REVIEW OF THE VKI DOCTORAL RESEARCH

2013 - 2014



von Karman Institute for Fluid Dynamics

Covert art : *Front cover: Fluorescent PIV technique applied on a flow experiencing cavitation in a safety relief valve. Both liquid and vapor phases are separated by different colors*
Back cover: Averaged velocity field of a flow experiencing cavitation in a safety relief valve
©2014 by the von Karman Institute for Fluid Dynamics
Waterloosesteenweg 72, B-1640 Sint-Genesius-Rode
To order: https://www.vki.ac.be

ISBN 978-2-87516-079-9

D/2014/0238/646, T. Magin, Editor-in-Chief

The contents of this book are the property of the von Karman Institute for Fluid Dynamics. No part of this book may be reproduced or distributed in any form of by any means, or stored in a database or retrieval system, without the prior written permission from the Publisher.

PREFACE

The fifth symposium on the doctoral research of the von Karman Institute for Fluid Dynamics took place during the period March 10 to 12, 2014. The doctoral students have presented the progress of their research work carried out in the three departments: Aeronautics and Aerospace, Environmental and Applied Fluid Dynamics, Turbomachinery and Propulsion. The first year students have presented a poster on their research plans and some preliminary results, while the most advanced students have proposed a presentation followed by a session of questions.

This event was attended by the faculty of the von Karman Institute as well as by colleagues from universities and industrial partners. The Symposium was open to external attendees free of charge. In addition to the presentations of the PhD candidates, we had the pleasure to welcome three prominent keynote lecturers who have opened each day the Symposium:

- Richard Schwane, ESA ESTEC, The Netherlands, *"Multi-disciplinary flow investigations at the European Space Agency,"*
- Gérard Bois, Laboratoire de Mécanique de Lilles 3, France, *"Some research aspects on hydraulic rotating pumps,"*
- Mario Ricchiuto, INRIA Bordeaux, France, *"Upwind Residual discretizations for depth averaged wave propagation."*

This year, the best presentation award has been attributed to Jorge Pinho for his research on "*Experimental Study and Modeling of Two-phase Flow cavitation through Complex Valves*." We would like to congratulate him on this achievement. The illustrated cover art of these proceedings is based on his research results.

This proceedings volume contains 38 papers which are divided into the following topics: "*Multiphase Flows*," "*Uncertainty Quantification*," "*Aero-Thermal Investigations in Turbomachinery*," "*Optimization in Turbomachinery*," "*Noise and Aeroacoustics*," "*Numerical Approach for Hypersonic and Plasma Flows*," "*Development of Advanced CFD*," "*Ablation*," "*Ground and Flight Experiments*," "*Numerical Modeling for Aerothermodynamics.*"

We would like to emphasize that this publication serves as a tool for communication and aims to enhance exchange between the doctoral candidates, the faculty and external attendees. The annual publication of their results in proceedings is of crucial importance to the VKI research providing a thorough review of the different activities within the three departments.

As such, the doctoral candidate students play a key role in strengthening the expertise in experimental research, computational methods, and physical modelling. In addition to basic research, works carried out at the von Karman Institute often leads to implementation of real life industrial applications critical to the fluid dynamics community.

We would like to thank Dr. Patrick Rambaud for having initiated this symposium and made it such a successful event.

Clara Garcia Sánchez Jérôme Sans Phd Representatives and Symposium co-Chairs	Thierry Magin Mario Rosaria Vetrano Professors Symposium Chairs	Jean Muylaert VKI Director

The contribution of all VKI members who helped with this event is deeply acknowledged in particular the faculty, library and printing office staff.

TABLE OF CONTENTS

Editorial notes i

Table of contents iii

Multiphase Flows

Nicolas De Cock (first year doctoral summary) 3
Splash plate nozzle design optimization

Sara Gonzalez Ruiz (first year doctoral summary) 5
Development of a remote sensing technique for airborne droplets and particles using the glory and speckle pattern

Imre Horváth 7
Understanding modelling and applying: light extinction by complex geometries

Bart Janssens 17
The finite element method and the equilibrium Eulerian method for disperse two-phase flow

Miguel Alfonso Mendez (first year doctoral summary) 31
Dynamics of gas jet impingement on vertical falling liquid films

Jorge Pinho 33
Cavitation in valves: modeling and experiments

Alessia Simonini 45
Sloshing dynamics in partially filled cylinder subjected to horizontal sinusoidal excitations

Chiara Spaccapaniccia 55
Experimental study of natural convective internal flows

Uncertainty Quantification

Clara García Sánchez 69
Quantifying inflow uncertainties for CFD simulations of dispersion in the atmospheric boundary layer

Gennaro Serino 79
Characterization of boundary layer perturbations via linear stability analysis

Aero-Thermal Investigations in Turbomachinery

Francesco Baldani 89
Heat transfer in high subsonic velocity environments behind the fan of a gas turbine

Giulia Dell'Era (first year doctoral summary) 103
Experimental and numerical investigation of the three dimensional unsteady flow field in a high speed axial compressor

Fabrizio Fontaneto 105
Detail aero-thermal characterization of cooled high pressure turbine components in view of numerical codes calibration and validation

Jérôme Sans 107
The effect of solidity on compressor performance and stability

Sebastian Scholl 121
Large eddy simulation and conjugate heat transfer in a rib-roughened cooling channel

Roberto Tomassini (first year doctoral summary) 131
Blade tip timing and blade tip clearance measurement system based on magnetoresistive sensors

Optimization in Turbomachinery

Julien Clinckemaillie (first year doctoral summary) 135
Analysis and consequences of the separation / transition mechanism of the flow on a modern low pressure gas turbine airfoil

Noise and Aeroacoustics

Filip Baillien 139
Development of a high fidelity acoustic simulation platform for detached flows

Gabriele Grasso (first year doctoral summary) 147
Tonal and broadband fan noise production and propagation

Daniel Guariglia (first year doctoral summary) 149
Shock-cells noise investigation on a subsonic/supersonic coaxial jet

Ugur Karban 153
Stochastic modeling of installation effects in environmental control systems

Numerical Approach for Hypersonic and Plasma Flows

Alejandro Alvarez Laguna (first year doctoral summary) 165
Multi-fluid modeling of magnetic reconnection in astrophysical and laboratory plasmas

Aurélie Bellemans (first year doctoral summary) 171
SPARK: simplified plasma models based on reduced kinetics

Koen Groot (first year doctoral summary) 173
Non-linear extensions of global flow stability theory

Development of Advanced CFD and Optimization

Christopher Chahine 177
Robust multidisciplinary optimization of composite fan blades

Mohamed Hassanine Aissa 185
Efficient high performance computing techniques for multi-disciplinary optimisation

Stefano Vagnoli 191
Numerical Investigation of inlet distortion on the stall inception of a radial compressor

Martin Vymazal 203
Residual distribution schemes with variable distribution coefficients

Ablation

Bernd Helber 213
Recession and boundary layer characterization of carbon-phenolic ablation in plasma flows

Pierre-Louis Schrooyen 225
Development of a numerical simulation tool for the aerothermal flow through an ablative thermal protection system for atmospheric entry

James B. Scoggins 235
An extension of the Gibbs function continuation method for linearly constrained multiphase equilibria

Ground and Flight Experiments

Lamberto Dell'Elce 245
Uncertainty quantification of the orbital lifetime of a LEO spacecraft

Guillaume Grossir 257
Natural boundary layer transition on a 7 degree half-angle cone at large hypersonic Mach numbers

Işil Şakraker 269
In-flight experiment design and ground testing for a re-entry cubesat

Bart Van Hove 283
Post flight reconstruction using conventional and novel instrumentation

Numerical Modeling for Aerothermodynamics

Jesús Garicano Mena 297
On the heat flux prediction capabilities of residual distribution methods applied to hypersonic flows

Erik Torres 311
Physico-chemical models for rarefied gas-kinetic simulations with application to atmospheric entry flows

Alan Viladegut 327
Assessment of gas-surface interaction modeling for lifting body re-entry flight design

Who's who 335

MULTIPHASE FLOWS

Splash Plate Nozzle Design Optimization

Nicolas De Cock

PhD candidate, Environmental and Applied Fluid Dynamics Department, von Karman Institute for Fluid Dynamics, Belgium, Nicolas.DeCock@vki.ac.be

Supervisor: Maria Rosaria Vetrano

Associate professor, Environmental and Applied Fluid Dynamics Department, von Karman Institute for Fluid Dynamics, Belgium, vetrano@vki.ac.be

University Supervisor: Frédéric Lebeau

Associate professor, Département d'Agriculture de Précision, Gembloux Agro-Bio Tech, Université de Liège, Belgium, F.Lebeau@ulg.ac.be

Nowadays, pesticides use is necessary to satisfy the growing demand for agricultural products. During field treatment a key parameter is the droplets sizes. Each kind of treatment has a droplet size which maximizes the spray application efficiency. However agricultural sprays have wide droplet size distribution because of their break up mode. This results in non-optimal application and therefore losses of product into the environment.

This statement brings the goal of this project which is to design a splash plate nozzle in order to produce a narrow drop size distribution and therefore increase the spray application efficiency. The three parameters illustrated on the Figure 1 are the followings: the shape of the orifice, the shape of the plate (angle, curvature and length), and surface structure (canals). The effect of surface tension which is the principal changing fluid characteristic will be also studied.

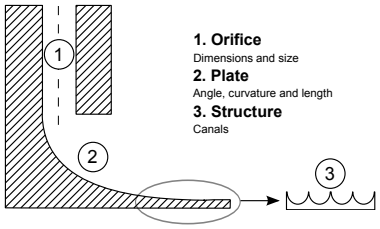

Figure 1: Geometrical parameters of a splash plate nozzle

Numerical simulations of the two-phase flow on a splash plate atomizer have already been realized by Fard et al. (2003). However, the high viscosity of the simulated liquid, black liquor, allow them to consider a laminar flow which is not valid for this agricultural case. Therefore, one key component of this work will be to take in account the turbulence.

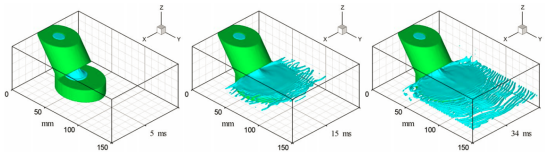

Figure 2: Numerical simulations of a laminar two phase flow on a splash plate atomizer (Fard et al.).

The first part of this project will be dedicated to a literature study in order to determine the aim in term of speed and diameter of the droplets which maximize the spray efficiency. Then, a test case will be study experimentally and numerically in order to validate the numerical simulations and select the proper numerical parameters for the further simulations. The numerical simulation will be performed with OpenFoam using a Volume of Fluid (InterFoam) solver. The experimental measurement will be realized by optical techniques as light absorption technique, high speed imaging in order to retrieve the thickness and the velocity of the liquid sheet on the plate respectively. The third step of this work will be dedicated to the optimization of the geometrical parameters numerically. Finally, the optimized geometry will be realized by rapid prototyping and assessed experimentally in order to validate the final simulations and also assess agronomical quality of the spray generated by the nozzle (drop size distribution and drift potential).

Keywords: agricultural nozzle, drop size distribution, multiphase flow.

Development of a Remote Sensing Technique for Airborne Droplets and Particles using the Glory and Speckle Pattern

Sara González Ruiz

Environmental and Applied Fluid Dynamics Department, von Karman Institute for Fluid Dynamics, Belgium, sara.gonzalez.ruiz@vki.ac.be

Supervisor: Jeroen van Beeck

Professor, Environmental and Applied Fluid Dynamics Department, von Karman Institute for Fluid Dynamics, Belgium, vanbeeck@vki.ac.be

University Supervisor: Steve Vanlanduit

Professor, Mechanical Engineering Department, Vrij Universiteit Brussel, Belgium, steve.vanlanduit@vub.ac.be

Since 1990, more than one hundred engine power-losses have occurred, on both commuter and large transport airplanes, due to the presence of ice crystals in convective weather. In some cases, in order to avoid these hazardous conditions, pilots have been using a visual inspection of what is known as the glory, an optical phenomenon produced in the atmosphere when the sunlight is backscattered by the water droplets contained in the clouds. However, a more reliable particle characterization technique is needed. Optical techniques are the most suitable, due to their non intrusivity, but challenges arise due to the presence of irregular particles in the flow, and to the compact characteristics imposed to the experimental apparatus.

Based on these observations, the final goal of this PhD project is to use backscattered laser light to develop a reliable measurement technique for particle characterization. This technique will detect the presence of irregular particles in the flow, and will measure particle size for both spherical and irregular particles in the size range from microns to millimeters. The main advantage of this technique is related to the position of the emitting and receiving optical elements, which are located at the same angle of observation, making the experimental apparatus extremely compact and useful in applications where only one optical window is available.

The PhD research concerns the study of the interference patterns produced by the backscattered laser light, in order to relate their angular frequency to the particle size, for both spherical and irregular particles. These interference patterns depend on several parameters, such as the particle size and morphology, the refractive index of the particle and surrounding medium, etc.

When the particle scattering the light is an homogeneous sphere, the interference pattern consists in concentric rings. In this case, the scattered light is mathematically described by the Lorenz-Mie theory. This theory will be used to perform numerical simulations, while a simpler model, based on a geometrical optics approach, will be developed in order to retrieve the particle size from the backscattered light.

On the contrary, when the particle scattering the light is irregular, the intensity of the interference pattern has a random granular distribution, called speckle pattern. The Lorenz-Mie theory can not be applied in this case, but the geometrical optics approach can still be used to develop a model based on the glare points, which are bright spots appearing in the surface of a particle when it is illuminated by parallel light.

In both cases, numerical simulations will be coupled with experimental campaigns, in order to validate the models.

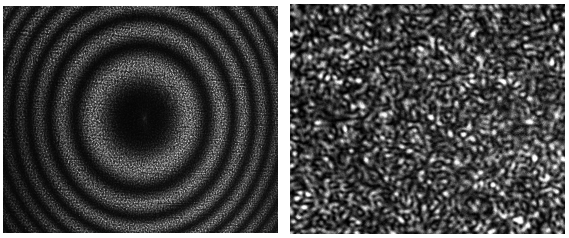

(a) glory (b) speckle pattern

Keywords: laser, backscattering, particle sizing, glory, speckle pattern.

Understanding Modelling and Applying: Light Extinction by Complex Geometries

Imre T. Horváth

Environmental and Applied Fluid Dynamics Department, von Karman Institute for Fluid Dynamics, Belgium, imre.horvath@vki.ac.be

Supervisor: Maria R. Vetrano

Assistant Professor, Environmental and Applied Fluid Dynamics Department, von Karman Institute for Fluid Dynamics, Belgium, vetrano@vki.ac.be.

University Supervisor: Pierre Colinet

FNRS Senior Research Associate, Transfers, Interfaces and Processes Department (TIPs), ULB, pcolinet@ulb.ac.be.

Abstract

The ultimate goal of the present paper is to examine two advanced applications of the Light Extinction Spectroscopy (LES) technique: characterization of particle aggregates and characterization of particles on a liquid-gas interface. The beginning of the paper demonstrates the underlying phenomenon behind the Light Extinction Spectroscopy technique by providing intuitive insight into the mechanism of scattering and extinction of light by particles. Afterwards a short summary to common modeling approaches is given, which allow the computation of light extinction by advanced geometries. Based on simulation results, the paper concludes the potential applicability of the LES technique for the characterization of particle aggregates composed of monodisperse spheres.

Keywords: light extinction spectroscopy, light scattering, particle aggregate, plane interface

1. Introduction

The characterization of sub-micron sized particles became an important subject of research during the past decades. Such particles are used at numerous fields of science and industry e.g. food and pharmaceutical industry, material science, biotechnology. The online and non-intrusive characterization of particles of such small size still represents a challenge. One possibility is to obtain quantitative information from measurements of light scattering by the investigated particles. The most flexible method of such kind is the Light Extinction Spectroscopy (LES) technique. Its operation relies on the measurement of the spectral extinction of a broadband (UV-NIR) light beam traveling through a medium containing the particles of interest. Fundamentally, the particle properties can be retrieved from the inversion of a suitable light extinction model. Contrary to the simplicity of its experimental apparatus, the processing of the experimental data requires the thorough understanding and modeling of the underlying phenomenon: light extinction by particles. The final step of data processing is the solution of an inverse light scattering problem, which is performed by a regularized inverse algorithm [1].

The LES technique has been established by the authors for the characterization of simple particle systems i.e. ensembles of single, spherical particles. Droplet clouds as well as solid particle aerosols have been successfully characterized.

Figure 1 shows the result of measuring a solid particle aerosol composed of Potassium Chloride (KCl) particles. The measurement has been validated by Scanning Mobility Particle Sizing measurements. The reference particle size distribution function (PSD) is also shown. Figure 1 displays satisfactory agreement both in terms of PSD function and total particle concentration.

Polystyrene particles of calibrated size have also been characterized. The Polysciences Inc. Polybeads particles were used with nominal diameters as follows: 356 nm, 535 nm, 1053 nm. Their PSD function

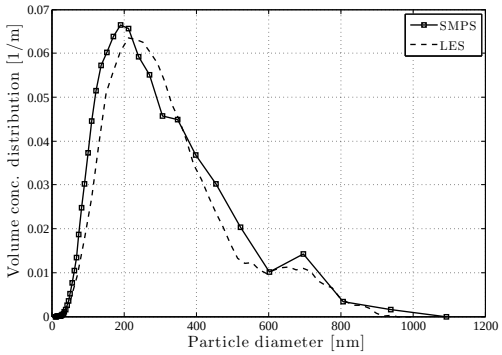

Figure 1: Volumetric particle size distribution function of a solid particle aerosol of KCl. The result is compared to a Scanning Mobility Particle Sizing (SMPS) measurement.

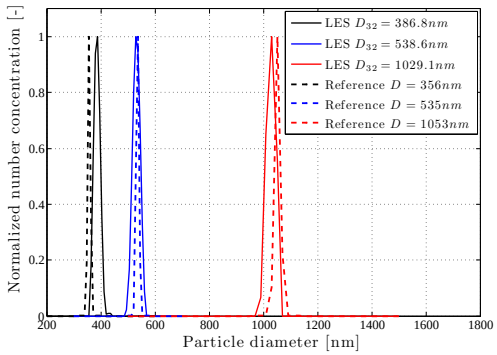

Figure 2: Measured PSD functions of Polystyrene standard particles as compared to the nominal PSD.

is monodisperse with standard deviation 0.01. The latter particles are dispersed in water thus they had to be aerosolized before the measurements. The measurement results and their comparison to the nominal PSD functions is shown in Figure 2. The LES measurements have successfully retrieved the highly monodisperse PSD functions. The variation of the mean diameter remained within 10%. The two above measurements show that the LES technique is an accurate particle sizing method.

The same Polystyrene particles can also be characterized when they are dispersed in water. It was found that the refractive index contrast between the particles and the surrounding medium has an important effect on the LES measurements: in case of low contrast such as water - polystyrene, the measurement range shifts towards larger particle size. The measurement result of the 1053 nm particles in water is shown on Figure 3. Good agreement was found with respect to the nominal PSD function.

The LES technique allows equally the characterization of aerosols composed of liquid drops. Figure 4 displays the result of investigating the coagulation of DEHS oil droplets. PSD functions were measured at the start of the coagulation experiment and were compared to those measured 10 and 20 minutes later. The LES measurements reproduce the expected evolution of the drop size distribution.

The particle size range of the LES technique strongly depends on the interval of wavelengths used for the extinction experiment. Using a Near Infrared (NIR) light source and a corresponding spectrometer allows to shift the measurable particle size range into the micrometric region. Figure 5 shows the result of measuring a water aerosol produced by a supersonic nozzle atomizer.

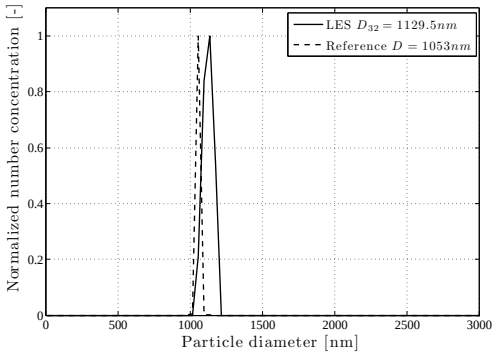

Figure 3: Measured PSD function of Polystyrene standard particles dispersed in water as compared to the nominal PSD.

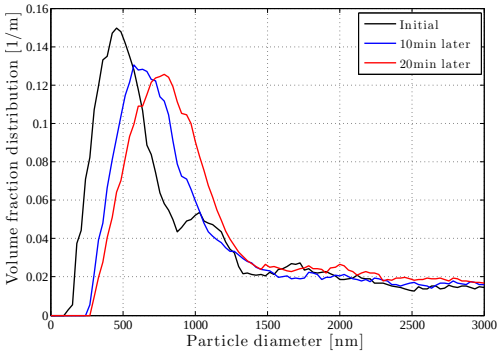

Figure 4: Evolution of the PSD function of a DEHS oil droplet aerosol due to particle coagulation. The LES measurements were taken at the start of the experiment, 10 minutes later and 20 minutes later.

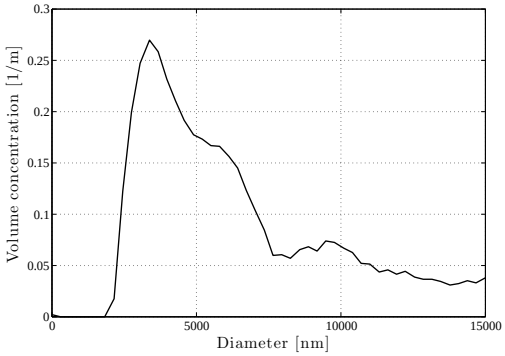

Figure 5: PSD function of a water aerosol obtained using a Near Infrared light source and spectrometer.

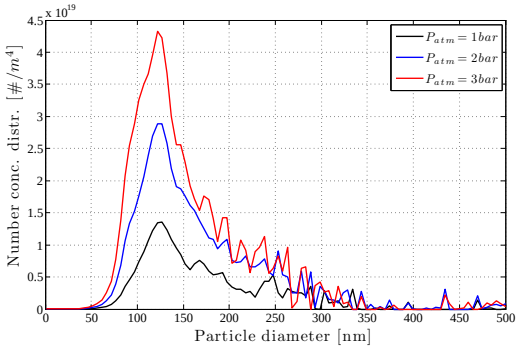

Figure 6: PSD functions of a SiC (Silicon Carbide) aerosol. The atomization pressure was varied between 1 and 3 bars.

When a UV-NIR light source and corresponding spectrometer are used, the measurable particle size interval well-penetrates the nanometric range. Figure 6 shows the PSD function of a SiC (Silicon Carbide) solid particle aerosol, which has been obtained by aerosolizing a precursor water dispersion of SiC powder. The nominal mean diameter of the tested sample was 76nm while the LES technique retrieved 110nm. This discrepency is a subject of further investigation.

The above measurements illustrate the wide range of applicability of the LES technique as an accurate particle sizing method: droplet aerosols, solid particles dispersed in gas or liquid with particle size ranging from 30nm up to 10 microns. In the other hand the simple experimental setup and measurement procedure allow the online and real-time monitoring of the above particle systems.

One important limitation of the LES technique arises when the measured particles are not independent scatterers or their shape cannot be approximated as spherical. In these situations the Mie theory for modelling light extinction loses its validity and the recovered particle properties become erroneous. The following sections attempt to understand the effect of these non-idealities on particle characterization experiments. Section 2 presents the physical explanation of light extinction. Section 3 introduces the most relevant approaches to model light extinction by two different types of geometries: aggregates of spheres and particles on- or near a plane interface. Section 4 applies the introduced modelling approaches and presents some simulation results. The paper draws preliminary conclusions concerning the influence of the scattering geometry on particle sizing experiments with the LES technique.

2. Light extinction by particles

The fundamental phenomenon of light extinction is often encountered in everyday life. Every object exposed to light casts a well-defined shadow. The approach of geometrical optics is usually used to interpret this phenomenon: the light rays intercepted by the surface of the object are reflected, refracted or absorbed, prohibiting them from illuminating the area just behind the object. It is expected therefore, that the energy removed from the incident direction by the object is proportional to the geometrical cross-section of the object C_{geo}. This explanation first seemed to fail when astronomical observations were made about meteorites passing in front of a distant light source e.g. a star. The surprising result was found, that the energy removed by the object exposed to light is proportional to exactly two times its geometrical cross-section. The latter is well-known as the *extinction paradox* and its explanation will be given in Section 2.2. The extinction paradox has been observed for particles large enough compared to the illuminating wavelength but also for small, highly refractive particles.

2.1. Interaction of light and matter

First, the fundamental interaction between light (an electromagnetic wave) and matter should be understood. The explanation of [2] is cited. "Consider an arbitrary particle, which we conceptually subdivide into small regions. An applied oscillating field (e.g., an incident electromagnetic wave) induces a dipole moment in each region. These dipoles oscillate at the frequency of the applied field and therefore scatter secondary radiation in all directions. In a particu-

lar direction (i.e., at a distant point P), the total scattered field is obtained by superposing the scattered wavelets, where due account is taken of their phase differences: scattering by the dipoles is coherent." The cited explanation shows, that upon illuminating an object, an internal electromagnetic field is induced, which strongly depends on the properties of the particle: size, shape, material (index of refraction). This concept is essential for understanding the explanation of the extinction paradox.

2.2. The extinction paradox

Several phenomenological explanations rose during the past 60 years, which seemed to resolve the extinction paradox. The most known among all is the explanation given by van de Hulst [3]. The latter relies on accounting to diffraction (small angular deviation of light rays) on the borderline of the shadow, which contributes to additional removal of energy. Despite some unexplained aspects, this concept endured through the past decades. It was only in 2011 when the paradox was finally explained by [4]. The author gave the complete explanation of the phenomenon while providing important insight into the mechanism of light extinction and scattering by objects. Central to his explanation is the Ewald-Oseen extinction theorem [5]: when an object is exposed to an incident electromagnetic wave, surface electromagnetic fields are formed on its boundaries. These fields are the sources of the internal wave, which cancels the incident wave everywhere within the object boundaries by means of destructive interference. In case of large or highly refractive small particles, these sources are located uniquely on the illuminated side of the particle. The very same sources are responsible for the scattered wave exterior to the particle including also its shadow. It is due to this *dual role*, that the latter sources have twice the expected magnitude.

2.3. Summary

The presented explanation of the extinction paradox puts the mechanism of scattering and extinction in a new light and it emphasizes the wave nature of extinction. Summarizing: scattering of light is entirely caused by the Ewald-Oseen cancellation wave, which forms in the interior of the particle. The latter wave propagates to the exterior of the particle and its interaction with the incident wave forms the scattered wave. Extinction of light can be explained as the destructive interference between the internal wave and the incident wave inside and outside the particle.

The amplitude of the electric field produced inside and outside an illuminated spherical water droplet can be examined on Fig. 7. The size of the droplet is close to that of the illuminating wavelength, therefore no distinct shadow is observed behind it. The cancellation of the incident field inside the droplet is well observable, such as some interference pattern outside its boundaries.

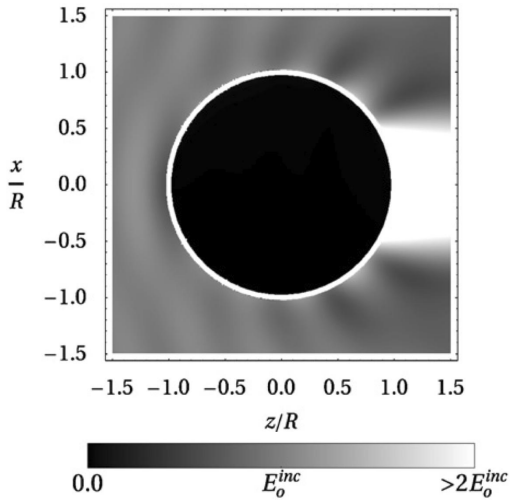

Figure 7: Superposition of the incident electric field and the cancellation wave inside and around a spherical water droplet with size close to that of the illuminating wavelength, from [4]. The refracted wave interior to the drop is not shown thus the internal field is zero.

3. Modelling of light extinction by particles

3.1. Single sphere: Mie's solution

The simplest case of electromagnetic scattering problems has been first solved by Gustav Mie in 1905 [3]. The case of a single sphere is one of the few cases, which can be solved in an analytic manner. First, general spherical vector wave functions are needed, which satisfy the Maxwell equations. Such functions are represented as infinite series, with appropriately chosen coefficients. The incident and the internal fields are expanded in terms of regular spherical vector wave functions, while the scattered field is expanded in radiating spherical vector wave functions. The coefficients of the latter expansions should be determined from the boundary conditions, which apply to the electromagnetic fields on the boundary of two

different media. Two of these standard boundary conditions are sufficient: the tangential components of the electric and magnetic fields are continuous across the boundary.

Solving the above boundary value problem provides the expansion coefficients (a_n and b_n) of the scattered electromagnetic field. The result can be numerically evaluated by truncating the infinite series expansion to a finite value.

3.2. Aggregate of spheres

Several different methods can be used for solving the scattering problem for an aggregate of spherical particles. Unfortunately, no analytical solution exists for the present case. The difficulty is caused by the multiple scattering interactions occurring between the constituent spheres. The incident field of one sphere is different from that of the aggregate: it is the superposition of the incident field and the scattered fields of all other member spheres.

One possibility for solving the present problem is to apply the Generalized Multi-particle Mie solution (GMM) [6]. The latter formulation allows the numerical evaluation of light scattering characteristics of aggregates of spheres in a fixed orientation. Ensemble average over individual orientations can also be computed.

First, the incident wave (plane wave propagating in the positive z-direction) is expanded in terms of Vector Spherical Wave Functions (VSWF) in the aggregate centred coordinate system:

$$\mathbf{E}_{inc} = -\sum_{n=0}^{N}\sum_{m=-n}^{n} iE_{mn}\Big[a_{mn}\mathbf{N}_{mn}^{(1)}(\rho,\theta,\phi) + b_{mn}\mathbf{M}_{mn}^{(1)}(\rho,\theta,\phi)\Big] \tag{1}$$

In the above equation $i = \sqrt{-1}$, E_{mn} is a normalization factor, a_{mn} and b_{mn} are the expansion coefficients of the incident field in the aggregate coordinate system, $\mathbf{N}_{mn}^{(1)}$ and $\mathbf{M}_{mn}^{(1)}$ are the regular vector spherical wave functions, with the spherical Bessel function of the first kind as their generating function. In order to apply the incident field to the jth individual constituent sphere, the incident wave expansion coefficients should be transformed into the coordinate systems of the individual spheres (X^j, Y^j, Z^j). The expansion of the incident wave in the jth sphere centered coordinate system can be obtained by adding a phase term to the expansion coefficients valid in the aggregate coordinate system. Denoting the wavenumber with k, the latter reads:

$$a_{mn}^j = e^{ikZ^j}a_{mn} \quad \text{and} \quad b_{mn}^j = e^{ikZ^j}b_{mn} \tag{2}$$

Similarly to the incident field, the individual scattered field of the lth component sphere can be expanded in terms of VSWFs as well. In the following expansion, radiating VSWFs are used, which are denoted by the superscript (3). Their generating function is the spherical Hankel function of the first kind.

$$\mathbf{E}_{sca}^l = \sum_{n=1}^{N^l}\sum_{m=-n}^{n} iE_{mn}\Big[p_{mn}^l\mathbf{N}_{mn}^{(3)}\left(\rho^l,\theta^l,\phi^l\right) + q_{mn}^l\mathbf{M}_{mn}^{(3)}\left(\rho^l,\theta^l,\phi^l\right)\Big] \tag{3}$$

where p_{mn}^l and q_{mn}^l denote the individual scattered wave expansion coefficients of the lth sphere. If $\bar{p}_n^l$ and $\bar{q}_n^l$ represent the Lorenz-Mie scattering coefficients of the lth isolated sphere and A_{mn}^l and B_{mn}^l are the expansion coefficients of the total field incident upon the *lth* sphere, one obtains the partial scattered field coefficients in the form:

$$p_{mn}^l = \bar{p}_n^l A_{mn}^l \quad \text{and} \quad q_{mn}^l = \bar{q}_n^l B_{mn}^l \tag{4}$$

with

$$A_{mn}^l = a_{mn}^l - \sum_{j\neq l}^{(1,L)}\sum_{\nu=1}^{N^j}\sum_{\mu=-\nu}^{\nu}\left(P_{mn\mu\nu}^{jl}p_{\mu\nu}^j + Q_{mn\mu\nu}^{jl}q_{\mu\nu}^j\right) \tag{5}$$

and

$$B_{mn}^l = b_{mn}^l - \sum_{j\neq l}^{(1,L)}\sum_{\nu=1}^{N^j}\sum_{\mu=-\nu}^{\nu}\left(Q_{mn\mu\nu}^{jl}p_{\mu\nu}^j + P_{mn\mu\nu}^{jl}q_{\mu\nu}^j\right) \tag{6}$$

In Eq. 5 and Eq. 6 $P_{mn\mu\nu}^{jl}$ and $Q_{mn\mu\nu}^{jl}$ are vector translation coefficients, which characterize the transformation of the scattered field of the jth particle into the incident field of the lth particle. The partial scattered fields p_{mn}^l and q_{mn}^l can be obtained by solving the large dimensional linear system consisting of

$$a_{mn}^l = \frac{p_{mn}^l}{\bar{p}_n^l} + \sum_{j\neq l}^{(1,L)}\sum_{\nu=1}^{N^j}\sum_{\mu=-\nu}^{\nu}\left(P_{mn\mu\nu}^{jl}p_{\mu\nu}^j + Q_{mn\mu\nu}^{jl}q_{\mu\nu}^j\right) \tag{7}$$

$$b_{mn}^l = \frac{q_{mn}^l}{\bar{q}_n^l} + \sum_{j\neq l}^{(1,L)}\sum_{\nu=1}^{N^j}\sum_{\mu=-\nu}^{\nu}\left(Q_{mn\mu\nu}^{jl}p_{\mu\nu}^j + P_{mn\mu\nu}^{jl}q_{\mu\nu}^j\right) \tag{8}$$

Once the partial scattered field coefficients are obtained in the respective sphere-centred coordinate systems, the total scattered field of the aggregate is sought

in the form:

$$\mathbf{E}_{sca} = \sum_{n=1}^{N^l} \sum_{m=-n}^{n} iE_{mn} \Big[p_{mn} \mathbf{N}_{mn}^{(3)}(\rho, \theta, \phi) + q_{mn} \mathbf{M}_{mn}^{(3)}(\rho, \theta, \phi) \Big] \tag{9}$$

Fortunately, due to the existence of an asymptotic form in the far-field for translating VSWFs between displaced coordinate systems, the total scattered field coefficients can be obtained without invoking any general addition theorem:

$$p_{mn} = \sum_{l=1}^{L} e^{-ik\Delta^l} p_{mn}^l \quad , \quad q_{mn} = \sum_{l=1}^{L} e^{-ik\Delta^l} q_{mn}^l \tag{10}$$

with $\Delta^l = X^l \sin\theta\cos\phi + Y^l \sin\theta\sin\phi + Z^l \cos\theta$. When only the computation of the extinction cross-section C_{ext} is needed, the last step can be omitted, since:

$$C_{ext} = \sum_{l=1}^{L} C_{ext}^l = \frac{4\pi}{k^2} \sum_{l=1}^{L} \sum_{n=1}^{N^l} \sum_{m=-n}^{n} \mathrm{Re}\left(a_{mn}^{l*} p_{mn}^l + b_{mn}^{l*} q_{mn}^l \right) \tag{11}$$

therefore the extinction cross-section of the aggregate can be obtained from the partial scattered field coefficients.

3.3. Particles on or near a plane interface

A solution for the light scattering problem by particles on or near a plane interface has been first proposed by [7]. It has also been formulated in the framework of the Null Field Method (NFM) [8]. The latter is publicly available as part of the program package NFM-DS r1.1, which is used in the present study. In the following the formulation in the NFM framework is presented.

3.3.1. Null-Field Method

The formulation implemented by the NFM-DS program is known as the Null-Field Method or equivalently the Extended Boundary Conditions method. This modelling approach shows great analogy with the physics of light extinction introduced in 2.2. The general Null-Field equation (equivalent to Ewald-Oseen extinction theorem) states, that the incident wave is extinguished internal to the particle by fields radiated from the particle surface. This principle can be used to derive integral equations for the surface fields. The scattered field outside the particle is produced by the same surface fields and can be evaluated using Huygens's principle [9].

Additional to Eq. 1 and Eq. 3 the internal field of the particle is also expanded in regular VSWFs, with expansion coefficients c_{mn} and d_{mn}. Based on the general null-field equation, the latter expansion coefficients can be obtained. Due to the VSWF expansions and the linearity of the Maxwell equations, the internal and incident field coefficients can be related by a linear operator [10]:

$$\begin{bmatrix} \mathbf{a} \\ \mathbf{b} \end{bmatrix} = \begin{bmatrix} \mathbf{Q}^{11} & \mathbf{Q}^{12} \\ \mathbf{Q}^{21} & \mathbf{Q}^{22} \end{bmatrix} \begin{bmatrix} \mathbf{c} \\ \mathbf{d} \end{bmatrix} \tag{12}$$

where $\mathbf{Q}^{ij}$ are the mentioned surface integrals, which are evaluated along the particle surface. The scattered field expansion coefficients are than obtained be evaluating similar surface integrals $\mathbf{RgQ}^{ij}$:

$$\begin{bmatrix} \mathbf{p} \\ \mathbf{q} \end{bmatrix} = \begin{bmatrix} \mathbf{RgQ}^{11} & \mathbf{RgQ}^{12} \\ \mathbf{RgQ}^{21} & \mathbf{RgQ}^{22} \end{bmatrix} \begin{bmatrix} \mathbf{c} \\ \mathbf{d} \end{bmatrix} \tag{13}$$

The transition matrix $\mathbf{T} = \mathbf{RgQ} \cdot \mathbf{Q}^{-1}$ relates the incident and scattered field coefficients directly:

$$\begin{bmatrix} \mathbf{p} \\ \mathbf{q} \end{bmatrix} = \begin{bmatrix} \mathbf{T}^{11} & \mathbf{T}^{12} \\ \mathbf{T}^{21} & \mathbf{T}^{22} \end{bmatrix} \begin{bmatrix} \mathbf{a} \\ \mathbf{b} \end{bmatrix} \tag{14}$$

The T-matrix does not depend on the incident field direction; therefore its use is very advantageous when particles in random orientations are simulated.

3.3.2. Modelling the interface

When a plane interface is present in the scattering geometry, the problem becomes more complicated by the reflection of both the incident and scattered fields from the interface. Two incident fields should be considered: the direct one and the one reflected from the surface. In addition, a field called interacting field also plays a role. The latter is the scattered field reflected back to the particle once again. The interacting field coefficients can be obtained using the reflection matrix $\mathbf{A}$:

$$\begin{bmatrix} \mathbf{p}^R \\ \mathbf{q}^R \end{bmatrix} = \mathbf{A} \begin{bmatrix} \mathbf{p} \\ \mathbf{q} \end{bmatrix} \tag{15}$$

The reflection matrix is computed using the integral representation of the radiating VSWFs. The computations also assume that the interacting radiation strikes the interface at normal incidence. Therefore the scattered field coefficients can be obtained using the particle T-matrix:

$$\begin{bmatrix} \mathbf{p} \\ \mathbf{q} \end{bmatrix} = \mathbf{T} \left(\begin{bmatrix} \mathbf{a} \\ \mathbf{b} \end{bmatrix} + \begin{bmatrix} \mathbf{p}^R \\ \mathbf{q}^R \end{bmatrix} \right) \tag{16}$$

Combining Eq. 15 and Eq. 16 gives

$$(\mathbf{I} - \mathbf{T} \cdot \mathbf{A}) \begin{bmatrix} \mathbf{p} \\ \mathbf{q} \end{bmatrix} = \mathbf{T} \begin{bmatrix} \mathbf{a} \\ \mathbf{b} \end{bmatrix} \tag{17}$$

The computation of the resulting extinction cross-section can be performed by the formula similar to Eq. 11 except that the total incident and scattered field coefficients should be used and the first summation should be omitted.

After the incident light hits the interface two different propagation directions exist: transmitted beam and reflected beam. Therefore two different extinction cross-sections can be defined: extinction of the transmitted beam and extinction of the reflected beam. The choice of the configuration should be in agreement with the experiments.

Since the NFM method does not allow to compute scattering by objects with intersecting domains (such as a particle intersecting the air-water interface), only such cases can be considered when the particle is completely above or below the interface. The latter is an important limitation and will prohibit the analysis of experimental data. Future work on this field will consist of analysing the dependency of the extinction spectrum on the particle-interface distance at both sides of the interface using the NFM.

4. Simulation results

The purpose of performing light extinction simulations of different geometries is to identify whether spectral light extinction is sensitive to the geometrical parameters of the scattering objects or not. If sensitivity is identified, the measurements performed on the complex geometries should be processed by taking the complex geometries into account. This case provides the theoretical possibility of retrieving the representative parameters of the scattering geometries e.g. number of particles in an aggregate or distance between the particle and an interface. If no sensitivity is found, the standard Mie solution could be used for all the cases without committing modelling errors.

4.1. Numerical model for particle aggregation

The light scattering simulations require the numerical generation of scattering geometries, which are likely to be found in experiments. A widely applied particle aggregation model is used, which is called the Filippov algorithm. The latter is implemented in the program Aggregate Workshop v1.0 [12]. The algorithm performs the random walk of particles, which

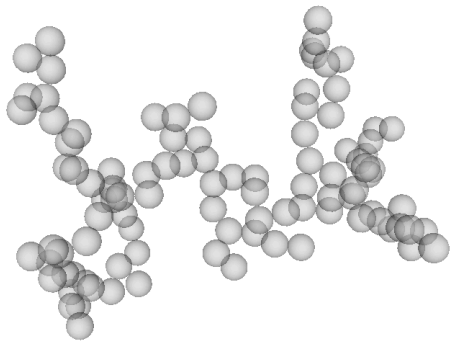

Figure 8: Aggregate of 100 spherical particles

are introduced to the computational domain one-by-one. Upon collision, the particles remain attached. A particle is accepted if after its attachment the prescribed fractal dimension is conserved. Such algorithms can be effectively applied for simulating realistic, three dimensional complex aggregates as shown on Fig. 8.

4.2. Light extinction spectra of aggregates of spheres

Fig 9 shows simulation results obtained with the GMM approach. The displayed quantity is the extinction efficiency factor Q_{ext}. The latter is a normalization of the extinction cross-section (C_{ext}) with the cross section area of a sphere with volume equivalent to that of the aggregate.

$$Q_{ext} = \frac{C_{ext}}{C^{v}_{geo}} \tag{18}$$

Therefore Q_{ext} should not depend on the volume of the aggregate.

Aggregates of spherical SiC particles were simulated with fractal dimension equal to 1,8. Each of the aggregates contain only spheres of equal size. The number of spheres within the aggregates was varied from 1 to 64.

Fig. 9a shows the extinction efficiency spectra of aggregates consisting of 25 nm diameter spheres. The obtained extinction efficiency spectra show variation both in magnitude and spectral features. The results obtained with larger sphere sizes (75 nm and 150 nm) conclude the same but display even stronger spectral variation.

The effect of the aggregate fractal dimension is shown on Figure 10, for aggregates composed of 16 spheres. Large fractal dimension results in a more

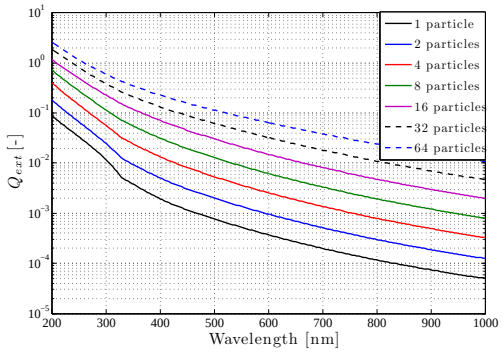

(a) D_0 = 25*nm*

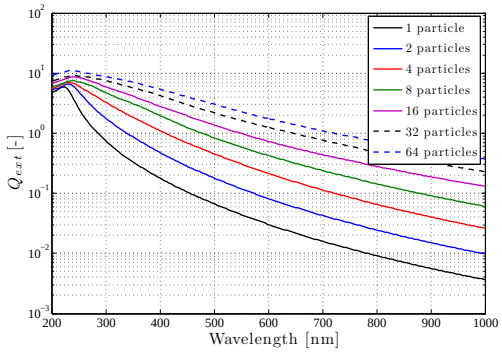

(b) D_0 = 75*nm*

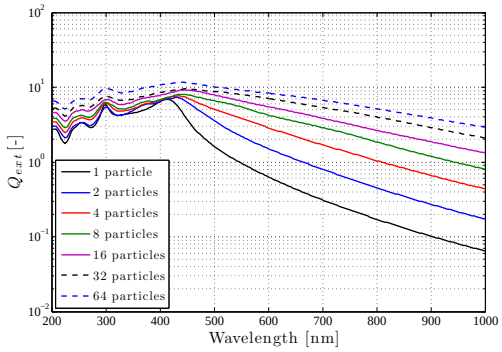

(c) D_0 = 150*nm*

Figure 9: Extinction efficiency spectra obtained for various sphere sizes. The material of the spheres is SiC [11].

compact structure, therefore stronger scattering interactions occur. It is observed that increasing the fractal dimension of the aggregate results in a similar spectral distortion to that caused by increasing the number of spheres. One important difference is that the variation of fractal dimension seems to conserve the spectral averaged extinction efficiency. At this point it is not clear, whether the effects of the number of spheres

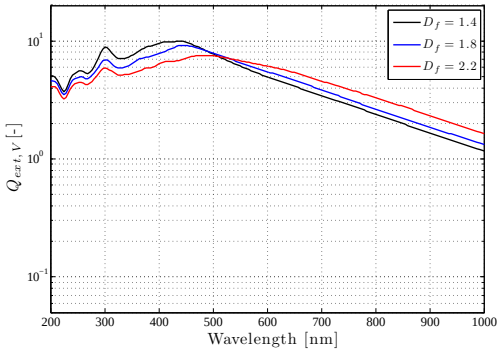

Figure 10: Extinction efficiency spectra obtained for various aggregate fractal dimensions. The aggregates consist of 16 150nm diameter SiC spheres.

and fractal dimension are distinguishable or not.

The presented figures suggest that the light extinction spectrum of an aggregate of mono-size spheres is dominated by the spectrum of the the individual component sphere. When more or stronger multiple scattering interactions occur, the latter spectrum is broadened and slightly red-shifted.

5. Conclusions

The present work intends to provide an intuitive understanding of the process of light extinction and its use for the determination of particle properties. A short summary of related simulation techniques is also given. The preliminary simulation results presented in the final section of the paper suggest, that the Light Extinction Spectroscopy (LES) technique can be used for the advanced determination of small particles: to retrieve morphology parameters of aggregates.

References

[1] I. T. Horvath, M. R. Vetrano, P. Colinet, Validation of the Multi Wavelength Light Extinction Technique on a submicron KCl aerosol by Scanning Mobility Particle Sizing measurements, Summary of VKI PhD Research 2012-2013.

[2] C. F. Bohren, D. R. Huffman, Absorption and scattering of light by small particles, Vol. 77, John Wiley & Sons Inc., 1983. doi:10.1119/1.3088878.

[3] H. van de Hulst, Light scattering by small particles, Dover Publications Inc., New York, 1957.

[4] M. Berg, C. Sorensen, a. Chakrabarti, A new explanation of the extinction paradox, Journal of Quantitative Spectroscopy and Radiative Transfer 112 (7) (2011) 1170–1181. doi:10.1016/j.jqsrt.2010.08.024.

[5] M. Born, E. Wolf, Principles of optics, 6th Edition, Pergamon Oxford (Ed.), 1986.

[6] Y.-l. Xu, B. A. S. Gustafson, An analytical solution to electromagnetic multisphere-scattering - the scattering formulation used in codes gmm01f.f and gmm01s.f, Tech. rep., University of Florida, Gainsville (2001).
[7] G. Videen, Light scattering from an irregular particle behind a plane interface, Optics communications 128 (1996) 81–90.
[8] T. Wriedt, A. Doicu, Light scattering from a particle on or near a surface, Optics communications 152 (1998) 376–384.
[9] A. Doicu, T. Wriedt, Y. Eremin, Light scattering by systems of particles, Springer-Verlag, Berlin, 2006.
[10] M. Mishchenko, L. Travis, D. Mackowski, T-matrix computations of light scattering by nonspherical particles: A review, Journal of Quantitative Spectroscopy and Radiative Transfer 55 (5) (1996) 535–575.
[11] A. M. Hofmeister, K. M. Pitman, A. F. Goncharov, A. K. Speck, Optical Constants of Silicon Carbide for Astrophysical Applications. Ii. Extending Optical Functions From Infrared To Ultraviolet Using Single-Crystal Absorption Spectra, The Astrophysical Journal 696 (2) (2009) 1502–1516. doi:10.1088/0004-637X/696/2/1502.
[12] K. Skorupski, A fast and accurate implementation of tunable algorithms used for generation of fractal-like aggregate models (Accepted 27 Feb 2014), Physica A: Statistical Mechanics and its Applications.

The Finite Element Method and the Equilibrium Eulerian Method for Disperse Two-Phase Flow

Bart Janssens

Department of Mechanical Engineering, Royal Military Academy, Belgium, bart.janssens@rma.ac.be

Promoter: Tony Arts

Professor, Head of Department, Turbomachinery and Propulsion Department, von Karman Institute for Fluid Dynamics, Belgium, arts@vki.ac.be.

Promoter: Walter Bosschaerts

Professor, Head of Department, Department of Mechanical Engineering, Royal Military Academy, Belgium, walter.bosschaerts@rma.ac.be

Promoter: Karim Limam

Professor, Laboratoire d'Étude des Phénomènes de Transfert et de l'Instantanéité, La Rochelle University, France , klimam01@univ-lr.fr

Abstract

We present our finite element solver for incompressible flow laden with a small volume fraction of fine particles. In the present paper, we provide details of the segregated semi-implicit scheme for the PSPG/SUPG/grad-div stabilized method for the fluid. The dispersed phase is modeled using the equilibrium Eulerian approach, where we extend existing work to apply a locally implicit method to an equation that is valid for both bubbles and dense solid particles. The code is validated using the Taylor-Green vortex flow.

Keywords: Multiphase flow, Disperse flow, coagulation, nanoparticles, Eulerian

Nomenclature

$\tilde{u}$	Value of unknown u interpolated by its associated shape functions
β	Density ratio parameter
Δt	Time step
η_k	Kolmogorov length scale
μ	Dynamic viscosity of the fluid
ν	Kinematic viscosity of the fluid
ν	Kinematic viscosity
Ω	The volume of the computational domain. When used with an index: the volume of a single element.
ω	Vorticity
ρ_f	Density of the fluid
ρ_p	Density of the particle
τ_{xx}	Stabilization coefficient. Index indicates type of stabilization.
τ	Generalized particle relaxation time
τ_k	Kolmogorov time scale
τ_p	Particle relaxation time
θ	Parameter for the theta-scheme
$\mathbf{a}$	Acceleration
$\mathbf{g}$	Acceleration associated with the body force
$\mathbf{u}$	Fluid velocity vector
$\mathbf{u}$	Velocity vector
$\mathbf{v}$	Particle velocity vector

$\mathbf{x}_e$	Element vector of unknowns
A	Stiffness matrix
c	Particle volume fraction
D_b	Diffusion coefficient due to Brownian motion
d_p	Particle diameter
h	Element length scale
N	Number of elements
N_u	Element shape function vector for the variable u
p	Kinematic pressure
T	Mass matrix
U_a	Horizontal Taylor-Green background velocity
V_a	Vertical Taylor-Green background velocity
V_s	Initial maximal Taylor-Green swirl velocity

1. Introduction

The purpose of the current work is to develop a model for particle-laden flow in the context of air pollution problems. Potential health risks are discussed in i.e. [1] and [2]. We seek to model the behavior of ultra fine particles, as well as inter-particle collision and coagulation.

In order to build a reusable and extensible code, much time was spent on the development of a generic framework for the development of finite element models. This resulted in the creation of a Domain Specific Embedded Language, which was presented at ICCAM 2012 in Gent. The system can be compared to FEniCS [3] and Life [4]. OpenFOAM also has a similar language to express finite volume problems [5]. We have previously used this system to implement the PSPG/-SUPG method for the fluid phase, solving a single coupled linear system each time step [6].

In the remainder of this paper, we first present the coupled SUPG/PSPG method. We then show how this formulation can be transformed into a segregated semi-implicit formulation that should be more scalable when small time steps are imposed based on physical considerations.

In the second part, the equilibrium Eulerian method is applied to obtain a finite element model for the dispersed phase. We extend previous work by accounting for both the locally-implicit terms [7] and for forces that are important in the case of bubbles.

In the final part of the paper, we validate the model using the Taylor-Green vortex flow, also comparing with results from [8].

2. Fluid model

We present an overview of the implicit SUPG method as detailed in [6]. This implicit method is then reformulated in a semi-implicit way in an attempt to improve scalability for large, unsteady 3D problems requiring small time steps.

2.1. Coupled formulation

The conservation equations for incompressible flow are:

$$\nabla \cdot \mathbf{u} = 0 \tag{1}$$

$$\frac{\partial \mathbf{u}}{\partial t} + (\mathbf{u} \cdot \nabla)\,\mathbf{u} + \frac{\mathbf{u}(\nabla \cdot \mathbf{u})}{2} + \nabla p - \nu \nabla^2 \mathbf{u} = \mathbf{0} \tag{2}$$

We use the skew symmetric formulation for the advection term in the momentum equation for improved conservation of energy [9]. To obtain the finite element formulation, we multiply the equations with a set of weighting functions, interpolate the unknowns between discrete nodes using shape functions and integrate over the domain. The weighting and shape functions are chosen to be identical, yielding a Galerkin formulation. The time derivative is approximated using the θ-method. This procedure yields a discrete system, with an unknown pressure and velocity at time level $n + 1$ to be computed at each node in the mesh. The global shape functions are non-zero only in a node and its surrounding elements. This means that the integrals can be evaluated as a sum of integrals over these elements. This global system can thus be written as the sum of N element contributions:

$$\sum_{e=1}^{N} \left(\frac{1}{\Delta t} T_e + \theta A_e \right) \left(\mathbf{x}_e^{n+1} - \mathbf{x}_e^n \right) = -A_e \mathbf{x}_e^n \tag{3}$$

The parameter θ controls the time stepping and should be set to 1 for a forward Euler method and 0.5 for the Crank-Nicolson scheme. The vector of unknowns at the element level is laid out by grouping the nodal values per unknown, i.e. for a 3D element with $m + 1$ nodes:

$$\mathbf{x}_e^n = [p_0^n \cdots p_m^n \, (u_0^n)_0 \cdots (u_0^n)_m \cdots (u_2^n)_m] \tag{4}$$

This results in the following block structure for the matrices A_e and T_e:

$$A_e = \begin{bmatrix} A_{pp} & A_{pu} \\ A_{up} & A_{uu} \end{bmatrix} = \begin{bmatrix} A_{pp} & A_{pu_0} & A_{pu_1} & A_{pu_2} \\ A_{u_0p} & A_{u_0u_0} & A_{u_0u_1} & A_{u_0u_2} \\ A_{u_1p} & A_{u_1u_0} & A_{u_1u_1} & A_{u_1u_2} \\ A_{u_2p} & A_{u_2u_0} & A_{u_2u_1} & A_{u_2u_2} \end{bmatrix} \tag{5}$$

We now apply the stabilized finite element method to equations (1) and (2) to obtain the following expressions for each block:

$$A_{pp} = \int_{\Omega_e} \tau_{\text{PS}} \nabla N_p^\intercal \nabla N_p \mathrm{d}\Omega_e \tag{6}$$

$$A_{pu_i} = \int_{\Omega_e} \Big((N_p + \frac{\tau_{\text{PS}} \tilde{\mathbf{u}}_{\text{adv}} \cdot \nabla N_p}{2})^\intercal (\nabla N_u)_i + \tau_{\text{PS}} \left(\nabla N_p\right)_i^\intercal \tilde{\mathbf{u}}_{\text{adv}} \nabla N_u \Big) \mathrm{d}\Omega_e \tag{7}$$

$$A_{u_iu_j} = \int_{\Omega_e} \Big(\tau_{\text{BU}} (\nabla N_u)_i + \frac{1}{2} (\tilde{\mathbf{u}}_{\text{adv}})_i (N_u + \tau_{\text{SU}} \mathbf{u} \nabla N_u) \Big)^\intercal (\nabla N_u)_j \, \mathrm{d}\Omega_e \tag{8}$$

$$A_{u_iu_i} = \int_{\Omega_e} \Big(\nu \nabla N_u^\intercal \nabla N_u + (N_u + \tau_{\text{SU}} \tilde{\mathbf{u}}_{\text{adv}} \nabla N_u)^\intercal \tilde{\mathbf{u}}_{\text{adv}} \nabla N_u \Big) \mathrm{d}\Omega_e + A_{u_iu_j} \tag{9}$$

$$A_{u_ip} = \int_{\Omega_e} (N_u + \tau_{\text{SU}} \tilde{\mathbf{u}}_{\text{adv}} \nabla N_u)^\intercal \left(\nabla N_p\right)_i \mathrm{d}\Omega_e \tag{10}$$

$$T_{pu_i} = \int_{\Omega_e} \tau_{\text{PS}} \left(\nabla N_p\right)_i^\intercal N_u \mathrm{d}\Omega_e \tag{11}$$

$$T_{u_iu_i} = \int_{\Omega_e} (N_u + \tau_{\text{SU}} \tilde{\mathbf{u}}_{\text{adv}} \nabla N_u)^\intercal N_u \mathrm{d}\Omega_e \tag{12}$$

Here, N_u and N_p are the shape functions for the velocity and pressure, respectively. They are row vectors of size m+1 with coefficients depending on the spatial coordinates. We use mapped coordinates so the integrals can easily be evaluated numerically using Gaussian quadrature. The indices i and j iterate over the number of dimensions of the problem, indicating a single component of a vector variable or a row of a gradient matrix ∇N. The stabilization terms are multiplied with their respective stabilization coefficients τ_{PS} for the PSPG stabilization, τ_{SU} for the SUPG stabilization and τ_{BU} for the bulk viscosity term. The PSPG term allows the use of equal-order interpolation for the velocity and the pressure. It introduces a non-zero A_pp block, consisting of the Laplacian of the pressure. The SUPG stabilization corresponds to upwinding in the streamwise direction, i.e. the weight of upstream nodes is increased. The bulk viscosity term is necessary for flows that are strongly dominated by advection, and is sometimes called grad-div stabilization [10] or the least squares on incompressibility constraint [11]. The values for the stabilization parameters must be chosen carefully: they should be large enough to obtain the stabilizing effect, but if they are too large the scheme becomes too dissipative and accuracy suffers. We follow the definitions given in [11]:

$$\tau_{\text{SU}1} = \frac{h}{2 \left\| \tilde{\mathbf{u}}_{\text{adv}} \right\|} \tag{13}$$

$$\tau_{\text{SU}2} = \frac{\Delta t}{2 c_1} \tag{14}$$

$$\tau_{\text{SU}3} = \frac{h^2}{c_2 \nu} \tag{15}$$

$$\tau_{\text{SU}} = \left(\frac{1}{\tau_{\text{SU}1}} + \frac{1}{\tau_{\text{SU}2}} + \frac{1}{\tau_{\text{SU}3}} \right)^{-1} \tag{16}$$

$$\tau_{\text{PS}} = \tau_{\text{SU}} \tag{17}$$

$$\tau_{\text{BU}} = \tau_{\text{SU}} \left\| \tilde{\mathbf{u}}_{\text{adv}} \right\|^2 \tag{18}$$

Here, h is a characteristic element length. In [12], a systematic study comparing different definitions of h was conducted, concluding that a length scale based on the minimal edge length of an element gives the best result in the case of high aspect ratio elements. For aspect ratios closer to one, results were comparable to other possible definitions (maximum edge length and edge length in the streamwise direction). This leads us to choose the minimum element edge length as our definition for h. The parameters c_1 and c_2 are introduced in [13] and allow further control of the stabilization. Values $c_1 = 1$ and $c_2 = 4$ correspond to the definitions in [11], while in [13] the authors choose $4 \leq c_1 \leq 16$ and $c_2 = 36$.

The advection velocity $\mathbf{u}_{\text{adv}}$ is calculated using a Taylor series expansion:

$$\mathbf{u}_{\text{adv}} = 2.1875\mathbf{u}^n - 2.1875\mathbf{u}^{n-1} + 1.3125\mathbf{u}^{n-2} - 0.3125\mathbf{u}^{n-3} \tag{19}$$

This technique allows us to linearize the equations without resorting to an iterative technique, thus solving only one linear system per time step, at the cost of storing the velocity for the previous 4 time steps for every node.

In [6], the global linear system 3 is solved by directly applying the GMRES method. It is preconditioned either with algebraic multigrid or ILU factorization. There is no stability condition for the time

step if we set $0.5 \leq \theta \leq 1$, and the scheme is second order accurate in time when setting $\theta = 0.5$. Storing the coupled system is expensive, and depending on the mesh and the flow configuration the iterative method may converge slowly.

2.2. Segregated formulation

An alternative to solving the complete system is to split it into separate linear systems for the velocity and the pressure. We follow the method proposed in [14]. Introducing the velocity- and pressure differences between two time levels $\Delta\mathbf{u}$ and Δp, we can rewrite the momentum equation as a function of the acceleration $\mathbf{a} = \Delta\mathbf{u}/\Delta t$:

$$\begin{aligned}(T_{uu} + \theta\Delta t A_{uu})\,\mathbf{a} + \theta A_{up}\Delta p \\ = -A_{uu}\mathbf{u}^n - A_{up}p^n \quad (21)\end{aligned}$$

Defining $\mathbf{a}^* = \mathbf{a} + (T_{uu} + \theta\Delta t A_{uu})^{-1}\theta A_{up}\Delta p$ we obtain a linear system that can be solved for $\mathbf{a}^*$:

$$(T_{uu} + \theta\Delta t A_{uu})\,\mathbf{a}^* = -A_{uu}\mathbf{u}^n - A_{up}p^n \quad (22)$$

The continuity equation is:

$$\begin{aligned}\left(T_{pu} + \Delta t A_{pu}\right)\mathbf{a} + A_{pp}\Delta p \\ = -A_{pu}\mathbf{u}^n - A_{pp}p^n \quad (23)\end{aligned}$$

Using the definition of a^*, we can rewrite this into a linear system for the pressure difference Δp between two time steps:

$$\begin{aligned}\left(\left(T_{pu} + \Delta t A_{pu}\right)(T_{uu} + \theta\Delta t A_{uu})^{-1}\,\theta A_{up} - A_{pp}\right)\Delta p \\ = T_{pu}\mathbf{a}^* + A_{pu}\left(\mathbf{u}^n + \Delta t\mathbf{a}^*\right) + A_{pp}p^n \quad (24)\end{aligned}$$

Note that the system matrix for the pressure is the Schur complement of the velocity block in the original system. We can now first solve the linear system for $\mathbf{a}^*$, then solve the Δp system and finally get the acceleration from

$$\mathbf{a} = \mathbf{a}^* - (T_{uu} + \theta\Delta t A_{uu})^{-1}\theta A_{up}\Delta p \quad (25)$$

So far, we have only solved the coupled system in a different way, algebraically equivalent to a direct solution. In addition to solving a separate linear system for the velocity and the pressure, we also need the inverse $(T_{uu} + \theta\Delta t A_{uu})^{-1}$ to construct the matrix for the pressure system. Doing this directly is not possible on a large mesh, so simplification is needed to obtain an efficient method. When we simplify steps in the algorithm, the result will no longer be identical to the solution of the coupled system, so we introduce an iterative algorithm that can be executed M times each time step. The linear systems will be solved for the difference between two inner iterations m and $m+1$, i.e. $\Delta\mathbf{a} = \mathbf{a}^{m+1} - \mathbf{a}^m$ and $\Delta p^{m+1} = p^{m+1} - p^m$. From this, we also have $\mathbf{u}^m = \mathbf{u}^n + \Delta t\mathbf{a}^m$ and $p^m = p^n + \sum_{i=0}^{m}\Delta p^i$. The modified $\mathbf{a}^*$ is then:

$$\mathbf{a}^{*m} = \mathbf{a}^m + (T_{uu} + \theta\Delta t A_{uu})^{-1}\theta A_{up}\left(\sum_{i=0}^{m}\Delta p^i\right) \quad (26)$$

Filling this into the original system (22) and using the definition of $\mathbf{a}^*$ yields:

$$\begin{aligned}(T_{uu} + \theta\Delta t A_{uu})\,\Delta\mathbf{a}^* = -A_{uu}\mathbf{u}^m - A_{up}p^m \\ - (T_{uu} + \theta\Delta t A_{uu})\,\mathbf{a}^m + A_{uu}\Delta t\mathbf{a}^m \\ + (1-\theta)\,A_{up}\left(\sum_{i=0}^{m}\Delta p^i\right) \quad (27)\end{aligned}$$

For the continuity equation we start from:

$$\begin{aligned}(T_{pu} + \Delta t A_{pu})\Delta\mathbf{a} + A_{pp}(\sum_{i=0}^{m+1}\Delta p^i) = \\ - A_{pu}\mathbf{u}^n - A_{pp}p^n - (T_{pu} + \Delta t A_{pu})\mathbf{a}^m \quad (28)\end{aligned}$$

With $\Delta\mathbf{a} = \Delta\mathbf{a}^* - (T_{uu} + \theta\Delta t A_{uu})^{-1}\theta A_{up}\Delta p^{m+1}$ this becomes:

$$\begin{aligned}\left(\left(T_{pu} + \Delta t A_{pu}\right)(T_{uu} + \theta\Delta t A_{uu})^{-1}\,\theta A_{up} - A_{pp}\right)\cdot \\ \Delta p^{m+1} = T_{pu}\Delta\mathbf{a}^* + A_{pu}\left(\mathbf{u}^m + \Delta t\Delta\mathbf{a}^*\right) \\ + A_{pp}p^m + T_{pu}\mathbf{a} \quad (29)\end{aligned}$$

With the problem formulated this way, we can now apply a predictor-multicorrector iterative scheme:

1: $\mathbf{u}^0 = \mathbf{u}^n$
2: $p^0 = p^n$
3: $\mathbf{a}^0 = \mathbf{0}$
4: **for** $m = 0$ to $M - 1$ **do**
5: Solve linear system (27) for $\Delta\mathbf{a}^*$
6: Solve linear system (29) for Δp^{m+1}
7: Compute:
$\Delta\mathbf{a} = \Delta\mathbf{a}^* - (T_{uu} + \theta\Delta t A_{uu})^{-1}\,\theta A_{up}\Delta p^{m+1}$
8: Update $\mathbf{u}^{m+1} = \mathbf{u}^m + \Delta t\Delta\mathbf{a}$
9: Update $p^{m+1} = p^m + \Delta p^{m+1}$
10: **end for**

Without simplifications to the systems, executing the iteration once will immediately provide the correct velocity- and pressure updates. The solution of the velocity system is difficult due to the advective terms.

These terms have an important impact on the convergence rate of the iterative solvers and introduce a direct dependency of the matrix coefficients on the velocity. An easy fix is to drop the advection terms from the velocity system matrix, treating them explicitly (i.e. setting θ=0 for those terms). We assemble the simplified velocity matrices $\widetilde{A_{uu}}$ and $\widetilde{T_{uu}}$ using the following expressions:

$$\widetilde{A_{u_i u_i}} = \int_{\Omega_e} (\nu + \tau_{\text{BU}}) \nabla N_u^\intercal \nabla N_u \, \mathrm{d}\Omega_e \tag{30}$$

$$\widetilde{A_{u_i u_j}} = \int_{\Omega_e} \tau_{\text{BU}} (\nabla N_u)_i^\intercal (\nabla N_u)_j \, \mathrm{d}\Omega_e \qquad (i \neq j) \tag{31}$$

$$\widetilde{T_{u_i u_i}} = \int_{\Omega_e} N_u^\intercal N_u \, \mathrm{d}\Omega_e \tag{32}$$

The system matrix of this simplified velocity system is now symmetric and much better conditioned, due to the removal of the advective terms. The coefficients only depend on the viscosity and τ_{BU}, so they do not vary much in time, especially if the time step is small. This allows us to reuse the same velocity matrix over a range of time steps, reducing the time required for assembly and preconditioner setup. For the pressure system, we first need an approximation for $(T_{uu} + \theta \Delta t A_{uu})^{-1}$. As suggested in [14], the inverse of the lumped velocity mass matrix M_L is a good candidate, i.e. we sum all the elements of a row and then put that value on the diagonal, making the inverse trivial to compute. The same approximation is used in [11]. After this change, the pressure system matrix becomes:

$$\left((T_{pu} + \Delta t A_{pu}) M_L^{-1} \theta A_{up} - A_{pp} \right) \tag{33}$$

If we ignore the stabilization terms and apply partial integration to the pressure gradient term in the momentum equation, we have $A_{up} = -A_{pu}^\intercal$, hinting that the structure of the pressure matrix and the Poisson problem are similar. This leads us to simplify the pressure matrix as follows:

$$\begin{aligned} ((T_{pu} + \Delta t A_{pu}) M_L^{-1} \theta A_{up} - A_{pp}) \approx \\ - \theta(\tau_{\text{PS}} + \Delta t) \int_{\Omega_e} \nabla N_p^\intercal \nabla N_p \, \mathrm{d}\Omega_e \end{aligned} \tag{34}$$

This approximation is remarkably similar to the approximation of the Schur complement of the velocity block for reaction-dominated flows as described in [15]. We are indeed in the situation of reaction-dominated flows since the time term is large due to the small time steps under consideration. The validity of our approximation is further confirmed by the Taylor-Green test case. The resulting matrix is symmetric and only depends on the solution through the value of τ_{PS}. Numerical experiments show that the adjustment of τ_{PS} in the matrix has no effect on the accuracy, so we can reuse the same pressure matrix during the complete calculation. This opens up the possibility of using a direct solution method or reuse of the preconditioner. While the original matrix required a sparse matrix product, the simplification can be assembled on a per-element basis. This greatly simplifies the code and speeds up the assembly. This can be important in the case of deforming meshes or variable time steps, where the pressure matrix does change with each time step.

3. Particle model

For monodisperse flows, it is possible to write a single transport equation for the particle concentration. We follow the approach of Ferry et al. [16], which is a fairly intuitive description of how the transport equation can be obtained. Similar models are also described by Simonin [17] and Zaichik et al. [18], where the model is obtained by integrating a probability density function in phase space. While more rigorous, this approach is much harder to follow and the resulting transport equation is the same.

The basic assumption is that we can write a transport equation for the particle volume fraction c as follows:

$$\frac{\partial c}{\partial t} + \nabla \cdot (c\mathbf{v}) = D_b \nabla^2 c \tag{35}$$

The velocity $\mathbf{v}$ is the particle velocity, and the above equation is valid only if we suppose that the particle velocity can be represented as an Eulerian field. This is a strong hypothesis, since the particle velocity not only depends on the fluid velocity but also on the particle initial conditions. Two particles with different initial velocities might still have different velocities at the same time t and position $\mathbf{x}$. If the particle relaxation time τ_p is sufficiently small with respect to the fluid velocity time scale, it can be shown (see [16]) that the effect of particle initial conditions decreases exponentially fast, and an Eulerian velocity field may be used.

Generally speaking, the particle velocity field $\mathbf{v}$ is obtained from a transport equation, as computed from the probability density function in i.e. [18]. For the small particle relaxation times considered here, however, it is possible to omit this extra set of transport

equations and to write the particle velocity as an expansion of the fluid velocity, resulting in the equilibrium Eulerian method. The expansion can be obtained from the particle equation of motion, to be discussed in detail in the following section.

3.1. Particle equation of motion

The Maxey and Riley [19] equation describes the motion of a small spherical particle moving in a constant density flow and reads:

$$\begin{aligned}\frac{\mathrm{d}\mathbf{v}}{\mathrm{d}t} = &\underbrace{\frac{\rho_p-\rho_f}{\rho_p}\mathbf{g}}_{\text{Buoyancy}} + \underbrace{\frac{\rho_f}{\rho_p}\frac{\mathrm{D}\mathbf{u}}{\mathrm{D}t}}_{\text{Fluid acceleration}} \\ &\underbrace{-\frac{1}{\tau_p}(\mathbf{v}-\mathbf{u})}_{\text{Stokes drag}} + \underbrace{\frac{\rho_f}{2\rho_p}\left(\frac{\mathrm{D}\mathbf{u}}{\mathrm{D}t}-\frac{\mathrm{d}\mathbf{v}}{\mathrm{d}t}\right)}_{\text{Added mass}} \\ &\underbrace{-\frac{9\sqrt{\mu\rho_f}}{d_p\rho_p\sqrt{\pi}}\int_0^t \frac{1}{\sqrt{1-s}}\frac{\mathrm{d}}{\mathrm{d}s}(\mathbf{v}-\mathbf{u})\,\mathrm{d}s}_{\text{Basset history}} \end{aligned} \tag{36}$$

Here, $\mathrm{d}/\mathrm{d}t$ denotes the total derivative following the particle, while $\mathrm{D}/\mathrm{D}t$ is the total derivative following the fluid. The first term is the buoyancy or Archimedes force felt by the particle. The second term, labeled "fluid acceleration" here, represents the force that the particle would feel if its density were equal to the fluid density. Together with the $\rho_f\mathbf{g}$ term in the buoyancy, this is an effect that can be computed from the undisturbed flow. The remaining terms take into account the effect of the disturbed flow, and are obtained from the solution of an unsteady Stokes problem around a sphere. Note that the Stokes flow alone is written as [20]:

$$\frac{\mathrm{d}\mathbf{v}}{\mathrm{d}t} = \frac{18\mu}{\rho_p d_p^2}(\mathbf{u}-\mathbf{v}) \tag{37}$$

The factor on the right hand side has dimensions [s^{-1}], so the particle response time appears naturally as:

$$\tau_p \equiv \frac{\rho_p d_p^2}{18\mu} \tag{38}$$

The approximation using Stokes flow implies that the Reynolds number associated with the relative velocity between fluid and particle is assumed to be small. The added mass term can be interpreted as an inertia term that is also derived from the disturbed flow computation. Finally, the Basset history term models the unsteady development of the flow around the particle.

Before we exploit this equation, we will examine possible simplifications, based on the expected importance of the different terms. The fluid acceleration, added mass and Basset history forces are present only when unsteady flow or particle motion is considered. They are usually important if $\rho_p \lesssim O(\rho_f)$. As found in [21], with $\rho_p \gg \rho_f$ their importance must be evaluated using the ratio d_p/η_k, where η_k is the Kolmogorov length scale, i.e. the smallest fluid length scale in the present context of incompressible flow. If $d_p < \eta_k$, the unsteady terms can be neglected. In [7], numerical tests are performed using the equilibrium Eulerian approach, indicating that the model remains valid when the particle response time stays below the order of the Kolmogorov time scale, i.e. $\tau_p \lesssim \tau_k$. For particles with $\rho_p \gg \rho_f$, this results in $d_p < \eta_k/2$. This means that for the entire validity range of the equilibrium Eulerian approach, the unsteady terms can be neglected, since we are in the case $\rho_p \gg \rho_f$ and $d_p < \eta_k$.

Nevertheless, we choose to retain the fluid acceleration and added mass terms, since they bring no significant complexity to the model and including them allows a comparison with the bubble simulations of [8]. The Basset history force greatly complicates the implementation of the model, so we will always neglect it. This is perfectly valid for the targeted applications, but care should be taken if the flow strays too much from the criteria $\rho_p \gg \rho_f$ and $d_p < \eta_k$. Armenio et al. [22] show that for larger particles, the Basset force is important for all density ratios. The importance of memory effects is also demonstrated in [23] and [24], again showing stronger effects for larger and lighter particles. Efficient methods to evaluate the Basset term can be found in i.e. [25; 26].

In equation (36) we also omitted the so-called Faxén correction terms, which are proportional to $d_p^2\nabla^2\mathbf{u}$. These terms become important only when $d_p > \eta_k$ [27; 28], so they can be neglected on the same grounds as the unsteady terms.

Rewriting equation (36) by regrouping terms and removing the Basset force yields:

$$\left(1+\frac{\rho_f}{2\rho_p}\right)\frac{\mathrm{d}\mathbf{v}}{\mathrm{d}t} = \frac{\rho_p-\rho_f}{\rho_p}\mathbf{g} - \frac{1}{\tau_p}(\mathbf{v}-\mathbf{u}) + \frac{3}{2}\frac{\rho_f}{\rho_p}\frac{\mathrm{D}\mathbf{u}}{\mathrm{D}t} \tag{39}$$

We now look for an approximate solution for the particle velocity from the above equation. First we have:

$$\mathbf{v} = \mathbf{u} - \tau_p\left[\left(1+\frac{\rho_f}{2\rho_p}\right)\frac{\mathrm{d}\mathbf{v}}{\mathrm{d}t} - \frac{\rho_p-\rho_f}{\rho_p}\mathbf{g} - \frac{3}{2}\frac{\rho_f}{\rho_p}\frac{\mathrm{D}\mathbf{u}}{\mathrm{D}t}\right] \tag{40}$$

If we consider τ_p as a small parameter, we can already see that this equation yields the trivial zeroth order ap-

proximation $\mathbf{v} = \mathbf{u}$, valid only for perfect tracer particles. Recursively replacing $\mathbf{v}$ on the right hand side using equation (40) itself yields the first order approximation:

$$\mathbf{v} = \mathbf{u} - \tau_p \left[\left(1 + \frac{\rho_f}{2\rho_p} \right) \frac{\mathrm{d}\mathbf{u}}{\mathrm{d}t} - \frac{\rho_p - \rho_f}{\rho_p} \mathbf{g} - \frac{3}{2} \frac{\rho_f}{\rho_p} \frac{\mathrm{D}\mathbf{u}}{\mathrm{D}t} \right] + O(\tau_p^2) \quad (41)$$

Higher order expansions can be obtained by writing out the $O(\tau^2)$ part and recursively substituting again the expression for $\mathbf{v}$. However, as concluded in [16] the second order approximation does not always yield better results, so it is not worth the effort in practice and we will use equation (41) without the $O(\tau_p^2)$ terms to obtain the particle velocity. Note that this is equivalent to the approximation $\mathrm{d}\mathbf{v}/\mathrm{d}t \approx \mathrm{d}\mathbf{u}/\mathrm{d}t$ and results in the locally implicit method as formulated in [7].

The equation is still implicit in $\mathbf{v}$ due to the definition of the total derivatives:

$$\frac{\mathrm{d}\mathbf{u}}{\mathrm{d}t} = \frac{\partial \mathbf{u}}{\partial t} + \mathbf{v} \cdot \nabla \mathbf{u} = \frac{\mathrm{D}\mathbf{u}}{\mathrm{D}t} + (\mathbf{v} - \mathbf{u}) \cdot \nabla \mathbf{u} \quad (42)$$

In [16], this is avoided by approximating $\mathrm{d}\mathbf{v}/\mathrm{d}t \approx \mathrm{D}\mathbf{u}/\mathrm{D}t$. This is less accurate because now $(\mathbf{v} - \mathbf{u}) \cdot \nabla \mathbf{u}$ is neglected. As indicated in [7], this term is important in the prediction of wall-normal transport of streamwise velocity, since the wall-normal component of $\mathbf{v}$ may differ significantly from that of $\mathbf{u}$. Filling in equation (42) into equation (41) results in:

$$\mathbf{v} = \mathbf{u} - \tau_p \left(1 - \frac{\rho_f}{\rho_p} \right) \left(\mathbf{I} + \tau_p \left(1 + \frac{\rho_f}{2\rho_p} \right) \nabla \mathbf{u} \right)^{-1} \left(\frac{\mathrm{D}\mathbf{u}}{\mathrm{D}t} - \mathbf{g} \right) \quad (43)$$

Here, $\mathbf{I}$ is the identity matrix. The matrix that needs to be inverted is only size 3x3 for three dimensional problems, so this equation is still very cheap to solve compared to a full momentum transport equation for the particle phase.

Equation (43) is difficult to apply to the limit case of bubbles, where $\rho_f/\rho_p \to \infty$ and $\tau_p \to 0$. This can be avoided by introducing the density ratio parameter β and the generalized relaxation time τ as defined in [16]:

$$\beta \equiv \frac{3}{2\rho_p/\rho_f + 1} \quad (44)$$

$$\tau \equiv \tau_p \left(1 + \frac{\rho_f}{2\rho_p} \right) \quad (45)$$

Substituting into equation (43) yields:

$$\mathbf{v} = \mathbf{u} - \tau (1 - \beta) (\mathbf{I} + \tau \nabla \mathbf{u})^{-1} \left(\frac{\mathrm{D}\mathbf{u}}{\mathrm{D}t} - \mathbf{g} \right) \quad (46)$$

Comparing with the equations found in literature, equation (46) is identical to the result found in [7] except for the factor $(1-\beta)$. This stems from the fact that [7] only accounts for gravity and Stokes drag forces. This also corresponds to $\beta = 0$, which is the limit for heavy particles with $\rho_p/\rho_f \to \infty$ and $\tau \to \tau_p$. It is another way to illustrate that the added mass and fluid acceleration forces become negligible as the density ratio increases. If we neglect the locally implicit contribution $(\mathbf{I} + \tau \nabla \mathbf{u})^{-1}$ we recover the general formulation of [16]. Finally, in the limit case of bubbles we have $\beta = 3$ as $\rho_p/\rho_f \to 0$ and we obtain the equation given in [8]. Note that for bubbles we have, using equations (45) and (38) with $\tau_p \to 0$:

$$\tau = \tau_p \frac{\rho_f}{2\rho_p} = \frac{d_p^2}{36\nu} \quad (47)$$

This is exactly the bubble relaxation time as given in [8].

In conclusion, with equation (46) we have generalized the locally-implicit approach of [7], accounting for the added mass and fluid acceleration forces, thus making the equation applicable to both bubbles and heavy solid particles.

3.2. Finite element formulation

Equation (35) is basically a scalar advection-diffusion equation, where the velocity field is not divergence free. We apply the same SUPG stabilization as for the flow field, resulting in the following expressions for the element matrices:

$$A_c = \int_{\Omega_e} (N_c + \tau_{\mathrm{SU}} \tilde{\mathbf{v}} \nabla N_c)^{\mathsf{T}} \left(\tilde{\mathbf{v}} \nabla N_c + \operatorname{div} \tilde{\mathbf{v}} N_c \right) + D_b \nabla N_c^{\mathsf{T}} \nabla N_c \, \mathrm{d}\Omega_e \quad (48)$$

$$T_c = \int_{\Omega_e} (N_c + \tau_{\mathrm{SU}} \tilde{\mathbf{v}} \nabla N_c)^{\mathsf{T}} N_c \, \mathrm{d}\Omega_e \quad (49)$$

As for the fluid model, we assemble a linear system, using θ time integration:

$$\sum_N \left(\frac{1}{\Delta t} T_c + \theta A_c \right) \left(\mathbf{c}_e^{n+1} - \mathbf{c}_e^n \right) = -A_c \mathbf{c}_e^n \quad (50)$$

Before the previous equation can be solved, we need to supply it with the particle velocity. The finite element formulation for equation (46) reads, when omitting the local-implicit term for clarity and only

writing the time step at $(n-1)$:

$$\left(\int_{\Omega_e} N_v^{\mathsf{T}} N_v \, \mathrm{d}\Omega_e\right)(\mathbf{v}_e)_i = \int_{\Omega_e} N_u^{\mathsf{T}} \Big[\tilde{\mathbf{u}} - \tau\,(1-\beta)\left(\frac{\tilde{\mathbf{u}} - \tilde{\mathbf{u}}^{n-1}}{\Delta t} + \tilde{\mathbf{u}} \cdot \operatorname{grad} \tilde{\mathbf{u}}\right)\Big]_i \, \mathrm{d}\Omega_e \quad (51)$$

On the left hand side, $\left(\mathbf{v}_e^{n+1}\right)$ appears next to a mass matrix, so we need to solve a linear system of equations over the domain in order to find the particle velocity. Even though a linear system involving only the mass matrix is easy to solve, the cost is still much greater than a direct application of the locally implicit formulation of equation (46). This becomes prohibitive especially when polydisperse particle distributions need to be considered. One easy fix would be to lump the mass matrix, resulting in a diagonal system that is trivial to solve. As another alternative, we can also approximate the gradient matrix $\nabla \mathbf{u}$ as the average of the gradient at the center of each element surrounding a node. The resulting gradient field can then be used to evaluate the particle velocity at each node k using equation (46) with a first-order difference in time:

$$\mathbf{v}_k = \mathbf{u}_k - \tau\,(1-\beta)\,(\mathbf{I} + \tau\,(\nabla \mathbf{u})_k)^{-1}\left(\frac{\mathbf{u}_k - \mathbf{u}_k^{n-1}}{\Delta t} + \mathbf{u}_k\,(\nabla \mathbf{u})_k - \mathbf{g}_k\right) \quad (52)$$

Numerical experiments in section 4 show that this approach maintains second order accuracy and is more accurate than lumping the mass matrix of the full finite element formulation.

4. Taylor-Green vortex flow

4.1. Carrier phase

We now apply the flow solver to the Taylor-Green periodic vortices, advected by a constant velocity field. The advantage of this test case is that it is a time dependent problem with an analytical solution in closed form. The velocity components, the pressure and the vorticity as a function of spatial coordinates and time are:

$$u = U_a - V_s \cos\left(\frac{\pi}{D}(x - U_a t)\right)\sin\left(\frac{\pi}{D}(y - V_a t)\right) e^{-\frac{2\nu\pi^2}{D^2}t}$$

$$v = V_a + V_s \sin\left(\frac{\pi}{D}(x - U_a t)\right)\cos\left(\frac{\pi}{D}(y - V_a t)\right) e^{-\frac{2\nu\pi^2}{D^2}t}$$

$$p = -\frac{V_s^2}{4}(\cos(2\frac{\pi}{D}(x - U_a t)) + \cos(2\frac{\pi}{D}(y - V_a t)))e^{-\frac{4\nu\pi^2}{D^2}t}$$

$$\omega = \frac{2V_s\pi}{D}\cos(\frac{\pi}{D}(x - U_a t))\cos(\frac{\pi}{D}(y - V_a t))e^{-\frac{4\nu\pi^2}{D^2}t}$$

This flow field represents two-dimensional, periodic vortices with diameter D and initial maximal swirl velocity V_s, advected by the advection velocity (U_a,V_a), and dissipating due to the kinematic viscosity ν. We use the following values in our tests (based on [6]): D = 0.5 m, V_s = 1 m/s, U_a = 0.3 m/s, V_a = 0.2 m/s and ν = 0.001 m^2/s. The flow field is visualized in figure 1, using contours of the dimensionless vorticity ω/ω_0 and dimensionless time $(tV_s)2D$. From these images, it is clear that the vortex centers move along the advection velocity vector. Viscosity redistributes the vorticity until it uniformly reaches zero everywhere in the domain, as indicated by the decrease in vorticity magnitude in the figures. For the numerical simulations, we initialize the flow with the analytical solution at time t = 0 s and set periodic boundary conditions in both directions. Since this determines the pressure only up to a constant, we impose the pressure in the center of the domain, setting it equal to the analytical solution at every time step. In a first test, we will determine the effect of the number of inner iterations M, using a grid of 64x64 quadrilaterals that are triangulated for the triangle element tests. In figure 2, the error of the segregated solution is compared to the fully coupled solution, defining the relative difference with the coupled solution as, for the x-component of the velocity:

$$\frac{\max_\Omega |u_c - u_s|}{\max_\Omega (u_c - u_{th})} \quad (53)$$

Here, u_c is the solution of the coupled system of equations, u_s is the segregated solution and u_{th} is the analytical solution. For $M = 1$ and at time 6, the difference between the segregated and the coupled solution is about 10 times greater than the error between the fully coupled solution and the analytical solution, i.e. the absolute error is an order of magnitude greater. When we increase the number of iterations to two, the difference between both methods is two orders of magnitudes smaller than the absolute error, i.e. the difference is negligible and increasing the number of iterations further is not necessary. The difference flattens off after 4 iterations. At the first time step (time 0.004), the iterative technique converges towards the coupled solution as the number of iterations increases. Again, the difference with the coupled solution de-

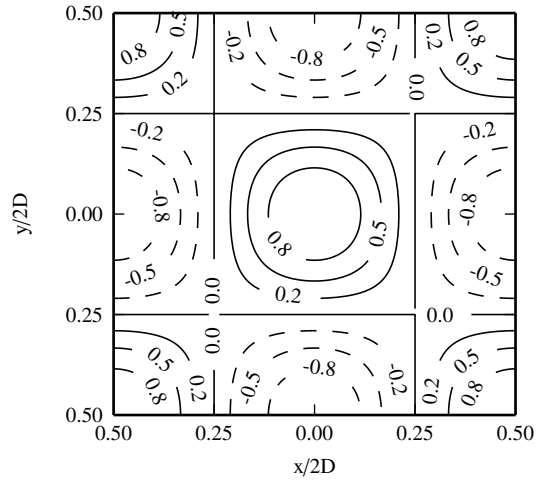

(a) $t = 0$

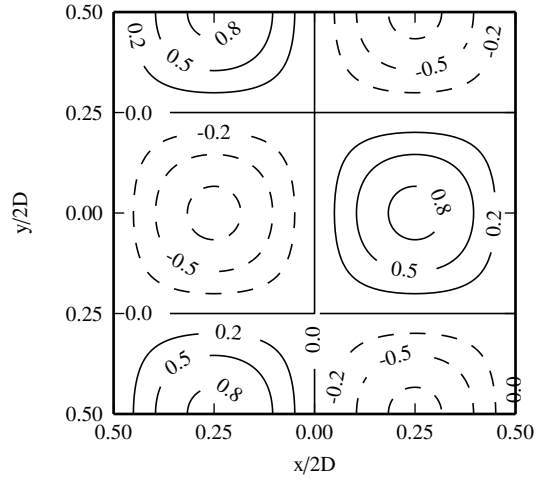

(b) $t = 2.5$

Figure 1: Contours of dimensionless vorticity, at dimensionless time 0 (a) and 2.5 (b).

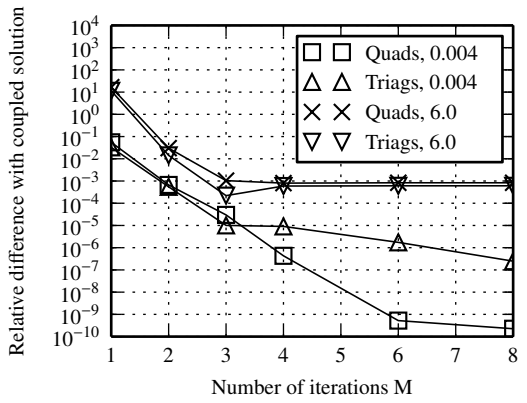

Figure 2: Comparison between the fully coupled solution of the linear system and the current method, as a function of the number of inner iterations and at two dimensionless times 0.004 (i.e. after one time step) and 6.0.

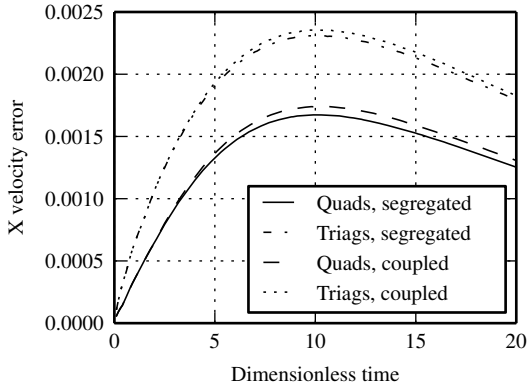

Figure 3: Maximum error over the domain for the x-component of the velocity, for triangles and quadrilaterals and using the coupled and segregated solution method using two inner iterations.

creases with two orders of magnitude when using two iterations instead of one. We conclude from these observations that two inner iterations offer a good balance between computational cost and accuracy. This is no surprise: in [14] the authors point out that the term including the effect of the mass matrix on the acceleration in the right hand side of the velocity system only contributes from the second iteration onwards, since we initialize the acceleration to zero each time step.

From figure 2, it is clear that the difference between the two methods is greater at time 6 than after the first time step. This effect is better illustrated in figure 3, where we have plotted the errors $\max_\Omega |u_c - u_{th}|$ and $\max_\Omega |u_s - u_{th}|$ as a function of time. Both errors reach a maximum around time 10, and so does the difference between both methods. This difference between the segregated and coupled solution remains small, varying between 2 % and 4 % of the difference with the analytical solution. This confirms that two inner iterations suffice to reproduce the results of the fully coupled solution.

Figure 4 shows the error for a series of meshes with

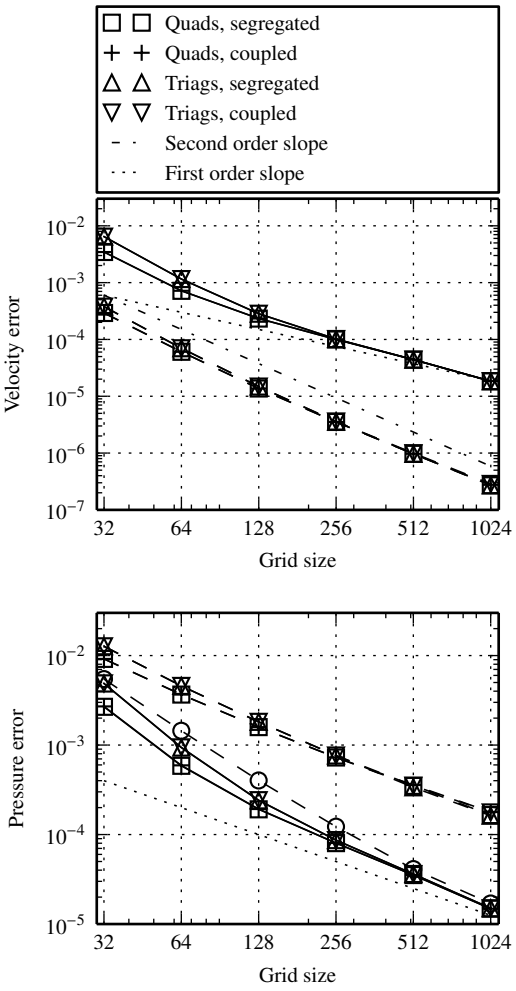

Figure 4: Maximum norm of the error for the velocity vector and the pressure, as a function of mesh size and with a constant Courant number of 0.32. The dashed lines connect the errors after one time step, the solid lines those at time 10. The lower plot also shows pressure error for quadrilateral elements computed at Courant number 0.03, denoted by the circles.

NxN quadrilaterals (triangulated for the triangle results). The time step was adapted to maintain a constant Courant number of 0.32 at the start of the simulation, using $\Delta t = 0.256/N$. We calculate the error as the maximum of the absolute value of the difference with the analytical solution over the entire domain, taking the maximum of either component for the velocity error. The velocity error after one time step (dashed line) follows the second order slope, while the pressure error follows the first order slope. The errors at time 10 (i.e. near the maximum of figure 3) decrease with a slope between first and second order. These effects are due to the time stepping: if we lower the Courant number to 0.03, the pressures also follow the second order law, as illustrated in figure 4. The errors for the coupled and the segregated method overlap, further confirming the equivalence of both methods at the time steps considered here.

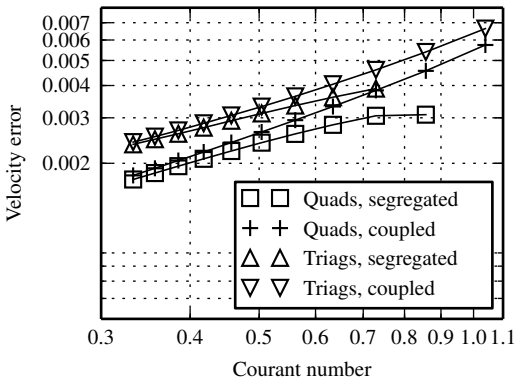

Figure 5: Maximum norm of the error for the velocity vector as a function of Courant number on the 64x64 grid.

Figure 5 shows the evolution of the maximum norm of the velocity error for increasing Courant numbers. The Courant number is computed here using the maximum velocity projection for all element edges. The segregated method becomes unstable when the Courant number reaches values close to 0.8, which is in line with the theoretical limits from [14]. Although we are using Crank-Nicolson time stepping, the errors in figure 5 do not decrease along a second order slope. Further tests with the fully coupled scheme show that second order in time is only visible at Courant number 2 and higher. In [29], a similar effect is visible in the numerical tests and this is attributed to the spatial component of the error.

4.2. Disperse phase

In [8], the preferential concentration of bubbles in the Taylor-Green vortex flow was studied, using equation (46), except for the locally-implicit factor. We repeat the same test here, to verify the correctness of our implementation. We adapt the parameters to match the study [8], so we set $U_a = V_a = 0$, $V_s = 1/4\pi$ m/s and $\nu = 1/5000$ m^2/s. For the particle phase, we set $\tau = 1/4$ s and β is set to 0 for solid particles and 3 for

bubbles. To stay coherent with the reference data, we use the non-dimensional time $4\pi V_s t/2D$.

Before moving on to the particle concentration field, we examine the particle velocity itself. Due to the explicit nature of equation (46) and the simple analytical solution of the flow field, it is possible to compute an analytical solution of the particle velocity field and use that to investigate the errors resulting from different approximations (discussed in section 3.2) of the velocity gradient. The analytical solution was obtained using computer algebra software and is omitted here for the sake of brevity. Figure 6 shows the evolution of the error as we increase the grid size from 32x32 to 512x512. The grid is graded in the vertical direction, to assess the effect of a non-uniform mesh. The complete finite element formulation (equation (51)) yields the most accurate result. The node-based formulation of equation (52) has an error that is almost twice as large, but still follows the second order slope. Finally, the finite eelement formulation that makes use of a lumped mass matrix is almost an order of magnitude less accurate than the other methods. Given the large gain in performance and the small cost in accuracy, the node-based formulation is chosen for this work. Figure 7 shows the particle velocity field,

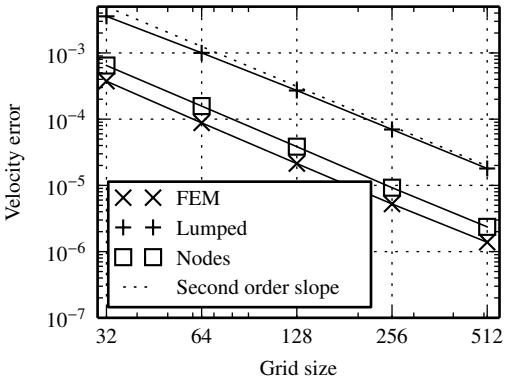

Figure 6: Maximum norm of the particle velocity error over the domain when compared with the analytical solution, at non-dimensional time 2

using vectors and contours of the X-velocity. The contours for the Y-velocity are not shown, but could be obtained by rotating the figure 90° counter clockwise. Due to the particle inertia, solid particles migrate out of the vortices. Bubbles tend to accumulate near the vortex centers, due to the effect of the fluid acceleration force. These effects can be seen in the velocity vector field, where the vectors circling the central vortex are directed more towards the center for bubbles than for solid particles.

The velocity vectors also indicate that the particle velocity field is not divergence-free. Around the point $(1/4, 1/4)$ in figure 7a for example, the horizontal vectors are shorter than the vertical vectors at an equal distance from this point, resulting in a non-symmetric distribution of the particles. This effect is reflected in

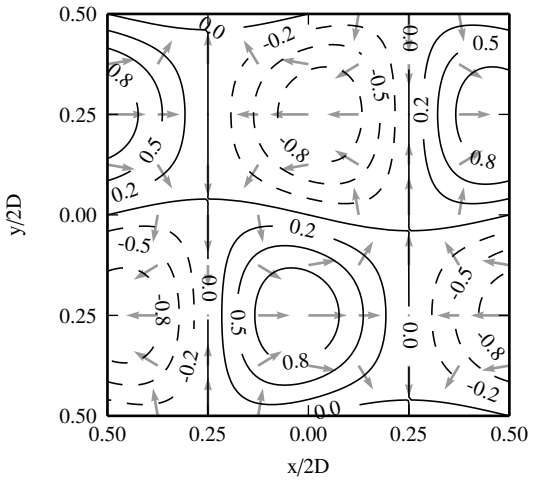

(a) Bubbles ($\beta = 3$)

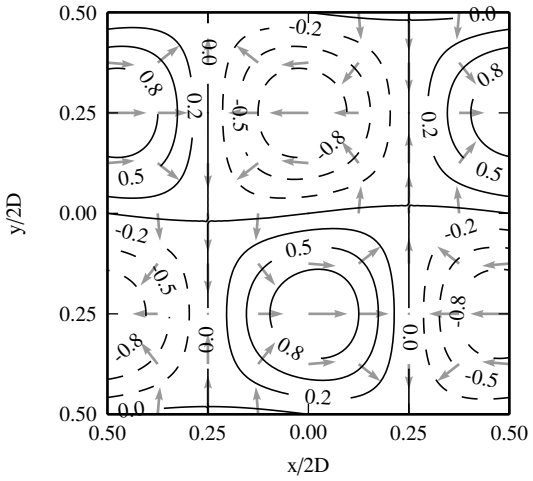

(b) Solid particles ($\beta = 0$)

Figure 7: Velocity vectors and contours of the X-velocity for the particles, normalized by V_s, at non-dimensional time 2.

the particle concentration distributions, shown in figure 8. For both bubbles and solid particles, the concentration field shows stretched patches at the corners

between vortices, which are the result of the different magnitudes for the horizontal and vertical velocity components. As expected, the concentration field for the bubbles shows a maximum near the vortex centers, while the solid particles migrate away from the vortex centers. The streamlines also show the particles spiraling outwards for solid particles and inwards for bubbles. To do a quantitative analysis of the obtained concentration field, it is possible to obtain an analytical solution of the particle concentration evolution with time, as was also done in [8]. We extend the analysis to be applicable for all values of β and we retain the locally implicit term. The equation is obtained by observing that the concentration reaches an extremum at the vortex center, so its gradient reaches zero. Neglecting Brownian motion, we obtain the following equation for the concentration:

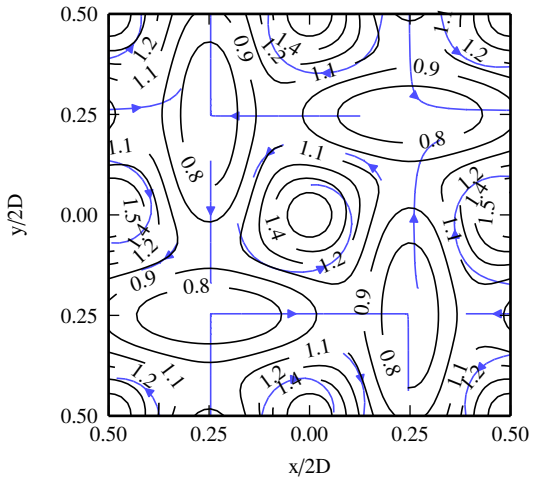

(a) Bubbles ($\beta = 3$)

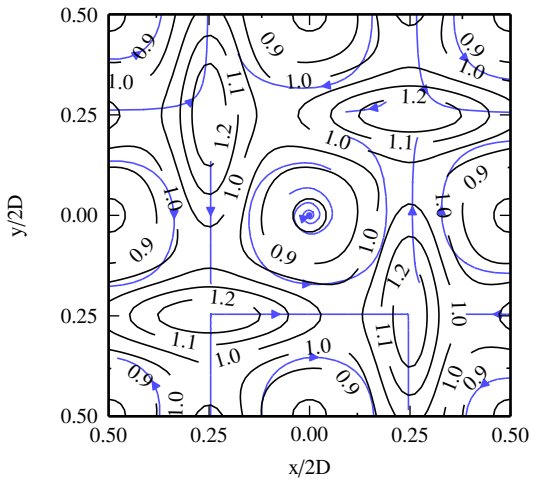

(b) Solid particles ($\beta = 0$)

Figure 8: Particle streamlines and volume fraction contours, normalized by the initial uniform volume fraction and shown at non-dimensional time 2.

$$\frac{\mathrm{d}c}{\mathrm{d}t} + c(t)\,(\nabla \cdot \mathbf{v})_{x=0,y=0} = 0 \tag{54}$$

Filling in the expression for the divergence of the Taylor-Green particle velocity field, evaluated at the origin, yields the time evolution of the concentration at the vortex center:

$$\begin{aligned} c(t) = c_0 \exp\Bigg[(\beta-1)\left(\frac{1}{2\nu\pi^2\tau} + \frac{1}{D^2}\right)\Bigg(4\nu\pi^2 t \\ - D^2 \log\left(D^2 \exp\left(\frac{4\nu\pi^2 t}{D^2}\right) + (\pi V_s \tau)^2\right)\Bigg)\Bigg] \\ \cdot \left(D^2 + (\pi V_s \tau)^2\right)^{(\beta-1)(D^2/(2\nu\pi^2\tau)+1)} \end{aligned} \tag{55}$$

We can compare this with the result from [8], adapted to our notation and generalized for any β:

$$c(t) = c_0 \exp\left[\frac{V_s^2(\beta-1)\tau}{2\nu}\left(1 - \exp\left(-\frac{4\nu\pi^2 t}{D^2}\right)\right)\right] \tag{56}$$

Figure 9 plots both equations, together with the numerical result on a 64x64 uniform mesh. Both analytical solutions and the numerical solution appear to be very close together. The excellent agreement can be explained by the small particle relaxation time ($\tau = 1/4$) which satisfies the hypothesis of the equilibrium Euler model very well. When we increase the relaxation time to $\tau = 3/4$, the simpler analytical model (55) predicts peak concentrations that are more than twice as large as the values from the locally implicit approach. This indicates that the higher accuracy of the approximation $\mathrm{d}\mathbf{v}/\mathrm{d}t \approx \mathrm{d}\mathbf{u}/\mathrm{d}t$ becomes more important as τ increases. At this relatively high relaxation time, steep concentration gradients appear in the solution, and a mesh size of 512 was necessary to avoid oscillations and negative concentrations.

When increasing τ, we should mind the basic hypothesis of the equilibrium Euler approach, namely that the particle velocity field can be represented as a unique vector field over the domain. In [16], a rigorous condition was established to verify that this is the case. The condition is that all eigenvalues of the matrix

$$\frac{1}{2}\left(\nabla\mathbf{v} + \nabla\mathbf{v}^{\mathsf{T}}\right) \tag{57}$$

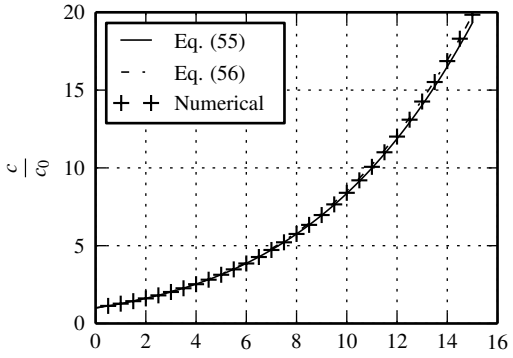

(a) $\tau = 1/4$, mesh size 64

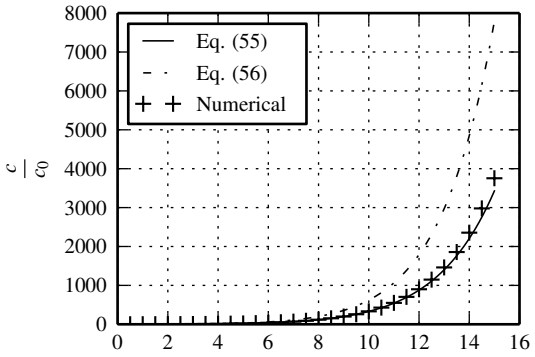

(b) $\tau = 3/4$, mesh size 512

Figure 9: Particle volume fraction at the domain center for bubbles ($\beta = 0$), relative to the initial concentration c_0, for relaxation times $\tau = 1/4$ and $\tau = 3/4$

are greater than $-1/\tau$ at every node in the domain. We have verified that this condition is satisfied for both relaxation times used in the current test.

In figure 10, we plot the evolution of the error at the vortex center as a function of the mesh size. For each grid, the simulation was run up to time 0.1 and the time step was adjusted to keep a constant Courant number as $3.2/N$, where N is the number of grid points. The expected second order slope is almost recovered, with a slight deviation that is likely due to errors introduced by the time discretization.

5. Conclusion and future work

The objective of the current work is to provide a meaningful contribution to the numerical modeling of dispersed phase flow. The inclusion of nanoparticles and coagulation effects constitute new challenges, and should extend the applicability of the method.

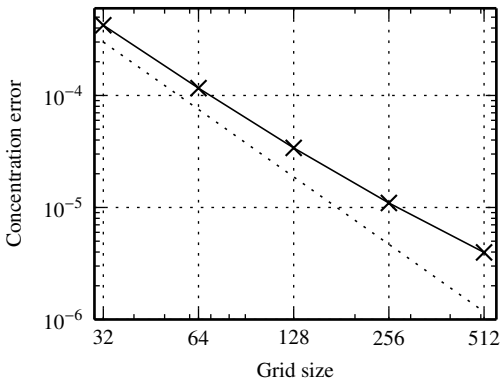

Figure 10: Error of the bubble volume concentration at the vortex center at time 0.1, normalized by the initial concentration. Evolution as a function of uniform mesh size, with the second order slope as reference (dotted line).

We presented a semi-implicit scheme for the solution of the linear system arising from the finite element discretization, demonstrating the accuracy and convergence rate using the Taylor-Green test case.

The equilibrium Eulerian approach was implemented for a single phase and also validated using the Taylor-Green vortex flow. Formulations found in literature were extended by combining a generic formulation for both dense particles and bubbles with the inclusion of the locally implicit factor introduced in [7].

In future work, we will extend the current model to account for coagulation using the techniques from [30] and [31]. The resulting model will be compared with our own experimental data.

Acknowledgments

The current implementation of the Navier-Stokes solver was realized thanks to the valuable assistance and comments of Tamás Bányai. For the PIV setup, the assistance from Elmar Recker was greatly appreciated.

References

[1] C. A. Pope, D. W. Dockery, Health Effects of Fine Particulate Air Pollution: Lines that Connect, J. Air & Waste Manage. Assoc. 56 (2006) 709–742.

[2] G. Oberdörster, E. Oberdörster, J. Oberdörster, Nanotoxicology: An Emerging Discipline Evolving from Studies of Ultrafine Particles, Environ Health Perspect 113 (2005) 823–839. doi:10.1289/ehp.7339.

[3] M. S. Alnæs, K.-A. Mardal, On the efficiency of symbolic computations combined with code generation for finite element methods, ACM Transactions on Mathematical Software 37 (1) (2010) 1. doi:10.1145/1644001.1644007.
[4] C. Prud'homme, Life: Overview of a Unified C++ Implementation of the Finite and Spectral Element Methods in 1D, 2D and 3D 4699 (2007) 712.
[5] H. G. Weller, A tensorial approach to computational continuum mechanics using object-oriented techniques, Computers in Physics 12 (6) (1998) 620. doi:10.1063/1.168744.
[6] T. Bányai, D. Vanden Abeele, H. Deconinck, A fast fully-coupled solution algorithm for the unsteady incompressible Navier-Stokes equations, in: Conference on Modelling Fluid Flow (CMFF'06), Budapest, Hungary, 2006.
[7] J. Ferry, S. L. Rani, S. Balachandar, A locally implicit improvement of the equilibrium eulerian method, International journal of multiphase flow 29 (6) (2003) 869–891.
[8] O. Druzhinin, S. Elghobashi, Direct numerical simulations of bubble-laden turbulent flows using the two-fluid formulation, Physics of Fluids 10 (1998) 685.
[9] T. A. Zang, On the rotation and skew-symmetric forms for incompressible flow simulations, Applied Numerical Mathematics 7 (1) (1991) 27–40.
[10] M. Braack, E. Burman, V. John, G. Lube, Stabilized finite element methods for the generalized oseen problem, Computer methods in applied mechanics and engineering 196 (4) (2007) 853–866.
[11] T. Tezduyar, S. Sathe, Stabilization parameters in supg and pspg formulations, Journal of computational and applied mechanics 4 (1) (2003) 71–88.
[12] S. Mittal, On the performance of high aspect ratio elements for incompressible flows, Comput. Methods Appl. Mech. Engrg. 188 (2000) 269–287.
[13] A. V. Trofimova, A. E. Tejada-Martínez, K. E. Jansen, R. T. Lahey, Direct numerical simulation of turbulent channel flows using a stabilized finite element method, Computers & Fluids 38 (4) (2009) 924–938.
[14] A. N. Brooks, T. J. Hughes, Streamline upwind/petrov-galerkin formulations for convection dominated flows with particular emphasis on the incompressible navier-stokes equations, Computer methods in applied mechanics and engineering 32 (1) (1982) 199–259.
[15] T. Heister, G. Rapin, Efficient augmented lagrangian-type preconditioning for the oseen problem using grad-div stabilization, International Journal for Numerical Methods in Fluids 71 (1) (2013) 118–134.
[16] J. Ferry, S. Balachandar, A fast eulerian method for disperse two-phase flow, International Journal of Multiphase Flow 27 (7) (2001) 1199–1226.
[17] O. Simonin, Statistical and continuum modelling of turbulent reactive particulate flows, in: Theoretical and experimental modelling of particulate flow, von Karman Institute Lecture Series, 2000.
[18] L. Zaichik, N. Drobyshevsky, A. Filippov, R. Mukin, V. Strizhov, A diffusion-inertia model for predicting dispersion and deposition of low-inertia particles in turbulent flows, International Journal of Heat and Mass Transfer 53 (1) (2010) 154–162.
[19] M. R. Maxey, J. J. Riley, Equation of motion for a small rigid sphere in a nonuniform flow, Physics of fluids 26 (1983) 883.
[20] C. Clayton, S. Martin, T. Yutaka, Multiphase Flows with Droplets and Particles, CRC, 1997.
[21] Y. Ling, M. Parmar, S. Balachandar, A scaling analysis of added-mass and history forces and their coupling in dispersed multiphase flows, International Journal of Multiphase Flow 57 (2013) 102–114.
[22] V. Armenio, V. Fiorotto, The importance of the forces acting on particles in turbulent flows, Physics of Fluids 13 (8) (2001) 2437–2440. doi:10.1063/1.1385390.
URL http://link.aip.org/link/?PHF/13/2437/1
[23] A. Daitche, T. Tél, Memory effects are relevant for chaotic advection of inertial particles, Physical Review Letters 107 (24) (2011) 244501.
[24] K. Guseva, U. Feudel, T. Tél, Influence of the history force on inertial particle advection: Gravitational effects and horizontal diffusion, Physical Review E 88 (4) (2013) 042909.
[25] A. Daitche, Advection of inertial particles in the presence of the history force: Higher order numerical schemes, Journal of Computational Physics 254 (2013) 93–106.
[26] M. Van Hinsberg, J. ten Thije Boonkkamp, H. Clercx, An efficient, second order method for the approximation of the basset history force, Journal of Computational Physics 230 (4) (2011) 1465–1478.
[27] E. Calzavarini, R. Volk, M. Bourgoin, E. Lévêque, J.-F. Pinton, F. Toschi, et al., Acceleration statistics of finite-sized particles in turbulent flow: the role of faxén forces, Journal of Fluid Mechanics 630 (2009) 179.
[28] H. Homann, J. Bec, et al., Finite-size effects in the dynamics of neutrally buoyant particles in turbulent flow, Journal of Fluid Mechanics 651 (2010) 81.
[29] R. Codina, J. Principe, O. Guasch, S. Badia, Time dependent subscales in the stabilized finite element approximation of incompressible flow problems, Computer Methods in Applied Mechanics and Engineering 196 (21) (2007) 2413–2430.
[30] D. L. Marchisio, R. O. Fox, Solution of population balance equations using the direct quadrature method of moments, Journal of Aerosol Science 36 (1) (2005) 43–73.
[31] L. Zaichik, R. Mukin, L. Mukina, V. Strizhov, Development of a diffusion-inertia model for calculating bubble turbulent flows: Isothermal polydispersed flow in a vertical pipe, High Temperature 50 (5) (2012) 621–630.

Dynamics of Gas Jet Impingement on Vertical Falling Liquid Films

Miguel Alfonso Mendez

Environmental and Applied Fluid Dynamics Department, von Karman Institute for Fluid Dynamics, Belgium, mendez@vki.ac.be

Supervisor: Jean-Marie Buchlin

Professor, Environmental and Applied Fluid Dynamics Department, Belgium, buchlin@vki.ac.be

University Supervisor: Prof. Herman Deconinck

Professor, Aeronautics and Aerospace Department, von Karman Institute for Fluid Dynamics, Belgium, deconinck@vki.ac.be
Département d' Aéro-Thermo-Mécanique, Faculté des Sciences Appliquées, Université Libre de Bruxelles, Belgium

A turbulent plane gas jet impinging the interface of a thin liquid film is a flow topology encountered in many industrial coating processes, such as in the manufacturing photographic and video tape, the paint industry and the galvanization industry. Typically, the impinging jet has the role of controlling the final coating thickness on an upward moving substrate, which is previously dipped in a bath of liquid coat so that it drags along its surface a thin liquid flow.
The technique is known as gas jet wiping or air-knife coating. The process is continuous and does not require wearing surfaces in contact with the coating liquid, a key advantage in applications such as hot dip galvanizing, where the liquid coat is typically molten Zinc at a temperature of the order of 450 ^oC.
On the other hand, jet wiped products exhibit unevenness in the coating thickness, typically featuring low amplitude and long wavelength undulations. As the paint and coating industry evolves toward products with higher surface finish quality, more attractive from an ecological and economical point of view, such undulations are becoming a main industrial concern. Yet, despite being a major industrial stake, the hydrodynamic instability at the origin of the undulation is still far from being understood.
This project is part of a long-standing VKI research program in Jet Wiping technique, which has already achieved the development of simplified engineering models ([1]), the experimental investigation of different unsteady impingement conditions ([2]), and advanced CFD modeling ([3]) of the flow configuration. These works prove that undulations in the final coat are the results of an hydrodynamic instability of the impingement configuration which produces continuous oscillations of the wiping position. Furthermore, it has been proven that this *global* instability does not originate from any of the two flows taken separately but from their interaction. As the dynamic of the gas flow results to be tightly linked to that of the liquid flow, the phenomenon has been referred to as the *coupling instability*.
This project aims to understand the origins of this instability and seeks to propose a control strategy. In a preliminary work ([4]), a new VKI Facility, capable of reproducing the coupling instability, has been designed, constructed and tested. The flow interaction can now be studied experimentally: Light Absorption and LeDaR techniques will reveal the liquid film's dynamic while Flow Visualizations and Image processing techniques will be used to infer the characteristic jet's response. The data collected will be utilized in the design of a simplified numerical model where different solution strategies, includying nozzle design and multi-jet configurations will be analyzed. Finally, the most promising solution will be constructed and tested in the Ondule Facility, a VKI prototype of a real jet wiping line.

Keywords: Jet Wiping Coating, Thin Films Liquid, Flow Instabilities, Self-Sustained Jet Oscillation

References

[1] J-M.Buchlin, Modelling of Gas Jet Wiping, in: Thin Liquid Films and Coating Processes, VKI-Lecture Series, 1997.
[2] A.Gosset,J.M.Buchlin, Jet wiping in hot-dip galvanization, J.Fluids.Eng. 129 (4) (2006) 466–475.
[3] K. Myrillas,A.Gosset, P.Rambaud, J.M.Buchlin, CFD simulation of gas-jet wiping processes, Eur.Phys.J.Special Topics 166 (2009) 93–97.
[4] M.A. Mendez, Experimental Study of Gas Jet-Falling Liquid Film Interaction, von Karman Institute, RM Project Report, 2013.

Cavitation in Valves : Modeling and Experiments

Jorge Pinho

Environmental and Applied Fluid Dynamics Department, von Karman Institute for Fluid Dynamics, Belgium, pinho@vki.ac.be

Supervisor: Patrick Rambaud

Associate Professor, Environmental and Applied Fluid Dynamics Department, von Karman Institute for Fluid Dynamics, Belgium

Co-Supervisor: Jean-Marie Buchlin

Professor, Head of Department, Environmental and Applied Fluid Dynamics Department, von Karman Institute for Fluid Dynamics, Belgium

Industrial Promotor: Saïd Chabane

CETIM, Centre Technique des Industries Mécaniques, 74 route de la Jonelière, Nantes, France

Abstract

Previous experiments were conducted and reported in two different safety relief valves. It was noticed that in presence of cavitation, the mass flux tends to be reduced due to the two-phase mixture compressibility. The first goal of this study is to propose a mathematical model capable of predicting the mass flux of a valve experiencing cavitation at initial high subcooling conditions. An extension of the actual recommended sizing equations of IEC 60534-2-3 is proposed, including a formulation of the semi-critical region, based on the hypothesis that compressibility of a two-phase mixture may be considered as an ellipse. It is verified that at chocking flow conditions, the critical section is partially filled by vapor as the fluid velocity equals the local speed of sound.

In the second part of the research, optical measurement techniques are applied to characterize a challenging two-phase flow through a transparent model of a safety relief valve. Results of f-PIV show the existence of a submerged jet just downstream the geometrical section, with two non-symmetric shear layers at its sides. Under cavitation conditions, it is confirmed that vapor bubbles are formed in the shear layers, characterized by a higher vorticity content. Finally, the phenomenon of mass flow limitation is reproduced and interaction between cavitation and flow topology is highlighted and understood for the first time.

Keywords: cavitation, safety relief valve, two-phase flow, choked flow, f-PIV

NOMENCLATURE

a Dimensionless flow rate at cavitation inception q_m/q_{max} [-]
A_1 Upstream Section [m^2]
A_2 Downstream Section [m^2]
b Critical pressure ratio [-]
c Speed of sound [m/s]
c_1 Upstream speed of sound [m/s]
c_2 Downstream speed of sound [m/s]
$_{com}$ Compressible
K_V Flow coefficient [m^3/h]
F_h Hydrodynamic force applying on SRV disk [N]
F_L Liquid pressure recovery factor[-]
F_F Liquid critical pressure ratio factor[-]
h_r Local hydraulic resistance coefficient [-]
$_{inc}$ Incompressible
k Ratio of specific heats [-]
Ma_1 Upstream velocity ratio u_1/c_1 [-]
Ma_1 Downstream velocity ratio u_2/c_2 [-]
P Pressure [bar]
P_1 Upstream Pressure [bar]
P_2 Downstream Pressure [bar]
P_b Backpressure [bar]
P_c Thermodynamic critical pressure [bar]
P_{FZ} Pressure at cavitation inception [bar]
P_{sat} Saturation pressure at inlet temperature conditions [bar]

P_t Total Pressure [bar]
P_{vc} Pressure at the vena contracta [bar]
Q_{max} Maximum volumetric flow rate [m^3/h]
q_m Mass flow rate [kg/s]
q_{max} Maximum mass flow rate [kg/s]
R Universal gas constant [J/kg K]
R Radius [m]
S Section [m^2]
SRV Safety Relief Valve
T_1 Upstream Fluid Temperature [K]
u Velocity [m/s]
u_1 Upstream velocity [m/s]
u_2 Downstream velocity [m/s]
α Dimensionless flow coefficient [-]
β_0 Residual initial void fraction [-]
β_2 Void fraction at minimum cross section [-]
ΔP Pressure differential [bar]
ΔP_L Linear and singular Pressure drop [bar]
ΔP_s Systematic Pressure drop [bar]
η Pressure ratio P/P_1 [-]
η_{FZ} Incipient cavitation pressure ratio P_{FZ}/P_1 [-]
η_{vc} Pressure ratio at the vena contracta P_{vc}/P_1 [-]
ρ Fluid Density [kg/m^3]
ρ_0 Water density at 15.5 C and 1 bar. [kg/m^3]
ρ_1 Upstream fluid density [kg/m^3]
ρ_2 Downstream fluid density [kg/m^3]
ξ Auxiliary variable Eq. **??**
ζ Coefficient friction [-]

1. Introduction

Two-phase flows are present in daily-life and in numerous technical and industrial processes such as nuclear, chemical or mechanical engineering where different gas-liquid reactors, boilers, condensers, evaporators and/or combustion systems can be found. In nuclear and thermal engineering systems the use of SRV is mandatory since it protects them against any over pressure, representing the ultimate protection before an accident occurs. The complete understanding of the multi-physics taking place in the flow through a SRV is therefore important for the security of the protected process. In single phase flow such as liquid or gas discharge, reliable and well established methods are available for the SRV design. On the other hand, when the static pressure of an initially subcooled liquid falls below the saturation pressure, vapor bubbles will form which tend to locally reduce the medium speed of sound. Similarly to a compressible flow, this decrease of the speed of sound will be linked to a limitation on the mass flow evacuated and therefore, the single phase flow methodology becomes inadequate. There are some calculation methods available in literature, that attempt to predict the critical flow onset in SRV for two-phase systems knowing the inlet flow conditions and the outlet pressure; however none of them is acknowledged as being fully reliable in the entire domain of two-phase flow. In the current study a new model is proposed for the prediction of the mass flux through a SRV experiencing cavitation. This model is an extension of the actual recommended sizing equations of IEC 60534-2-3[1], including a formulation of the semi-critical region based on the hypothesis that compressibility of a two-phase mixture may be considered as an ellipse. The experimental database supporting the validation of the proposed model has been described and presented by the same authors[2]. For the present case, experiments performed on a API 2J3 SRV were considered. Instead of using a spring, the design of the valve was changed to allow the adjustment of the disk at any fixed desired lift, as illustrated in Figure 1. Measurements of flow rate were compared against the pro-

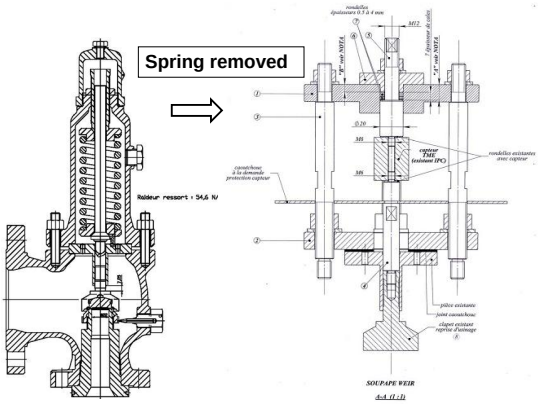

Figure 1: Drawing of the API 2J3 SRV tested[2].

1.1. IEC 60534-2-3

Different methodologies exist in the literature providing general guidelines to the sizing of SRV. The most widely known are the Homogeneous Equilibrium Models (HEM) and more recently the HNE-DS[3][4] model, integrating the thermodynamic and mechanical non-equilibrium in the two-phase flow formulation. However, these models are better suitable for the case of an initial void content at inlet conditions, resulting in the well known Bernoulli equation for the case of a high subcooled flow experiencing vaporization at the critical section. In such conditions, the formulation adopted by the international standard

IEC 60534-2-3[1] seems to be more reliable since it is assumed that at inlet conditions the flow is mainly incompressible. It defines several criteria for the proper sizing of a control valve, by providing testing procedures for the determination of functional parameters, such as the flow coefficient K_V and the liquid recovery factor F_L. The flow rate of an incompressible fluid through a valve is normally defined as a function of $\sqrt{\Delta P}$ for a constant upstream pressure, as it is shown in Figure 2.

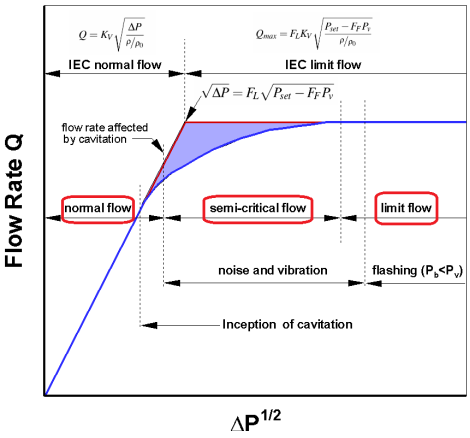

Figure 2: Flow rate diagram of an incompressible fluid through a valve according to IEC 60534-2-3[1].

This function can be divided into three distinct regions:

Normal flow: the flow rate is proportional to $\sqrt{\Delta P}$. This region is established while there is no limitation on the flow rate due to the cavitation.

Semi-critical flow: the flow rate increases with the increment of $\sqrt{\Delta P}$ but not linearly. In this region, the valve capacity in converting pressure loss into flow rate is reduced, due to the liquid vaporization and consequently cavitation. Although cavitation starts in the normal flow region, the bubble nucleation only becomes permanent at the beginning of the semi-critical flow in which the flow rate becomes limited.

Limit flow or choked flow: the flow rate becomes constant and limited even with further increment of $\sqrt{\Delta P}$. In case the downstream pressure is less than the saturation pressure, vaporization and flashing phenomenon occurs.

Sizing equations recommended by IEC 60534-2-3[1] take into account the shadow area of Figure 2, since they neglect the semi-critical flow region. The parameter that defines the beginning of the critical flow region is the liquid pressure recovery factor F_L, originally proposed by Baumann[5], and that depends on the valve body geometry. Its value represents the capacity of the valve in transforming the fluid kinetic energy in pressure, in the vena contracta region. It is defined by:

$$F_L = \sqrt{\frac{P_1 - P_2}{P_1 - P_{vc}}} \tag{1}$$

Due to the difficulties of measuring the pressure in the vena contracta P_{vc} with high accuracy, this factor is normally determined in critical flow conditions, being only dependent on the maximum flow rate Q_{max} for a given upstream pressure P_1. With fixed inlet conditions, choked flow is evidenced by the failure of increasing pressure differentials to produce further increases in the flow rate and therefore, Eq. (1) is replaced by:

$$F_L = \frac{Q_{max}}{K_V}\sqrt{\frac{\rho/\rho_0}{P_1 - F_F P_{sat}}} \tag{2}$$

The liquid critical pressure ratio factor F_F introduced in Eq. (2) is the ratio between the pressure in the vena contracta and the saturation pressure in a choked flow regime. In experiments performed by Stiles[6], the author has remarked that vaporization of the liquid starts below the saturation pressure of the fluid. The following relation was proposed:

$$F_F = 0.96 - 0.28\sqrt{\frac{P_{sat}}{P_c}} \tag{3}$$

For the case of water at ambient temperature, this factor reduces to F_F=0.96.

1.2. Choked flows

A flow is said critical, limited or choked when the mass flow becomes independent of the downstream flow conditions (Shapiro[7]). Typically when a flow is choked in a pipe connecting two vessels at different pressures, any further decrease of the pressure in the downstream vessel does not result in a change of the mass flow rate. This limit, which corresponds to the maximum flow rate between both vessels, exist because the acoustic signal related to the pressure decrease can no longer propagate upstream of the critical section. This condition occurs when the flow velocity reaches the propagation velocity or the speed of sound[8].

In the present study, the prediction of the critical flow condition is based on the hypothesis that the flow compressibility may be approximated by the geometrical form of an ellipse. As proposed by Chabane[9] for the case of a purely compressible flow, this approximation gives very satisfactory results for most of the pneumatic components used in industry. Calculated mass flow rates using this formulation have shown a good agreement against experimental data obtained with pipes for several diameters and lengths, even for variable upstream pressure conditions. As illustrated in Figure 3, this model assumes that for very small pressure ratios ($\eta \approx 1$), the flow is mainly incompressible and the derivative of q_m/q_{max} tends to infinity. On the other hand, when the flow reaches its critical point, the flow rate is maximum and therefore, the derivative

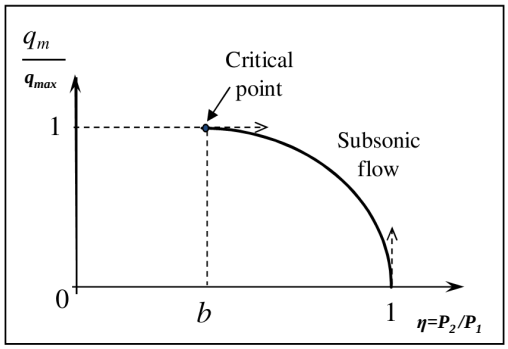

Figure 3: Elliptic shape of mass flow rate ratio for most of pneumatic components for constant upstream conditions[9].

1.3. Optical techniques in cavitation

During the last years, an increase of PIV measurement techniques have been developed and applied for two phase flows. In order to suppress the intense reflections at the liquid/gas interface the standard PIV has been replaced by fluorescent Particle Image Velocimetry (f-PIV). This adaptation for two-phase flows uses fluorescence-emitting particles. The emission occurs with a different wavelength from the light excitation source. Using the appropriate optical filter, liquid and gas phase can be separated without any disturbance from the light source. This approach has been recently used by Iliescu[10] on the analysis of a cavitating draft tube vortex in a francis turbine, where two cameras were used simultaneously. The first camera had an antireflection-coated filter, focused on the laser wavelength, to record the reflections in the laser light from the cavitation rope/water interface; while the second camera had a cut-off filter on the emission wavelength of fluorescent particles. The vortex core boundary was extracted by image processing of the first camera image and the velocity field was extracted of the second camera image.

2. Modeling

Following the same reasoning applied in the case of a purely compressible flow[9], one may considers that the compressibility of a two-phase flow is also governed by the geometrical form of an ellipse.

2.1. Ellipse approach

It is important to notice that at initial high subcooling conditions (where only liquid phase is present), the flow is essentially incompressible and therefore is governed by the well known Bernoulli equation, which for the present case, will be applied from an inlet pressure P_1, velocity u_1 and section A_1, through a convergent with outlet pressure P_2, velocity u_2 and section A_2:

$$P_1 + \rho\frac{{u_1}^2}{2} = P_2 + \rho\frac{{u_2}^2}{2} + \Delta P_L \tag{4}$$

Both linear and singular pressure drops are included in the last term ΔP_L, being function of the coefficient friction ζ:

$$\Delta P_L = \zeta\rho\frac{{u_2}^2}{2} \tag{5}$$

From mass conservation, Eq. (4) can be rewritten as function of the mass flow rate q_m:

$$\Delta P = P_1 - P_2 = \frac{{q_m}^2(1 - {A_2}^2/{A_1}^2 + \zeta)}{2\rho{A_2}^2} \tag{6}$$

For the purpose of simplification, the dimensionless flow coefficient α will be defined as:

$$\alpha = \sqrt{\frac{1}{1 - {A_2}^2/{A_1}^2 + \zeta}} \tag{7}$$

Finally, by re-arranging the above equations and substituting $\Delta P = P_1(1 - \eta)$, the mass flow rate of an incompressible fluid is simply given by:

$$q_m = A_2\alpha\sqrt{2\rho P_1(1 - \eta)} \tag{8}$$

The flow at initially subcooling conditions passing through a convergent will remain incompressible till the occurrence of liquid vaporization. This condition

is normally identified by the incipient cavitation pressure ratio η_{FZ}:

$$\eta_{FZ} = \frac{P_{FZ}}{P_1} \tag{9}$$

For pressure ratios $\eta < \eta_{FZ}$, the flow will experience vaporization and therefore, compressibility has to be taken into account. Similar to the case of a purely compressible flow, the geometrical curve of an ellipse is proposed for this region as illustrated in Figure 4, where the mass flow rate is rendered dimensionless relatively to its maximum.

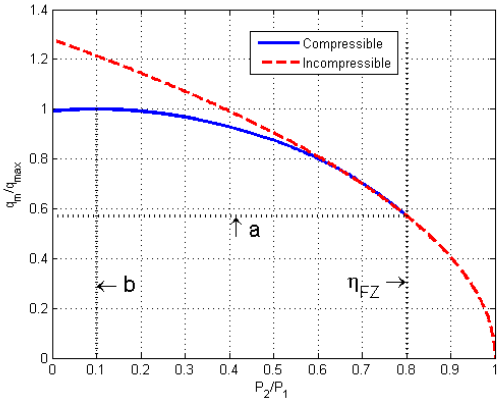

Figure 4: Modeling of two-phase flow as an ellipse.

As evidenced in Figure 4, the equation of an ellipse can be simply defined by 3 different points: a, b and η_{FZ}. The variable a corresponds to the flow rate at cavitation inception; and the variable b represents the critical pressure ratio in which $q_m/q_{max} = 1$. The following equation of an ellipse is retrieved:

$$q_m = q_{max}\sqrt{1 - \frac{(\eta - b)^2(1 - a^2)}{(\eta_{FZ} - b)^2}} \tag{10}$$

At the cavitation inception pressure ratio η_{FZ}, both incompressible and compressible formulations should result in the same mass flow rate. By equaling Eq. 8 to Eq. 10, and substituting η=η_{FZ}, the maximum flow rate q_{max} can be determined:

$$q_{max} = \frac{A_2\alpha\sqrt{2\rho P_1(1 - \eta_{FZ})}}{a} \tag{11}$$

To correctly define the ellipse, both the variables a, b and η_{FZ} have to be known. This means three additional relations should be set. At the cavitation inception point $\eta = \eta_{FZ}$, a condition of tangency can be defined between the incompressible and compressible curves:

$$\left(\frac{\partial(q_m/q_{max})_{inc}}{\partial\eta}\right)_{\eta=\eta_{FZ}} = \left(\frac{\partial(q_m/q_{max})_{com}}{\partial\eta}\right)_{\eta=\eta_{FZ}} \tag{12}$$

Solving the derivatives of Eq. 12, the first relation is retrieved for the variable a:

$$a = \sqrt{\frac{2(\eta_{FZ} - 1)}{(b + \eta_{FZ} - 2)}} \tag{13}$$

Concerning the second relation, one needs to recall the definition of the liquid recovery factor F_L,

$$F_L = \sqrt{\frac{P_1 - P_2}{P_1 - P_{vc}}} = \sqrt{\frac{1 - \eta}{1 - \eta_{vc}}} \tag{14}$$

It is well known that the liquid recovery factor F_L is the projection point of the maximum flow rate against the incompressible one given by Eq. 8. Therefore, one gets:

$$q_m = q_{max} \Leftrightarrow (1 - \eta_{FZ}) = a^2(1 - \eta) \tag{15}$$

By replacing the previous relation in the definition of F_L from Eq. 14, the second relation of the ellipse is retrieved:

$$(1 - \eta_{FZ}) = {F_L}^2 a^2(1 - \eta_{vc}) \tag{16}$$

At this moment, a third relation is needed for the critical pressure ratio b. The solution proposed hereafter is based on the application of mass conservation in a two-phase flow passing through a convergent:

$$\rho_1 u_1 A_1 = \rho_2 u_2 A_2 \Leftrightarrow \rho_1 Ma_1 c_1 A_1 = \rho_2 Ma_2 c_2 A_2 \tag{17}$$

Taking into account the definition of Mach number $Ma = u/c$ and replacing the expressions of the maximum flow rate derived in Eq. 11, the following relation apply for a critical condition at the outlet ($Ma_2 = 1$):

$$\rho_2 c_2 = \frac{\alpha}{a}\sqrt{2P_1\rho_1(1 - \eta_{FZ})} \tag{18}$$

Eq. 17 and Eq. 18 introduce 2 new unknowns in the system (ρ_2 and c_2). Therefore, additional relations have to be defined concerning the variation of the fluid mixture density and speed of sound towards the critical pressure ratio. Assuming that the gaseous phase present in the mixture behaves as a perfect gas, and it expands polytropically $\left(\rho^k \propto P\right)$ from a residual initial void fraction β_0 to the actual void fraction β_2 located

at the minimum cross section, Liuzzi [11] proposed the following relations:

$$\rho_2 = \rho_1 \frac{(1-\beta_2)}{(1-\beta_0)} \tag{19}$$

$$\frac{1}{{c_2}^2} = \frac{\beta_2}{kP_{sat}}\left[\rho_1(1-\beta_2) + \frac{P_{sat}}{RT_1}\beta_2\right] \tag{20}$$

Where k is the ratio of specific heats for vapor and the last term of Eq. 20 can be simply retrieved by the definition of an homogeneous flow:

$$\rho_2 = \rho_1(1-\beta_2) + \frac{P_{sat}}{RT_1}\beta_2 \tag{21}$$

Please notice that the above relations assume that the vapor phase is always at equilibrium, i.e., at saturation pressure P_{sat} conditions. Finally, the critical pressure ratio b is then given by:

$$b = \frac{P_2}{P_1} = \left[\frac{\beta_0\rho_2}{\rho_1 - (1-\beta_0)\rho_2}\right]^k \tag{22}$$

The set of 5 relations derived in Eq. 18, Eq. 19, Eq. 20, Eq. 21 and Eq. 22 can be solved to determine the critical pressure ratio b. Typically, for water at ambient temperature this system reduces to $b \approx 0$, meaning that the flow will only attend critical conditions if the backpressure is lowered to the saturation pressure, which is extremely difficult to obtain experimentally at room conditions. Nevertheless, the same criterion is foreseen by the European normative ISO 4126-10[12] when the flow conditions fall in the high subcooling case.

This model is an extension of the actual recommended sizing equations of IEC 60534-2-3[1], which originally do not include any formulation at the semi-critical region. The proposed model can be easily set in a numerical routine to solve simultaneously 9 equations with 9 unknowns, as summarized in Table 1.

In order to evaluate the robustness of the proposed model, a simple test case is presented for a liquid flow through a convergent with minimum section diameter of $22mm$. As initial conditions, an upstream pressure $P_1 = 3.0bar$ and temperature $T_1 = 293K$ were defined. Regarding the experimental inputs, it was considered a flow coefficient $K_V = 2$ and $F_L = 0.8$. The dimensionless flow coefficient α can be simply retrieved by:

$$\alpha = \frac{K_V}{3600A_2}\sqrt{\frac{\rho_1}{2\cdot 10^5}} \tag{23}$$

Inputs	Model 9 Equations	Outputs
Experimental	Eq. 10	q_m
K_V, F_L	Eq. 11	q_{max}
Geometrical	Eq. 13	a
A_2	Eq. 16	η_{FZ}
Initial Conditions	Eq. 18	ρ_2
P_1, $P_{sat}(T_1)$, η	Eq. 19	β_0
	Eq. 20	c_2
$\alpha(K_V, A_2, \rho_1(T_1))$	Eq. 21	β_2
Eq. 23	Eq. 22	b

Table 1: Equations system of the proposed two-phase ellipse model.

Equations detailed in Table 1 were then solved according to the proposed model, at different pressure ratios η to cover the entire flow regimes. Results presented in Figure 5 were rendered dimensionless for the sake of clarity. These results illustrate well the improvement of the ellipse model against the original IEC 60534-2-3[1] recommended sizing equations. In the region of semi-critical flow, the ellipse modeling takes into account the two-phase fluid compressibility, while the original IEC 60534-2-3 equations simply project the maximum flow rate to the incompressible linear part (normal flow region). Furthermore, the present model allows to determine the void fraction β_2 at the minimum geometrical section. For the tested initial conditions, it is found that the flow experiences vaporization at $\sqrt{1-\eta_{FZ}} = 0.51$ and becomes choked for a void fraction of $\beta_2 = 0.58$.

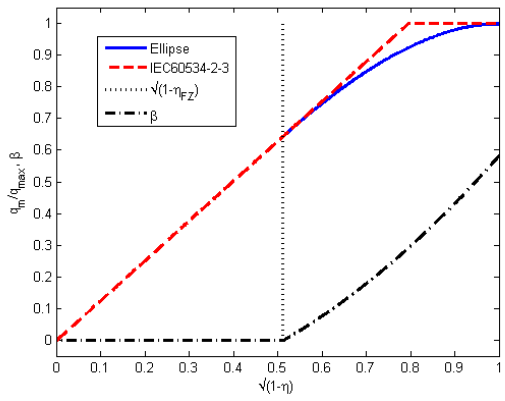

Figure 5: Comparison between the proposed ellipse modeling and IEC 60534-2-3[1] recommended equations - test case.

In fact, the chocking flow condition occurs when the critical section is still partially filled by the liquid

phase. This can be explained by the sudden decrease of the speed of sound when the liquid experiences vaporization as evidenced in Figure 6(a) and Figure 6(b).

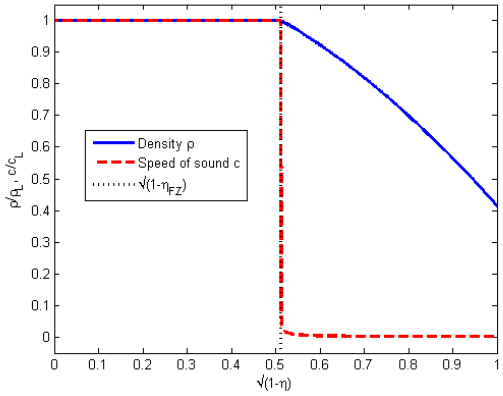

(a) Density and speed of sound evolution.

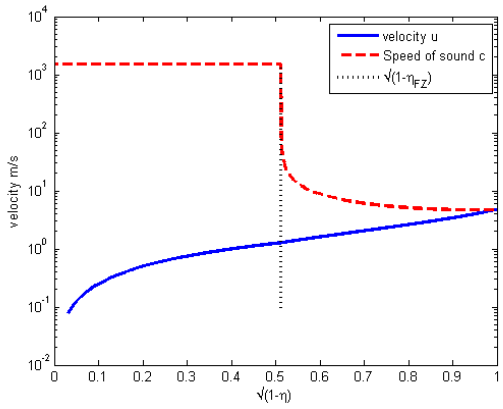

(b) Comparison between fluid velocity and mixture speed of sound.

Figure 6: Flow variables of the proposed ellipse model.

The comparison between the proposed model against available experimental data of a SRV is presented in the following subsection.

2.2. *Results and discussion*

Experimental data obtained for the API 2J3 SRV at a fixed lift of 5.0mm is used for the validation of the present model, and is presented in Figure 7(a) as function of the squared pressure drop. Measurements were performed at different inlet pressure conditions: 6.0bar, 8.0bar and 9.5bar. The influence of the upstream pressure is well evidenced in this plot in the critical flow region. On the other hand, for smaller pressure drops the flow remains liquid and therefore, the incompressible relation given by Bernoulli equation applies. The overall deviation of the proposed model against experimental data is shown in Figure 7(b), and was found to be less than 1.1% for the data considered.

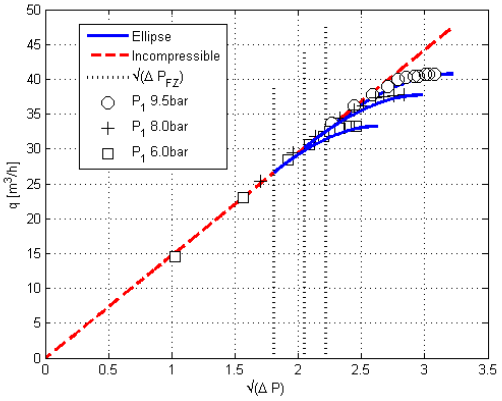

(a) Comparison of the proposed model against experimental data.

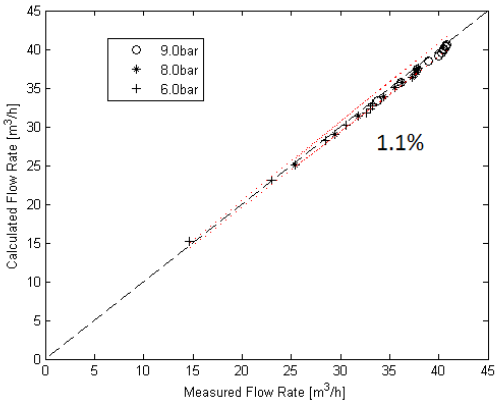

(b) Overall deviation of the proposed model against experimental data.

Figure 7: Evaluation of the ellipse model against experimental data on API 2J3 SRV at fixed lift 5.0mm

It is important to enhance that the proposed model still requires experimental data (flow coefficient K_V and the liquid recovery factor F_L) for the proper valve sizing. The reproduction of the liquid compressibility is evidenced in the ellipse modeling. However, no theoretical evidence has been shown so far, that the curve of an ellipse may reproduce correctly a two-phase flow. The proposed model is seen as an improvement of the existent sizing equations recommended by the international standard IEC 60534-2-3[1].

3. Experiments

Following a similar approach proposed by Iliescu [10], an experimental campaign is performed by means of optical techniques. The goal is to characterize a challenging flow experiencing cavitation in a safety relief valve.

3.1. Experimental setup

A FlowMaster 2D PIV system is used for measuring the two-dimensional unsteady velocity fields. As illustrated in Figure 8, the light is generated by a double pulsed Nd:YAG EverGreen laser system delivering 100mJ per pulse. A laser sheet with thickness of 1mm is adjusted by passing the light through a cylindrical and spherical lenses. Two charge couple device (CCD) ImagerProSX cameras are used to visualize the illuminated zone, with a series of 300 paired images acquired at a frequency of 15Hz with a 18μs time delay. Both cameras resolution are 2500×1700pixels^2 for a 60×40mm^2 spatial domain. To focus both cameras on the same area, a beam splitter is used. The first camera uses a 532 ± 10*nm* pass-band filter, selecting on the laser wavelength, and a polarizer to attenuate the light intensity. The second camera has a stop-band filter (532 ± 5*nm*) allowing to separate the fluorescent seeding particles emission. The two cameras are synchronized (PTU, Figure 8) with the luminous flashes and then simultaneously exposed. The vector processing is performed with LaVision DaVis 8 commercial software, based on the cross-correlation technique. The shape of the cavitation bubbles is determined through image processing from the first camera, while unsteady velocity fields are obtained from the second one.

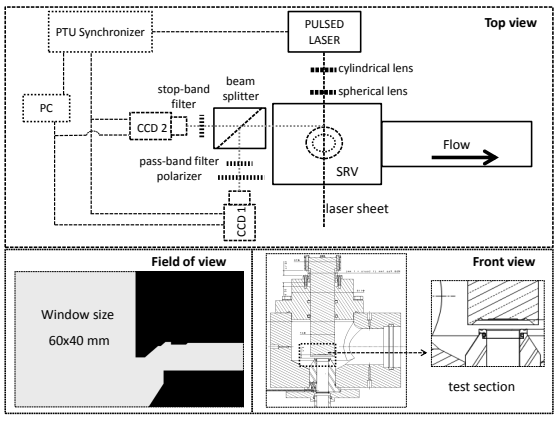

Figure 8: Optical Setup for f-PIV measurements.

Measurements are performed at different cavitation and opening conditions of the valve. The experimental test matrix is summarized in Table 2.

Valve opening	Upstream	Downstream	Points
3.0 mm			7
4.0 mm	P_1	P_2	7
5.0 mm	2.5barg	-0.5~1.0 barg	7
8.0 mm			7

Table 2: Experimental test matrix.

3.2. Calibration

For the proper evaluation of the 2D displacement of the particles, and a correct overlapping of images taken from both cameras, a calibration of the two fields of view is necessary. The camera calibration consists in defining the coefficients of a third order polynomial function that relates the real spatial locations in the measurement plane to the corresponding positions in the recording one. This function includes the geometrical and optical characteristics of the cameras setup, taking into account optical distortions, lens aberrations and interposed media with different refractive indices (water, polymethylmethacrylate (PMMA), and air). By acquiring images of a target with well specified spatial markers, their corresponding positions in the image plane are known, and thus the polynomial coefficients can be determined.

The calibration is performed by placing a 2D metallic target 120×120mm^2 with 28×9 equidistant holes (2mm diameter), in the measurement plane position. The test section is then filled with water for reproducing the optical configuration during measurements. Both cameras are focused on the target and the calibration images are acquired. The laser sheet is then aligned with the target surface and finally the valve disk is placed without modifying the optical arrangement. Figure 9 shows the sum of both images acquired, after the calibration correction has been applied. The maximum deviation of the calibration was found to be 1.84 pixel and 2.00 pixel for the first and second camera, respectively.

These values are in agreement with the ones recommended in the literature [13], for the present cameras resolution.

3.3. Seeding intrusiveness

Fluorescent red polyethylene microspheres are used as seeding particles, with an emission peak at 605nm.

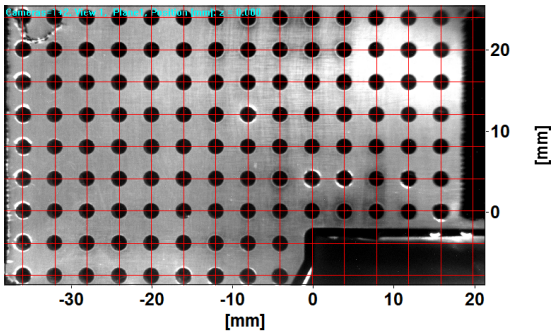

Figure 9: Sum of corrected images taken by both cameras.

The concentration of particles inside the facility is around 20g per 1000 liter of water. The relative density of 0.995 against the water one and the range size of 53-63μm allow these particles to accurately follow the flow. In order to evaluate the particles intrusiveness against the cavitation occurring in the test section, two different criteria are defined and reported in Figure 10: the flow rate and the noise produced by the flow passing through the valve.

Both criteria are measured before and after the particles seeding, at different valve openings and cavitation conditions. It is shown that particles do not have a significant influence on the cavitation phenomenon. Both the flow rate and unsteady pressure measurements, presented in Figure 10(a) and Figure 10(b) respectively, confirm this independence for the different valve openings and cavitation conditions. This can be explained by the low particle concentration used in the present experiments, which does not increase significantly the number of cavitation nucleation sites. Furthermore, the seeding particles range size of 53-63μm is well above experimental data reported in the literature [14], that promotes significantly the cavitation inception (less than 10 μm).

Another important remark concerning the seeding intrusiveness, is the spatial location of both particles and vapor bubbles. In certain experiments, it is found that both bubbles and particles (captured by two different cameras) are visible in the same region, as enhanced in Figure 11.

Physically, the existence of particles inside the bubble is not possible for two main reasons: 1) The nucleation site is much smaller than the particles size; 2) The bubble inception tends to expel its surroundings so the particle is more probable to be pushed by the bubble rather than be present inside it. The most suitable explanation for the results presented is the fact

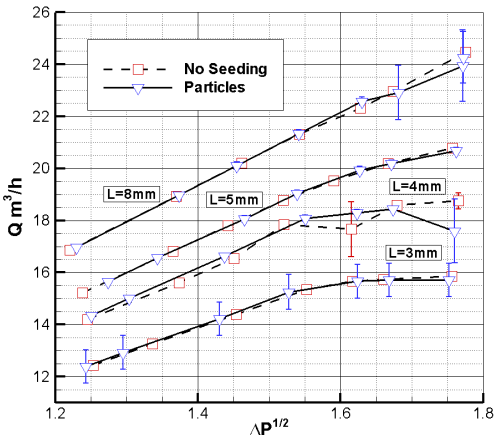

(a) Influence of seeding particles on the flow rate.

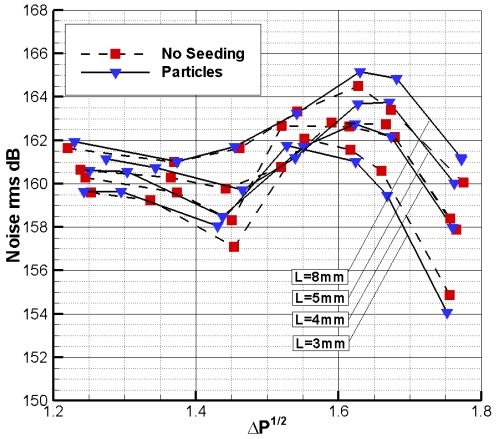

(b) Influence of seeding particles on the noise level

Figure 10: Analysis on the particles seeding intrusiveness.

that bubbles registered from camera 1 (Figure 11(a)) are located between the laser sheet and the camera, while the particles taken from camera 2 (Figure 11(b)) are mainly those on the laser sheet. This supports why such behaviour is not evidenced in all the experiments. Due to the highly unsteadiness of the cavitation inception, bubbles can be formed outside the laser region and be illuminated by the light reflection coming from particles or even from other bubbles present in the flow.

3.4. Data Processing

The two cameras images are processed separately. The distortion correction is performed to both cameras images with the calibration transform prior to processing. The camera 1 images are processed to extract the

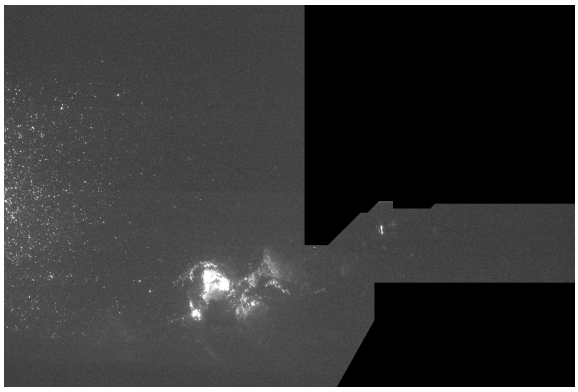

(a) Cavitation structure taken from CCD 1.

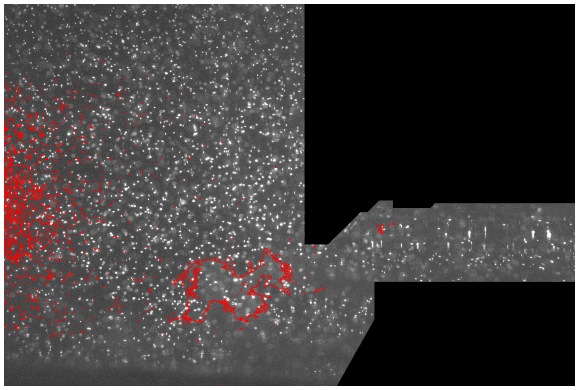

(b) Particle image taken from CCD 2, enhancing vapor regions reconstructed from camera 1.

Figure 11: Interaction between seeding particles and vapor bubbles.

vapor phase, by averaging the intensity levels of all the images taken at a given experimental point. Then, the contrast is amplified by histogram analysis and finally the image is rendered binary through the definition of a threshold. On the other hand, camera 2 images are processed to extract the liquid velocity fields. The instantaneous velocity field is retrieved by cross correlation of the two frames. Results are filtered by local mean value and peak (the relative height of the highest cross correlation peak compared to the second highest is chosen 1.5) validation criteria. An example of instantaneous velocity field is presented in Figure 12 for the case of single phase flow at 8mm opening of the valve. Statistical convergence is reached with 200 velocity fields for 5% uncertainty.

3.5. Flow analysis

It is noticed from the instantaneous velocity fields, that the flow presents significant instabilities downstream the geometrical section for both the liquid and

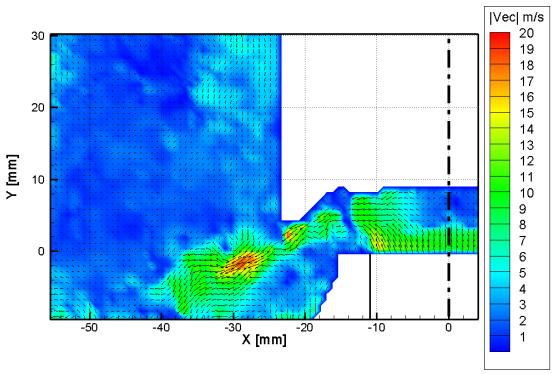

Figure 12: Instantaneous velocity field for single phase flow.

cavitation experiments. Unfortunately, the characterization of such instabilities in the frequency domain is not possible at the moment, since it requires time resolved data which is not available. Therefore, the analysis presented hereafter is based on statistical convergence of the data obtained from the ensemble of instantaneous velocity fields. Results presented in Figure 13 refer to the mean velocity and rms measured at 5.0mm opening of the valve, for single phase and cavitating flow conditions.

Results reveal the flow topology through the valve. The existence of a liquid jet downstream the critical section is evident from the chart of the velocity magnitude. This region is characterized by a high rms present in the velocity measurements which can lead to turbulence intensities up to 50%. It is concluded that such high levels can not be consequence of turbulence but rather on instabilities present on the flow downstream the critical section, which were already discussed in the instantaneous velocity field given in Figure 12. For the moment, the analysis will focus on the main differences of the flow topology between a single phase and cavitating flow. It can be seen that the maximum velocity increases considerable between the two operative conditions. This feature was already predicted by the proposed model in Figure 6(b). Furthermore, the location of the maximum velocity is shifted upstream towards the critical section. As a consequence, the liquid jet downstream the valve tends to be much larger due to mass conservation that has to be respected along the flow path. Concerning the rms, it is evident from the above results that instabilities of the flow tend to increase with the velocity. Velocity profiles were integrated through the axisymmetric domain to check the measurment uncertainty on the mass flux. Results are in agreement with the flux measured by a flow meter located

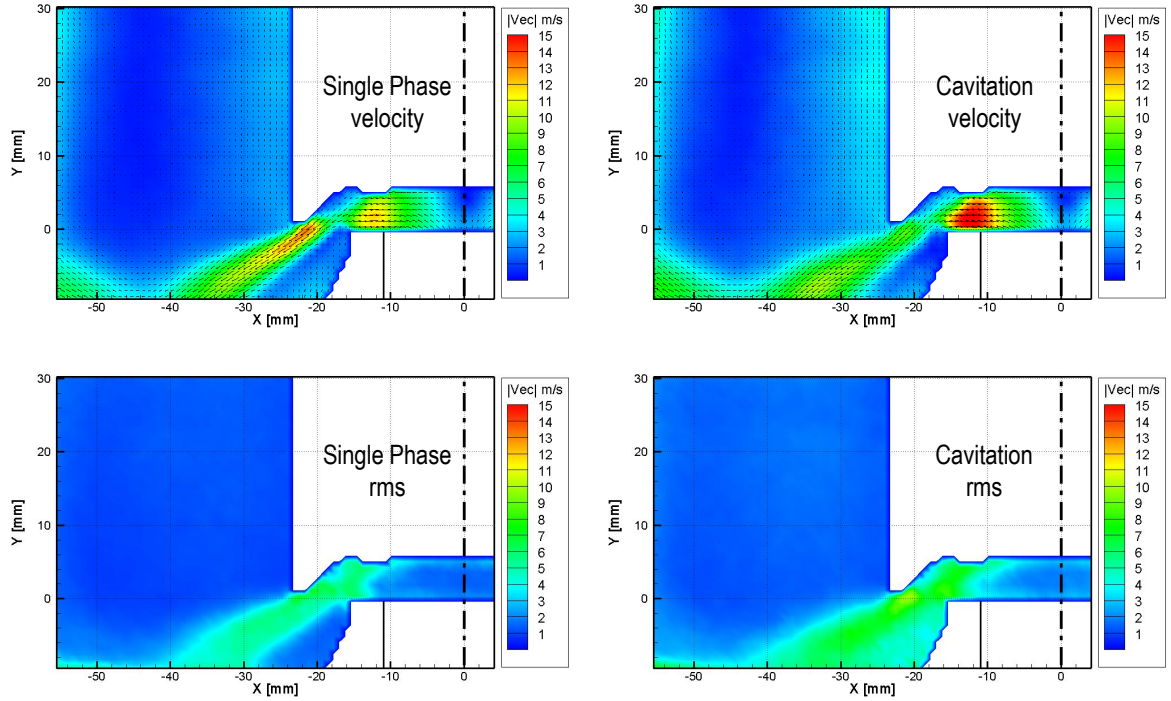

Figure 13: Mean velocity and rms fields for single phase and cavitating flow. Valve opening 5.0mm.

upstream of the test section.

After changing direction due to the presence of the disk, the flow enters the chamber with large recirculation areas from both sides and consequent vortices generation. In order to detect the location of the shear layers the absolute value of the vorticity is computed. Results of vorticity fields are shown in Figure 14, as well the light intensity captured from the first camera for single phase and cavitating flow conditions.

It is shown the presence of two non-symmetric shear layers located downstream the valve. Under cavitation conditions, it is confirmed that vapor bubbles are formed in the shear layers, characterized by a high vorticity. These results are in agreement with the predictions of the proposed model, in which critical flow conditions are obtained with the geometric section partially filled by vapor.

4. Conclusions

A new model is proposed for the prediction of the mass flux passing through a valve experiencing cavitation. This model is an extension of the actual recommended sizing equations of IEC 60534-2-3, including the formulation of the semi-critical region which is currently neglected by the same standard. Calculated flow rates confirm a good agreement against experimental available data. Furthermore, the proposed model allows to determine at which void content, the flow becomes choked. The model still requires both the flow coefficient and liquid recovery factor to be determined experimentally. The reproduction of the liquid compressibility is evidenced through the ellipse modeling. This model aims to be an important improvement on the current methodology adopted by IEC 60534-2-3.

Then, experimental results by means of optical techniques are presented and discussed. The use of fluorescent particles have proved their effectiveness in the results obtained, without interfering with the dynamics of the cavitation phenomenon. The velocity field shows a topology of the flow similar to a jet, characterized by a high velocity in the center and shear layers on both sides of the jet. The comparison between single phase and cavitation flow conditions reveals an important increase on the maximum velocity and consequent instabilities. Finally, it is concluded that limitation of the mass flux is occurring when the geometric section is still partially filled of vapor.

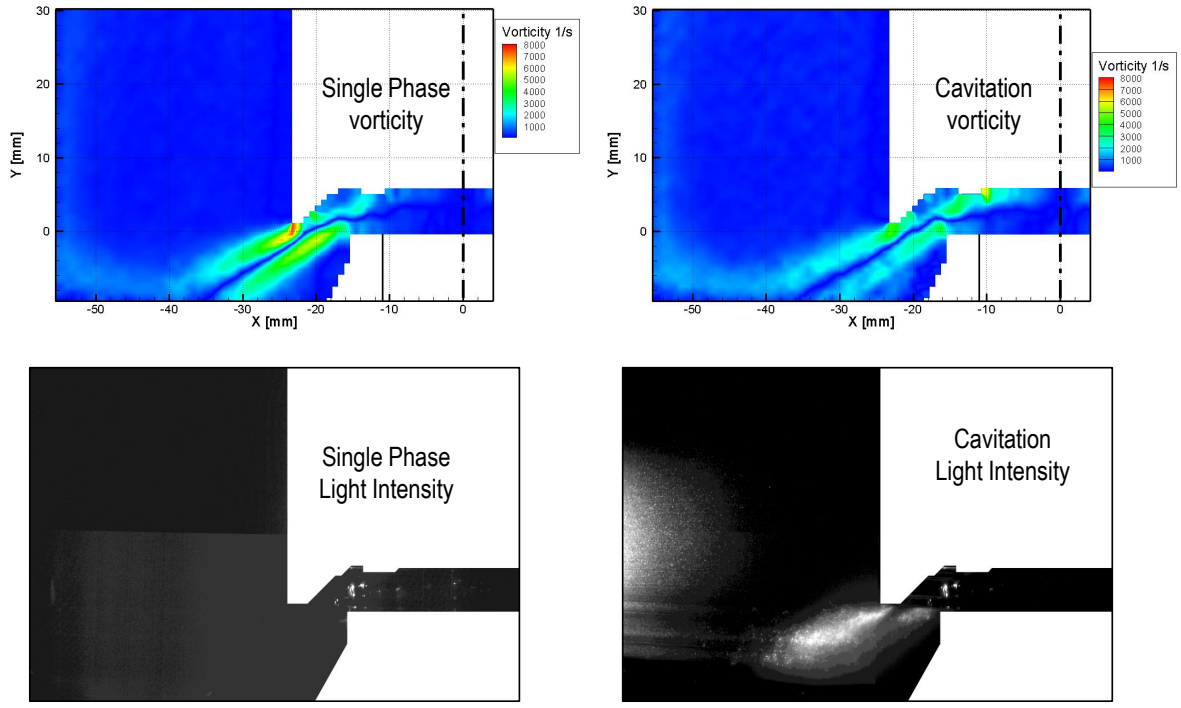

Figure 14: Vorticity field and vapor content from light intensity for single phase and cavitating flow. Valve opening 5.0mm.

Acknowledgments

The authors would like to thank Giuseppe Caridi for his contributions in the experimental work presented in this paper.

The financial support of the French company CETIM (Centre Technique des Industries Mécaniques) situated in Nantes, France is gratefully acknowledged.

References

[1] IEC 60534-2 3, Control valve capacity test procedures (1997).

[2] J. Pinho, P. Rambaud, S. Chabane, Experimental study of two-phase flow induced by cavitation through a safety relief valve, Proceedings of ASME 2013 Pressure Vessels Piping Division Conference.

[3] R. Diener, J. Schmidt, Sizing of throttling device for gas-liquid two-phase flow part1: Safety valves, Process Safety Progress Vol. 23, No.4 (2004) 335–344.

[4] R. Diener, J. Schmidt, Sizing of throttling device for gas-liquid two-phase flow part 2: Control valves, orifices and nozzles, Process Safety Progress Vol. 24, No.1 (2005) 29–37.

[5] H. D. Baumann, The introduction of a critical flow factor for valve sizing, ISA Transactions Vol. 2 (1963) 107–111.

[6] G. Stiles, Cavitation and flashing considerations, ISA Handbook of Control Valves. 2nd Edition by Hutchinson, J.W. (1976) 206–211.

[7] A. Shapiro, The dynamics and thermodynamics of compressible fluid flows, Ronald Press.

[8] Y. Bartosiewicz, Modeling of two-phase choked flows, Flow Characteristics and Performance of Safety Valves. Lecture Series 2013-08, von Karman Institute for Fluid Dynamics.

[9] S. Chabane, S. Sesmat, D. Hubert, D. Gautier, C. Wartelle, E. Bideaux, Mass flow rate of pneumatic pipes using friction factor, Journal of Systems and Control Engineering.

[10] G. Ciocan, M. Iliescu, The Particle Image Velocimetry - Characteristics, Limits and Possible Applications, InTech, 2012.

[11] D. Liuzzi, Two-phase cavitation modelling, Ph.D. thesis, Faculty of Cicil and Industrial Engineering, University of Rome, La Sapienza (2012).

[12] ISO 4126-10, Safety devices for protection against excessive pressure – Part 10: Sizing of safety valves and connected inlet and outlet lines for gas/liquid two-phase flow (2006).

[13] FlowMaster Getting Started, Product Manual 1105011-4 for DaVis 8.1, La Vision (2013).

[14] C. E. Brennen, Fundamentals of Multiphase Flows, 2005.

Sloshing Dynamics in Partially Filled Cylinder Subjected to Horizontal Sinusoidal Excitations

Alessia Simonini

Environmental and Applied Fluid Dynamics Department, von Karman Institute for Fluid Dynamics, Belgium, simonini@vki.ac.be

Supervisor: Maria Rosaria Vetrano

Associate Professor, Environmental and Applied Fluid Dynamics Department, von Karman Institute for Fluid Dynamics, Belgium, vetrano@vki.ac.be

University Supervisor: Pierre Colinet

Professor, Fluid Physics - Transfer Interfaces and Processes Department, Université Libre de Bruxelles, Belgium, pcolinet@ulb.ac.be

Abstract

The asymmetric water sloshing in a partially filled circular cylindrical container subjected to horizontal harmonic excitations is investigated. The understanding of this phenomenon is fundamental for the design of propellant management devices. The dynamic response of the moving liquid inside the tank can dramatically influence the trajectory of vehicles. Above all, the behaviour of the free liquid surface is of major interest. The analytical and equivalent mechanical models of the simplified undamped problem are introduced. The asymmetric sloshing is controlled by the liquid depth, forcing frequency and amplitude. Fluorescent Particle Image Velocimetry is used to investigate the velocity field in the liquid phase. The f-PIV is phase locked with a selected phase of the external excitation in order to provide statistical data. Results are shown and a first comparison with the aforementioned analytical theory is given.

Keywords: sloshing, f-PIV, fluorescence, circular cylinder, mechanical model, undamped, free surface

NOMENCLATURE

Bo Bond number [-]
F External excitation frequency [Hz]
f Natural frequency [Hz
f-PIV Fluorescent Particle Image Velocimetry
g gravitational acceleration [m/s^2]
Ga Galilei number [-]
m subscript for diametral nodes [-]
n subscript for circumferential nodes [-]
PIV Particle Image Velocimetry
h Liquid level [cm]
r Polar coordinate coordinate(see fig.1) [mm]
R Radius of the sloshing cell [cm]
Re Reynolds number [-]
T Period [s]
t Time [s]
x Cartesian coordinate(see fig.1) [mm]
y Cartesian coordinate(see fig.1) [mm]
z Cartesian coordinate(see fig.1) [mm]
η Free surface displacement [mm]
θ Polar coordinate(see fig.1) [rad]
ν Viscosity [Pa·s]
ξ Roots of the Bessel function of first order and first kind.
ρ Density [kg/m^3]
σ Surface tension [N/m]
Φ Velocity potential function [m^2/s]
Ω External excitation frequency [rad/s]
ω Natural frequency [rad/s]

1. Introduction

The motion of the free liquid surface inside its container is called ‘sloshing‘. It is strongly affected by external excitations applied to the partially filled container. The understanding and the prediction of this

particular motion is of special importance in many fields. Indeed, the motion of liquids inside containers can refer to embarked containers filled of fluid, motion of cooling liquids in systems subjected to earthquake or motion of propellant inside the tank. The latter can influence the dynamic stability and performance of the vehicle, be a ship, a missile, a rocket or a satellite.
The motion of a liquid inside its container can have an infinite number of natural frequencies, but the lowest few modes are most likely to be excited from the vehicle motion[1]. Analytical and mechanical analogy are well-known in literature, while numerical simulations are still far from the desired reliability, especially for fluids used in space propulsion like cryogenic fluids at low gravity environmental conditions.
The motivation behind this paper is the characterization of the sloshing motion inside a partially filled cylinder in order to build a test case and provide experimental data for calibrating and validating numerical codes. The velocity in the liquid phase and the behavior of the free surface will be studied. The geometry chosen is a circular cylinder: this is a common shape for liquid storage due to pressurization issues. For this geometry the analytical results are well known. In this work the experiments were performed with water in a partially filled circular cylinder subjected to sinusoidal lateral excitations. Water was chosen in order to figure out the experimental procedures and the post-processing strategies. Fluorescent 2D Particle Image Velocimetry (f-PIV) has been applied to characterize the velocity field in the meridional plane which is the plane of the motion. In the future the same technique will be used, applied to a container filled with LN_2, a cryogenic fluid.

2. Sloshing theory

The theory of liquid sloshing dynamics in partially filled containers consists in developing the fluid field equations. The Navier-Stokes equations are integrated taking into accounts different hypotheses and boundary conditions relative to the particular problem. For an open surface the boundary condition specifies either the values of the field at every point of the surface, the normal gradient to the container walls or both. Explicit solutions are possible only for few cases such as the upright partially filled cylinder. The boundary value problem is usually solved for modal analysis(free sloshing) and for the dynamic response characteristics to external excitations(forced oscillations). The fluid free-surface motion and the resulting hydrodynamic forces and moments can be estimated from the system of fluid field equations. Mechanical analogies can be found in literature beside the analytical solutions[2; 3; 4; 5; 1].

2.1. Analytical solution

Free oscillations. The container-fluid system investigated is shown in figure 1.

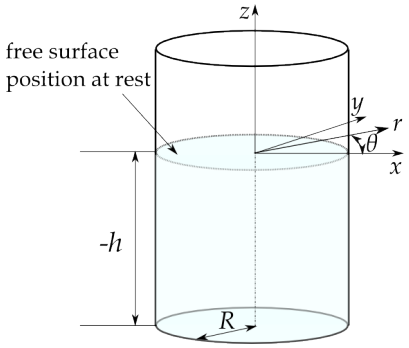

Figure 1: Circular cylindrical tank of radius R, partially filled to an arbitrary depth h.

As a first approximation, the analysis of the fluid dynamic problem is generally simplified with the following assumptions:

- rigid and impermeable container
- inviscid, incompressible and irrotational fluid
- if the system is in normal gravity environment, the effect of surface tension can be neglected

It is of interest to determine the regime of validity of these simplifications. The dimensionless parameters controlling the validity of the inviscid and negligible surface tension assumptions are the Reynolds number and the Bond number, respectively. The Reynolds number in the sloshing field is often express in terms of importance of gravity forces with respect to viscous forces, the so called Galilei number (eq.1)[6; 7]. The Bond number(eq.2) gives information on the relative importance of gravity forces with respect to surface tension ones(capillary forces). Physically the bond number can give a prediction on the shape of the interface: for Bo$\gg$1, gravitational forces are dominant and the free surface is flat (except right at the wall where the contact angle condition must be satisfied) while for Bo$\ll$1, capillary forces are dominant and the free surface will be highly curved.

$$Re = \frac{VR}{\nu} \rightarrow Ga = \frac{gR^3}{\nu^2} \tag{1}$$

$$Bo = \frac{\rho g R^2}{\sigma} \tag{2}$$

From the hypothesis stated here-above, the field equation can be written as:

$$\nabla^2\Phi = 0 \quad \text{in} \quad \begin{cases} 0 \le r \le R \\ 0 \le \theta \le 2\pi \\ -h \le z \le 0 \end{cases} \tag{3}$$

The non permeability conditions at the rigid container are:

$$\frac{\partial \Phi}{\partial r} = 0 \qquad \text{at} \quad r = R \tag{4}$$

$$\frac{\partial \Phi}{\partial z} = 0 \qquad \text{at} \quad z = -h \tag{5}$$

Calling $\eta(r, \theta, t)$(fig.2) the vertical displacement of the free surface above the undisturbed free surface and, for simplicity, setting the value of the pressure on the free surface to zero, the dynamic condition at the free surface can be derived.

A second condition has to be expressed on the kinematic of the problem: the vertical velocity of a fluid particle located on the free surface $z = \eta(r, \theta, t)$ is equal to the vertical velocity of the free surface itself. Assuming amplitude excitations and fluid responses to be small, the problem can be linearized and the two conditions are expressed in equations 6 and 7.

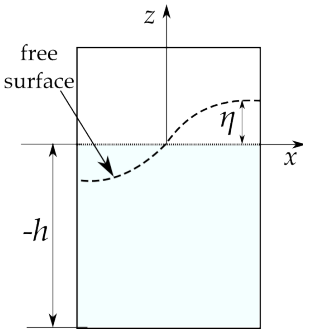

Figure 2: Surface wave in a cylindrical tank.

$$g\eta - \frac{\partial \Phi}{\partial t} = 0 \qquad \text{at} \quad z = \eta(r, \theta, t) \tag{6}$$

$$-\frac{\partial \Phi}{\partial z} = \frac{\partial \eta}{\partial t} \qquad \text{at} \quad z = \eta(r, \theta, t) \tag{7}$$

Combining equations 6 and 7 we obtain the linearized condition of the free surface:

$$\frac{\partial^2 \Phi}{\partial t^2} + g\frac{\partial \Phi}{\partial z} = 0 \qquad \text{at} \quad z = \eta(r, \theta, t) \tag{8}$$

Taking equation 8 and substituting a possible solution of the Laplace equation 3, which satisfies conditions 4 and 5, the natural frequencies of the liquid free-surface can be calculated from the following expression:

$$\omega_{mn}^2 = \frac{g\xi_{mn}}{R} \tanh\left(\frac{\xi_{mn} h}{R}\right) \tag{9}$$

where m refers to the diametral nodes and n to the circumferential nodes for the different kind of vibration[1]; ξ_{mn} are the roots $dJ_1(\xi_{mn} r/R)/dr|_{r=R} = 0$, where J_1 is the Bessel function of first order and first kind[2]. The asymmetric modes are of major concern since they are associated to a horizontal oscillation of the center of mass(fig. 3). Symmetrical modes about the vertical axis are possible but not excited so often[8]. In the case of a lateral excitation, the first asymmetric mode(m=1,n=1) is the predominant[9] and it is related to the lowest natural frequency of the system. For the first mode, m=1, we have a nodal diameter perpendicular to the direction of motion.

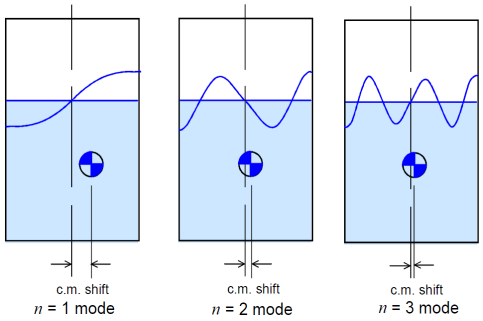

Figure 3: Scheme of first asymmetrical modes[5].

Small amplitude forced oscillations. It is possible to determine the linear response to a sinusoidal external excitation of the liquid contained inside the cylindrical tank of figure 1. We assume that the excitation is only acting in the x-direction and it has the form:

$$\mathbf{V}_0 = X_0 \sin(\Omega t)\mathbf{i} \tag{10}$$

The linearized fluid field equation is the same equation 3, while the linearized free surface condition (eq. 8) becomes:

$$\frac{\partial^2 \Phi}{\partial t^2} + g\frac{\partial \Phi}{\partial z} = -X_0 \Omega^3 \cos(\Omega t) r \cos\theta \quad \text{at} \quad z = \eta(r, \theta, t) \tag{11}$$

[1]The number n is always referred as n-1 circumferential nodes.

Substituting the general solution of the potential function Φ it is possible to determine the surface wave height function:

$$\eta(r,\theta,t) = \frac{X_0\Omega^2}{g}\cos\theta\cos\Omega t\,[r+B] \qquad (12)$$

with

$$B = \sum_{n=1}^{\infty} \frac{2R}{(\xi_{1n}^2-1)}\frac{\Omega^2}{(\omega_{1n}^2-\Omega^2)}\frac{J_1(\xi_{1n}r/R)}{J_1(\xi_{1n})}$$

and where only the first asymmetric mode is considered(m=1). It is obvious from equation 12 that as the applied external pulsation, Ω, approaches a natural frequency, ω_{mn}, the solution becomes unbounded due to the lost of validity of the linearized theory.

2.2. Mechanical Modeling

An equivalent mechanical model of the linear sloshing phenomenon can be studied. The liquid motion inside the container can be distinguished in two different components: one part which is moving in unison with the rigid tank and a second part which experiences the sloshing motion. Experiments have shown that the fluid velocity decreases exponentially with depth[1; 9]. For this reason, the fluid dynamics of an undamped fluid inside a container in response to a lateral excitation might be represented by a nonsloshing mass and an infinite series of oscillating spring masses[9]. Each spring-mass element represents a single slosh mode.

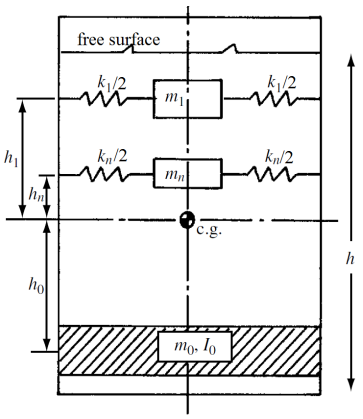

Figure 4: Equivalent spring-mass system for undamped propellant slosh in a cylindrical tank.

For the pure translational excitation of eq. 10 and zero damping, the sloshing equation for each mass n takes the form:

$$m_n\ddot{x}_n + k_n x_n = m_n X_0\Omega^2\sin\Omega t \qquad (13)$$

Comparing the results from the analytical solution with those of the mechanical model and considering only the fundamental mode, we obtain the following equivalent parameters[1]:

$$K_1 = m_f\left(\frac{g}{1.19h}\right)\left(\tanh\frac{1.84h}{R}\right)^2 \qquad (14)$$

$$m_1 = m_f\left(\frac{R}{2.2h}\right)\tanh\frac{1.84h}{R} \qquad (15)$$

$$m_0 = m_f - m_1 \qquad (16)$$

$$h_1 = \frac{h}{2} - \frac{R}{1.84}\tanh\frac{1.84h}{R} \qquad (17)$$

$$h_0 = \frac{m_f}{m_0}\left[\frac{h}{2} - \frac{R^2}{2h}\right] - h_1\frac{m_1}{m_0} \qquad (18)$$

Where m_0 is the non-sloshing mass, m_f is the total fluid mass, m_1 and K_1 are the mass and the spring costant concerning the first sloshing mode. An interesting result from this mechanical model is the dependence of the non-sloshing mass ratio, m_0/m_f, and modal slosh mass ratio, m_n/m_f, on the liquid-depth ratio, h/R, for the firsts three modes, as shown in figure 5. It can be observed that the size of the slosh mass rapidly decreases for all modes exceeding the first.

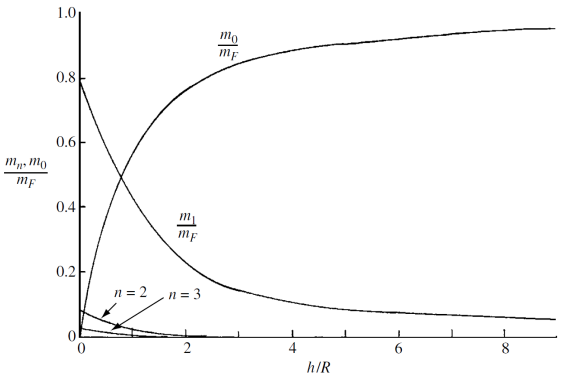

Figure 5: Ratio of mechanical model masses and fixed mass to the total fluid mass for a circular cylindrical tank[1].

3. Experimental Facility

A scheme of the experimental facility to characterize the behavior of a fluid contained in a cylindrical cell subjected to sinusoidal excitation is shown in figure 6. The principal element of the experimental setup consists in a partially filled cylindrical cell with a diameter R = 40mm. The cylindrical cell is designed

in order to limit image distortion due to the curved walls by means of refractive index matching. Since the fluid chosen is water (RI=1.333), the cell was designed with a double layer containing water(perfect index mathcing) and the material chosen was Plexiglass(RI=1.489). The drawing of the cell with its dimensions is shown in figure 7. The cell is bolted to a table that can generate harmonic oscillations. From now on this table is here called sloshing table. The latter is able to produce a sinusoidal motion in one direction with an amplitude in the range $[1-10]$mm and with a frequency in the range $[0.1-6.6]$Hz. The accuracy on the selected frequency is 0.02Hz.

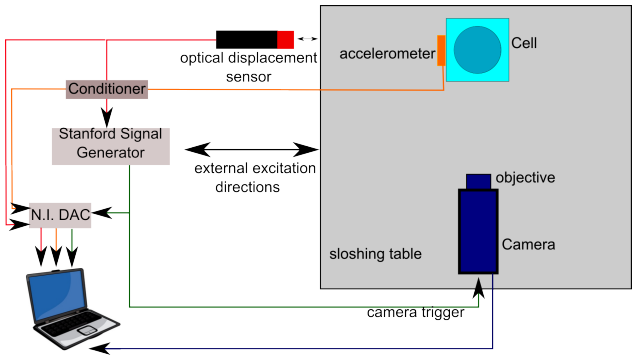

Figure 6: General sketch of the sloshing facility.

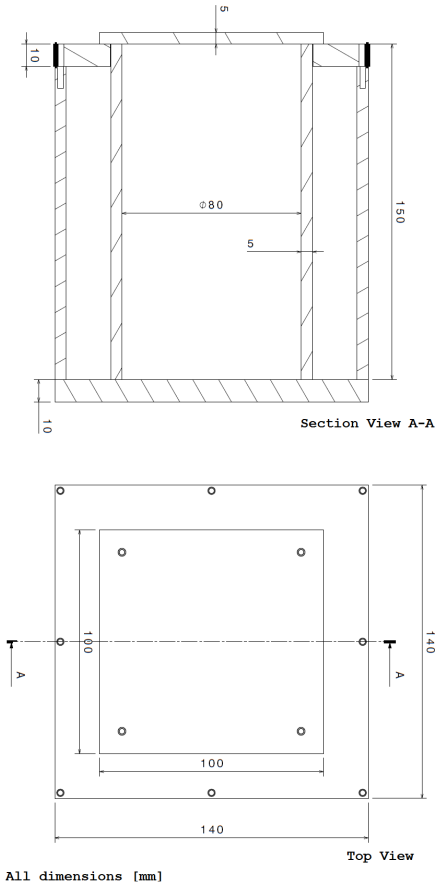

Figure 7: Drawing of the sloshing cell.

The position of the table is recorded online by an Optical Displacement Sensor(ODS) which has an accuracy of 18μm (C.L.95%). An accelerometer can be mounted on the cell to record the accelerations experienced by the cell itself. The uncertainty on the acceleration is 0.01mm/s^2(C.L.95%). The signal of the ODS can be used as input for a synchronizer in order to perform phase locked image acquisitions with the sinusoidal motion.

In this setup it is possible to study the behavior of the fluid during sloshing by means of backlighting high speed visualizations and Particle Image Velocimetry phase locked measurements. The optical arrangement for f-PIV is shown in figure 8. Fluorescent particles from the brand Cospheric were used in order to have less light noise due to laser reflections inside the transparent cell. The properties of the particles are summarized in table 1 where also the order of magnitude of the Stokes number for this application is shown. The density of the particles is almost the same as that one of water. For this reason some particles can float on the free surface.

4. Results and discussions

In this section the results of f-PIV applied to the sloshing phenomena are shown. The plane of measurement is the meridional plane parallel to the vector of the external excitation (referring to fig. 1 is the plane xz). The measurements done with the aforementioned cell of radius 4 cm are shown. In order to compare the results with the inviscid linearized theory, the respect of the assumption on the Bond number is verified. The table 2 shows the values of the Galilei and Bond number in gravitational conditions, using water as working fluid.

Table 1: Properties of fluorescent particles.

diameter μm	density kg m^{-3}	Stokes -	Absorption nm	Emission peak nm
10-45	998	$\approx 10^{-4}$	460-650	605

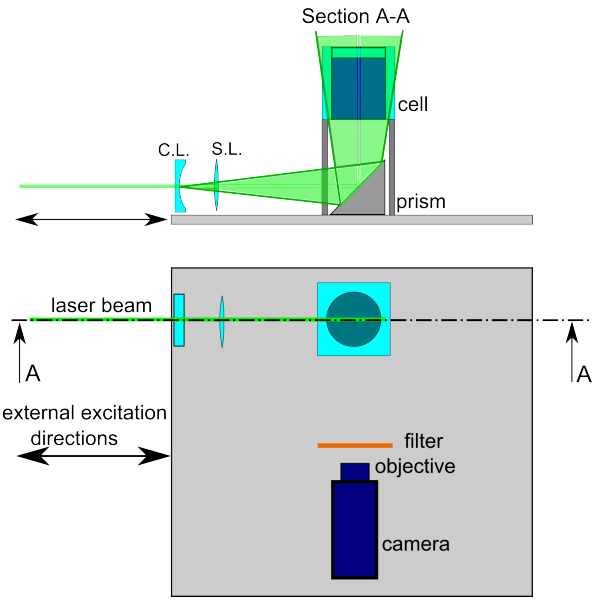

Figure 8: Optical arrangement for f-PIV.

Table 2: Galilei and Bond numbers.

	Galilei	Bond
R = 4cm	6.2e+08	216

PIV images are acquired phase locked with a selected phase of the sloshing table motion. The test matrix of the experiments discussed is shown in table 3. Test 1 and 3 correspond to the position of the free surface when its amplitude is close to its maximum position, while Test 2 and 4 correspond to the horizontal position of the free surface. The separation time between frames is such to have a maximum value of ≈4-10 pixel displacement in the region close to the free surface position. For each test, 225 frames are acquired in phase locked configuration.

Table 3: Test conditions matrix.

Test	R	h/R	f_{11}	F	X_0	Phase
	cm	-	Hz	Hz	mm	s
1	4	2.4	3.38	2.00	1.20	0.30T
2						0.50T
3				3.00		0.27T
4						0.48T

In figure 9 the typical f-PIV images for the tests at 2Hz and 3Hz are shown. It can be seen that the free surface is not immediately detectable. Indeed a common issue of doing PIV in presence of liquid/gas interface is the presence of so called 'ghost particles'[10; 11]. In figure 9 it can be noticed also that in the case of 2Hz, the amplitude of oscillations of the free surface is such that many particles remains on the free surface while, for the case of 3Hz, the particles are more mixed inside the fluid. It has to be underline that F = 3Hz is approaching the first natural frequency, f_{11} = 3.38 and the free surface is not anymore flat.

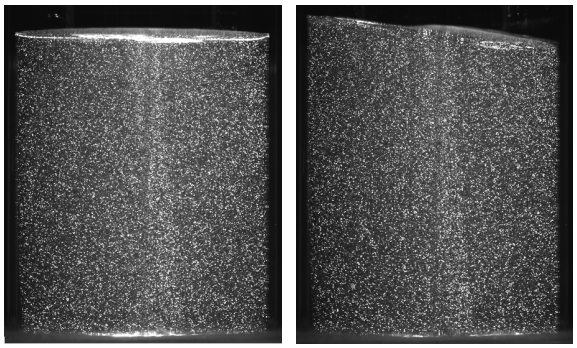

(a) F=2Hz (b) F=3Hz

Figure 9: Typical f-PIV images for the test at 2Hz and 3Hz.

In figure 10 the rms of the intensity over 225 images is shown, zooming in the free surface region. The two images presents different aspect: for the test at 2Hz the free surface is enlightened due to the presence of many particles on it; for the test at 3Hz the particles on the surface are continuously mixed inside the fluid and the free surface become a dark line. For the four tests the detection was done manually, following the rms contour.

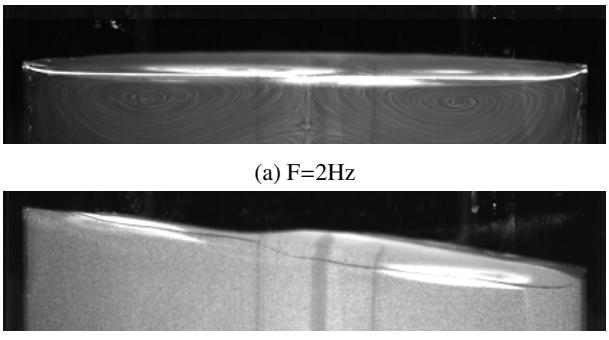

(a) F=2Hz

(b) F=3Hz

Figure 10: Rms of intensity over 225 phase locked f-PIV images for the test at 2Hz and 3Hz.

After the masking, the images were processed with a structured grid of final size 48x48 pixel and 75% of overlap obtaining a resolution of ≈1.25mm. In figure 11 an example of the mean velocity map obtained doing the phase locked f-PIV for the case at 3Hz is shown. The rms of the velocity is presented in figure 12a while figure 12b shows the mean Signal to Noise (SN) of the PIV processing. The repeatability was tested and the deviations were found inside the rms value. Tests at 2Hz will be analyzed separately from those at 3Hz since the latters are close to the first natural frequency and they present a different topography. The synchronization of the phase locked acquisition respect to a period of the motion are shown in figure 13 for each test.

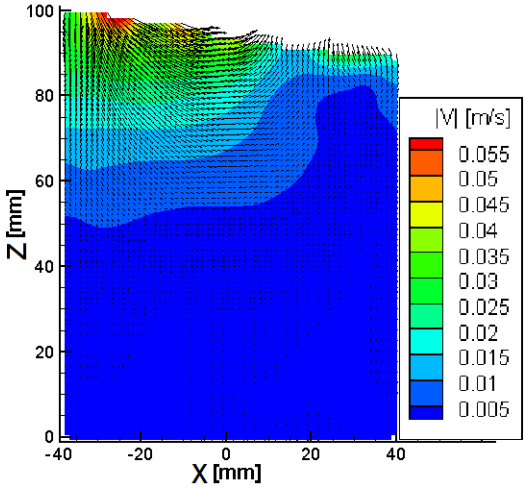

Figure 11: Mean velocity map over 225 instantaneous velocity maps

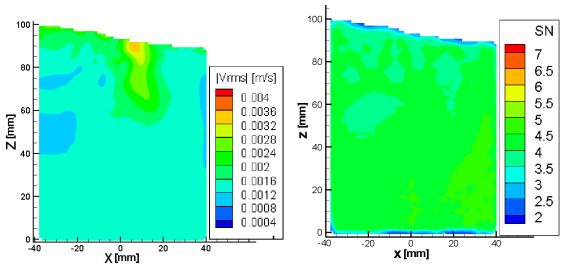

(a) Rms of the velocity (b) Mean SN over 225 processed images

Figure 12: Velocity result for test 3.

Test at 2Hz. The experimental results from the test 1-2 are expected to be comparable with the linearized

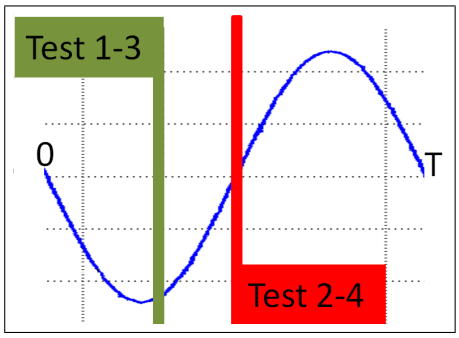

Figure 13: Syncronization for the phase locked measurements.

analytical theory, keeping in mind that the analytical theory considers the fluid inviscid, incompressible and irrotational and that the effect of surface tension has been neglected. In figure 14 and 15 the vertical profiles of the component V_x, respectively for the Test 1 and Test 2, at x=[-20,0,+20], are shown. The component V_x is found to be exponential with the liquid depth and its maximum value is on the vertical axis of the container as expected. In particular the test 2 is expected to be symmetric since it is the case in which the free surface is in the flat position. In the bottom of the container the velocity is supposed to be zero. In both tests there is a residual velocity measured with f-PIV, but this value is so small to be comparable with the rms of the velocity itself(≈1e-4 m/s). For this reason those small values of velocity are not considered.

The comparison between the vertical velocity V_z at the position of the free surface for both Tests 1-2 is shown in figure 16. Several considerations can be done on this plot:

- the profile V_z at the free surface position is linear in the central part as expected from the excited mode (1,1).
- The coordinate $x = 0$ is a nodal point for the free surface motion.
- Approaching the external wall ($x \rightarrow R$) the velocity decreases, reaching a maximum and then decreasing again; this is due to the presence of the meniscus which has a damping effect on the moving of the free surface.
- Test 1 is acquired when the inversion of the direction of the free surface motion happens: due to the presence of the meniscus the free surface is ”frozen” for some ms. Even if the free surface

seems at its maximum displacement, from the trigger signal compared to ODS signal(fig.13) it can be seen that the motion of the tank is already in the accelerating part. Moreover, the value of velocity found in Test 2 is higher than that one found in Test 1 in agreement with the phase of the motion in which the measurements are done(see fig.13).

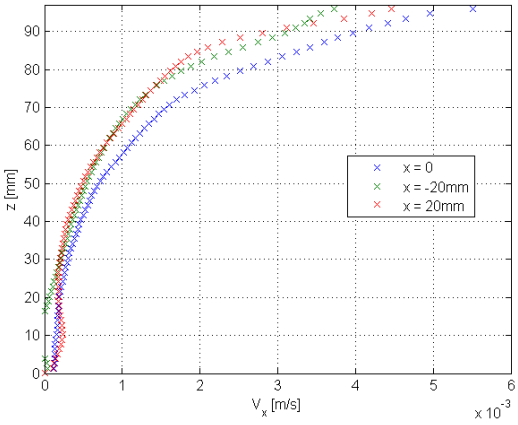

Figure 14: Test 1, 2Hz-0.3T V_x in three different x position.

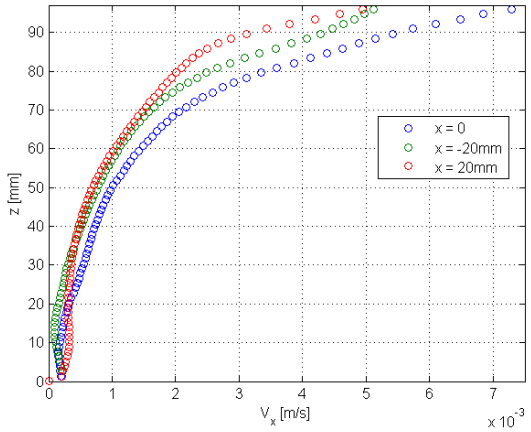

Figure 15: Test 2, 2Hz-0.5T V_x in three different x position.

Considering equation 12 and the condition 7 we can calculate the profile of V_z at the free surface position and compare it with the measured V_z obtained from the first PIV window at the free surface position. The result of the comparison is shown in figure 17. It can be seen that the V_z measured has a linear behavior in the central position of the field as well as the theoretical profile of the free surface velocity. The deviation is due to the fact that the analytical theory is neglecting the surface tension effect and so it does not take into account the presence of the meniscus at the wall.

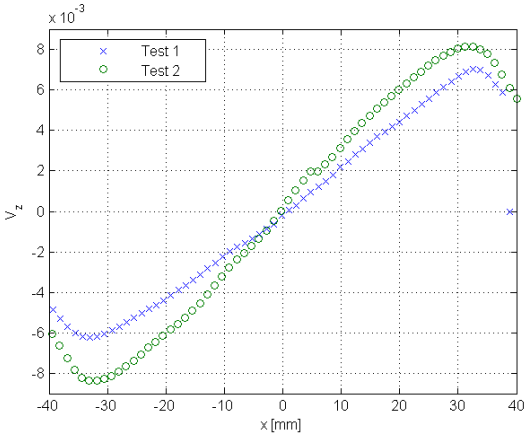

Figure 16: Test 1-2, 2Hz, V_z at the free surface.

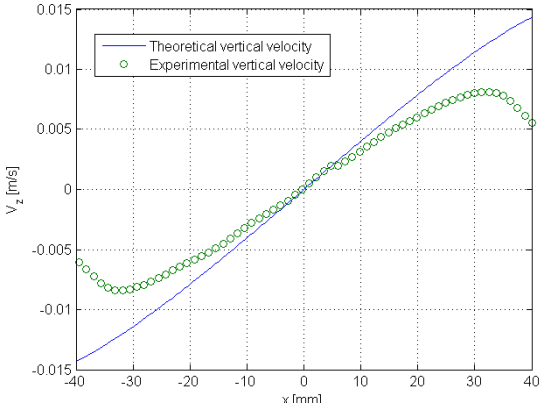

Figure 17: Test 2 - Comparison with the theoretical velocity of the free surface.

Test at 3Hz. The Tests 3 and 4 are done exciting the container almost at the natural frequency ($f_{1,1}$ = 3.38Hz). Even if those tests are done with a frequency close to the natural frequency, the shape of the free surface appears still continuous(no wave-breaking) but a system of small waves is generated as it can be seen from figure 10b. The vertical profiles of V_x in the coordinates x=[-20,0,+20] are shown in figure 18 for Test 4. It can be noticed that the maximum velocity at the free surface appears at the coordinate x=-20 on the contrary of what happens for Test 2(fig. 15),

even if both tests are done in the same phase of the external motion(fig. 13). The central profile shows the maximum value just below the interface to decrease from that position towards the free surface. Figure 19 shows the vertical component of the velocity V_z at the free surface for both Tests 3 and 4. Some considerations can be done on this plot:

- the profile V_z at the free surface position is not linear anymore since the experiments are done close to the natural frequency $f_{1,1}$: the velocity is fluctuated all along the free surface and other modes can be excited.
- The coordinate $x = 0$ is still a nodal point for the free surface motion.
- Approaching the external wall ($x \to R$) the velocity reaches a maximum value followed by a decreasing in correspondence of the meniscus, similarly to the Tests 1 and 2. In those tests the effect is less evident than Test 1 and 2 due to the presence of a small waves system. Those waves start to appear close to the natural frequency.
- Velocities of Test 3 are smaller than those of Test 4 since the two instants of the motion are in sequence on the accelerating phase of the oscillation.

Even if the linearized theory is not completely valid anymore, the comparison of it with Test 4 (fig.20) shows that the theory is still able to predict the order of magnitude of the vertical velocities at the free surface position. The maximum deviation is found at the wall of the container where the theory does not take into account the presence of the meniscus. Comparing figures 17 and 20, we can have the impression that the theory is better approximated by the test at 3Hz. In reality we have to take into account that the theory is predicting the velocity profile of the free surface in terms of wavelength of disturbances. In this sense it can be affirmed that Test 2 is better approximated by the theory. Moreover, the deviation of Test 4 respect to the theory is smaller than the case of Test 2 because the amplitude of oscillations is much higher in Test 4 due to instabilities generated close to the natural frequencies.

General behavior. The component V_x in the central position was compared between all tests. The vertical position is made dimensionless with the undisturbed liquid height and the velocity was rendered dimensionless with the maximum V_x of the profile. The result of this comparison is shown in figure 21. It can be

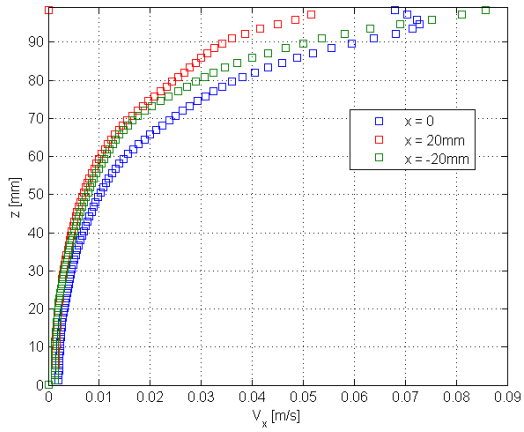

Figure 18: Test 4, 3Hz-0.48T V_x in three different x position.

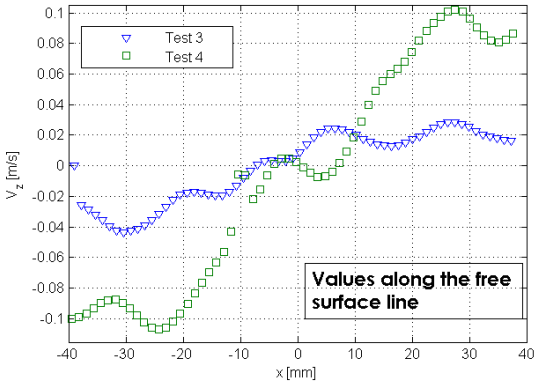

Figure 19: Test 3-4, 3Hz, V_z at the free surface.

noticed that the behavior of V_x/V_xmax is similar for all tests, despite the differences on the typology of behavior for the cases at 2Hz and 3Hz. It could be interesting to find if it exists a relation between the results in order to be able to predict the behavior of the fluid, knowing the boundary conditions of the problem (e.g. from the external excitation.)

5. Conclusions and future work

A first step on the characterization of the velocity field of the sloshing phenomenon in the first mode has been done. Particle Image Velocimetry in the form of phase locked measurements has been found a reliable tool for this characterization, with a high repeatability. Future steps have to be done in order to improve the detection of the free surface from f-PIV images. The

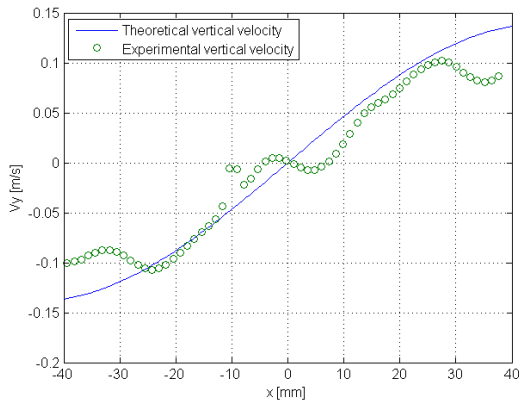

Figure 20: Test 4 - Comparison with the theoretical velocity of the free surface.

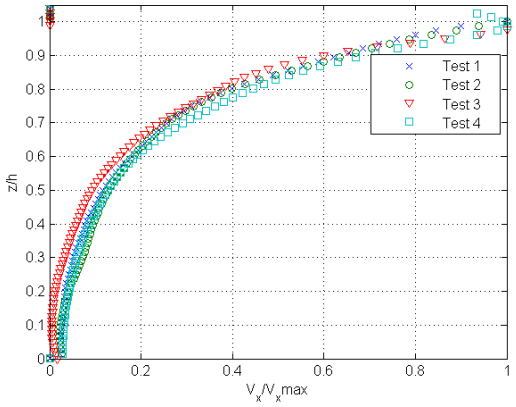

Figure 21: Dimensionless comparison of V_x along the axis for all tests.

precision of this detection has been found fundamental for the accuracy of the results[12; 10; 13]. Standard adaptive PIV with Cartesian grid can not properly resolve the velocity at the free interface when the pulsation of the excitation is approaching the natural frequency due to the high deformation of the free surface itself. The next step will be to implement the work of Berger[10] and Theunissen[13] in order to improve the accuracy of the results at the free surface. The inviscid, linearized theory and considering the effect of the surface tension negligible is not approximating well the experiments even if the excitation was far from the natural frequency of the system. An improvement can be done using the work of Bauer[14; 15; 16] who analyzed the viscous sloshing phenomenon for a partially filled cylinder under translational excitation considering the case of slipping and anchored contact line. Finally it could be of great interest to find a correlation between the external excitation and the measured fluid velocities.

References

[1] R. Ibrahim, Liquid Sloshing Dynamics: Theory and Applications, Cambridge University Press, Cambridge, 2005.

[2] H. Abramson, The dynamic behavior of liquids in moving containers, SP 106, NASA (1966).

[3] J.W. Tedesco and D.W. Landis and C.N. Kostem, Seismic analysis of cylindrical liquid storage tanks, Computers & Structures 32 (5) (1989) 1165–1174.

[4] H.F. Bauer and W.Eidel, Axysimmetric viscous liquid oscillations in a cylindrical container, Engineering Research 63 (1997) 189–201.

[5] F. Dodge, The new "dynamic behavior of liquids in moving containers", SP 106, SRI (2000).

[6] T. Arndt and M. Dreyer, Damping behavior of sloshing liquid in laterally excited cylindrical propellant vessels, Journal of Spacecraft and Rockets 45 (5).

[7] E.J. Hopfinger and V. Baumbach, Liquid sloshing in cylindrical fuel tanks, Progress in Propulsion Physics 1 (2009) 279–292.

[8] T. S. C. Institute, Fluid structure interaction effects on and dynamic response of pressure vessels and tanks subjected to dynamic loading, RR 527, HSE-UK (207).

[9] T. Lance, Analysis of propellant slosh dynamics and generation of an equivalent mechanical model for use in preliminary voyager autopilot design studies., TM 33-306, NASA (1966).

[10] R. Berger, Intgration et validation exprimentale de la mthode VOF dans les calculs arodynamiques automobiles : application au cas de l'entrainement d'eau dans les conduits de climatisations, Ph.D. thesis, Universite Libre de Bruxelles - von Karman Institute (2010).

[11] A. Sanchis and A. Jensen, Dynamic masking of PIV images using the Radon transform in free surface flows., Experiments in Fluids 51 (2011) 871–880.

[12] G.A. Zarruk, Measurement of free surface deformation in PIV images, Measurement Science and Technology 16 (2005) 1970–1975.

[13] R. Theunissen, Adaptive image interrogation for PIV - Application to compressible flows and interfaces, Ph.D. thesis, Vrije Universiteit Brussel - Technische Universiteit Delft - von Karman Institute (2010).

[14] H.F. Bauer, Liquid oscillations in a circular cylindrical container with "sliding" contact line, Engineering Research 58 (10) (1992) 240–251.

[15] H.F. Bauer, Oscillations of a viscous liquid in a cylindrical container, Aerospace Science and Technology (8) (1992) 519–532.

[16] H.F. Bauer and W.Eidel, Free oscillations and response of viscous liquid in rigid circular cylindrical tank, Aerospace Science and Technology (3) (1999) 495–512.

Experimental Study of Natural Convective Internal Flows

Chiara Spaccapaniccia

Environmental and Applied Fluid Dynamics Department, von Karman Institute for Fluid Dynamics, Belgium,
chiara.spaccapaniccia@vki.ac.be

Advisor: Philippe Planquart

Research Engineer, Environmental and Applied Fluid Dynamics Department, von Karman Institute for Fluid Dynamics, Belgium,
philippe.planquart@vki.ac.be

Supervisor: Jean-Marie Buchlin

Professor, Environmental and Applied Fluid Dynamics Department, von Karman Institute for Fluid Dynamics, Belgium,
Professor, Faculté des Science Appliquées, Université Libre de Bruxelles
buchlin@vki.ac.be

University Supervisor: Gérard Degrez

Professor, Aeronautics and Aerospace Department, von Karman Institute for Fluid Dynamics, Belgium,
Professor, Faculté des Science Appliquées, Université Libre de Bruxelles
buchlin@vki.ac.be

Abstract

The developing of new generation liquid metal cooled reactors lead to numerous advantages in the nuclear energy technology, such as a higher power density and improved operating safety. The Belgian nuclear research institute SCK•CEN is developing MYRRHA, a subcritical liquid metal cooled reactor. The reactor is designed to operate in natural convection decay heat removal conditions. The consequent stratification developing in the upper vessel could affect the heat removal efficiency. The factors influencing the temperature profile should be analyzed by experimental and numerical methods considering a scaled facility.

Keywords: Natural Convection, Stratification, Planar Laser Techniques

1. Introduction

Natural circulation occurs often in energy systems: the simplicity of the principle of working of natural recirculation loops (*thermosyphons*) make this kind of systems reliable and very attractive. However this can of heat removal should be assessed when nuclear reactor is concerned. The present study is undertaken in collaboration with the SCK•CEN, that is developing the LMFBR Myrrha. The coolant of the primary loop of Myrrha is LBE. In passive heat removal conditions a LBE mass flow is driven by the difference in hydrostatic pressure of the core and the heat exchangers [1]. A flow rate is established as a consequence of a balance between frictional pressure losses of the hydraulic loop and Archimedes force driven by the heating power [2]. In these conditions a buoyant jet rises in the upper vessel. Since the height of the vessel is limited by the free level surface a thermal stratification may take place [3].A too strong stratification in the upper plenum is undesired because it affects the efficiency of the heat removal [4] and could compromise the integrity of the structure. The object of this analysis is to determine, which are the geometrical features of the upper vessel that affect mostly the thermal pattern. For such an investigation, a simple water model has been designed as described in [5]. The model is a thermosyphon closed loop. As shown in Fig.2 the model is provided with an upper tank in which are indicated the position of the barrel holes and the high of the buffer plate from the free surface level h_b. Number of holes and as a consequence their

position, are changing during the study; that originates different flow topologies and temperature profiles with respect to the nominal case. The analysis is performed for different heights of the buffer plate hp, in order to simulate different heat exchangers entrances, different pressure drops, by means of a regulating valve placed in the bottom part of the loop. The measurement techniques selected for the analysis are thermocouples (TC) , Particle Image Velocimetry and Laser Induced Fluorescence. Differently from TCs the LIF technique delivers mapping of thermal field. The simultaneous acquisition of velocity and temperature map is appealing for validation of numerical models. The coupling of these two planar techniques (PIV-LIF) were tested for the first time in a small setup presented in Section 11.

2. Scaling

If no externally induced flow is provided and flow arises simply due to the effect of a density difference resulting from a temperature or concentration gradient in a body force field (such as the gravitational field) the process is termed as natural convection [4]. In the present case the flow is generated by a difference of density due to the presence of cooling and heating elements. Since the flow evolves stationary in a hydraulic closed loop the pressure drops are equally important and must be considered in the scaling of the hydraulic system. Fig. 1 shows a schematic of the reactor primary loop in which are indicated the main components, such as heat source and heat sink. The highest pressure drops occur in the barrel holes and in the heat exchangers exit.

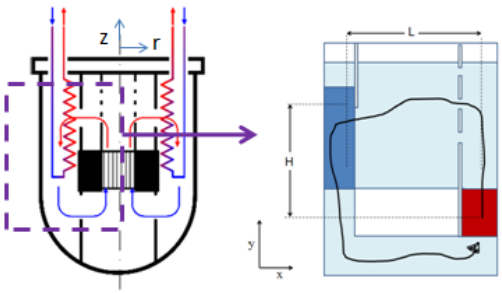

Figure 1: schematic of Myrrha primary loop working in passive heat removal conditions. The red section represents the heater, while the blue section is representing the heat sink.

As depicted in Fig. 1 the fluid motion in the following analysis is approximated as two dimensional. Given that the buoyancy acts only in vertical direction the basic equations of continuity, momentum and energy are, respectively:

$$\frac{\partial u}{\partial x} + \frac{\partial v}{\partial y} = 0 \tag{1}$$

$$u\frac{\partial u}{\partial x} + v\frac{\partial u}{\partial y} = -\frac{1}{\rho}\frac{\partial P_x}{\partial x} + \nu\frac{\partial^2 u}{\partial x^2} + \nu\frac{\partial^2 u}{\partial y^2} \tag{2}$$

$$u\frac{\partial v}{\partial x} + v\frac{\partial v}{\partial y} = -\frac{1}{\rho}\frac{\partial P_y}{\partial y} + \nu\frac{\partial^2 v}{\partial x^2} + \nu\frac{\partial^2 v}{\partial y^2} + g\frac{\rho_0}{\rho} \tag{3}$$

$$u\frac{\partial T}{\partial x} + v\frac{\partial T}{\partial y} = \alpha\frac{\partial^2 T}{\partial x^2} \tag{4}$$

Selecting proper characteristic quantities for length, pressure drops and temperature we can retrieve the following non dimensional variables:

$$X = x/L \quad Y = y/H$$
$$\mathcal{P}_x = P_x/P_{cx} \quad \mathcal{P}_y = P_y/P_{cy} \tag{5}$$
$$\Theta = (T - T_C)/(T_H - T_C)$$

Where H and L are the relative vertical distance and horizontal distance between heat source and heat sink, respectively. P_{cx} and P_{cy} are the pressure drops in horizontal and vertical directions and T_C and T_H are the smallest and the highest temperatures in the flow, respectively. A particular consideration should be given for the selection of a characteristic velocity value V_c . In the present analysis V_c is determined from a balance between buoyant and frictional forces in the loop [1]:

$$f\rho\frac{V_c^2}{2} = gH\Delta\rho \quad \Rightarrow \quad V_c = \sqrt{\frac{2gH\Delta\rho}{f\rho}} \tag{6}$$

From an analysis of order of magnitude applied to the non dimensional continuity equation we get:

$$\frac{\partial U}{\partial X} + \frac{\partial V}{\partial Y} = 0 \quad \Rightarrow \quad U_c = \frac{L}{H}V_c \tag{7}$$

Therefore the non dimensional equations become:

$$U\frac{\partial U}{\partial X} + V\frac{\partial U}{\partial Y} = -f_x\frac{\partial \mathcal{P}_x}{\partial X} + \sqrt{\frac{f}{Gr_H}}\left(A\frac{\partial^2 U}{\partial X^2} + \frac{\partial^2 U}{\partial Y^2}\right) \tag{8}$$

$$U\frac{\partial V}{\partial X}+V\frac{\partial V}{\partial Y}=-f_y\frac{\partial \mathcal{P}_y}{\partial Y}+\sqrt{\frac{f}{Gr_H}}\left(A\frac{\partial^2 V}{\partial X^2}+\frac{\partial^2 V}{\partial Y^2}\right)-f \tag{9}$$

$$U\frac{\partial \Theta}{\partial X}+V\frac{\partial \Theta}{\partial Y}=A^2\frac{1}{Pr}\sqrt{\frac{f}{Gr_H}}\frac{\partial^2 \Theta}{\partial X^2}=A^2\sqrt{\frac{f}{PrRa_H}}\frac{\partial^2 \Theta}{\partial X^2} \tag{10}$$

The dimensionless numbers to be respected for the scaling of the facility are:

$$f=f_x+f_y \text{ =The Friction Factor}$$

$$Ra_H=\beta g\Delta T H^3/\nu\alpha=Gr_H Pr \text{ =The Rayleigh Number}$$

$$A=H/L \text{ =The geometrical Aspect Ratio} \tag{11}$$

3. Aquarium

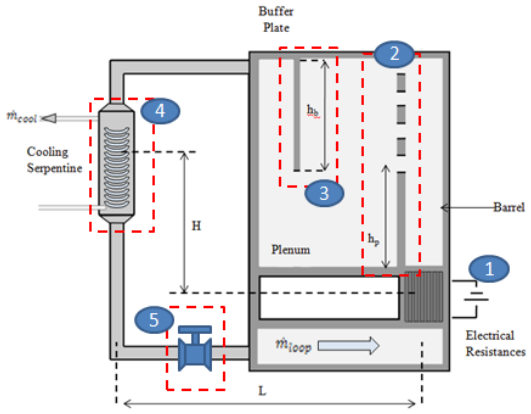

Figure 2: sketch of Aquarium Facility: 1- electrical resistances, 2- barrel plate, 3- buffer plate, 4- heat exchangers, 5- valve.

Fig. 2 shows a sketch of the water model, Aquarium, designed for this study. The main elements of the system are:

1. Core: a series of flat electrical resistances
2. Upper Core Barrel: a inter exchangeable plate provided with holes.
3. Buffer Plate: a plate with adjustable high to simulate the Heat Exchangers entrance level.
4. Heat Exchanger: Helical coil circulating water cooled by an external refrigerating system.
5. Valve: adjustable pressure drops.

The facility has a height of 1 m, width of 0.5 m and a depth of 10 cm. The flow circulates in a clockwise direction The flow circulates in a clockwise direction. Table 1 shows the values of the non dimensional numbers obtained with the Aquarium design and the comparison with the non dimensional number calculated for Myrrha.

Table 1: Non dimensional number values achieved for Aquarium and compared with the values calculated for Myrrha.

N	$N_{Aquarium}$	$N_{Aquarium}/N_{MYRRHA}$
Ra_H	$1.56\ 10^{11}$	1/20
A	0.3	1
f	186	1/1.2

The value of the Rayleigh number indicates that the difference with respect to the reactor is of one order of magnitude. However it indicates also that the natural convection in Aquarium, as well as in Myrrha, is turbulent. In the present analysis f is estimated from experimental correlations [6].

4. Experimental techniques

ΔT_{loop} and mass flow should be measured continuously to qualify the steadiness of the system. Moreover the spreading of the plume in the upper vessel and the consequent stratification of the plenum should be analyzed in detail. For these reasons the techniques applied are:

- Temperature measurements by thermocouples: TC probes were used to measure the minimum and maximum temperature of the loop and the temperature profile in the upper vessel. The thermocouples arrangement is presented In Fig. 3.
- Particle Image Velocimetry: a PIV camera is placed in front of the Plenum to measure the flow topology at the exit of the barrel holes.
- Coupled PIV and Laser Induced Fluorescence: planar velocity and temperature fields were measured at the exit of the barrel holes.

The red window in Fig.3 indicates the region analyzed by means of optical techniques. Section 11 discusses how to realize a coupled PIV and LIF measurement

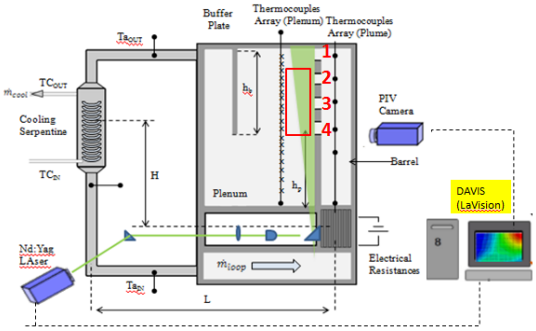

Figure 3: PIV set up for Aquarium (Nd-Yag double pulsed Laser, Camera and Acquisition/synchronization system). The investigation area cover the exit of the last three holes of the barrel plate.

5. Parametric study

Table 2 gives the range each parameter together with the setting selected as a reference case. The experiments were performed by changing only one of the parameters at once. In the following chapter the results obtained for the reference case are explained in detail. Each test lasts about 49 minutes. Temperature and velocity measurements are gathered for all the duration of the test. The start of the experiment coincides with the switching on of the electrical resistances.

Table 2: geometrical details changing during the analysis. The parametric study was performed changing one element at a time.

Variable Geometry	Values	Reference
h_p	20,40,55 cm	40 cm
Holes Number	2,4,6	4
f Number	186,201,240	186

The cooling system is switched on after 8 minutes from the beginning of the experiment to guaranty an established stratified plenum as an initial condition.

6. Reference Case

The characteristic values of Ra_H and f for the benchmark case are indicated in Table 3. Through an energy balance at the heat exchanger it is possible to evaluate the mass flow circulating in the thermosyphon loop at any time using the following relation:

$$\dot{m} = \dot{m}_c \frac{c_{p,cool}\,(T_{c,out} - T_{c,in})}{c_{p,hot}\,(T_{HE,in} - T_{HE,out})} \tag{12}$$

where $T_{c,out}$ and $T_{c,in}$ are the outlet and inlet temperature, respectively, of the secondary mass flow $\dot{m}_c$ in the heat exchanger whereas $T_{HE,in}$ and $T_{HE,out}$ are the inlet and outlet temperature of Aquarium primary loop. In Fig. 4 is plotted the evolution of the mass flow during the experiment; each point is the result of an average carried out over 3 minutes. Stability in the flow is reached after about 20 minutes. In Fig. 5 is plotted the evolution of the temperature profile measured by the 15 thermocouple rack placed in the upper plenum. In the bottom part of the domain we observe a gradient that is increasing in time while the upper part experiences an almost constant temperature. This temperature increases until the cooling loop is switched on, and then starts to decrease after approximately 15 minutes.

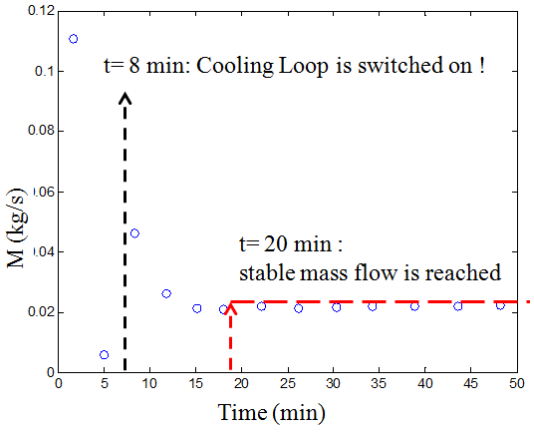

Figure 4: mass flow evolution in time for the benchmark case. Each point of the graph is the result of an average performed on 3 minutes of experiments. The data were acquired at 50 Hz.

The vertical location of the separation between these two regions moves downward with time and it reaches a stability after 30 minutes from the beginning of the experiment.

Fig.6 displays the velocity fields acquired with PIV. The flow topology is reported for different moments. At the start we observe entrainment of the flow of the plenum through all the holes observed. The stratification is not developed yet and the plume in the barrel is free to rise in the plenum. The second frame corresponds to a time after the starting of the cooling loop, when fluid cooler than the fluid in the upper plenum is rising and exits the first two holes with downward

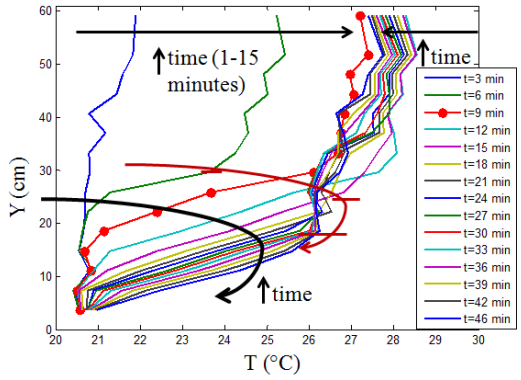

Figure 5: Temperature profile evolution in time for the benchmark case. Each profile is the result of an average performed on 3 minutes of experiments. The data were acquired at 50 Hz.

component of velocity. As stated previously temperature stabilizes after 30 minutes; however the velocity field is not totally stable. As a reference for the parametric study we select the flow topology obtained at $t_r \sim 41min$, when steadiness is quasi reached.

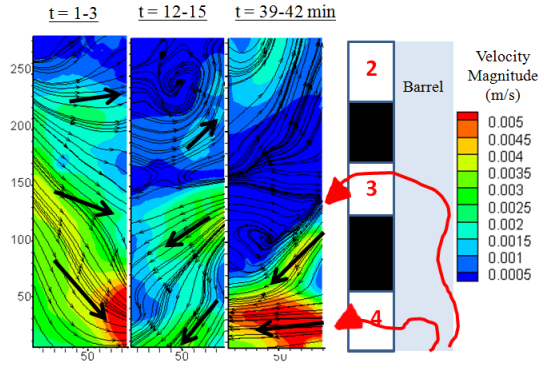

Figure 6: Velocity fields are the result of the average of 600 vector fields, acquired at 3 Hz, with a separation time of 333 ms. The post processing was performed with WIDIM, two step refinement, final window size=16x16 px

Fig.7 compares the temperature profile and the velocity field at t_r. Three different zones can be identified in the upper plenum:

- zone I: stagnation region
- zone II: mixing region
- zone III: diffusion region.

In zone I no fluid motion is detected and the thermal field is uniform. In zone II the temperature is lower with respect to the first zone due to the colder flow outgoing from the first two holes of the barrel. In zone III, the temperature profile results from diffusion.

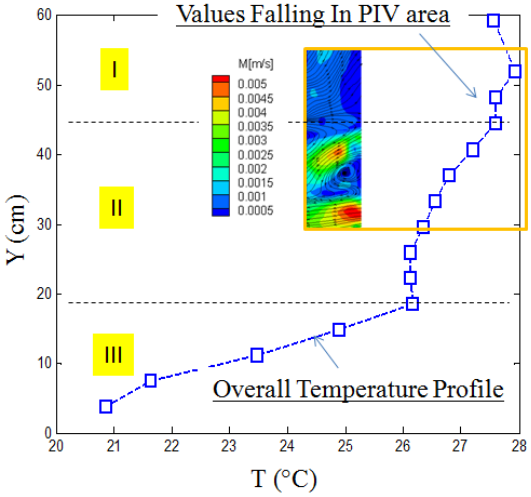

Figure 7: coupling of temperature profile and velocity field. The flow streamlines are fundamental to explain the temperature trend in the upper vessel

7. Influence of Buffer Plate position (h_p)

Results obtained with different values of buffer plate height, representing different inlet of the heat exchangers side, are compared to the reference case in terms of temperature profiles and flow topology at t_r.

Fig.8-a shows the streamlines obtained with a reduced buffer plate height h_p: we observe outgoing jets from the second and third hole and a weak entrainment in the lowest hole. The corresponding temperature profile is plotted in Fig.9 the region where the temperature exhibits a uniform trend is extended, as a sign of a higher degree of mixing with respect to the nominal case (in the part of vessel investigated).

On the contrary the case of Fig.8-b, which corresponds to an incremented buffer plate height h_p, shows a downward jet outgoing from the first hole while the upper region results is almost motionless. Observing the corresponding temperature profile in Fig.9 we can conclude that for the case of the increased h_p the stagnation region results is extended to a lower level of the plenum, reducing the mixing region.

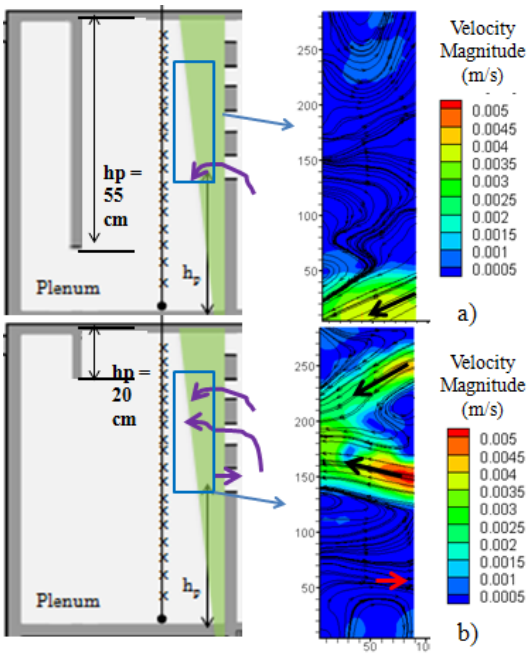

Figure 8: (a) hp=55 cm, (b) hp=20 cm. The streamlines are the results of an average performed on the minutes 39-42 (600 images at 3 Hz) of each experiment.

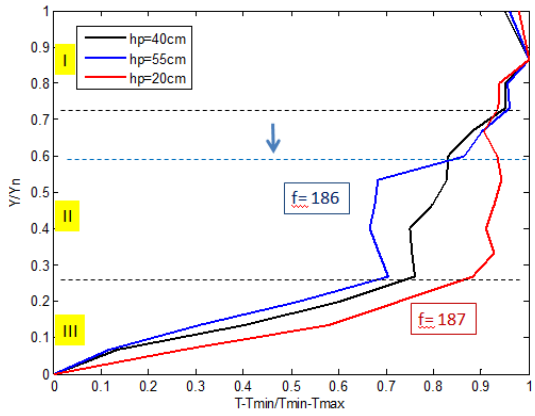

Figure 9: normalized temperature profiles. The profiles changing as a function of hp. Data are the results of an average over 3 minutes of experiment, data were acquired at 50 Hz.

8. Influence of free barrel area (holes N°)

Fig.10 and Fig.11 presents the results obtained for different porosity of the barrel area, expressed in number of holes. In Fig.10-a the streamlines correspond to the case where the number of holes is reduced from 4 to 2. The holes are occupying the higher position of the plate. Two jets are exiting the holes with a positive vertical component of velocity, entraining the surrounding fluid and enhancing the mixing in the region included between the barrel plate and the buffer plate. That leads to an extended mixing region, as confirmed by the temperature profile shown in Fig.11: the size of the diffusion region, characterized by a constant gradient, is reduced to the half.

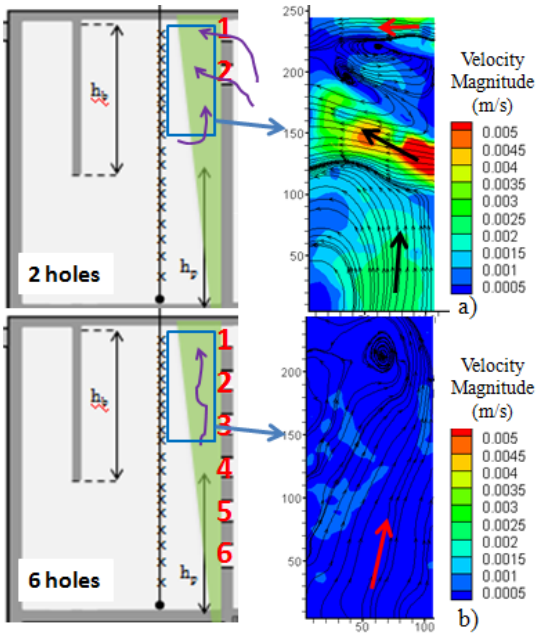

Figure 10: (a) 2 holes, (b) 6 holes. The streamlines are the results of an average performed on the minutes 39-42 (600 images at 3 Hz) of each experiment.

An extended mixing region is also observed when increasing of the holes number from 4 to 6. The holes are in this case distributed all along the buffer plate.

Observing Fig.10-b, we can conclude that since no jets come out from the top holes the fluid is outgoing from the bottom holes and only a weak component of buoyancy is remaining in the upper barrel. Fig.11 reveals lower temperatures for the case with a greater number of holes when compared to the case of Fig.10-a. This is due to a decreased hydraulic resistance (f number) in the loop that leads to a higher circulating mass flow and, as a consequence, to a drop of the temperature in the flow.

9. Influence of f Number (Pressure Drops)

The increase of the pressure drops (or f number) obtained by adjusting the valve placed in the horizontal branch right after the heat exchangers is illustrated in 12.

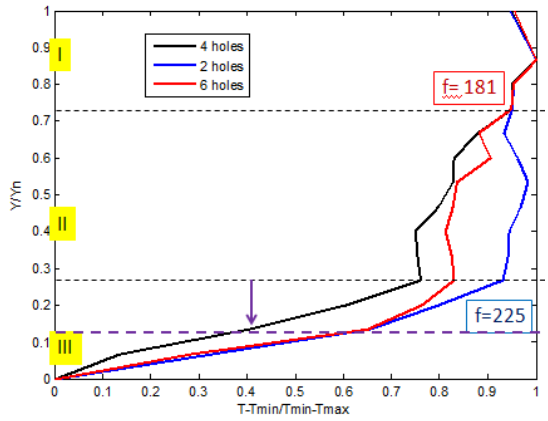

Figure 11: normalized temperature profiles. The profiles changing as a function of the hole number and distribution. Data are the results of an average over 3 minutes of experiment, data were acquired at 50 Hz.

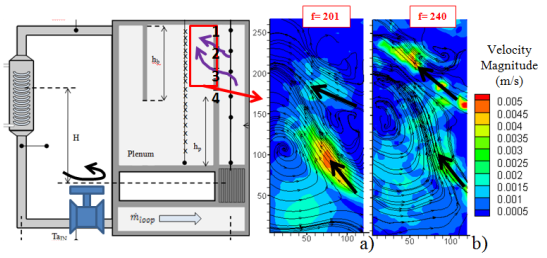

Figure 12: (a) f=201, (b) f=240. The streamlines are the results of an average performed on the minutes 39-42 (600 images at 3 Hz) of each experiment bad quality of flow topology can be due to a missing application of background subtraction as explained in [7].

Fig.12 compares the velocity field obtained with an incremented pressure drop compared to the reference case.

We notice that for both Fig.12-a (f =201) and Fig.12-b (f =240) jets own an upward component due to buoyancy. The effect of increasing the f number is a decrease in the mass flow rate and a subsequent augmentation of the fluid temperature of the fluid leaving the heating core. This increment is apparent in the temperature profiles plotted in Fig. 13. For this case it is however not possible to define a stagnation region, since the flow topologies a and b don't show motionless areas.

10. Conclusion Parametric Study

Changes in the geometry of the vessel and the loop lead to different flow topologies and resulting thermal fields. Velocity and temperatures were measured for

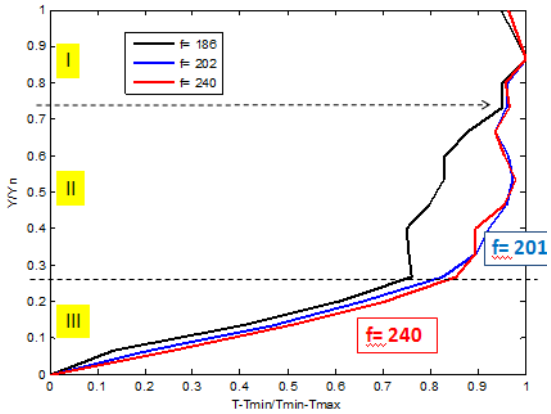

Figure 13: normalized temperature profiles. The profiles changing as a function of hp. Data are the results of an average over 3 minutes of experiment, data were acquired at 50 Hz.

all the cases tested, by PIV and thermocouples. Since the study was performed by changing only one variable at a time, it was not possible to keep the hydraulic resistance (f number) constant (it depends on the geometry itself). The objective was to determine which ensures the highest level of mixing. An increase of the pressure drops, even if it eliminates the stagnation region, does not represent a good strategy, since it increases at the same time the temperature in the vessel. Decreasing the buffer plate high h_p leads to a higher uniformity of temperatures in the vessel, and keeps the temperature level low, since the hottest fluid is in direct contact with the heat exchangers. The highest benefits are however achieved by increasing the porosity of the barrel plates, that allows a enlargement of the mixing region and at the same time helps keeping the hydraulic resistance of the loop at a low value. Differently from the velocity the temperature data are measured only along one vertical line We discuss in Section 13 and 13 the issues arising with the application of a fluorescence based technique for temperature measurements.

11. Cavity with differentially heated walls

In order to understand the applicability of the LIF technique a stratification was first measured in a small cavity provided with heat source and heat sink. The cavity was filled with a solution of water and Rhodamine B. The non dimensional analysis proposed for the cavity is similar to the one performed in Section 2. In the case of the cavity however it is possible to neglect the pressure drop term and the a different expres-

sion for the characteristic value of velocity V_c should be selected. The typical geometrical lenght quantities are now the high of the cavity H and the boundary layer thickness δ. As Prandtl number is higher than 1 (Pr > 1) the velocity boundary layer is thicker than the thermal boundary layer. The non dimensional variables X and Y are expressed as:

$$X = \frac{x}{\delta} \qquad Y = \frac{x}{\delta} \qquad V = \frac{v}{V_c} \tag{13}$$

Replacing the previous identities in the continuity equation and performing an order of magnitude analysis leads to:

Continuity:

$$\frac{\partial U}{\partial X} + \frac{\partial V}{\partial Y} = 0 \quad \Rightarrow \quad U_c = \frac{\delta}{H} V_c \tag{14}$$

Momentum

$$\left(U\frac{\partial V}{\partial X} + V\frac{\partial V}{\partial Y}\right)\frac{V_c^2}{H} = \nu\frac{V_c}{\delta^2}\left(\frac{\partial^2 V}{\partial X^2} + \frac{\delta^2}{H^2}\frac{\partial^2 V}{\partial Y^2}\right) + g\beta\Delta T\Theta \tag{15}$$

where Θ is defined as seen in Section 2. The left term of the momentum equation represents the inertia; the first term on the right side represents the friction and the last term the buoyancy. For fluids with Pr > 1 the inertia term is negligible and the buoyancy is balanced by friction. As a consequence we can write:

$$\nu\rho\frac{V_c}{\delta^2} \sim g\beta\Delta T \quad \Rightarrow \quad V_c \sim \frac{g\beta\Delta T\delta^2}{\nu} \tag{16}$$

Then, the non dimensional form of the energy equation is:

$$U\frac{\partial\Theta}{\partial X} + V\frac{\partial\Theta}{\partial Y} = \tag{17}$$

$$\frac{\alpha}{\delta^2}\frac{H}{V_c}\frac{\partial^2\Theta}{\partial X^2} = \frac{\alpha\nu}{g\beta\Delta T\delta^2}\frac{H}{\delta^2}\frac{\partial^2\Theta}{\partial X^2} = Ra_H^{-1}\frac{H^4}{\delta^4}$$

Applying an order of magnitude analysis to (17), we obtain:

$$\frac{\delta}{H} \sim (Ra_H)^{-1/4} \tag{18}$$

From which we conclude that the boundary layer thickness-to-cavity height ratio depends only on the Rayleigh number [8] expressed as:

$$Ra_H = \frac{\beta g\Delta T H^3}{\nu\alpha} \tag{19}$$

12. Experimental Set Up

The model is 8.3 cm high, 4 cm large and 8 cm long. The test section is provided with two optical accesses, one for the camera and the other for the Laser sheet. The fluid is water with a proper concentration of Rhodamine B. The tracers for PIV are 32 m of diameter hollow glass spheres. The metal side vertical walls are in contact with Peltier cells, the heat flux of which is adjusted to obtain a stable wall temperature. Fig.14b shows the optical arrangement. A double cavity YAG source produces a Laser beam at 532 nm. The Laser illuminates a section of the cavity, one camera, with a band pass filter centered on 580 nm, detects the fluorescent signal and the other camera, with a band pass filter centered on 532 nm, detects the light scattered by the particles

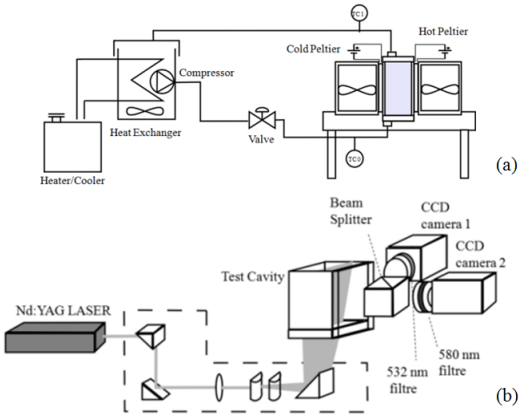

Figure 14: (a)Experimental set up. In the calibration phase the Peltier cells are off, while the flow is circulating through heat exchanger and cavity. (b) The images are obtained by two cameras CCD LaVision, Imager intense, 16bit, with a resolution of 1.4 million of pixels, simultaneously thank to a beam splitter.

13. LIF principle and calibration

The LIF technique is based on the fluorescent emission of an organic dye. The intensity of this re-emitted light is function of the liquid temperature. In the present experiment the molecules of Rhodamine are excited by a 532 wavelength photon flux. The probability of absorption of one photon by a RhB molecule depends on the absorption cross section ε_{RhB} that is only a function of the incident photon wavelength on the range of temperatures [0-100]°C[9].

The excited molecule emits a photon characterized by a lower energy level (fluorescence). The intensity

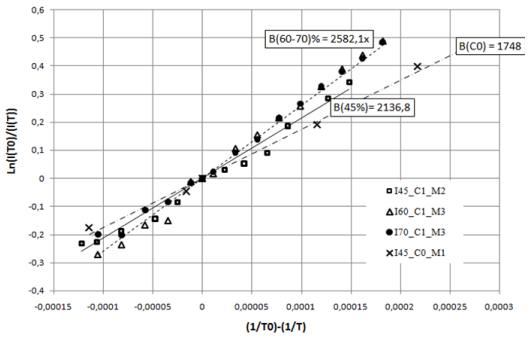

Figure 15: Laser Intensities: I45=45% of total power, I60=60%, I70=70%, Concentrations: C0=10^{-7}mol/l, C1=2.6 10^{-6}mol/l, Magnification factor: M1=0.09 mm/px, M2= 0.03 mm/px, M3= 0.06 mm/px

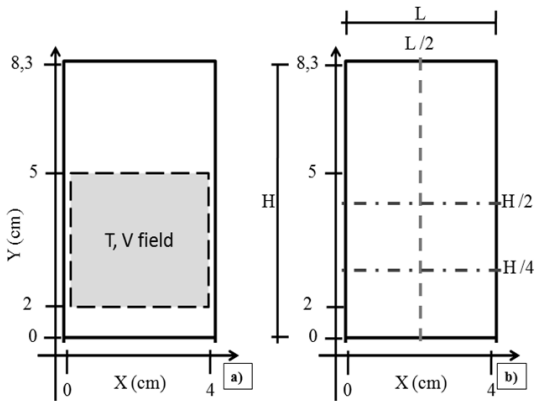

Figure 16: Domain for mapping (a) and lines selected for the extrapolation of velocity and temperature profiles (b)

of the emitted photon flux decreases for higher temperatures. For a given temperature and optical set up, the fluorescent signal detected by each pixel of the CCD camera, and as a consequence the resolution of the technique, will depend on:

- The concentration of the fluorescent dye [10]
- The incident Laser light intensity [11]
- The optical magnification factor [12]

Typical calibration curves are drawn in Fig.15 for different magnification factors, concentration and Laser intensity. The fitting correlation is [9]:

$$\ln \frac{I(T_0)}{I(T)} = B\left(\frac{1}{T_0} - \frac{1}{T}\right) \tag{20}$$

The resolution of LIF measurements decreases as the slope of the calibration curve, B, lessens.

14. LIF and PIV coupled - Results

Fig.16a shows the domain investigated mapping velocity and temperature. The vertical gradient of temperature is measured in the middle of the cavity (X=L/2) while horizontal profiles of velocity and temperature are drawn for Y=H/2 and Y=H/4 (Fig.16-b)

Tests were carried out for different heat fluxes but in the present paper only results obtained with a power 36 W are presented. Further results are reported [13]. Fig.17 proposes comparisons of LIF and thermocouple measurements. The agreement is rather satisfactory because the difference between the two techniques doesnt exceed 2°C. and because this discrepancy could be explained by the same difference observed on the cold wall temperature between the thermocouple and the LIF tests.

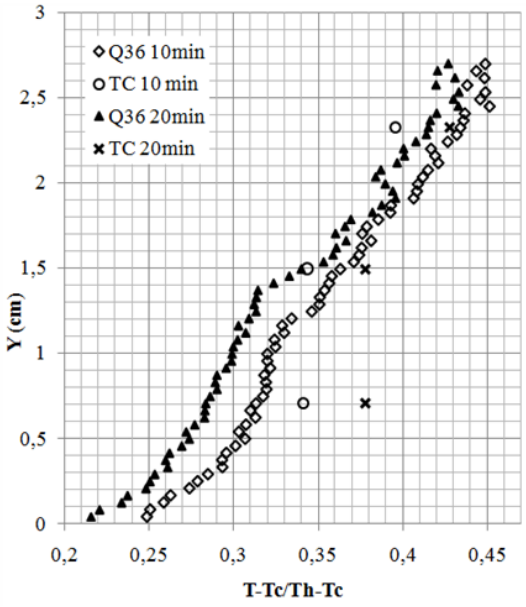

Figure 17: Comparison between thermocouples and LIF measurements, Q36 labels LIF measurements, TC labels thermocouple measurements

The profile of the axial velocity component and temperature are plotted in Fig.18 for Y=H/2 (a) and Y=H/4 (b).

The graphs focus on the region close to the cold wall of the cavity. Table 3 indicates the highest and lowest temperatures measured at the cavity walls by means of thermocouples.

The Ra_H value of the experiments corresponds to

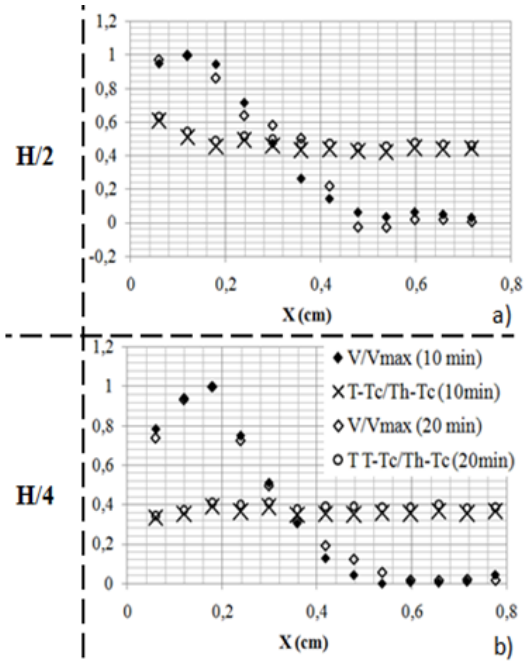

Figure 18: Normalized velocity and temperature values at the cold wall, Q=36W. The profiles are drawn for Y=H/2 (a) and Y=H/4 (b).

a regime characterized by very thin boundary layer. The boundary layers are confined in the wall region and they dont interact [4]. The theoretical value of the boundary layer thickness retrieved with the formulation expressed in Section 11 is 1 mm; that fits reasonably with the one estimated from Fig.18. As the Prandtl number is greater than the unity, the thickness δ_T of the thermal boundary layer is smaller than the thickness δ of the velocity boundary layer. While it is possible to resolve the last one, the spatial resolution is not sufficient to measure the thermal boundary layer. Table 3 compares the experimental values of δ and δ_T for Y=H/4. The ratio between the two thickness is in good agreement with the correlation proposed by [8]:

$$\frac{\delta_T}{\delta} < \frac{1}{\sqrt{Pr}} = 0.36 \tag{21}$$

Table 3: Rayleigh and Prandtl number are calculated thorough an average of water properties performed on the range of temperature observed during the experiment. and T are evaluated for Y=H/4.

T_{cold}	21°C
T_{hot}	37°C
Ra_H	1.8 10^8
Pr	5.8
δ (theory)	~ 1 mm
δ	~ 5.3 mm
δ_T	~ 1.9 mm
δ_T/δ	0.358

15. Discussion

Planar calibration and experiments have been performed in the cavity without changing the optical system or fluorescent dye concentration. An analysis of uncertainty, based on 100 samples revealed 1.25 K of uncertainty in line with recent study which indicates 1.8 K [14]. Beside the relative high uncertainty the main drawback of one color LIF for temperature measurement is the dependency of the fluorescent signal on the input laser light. In the case of a laser light not constant in time, only time averaged temperature mapping is possible. However, the technique is judged suitable to measure temperature gradients higher than 0.2°C/cm, and was as a consequence applied to Aquarium [14].

16. Future Work

Two set up for experimental natural convection studies were proposed. The scaling of the large scale facility (Aquarium) was performed in order to respect as much as possible the non dimensional numbers values of the nuclear reactor Myrrha. A parametric study was performed in order to understand the influence of the geometry of the upper vessel on the development of temperature profiles. However the flow in Aquarium is characterized by two main components of velocity, vertical and radial, while the tangential component of mixing, that occurs instead in the real case, is not considered. As a consequence the mixing is underestimated in all the cases analyzed and the stratification is overestimated with respect to the real case. For this reason it would be more correct to rely on the data retrieved from a larger scale, three dimensional water model of the reactor. A numerical study on Aquarium is furthermore foreseen in order to extend the range investigated for each geometrical details considered in the previous analysis. Stratification in the small cavity with differentially heated walls was detected and measured by LIF. More experimental work is foreseen in order to measure the thermal boundary layer at the wall the cavity. In particular the spatial resolution in correspondance of the boundary

layer region should be increased in order to measure with higher precision thermal and velocity profiles.

References

[1] N. E. Todreas, M. S. Kazimi, Nuclear system II-Elements of Thermal Hydraulic Design, Hemisphere, New York, 1990.

[2] P. K. Vijayan, A. Nayak, D. Saha, M. R. Gartia, Effect of Loop Diameter on the Steady State and Stability Behaviour of Single-Phase and Two-Phase Natural Circulation Loops, Science and Technology of Nuclear Installations 2008.

[3] W. D. Bainest, J. S. Turner, Turbulent buoyant convection from a source in a confined region, Journal of Fluid mechanics 37 (1) (1969) 51–81.

[4] Y. Jaluria, Natural Convection Heat and Mass Transfer, Pergamon Press, HMT- The Science and Application of Heat and Mass Transfer, 1980.

[5] D. S. Martinez Hernandez, C. Spaccapaniccia, P. Planquart, J. M. Buchlin, Experimental and numerical study of natural convection in fuel assembly bundles, Vki internal report, Von Karman Institute for Fluid Dynamics (2012).

[6] I. E. Idelchik, Handbook of Hydraulic Resistance, Jaico Publishing House, New York, 2008.

[7] I. A. Horvat, Simultaneus and Istantaneus Velocity and Concentration Measurements on Model and Real Scale Car Park Fire Scenarios, Ph.D. thesis, Universite Libre de Bruxelles (2012).

[8] A. Bejan, Convection Heat Transfer, Wiley, New York, 2004.

[9] F. Lemoine, Y. Antoine, M. Wolff, M. Lebouche, Simultaneous temperature and 2D velocity measurements in a turbulent heated jet using combined laser-induced fluorescence and LDA, Experiments in Fluids 26 (1999) 315–323.

[10] K. E. Meyer, P. S. Larsen, Temperature and Velocity field in Natural convection by PIV and LIF, no. 11th Int. Symposium on Application of Laser Techniques to Fluid Mechanics, Lisbon, Portugal, 2002.

[11] C. Tropea, A. Yarin, J. Foss, Handbook for Experimental Fluid Mechanics, Springer, New York, 2007.

[12] B. Hiller, R. K. Hanson, Properties of the Iodine Molecule relevant to Laser Induced Fluorescence experiments in gas flows, Experiments in Fluids 10 (1990) 1–11.

[13] C. Spaccapaniccia, Ph. Planquart, M. R. Vetrano, J. M. Buchlin , Simultaneus measurements of temperature and velocity by PIV and LIF techniques in a rectangular cavity with heat fluxes at the walls, no. 13ime Congrs Francophone de Techniques Laser, CFTL , Rouen, France, 2012.

[14] Z. E. Yildirim, C. Spaccapaniccia, P. Planquart, J. M. Buchlin, Study of Stratification in a Natural Convection Loop, Vki internal report, Von Karman Institute for Fluid Dynamics (2013).

UNCERTAINTY QUANTIFICATION

Quantifying Inflow Uncertainties for CFD Simulations of Dispersion in the Atmospheric Boundary Layer

Clara García Sánchez

Environmental and Applied Fluid Dynamics Department, von Karman Institute for Fluid Dynamics, Belgium, clara.garciasanchez@vki.ac.be

EMAT, Department of Physics, University of Antwerp, Groenenborgerlaan 171, 2020 Antwerp

Supervisor: Jeroen van Beeck

Professor, Environmental and Applied Fluid Dynamics Department, von Karman Institute for Fluid Dynamics, Belgium, vanbeeck@vki.ac.be

Co-Supervisor: Catherine Gorlé

EMAT, Department of Physics, University of Antwerp, Groenenborgerlaan 171, 2020 Antwerp, gorle@vki.ac.be

University Supervisor: Gustaaf van Tendeloo

Professor, Department Fysica, Antwerp University, Belgium, staf.vantendeloo@uantwerpen.be

Abstract

When using Computational Fluid Dynamics (CFD) methods to investigate wind flow and dispersion in urban environments validation with field experiments that represent the full complexity of the problem should be performed to assess the predictive capabilities of the computations. In this context it will be necessary to quantify the effect of uncertainties in simulations of the full-scale problem. This research aims at quantifying the uncertainty related to the variability in the inflow boundary conditions for Reynolds-averaged Navier-Stokes simulations of the flow in downtown Oklahoma City to address validation with the Joint Urban 2003 field measurements.

Keywords: computational fluid dynamics, Joint Urban 2003, pollution, uncertainty quantification, boundary conditions

1. Introduction

Continuous population growth is linked to a progressive expansion of urban environments and building structures. As a consequence, there is increasing interest in understanding and accurately determining wind distributions within cities for different purposes such as assessing pedestrian wind comfort, wind loads on buildings, air quality levels, or potential wind energy resources [1; 2]. Nevertheless, the prediction of the flow pattern in urban canopies is a challenging task, as it is characterized by complex turbulent structures with multiple separation and recirculation zones created by the presence of buildings. Additionally the intrinsic variability in atmospheric conditions further compromises the predictive capability of computations of the flow field inside the urban canopy [3].

Increasing computer resources have resulted in a relatively widespread use of computational fluid dynamics (CFD) to solve the Reynolds-averaged Navier-Stokes (RANS) equations for predicting flow and dispersion in realistic urban canopies [4]. In the RANS approach the flow variables are decomposed into mean values and their turbulent fluctuations, and a turbulence model, e.g. a k-ε, k-ω, or a second-moment closure model [5], is used to model the Reynolds stress tensor in the Reynolds-averaged momentum equations. Numerous, often more academic, validation studies have shown the limitations of this methodology in terms of accurately predicting complex separated flows [6]. As a result, a tendency towards using Large Eddy Simulations (LES) of atmospheric boundary layer flows can be observed [7; 8; 9]. LES resolves the larger scales of turbulence that characterize the flow, and models only the smaller scales [10]. A

well-resolved LES certainly provides improved turbulence model accuracy, but the approach is significantly more expensive, which inhibits its practical and operational application for modeling flow and dispersion in urban environements.

While validation studies often show the superior performance of LES, it is important to remember that these studies mainly focus on validation with wind tunnel measurements. The reason for that is twofold. First, a large number of wind tunnel experiments have been carried out to study the flow and dispersion around scaled building geometries [11; 12], some of them providing comprehensive validation data sets in a wide range of configurations [13]. Second, the flow conditions and model configuration in the wind tunnel can be accurately measured and documented to reconstruct the wind tunnel model in the CFD simulations. Field measurements, on the other hand, are prohibitively expensive and only a few full-scale measurements have been performed during the last decade, e.g. in New York, London, Oklahoma City and Salt Lake City [14; 15; 16; 17]. Validating computations with field experiments is complicated by the uncertainty in the input parameters required to set up the computations. There is only a limited amount of data available to infer the inflow conditions that have to be specified in the simulations, and it is impossible to represent the level of detail present in reality through any numerical model. Klein et al. [3] addressed comparisons between field and wind tunnel measurements, demonstrating the relatively large discrepancy between field and wind tunnel data. This indicates that the capability of a simulation to reproduce a specific wind tunnel measurement is no guarantee of its predictive capabilities when applied to a full-scale problem where bigger scale motions, such as mesoscale phenomena have an important influence.

To assess the predictive capabilities of the computations, it is necessary to quantify the effect of uncertainties in simulations of the actual full-scale problem and perform validation studies with field experiments. Two different kinds of uncertainties can be identified: uncertainties due to the physical variability of the system (aleatory uncertainty) and uncertainty due to a lack of knowledge (epistemic uncertainty) [18]. Epistemic uncertainty can be reduced by developing and using more accurate models, but aleatory uncertainty is inherent to the modeled system. Reducing the epistemic uncertainty in a system with significant aleatory uncertainty might only result in a small improvement of the predictive capabilities of the simulations, while coming at a significantly higher computational cost. For example, the use of LES simulations for modeling the flow inside urban canopies will result in a smaller epistemic uncertainty than RANS simulations, but the increased cost per simulation in combination with an increased number of uncertain input variables, necessary to define the unsteady turbulent boundary conditions, renders the approach orders of magnitude more expensive. If other uncertain parameters induce considerable uncertainty in the solution, this higher computational cost might not be justifiable for practical applications.

The present study therefore investigates the feasibility of using RANS simulations in combination with non-intrusive polynomial chaos to quantify the uncertainty in the solution for the flow field induced by uncertainty in the inlet conditions for the simulations. The methodology is applied to simulate the flow field in downtown Oklahoma City (OKC) and a comparison with field measurement data from the Joint Urban 2003 (JU2003) field measurement campaign, is performed. The selected inflow uncertainty is only one of the many uncertainties in these simulations, but it is expected to be of primary importance because the inflow conditions largely determine flow and dispersion patterns within the urban canopy, and they are directly related to the irreducible atmospheric variability. Consequently, characterizing the inflow uncertainty is a good starting point for exploring the capabilities of a stochastic framework for performing environmental flow simulations and addressing validation with field experiments.

2. Joint Urban 2003

The main purpose of the Joint Urban 2003 (JU2003) field experiment in Oklahoma city was to provide quality-assured meteorological and tracer data sets for the validation of indoor and outdoor dispersion models in urban environments. The large-scale measurement campaign took place during one month of the summer in 2003. Wind velocity, wind direction, and concentration of sulfur hexafluoride (SF_6) were determined based on sonic anemometers, airplane-based meteorological sensors, and fast-response tracer analyzers. The final data set provided by JU2003 also included an accurate geometrical description. Most of the geometrical complexity is related to the presence of buildings, since the state has a flat natural topography. For the dispersion measurements, ten eight-hour intensive observation periods (IOPs) were completed during the study period.

The tracer was released in downtown OKC at different locations for each IOP, and sampled in and around downtown. Allwine and Flaherty [16] provide a summary of all the institutions participating in the measurements with their specific locations for the experiments, and an overview of the measurement techniques.



Figure 1: PWIDS locations inside downtown Oklahoma city. Red color indicate the southest station: PWIDS 15 [16].

Additional studies have focused on analyzing the dispersion measurements, pointing out the challenge introduced by the atmospheric variability found in 'real-life' experiments [19]. The influence of the varying atmospheric stability and its effect on turbulence within urban environments were also investigated in [20; 21]. Other publications focused on the mesoscale phenomena over Oklahoma city during the measurement campaign concluding that mesoscale motions have a relatively important influence on turbulent mixing and atmospheric variability, which CFD simulations with boundary conditions that represent a neutral atmospheric boundary layer do not include [22; 23]. Several studies have investigated computational modeling of the experiment. RANS simulations for the flow and dispersion in Oklahoma city are described in [24; 25]. In [25] it was noted that the validation of efforts to better model the effects of turbulence anisotropy on dispersion in the complex urban geometry was hindered by uncertainty in the mean flow field. A validation of FEM3MP (Finite Element Model in 3-Dimensions and Massively Parallelized), is presented in [26]. Through the validation process they point out the relevance of considering stability effects during day releases for dispersion [27], and they justify the use of neutral stability assumption in the urban simulations for determined night time measurements. Lastly, some studies have used LES to model JU2003 [9; 28]. Neophytou et al. [28] compared three different approaches, a mass-consistent empirical diagnostic code, RANS, and LES. The study demonstrates that only a slight improvement was obtained by resolving the large scale turbulent structures with LES, compared to the RANS and empirical code. They point out the relevance of the variability of atmospheric flows, and the unrealistic definition of the boundary conditions in CFD simulations used at present.

This study describes a computational approach that enables analyzing the influence of the variability in the boundary conditions, specifically investigating the influence of varying the wind direction and velocity, and the roughness length. The actual ranges of the variables for the uncertainty quantification study were defined based on the field measurement data obtained with the Portable Weather Information Display System (PWIDS), operated by Dugway Proving Ground. The PWIDS measure the velocity magnitude and direction each second and average the values each 10 seconds before recording. Figure 1 illustrates the locations of the measurement station.

3. Computational model

This section describes the governing equations and their discretization, and the computational model used. It includes the influence of the selected domain size and the grid sensitivity study on the results. These preliminary simulations were performed for a south wind direction, which was the dominant direction during the complete measurement campaign. For this, the field measurement data was extracted by parsing all measurement times with wind direction south at PWIDS 15, represented in red in figure 1. This sensor is positioned south of the downtown region of the central business district (CBD), in a location amenable to providing inflow conditions for the flow coming from the south direction.

3.1. Governing equations and discretization schemes

The governing equations for neutral conditions are given by the steady, incompressible Reynolds-averaged Navier-Stokes equations:

$$\frac{\partial \overline{u_j}}{\partial x_j} = 0, \tag{1}$$

$$\overline{u_j}\frac{\partial \overline{u_i}}{\partial x_j} = -\frac{1}{\rho}\frac{\partial \overline{p}}{\partial x_i} + \nu\frac{\partial^2 \overline{u_i}}{\partial x_j^2} - \frac{\partial \overline{u_i' u_j'}}{\partial x_j}, \tag{2}$$

where $\overline{u_i}$ are the time-averaged velocity components, ρ is the density, $\overline{p}$ the pressure, ν the kinematic viscosity and $\overline{u_i' u_j'}$ the Reynolds stress tensor. The RANS equations need to be closed by a model for the Reynolds stress tensor. In the present simulations the standard k-ε turbulence model is used, which computes the Reynolds stresses based on the linear eddy viscosity hypothesis:

$$\overline{u_i' u_j'} = \frac{2}{3}k\delta_{ij} - 2\nu_t S_{ij}, \tag{3}$$

where k is the turbulence kinetic energy, δ_{ij} the Kronecker delta, S_{ij} the time-averaged shear stress tensor and ν_t the turbulent viscosity, given by:

$$\nu_t = C_\mu \frac{k^2}{\varepsilon} \tag{4}$$

with C_μ a constant equal to 0.09, and the turbulence kinetic energy k and turbulence dissipation rate ϵ obtained from solving their respective transport equations:

$$u_i\frac{\partial k}{\partial x_i} = \frac{\partial}{\partial x_j}\left[\left(\nu + \frac{\nu_t}{\sigma_k}\right)\frac{\partial k}{\partial x_j}\right] + P_k - \varepsilon, \tag{5}$$

$$u_i\frac{\partial \varepsilon}{\partial x_i} = \frac{\partial}{\partial x_j}\left[\left(\nu + \frac{\nu_t}{\sigma_\varepsilon}\right)\frac{\partial \varepsilon}{\partial x_j}\right] + C_{\varepsilon 1}\frac{\varepsilon}{k}P_k - C_{\varepsilon 2}\frac{\varepsilon^2}{k}, \tag{6}$$

with P_k the turbulent production term and σ_k, σ_ε, $C_{\varepsilon 1}$, $C_{\varepsilon 2}$ model constants, respectively equal to 1.0, 1.3, 1.44 and 1.92.

It is noted that this turbulence model does not qualify as the most accurate or reliable turbulence model available. However, the goal of this study is not to investigate to what extent the turbulence model correctly represents the flow, but to quantify the influence of uncertainty in the inflow conditions on the result. This effect is likely to be similar for different turbulence models available. In ongoing work, the turbulence model inaccuracy will be further addressed, not by testing different turbulence models in an attempt to find the most accurate one, but by incorporating a turbulence model form uncertainty quantification method [29; 30].

The continuous equations were discretized using second order upwind schemes for velocity, turbulence kinetic energy, and turbulent dissipation. The gradients were computed using a least squares cell based interpolation, and the pressure-velocity coupling was done with the SIMPLE algorithm. The simulations were run for 1600 iterations, which resulted in a converged solution with residuals below 10^{-7} for velocity and turbulence kinetic energy, and below 5^{-6} for mass conservation and the turbulent dissipation.

3.2. Boundary Conditions

In CFD simulations, the boundary conditions are known to be of paramount importance [31]. It is recognized that these boundary conditions are highly variable when considering realistic, full-scale applications [3; 28; 32]. The definition of the boundary conditions therefore becomes extremely relevant, as they represent a major source of uncertainty, given the variability of the atmospheric conditions. In the present work we address a comparison with field measurement data obtained at night time, when the boundary layer was neutrally stable. The inflow boundary conditions therefore specify a fully-developed neutral atmospheric boundary layer, which can be represented by the following profiles for velocity, turbulence kinetic energy and dissipation [33]:

$$U = \frac{u_*}{\kappa} ln\left(\frac{z + z_0}{z_0}\right), \tag{7}$$

$$k = \frac{u_*^2}{\sqrt{C_\mu}}, \tag{8}$$

$$\varepsilon = \frac{u_*^3}{\kappa(z + z_0)}, \tag{9}$$

where κ is the von Karman constant with a value of 0.41. The friction velocity u_* and the aerodynamic roughness z_0 are the parameters that will be varied to quantify the effect of inflow variability. The friction velocity is determined from the specified aerodynamic roughness, and the reference velocity U_{ref} measured at $z_{ref} = 30\ m$ for PWIDS 15 [16], which is the southmost sensor near the downtown region (figure 1). For the preliminary simulations, the parameters used were $U_{ref} = 6.3\ ms^{-1}$ and $z_0 = 0.5\ m$, and the wind direction was south. The ranges considered for the uncertainty quantification study are presented in Section 4.

The use of wall functions is unavoidable for this type of high Reynolds number applications where relatively coarse meshes are used. In the present simulations we use a wall function based on the aerodynamic roughness at the ground wall [34], to ensure that there is no unintended horizontal gradient in the specified velocity inlet profile in the region upstream of the buildings [35]. On the building walls a standard log law wall function for smooth surfaces is applied.

3.3. Computational Domain and Mesh

The domain is a rectangular box with the dimensions indicated in figure 2, containing the buildings of downtown and suburban Oklahoma city. The buildings represented are located within a circle of diameter 1.6 km, centered around the location of the tracer release "Park" for IOP9. This release will be used in future research to introduce a pollutant source and to compare dispersion predictions against tracer measurements. The proposed domain configuration satisfies the guideline formulated in COST 732 [31], which states that a building with height H_n may have a minimal influence if its distance from the region of interest is greater than 6 to $10H_n$, where the region of interest is defined as the area within which concentration measurements where performed.

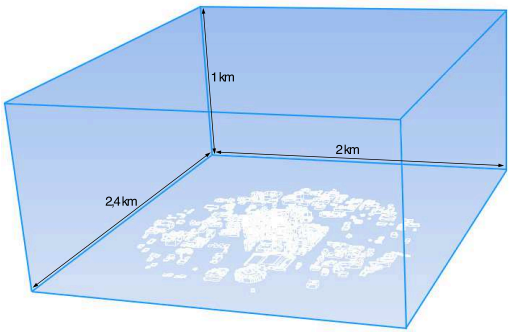

Figure 2: Domain size specifications.

Prior to using these settings for the uncertainty quantification study, simulations with a larger domain and a finer mesh were performed to determine the influence of the domain size and the mesh refinement. The meshes were generated with Tommie, a fully automated parallel mesh generator developed at Stanford [36]. It reads surface descriptions from an STL, and generates a Cartesian grid with locally defined anisotropic refinements such that a user-specified resolution is guaranteed throughout the grid. When modeling different wind directions during the uncertainty quantification investigation, the STL is rotated inside the domain, and a new mesh is automatically generated. A resume with the domain and meshes size is presented in table 1

	Nominal	Extended	Fine
Number of cells (10^6)	5.5	10	29
Domain size (10^6 km^3)	4.806	8.759	4.806

Table 1: Nominal, extended and fine cases properties.

The differences between the nominal and the extended domain are limited, the average discrepancy in the velocity magnitude is 0.26% of U_{ref}. For the wind direction the discrepancy is lower than 15° in 11 out of 14 measurement stations. Regarding the finer mesh case, in terms of velocity magnitude the differences between both meshes are small, with an average difference of 0.3% of U_{ref}. The discrepancy in the direction is also limited, with 8 out of 14 measurement stations producing results that agree within 15°. The differences do remain small, and extending the domain size or increasing the mesh size does not consistently provide a better agreement with the measurement data, therefore, it was decided to use the baseline mesh and domain for the large number of simulations that will be performed for the UQ study. This will significantly decrease the required computational time.

4. Uncertainty Quantification Study

Uncertainty quantification is generally focused on two main objectives: the construction of a framework to estimate the error bars associated to given predictions, and the evaluation of the likelihood of a certain outcome. Two different kinds of uncertainties can be identified: aleatory uncertainty, which is due to the physical variability of the system, and epistemic uncertainty, which is due to the lack of knowledge [18]. Developing and using more accurate models can reduce epistemic uncertainty, but aleatory uncertainty is always inherent to the modeled system. The number of uncertainties in simulations of atmospheric flow is large, and their importance will have to be characterized to develop predictive simulation tools. This work presents a first step towards quantifying the aleatory uncertainty related to the inflow conditions, which can be expected to be of primary importance.

The simulations focus on a 25 minutes period over the night of the 26th of July. The selection of this

specific period is based on two reasons: the conditions were near neutral at that time, and there was a 30 min continuous tracer release during that night in the Park area, which will be useful for future work focused on dispersion. The aim of the UQ study is to determine error bars for the predicted velocity field related to the uncertainty in the inflow. The result will be compared to the field measurement data at the locations of the PWIDS measurement stations (Figure 1). A validated prediction is defined as a result where the time-averaged field measurement over the 25 min period is within the range predicted by the UQ study.

4.1. Uncertain variables

The boundary conditions used in this study were presented in section 3.2. The uncertain parameters have been determined to be the inflow velocity magnitude and direction at the reference height, and the atmospheric roughness height used to compute the friction velocity of the incoming atmospheric boundary layer. The friction velocity will determine the shape of the logarithmic inlet velocity profile, the inlet turbulence kinetic energy and the inlet dissipation [33].

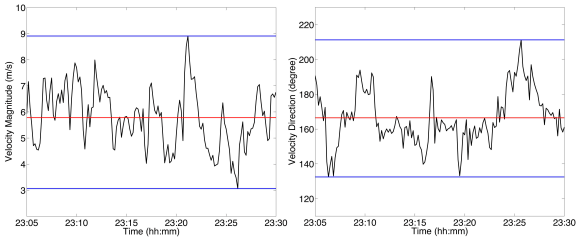

Figure 3: Time series for velocity magnitude and direction neutral case 26 of July 23:05-23:30 (UTC).

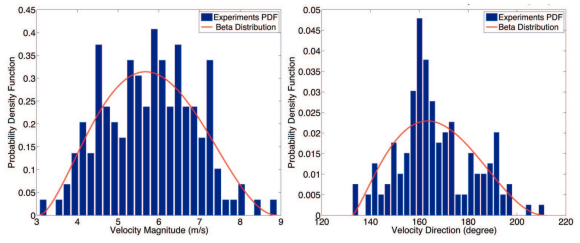

Figure 4: Histogram for velocity magnitude and direction neutral case 26 of July 23:05-23:30 (UTC).

The selection of the range of values to be considered for the roughness length was based on [37], where the values for the roughness length are related to the building density and vegetation. For the wind speed and direction, the range of values is based on the JU2003 measurements obtained during the time period selected for the study. Figure 3 and 4 present the time series and probability density distributions for wind speed and direction measured by PWIDS 15 during this 25 minutes period. The data is extracted from this station since it is the furthest south of downtown Oklahoma City, and the dominant wind direction during the measurement period was southern. The input ranges of the values for the velocity magnitude and direction are determined by the maximum and minimum values extracted from figure 3.

In figure 5 the different velocity profiles used at the inlet boundary conditions are presented in a 2D and 3D plot. The 2D plot presents the difference in velocity inlet profile when the roughness length and the velocity magnitude are modified, the inlet profile used for the nominal simulation is presented in the squared black line. The 3D plot shows the different planes that represent the variation in wind direction, as it can be seen in the front plane, each different shape for the inlet profile showed in the 2D plot is applied in each one of the different wind directions presented by the planes.

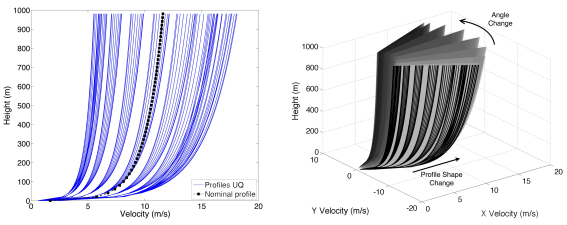

Figure 5: 2D and 3D representation of the different profiles applied for the inflow conditions in the UQ case.

4.2. Propagation algorithm

A non-intrusive polynomial chaos expansion (PCE) method was used for the uncertainty quantification. In non-intrusive PCE, the simulation tool is used as a black box. The calculation of the chaos expansion coefficients for known orthogonal polynomial basis functions that represent response metrics of interest is based on a set of simulation response evaluations [38]. Legendre basis polynomials were used to construct the response surfaces and the coefficients were computed using Clenshaw-Curtis quadrature with 729 response evaluations. Once the PCE response surfaces for the different quantities of interest were determined, 10.000 samples from these representations were drawn according to the beta distributions for the wind speed and direction. The mean and confidence

levels were subsequently determined from the probability density functions of the samples. The non-intrusive code Ray, developed at the Stanford UQ lab, was used to define the collocation points, queue the simulations, and post-process the results in a parallel Linux environment [39].

4.3. Results

Figure 6 presents the results obtained for the velocity at the different field measurement locations using the UQ approach described above. The black arrows represent the time-average from the experiment for the 25 minute period under consideration. The blue arrows represent the mean from 10.000 samples drawn from the PCE according to the beta distributions plotted in figure 4. The 95% confidence interval for both the measured and predicted velocities is represented by the arcs. The range of velocity magnitudes is represented by the arc radius, while the range of the directions is represented by the angle. The 95% confidence intervals are bounded at the values where the cumulative density function is 0.025 and 0.975. For the simulation results those are obtained from the 10.000 samples drawn from the PCE response surface, while for the experiments they are obtained from the 150 measured samples during the 25 minute period considered. As stated before, the goal of this paper is to obtain confidence intervals from the CFD that encompass the mean value of the experiments. It is noted that a direct comparison of the confidence intervals from the measurements and CFD simulations is not possible because the measured samples represent the instantaneous turbulent velocities, while the RANS simulations solve for the mean velocity and the confidence intervals are intended to represent fluctuations due to large scale variations in the inflow conditions.

Table 2 presents some further details on the results. N represents the number of the PWIDS station (station 9 is missing as the measurements for the period selected were not recorded). $\Delta\mathbb{E}[U_m]$ represents the difference in the expected values for the velocity magnitude from the experimental time series and the CFD UQ study in percentage values; $\Delta\mathbb{E}[\theta_U]$ represents the difference in the expected values for the flow direction between the experiments and the CFD UQ study in absolute values. In the 'UQ Range Validated' column a '✓' indicates that the mean from the experiments is within the 95% confidence interval from the UQ study for the velocity magnitude or direction. When the UQ result does not encompass the experimental mean the

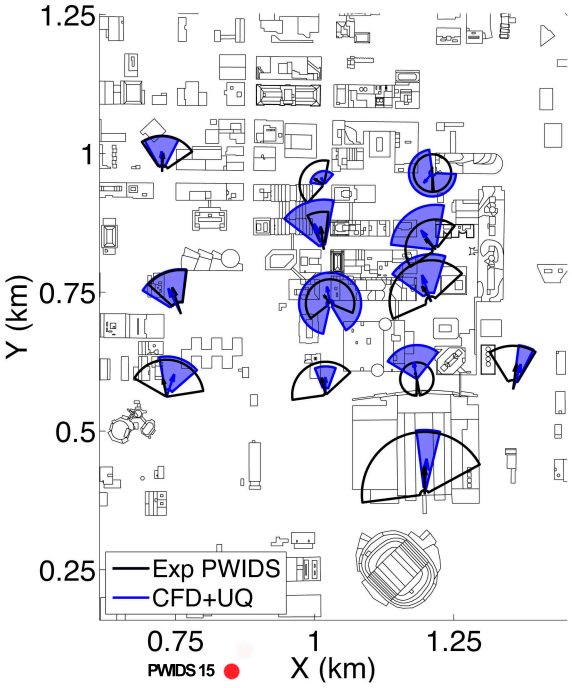

Figure 6: Comparison of the measurements on July 26th from 23:05-23:30 with the uncertainty quantification study results.

discrepancy between the bound of the confidence interval and the experimental mean is reported.

Considering the velocity magnitude the mean experimental velocity magnitude is covered by the range of magnitudes predicted by the UQ study in all stations. In terms of the direction, the experimental mean velocity direction is within the range predicted by the CFD in 11 out of 13 locations. In section 3, the deviations from the nominal simulation when extending the domain or refining the mesh were presented. It is important to remark that the stations that had larger discrepancies in the wind direction compared to the nominal case also correspond to a relatively wide UQ range for the wind direction in figure 6.

The result confirms the initial hypothesis that the variability in the inflow conditions is indeed an important contributor to uncertainty in the prediction of the mean flow in the urban canopy. The present UQ study allows the quantification of this effect. More specifically, it indicates locations in the flow that are particularly sensitive to the inflow conditions, such as the regions near PWIDS 3 and 7. The comparison with the experimental data in figure 6 also allows to identify the stations where there remains a discrepancy with the CFD results that is most likely induced by additional uncertainties. Probable candidates are

geometric uncertainties, or the epistemic uncertainty related to the limited accuracy of the turbulence model for computing the complicated bluff body flow inside the urban canopy.

N	$\Delta\mathbb{E}[U_m]$ [%]	UQ Range Validated	$\Delta\mathbb{E}[\theta_U]$ [°]	UQ Range Validated
1	0.08	✓	4.26	✓
2	0.33	✓	37.80	✓
3	1.18	✓	133.78	2.44°
4	0.18	✓	12.16	✓
5	0.56	✓	7.52	✓
6	0.02	✓	8.03	✓
7	0.62	✓	25.48	✓
8	0.52	✓	11.12	✓
10	0.28	✓	30.17	0.83°
11	0	✓	12.00	✓
12	1.63	✓	3.57	✓
13	0	✓	9.16	✓
14	0.26	✓	3.72	✓

Table 2: Velocity magnitude and direction differences from the experiments and the uncertainty quantification study.

5. Conclusion and Future Work

5.1. Conclusions

We performed an uncertainty quantification study that aims to characterize the influence of inflow variability on the prediction of flow in a real urban canopy. The study is a first step towards developing a Quantification of Margins and Uncertainties (QMU) framework that accommodates validation with full scale measurements, which is essential for evaluating the predictive capabilities of CFD simulations for urban flow and dispersion processes [40]. The JU2003 measurement campaign in Oklahoma City was selected as the test case because of the large data set available.

A 25 minute measurement period was considered and the inflow uncertainty was introduced through 3 uncertain variables: the inflow velocity magnitude and direction at a reference height, and the atmospheric roughness of the logarithmic inflow profile. For the first two variables probability distributions were obtained from the time series recorded by the southmost field measurement station. For the aerodynamic roughness the possible range of values was based on an empirical estimate of the roughness as a function of the upstream terrain characteristics. These uncertainties were propagated using a non-intrusive polynomial chaos approach, generating a polynomial chaos expansion response surface for the quantities of interest. Statistics of these quantities were obtained by sampling from this response surface according to the input distributions. The statistics of interest are the mean and the 95% confidence interval, which is defined by the values where the cumulative distribution function is 0.025 and 0.975. A prediction is considered validated when the time-average over the measurement period is within the confidence bounds obtained from the CFD UQ study.

Considering the velocity magnitude the mean experimental velocity magnitude is encompassed within the 95% confidence interval for the magnitudes predicted by the UQ study in all stations. In terms of the direction a validated prediction is obtained in 11 out of 13 locations. The results confirm that the variability in the inflow conditions is indeed an important contributor to uncertainty in the prediction of the mean flow in the urban canopy and they demonstrate the potential of applying advanced uncertainty quantification methods to address validation with field measurements.

Additionally, the results clearly identify locations in the flow that are particularly sensitive to the inflow conditions. This is very valuable information given the difficulty of defining accurate boundary conditions. The comparison with the field data also indicates in which regions there remains a discrepancy with the CFD results, i.e. regions where additional uncertainties are likely to be important. Probable candidates are geometric uncertainties, or the epistemic uncertainty related to the RANS turbulence model.

A number of questions and challenges remain to be addressed in future studies. First, the results for the velocity magnitude and the velocity direction indicate a somewhat different trend for both variables. The confidence levels for the magnitude encompass the time-average from the field experiment at all locations, and the results are rather conservative. For the wind direction on the other hand, the inflow variability as defined in this study can not fully explain the discrepancies with the field measurements. A possible explanation for this difference could be the variable extent to which both inflow variations are inherently represented as turbulence by the RANS model. Second, approaches that predict a non-dimensional velocity field that can be scaled with a varying reference velocity will be explored, since this might allow a reduction in the number of uncertainties.

5.2. Future work: coupling with mesoscale

In order to make the UQ approach available to cases for which no field measurement data is available, coupling with a mesoscale code will be considered. Mesoscale simulation results could be used to extract the necessary boundary conditions that drive the microscale simulations. This will be done through the coupling with the Numerical Weather Prediction (NWP) model Weather Research and Forecasting (WRF). This model is an open-source tool developed by Skamarock et al. [41]. This mesoscale code covers a range of scales from near synoptic scales (2000 km) to individual cloud cells ($\sim$ 1 km), based on reanalysis data. The code provides a nesting capability that allows higher resolution through embedded nests.

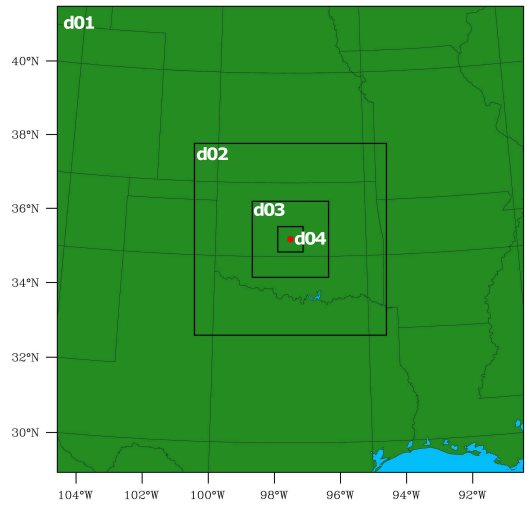

Figure 7: Mesoscale domains configuration over Oklahoma City. d0# represents the number of domain; the red point indicates the release location for IOP9.

In figure 7, the domain configuration is presented. The simulation is set up around the release location point of the Intense Observation Period 9 (latitude: 35.46871; longitud: 97.51556). The nesting technique is used reaching a maximum resolution of 1km in the fourth domain. The mesoscale initial and boundary conditions are extracted from the National Centre for Environmental Prediction North American Regional Reanalysis data (NARR), which supply 3h resolution data. The simulation covers one day in advance of the period of interest, in order to allow the spin-up of the mesoscale content in the simulation, as recommended in [22]. The parent domain is based on the resolution of NARR data, in order to extract enough information from the reanalysis data.

Acknowledgments

The author's contribution was supported by the Agency for innovation by Science and Technolodgy (IWT) in Belgium. The author acknowledges the following award for providing computing resources that have contributed to the research results reported within this paper: MRI-R2: Acquisition of a Hybrid CPU/GPU and Visualization Cluster for Multidisciplinary Studies in Transport Physics with Uncertainty Quantification. This award is funded under the American Recovery and Reinvestment Act of 2009 (Public Law 111-5). The WRF boundary conditions data were provided by the Data Support Section of the Scientific Computing Division at the National Center for Atmospheric Research (NCAR).

References

[1] W. Janssen, B. Blocken, T. van Hooff, Pedestrian wind comfort around buildings: Comparison of wind comfort criteria based on whole-flow field data for a complex case study, Building and Environment 59 (2013) 547–562.

[2] A. A. Razak, A. Hagishima, N. Ikegaya, J. Tanimoto, Analysis of airflow over building arrays for assessment of urban wind environment, Building and Environment 59 (2013) 56–65.

[3] P. Klein, B. Leitl, M. Schatzmann, Driving physical mechanisms of flow and dispersion in urban canopies, International Journal of Climatology 27 (2007) 1887–1907.

[4] B. Blocken, Y. Tominaga, T. Stathopoulos, CFD simulation of micro-scale pollutant dispersion in the built environment, Building and Environment 64 (2013) 225–230.

[5] D. C. Wilcox, Turbulence Modeling for CFD, DCW Industries, 1993.

[6] Y. Cheng, F. Lien, E. Yee, R. Sinclair, A comparison of large eddy simulations with a standard k-ε Reynolds-averaged Navier-Stokes model for the prediction of a fully developed turbulent flow over a matrix of cubes, Journal of Wind Engineering and Industrial Aerodynamics 91 (2003) 1301–1328.

[7] T. Stoesser, F. Mathey, J. Frohlich, W. Rodi, LES of flow over multiple cubes, ERCOFTAC Bulletin 53.

[8] Z.-T. Xie, I. P. Castro, LES and RANS for turbulent flow over arrays of wall-mounted cubes, Flow,Turbulence and Combustion 76 (3) (2006) 291–312.

[9] F. Harms, B. Leitl, M. Schatzmann, G. Patnaik, Validating LES-based flow and dispersion models, Journal of Wind Engineering and Industrial Aerodynamics 90 (2011) 289–295.

[10] F. Porté-Agel, H. Lu, Y.-T. Wu, CFD for atmospheric flows and wind engineering: Application of large-eddy simulation to atmospheric flows, Von Karman Institute for Fluid Dynamics Lecture Series, 2011-2012.

[11] P. Klein, B. Leitl, M. Schatzmann, Concentration fluctuations in a downtown urban area. Part II: analysis of Joint Urban 2003 wind-tunnel measurements, Environmental Fluid Mechanics 11 (2011) 43–60.

[12] E. Fedorovich, Dispersion of passive tracer in the atmospheric convective boundary layer with wind shears: a review of laboratory and numerical model studies, Meteorology and Atmospheric Physics 87 (2004) 3–21.

[13] U. Hamburg, CEDVAL Data Base, http://www.mi.uni-hamburg.de/Data-Sets.432.0.html (-).

[14] K. J. Allwine, J. E. Flaherty, Urban Dispersion Program MSG05 Field Study: Summary of Tracer and Meteorological Measurements, Tech. rep., Pacific Northwest National Labora- tory, Richland, Washington 99352 (August 2006a).

[15] S. Arnold, H. ApSimon, J. Barlow, S. Belcher, M. Bell, J. Boddy, R. Britter, H. Cheng, R. Clark, R. Colvile, S. Dimitroulopoulou, A. Dobre, B. Greally, S. Kaur, A. Knights, T. Lawton, A. Makepeace, D. Martin, M. Neophytou, S. Neville, M. Nieuwenhuijsen, G. Nickless, C. Price, A. Robins, D. Shallcross, P. Simmonds, R. Smalley, J. Tate, A. Tomlin, H. Wang, P. Walsh, Introduction to the DAPPLE Air Pollution Project, Science of The Total Environment 332 (1-3) (2004) 139–153.

[16] K. J. Allwine, J. E. Flaherty, Joint Urban 2003: Study Overview and Instrument Locations, Tech. rep., Pacific Northwest National Laboratory, Richland, Washington 99352 (August 2006b).

[17] K. J. Allwine, J. E. Flaherty, OVERVIEW OF URBAN 2000: A Multiscale Field Study of Dispersion through an Urban Environment, American Meteorological Sociaty 83 (4) (2002) 521–536.

[18] G. Iaccarino, Introduction to uncertainty representation and propagation, Tech. rep., NATO Research and Technology Organization Neuilly-sur-Seine (France) (2009).

[19] P. Klein, D. Young, Concentration fluctuations in a downtown urban area. Part I: analysis of Joint Urban 2003 full-scale fast-response measurements, Environmental Fluid Mechanics 11 (2011) 23–42.

[20] J. Lundquist, S. T. Chan, Consequences of Urban Stability Conditions for Computational Fluid Dynamics Simulations of Urban Dispersion, Journal of Applied Meteorology and Climatology 46 (2006) 1080–1097.

[21] P. Ramamurthy, E. R. Pardyjak, Observations of the Effects of Atmospheric Stability on Turbulence Statistics Deep within an Urban Street Canyon, Journal of Applied Meteorology and Climatology 46 (2007) 2074–2085.

[22] J. K. Lundquist, J. D. Mirocha, Interaction of Nocturnal Low-Level Jets with Urban Geometries as seen in Joint Urban 2003 Data, Journal of Applied Meteorology and Climatology 47 (2007) 44–58.

[23] X.-M. Hu, P. M. Klein, M. Xue, J. K. Lundquist, F. Zhang, Y. Qi, Impact of Low-Level Jets on the Nocturnal Urban Heat Island Intensity in Oklahoma City, Journal of Applied Meteorology and Climatology 52 (2013) 1779–1802.

[24] C. Gorlé, Dispersion of fine and ultrafine particles in urban environment, Ph.D. thesis, Universiteit Antwerpen (2010).

[25] D. A. Philips, Modeling Scalar Dispersion in Urban Environments, Ph.D. thesis, Stanford University (2012).

[26] S. T. Chan, M. J. Leach, A Validation of FEM3MP with Joint Urban 2003 Data, Journal of Applied Meteorology and Climatology 46 (2006) 2127–2146.

[27] J. Allegrinia, V. Dorer, J. Carmeliet, Buoyant flows in street canyons: Validation of CFD simulations with wind tunnel measurements, Building and Environment 72 (2014) 63–74.

[28] M. Neophytou, A. Gowardhan, M. Brown, An intercomparison of three urban wind models using Oklahoma City Joint Urban 2003 wind field measurements, Journal of Wind Engineering and Industrial Aerodynamics 99 (2011) 357–368.

[29] M. Emory, J. Larsson, G. Iaccarino, Modeling of structural uncertainties in Reynolds-averaged Navier-Stokes closures, Physics of Fluids 25 (2013) 110822.

[30] C. Gorlé, G. Iaccarino, A framework for epistemic uncertainty quantification of turbulent scalar flux models for reynolds-averaged navier-stokes simulations, Physics of Fluids 25 (2013) 055105.

[31] J. Franke, A. Hellsten, H. Schlünzen, B. Carissimo, Best practice guideline for the CFD simulation of flows in the urban environment, Tech. rep., COST Action 732 (May 2007).

[32] Z.-T. Xie, I. P. Castro, Coupled modelling of flow and dispersion in urban environments, in: The 5th International Symposium on Computational Wind Engineering, North Carolina (US), 2010, 2010.

[33] P. Richards, R. Hoxey, Appropriate boundary conditions for computational wind engineering models using the k-ε turbulence model, Journal of Wind Engineering and Industrial Aerodynamics 46 (1993) 145–153.

[34] A. Parente, C. Gorlé, J. van Beeck, C. Benocci, A Comprehensive Modelling Approach for the Neutral Atmospheric Boundary Layer: Consistent Inflow Conditions, Wall Function and Turbulence Model, Boundary Layer Meteorology 140 (2011) 411–428.

[35] B. Blocken, T. Stathopoulos, J. Carmeliet, CFD simulation of the atmospheric boundary layer: wall function problems, Atmospheric Environment 41 (2) (2007) 238–252.

[36] B. Khalighi, S. Jindal, J. J. andK.H. Chen, G. Iaccarino, Validation of the Immersed Boundary CFD Approach for Complex Aerodynamic Flows, Lecture Notes in Applied and Computational Mechanics 41 (2009) 21–38.

[37] J. Wieringa, Updating the Davenport roughness classification, Journal of Wind Engineering and Industrial Aerodynamics 41-44 (1992) 357–368.

[38] M. Eldred, J. Burkardt, Comparison of non-intrusive polynomial chaos and stochastic collocation methods for uncertainty quantification, AIAA Paper 2009-0976.

[39] G. Iaccarino, F. Ham, LES on Cartesian Grids with Anisotropic Refinement. Complex Effects in Large Eddy Simulations, Springer Berlin Heidelberg 56 (2007) 219–233.

[40] Y. Tominaga, T. Stathopoulos, CFD simulation of near-field pollutant dispersion in the urban environment: A review of current modeling techniques, Atmospheric Environment 79 (2013) 716–730.

[41] W. Skamarock, J. Klemp, J.Dudhia, D. Gill, D. Barker, M. Duda, X.-Y. Huang, W. Wang, J. Powers, A Description of the Advanced Research WRF version 3, NCAR/TN-475+STR, NCAR (June 2008).

Characterization of Boundary Layer Perturbations via Linear Stability Analysis

Gennaro Serino

Aeronautics and Aerospace Department, von Karman Institute for Fluid Dynamics, Belgium, gennaro.serino@vki.ac.be

Supervisors: Thierry E. Magin and Patrick Rambaud

Associate Professors, Aeronautics and Aerospace Department, von Karman Institute for Fluid Dynamics, Belgium, thierry.magin@vki.ac.be, patrick.rambaud@vki.ac.be.

Promoter: Vincent Terrapon

Assistant Professor, Aerospace and Mechanical Engineering Department, University of Liege, Belgium, vincent.terrapon@ulg.ac.be.

Abstract

This work aims at characterizing the free stream perturbations causing laminar to turbulent transition in hypersonic boundary layer. The e^N transition prediction method and Linear Stability analysis are used to compute the amplitudes of the perturbations at selected streamwise locations where experimental data are available. Normal probability distributions are obtained for the frequency spectrum for different free stream conditions. These perturbations are used to quantify the uncertainties on the transition onset when the frequencies have such a distribution. The initial amplitude of the perturbations in the boundary layer is also computed showing the dependency respect with the Frequency and the Reynolds number. Finally a comparison with experimental data is performed showing good agreement between the computed amplitudes and the pressure measurements along the model tested.

Keywords: Laminar to turbulent transition, hypersonic flows, Uncertainty Quantification, Linear Stability Theory, Reynolds Averaged Navier-Stokes, intermittency factor, pressure fluctuations in supersonic boundary layer.

Nomenclature

Symbols

A_0	initial amplitude of the disturbances
F	dimensional frequency (kHz)
M	Mach number
N	amplification ratio
N_{crit}	critical N for transition onset
Re	Reynolds number
St	Stanton number
p_T	probability of transition
$\hat{v}(y)$	amplitude of the perturbations
x	streamwise coordinate (m)
y	normal coordinate (m)
z	spanwise coordinate (m)

Greek symbols

α	streamwise wave number
β	spanwise wave number
δ_{μ_F}	MCMC increment for the mean
δ_{σ_F}	MCMC increment for the variance
γ	intermittency factor
μ	mean
ω	non-dimensional frequency
σ	variance

Abbreviation

CFD	Computational Fluid Dynamics
DNS	Direct Numerical Simulations
$MCMC$	Markov chain Monte Carlo
QoI	Quantity of Interest
$RANS$	Reynolds Averaged Navier-Stokes
TPS	Thermal Protection System
UQ	Uncertainty Quantification
VKI	von Karman Institute for Fluid Dynamics
cdf	cumulative distribution function
pdf	probability distribution function

1. Introduction

Laminar to turbulent transition in high speed flows has been the objective of an extensive experimental and numerical work during the years. Experiments have been carried out to improve the understanding of the physical mechanisms underlaying transition. On the other hand, numerical simulations have allowed to investigate several cases and conditions not reproducible in the tests. Both aim at developing criteria for scientific purposes and applicable in industrial design.

The study and prediction of laminar to turbulent transition is fundamental for high speed flow applications. The uncertainty on laminar-to-turbulent boundary layer transition is one of the most significant obstacle in the design and development of hypersonic vehicles since transition is a critical mechanism of high importance for system drag, thermal load, propulsive efficiency, and stability [1]. Because of the uncertainties and variations in the entry environment and the resulting thermal response of the material, it is common practice to provide a margin of safety by increasing the Thermal Protection System (TPS) thickness. It is important to use standardized quantitative methods in specifying the appropriate margin, because the addition of TPS mass reduces the mass available for payload. A common way is to use a sensitivity analysis by perturbing one parameter at a time in numerical simulations and by observing the variability in the output [2], accordingly. The heat flux at the wall of the vehicle is the leading parameter in the TPS design, since it changes dramatically in case of laminar or turbulent flow, as is experimentally observed [3]. Thus, the variability of the input conditions reflect in a change of the transition onset and on a variation of the thermal loads which are typically distributed within a range of expected values. A probabilistic approach is most suitable for such an approach since the variability of the input conditions yields the variability of the output quantity of interest that is related to the estimation of the TPS thickness. A complete sensitivity analysis can be very expensive in terms of computational resources and time, thus a faster approach is needed. The Uncertainty Quantification (UQ) approach has been demonstrated to be a valid tool to quantify and eventually reduce the error bars mostly used in industrial design in the applications considered currently [4].

The difficulty in transition prediction is related to the large number of parameters that can influence it. There is a variety of transition mechanisms to be dealt with when creating a mathematical model to describe the transition process. In flows with low freestream turbulence, mostly natural transition is expected to occur critically involving Tollmien-Schilichting (TS) waves [6] in the boundary layer (BL). In applications with higher freestream turbulence (more than 1%), the natural transition phase is bypassed since turbulent spots occur immediately. This phenomenon is called Bypass-Transition. For flow conditions where separated bubbles occur, disturbances in the shear layer above these bubbles can cause laminar to turbulent transition as well. In the hypersonic regime shocks are generating disturbances that can also yield transition. Another impact factor is the variability intrinsic to every physical environment. To take this all into account, a probabilistic approach has been used to study transition and satisfying results have been obtained focusing on high speed flows [5]. Uncertainty Quantification methods are used to take into account the variability of the physics in numerical simulations. First, probabilistic distributions of the input parameters are inferred. Second, these distributions are fed thorugh the deterministic algorithm to yield output distributions. Comparison with experimental data demonstrated the efficiency of the approach, but a justification of the assumptions made on the input distributions was still lacking. This paper will comment on the main results obtained in previous works with a physical justification of the assumptions made. The main question that rose from previous work is how to justify a probabilistic distributions for the input parameters. In particular, a probabilistic distribution of the frequency of the perturbations upstream of the transition onset was assumed and this paper will justify this via experimental observations.
This paper thus represents the integration of the previous work by linking experiments and deterministic computations through the stochastic approach. It is in fact demonstrated that the probabilistic distributions assumed as the input of the deterministic simulations agree with what can be experimentally measured in transition experiments.

2. State of the Art

Theoretical studies address laminar to turbulent transition to the amplification of freestream perturbations in the boundary layer. These perturbations, often called modes, originate in the laminar boundary layer and, once excited, grow exponentially until non-linear physics take over which includes the final breakdown

to turbulebce [6]. In high speed flows, the most unstable perturbations are the second modes as demonstrated by numerous calculations [7] and observations.

In order to develop reliable methods for transition prediction, experimental measurements are necessary. The most useful are those regarding the boundary-layer instabilities in terms of pressure or velocity fluctuations, which are achieved via pressure sensors and hot wire anemometers [8]-[9]-[12]. These measurements are performed at selected streamwise locations on the surface of the model and requires several runs of the same test. These tests are therefore very expensive, but necessary, in order to improve methods for predicting transition. An example of these measurements is shown in Fig.1 for data acquired in the VKI-H3 wind tunnel by Masutti[10].

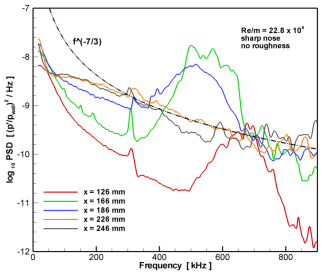

Figure 1: Measurements of pressure fluctuations via pressure transducers [10], VKI-H3 WT ($M = 6$, $Re = 22 \times 10^6$)

It is shown that the different pressure transducers placed on the model, a 7° half angle cone in this case, acquire the pressure fluctuations showing transition from laminar to turbulent flows.

Different methods have the aim to link the pressure fluctuations to the transition onset using the e^N method [11]. The latter method is one of the most used semi-empirical transition prediction method. The transition location is predicted by using the growth of the instabilities computed via a stability analysis. This growth is the ratio between the amplitude A of the perturbations at a given location and the amplitude A_0 that the instability had when it first becomes unstable. The ratio A/A_0 is e^N from which the method takes its name. Transition is empirically correlated to a certain N-factor. This method has been extensively applied in the years with success [13]. However, much is still uncertain when using e^N to predict transition. In fact, the initial amplitude A_0 of the instabilities is not accounted for, nor is it known at what amplitude the instabilities will break down. Moreover, the N-factor at which transition occurs is related to the noise of wind tunnel used for the experiments [14]. In flight conditions and quiet wind tunnels, the N-factor used for transition prediction is around 7. In common wind tunnels, where the disturbances environment is much higher, the threshold value is around 4-5 [15]. In this paper, an estimation of the amplitude A_0 of the perturbations at the onset of transition is shown for different experimental data acquired in several hypersonic wind tunnels. Moreover, the variability of the N-factor has been introduced since its exact value is not known and it depends on the wind tunnel and its conditions. The probabilistic approach has been extended to this additional parameter to study the effect on the results.

Due to its intrinsic seamingly random nature, transition prediction represents a significant challenge, which is compounded by the complexity of the physics of high-speed flows. The difficulty linked to the development of a general model for laminar-turbulent transition lies in the multitude of possible instability modes and the various ways each of those can be triggered. Moreover, uncertainties related to the application of transitional method as e^N makes transition prediction even more challenging. Therefore, in this paper, a relation between the computed N factor and the freestream perturbations is presented in order to justify the application of the e^N method.

2.1. The e^N Method

In the e^N method, the N-factor quantifies the amplification of the free stream perturbation within the boundary layer. The standard definition of the N factor is the following:

$$N = \int_{x_0}^{x} -\alpha_i dx = ln\frac{A}{A_0} \tag{1}$$

Thus, the N-factor depends on the initial amplitude A_0 at which the perturbations start to be amplified. Properties of integrals and logarithms can be used to manipulate Eq.(1) as follows:

$$N = \int_{0}^{x} -\alpha_i dx - \int_{0}^{x_0} -\alpha_i dx = ln(A) - ln(A_0) \tag{2}$$

We can therefore define the initial amplitude A_0 as

$$A_0 = exp\left(\int_{0}^{x_0} -\alpha_i dx\right) \tag{3}$$

and the amplitude of the perturbations at a given location x as follows

P_∞ [Pa]	T_∞ [K]	ρ_∞ [kg/m^3]	U_∞ [m/s]	Re_∞ [1/m]	T_{wall} [K]
1330.06	60.863	0.07601	939.10	1.80E+07	294.73
1640.41	59.875	0.09529	931.45	2.28E+07	294.73
1950.75	59.880	0.11331	931.48	2.71E+07	294.73

Table 1: Free stream conditions (subscript ∞) for the test cases.

$$A = exp\left(\int_0^x -\alpha_i dx\right) \tag{4}$$

Eq.(3) and Eq.(4) can be applied to the results of stability computations (α_i) to determine the initial amplitudes A_0 and the amplitudes of the perturbations at different locations x for selected frequencies. Results can be then compared to experimental data.

3. Results

Focus has been placed on VKI-H3 conditions corresponding to Low-Reynolds ($1.80E+07$), Medium-Reynolds ($2.28E+07$) and High-Reynolds ($2.71E+07$) for which experimental data are available. Conditions are reported in the Tab.1:

3.1. Determination of the initial amplitude A_0

Frequencies have been varied between 400 to 800 kHz for the Low-Reynolds case, between 500 to 900 kHz for the Medium-Reynolds case and between 500 to 1000 kHz for the High-Reynolds. The variation step has been set to 25 kHz in order to compare with experimental data acquired by Masutti [10]. Results are presented in Tab. 2, Tab. 3 and in Tab. 4.

F [kHz]	400	500	600	700	800
A_0	0.0082	0.0185	0.0302	0.0462	0.0659

Table 2: Initial amplitude A_0 for the Low-Reynolds case.

F [kHz]	400	500	600	700	800	900
A_0	0.0030	0.0086	0.0165	0.0256	0.0378	0.0544

Table 3: Initial amplitude A_0 for the Medium-Reynolds case.

An exponential fit is proposed as represented in Fig.2. Using a least squares approach, the fit aligns rather well with the numerical data. The formula for the fitting model is reported in Eq.(5) in which A_0 is a function of the frequencies for the selected condition. The coefficients are reported in Tab.5. It can be seen

F [kHz]	500	600	700	800	900	1000
A_0	0.0039	0.0089	0.0158	0.0229	0.0320	0.0431

Table 4: Initial amplitude A_0 for the High-Reynolds case.

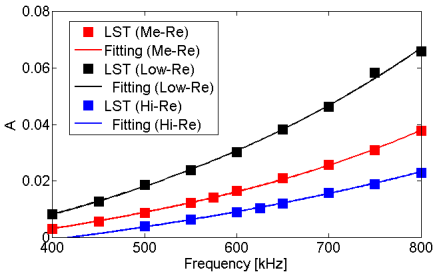

Figure 2: Initial amplitude A_0 computed for all the Reynolds case in the VKI-H3 wind tunnel (numerical data and exponential fitting)

.

that the initial amplitude of the perturbations increases when reducing the Reynolds number for a selected frequency. This means that a single perturbation will be more amplified at the very same frequency by decreasing (less viscous damping) the Reynolds number in agreement with the Linear Stability theory.

$$A_0(F) = a \cdot exp(b \cdot F) + c \cdot exp(d \cdot F) \tag{5}$$

3.2. Determination of the amplitude A

The amplitudes of the perturbations have been determined at the streamwise location x where pressure sensors are placed on the cone model in order to compare with the experimental data. Results are presented in Tab. 6, Tab. 7 and in Tab. 8 and in Fig. 3, Fig. 4 and in Fig. 5 with a normal distribution fit.

Using a least squares approach, the fit aligns with the numerical data. The formula for the fitting model is reported in Eq.(6) in which A is a function of the frequencies for the selected condition. The coefficients are reported in Tab. 9, Tab. 10 and in Tab. 11.

$$A(F) = k \cdot exp\left[-\left(\frac{F-\mu}{\sigma}\right)^2\right] \tag{6}$$

Re	a	b	c	d
1.80E+07	0.001582	0.002306	-0.03035	0.0001092
2.28E+07	0.0032	0.003225	-0.01735	-0.001755
2.71E+07	0.001296	0.0017	-0.002562	0.002316

Table 5: Coefficient of the exponential model for the fitting of the initial amplitude A_0

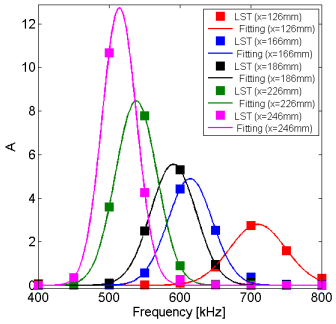

Figure 3: Amplitude A_0 computed for the Low-Reynolds case for the VKI-H3 wind tunnel (numerical data and normal distribution fitting)

.

F [kHz]	400	500	600	700	800
A (x = 1.26 mm)	0.0792	0.0262	0.1031	2.7485	0.3285
A (x = 1.66 mm)	0.0296	0.0323	4.4406	0.3698	0.0142
A (x = 1.86 mm)	0.0196	0.1115	5.3122	0.1283	0.0059
A (x = 2.26 mm)	0.0086	3.5997	0.8923	0.0178	0.0010
A (x = 2.46 mm)	0.0087	10.6692	0.2745	0.0084	5.04e-4

Table 6: Amplitude A for the Low-Reynolds case.

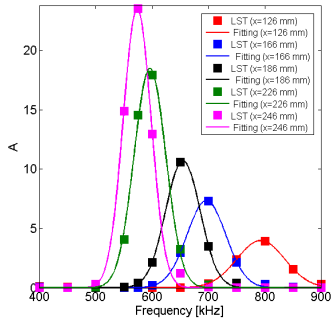

Figure 4: Amplitude A_0 computed for the Medium-Reynolds case for the VKI-H3 wind tunnel (numerical data and normal distribution fitting)

.

F [kHz]	500	600	700	800	900
A (x = 1.26 mm)	0.0372	0.0129	0.1586	5.4716	1.1083
A (x = 1.66 mm)	0.0088	0.0897	8.7840	0.5421	0.0135
A (x = 1.86 mm)	0.0049	0.9143	4.6588	0.0949	0.0016
A (x = 2.26 mm)	0.0139	15.8442	0.4265	0.0039	3.5e-05
A (x = 2.46 mm)	0.1140	11.5110	0.0826	5.2e-04	3.4e-06

Table 7: Amplitude A for the Medium-Reynolds case.

F [kHz]	500	600	700	800	900
A (x = 1.26 mm)	0.0620	0.0187	0.0229	1.3831	4.3884
A (x = 1.66 mm)	0.0173	0.0124	5.2604	0.5421	0.1205
A (x = 1.86 mm)	0.0083	0.0678	16.7516	1.3864	0.0157
A (x = 2.26 mm)	0.0039	4.1073	9.5166	0.0795	4.45e-04
A (x = 2.46 mm)	0.0065	23.2927	3.4392	0.0167	7.29e-05

Table 8: Amplitude A for the High-Reynolds case.

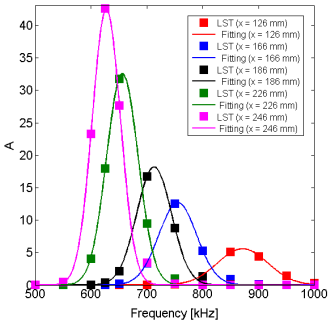

Figure 5: Amplitude A_0 computed for the High-Reynolds case for the VKI-H3 wind tunnel (numerical data and normal distribution fitting)

.

x (mm)	k	μ [kHz]	σ [kHz]
126	2.79	709.5	55.58
166	4.89	614.2	44.68
186	5.55	590.4	39.21
226	8.46	538.1	33.24
246	12.74	514.4	29.12

Table 9: Coefficient of the normal distribution model for the fitting of the amplitude A (Low-Reynolds)

x (mm)	k	μ [kHz]	σ [kHz]
126	5.545	814.7	59.61
166	8.471	702.6	46.16
186	10.52	663.4	41.7
226	15.77	606.8	35.12
246	20.66	577.4	31.44

Table 10: Coefficient of the normal distribution model for the fitting of the amplitude A (Medium-Reynolds)

The amplitudes are well represented by normal distributions with a scale coefficient (k), mean (μ) and variance (σ) varying with respect to streamwise location as represented in Fig. 6, Fig. 7 and Fig. 8. A similar behavior is observed in all the conditions experienced in the VKI-H3 wind tunnel.

4. Comparison with experiments

In order to verify the goodness of the method, the same procedure is applied to Longshot conditions for which experimental data are available. The reference conditions of the test are reported in Tab. 12. In this case the test has been carried out with nitrogen to avoid real gas effect for such an high Mach number.

An LST analysis has been carried out at the selected conditions for the Longshot in order to obtain the N-

x (mm)	k	μ [kHz]	σ [kHz]
126	5.579	871.5	63.61
166	12.68	755.1	48.35
186	18.17	712.8	43.91
226	32.57	655.9	39.69
246	42.41	627.2	35.48

Table 11: Coefficient of the normal distribution model for the fitting of the amplitude A (High-Reynolds)

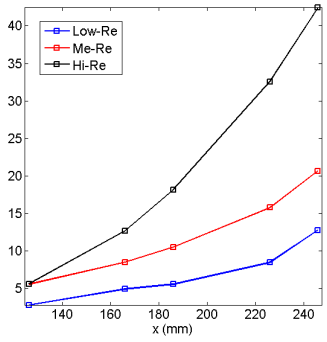

Figure 6: Scale coefficient k computed for all the Reynolds cases in the VKI-H3 wind tunnel (numerical data and quadratic distribution fitting)

.

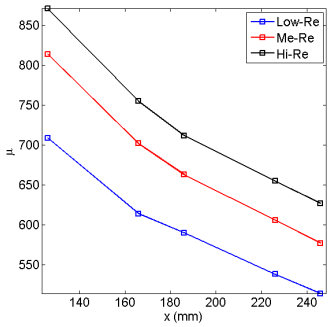

Figure 7: Mean μ computed for all the Reynolds cases in the VKI-H3 wind tunnel (numerical data and quadratic distribution fitting)

.

P_∞ [Pa]	T_∞ [K]	U_∞ [m/s]	Re_∞ [1/m]	T_{wall} [K]
277	69.5	1689	5.3E+06	293

Table 12: Free stream conditions (subscript ∞) for the Longshot test cases.

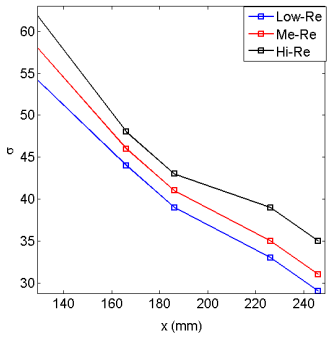

Figure 8: Variance σ computed all the Reynolds cases in the VKI-H3 wind tunnel (numerical data and quadratic distribution fitting)

.

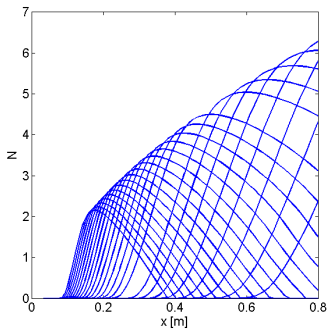

Figure 9: N-factor computations for the Longshot conditions (F = 150 ÷ 500 kHz, ΔF = 10 kHz).

factor curves as reported in Fig. 9. These curves can be used in the e^N transition method to determine the critical N-factor for transition onset.

The comparisons with experimental data has been carried out at selected streamwise locations (x) where pressure sensors have been placed on the cone model. The selected x coordinates are x = 270, x = 490 and x = 710 mm while frequencies in the range of F = 150 ÷ 500 kHz have been considered. The initial amplitude A_0 and the amplitude of the perturbations A are reported in Tab. 13. In Fig. 10, experimental data are compared with the results of the stability analysis. Pressure fluctuations, acquired via pressure transducers placed along the cone model, are compared with the amplitude of the perturbations. As it can be noticed, the peak of the perturbations well agree with the peak of the measured amplitudes for all the selected coordinates. Moreover, both the shape of amplitudes and of the pressure fluctuations resemble a Gaussian distribution with a comparable mean and variance. Respect to Fig. 6, Fig. 7 and Fig. 8, the amplitude is presented in logarithmic scale in order

F [kHz]	200	300	400	500
A_0	0.1319	0.2478	0.4458	0.7378
A (x = 270 mm)	0.1485	5.4792	1.7024	0.3094
A (x = 490 mm)	2.0508	2.5585	0.1203	0.0338
A (x = 710 mm)	38.6032	0.2296	0.0336	0.0032

Table 13: Amplitude A_0 and A for the LongShot conditions.

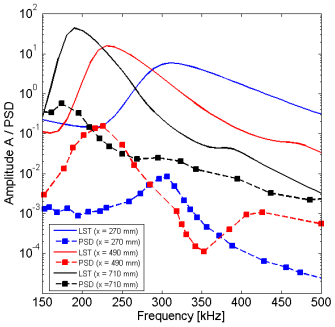

Figure 10: Comparison between LST computations and experimental data for the LongShot conditions

.

to better compare with the experimental data. Moreover the initial amplitude is represented along with the amplitudes for the previous case respect with the non dimensional frequency $\overline{F}$ defined in Eq. 7. The amplitudes have been scaled respect with the length of the cone model ($\overline{A_0} = A_0/L$) which is equal to $L = 265$ mm for the H3 wind tunnel and equal to $L = 800$ mm for the Lonshot facility. In Fig. 11 it can be seen that the initial amplitudes collapse for the H3 wind tunnel and they distinguish respect that of the Longshot. It is demonstrated then, that the initial amplitude of the perturbations depends only on the facility since the non dimensional quantity are considered both respect with the geometry and the free stream conditions. Finally, in Fig. 12, the coefficients for the fitting model of the amplitude are represented. The proposed model is a Gaussian distribution as reported in Eq. 6 where the amplitude k, the mean μ and the variance σ have been properly non dimensionalized showing a quadratic behavior respect with the streamwise coordinate.

$$\overline{F} = 2\pi F\nu/U_e^2 \tag{7}$$

5. Conclusions

In previous works, a normal distribution was assumed for the frequency distribution in transition prediction for high speed flows. This assumption has now

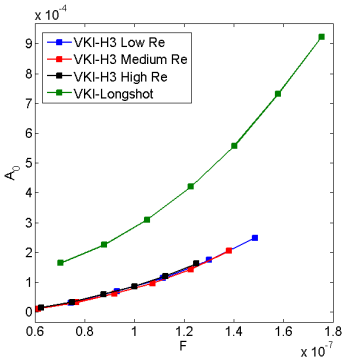

Figure 11: Comparison of the initial amplitude A_0 between LST computations and experimental data for the LongShot conditions

.

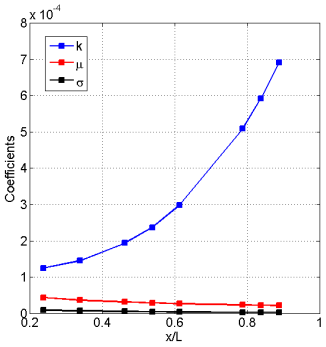

Figure 12: Coefficients for the fitting model of the amplitude respect with the non dimensional streamwise location (x/L)

.

been reasonably justified by computations of the amplitude A, profiles/distributions at selected streamwise locations. In fact, the amplitudes show a normal distribution with the characteristic coefficients (k, μ and σ) varying along the model. In the previous approach, the frequency distribution was assumed constant respect with the x-coordinate, therefore a streamwise varying distribution could be more representative of the experimental conditions. A variation of this distribution could be assumed in future works by taking a probability distribution for the frequency as shown in the present work. Moreover, the comparison with the experimental data for the Longshot conditions has demonstrated the quality of the approach. The non-dimensionalization proposed for the initial amplitude has shown that this quantity only depends on the wind tunnel used for the test. This has a crucial role in transition onset since the N-factor is computed as the amplification of the perturbations respect with this quantity.

References

[1] H. L. Reed, E. Perez, J. Kuehl, T. Kocian, N. Oliviero, "Hypersonic Stability and Transition Prediction," *21st AIAA Computational Fluid Dynamics Conference*, June 24-27, 2013, San Diego, CA.

[2] P. Kolodziej, "Strategies and approached to TPS design," *RTO AVT Lecture Series on Critical Technologies for Hypersonic Vehicle Development*, 10-14 May, 2004, von Karman Institute, Rhode-St-Genese, Belgium.

[3] S. Tirtey, L. Walpot, O. Chazot, "Characterization of Hypersonic Roughness Induced Transition for the EXPERT Flight Experiment," *16th AIAA/DLR/DGLR International space planes and hypersonic systems and technologies conference*, 19-22 October, 2009.

[4] I. Cozmuta, "Uncertainty Quantification and Statistical Engineering for Hypersonic Entry Applications ," *RTO-AVT-VKI short course on Uncertainty Quantification*, Stanford University, CA.

[5] G. Serino, O. Marxen, F. Pinna, P. Constantine, C. Gorle, G. Iaccarino, "Statistical inverse analysis and stochastic modeling of transition," *Center for Turbulence Research Proceedings of the Summer Program 2012*, June-July, 2009, Stanford University, CA.

[6] Schlichting, H., "Boundary Layer Theory. McGraw-Hill Book Company", seventh edition, 1979.

[7] L. M. Mack, "Boundary-Layer Linear Stability Theory, Special Course on Stability and Transition of Laminar Flow, AGARD-R-709, chap. 3, June 1984, pp. 31, 381.

[8] Stetson, K., Kimmel, R., Thompson, E., Donaldson, J., and Siler, L., A Comparison of Planar and Conical Boundary Layer Stability at a Mach Number of 8, Paper 91-1639, AIAA, June 1991.

[9] Stetson, K. F. and Kimmel, R. L., Example of Second-Mode Instability Dominance at a Mach Number of 5.2, AIAA Journal , Vol. 30, No. 12, December 1992, pp. 2974-2976.

[10] Masutti, D.,Ground Testing Investigation of Hypersonic Transition Phenomena for a Re-entry Vehicle", PhD thesis, VKI-TU Delft, 2013.

[11] Ingen, J. L. van, A Suggested Semi-empirical Method for the Calculation of the Boundary Layer Transition Region. Report ,VTH-74, 1956.

[12] Schneider, S. P., Hypersonic Laminar-Turbulent Transition on Circular Cones and Scramjet Forebodies, Progress in Aerospace Sciences, Vol. 40, 2004, pp. 150.

[13] E. Orlik, V. Kornilov, M. Ferrier, I. Fedioun and D. Davidenko, Hypersonic laminar/turbulent transition: computations and experiments,Progress in Flight Physics, Vol. 3, 2012, pp. 243 - 252.

[14] Beckwith, I. E. and Miller III, C. G., Aerothermodynamics and Transition in High-Speed Wind Tunnels at NASA Langley, Annual Review of Fluid Mechanics, Vol. 22, 1991, pp. 419439.

[15] Alba, C., Johnson, H., Bartkowicz, M., Candler, G., and Berger, K., Boundary Layer Stability Calculations for the HIFiRE-1 Transition Experiment, Journal of Spacecraft and Rockets, Vol. 45, No. 6, January 2008, pp. 11251133.

[16] Schneider, s. P., Developing Mechanism-Based Methods for Estimating Hypersonic Boundary-Layer Transition in Flight: The Role of Quiet Tunnels, 43rd AIAA Fluid Dynamics Conference, June 24-27, 2013, San Diego, CA.

AERO-THERMAL INVESTIGATIONS IN TURBOMACHINERY

Heat Transfer in High Subsonic Velocity Environments behind the Fan of a Gas Turbine

Francesco Baldani

Mechanics Department, Royal Military Academy, Belgium, francesco.baldani@rma.ac.be

Supervisor: Tony Arts

Professor, Head of the Department, Turbomachinery and Propulsion Department, von Karman Institute for Fluid Dynamics, Belgium, arts@vki.ac.be.

Promoter: Walter Bosschaerts

Professor, Head of the Department, Mechanics Department, Royal Military Academy, Belgium, Walter.Bosschaerts@rma.ac.be

Promoter: Souad Harmand

Professor, Head of the Department, University of Lille Nord de France, , France, Souad.harmand@univ-valenciennes.fr

Abstract

The work aims proposing a methodology to evaluate local heat convection coefficients in high subsonic speed environments via a dynamic analogy analysis, exploiting the IHCP solution by means of QIRT, performing high and low speed experiments and numerical simulations as validating tools. Near-wall and free flow boundary conditions are imposed using CTA and PIV. The methodology validation is presented for a flat plate, experiments are undergoing for a finned configuration.

Keywords: High Subsonic Speed, Local Heat Convection Coefficient, **IHCP** - Inverse Heat Conduction Problem , **QIRT** - Quantitative Infra Red Thermography, Dynamic Analogy, **CTA** - Constant Temperature Anemometry, **PIV** - Particle Image Velocimetry

NOMENCLATURE

Bi Biot number
Re Reynolds number
Pr Prandtl number
k thermal conductivity $\left[W\,m^{-1}K^{-1}\right]$
C_p specific heat capacity $\left[J\,kg^{-1}K^{-1}\right]$
h heat transfer coefficient $\left[W\,m^{-2}K^{-1}\right]$
ρ material density $\left[kg\,m^{-3}\right]$
e electrically injected heat flux density $\left[W\,m^{-2}\right]$
q heat flux density $\left[W\,m^{-2}\right]$
x coordinate in the flow direction $[m]$
y coordinate perpendicular to the flow $[m]$
ξ plate unheated starting length $[m]$
th plate thickness $[m]$
m,M discretization indices x direction
n,N discretization indices y direction
$\alpha_{x,y,z,t}$ case dependent parameters $[0, 1]$
$\alpha_{0,1,2}$ Tikhonov Regularization parameters
cond() condition number of a matrix

Superscripts

r iteration number
opt optimum
t matrix transpose
p time step

Acronyms

ACOC Air Cooled Oil Cooler
FCOC Fuel Cooled Oil Cooler
IHCP Inverse Heat Conduction Problem
QIRT Quantitative Infra Red Thermography
CTA Constant Temperature Anemometry
PIV Particle Image Velocimetry

1. INTRODUCTION

The work focuses on the development of a methodology to evaluate gas turbine Air Cooled Oil Coolers (ACOC) thermal performances at high subsonic speed with a specific interest in local heat convection coefficients.To report the background for the present research work it is worth consider turbine engines increased performances and reduced fuel consumption to understand the importance of turbine engines thermal management. The review of the available bibliography evidences the limited attention received by relevant aspects of ACOC thermal performance such as the local heat convection coefficients evaluation or their aerodynamic performance analysis. A lot of research work both numerical and experimental is performed on finned heat exchangers in their low speed application, i.e. for electronic devices cooling purposes but the research lacks a performance evaluation strategy for such heat exchangers submerged in a high subsonic speed flow.

1.1. Gas Turbines and Thermal Management

Among the means of producing thrust and mechanical power, the gas turbine engine is one of the most satisfactory and its main advantage is the high thrust-to-weight ratio. The purpose of the gas turbine determines the design so that the most desirable energy form is maximized. Being the gas turbines range of applications wide any small gain in thermal efficiency and performance translates into a major economic impact worldwide. The improvements in the

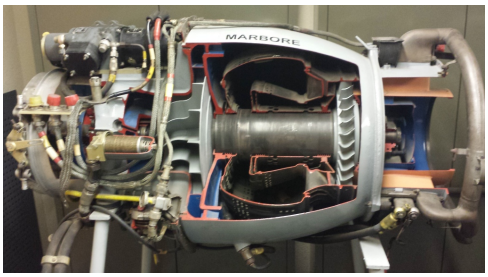

Figure 1: *Marboré* by Turbomeca - Cutaway at RMA

manufacturing techniques as well as in the available materials push the aero-thermal engineers to find better solutions to improve engine performances. Improving turbine engine performances for military and civil purposes has a deep impact on thermal efficiency, fuel consumption, life-time and consequently on the achievement of the working standards required by the new laws in matter of environment such as noise and pollutant emissions. The fuel consumed by an aircraft turbine engine is the preferred heat sink for its lubrication, hydraulic, and integrated drive generator oil systems. Reasons for this are, that a fuel/oil heat exchanger is more compact, if compared with an air/oil cooler, and causes no drag increase and no engine performance loss from air bleed or loss of momentum of the air. Furthermore, the energy exchanged in the fuel/oil cooler is conserved in the thermodynamic cycle. The capacity of the fuel as a heat sink is temperature limited, however, and the fuel pumps contribute to the fuel heating as well. Integration of the fuel and oil systems to a thermal management system is required, which performs its functions without exceeding fuel or oil temperature limits within the aircraft flight envelope. To make this possible, reduction of the oil system heat rejection, as well as the installation of air/oil heat exchangers, has to be considered early in the engine development program [1]. A continuous analysis of the heat loads from fuel and oil systems is required, until sufficient test evidence proves that the design meets the requirements.

The term thermal management is used for a system which connects the fuel and lubrication oil systems via the fuel cooled oil cooler (FCOC). Other systems and components, like an engine hydraulic system or an integrated drive generator (IDG), may also use FCOCs and belong to the thermal management system as well. Shown in Figure 2 is a schematic diagram of a typical heat management system. It includes a simplified fuel system scheme and an FCOC for lubrication oil cooling. The lube oil circuit is shown together with an air cooled oil cooler (ACOC). Because such an ACOC is not installed in all engines, it is indicated in dotted lines, like the other components which may not always be included. Fuel cooled

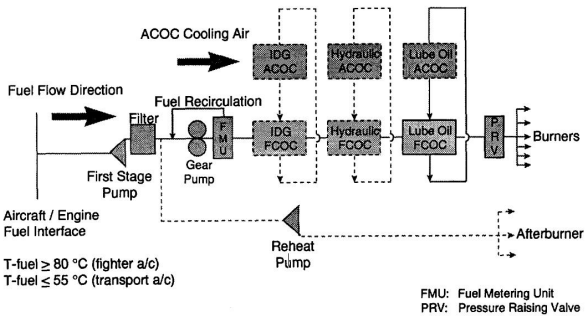

Figure 2: Heat Management System [2]

oil coolers are relatively compact, because of the high

density, specific heat, and thermal conductivity of the fluids. They can be installed within the engine bay or nacelle as required and cause no particular integration problems. The integration of an ACOC is more difficult. It either requires engine bleed air, an ejector system, a mechanically or electrically driven fan, or it is a ram air cooler with bypass air or ambient air. An external ram air cooler causes an additional interface with the aircraft. The ACOC has a negative effect on engine performance (bleed air, loss of momentum of the cooler or ejector air flow, mechanical power loss for fan drive), or increases the aircraft drag (ram air cooler). In a fighter aircraft flying at a high supersonic Mach number, the air flow through the cooler is choked and the high ram air temperature reduces the temperature difference between air and oil. At high altitude, the low air temperature increases the ACOC effectiveness, but the low air density reduces the air mass flow and, hence, cooling effectiveness. Because of the disadvantages of air/oil heat exchangers, the fuel is the preferred heat sink in a turbofan engine [2]. This criticism about ACOCs summarizes the approach to thermal management in the nineties when the today's greener approach was not topical. Indeed the ecologic and economic pressure as well as the fear of future fuel shortage claims major improvements from the next-gen aircraft especially from the engine point of view. Engine specialists foresee technological improvements concerning the turbomachinery and the power spilling (to move towards the more-electric aircraft). To accomplish these tasks the development of new cooling solutions is of crucial importance.

1.2. TechSpace Aero Patented ACOC

An example of new cooling solutions for aircraft turbine engine is given by the ACOC patented by TechSpace Aero. The finned heat exchanger placed just downstream of the fan (Figure 3(a), position 16) is submerged in a cold flow (by-pass engine flow). The patent is about an air-oil heat exchanger with the double purpose of i) cooling the engine oil and or engine installed equipment (electrical, electronic, gearing box) ii) serving as de-icing apparatus for the bypass duct nose.

Classical ACOC are realized by means of air scoop or airflow spilling leading to either an increase of drag (external scoop) and/or a reduction of the engine overall performance. But such an heat exchanger is from now on indispensable as complementary cooling system for the engine oil circuit besides the FCOC. Indeed new generation aircraft engines are characterized by a bigger heat generation mainly due to i) higher

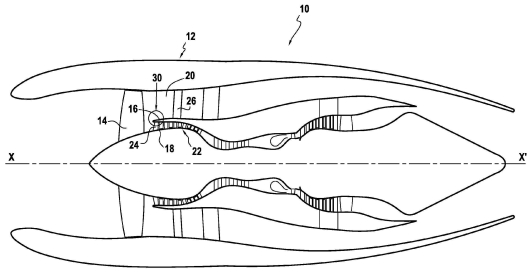

(a) Heat Exchanger Position (16)

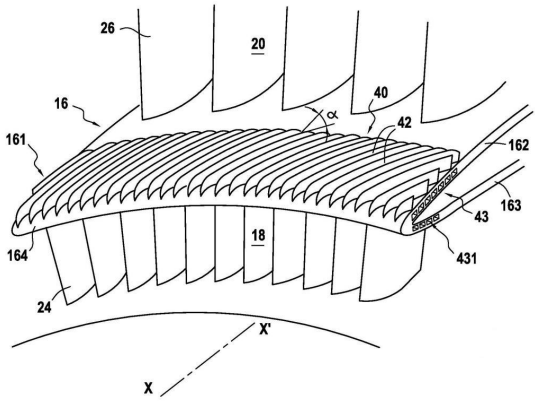

(b) Heat Exchanger Close-up View

Figure 3: Air Cooled Oil Cooler (ACOC) **Techspace Aero** Patented Design - http://www.freepatentsonline.com/EP2075194.pdf

mechanical stresses on the rolling bearing systems, ii) higher power gearing box and iii) the integration of new high power electrical machines such as S/G (Starter/Generator - turbine engine electrical feeding) and the PPS (Power Plant System - the engine/nacelle ensemble). Therefore to minimize the loss of performance due to the presence of the ACOC or of its scoop it is common to use surface heat exchangers. The new regulations in matter of pollutant and noise emissions raised questions about the heat exchangers positioning (integration constraints to create oil carters, reduction of the surfaces available for acoustic treatment). Several manufacturers focused on answering these technical questions prior to investigate the surface heat exchangers behavior in such environments [3; 4; 5].

2. STATE OF THE ART

Analysis of the state of the art for the topics of interest of this research study.

2.1. Extended surface heat transfer

A simple yet complete definition of heat exchanger, in its most general meaning, can be found in [6] where it is defined as a device that is used for transfer of thermal energy (enthalpy) between two or more fluids, between a solid surface and a fluid or between solid particulates and a fluid, at differing temperatures and in thermal contact, usually without external heat and work interaction. In 1922 an NACA report by Harper and Brown [7], inspired by a request from the Engineering Division of the U.S. Bureau of Standards in connection with the heat-dissipating features of air-cooled aircraft engines, appears to be the first really significant attempt to provide a mathematical analysis of the interesting interplay between convection and conduction in and upon a single extended surface. The work considered longitudinal fins of rectangular profile and trapezoidal profile and radial fins of rectangular profile introducing the concept of fin efficiency. From this modest, yet masterful beginning, the analysis and evaluation of the performance of individual components of extended surface and arrays of extended surface where individual components are assembled into complicated configurations has become an art [8]. Several generalized studies of the problem of heat transfer through convective fins can be found also in modern literature [9; 6; 8; 10]. Many research work focuses on the optimization of just the fin distribution/spacing/dimensions [11; 12; 13] or of a whole cooling configuration [14; 15]. Nowadays a lot of interest is dedicated to finned heat exchangers for electronic devices cooling, power plant cooling and similar; most of the research is devoted to natural convection cooling [16; 17] or forced convection at low Reynolds numbers ($Re \leq 10^4$) cooling [18; 19].

2.2. Coupled studies of flow field and heat transfer

Relatively few studies present a direct combination of flow field velocity analysis and heat transfer distribution analysis. This lack is regrettable as any insight on the origin and impact of the fluid motion in the cooling is greatly helpful to the designer. Furthermore, wide and trustworthy experimental databases reporting the velocity fields and/or the convective flows are necessary to assess the reliability of CFD codes. Most of the work is based on numeric computation and good examples are [20] and [21] in which fully numerical approaches are developed and validated against available experimental data. A good experimental work on heat transfer analysis, even if simplified and tuned for a planar wall jet, can be found in [22], where hot-wire anemometers and micro thermocouples are used to perform the study.
An inspirational work for this research study is reported in [23] where it is presented one of the first attempt to develop a novel experimental methodology to perform accurate measurements of the local heat transfer distribution.

2.3. Local heat transfer measurements

It is difficult to accurately determine local convection coefficients or to perform accurate local heat flux measurements. However, often the knowledge of the heat flux distribution is indispensable as for the design of optimal and efficient heat exchangers [24] and for finned heat exchangers this task is particularly challenging [25]. The heat transfer coefficient should be studied both locally and globally, since a global study of h is fundamental in the preliminary design phase while a local study of h is useful to understand the effects of the geometry on the local flow conditions and on the achievable heat exchange, to retrieve information on the heat transfer enhancement mechanisms and to get more insight in the design of more performing heat transfer enhancers.
The most used measurement methods are heat flux sensors, local temperature measurements (mostly in solids) and the solution of the inverse heat conduction problem. Heat flux sensors are seldom used, they need to be attached to the surface and give an average value for the heat flux through the sensor surface. Moreover the sensor placement adds an extra thermal resistance to the measurement surface, which influences the measurement and causes a redistribution of the heat flux over the surface. Heat flux sensors are not very accurate: a typical accuracy is of about ± 15 % [26].
Thermocouples are the most commonly used temperature sensing techniques for monitoring temperatures. Many studies use thermocouples that are embedded in the measurement surface to determine local heat fluxes. For instance in [24] a technique to measure local heat fluxes with two thermocouples is developed. This technique is especially useful for high heat fluxes and two phase heat transfer. It is however limited to one-dimensional conduction applications, and is not very useful if a heat flux distribution over a surface needs to be measured. The use of thermocouples has also other drawbacks. The number of thermocouples that can be imbedded is limited. The presence of thermocouples interfere with the local temperature and the heat flow, due to conduction into the thermocouple and thermocouple wires (this is called the fin effect

of thermocouples [27]).
Therefore the best practice is to determine the heat fluxes at the fin base indirectly by measuring the heat fluxes through the extended surface and the primary surface [28].
In recent years the technique exploiting the inverse heat conduction problem solution is becoming more and more popular for identifying local heat fluxes. This technique is mainly used to estimate temperatures or heat fluxes at locations that are not accessible for direct measurements. One can conclude that among the available techniques to perform heat transfer measurements [29], the solution of the IHCP is probably the most suitable for the case under analysis [30].

2.4. Transient IHCP

In words IHCP can be defined as the estimation of the surface heat flux history given one or more measured temperature histories inside a heat conducting body [31]. The advantage of this method is that experimental studies can be performed under similar conditions and environment as during operation [32]. Inverse methods are very valuable when an operational process is too complicated for direct measurement of physical parameters, or when measuring requires sophisticated or expensive instruments [33]. To solve an inverse heat conduction problem, a mathematical optimization method is required, which uses temperature measurements as input. Based on the surface temperatures of a solid object, the heat fluxes on one or more surfaces of the object can be estimated. So the need for internal temperature measurements can be omitted. Additionally the method has the advantage that the temperature field in the whole object can be reconstructed based on surface temperature measurements, together with the coupled heat flux distribution. Depending on the temperature measurement technique, the disturbance of the local temperature fields and heat flux distribution is limited or even absent, i.e. using the QIRT there is no effect neither on the temperature nor on the heat flux as it could happen applying thermocouples on the object surfaces. For instance in [34] thermocouples embedded in the heat conducting body are used to solve the IHCP. But the presence of thermocouples inside a heat-conducting body distorts the temperature field in the body and may lead to significant bias in the temperature measurement resulting in errors propagating into the IHCP results. Models can be used to generate correction kernels to eliminate bias in the thermocouple reading, or can be applied as sensitivity coefficients in the IHCP directly [34]. Another drawback of thermocouples is a poor spatial resolution (punctual temperature). Other techniques like the Liquid Crystal Thermography (LCT) might be exploited to perform temperature measurements in order to solve the IHCP [35; 36; 37]. It is to be said that the use of unmatched materials disturbs the local heat flux and also the local convective boundary layer, producing a potential error that must be compensated for [29].

3. MOTIVATION AND OBJECTIVES

The specific goals of this research are the identification and characterization of i) the local heat convection coefficient of an extended surface heat exchanger and of ii) the flow structures determinant for the heat transfer process in order to qualify the effectiveness of finned heat exchangers when submerged in a high subsonic flow retrieving finned heat exchangers capabilities from a low speed analysis.
The original contribution of this work with respect to most of the published reports in the same research field results from:

- proposing a simplified solution for the transient IHCP
- obtaining a high resolution heat convection coefficient analysis on the heat exchanger surfaces
- exploiting the low-to-high speed analogy for the heat transfer analysis obtained by means of i) a dynamic analogy analysis of the finned heat exchanger and of ii) the calculation of local heat convection coefficients solving the IHCP by means of QIRT(complex geometries reduced to flat plate representation decreasing IHCP ill-posedness related difficulties)
- design, manufacture and test a hot-wire probe rake with a specific design making it exploitable in a wide range of velocities (from 30 m/s to 230 m/s)

4. PROPOSED SOLVING METHODOLOGY

The experimental set up is thought to exploit QIRT which eliminates any disturbance of the temperature field possibly caused by other measurement techniques and at the same time allows for a reasonably high spatial resolution. To validate the proposed method a heated flat plate is examined. The plate has length L=0.45 m, width W=0.17m and thickness

th= $0.25 \cdot 10^{-5}$ m, and is painted in matt black with a known emissivity of 0.94. The plate is heated via

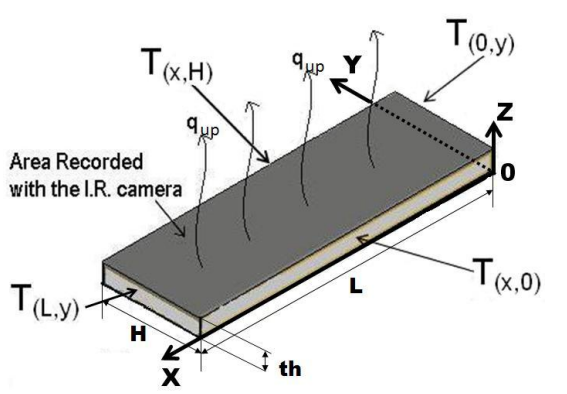

Figure 4: Heat Conducting Plate Sketch

electric power injection and subjected to a forced convection cooling on its upper surface in a wind tunnel. As the plate is mounted in an open wind tunnel, the measured flow field over the flat plate will be used as boundary condition for the numerical simulation. Using QIRT, the measured surface temperature will be used to calculate the local convective heat transfer coefficients following the numerical IHCP solution approach ([38; 39; 40]). The general expression for the plate temperature field variation is given in eq. 1.

$$\frac{1}{th} \cdot e + k \cdot \left(\alpha_x \frac{\partial^2 T}{\partial x^2} + \alpha_y \frac{\partial^2 T}{\partial y^2} + \alpha_z \frac{\partial^2 T}{\partial z^2} \right) = \frac{1}{th} \left[q_{down} + q_{up} \right] + \alpha_t \cdot \rho \cdot C_p \cdot \frac{\partial T}{\partial t} \quad (1)$$

The plate can be considered as "thermally thin" if $Bi < 0.1$ (sketch in Figure 4) so that the temperature gradient along the z direction can be neglected. The initial and boundary conditions on the plate surfaces are defined as follows:

- Initial Condition: imposed temperature field
- Boundary Conditions:
  - Upper and Side Surfaces: imposed $T_{surface}$
  - Lower Surface: thermally insulated ($q_{down} = 0$)

In the following $q = q_{up}$. The problem reduces to the expression in eq. 2.

$$\frac{1}{th} \cdot e + k \cdot \left(\alpha_x \frac{\partial^2 T}{\partial x^2} + \alpha_y \frac{\partial^2 T}{\partial y^2} \right) = \frac{1}{th} q + \alpha_t \cdot \rho \cdot C_p \cdot \frac{\partial T}{\partial t} \quad (2)$$

Equation 2 can be used to numerically minimize equation 3.

$$F = \sum_x \sum_y \left[T_{comp}(x,y) - T_{meas}(x,y) \right]^2 \quad (3)$$

The problem is ill-posed and has a high temperature measurement error sensitivity [31] which almost invariably leads to non-unique or erroneous results. Since the minimization of F will have no influence on the error amplification of the input data a regularization is needed. It is also known as ridge regression, it was first proposed by Tikhonov [41; 42] and it can be expressed as in eq. 4.

$$S = F + \alpha_0 \cdot S_0 + \alpha_1 \cdot S_1 + \alpha_2 \cdot S_2 \quad (4)$$

Applied to the IHCP one obtains:

- F: Minimization Criterion
- S_i: Heat Flux Related Functions
  - $S_0 = \sum_x \sum_y [q(x,y)]^2$
  - $S_1 = \sum_x \sum_y [grad(q(x,y))]^2$
  - $S_2 = \sum_x \sum_y [\Delta q(x,y)]^2$
- α_i: Regularization Parameters
  - 0th Order - α_0: limits the values q_{max}
  - 1st Order - α_1: limits q bigger variations
  - 2nd Order - α_2: limits q quick oscillations

The main source of the measurement error in QIRT is the noise on the readout of the thermal camera, resulting in temperature readout fluctuations. As a result, only to the 1st order term will be assigned a weight as it limits these fluctuations, reducing S to eq. 5.

$$S = \sum_x \sum_y \left[T_{comp}(x,y) - T_{meas}(x,y) \right]^2 + \alpha_1 \cdot \sum_x \sum_y \left[grad(q(x,y)) \right]^2 \quad (5)$$

To find the heat flux values of next iteration step (q^{r+1}) for the minimization of S in eq. 5, the derivative of eq. 5 with respect to the fluxes of the next time step q^{p+1} needs to be zero. After rearranging the spatial discretization field into a single m by n vector, the derivative of the first part of 5 (defined as F) with respect to q^{p+1} can be expressed in matrix form as in eq. 6:

$$\frac{\partial F}{\partial q^{p+1}} = 2J. \left[T^r_{comp}(q^{p+1}) - T_{meas} \right] \quad (6)$$

where J is the temperature sensibility matrix with respect to the variation of each heat flux of the next time step p+1.

$$J = \begin{bmatrix} \frac{\partial T^r_{meas}(1)}{\partial q^{p+1}(1)} & \cdots & \frac{\partial T^r_{meas}[(M-1).(N-1)]}{\partial q^{p+1}(1)} \\ \vdots & \ddots & \vdots \\ \frac{\partial T^r_{meas}(1)}{\partial q^{p+1}[(M-1).(N-1)]} & \cdots & \frac{\partial T^r_{meas}[(M-1).(N-1)]}{\partial q^{p+1}[(M-1).(N-1)]} \end{bmatrix} \tag{7}$$

The value of $T^r_{comp}(q^{p+1})$ remains unknown but it can be calculated through a Taylor expansion of the known $T^r_{comp}(q^p)$. In matrix form it is:

$$T^r_{comp}(q^{p+1}) = T^r_{comp}(q^p) + J^t \Delta q \tag{8}$$

Combining 6 and 8 results in eq. 9:

$$\frac{\partial F}{\partial q^{p+1}} = 2J.\left[T^r_{comp}(q^p) - T_{meas}\right] + 2JJ^t\Delta q \tag{9}$$

In a similar way the derivative to q^{p+1} of the first order term S_1 in eq. 5 can be expressed in matrix form as:

$$\frac{\partial S_1}{\partial q^{p+1}} = 2X_1 q^r + 2X_1 \Delta q \tag{10}$$

where X_1 is the regularization matrix obtained deriving the discretized version of S_1 with respect to the heat flux variation. Combining eq. 10 and 9 results in 11 which is set equal to zero in order to calculate the next iteration (r+1) values for heat fluxes q^r:

$$\begin{aligned} \frac{\partial S}{\partial q} =& 2J\left(T^r_{comp}(q^r) - T_{meas}\right) + \\ & 2\alpha_1 X_1 q^r + \left(2JJ^t + 2\alpha_1 X_1\right)\Delta q = 0 \end{aligned} \tag{11}$$

Re-arranging eq. 11 to Δq^{r+1} one obtains:

$$\begin{aligned} &\Delta q|_{r\to r+1} = \\ &-\left(JJ^t + \alpha_1 X_1\right)^{-1}\left[J\left(T^r_{comp}(q^i) - T_{meas}\right) + \alpha_1 X_1 q^r\right] \end{aligned} \tag{12}$$

To solve the system in eq. 12 the sensibility coefficients Q^r of matrix J need to be determined. As these coefficients represent the temperature variation caused by the flux variation for each point l they can be estimated using eq. 13

$$Q^r_l = \frac{\partial T^r_{comp}}{\partial q^{p+1}_l} = \frac{T^p_{comp}(q_l - \epsilon \cdot q_l) - T^p_{comp}(q_l)}{\epsilon \cdot q_l} \tag{13}$$

Once the matrix X_1 and the coefficients Q^r are known it is possible to determine the vector of corrections Δq which minimizes S.

The term α_1 is chosen to minimize the condition number of the solution matrix in order to minimize the sensitivity of the used system of linear equations to any errors in the data. Introducing α_1^{opt}:

$$cond\left(JJ^t + \alpha_1^{opt} X_1\right) = min\left[cond\left(JJ^t + \alpha_1 X_1\right)\right] \tag{14}$$

with $cond()$ the condition number of the solution matrix. Imposing α_1^{opt} as value for α_1 will result in the best possible conditioning of the posed mathematical problem (see Figure 5).

Switching back to the inverse problem, eq. 12 is solved iteratively using α_1^{opt}.

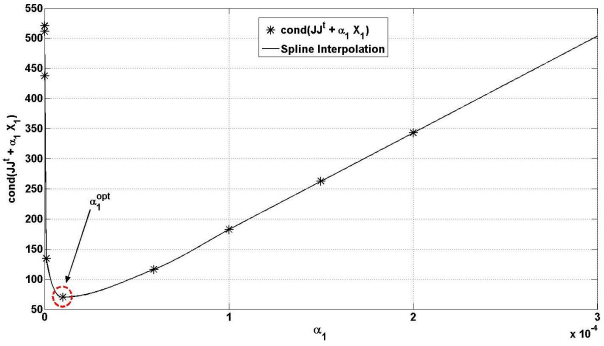

Figure 5: Condition number - α_1^{opt}

The iterative computation is stopped when the function S holds constant, within an imposed tolerance interval ϵ, for two consecutive iterations and the surface heat flux q(x,y) is found. Since the surface heat flux found is the total heat flux, it can be split into its convective and radiative part:

$$\begin{aligned} q(x,y) =& q_{conv.}(x,y) + q_{rad.}(x,y) \\ =& h(x,y)\left(T(x,y) - T_{ref.}\right) + \epsilon \cdot \sigma\left(T(x,y)^4 - T^4_{air}\right) \end{aligned} \tag{15}$$

As the emissivity of the paint on the plate surface and T_{air} are both known, the convective flux at the plate surface can be determined. Using a relevant reference temperature, the local convection coefficient at each point on the surface can be computed.

5. IHCP SOLUTION VALIDATION

The numerical validation is performed using a commercial CFD software package (*Fluent*©) and it can be summarized as follow:

1. Compute the $h(x)$ profile via the Nusselt correlation for a heated plate with unheated starting length. Equation 16 gives the Nusselt number for a turbulent, isothermal, local flow with $Pr > 0.6$ which holds true for the imposed flow velocity (U_∞) of 9.2 m/s and bulk flow temperature (T_∞) of 18 °C.

$$Nu(x) = \frac{0.0296 \cdot Re(x)^{0.8} \cdot Pr^{1/3}}{\left[1 - \left(\frac{\xi}{x}\right)^{9/10}\right]^{1/9}} \qquad (16)$$

   Some of the required fluid properties (particularly viscosity and diffusivity) have a high thermal dependency. To reduce ambiguity as to which temperature should be used to compute the property values the recommended approach is to use the film temperature, defined as the average of the wall and free-stream temperature, $T_{film} = \frac{T_{surface} + T_{air}}{2}$. After calculation of $Nu(x)$, $h(x)$ can be found directly.

2. Perform a direct simulation imposing the computed $h(x)$ in order to compute the 'hot' reference temperature field $T(x, y, t_1) = T_1$.

3. Perform a second direct simulation to compute the cooling phase and retrieve the surface 'cold' reference temperature field. $T(x, y, t_2) = T_2$.

4. Use T_1 and T_2 as IHCP boundary conditions to compute back $h(x)$

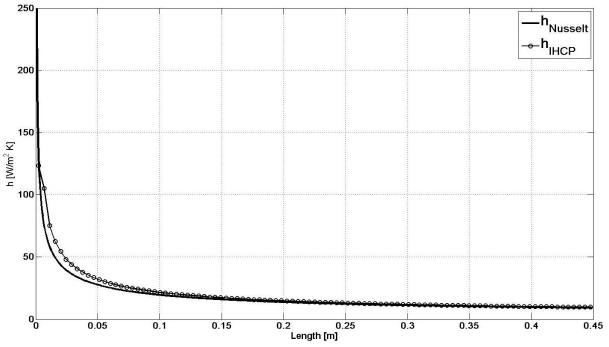

Figure 6: Theory - IHCP Solution Comparison

The problem solution reported in Figure 6 shows a very good agreement with the analytical solution except at the very beginning of the plate. In this area the asymptotic nature of the Nusselt correlation used for the theory is difficult to reproduce when using discretized solutions.

5.1. IHCP solution: experimental validation

Exploiting a heated flat plate allows an easy comparison between the experimental results and the direct numerical simulations already performed. A copper flat plate heated by an integrated electrical resistance is mounted in the test section of a low speed wind tunnel. The integrated circuit is glued on a bakelite plate placed on a polystyrene support to impose boundary conditions. Figure 7(a) and Figure 7(b) show the experimental setup and a cross section of the plate assembly. The surface temperature is measured using QIRT technique [43; 44; 45] with a *FLUKE - Ti50* I.R. camera. The camera has a 320 x 240 Focal Plane Array (FPA) and uses a vanadium oxide (VOX) uncooled microbolometer. The spectral band ranges from $8\mu m$ to $14\mu m$ with a thermal sensitivity lower than 0.070 °C at 30 °C and an accuracy of ±2 °C or ±2 %. It has a standard 20 mm $f/0.8$ Germanium lens with a 23°horizontal by 17°vertical field of view. The camera has a spatial resolution (IFOV) of 1.3 mrad and a minimum focus of 0.15 m. The refresh rate of the camera is 7.5 Hz. Emissivity correction is provided by user input, and ranges from 0.01 to 1 with a 0.01 step. The I.R. camera is calibrated using a black body as reference source.

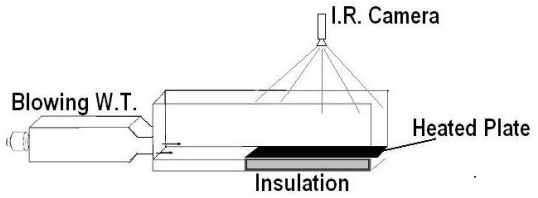

(a) Experimental Set Up Sketch



(b) Heated Plate Close Up View

Figure 7: Experimental Set Up Preparation Overview

The black body used for the camera calibration is the HGH Infrared Systems *ECN 100 blackbody* characterized by a radiant surface dimension ranging from 150 mm x 150 mm to 1 m x 1 m for temperatures up to +550 °C, enabling infrared sensor calibration without

collimator. The benchmarking of the plate's temperatures measured by the I.R. camera is made against the temperature measurement of a set of four thermocouples attached to the surface, repeated for several imposed temperatures [44]. The wind tunnel is set to have a bulk flow velocity in the test section of $9.2\,m/s$. To allow direct QIRT measurements of the flat plate, the upper part of the wind tunnel section is left open. As such, the actual flow field inside the wind tunnel has to be measured. To minimize any horizontal velocity gradients, the plate is mounted between two high vertical walls. The far field flow is measured using a *TSI* anemometer 'Velocicalc Plus Air Velocity Meter'. The anemometer has an uncertainty of $\pm 3\%$ of the reading or $0.015\ m/s$ with a resolution of $0.01\ m/s$ in the range from $0\ m/s$ to $40\ m/s$. The anemometer also incorporates a temperature sensor, with a resolution of 0.1 °C and uncertainty of ± 0.3 °C from -10 °C to 60 °C. To validate the turbulent boundary layer hypothesis used in eq. 16 the near wall flow is measured with a specific boundary layer hotwire probe (Dantec 55P15 probe) connected to a Dantec Streamline 90N10 acquisition box with a 90C10 module for CTA. The boundary layer is measured in a traverse of 77 points by means of a robotized system at different heights starting from 0.025 mm. As the output of I.R. camera temperature recording is incompatible for direct input in the IHCP solving code, the recorded images need to be adapted. After taking any I.R. image with a color map legend to link the colors to the temperature levels one has to retrieve a vector capable to translate the R(ed)-G(reen)-B(lue) data contained in the I.R. images into a matrix containing the corresponding temperatures. The last two steps consist in translating the image into any standard *Matlab*© exploitable matrix and crop the image to the area of interest. Once the I.R. images are converted for the analysis, the right surface dimensions, time step and plate material characteristics should be inserted in the script. As a last step to start the proposed solving procedure, the script requires the hot (T_1) and the cold (T_2) surface temperature matrices [46], which are recorded according to the the following procedure:

1. Heat the plate up to the wanted temperature and reach the intended target velocity.
2. Once the velocity and the plate T_{surf} are stabilized record the hot reference temperature (T_1).
3. Switch off the heating resistance.
4. After a time Δt record the cold reference temperature (T_2)

RESULTS

Figure 8 shows the velocity and the turbulence intensity profiles at the heated plate leading edge, (position $x = 0\ mm$), for both the boundary layer and the free flow region. The results show that the flow field generated for the experimental campaign meets the requirements of the theoretical reference case, with Figure 8(a) showing the typical figure of a turbulent boundary layer.

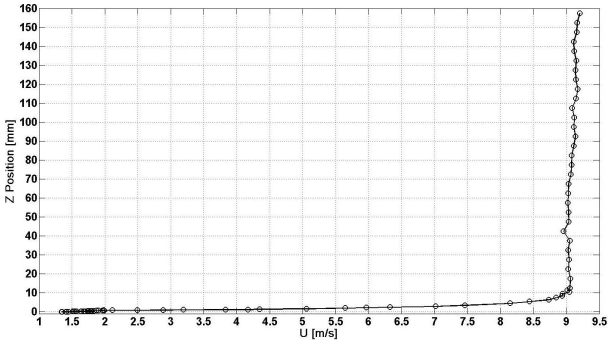

(a) Velocity Profile

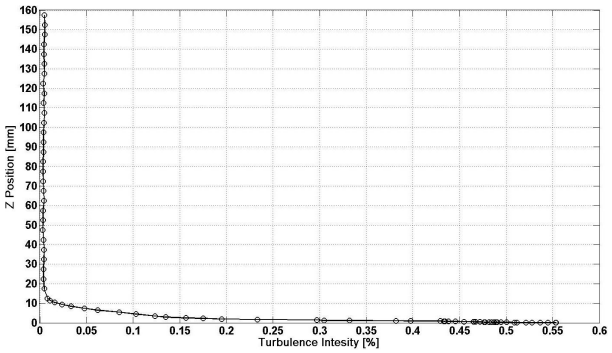

(b) Turbulence Intensity Profile

Figure 8: Boundary Layer Analysis

The effects of the regularization can be seen in Figure 9, where the upper figure show the results of the surface temperature using raw I.R. camera data and the contour plots in the lower figure the resulting temperatures obtained after regularization. To illustrate the effect of the parameter α_1 on the computed surface heat flux, Figure 10 plots the computed heat transfer coefficient as a function of α_1. The elimination of the fluctuation dampening ($\alpha_1 = 0$) shows the ill-posed character of the IHCP solution as measurements errors are amplified into large nonphysical oscillations on the calculated heat transfer coefficient profile. Fig-

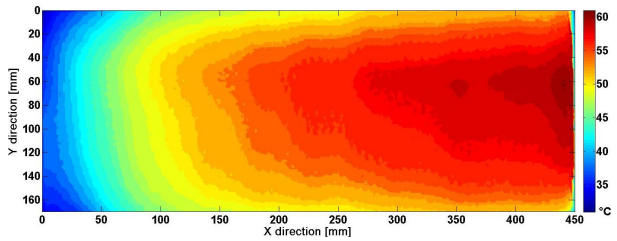

(a) T beginning - Raw data

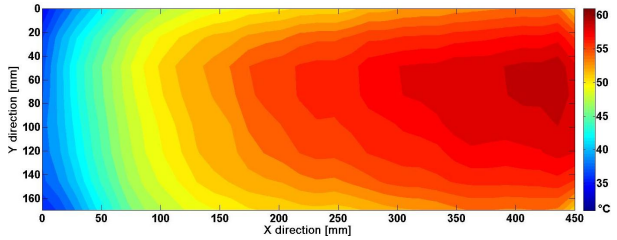

(b) T beginning - Regularization

Figure 9: Regularization Effect on the Measured Surface Temperature

ure 10 shows that the use of α_1^{opt} gives the best estimation for the heat transfer coefficient and that higher values of α_1 will lead to the underestimation of the heat transfer coefficient. A comparison between the theory and the results of the proposed IHCP methodology is given in Figure 11. The experiment was conducted with a time step of 5.41 seconds between two I.R. images. The theory uncertainty bounds come from a 3% of relative uncertainty on U_∞, while the error for $h(x)$ mainly originates from an average 2.8% of relative uncertainty on the measured T_{surf}. The biggest discrepancy can be seen on the leading edge the plate, where the steepness of the h curve becomes problematic due to the discretization of the calculated result. Nonetheless the quality of the obtained results can be controlled by a comparison of the heat flow lost per unit distance between the theoretical and the experimental case. The lost heat flow can be computed by eq. 17 as:

$$Q = \int h \cdot \Delta T_{surf} dS \tag{17}$$

which puts the heat flow at 2.35 W/m for the theory, and 2.5 W/m for the experimental result.Figure 12 plots the heat transfer coefficient $h(x, y)$ for the whole plate.

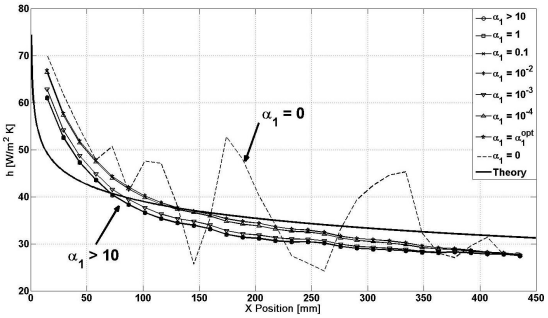

Figure 10: Regularization Effect on the IHCP Solution

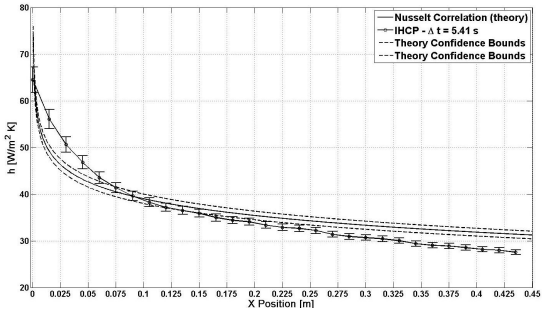

Figure 11: IHCP Solution Result - Comparison with Theory

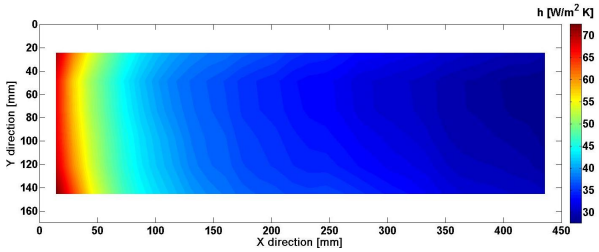

Figure 12: IHCP Solution Result - $h(x, y)$ Map

CONCLUSIONS

A solving methodology for the transient inverse heat conduction problem is proposed, using QIRT to measure the surface temperatures. To reduce the sensibility of the IHCP solution to the measurements noise a regularization method, based on the Tikhonov ridge regression, is applied. The methodology is first validated numerically, using a commercial CFD code to calculate the imposed surface temperatures. A very good match between the calculated values and the theoretical Nusselt correlation results was found. An experimental validation of the proposed methodology followed. The constant temperature anemometry technique was used to characterize the flow field.

The results shown a good agreement between theoretical and experimental data and proved the enhancements obtainable by applying the proposed regularization procedure, with the correct choice of parameter α_1 proven to be crucial.

WORK IN PROGRESS

A PIV experimental campaign on a scaled-up model of the finned heat exchanger has been conducted to investigate the flow field. The data analysis is partially performed. The region where the flow first impacts the heat exchanger is mainly investigated. Measurements are performed on several vertical and horizontal planes along the fins and between the fins. The measurements are performed at 3 different locations with respect to the heat exchanger fin edge. The horizontal planes are caught at 5 different heights per each location while the vertical plane measurements are performed at 5 different position between two fins. Figure 13 shows pictures of the experimental set-up while testing.

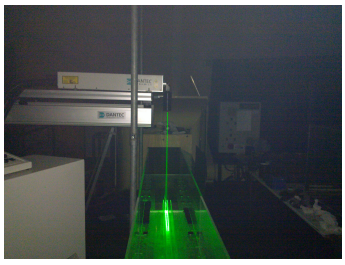

(a) PIV Experiments



(b) Scaled-up Model Close View

Figure 13: PIV Experimental Campaign

From the data analysis performed so far are obtained the plots reported in Figure 14 and Figure 15 .

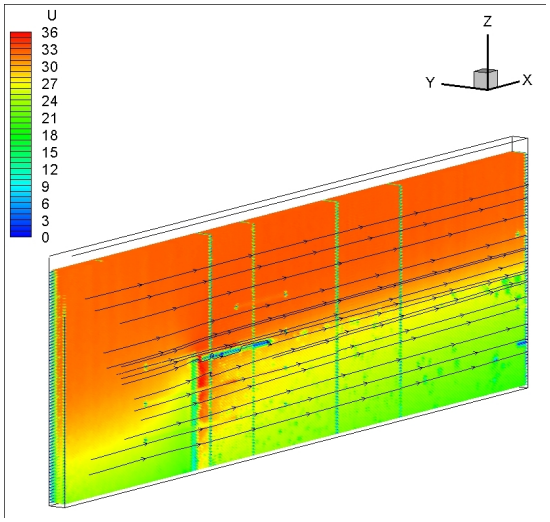

Figure 14: Average Field Reconstruction - U [m/s]

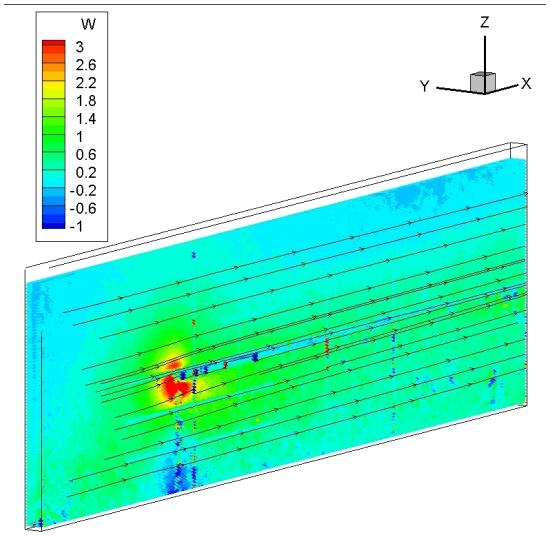

Figure 15: Average Field Reconstruction - W [m/s]

In the meanwhile the scaled-up model to close the thermal analysis at low speed has been manufactured and preliminary test performed. The design proposed is based on a 'sandwich fin' configuration. The heat source is obtained by means of a very thin (0.2 mm) copper streak glued on an aluminum plate. The interior of the assembly of the scaled-up fin is shown in figure 16. This assembly choice allows reducing manufacture complexity while granting heating uniformity all over the fin length.

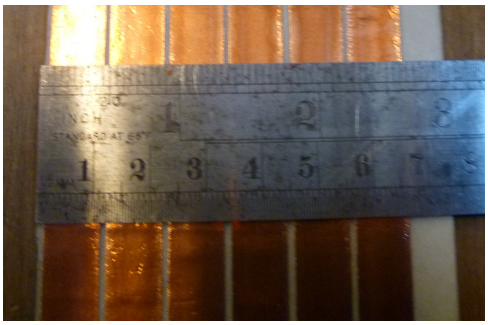

Figure 16: 'Sandwich Fin' Assembly - Interior

The pictures in Figure 17 show a comparison of an I.R. image and a color image of the first part of the fin during a preliminary test.

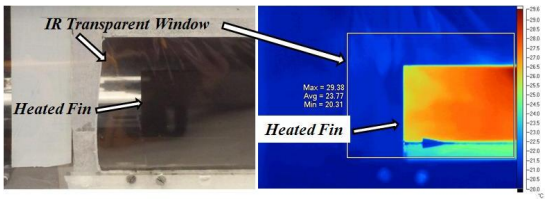

Figure 17: I.R. Vs. Color Image - 'Sandwich Fin'

In figure 18 the experimental set-up prepared to analyze a scaled-up single fin heat exchanger. The manufactured model is the same as for PIV experiments. It consists of a plexiglass base and an electrically heated fin (assembled as shown in figure 16) with the same dimensions of the fins used for the PIV experimental campaign. On a side wall an I.R. transparent window is created to allow QIRT measurements.



Figure 18: Experimental Set-up

To complete the overall heat exchange analysis a series of coupled experimental-numerical campaigns at high speed is under development. The proposed approach consists in solving a direct problem imposing the local heat transfer coefficients found at low speed as boundary conditions. The direct computation results will be compared with the surface temperature measurements performed at high subsonic velocity.

References

[1] G. Brines, D. E. Gray, Heat management in advanced aircraft gas turbine engines, ASME 86-GT-76.

[2] H. Streifinger, Fuel/oil system thermal management in aircaft turbine engines, RTO MP-8.

[3] J. Friedel, D. Bajusz, A. Cornet, N. Raimarckers, Air-oil exchanger arranged at the air separator nozzle of a jet engine and jet engine including such an air-oil exchanger, eP Patent App. EP20,070,150,441 (july 2009).
URL https://www.google.be/patents/EP2075194A1?cl=en

[4] S. Da, A. Roncatto, A. Belém, C. Da, Aircraft air inlet diverter assemblies with improved aerodynamic characteristics, eP Patent App. EP20,120,199,543 (july 2013).
URL http://www.google.com/patents/EP2610179A2?cl=en

[5] http://www.businesswire.com, Acoc applied to helicopter engines (unison), http://www.businesswire.com/news/home/20130617006273/en/Unison%E2%80%99s-Surface-Cooler-Helicopter-Applications (2013).

[6] R. Shah, D.P.Sekulic, Fundamentals of Heat Exchanger Design, John Wiley and Sons, INC., 2002.

[7] D. Harper, W. Brown, Mathematical equations for heat conduction in the fins of air cooled engines, NACA Report 158.

[8] A. Kraus, A. Aziz, J. Welty, Extended Surface Heat Transfer, John Wiley and Sons, INC., 2001.

[9] P. Razelos, A note on the heat transfer in convective fins, Thermo and Fluid Dynamics (12) (1979) 113–119.

[10] F. G. A. de Lieto Vollaro, S. Grignaffini, Optimum design of vertical rectangular fin arrays, International Journal of Thermal Science (38) (1999) 525–529.

[11] A. Bejan, E. Sciubba, The optimal spacing of parallel plates cooled by forced convection, International Journal of Heat and Mass Trasnfer 35 (12) (1992) 3259–3264.

[12] A. Aziz, A. B. Beers-Green, Performance and optimum design of convective-radiative rectangular fin with convective base heating, wall conduction resistance and contact resistance between the wall and the fin base, Energy Conversion and Management (50) (2009) 2622–2631.

[13] A. Kotcioglu, A. Cansiz, M. N. Khalaji, Experimental investigation for optimization of design parameters in a rectangular duct with plate-fins heat exchanger by taguchi method, Applied Thermal Engineering (50) (2013) 604–613.

[14] I. M. Didarul, O. Kenyu, Y. Minoru, S. Izuru, Study on heat transfer and fluid flow characteristics with short rectangular plate fin of different pattern, Experimental Thermal and Fluid Science (31) (2007) 367–379.

[15] P. D'Agaro, G. Comini, Thermal-performance evaluation of coolant passages with staggered arrays of pin fins, Heat Mass Transfer (44) (2008) 815–825.

[16] H. Azarkish, S. Sarvari, A. Behzadmehr, Optimum geometry design of a longitudinal fin with volumetric heat generation under the influences of natural convection and radiation, Energy Conversion and Management (51) (2010) 1938–1946.

[17] S. Mahmoud, R. Al-Dadah, D. Aspinwall, S. Soo, H. Hemida, Effect of micro fin geometry on natural convection heat transfer of horizontal microstructures, Applied Thermal Engineering (31) (2011) 627–633.

[18] M. Dogan, M. Sivrioglu, Experimental investigation of mixed convection heat transfer from longitudinal fins in a horizontal rectangular channel, Heat and Mass Transfer (53) (2010) 2149–2158.

[19] U. Akyol, K. Bilen, Heat transfer and thermal performance analysis of a surface with hollow rectangular fins, Applied Thermal Engineering (26) (2006) 209–216.

[20] Y. Lai, J. Lee, H. Nguyen, A coupled thermo-fluid analysis method with application to a novel thermodynamic vent system.

[21] J. E. Leland, V. Shanmugasundaram, J. E. Beam, R. Ponnappan, Effect of geometry on the conjugate heat transfer in a venturi-based cooling.

[22] R. AbdulNour, K. Willemborg, J. McGrath, J. Foss, B. AbdulNour, Measurements of the convection heat transfer coefficient for a planar wall jet: uniform temperature and uniform heat flux boundary conditions, ASME 86-GT-76.

[23] G. Cardone, T. Astarita, G. Carlomagno, Wall heat transfer in static and rotating 180 turn channels by quantittaive infrared thermography, Revue General Thermique.

[24] T. Wu, K. Vierow, A local heat flux measurement technique for inclined heat exchanger tubes, Experimental Heat Transfer 19 (1) (2006) 1–14. arXiv:http://www.tandfonline.com/doi/pdf/10.1080/08916150500317614, doi:10.1080/08916150500317614.
URL http://www.tandfonline.com/doi/abs/10.1080/08916150500317614

[25] A. Willockx, Using the inverse heat conduction problem and thermography for the determination of local heat transfer coefficients and fin effectiveness for longitudinal fins, Ph.D. thesis, University of Ghent (2009).

[26] H. Website, Rc01 radiation convection heat flux sensor, http://www.hukseflux.com/product/rc01?referrer=/product_group/heat-flux-sensors.

[27] T. Tszeng, V. Saraf., A study of fin effects in the measurement of temperature using surface-mounted thermocouples, Journal of heat transfer 125 (5) (2003) 926–935, eng.
URL http://www.refdoc.fr/Detailnotice?idarticle=9066425

[28] B. Cukurel, T. Arts, C. Selcan, Conjugate heat transfer characterization in a ribbed cooling channel, Conference Proceedings (ISAIF10 Paper nr.161).

[29] P. R. N. Childs, J. R. Greenwood, C. A. Long, Heat flux measurement techniques, Proceedings of The Institution of Mechanical Engineers Part C-journal of Mechanical Engineering Science 213 (1999) 655–677. doi:10.1243/0954406991524471.

[30] J. Beck, B. Blackwell, A. Hoji-Sheikh, Comparison of some inverse heat conduction methods using experimental data, International Journal of Heat Mass Transfer (Vol. 39, pp. 3649-3657).

[31] J. Beck, B. Blackwell, C. S.-C. Jr., Inverse Heat Conduction - Ill-posed Problems, first edition Edition, International Text Books in Mechanical Engineering, Wiley Interscience Publication, 1985.

[32] O. Alifanov, A. Nenarokomov, Three-dimensional boundary inverse heat conduction problem for regular coordinate systems, Inverse Problems in Engineering 7 (4) (1999) 335–362.
URL http://www.refdoc.fr/Detailnotice?idarticle=31127407

[33] M. G. Haghighi, M. Eghtesad, P. Malekzadeh, D. Necsulescu, Three-dimensional inverse transient heat transfer analysis of thick functionally graded plates, Energy conversion and management 50 (3) (2009) 450–457, eng.
URL http://www.refdoc.fr/Detailnotice?idarticle=20934653

[34] J. W. Woolley, K. A. Woodbury, Thermocouple data in the inverse heat conduction problem, Heat Transfer Engineering 32 (9) (2011) 811–825. arXiv:http://www.tandfonline.com/doi/pdf/10.1080/01457632.2011.525468, doi:10.1080/01457632.2011.525468.
URL http://www.tandfonline.com/doi/abs/10.1080/01457632.2011.525468

[35] D. Cavallero, G. Tanda, An experimental investigation of forced convection heat transfer in channels with rib turbulators by means of liquid crystal thermography, Experimental Thermal and Fluid Science 26 (2) (2002) 115–121. doi:doi:10.1016/S0894-1777(02)00117-6.
URL http://www.ingentaconnect.com/content/els/08941777/2002/00000026/00000002/art00117

[36] M. Lin, T. Wang, A transient liquid crystal method using a 3-d inverse transient conduction scheme, International journal of heat and mass transfer 45 (17) (2002) 3491–3501, eng.
URL http://www.refdoc.fr/Detailnotice?idarticle=9821056

[37] M. K. Das, A. Tariq, P. K. Panigrahi, K. Muralidhar, Estimation of convective heat transfer coefficient from transient liquid crystal data using an inverse technique, Inverse Problems in Science and Engineering 13 (2) (2005) 133–155. arXiv:http://www.tandfonline.com/doi/pdf/10.1080/10682760412331313414, doi:10.1080/10682760412331313414.
URL http://www.tandfonline.com/doi/abs/10.1080/10682760412331313414

[38] F. Kreith, Principles of Heat Transfer, second revised edition Edition, International Text Books in Mechanical Engineering, International Textbook Company Ltd, 158 Buckingham Palace Road London, 1965.

[39] P. H. Groeber, D. S. Erk, Fundamentals of Heat Transfer, third revised edition by dr. u. grigull Edition, McGraw-Hill Series in Mechanical Engineering, McGraw-Hill Book Company, INC., 1962.

[40] F. Coletti, A. Armellini, T. Arts, C. Scholtes, Aero-thermal investigation of a rib-roughened trailing edge channel with crossing jets - part ii: Heat transfer analysis, ASME paper No. GT2008 - 50695.

[41] A. Tikhonov, V. Arsenin, Solutions of ill-posed problems, WH Winston, Washington, DC.

[42] A. Tikhonov, V. Arsenin, Methods for solving ill-posed problems, Scripta Series in Mathematics (Scripta Mathematics, New York, 1977).

[43] G. Cardone, T. Astarita, G. Carlomagno, Wall heat transfer in static and rotating 180 degrees turn channels by quantitative infrared thermography, Rev. Gén. Therm. (37, 644-652).

[44] S. Rainieri, F. Bozzoli, G. Pagliarini, Characterization of an uncooled infrared thermographic system suitable for the solution of the 2-d inverse heat conduction problem, Experimental Thermal and Fluid Science (32, pages 1492-1498).

[45] J. Pellé, S. Harmand, Heat transfer measurement in an opened rotor stator system air gap, Experimental Thermal and Fluid Science.

[46] F. Baldani, W. Bosschaerts, R. Wagemakers, High velocities wind tunnel flow field investigation and heat exchanger infrared analysis. part 1: Experimental set-up, experiments and first results, Conference Proceedings (ISAIF10-11).

Experimental and Numerical Investigation of the Three Dimensional Unsteady Flow in a High Speed Axial Compressor

Giulia Dell'Era

Turbomachinery and Propulsion Department, von Karman Institute for Fluid Dynamics, Belgium, dellera@vki.ac.be

Supervisor: Jean-Francois Brouckaert

Associate Professor, von Karman Institute of Fluid Dynamics, Turbomachinery and Propulsion Department, Belgium, brouckaert@vki.ac.be

Co-Supervisor: Tony Arts

Professor, Turbomachinery and Propulsion Department, Head of the Department, von Karman Institute of Fluid Dynamics, Belgium, arts@vki.ac.be

University Supervisor: Philippe Chatelain

Professor, Université Catholique de Louvain, Institute of Mechanics, Materials and Civil Engineering, Belgium, philippe.chatelain@uclouvain.be

The development of the aircraft traffic, the decrease in fossil fuels availability during the last decades and the ambitious environmental goals set by several international bodies have made the improvement of the aero-engines technology a fundamental issue in pursuit of a safer, greener and cheaper engine operation. The compressor remains a critical component, not only in terms of weight but also regarding the performance and the stability of the machine. Modern compressors are characterized by high levels of unsteadiness due to both the rotor - stator interactions as well as the turbulence. The unsteady phenomena appearing in the blade passages have an important impact on the aerodynamic, mechanical and acoustic characteristics. Therefore their understanding is fundamental for the improvement of the performance of a compressor stage.

The accurate evaluation of the performance and stability characteristics of highly loaded low pressure (LP) axial compressor stages is the motivation for this PhD. The study comprises both an experimental and a numerical approach. The objective of this study is threefold. Firstly this research targets to find an optimum strategy to simulate numerically the flow in the compressor through the comparison of the experimental data with steady and unsteady simulations; the second aim is to analyze the flow field in order to point out the topology of the secondary flows and associated losses; the last objective is to understand the reason for the discrepancy between the predicted and the measured stall occurrence in the machine.

On one hand, an elaborate in-house experimental database exists of both time-mean and time-resolved measurements, at the rotor and stator exit stations as well as along the rotor over-tip casing. Those data are available along different speed lines, cover several throttling conditions from choke to stall and the stall transients. Since this detailed dataset constitutes the reference for the validation, it will be further analyzed in order to assess not only the uncertainty quantification on the unsteady data but also a better evaluation of the post-processing methodologies. The stall transient data will be further exploited to provide a clearer explanation of what occurs in terms of stall inception process.

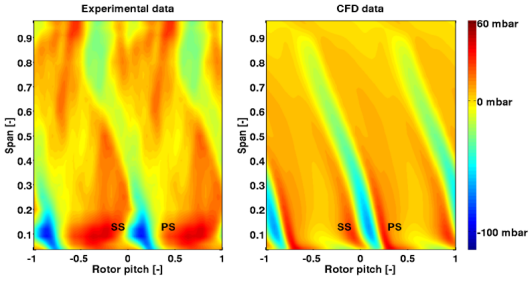

Figure 1: Fluctuations of total pressure around the mean level at the rotor outlet in the design condition

On the other hand, the available steady RANS computations need to be recomputed applying the proper measured inlet conditions and turbulence model. The unsteady computations are meant to be performed adopting both the non linear harmonic (NLH) and the traditional unsteady methodologies. The objectives are to determine up to which extent the unsteady computations improve the fidelity of the simulations and to understand the fluctuations in the aerodynamic parameters by using the time-resolved simulations.

Keyword: Axial compressors, unsteady flow, rotor-stator interaction, fast-response probes, unsteady computations, stability

Detail Aero-Thermal Characterization of Cooled High Pressure Turbine Components in View of Numerical Codes Calibration and Validation

Fabrizio Fontaneto

"'Jacques Chauvin"' Laboratory

Turbomachinery and Propulsion Department, von Karman Institute for Fluid Dynamics, Belgium, fontaneto@vki.ac.be

Supervisor: Tony Arts

Professor, Head of the Turbomachinery and Propulsion Department, von Karman Institute for Fluid Dynamics, Belgium, tony.arts@vki.ac.be

Promotor: Giovanna Barigozzi

Associate Professor, Faculty of Industrial Engineering, University of Bergamo (IT), giovanna.barigozzi@unibg.it

Nowadays companies are making a massive use of Computational Fluid Dynamics (CFD) since the early stages of the development of new components. Given therefore the critical role that numerical codes are playing, their reliability must be rigorously checked through detailed comparisons between numerical and experimental results. The present work briefly reports on the main findings of two different but complementary measurement campaigns, both focused on the creation of an experimental test-case for turbomachinery numerical codes validation.

The first experimental activity, funded by "Ansaldo Energia" and carried out at the *Energy Systems and Turbomachinery Laboratory* of the University of Bergamo (Italy), dealt with the characterization of the effect that the endwall cooling system of a high pressure turbine rotor had on both, the thermal and the aerodynamic performance, with a particular attention paid to the study of the interaction between the cooling jets and the secondary flows. Aerodynamic measurements, performed by means of a 5-hole miniaturized pressure probe, evidenced a marked asymmetry of the secondary flows between the upper and the lower semi-channels. The latter had to be related to the presence of the fillet between the blade and the cooled endwall and it demonstrated to provide a significant reduction of the aerodynamic losses. Injection seemed not to affect at all the secondary flows pattern: at every injection rate, the cooling jets kept attached to the endwall surface and confined in the boundary layer. Such a result was confirmed by the adiabatic effectiveness distribution which was retrieved by thermochromic liquid crystals. The thermal protection was continuously growing with the injection rate and no separation was identified. The high performance of the cooling system had to be related to the extreme tangential arrangement of the holes. In the end, a good agreement was found between the experimental data and the results of simulations run by the company.

The second measurement campaign was held at the von Karman Institute for Fluid Dynamics (VKI) (Belgium) and funded by the Japanese Central Research Institute of Electric Power Industry (CRIEPI). A film-cooled transonic turbine vane was investigated in a five blades linear cascade configuration and at engine-like conditions in terms of Reynolds number and Mach number. The inlet free-stream turbulence was fully characterized by means of hot-wire anemometry showing results in complete agreement with partial past results and literature. The aerodynamic performance of the cascade was assessed by traversing a 3-hole pressure probe in the downstream section. Injection was found to slightly enhance total pressure wakes, with a weak increase in terms of aerodynamic losses. In particular, it has been demonstrated how, in supersonic conditions, the presence of a strong shock in the rear part of the suction side is responsible for a marked degradation of the performance of the cascade. Thin-films thermometers have been used to retrieve the blade convective heat transfer coefficient (h) distribution. The non-cooled tests demonstrated that, for every main-stream condition, the tripping effect of the film-cooling holes is the responsible for a transition of the boundary layer state. The thermal protection of the suction side always increases with the injection rate, showing therefore a high re-

sistance to separation. On the pressure side, on the contrary, the portion of the blade surface placed immediately downstream the injection point is characterized by values of h higher than those of the non-cooled case: already at low injection rates, the coolant momentum is high enough to break down the boundary layer, putting therefore in direct contact the blade surface with the hot main-stream. In any case, the rear part of the pressure side always benefits from an enhanced injection.

Keywords:
Gas turbines, CFD validation, film-cooling, high pressure turbine blade/vane, aero-thermal performance, turbulence characterization

The Effect of Solidity on Compressor Performance and Stability

Jérôme Sans

Turbomachinery and Propulsion Department, von Karman Institute of Fluid Dynamics, Belgium, sans@vki.ac.be

Supervisor: Jean-François Brouckaert

Associate Professor, Turbomachinery and Propulsion Department, von Karman Institute of Fluid Dynamics, Belgium, brouckaert@vki.ac.be

Co-Supervisor: Tony Arts

Professor, Head of Turbomachinery and Propulsion Department, von Karman Institute of Fluid Dynamics, Belgium, arts@vki.ac.be

Promotor: Philippe Chatelain

Professor, Université Catholique de Louvain, Institute of Mechanics, Materials and Civil Engineering, Belgium, philippe.chatelain@uclouvain.be

Abstract

The solidity in a compressor is the ratio of the aerodynamic chord over the pitch. The following PhD project aims at investigating numerically and experimentally the effect of the solidity on both compressor performance and stability. Existing compressor correlations are reviewed to extract the influence of solidity on deviation, incidence, losses and blade loading. The effect of solidity is investigated by CFD with FINE/Turbo of NUMECA International. Two different blade profiles were selected and investigated within a linear cascade configuration that matches the VKI-C3 high-speed facility. The first airfoil is a standard double circular arc profile, extensively referenced in the literature, while the second profile uses a state-of-the-art controlled diffusion blade, representative of low pressure compressor stator mid-span profile. Performance of both cascades are analyzed and compared to the correlations. Finally, based on a given compressor geometry, solidity optimization are presented at the level of meridional design. This is performed with an axial compressor design tool implemented at VKI coupled with the VKI optimization code. The importance of the maximum diffusion factor and the loss correlations along the span is highlighted.

Keywords: Compressor, solidity, pitch, chord, blade number

Nomenclature

b	Deviation-rule exponent [-]	M	Mach number [-]
c	Chord [m]	P	Pressure [Pa]
i	Incidence angle [°]	Re	Reynolds number [-]
m	Deviation-rule slope factor [-]	V	Velocity [m/s]
m_c	Carter's rule slope factor [-]	α	Angle of attack [°]
n	Incidence-rule slope factor [-]	β	Flow angle [°]
s	Pitch [m]	δ	Deviation angle [°]
t	Thickness [m]	γ	Stagger angle [°]
y	Pitch direction [m]	κ	Blade metal angle [°]
z	Axial direction [m]	ϕ	Camber angle [°]
D	Diffusion factor [-]	σ	Solidity [-]
H	Shape factor [-]	θ	Momentum thickness [m]
K	Thickness correction coefficient [-]	ζ	Loss parameter [-]

ω	Total pressure loss [-]
AVDR	Axial Velocity Density Ratio [-]
CDB	Controlled Diffusion Blade
DCA	Double Circular Arc
RANS	Reynolds Averaged Navier Stokes

Subscripts

0	Zero-camber quantity
1	Cascade inlet quantity
2	Cascade outlet quantity
i	Incidence
s	Static quantity
t	Total or stagnation quantity
δ	Deviation
cr	Critical condition
fs	Free stream quantity

1. Introduction

The solidity is the ratio of the aerodynamic chord over the peripheral distance between two blades also called the pitch. This parameter must be selected early in the design process and the important role played by the solidity in the loading assessment makes its choice a crucial step that should be regarded with great care.

During the last decades, a constant increase of solidity in engine compressors has been noticed (Fig. 1). This reflects the need to satisfy more and more severe loading requirements that can only be achieved with high solidity. Unfortunately, even though either a chord extension or a blade count increase allows to work at higher loading, both methods present the undeniable disadvantage of increasing the engine weight, meaning a higher fuel consumption and pollutant emissions but also higher production and maintenance costs. In that prospect, the following PhD project aims at investigating numerically and experimentally the effect of the solidity on both compressor performance and stability. Focusing on solidity variations, the work also aims at validating and updating the low-speed correlations both with numerical simulations and high-speed cascade tests in the VKI-C3 facility. The research is driven by the need of improving the current practices regarding the solidity choice in compressor design.

The first part of the paper covers all the existing compressor cascade correlations and characterizes the influence of solidity on deviation, incidence and losses. The important role played by the solidity on the blade loading and stability is also addressed.

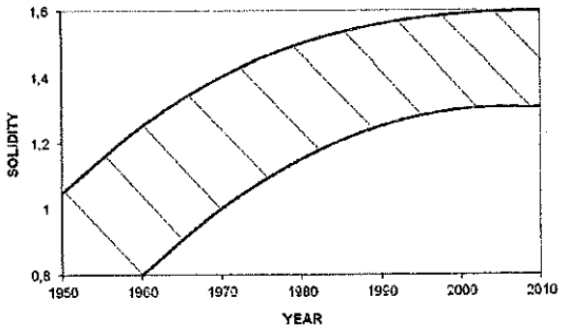

Figure 1: Evolution of the solidity in engine compressors over the last years [1] (Obrecht, 2013).

After reviewing the literature, the effect of solidity is assessed through CFD. Two different compressor profiles have been set-up within a linear cascade configuration. The first airfoil is a state-of-the-art controlled diffusion blade (CDB) representative of a low-pressure compressor stator profile. This geometry will be then tested in the VKI C3 facility. For the numerical investigation, a standard double circular arc (DCA) profile has also been considered. This choice is motivated by the extensive amount of data in the literature about this geometry which enables to evaluate the CFD predictions.

The last section of the paper exposes results of solidity optimization performed with an axial compressor design tool implemented at VKI together with the VKI CADO optimizer are presented. To support this investigation, a low-pressure compressor geometry studied both experimentally and numerically at VKI within the European DREAM project is considered.

Finally, the future perspectives of the work are presented.

2. Literature review

Despite the fact that the flow in axial compressors is mainly governed by three-dimensional effects, cascade theory allows to shed some light on the physical phenomena taking place in the three-dimensional machine. Cascade correlations, presented in this section, essentially come from the 1960's. They may have been corrected since then by engine manufacturers but all compressor designers once dealt with those data. The current section does not have the ambition of being exhaustive but tries to summarize the most relevant definitions and developments required to

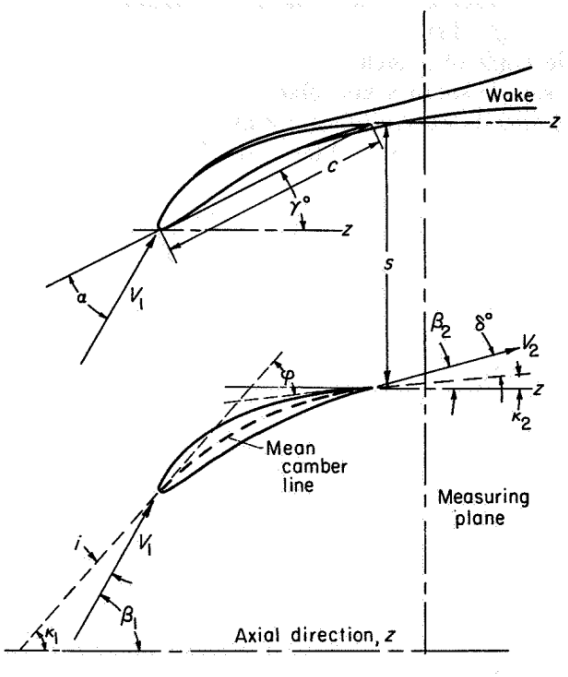

Figure 2: Geometrical configuration and angle definition in a compressor cascade

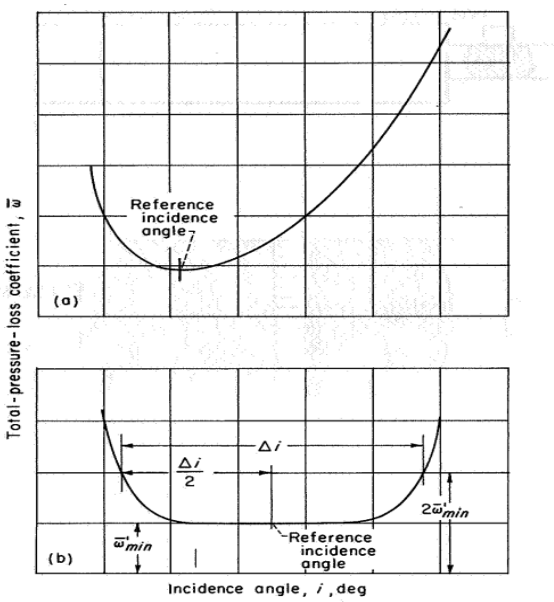

Figure 3: Definition of the optimum incidence [2]: (a) minimum loss incidence; (b) mid-range incidence

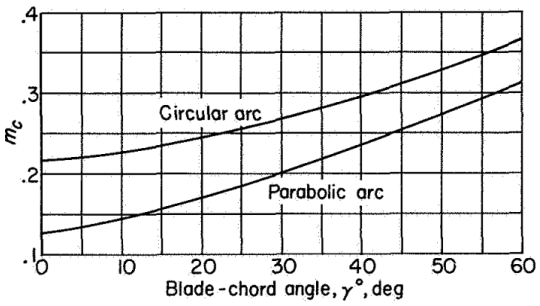

Figure 4: Empirical factor m_c of Carter's rule Eq. 3 [2]

understand the effect of solidity.

The nomenclature for the flow angles is established in Fig. 2. It follows the standards of the well-known NASA SP-36 axial compressor design manual ([2], 1965).

Most of the correlations only focus on reference incidence performance. The performance parameters are the deviation angle δ (cf. Fig. 2) and the total pressure losses ω, defined in Eq. 1.

$$\omega = \frac{p_{t1} - p_{t2}}{p_{t1} - p_{s1}} \tag{1}$$

The reference incidence of a given airfoil is the incidence that yields to minimum total pressure losses. It is therefore called optimum incidence or minimum loss incidence. When the loss curve shows a very flat region, the mid-range incidence is considered as the optimum incidence. This is illustrated in Fig. 3.

The manual from NASA [2] provides correlations to predict the optimum incidence in the form of Eq. 2.

$$i = K_i i_0 + n\phi \tag{2}$$

The empirical coefficients i_0, n and K_i in Eq. 2 are tabulated in [2] for DCA and NACA 65 series compressor profiles. For the sake of clarity, the plots are not given in the paper but one should know that the influence of solidity is hidden both in the zero-camber optimum incidence i_0 and the slope factor n. The coefficient K_i only takes into account the maximum thickness variation. The impact of solidity is not straightforward but it emerges that the optimum incidence decreases with solidity.

Regarding the deviation, the most important work comes from Carter ([3], 1949). Carter's deviation rule is defined in Eq. 3 where m_c is the Carter's empirical slope factor (given in Fig. 4) and ϕ stands for the camber angle.

$$\delta = m_c \frac{\phi}{\sqrt{\sigma}} \tag{3}$$

Eq. 3 clearly establishes the solidity impact on the

flow deflection. The deviation decreases as the solidity increases. A more complete definition of the deviation from the compressor design handbook of NASA [2] is given by Eq. 4. The empirical coefficients K_δ, δ_0, m and b used in Eq. 4 are tabulated in [2].

$$\delta = K_\delta \delta_0 + \frac{m\phi}{\sigma^b} \tag{4}$$

Most of the time, both rules (Eq. 3 and Eq. 4) offer comparable results for low Mach numbers and have been used for decades.

For high subsonic values, as mentioned in [2] or [4], the influence of Mach number is very limited on both the optimum incidence and deviation. Jansen et al. ([5], 1967) give turning corrections for Mach numbers equal or above the critical Mach number. The latter is defined as the Mach number inducing the appearance a sonic point along the blade suction side. It depends mainly on the profile thickness and camber distribution. An analytical function, based on empirical correlations that are only valid for NACA 65 series, is given in [5] in order to calculate the critical Mach number. Below critical conditions, no correction is suggested.

Regarding the loss prediction and the loading assessment, the greatest advancement comes from Lieblein et al. [6] and the definition of the diffusion factor in 1953. Since the suction side boundary layer, facing an adverse pressure gradient, is responsible for the limiting pressure rise and turning of the flow, Lieblein et al. linked the suction side deceleration of the flow to a local diffusion factor:

$$D_{loc} = \frac{V_{max} - V_2}{V_2} \tag{5}$$

where V_{max} is the peak suction side velocity and V_2 the outlet velocity. Under the form of Eq. 5, the calculation of the diffusion factor was not practical and, in most of the cases, not measurable as it requires the blade velocity distribution. A simplified diffusion factor was then defined to assess the loading of the blades. It is given in Eq. 6.

$$D = 1 - \frac{V_2}{V_1} + \frac{\Delta V_\theta}{2\sigma V_1} \tag{6}$$

This simplification brings up the outlet-inlet velocity ratio, the tangential velocity difference as well as the solidity. Gathering the results of measurements performed on various types of bladings (DCA, NACA65 or British C4 among others) having different solidities but also maximum thicknesses and camber angles, Lieblein linked the wake momentum thickness

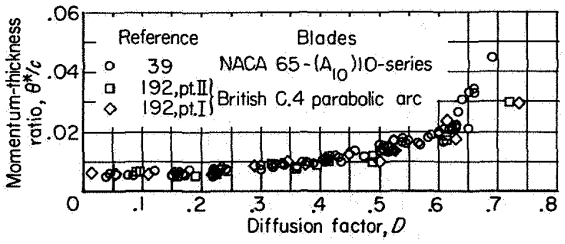

Figure 5: Evolution of momentum thickness as a function of diffusion factor of Lieblein [2]

to the diffusion factor. This is illustrated in Fig. 5 from [2]. For $D > 0.6$, it can be seen that the wake momentum thickness starts to rise more steeply. It was therefore commonly accepted that a diffusion factor of 0.6 could be considered as a stall limit.

Lieblein [7] derived the link between the momentum thickness to chord ratio and the total pressure losses, as shown in Eq. 7.

$$\frac{\theta}{c} = \frac{\omega \cos\beta_2}{2\sigma} \left(\frac{\cos\beta_2}{\cos\beta_1}\right)^2 \left\{ \frac{3H-1}{2H} \left[1 - \frac{\theta}{c} \frac{H\sigma}{\cos\beta_2}\right]^3 \right\} \tag{7}$$

Lieblein observed in [7] and [8] that the last term within braces in Eq. 7 was close to 1 and not subject to strong variation over a wide diffusion range. Therefore, he suggested the use of loss parameters to approximate the wake momentum thickness. Those loss parameters are given in Eq. 8 or Eq. 9 and referred as ζ_1 and ζ_2 in the following. They present the big advantage of relying only on total pressure losses and flow angle measurements. Plotted versus the diffusion factor, both loss parameters offer a good prediction of the wake momentum thickness. This is shown in Fig. 6.

$$\zeta_1 = \frac{\omega \cos\beta_2}{2\sigma} \approx \frac{\theta}{c} \tag{8}$$

$$\zeta_2 = \frac{\omega \cos\beta_2}{2\sigma} \left(\frac{\cos\beta_2}{\cos\beta_1}\right)^2 \approx \frac{\theta}{c} \tag{9}$$

Although Lieblein enlightens the physical relation between the total pressure deficit ω and the boundary layer development through the use of θ and H, Eq. 7 is based on incompressible relations. Consequently, ζ_1 and ζ_2 are not supposed to be employed at high subsonic Mach numbers. However, many authors as Jansen et al. (1967, [5]), Hearsey (1986, [9]), Roberts et al. (1988, [10]), Casey (1987, [11]) or Wright et al. (1991, [12]) refer to such loss parameters because it only relies on the inlet and outlet pressure and velocity diagrams as well as the solidity. Therefore, it makes a

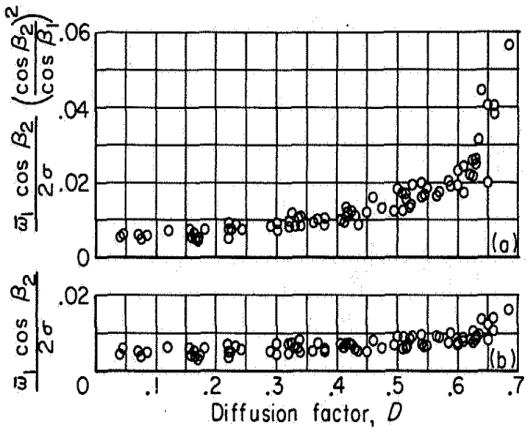

Figure 6: Evolution of loss parameters ζ_1 and ζ_2 versus [2]

very convenient tool to obtain a first guess of the total pressure losses induced by a blade row at the level of the meridional design.

Some corrections for compressible flow exist as presented by Jansen et al. [5]. Below the critical Mach number, no correction is considered. Above the critical Mach number, they suggest that the incompressible losses may be simply corrected by Eq. 10.

$$\omega_{comp} = \omega_{incomp}[2(M_1 - M_{1,cr}) + 1] \qquad (10)$$

One of the motivation of the current investigation is to assess both numerically and experimentally the validity of the low-speed correlations in the compressible regime at high subsonic Mach number. While the experimental campaign is still under progress in the VKI-C3 facility, the results of the numerical investigation are presented in the next section.

Finally, to conclude this section, it must be mentioned that the definition of an optimum solidity is an theoretical issue that has been tackled by many (e.g., Howell [13], Zweifel [14], Hearsey [9], McKenzie [15] or Liu [16]). However, in most cases, all the existing methods lead to different results and unfortunately, no general rule exists to help the designer selecting the best solidity. The solidity may be optimized at the level of the meridional design. Such a method has been used by Massardo et al. (1990, [17]), Joly et al. (2012, [18]) or Teichel et al. (2013, [19]) but did not focus on solidity. Solidity optimization obtained with a meridional design tool implemented at VKI together with the VKI optimzation code (CADO) are presented in a further section of this paper.

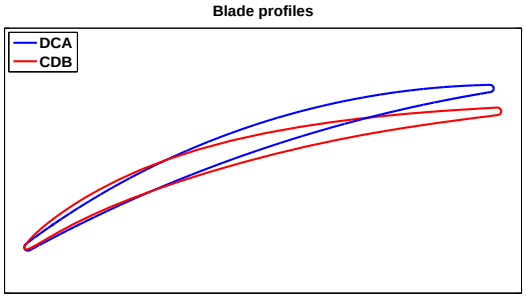

Figure 7: Investigated controlled diffusion blade (CDB) and double circular arc (DCA) profiles (not to scale)

	CDB	DCA
Chord	33.09 mm	
t_{max}/c	5%	
$\kappa_1 - \kappa_2$	28.3°	
γ	16.5°	19.3°
σ	1.38, 1.24, 1.10	

(a) List of blade parameters

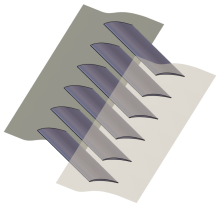

(b) View of the CDB cascade

Figure 8: List of blade design parameters (a) and view of the CDB linear cascade (b)

3. Numerical investigation

3.1. Geometrical model

Two blade profiles have been set-up into a linear cascade configuration. The first geometry involves a controlled diffusion blade that is representative of a state-of-the-art low pressure compressor stator profile while the second is a standard DCA blade. The CDB thickness distribution and camberline have been optimized. Since the camberline is not a circular arc like DCA blades or NACA 65 airfoils referenced in the literature, the camber angle may not be defined as $\phi = \kappa_1 - \kappa_2$ like it is presented in Fig. 2. The blade parameters that have been chosen to be kept constant are the aerodynamic chord c, the maximum thickness-to-chord ratio t_{max}/c and both inlet and outlet blade metal angles, i.e. the metal turning (κ_1-κ_2). As a consequence of this choice, the stagger angles γ are different as well as the achieved flow turning. The blade parameters are summarized in Fig. 8 and the profiles are displayed in Fig. 7.

Finally, both blades have a span 100 mm height to match the dimensions of the high-speed cascade facility of VKI. Given that the chord and the blade height

are not modified, the aspect ratio as well as the chord-based Reynolds number at a given Mach number are kept constant. A picture of the CDB profile within its cascade configuration is displayed in Table 8.

3.2. Numerical model

The FINE/Turbo software package (Numeca International) has been used both for meshing the domain and solving the Navier-Stokes equations. Within this investigation, only fully-turbulent steady RANS computations are considered. The mesh domain extends from one chord upstream the leading edge to one chord downstream the trailing edge and includes the whole blade passage. A standard O4H topology is considered and the grid counts 800.000 cells for one blade passage. It ensures a $y^+ < 1$ at the walls. A complete mesh sensitivity analysis at design and off-design conditions has been performed and is reported by Resmini (2013, [20]).

Regarding the turbulence model, the $k - \epsilon$ Yang-Shih turbulence model has been used. A turbulence intensity of 1% is set at the inlet of the computational domain to match the inlet conditions of the experimental facility C3 of the VKI. For the spatial discretization, the Jameson central scheme has been used, coupled with a 4th order Runga-Kutta time discretization. A study of the turbulence model and the numerical scheme effects is reported by Sans et al. (2014, [21]).

Total conditions and flow angle are imposed at the inlet and static pressure at the outlet (set to the standard atmospheric pressure level of 101325 Pa). The solidity is only varied by changing the pitch in order to keep the chord-based Reynolds number constant at a given inlet Mach number (Re$\approx$ 320.000 at $M_1 = 0.4$ and Re$\approx$ 540.000 at $M_1 = 0.7$). In the pitch direction, periodic boundary conditions are considered and the number of blades is infinite.

The cascade configuration has been considered in view of the measurement campaign. Therefore, as it can be seen in Fig. 8, the end-walls have not been removed. As a consequence, secondary flows and corner separation are growing as the incidence increases. The development and the topology of the secondary flows will not be addressed in the current paper. The emphasis is set on the mid-span performance and the comparison with the literature.

3.3. Results

The total pressure losses for the CDB and DCA blades are given as a function of incidence in Fig. 9 at inlet Mach numbers of 0.4, 0.5, 0.6 and 0.7. The minimum losses ω_{min} are indicated by a cross. The first and last incidences correspond to incidences yielding $2\omega_{min}$ and to match exactly this loss level, both first and last incidences have been interpolated. In the case of the controlled diffusion blade, at M_1=0.6 and M_1=0.7, the two lowest solidity blades stalled before reaching $2\omega_{min}$. Except those specific cases, the last incidence is not the last converged incidence. It has been chosen to present the results in a limited incidence range as the emphasis is set the performance at optimum incidence and the comparison with the correlations. The issue of the operating range and the stall limit are discussed in a further section.

Concerning the comparison of the two different blades, the CDB produces lower total pressure losses since its design is the result of an optimization process. Regarding the effect of solidity, both blades present the same behaviour. From choke to the minimum loss incidence, the total pressure losses increase with solidity. This can be explained by an enlarged wet area when the solidity is increased. Beyond the minimum loss incidence, the trend reverses. The loading and the diffusion increase and the losses increases faster for lower solidities.

As predicted by correlations [2], the minimum loss incidence varies with solidity. No influence of Mach number is noticed and the minimum loss incidence remains the same as the inlet Mach number increases. This is not true for the low solidity DCA for which the minimum loss incidence is changing at M_1=0.7. It must be pointed out that the influence of Mach number on the optimum incidence may be affected by the discretization of the incidence range and the impossibility of having a continuous incidence evolution.

Once the minimum loss incidence has been identified, one can compare the performance at this specific inlet flow angle with the existing correlations. First of all, the optimum incidences for both CDB and DCA are given in Fig. 10. As no influence of the Mach number has been noticed (except for the low solidity DCA), all the results are gathered in the same plot. The CFD results are compared with the NASA prediction available for the DCA and NACA 65 (cf. Eq. 2). The NASA rule for DCA is giving higher optimum incidences and the best agreement is achieved at high solidity where it predicts an optimum incidence 0.5° too high. For both blades, the calculated trend is definitely linear and the optimum incidence increases with solidity. Linear polynomials seem to fit the CDB and DCA quite well and are indicated by dashed lines in Fig. 10.

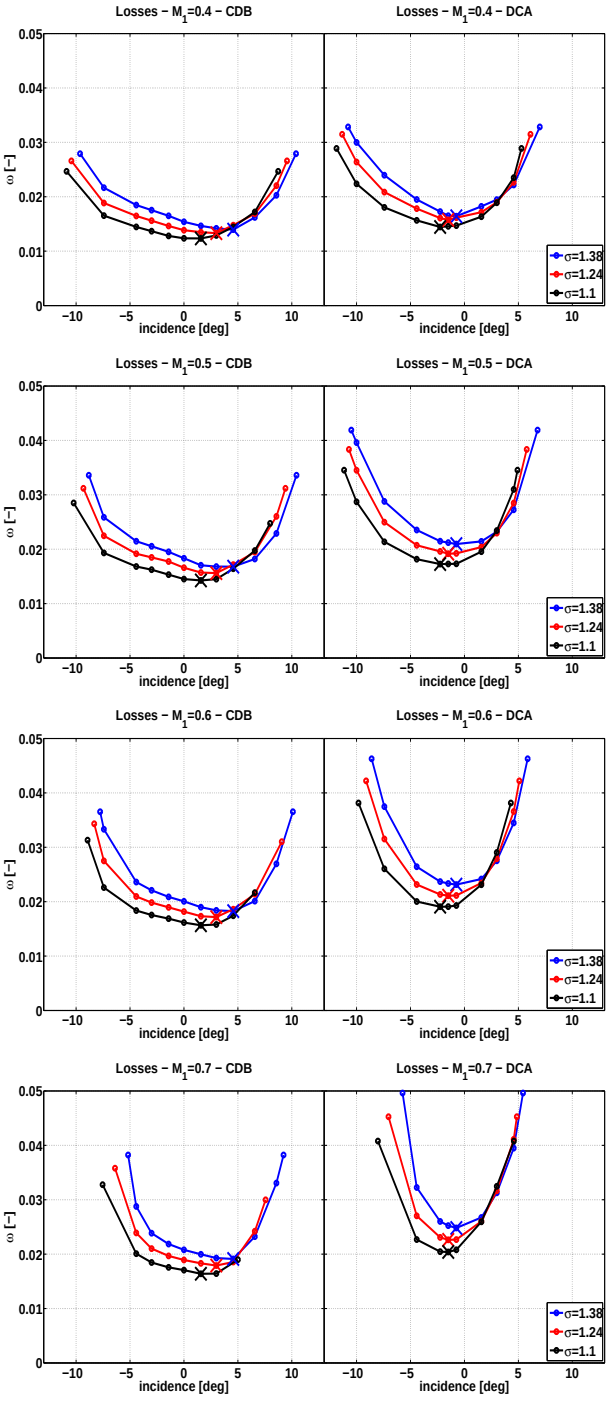

Figure 9: TOTAL PRESSURE LOSSES VERSUS INCIDENCE AT M_1=0.4, 0.5, 0.6 AND 0.7

The deviation at optimum incidence is plotted versus solidity in Fig. 11. Carter's DCA rule (cf. Eq. 3) as well as both the DCA and NACA 65 NASA rules

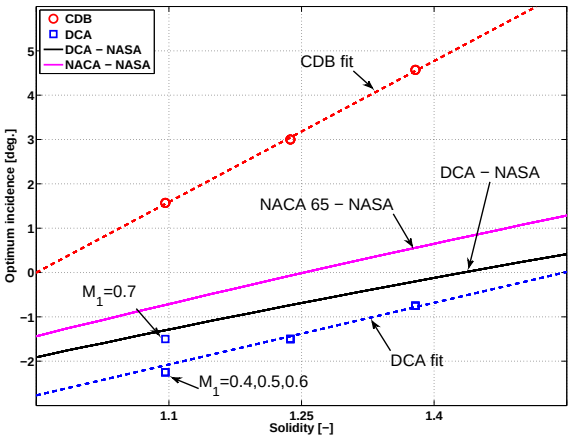

Figure 10: Minimum loss incidence versus solidity

(cf. Eq. 4) are also plotted. Carter's DCA predictions are in good agreement with the DCA results for all Mach numbers. At high solidity, it gives slightly higher values but the highest discrepancy is around 0.4°. It proves that, although the correlations are from low speed data, they are valid up to the critical Mach number. The NASA rule is very close to Carter's predictions but only at high solidity. Towards the low solidities, the NASA rule diverges from Carter's one. Regarding the CDB, none of the correlations match the CFD results. A curve fit matching the data at all Mach numbers can be obtained by applying an offset of −1.3° to the NASA rule for the NACA 65 series. The compressibility effect is very limited for the DCA and slightly stronger for the CDB. For the latter, the Mach number influence is higher at low solidity where a decrease of 0.6° is observed between M_1=0.4 and M_1=0.7. The typical measurement uncertainty on flow angle measured with a standard three-hole probe sits around 0.3° and those effects may not be validated during the measurement campaign.

The diffusion factor at optimum incidence and at stall are displayed in Fig. 12 in function of Mach number. It is very interesting to notice that the diffusion factor at minimum loss incidence remains approximately constant with solidity for both CDB and DCA. At stall, the diffusion factor corresponding to $2\omega_{min}$ is also independent of the solidity choice. Although the optimum diffusion factor (i.e at optimum incidence) varies with the type of blade and Mach number, it is an essential information for the designer. For a given Mach number and blading, the minimum loss conditions are encountered for a given value of the diffusion factor that is independent of the solid-

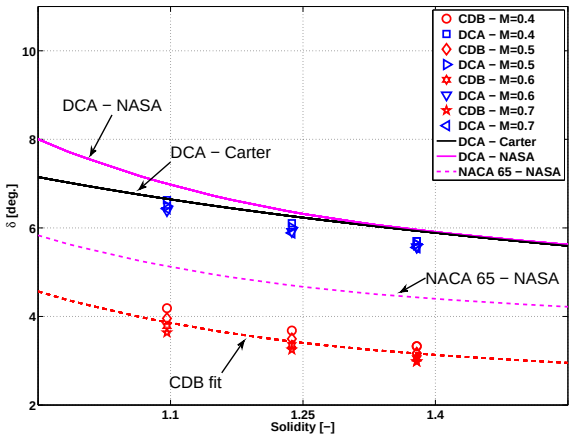

Figure 11: Deviation at optimum incidence versus solidity

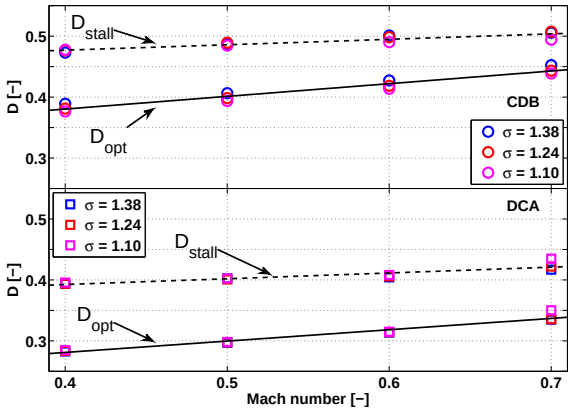

Figure 12: Diffusion factor at minimum loss incidence and at stall versus mach number

ity. The same conclusion can be drawn at stall, for the conditions yielding $2\omega_{min}$. It is thus possible to design for a given optimum diffusion factor before selecting an optimum incidence and a solidity.

The loss parameters ζ_1 and ζ_2 are supposed to provide an approximation of the wake momentum thickness. To assess the quality of this approximation, the wake momentum thickness has been calculated from the velocity wakes as exposed by Lieblein [7]. The obtained momentum thickness is shown at minimum loss incidence in Fig. 13 and Fig. 14 together with the loss parameter ζ_1 and ζ_2. In both figures, the black dashed line represents the NASA correlations of [2] (cf. Fig. 6). The dotted lines that pass through the minimum loss data represent the neighboring incidences, i.e. the off-design incidences.

Although a small effect of the Mach number can

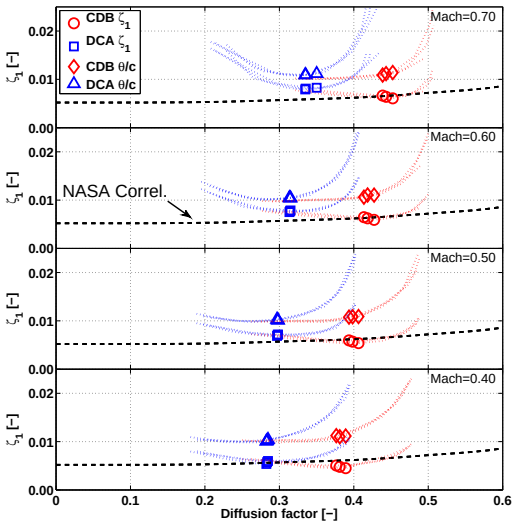

Figure 13: Loss parameter ζ_1 and wake momentum thickness to chord ratio versus diffusion factor with NASA correlations (dashed line) of Fig. 6 (b)

be noticed for the DCA, the calculated ζ_1 are in satisfactory agreement with the NASA correlation for both blades. Comparing both the correlation and the ζ_1 from the simulations with the computed wake momentum thickness to chord ratio, it appears that they are 0.5% too low. It indicates that ζ_1 may not be a good estimate of the wake momentum thickness and that some terms of Eq. 7 may not be negligible. Looking at Fig. 14, except at M_1=0.4, the use of ζ_2 to approximate θ/c appears satisfactory. Nonetheless, the CDB shows strong disagreement with the correlation. It points out that, for a state-of-the-art CDB, such correlation remains conservative but is not predicting correctly the performance of the profile. A possible explanation may be the presence of boundary layers at the end-walls that prevents to have theoretical two-dimensional flow conditions. For the DCA, the discrepancies with the correlation are acceptable but it would be more accurate to take into account some compressibility effect if accurate performance prediction are desired.

From a designer point of view, it must be pointed out that the quantity that must be predicted is the total pressure deficit ω and not the wake momentum thickness θ. In that sense, the correlation of ζ_1 appears very useful. Indeed, looking back at Fig. 13, it is a simple parameter that makes all the curves collapse on each other and that is not very sensitive to Mach number effects. At the level of the meridional design, it can provide a very good estimate of the total pressure losses

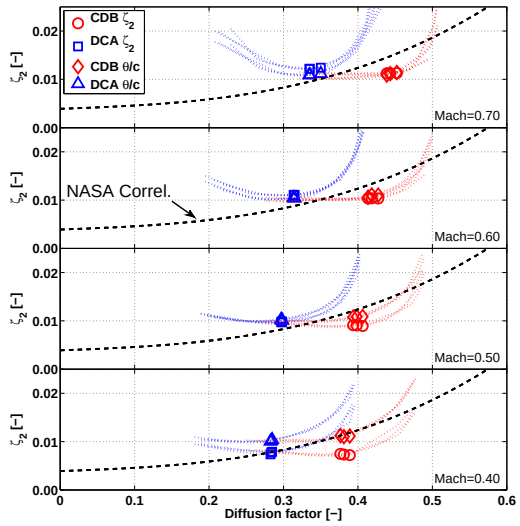

Figure 14: Loss parameter ζ_2 and wake momentum thickness to chord ratio versus diffusion factor with NASA correlations (dashed line) of Fig. 6 (a)

in function of the diffusion factor for various type of bladings and solidities.

3.4. Stall margin

The solidity plays an important role on the maximum loading that can be reached and the stall limit of the blade. The stall is a phenomenon widely commented and discussed in the literature and it is commonly agreed that CFD still fails at capturing the stall. Some examples can be found in [22] (Brouckaert et al., 2009) or [23] (Sans et al., 2013) from previous work at VKI. The works of Horlock et al. (2005, [24]) and Denton (2010, [25]) constitute excellent references that summarize the last advancements and the remaining hurdles of CFD for turbomachinery applications.

To analyze the impact of the solidity on the stability limit, it is firstly essential to define the last incidence. If the last converged incidence is considered, i.e. the numerical stability limit of the cascade, the analysis of the results would have been compromised by the appearance of strong secondary flow effects and corner stall. At such operating point, it is commonly accepted that the accuracy and the reliability of steady RANS computations are very questionable. Therefore, to remain consistent with the correlations, it has been decided to define the operating range like it is done in Fig. 3(b), i.e. by taking the difference Δi between the negative and positive incidence that both yield $2\omega_{min}$. As already mentioned, in the case of the

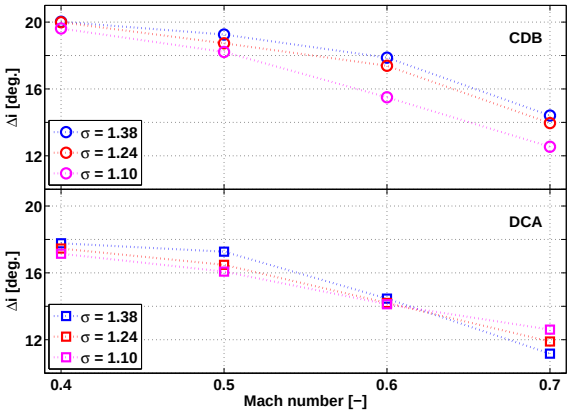

Figure 15: Operating range versus Mach number

CDB, the two lowest solidity cascades could not reach $2\omega_{min}$ above M_1=0.6. It is believed that the range of the profile at those specific points could be slightly extended by 1° or 2° without the presence of the endwalls. The operating range in function of Mach number is displayed in Fig. 15.

As already pointed out in Fig. 12 looking at the diffusion factors, the higher the Mach number the lower the working range. For the CDB, the incidence range also decreases when the solidity decreases. It confirms that, although some efficiency improvements can be achieved, the stability cannot be maintained if the solidity is reduced. A compromise must be found. In a real compressor configuration, another solution must be implemented in order to compensate the decrease of stability due to a blade count reduction. For rotors, a solution is for instance presented by Houghton et al. (2010, [26]) where casing treatment helps to delay the inception of stall caused by a solidity decrease. It must also be pointed out that for all solidities and Mach numbers, the optimized profile has a greater range than the DCA. Regarding the latter, it can be observed that, until M_1=0.6, increasing the solidity helps to improve the operating range. At M_1=0.7, the trend reverses and the low solidity DCA experiences the highest incidence range. This may be due to the appearance of supersonic pockets and shocks that induce a steeper and faster rise of losses. The $2\omega_{min}$ limit is then reached faster than expected. Some previous works of Schwenk et al. (1955, [27]) or Heilmann et al. (1968, [28]) done at high subsonic and low supersonic Mach numbers confirm that such an unexpected result should not be discarded. More specifically, Schwenk et al. observed that the solidity effects on three DCA compressor rotors were reversed

compared to the subsonic solidity trend as the rotational speed was increased to its design value. They concluded that, at high inlet relative Mach numbers, the stall margin was slightly extended and the losses increased when the number of blades was decreased.

4. Optimum solidity

The solidity is chosen at the stage of the meridional design. It consists of solving the NISRE equations iteratively until the desired pressure ratio or efficiency is met. The designer requires an estimation of the losses that comes from experimental correlations as provided in Fig. 6. Knowing the blade metal angles along the span, a three-dimensional blade can be drawn. This first guess can finally be opti through 3D RANS computation. During the opt tion process, the solidity does not change any In order to find an optimum solidity, the focus be set on the meridional design.
In industry, some axial compressor design enable off-design predictions at the level c meridional calculation. Such programs all specify a stall margin as a design target. F present work, a multi-stage axial compressor program (referred as *ACD* in the rest of the from Creveling et al. (1968, [29, 30]) has implemented at VKI and has bee VKI CADO algorithm to find the in terms of efficiency. In the curr program does not provide off-desigr

4.1. Input definitions

The R4 compressor stage studied pean DREAM project is used as tes vestigation. It is a 1.5 low-pressure involving three rows: IGV, rotor and nel geometry is imposed and divide axial stations where the radial equi will be solved (Fig. 16). The mass f pressure and temperature and the ro been set accordingly to the origina the stage. The following additional quired:

- a normalized rotor pressure ratio distribution;
- stator outlet tangential velocity distribution;
- rotor solidity distribution;
- stator solidity distribution.

Both rotor inlet and stator outlet tangential velocity profiles have been imposed following the original design specifications. The desired normalized rotor pressure ratio distribution is given in Fig. 17. The design mass-averaged rotor pressure ratio has been set to 1.25. During the optimization process, only the rotor solidity distribution has been optimized. Since the pressure ratio is fixed and that only the efficiency must be maximized, the designer is facing a single objective optimization problem. The stator solidity of the R4 stage is given and kept constant while the rotor solidity must be optimized in order to maximize the rotor efficiency. Despite the whole stage is calculated, only the rotor performance are considered.

Finally, the maximum spanwise diffusion factor

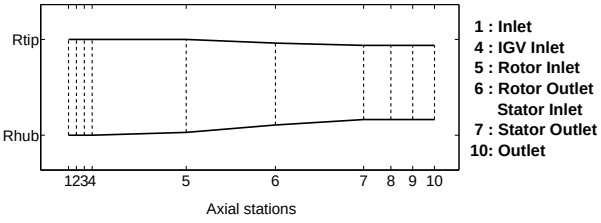

Figure 16: Channel and axial station repartition

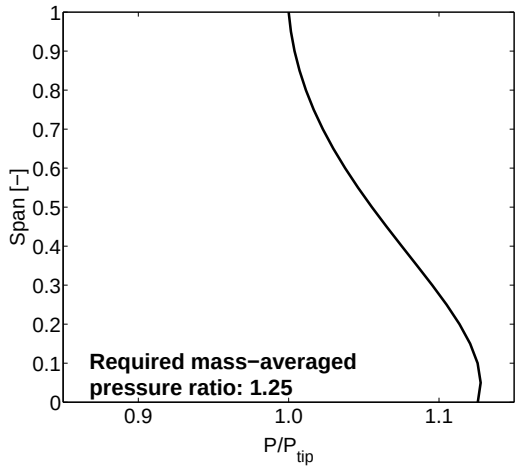

Figure 17: Normalized pressure ratio distribution to achieve a mass-averaged pressure ratio of 1.25.

4.2. Method and constraints

The VKI optimization code (CADO) is based on an evolutionary algorithm and is extensively explained

by Pierret (1999, [31]) or Verstraete (2008, [32]). Firstly, random solidity distributions are generated. This constitutes the first generation of individuals. For each solidity distribution, ACD gets the loading distribution yielding the desired pressure ratio. Only the individuals that have a diffusion factor below D_{max} are kept and considered as successful. All the others are discarded. The successful cases give birth to a new generation according to the evolutionary algorithm and produce new candidates providing better efficiency. For a given D_{max}, convergence was reached on one single solidity profile after 50 generations of 200 individuals.

4.3. Results

Optimization studies have then been performed with D_{max} of 0.38, 0.40, 0.42, 0.45 and 0.50. The optimum solidity distributions are given in Fig. 18. Firstly, it can be observed that when higher diffu-

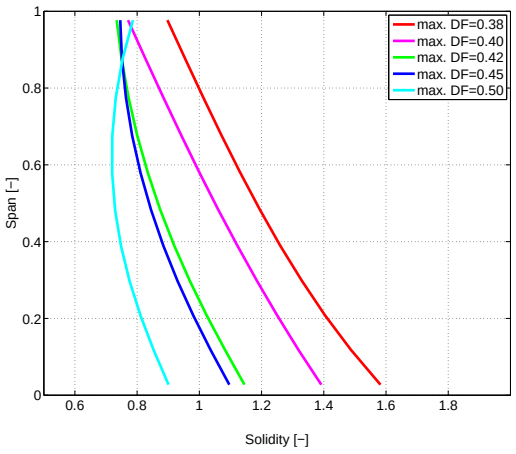

Figure 18: Optimum solidity distributions for various maximum diffusion factors

sion factors are allowed, the mean solidity level decreases. It is interesting to see that when $D_{max} \leq 0.42$, the optimum solidity profiles are quite linear. For $D_{max} > 0.42$, they are bended and the tip solidity remains between 0.7 and 0.8. It underlines that, around the tip sections, an optimum solidity may exist.

To understand better this behaviour, the diffusion factor spanwise distributions have been plotted in Fig. 19. When D_{max} is equal to 0.38, 0.40 or 0.42, the diffusion factor is uniform along the span and equals to the maximum allowed. Considering a D_{max} of 0.45 or 0.50, the diffusion factor reaches a maximum at 20% and decreases towards the tip to sit between 0.40 and

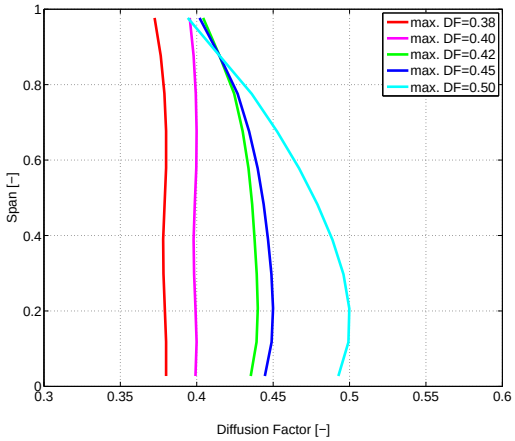

Figure 19: Diffusion factor distributions of the optimum solidity candidates

0.42. It confirms that an optimum solidity (and diffusion factor) may exist around the tip sections. This optimum solidity may not be reached if the constraint on the diffusion factor is too strong.

Looking at the rotor efficiencies in Fig. 20, it can be seen that from the hub to 70% of the blade height, the lower the solidity, the higher the efficiency. For the last 30%, the trend is less obvious and the most efficient solidity appears to be reached when $D_{max} = 0.42$.

To fully understand these results, one should look

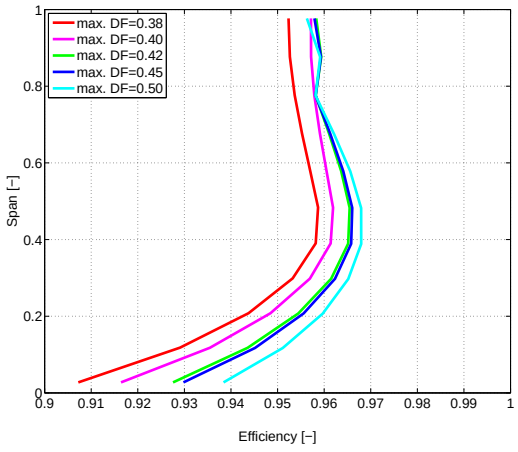

Figure 20: Efficiency distributions of the optimum solidity candidates

at the loss correlations used in ACD (directly coming from [2]). They vary along the span and have been plotted in Fig. 21. One can now understand that the resulting solidity distributions depend on both

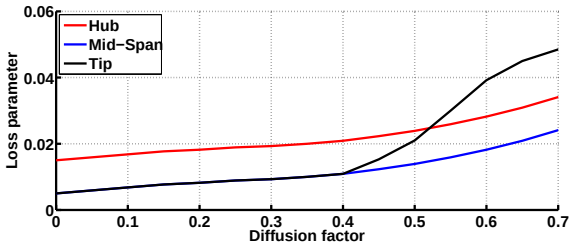

Figure 21: Loss correlations used in ACD

the maximum diffusion factor and the loss variation along the span. As displayed in Fig. 21, for a rotor, hub losses are greater than mid span losses but the profile is only translated from the mid-span curve to higher losses. Its dependence with respect to the diffusion factor is similar. It means that, for a given pressure ratio, the mid-span optimum solidity would be the same as the hub optimum solidity. However, for the same optimum solidity, the efficiency at the hub will be lower than at mid-span as the loss level is different. Tip losses start at the same level as the mid-span curve but when the diffusion factor reaches 0.40, the slope rises. It represents the loss increase observed in axial compressor due to the influence of the tip leakage vortex at high loading.

Such a loss evolution along the span explains the reason why the optimum solidity profiles yield to uniform loading distributions when $D_{max} \leq 0.40$. For higher D_{max}, the optimum solidity tries to keep the loading as close as possible to 0.40 in the tip region but allows higher loading at the hub sections.

5. Conclusion

The solidity effect has been reviewed in the literature to highlight its influence on the blade performance. A numerical investigation has been performed on two linear compressor cascade involving a state-of-the-art CDB profile and a standard DCA blade.

Both CDB and DCA performance at optimum incidence have been compared to existing correlations. The optimum incidence is increasing with solidity. The predictions of NASA gave higher optimum incidences. The famous Carter rule offered really good deviation prediction for the DCA. Regarding the CDB, it appears that the form of the NASA deviation rule is still valid but with empirical coefficients adapted for the CDB. Compressibility effects have been depicted but they are very limited. It demonstrates that, although they rely on low-speed data, the correlations can still be trusted as long as the critical Mach number is not reached. It has been highlighted that the minimum loss diffusion factor does not depend on the solidity. It reveals that the whole compressor design could be based on the choice of an optimum diffusion factor independent of the optimum incidence and the solidity. Regarding the total pressure losses, they can be predicted using Lieblein's simple ζ_1 loss parameter. However, coming back to the original work of Lieblein, the definition of the loss parameters as an approximation of the wake momentum thickness are only valid considering ζ_2. Analyzing the results from M_1=0.4 to M_1=0.7, compressibility effects have also been highlighted but they appeared very limited.

To optimize the solidity at the level of the meridional design, the software ACD, recently implemented at VKI and the CADO algorithm have been used to get optimum rotor solidity profiles for a given low-pressure compressor geometry. It has been observed that, for a given pressure ratio distribution, the optimum depends on the maximum diffusion factor allowed. Results have been compared in terms of efficiency and loading spanwise distributions. The analysis revealed the importance of the loss correlations in the determination of the optimum solidity.

In that prospect, the presented numerical investigation as well as the ongoing experimental campaign in the VKI C3 high-speed cascade facility will allow to update the correlations of ACD. Corrections for compressible flows as well as off-designs predictions may be added to ACD in order to provide optimum solidity not only in terms of efficiency but also with respect to the stall limit of the compressor.

Acknowledgments

The authors would like to thank Techspace Aero for supporting this research.

References

[1] Obrecht, T., HP compressor preliminary design, in: Advances in axial compressor aerodynamics, von Karman Institute for Fluid Dynamics Lecture Series, Rhode-Saint-Genese, Belgium, 2013, vKI-LS 2013-03.

[2] Lieblein, S., Aerodynamic design of axial-flow compressors - Chapter VI: Experimental Flow in Two-Dimensional Cascades, NASA SP-36 (1965).

[3] Carter, A. D. S., The Low-Speed Performance of Related Aerofoils in Cascades, A.R.C. Tech. Report, NGTE, report No.R.55 (1949).

[4] AGARD, Loss Mechanisms and Unsteady Flows in Turbomachines, AGARD CP-571 (1995).

[5] Jansen, W. and Moffat, W. C., The Off-Design Analysis of Axial-Flow Compressors, Journal of Engineering for Power 89 (4) (1967) 453–462.

[6] Lieblein, S., Schwenk, F. C., and Broderick, R. L., Diffusion Factor for Estimating Losses and Limiting Blade Loadings in Axial-Flow Compressor Blade Elements, NACA Research Memorandum, Lewis Flight Propulsion Laboratory, Cleveland, Ohio, rME53D01 (1953).

[7] Lieblein, S., Theoretical Loss Relations for Low-Speed Two-Dimensional Cascade Flow, NACA Research Memorandum, Lewis Flight Propulsion Laboratory, Cleveland, Ohio, tN 3662 (1956).

[8] Lieblein, S., Analysis of Experimental Low-Speed Loss and Stall Characteristics of Two-Dimensional Compressor Blade Cascades, NACA Research Memorandum, Lewis Flight Propulsion Laboratory, Cleveland, Ohio, rME57A28 (1957).

[9] Hearsey, R. M., Practical Compressor Aerodynamic Design, in: Advanced Topics in Turbomachinery Technology, Concept ETI Principal Lecture Series, Norwich, Vermont, USA, 1986.

[10] Roberts, W. B., Serovy, G. K., and Sandercock, D. M., Design Point Variation of Three-Dimensional Loss and Deviation for Axial Compressor Middle Stages, Journal of Turbomachinery 110 (4) (1988) 426–433.

[11] Casey, M. V., A Mean Line Prediction Method for Estimating The Performance Characteristic of An Axial Compressor Stage, in: Turbomachinery: Efficiency Prediction and Improvement, Proceedings of Institution of Mechanical Engineering, 1987, pp. 273–281, c264/87.

[12] Wright, P. I. and Miller, D. C., An Improved Compressor Performance Prediction Model, in: Turbomachinery: Latest Developments in a Changing Scene, Proceedings of Institution of Mechanical Engineering, 1991, pp. 69–75, c423/028.

[13] Howell, A. R., Fluid dynamics of axial compressors, in: Proceedings of Institution of Mechanical Engineering, Vol. 153, 1945, pp. 441–452.

[14] Zweifel, O., The Spacing of Turbo-Machine Blading, Especially With Large Angular Deflection, The Brown Boveri Review 32 (1945) 436–444.

[15] McKenzie, A. B., The Selection of Fan Blade Geometry for Optimum Efficiency, Proceedings of Institution of Mechanical Engineers, Part A: Journal of Power and Energy 202 (1988) 39–44.

[16] Liu, G. L., Simple Formulae for Optimal Solidity of Two-Dimensional Compressor Cascades Based on Diffusion Concept, International Journal of Turbo and Jet Engines 10 (1993) 127–134.

[17] Massardo, A., Satta, A., and Marini, M., Axial Flow Compressor Design Optimization: Part II - Throughflow Analysis, Journal of Turbomachinery 112 (1990) 405–410.

[18] Joly, M., Verstraete, T., and Paniagua, G., Full Design of Highly Loaded Fan by Multi-Objective Optimization of Throughflow and High-Fidelity Aero-Mechanical Performance, in: Proceedings of ASME Turbo Expo 2012, Copenhagen, Denmark, 2012, aSME Paper No. GT2012-69686.

[19] Teichel, S., Verstraete, T., and Seume, J., Optimized Preliminary Design of Compact Axial Compressors A Comparison of Two Design Tools, in: 31st AIAA Applied Aerodynamics Conference, San Diego, California, USA, 2013, aIAA-2013-2651.

[20] Resmini, M., Numerical Investigation of the Solidity Effect on a Linear Compressor Cascade Performance and Stability, Master's thesis, Politecnico de Milano - von Karman Institute for Fluid Dynamics (2013).

[21] Sans, J., Resmini, M., Brouckaert, J. F., and Hiernaux, S., The Impact of Turbulence Model and Numerical Scheme on The Performance of a Linear Compressor Cascade, in: Proceedings of ASME Turbo Expo 2014, Dusseldorf, Germany, 2014, aSME Paper No. GT2014-25531.

[22] Brouckaert, J.-F., de Wyer, N. V., Desset, J., Farkas, B., Perez, J. G., Capart, R., Thomas, J.-F., Isaac, N., and Hiernaux, S., Experimental and Numerical Investigation of a Single Stage low Pressure Compressor for Counter-Rotating Turbofan Engine Architechtures, in: The XVIIIth European Turbomachinery Conference, Austria, 2009.

[23] Sans, J., Desset, J., Dell'Era, G., and Brouckaert, J.-F., Performance Testing of a Low-Pressure Compressor, in: The Xth European Turbomachinery Conference, Finland, 2013.

[24] Horlock, J. H. and Denton, J. D., A Review of Some Early Design Practice Using Computational Fluid Dynamics and a Current Perspective, Journal of Turbomachinery 127 (1) (2005) 5–13.

[25] Denton, J., Some Limitations of Turbomachinery CFD, in: Proceedings of ASME Turbo Expo 2010, Glasgow, United-Kingdom, 2010, aSME Paper No. GT2010-22540.

[26] Houghton, T. and Day, I., Stability Enhancement by Casing Grooves: The Importance of Stall Inception and Solidity, in: Proceedings of ASME Turbo Expo 2010, Glasgow, United Kingdom, 2010, aSME Paper No. GT2010-22284.

[27] Schwenk, F. C. and Lewis, G. W. J., Experimental investigation of a transonic axial-flow compressor rotor with double-circular arc airfoil blade sections: III - comparison of blade element performance with three levels of solidity, NACA Research Memorandum, Lewis Fligh Propulsion, Cleveland, Ohio, rME55F01 (1955).

[28] Heilmann, W., Starken, H., and Meyer, H., Cascade wind tunnel tests on blades designed for transonic and supersonic compressors, Tech. rep., Institut fuer Luftstrahlantriebe, aGARD-CP-34 (1968).

[29] Creveling, H. F. and Carmody, R. H., Axial Flow Compressor Design Computer Programs Incorporating Full Radial Equilibrium - Part I : Flow Path and Radial Equilibrium of Energy Specified, Tech. rep., NASA, nASA CR-54532 (June 1968).

[30] Creveling, H. F. and Carmody, R. H., Axial Flow Compressor Design Computer Programs Incorporating Full Radial Equilibrium - Part II : Radial Distribution of Total Pressure and Flow Path or Axial Velocity Ratio Specified, Tech. rep., NASA, nASA CR-54531 (June 1968).

[31] Pierret, S., Designing Turbomachinery Blades by Means of the Function Approximation Concept Based On Artificial Neural Network, Genetic Algorithm and Navier-Stokes Equations, PhD Thesis, von Karman Institute for Fluid Dynamics - Faculté Polytechnique de Mons, Rhodes-Saint-Genese, Belgium (1999).

[32] Verstraete, T., Multidisciplinary Turbomachinery Component Optimization Considering Performance, Stress and Internal Heat Transfer, PhD Thesis, von Karman Institute for Fluid Dynamics - Universiteit Gent, Rhodes-Saint-Genese, Belgium (2008).

Large Eddy Simulation and Conjugate Heat Transfer in a Rib-Roughened Cooling Channel

Sebastian Scholl

Turbomachinery and Propulsion Department, von Karman Institute for Fluid Dynamics, Belgium, sebastian.scholl@vki.ac.be

Supervisor: Tom Verstraete

Assistant Professor, Turbomachinery and Propulsion Department, von Karman Institute for Fluid Dynamics, Belgium, tom.verstraete@vki.ac.be.

Promotor: Wolfgang Schröder

Professor, RWTH Aachen, Aerodynamisches Institut , office@aia.rwth.de.

Abstract

The following contribution focuses on the conjugate heat transfer computation of a rib-roughened internal turbine blade cooling channel via the coupling of two numerical in-house tools: an LES flow solver (AVBP) and a solid conduction solver (AVTP) developed by CERFACS. While interested in the thermal steady states of such problems, both solvers provide time dependent de-synchronized solutions. Different coupling strategies for Conjugate Heat Transfer are investigated: A loose coupling strategy first computes the fluid domain until it reaches a statistically steady state from which the mean temporal solution is obtained. Then, it solves the solid domain with the mean boundary conditions imposed from the fluid leading to an updated fluid boundary condition. This process is repeated until convergence of the coupled problem. A tight coupling strategy runs the fluid and solid solvers in parallel with in-memory exchange of boundary conditions. An acceleration procedure, detailed by Duchaine et al. (2009), is used to ensure the convergence of the coupled system toward the steady thermal state. We validated the results against experimental data provided by the von Karman Institute.

Keywords: Conjugate Heat Transfer, Coupling, Turbine Blade, Cooling Channel, Large Eddy Simulation

Nomenclature

Latin

c_s	solid heat capacity	$[JK^{-1}]$
D_h	Hydraulic diameter	$[m]$
c_p	fluid heat capacity	$[JK^{-1}]$
Bi	Biot number	
c	speed of sound	$[ms^{-1}]$
EF	enhancement factor	
F	flux tensor	
h	heat transfer coefficient	$[Wm^{-2}K]$
L	characterisitc length scale	$[m]$
Nu	Nusselt number	
P	pitch length in the ribbed channel	$[m]$
p	pressure	$[Nm^{-2}]$
Pr	Prandtl number	
q	heat flux	$[Wm^{-2}]$
Re	Reynolds number	
T	temperature	$[K]$
t	time	$[s]$
u,v,w	velocity components	$[ms^{-1}]$
x,y,z	Cartesian coordinates	$[m]$
y+	non-dimensional wall distance	

Greek

β	relaxation coefficient	
μ	dynamic viscosity	$[Pa^1 s^1]$
ν	kinematic viscosity	$[m^2 s^{-1}]$
ρ	density	$[kg^1 m^{-3}]$

Abbreviations

CFL	Courant-Friedrich-Levy number
LES	large eddy simulation
SGS	Sub-grid Scale

Super- and Subscripts

∞	free stream quantity
f	fluid domain
s	solid domain

1. Introduction

Trying to comply with the claims for environmental awareness and the rising use of energy, the turbomachinery industry is bound to improve the gas turbine efficiency in several regions, one of which consists in increasing the turbine inlet temperature. Since the life of a turbine blade is reduced by half with an increased temperature of 30 Kelvin [1], the prediction of local heat transfer coefficients and temperatures is a crucial step towards the design of turbine blades.

Current numerical methods lack the needed predictive capacity and call for new numerical strategies. Two reasons explain the current status: First, Reynolds averaged Navier-Stokes simulations fail to predict complex flow fields and can lead to wrong thermal predictions. Second, conjugate effects need to be taken into account for reliable thermal predictions, but are often neglected. Conjugate heat transfer describes the interaction between fluid and solid domain. If the temperature distributoin would be known at the interface a priori, the problem would reduce to a convetcive problem, but the temperature distribution (and the heat flux distribution) is unknown a priori and is part of the coupled solution of the fluid and solid energy equations, which is the conjugate heat transfer problem [2]. The coupling of fluid and solid solvers is a demanding task, stability problems can occur and the time scales in the fluid and solid domain vary by orders of magnitude.

Large Eddy Simulations (LES) improve the turbulent flow field and heat transfer predictions, but are expensive. Due to those challenges, only few computations of conjugate heat transfer (CHT) with LES have been done and research is still needed for an efficient LES based CHT Strategy.

The paper describes the used solvers, different approaches for the conjugate heat transfer problem, an investigation on the stability of the loose coupling strategy and finally results of the cooling channel flow simulation (adiabatic, convective and conjugate computations) showing the need for further investigations.

2. Coupling Procedures

Conjugate heat transfer methods for numerical simulations can be categorized by the interface: the two main approaches to solve conjugate heat transfer problems are the monolithic approach (often also referred to as the conjugate method or strong coupling) uses one solver for both domains. The partitioned approach (often also referred to as the coupled method or weak coupling) uses different solvers for each domain.

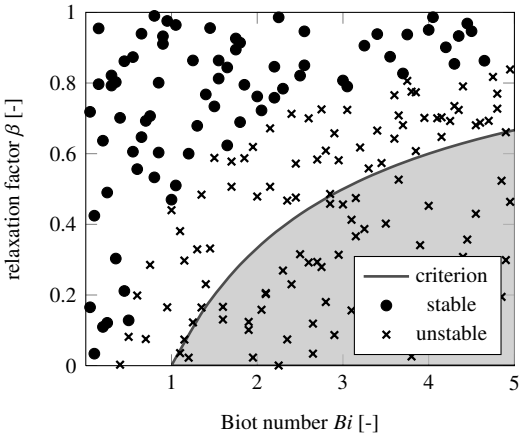

Figure 1: Stability diagram for the FFTB coupling method. Grey area indicates zone for which the stability criterion predicts the simulation to become unstable.

Further, the exchange method can be explicit (e.g. a Gauss-Seidel or a Jacobi scheme) or implicit. Last, the kind of exchanged boundary condition is important for convergence and stability. In this respect four different coupling procedures can be distinguished as described by Verstraete [3] [4]. Crucial for weak coupling procedures is the stability of the coupled computation. [3] showed that the stability depends on the Biot number:

$$Bi = \frac{hL}{\lambda_s}. \tag{1}$$

The physical meaning of this dimensionless number can be interpreted as the ratio of conductive resistance in the solid L/λ_s, with the solid conduction coefficient λ_s and the convective resistance in the fluid boundary layer 1/h with the heat transfer coefficient h.

The flux forward temperature back method (often referred to as the FFTB method, named from the perspective of the fluid domain) imposes a wall temperature distribution to the fluid solver. After the fluid calculation the resulting heat flux distribution is imposed to the

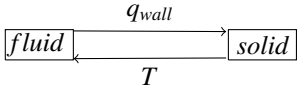

Figure 2: FFTB coupling.

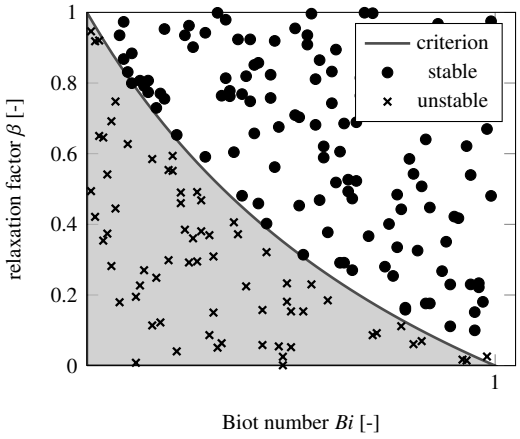

Figure 4: Stability diagram for the TFFB coupling. Grey area indicates zone for which the stability criterion predicts the simulation to become unstable.

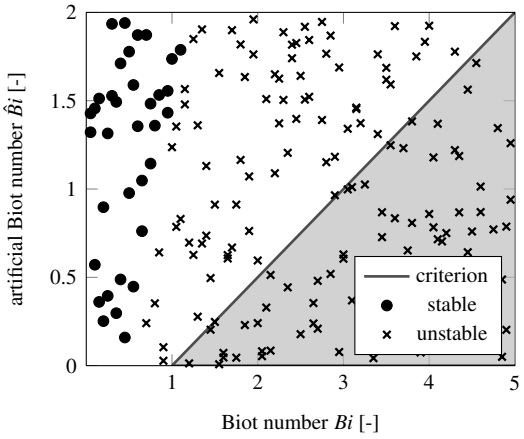

Figure 6: Stability diagram for the hFTB coupling. Grey area indicates zone for which the stability criterion predicts the simulation to become unstable. The artificial Biot number is defined as $\hat{Bi} = \frac{\hat{h}L}{\lambda}$, with the imposed heat transfer coefficient $\hat{h}$.

solid conduction solver, which returns an updated temperature in turn imposed to the fluid domain. The exchange of boundary conditions is repeated until continuous temperatures and heat fluxes between both domains are reached. The FFTB procedure is stable for $Bi < 1$. With a relaxation factor β simulations for $Bi > 1$ can be stabelized with the drawback of slower convergence. The relaxation is used for the exchange of the boundary conditions as follows [3]:

$$T_{wall}^{fluid,i} = \beta_T \cdot T_{wall}^{fluid,i-1} + (1-\beta_T) \cdot T_{wall}^{solid,i-1}, \quad (2)$$

and:

$$q_{wall}^{solid,i} = \beta_q \cdot q_{wall}^{solid,i-1} + (1-\beta_q) \cdot q_{wall}^{fluid,i-1}, \quad (3)$$

with the current iteration step i fluxes q and temperature T. The stability criterion is then: $Bi < \frac{1+r}{1-r}$.

The temperature forward flux back method (often referred to as the TFFB method, named from the perspective of the fluid domain) imposes a heat flux distribution as boundary condition to the fluid solver. The resulting temperature is imposed to the solid solver, which returns a new heat flux distribution to the fluid domain. The TFFB method is stable if $Bi > 1$. With a relaxation factor r simulations for $Bi < 1$ are possible; again, with the drawback of slower convergence. The stability criterion is then: $Bi > \frac{1-r}{1+r}$.

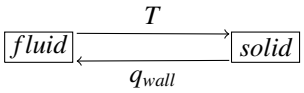

Figure 3: TFFB coupling.

The heat transfer coefficient forward flux back method (referred to as the hFTB method, named from the perspective of the fluid domain) starts with an initial temperature distribution as boundary condition for the fluid computation. It uses Newton's law of convective heat transfer to return a Robin (mixed type) boundary condition to the solid domain:

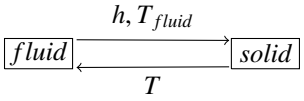

Figure 5: hFTB coupling.

$$q_{wall} = h \cdot (T_{wall} - T_{fluid}), \quad (4)$$

with the heat transfer coefficient h the heat flux q_{wall}, the temperature at the wall T_{wall} and the ambient fluid temperature T_{fluid}. T_{wall} and q_{wall} are passed to the solid solver as Robin condition. Note that h and T_{fluid} have to be computed for this method. This is done with the algorithm proposed in [3] that sets a fixed positive heat transfer coefficient.

The advantage of this method is that after the one-dimensional stability criterion, it is stable for $Bi < 1$, but also for $Bi >= 1$, if an appropriate heat transfer coefficient for the method is used: $\hat{h} < 2h$, with the imposed heat transfer

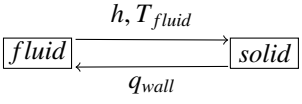

Figure 7: hFFB coupling.

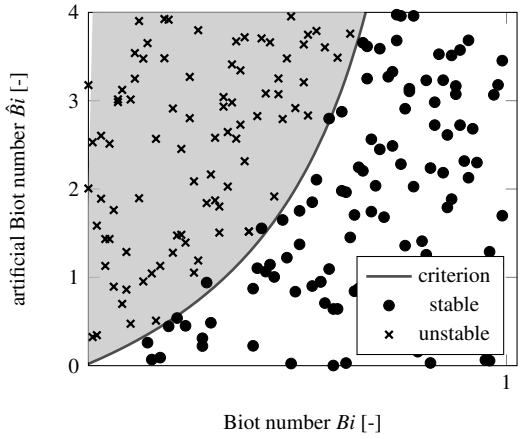

Figure 8: Stability diagram for the hFFB coupling. Grey area indicates zone for which the stability criterion predicts the simulation to become unstable. The artificial Biot number is defined as $\hat{Bi} = \frac{\hat{h}L}{\lambda}$, with the imposed heat transfer coefficient $\hat{h}$.

coefficient $\hat{h}$ and the actual heat transfer coefficient h. Verstraete [3] proposed a fourth method (referred to as the hFFB method, named from the perspective of the fluid domain), which imposes a heat flux distribution to the fluid domain returning mixed type boundary conditions to the solid solver. Again, for the mixed type boundary condition, Newton's law of convective heat transfer is used:

$$q_{wall} = h \cdot (T_{wall} - T_{fluid}). \tag{5}$$

This method is stable for $Bi > 1$ and also for $Bi <= 1$, if an appropriate heat transfer coefficient is used: $\hat{h} > \frac{h}{2}$, with the imposed heat transfer coefficient $\hat{h}$ and the actual heat transfer coefficient h.

Figures 1, 4, 6, 8 show the results of numerical experiments of flow over a solid flat plate with heat conduction. These experiments confirm the stability criteria by [3] especially for the flux backward methods for which the numerical experiments show a perfect match. For the temperature back methods the criteria are fair, but too optimistic.

3. Numerical Method

The applied method for the conjugate heat transfer in the cooling channel couple a parallel LES solver for the fluid domain with a parallel conduction solver for the solid domain.

3.1. Fluid solver

The fluid domain is computed by the CERFACS in-house solver AVBP. Applying Favre filtering to the compressible Navier-Stokes equations (see [5] or [6]), leeds to the following LES equations:

$$\frac{\partial \bar{w}}{\partial t} + \nabla \cdot \bar{F} = 0, \tag{6}$$

with the conservative variables $\bar{w} = (\bar{\rho}, \bar{\rho}\tilde{u}, \bar{\rho}\tilde{v}, \bar{\rho}\tilde{w}, \bar{\rho}\tilde{E})$ the flux tensor $\bar{F}$, the density $\bar{\rho}$, the velocity components $(\tilde{u}, \tilde{v}, \tilde{w})$, and the total Energy $\tilde{E}$. The conductive heat flux is included in the flux tensor and given by Fourier's law of conduction:

$$\bar{q}_i = -\bar{\lambda}\frac{\partial \tilde{T}}{\partial x_i}, \tag{7}$$

with the thermal conductivity

$$\bar{\lambda} = \frac{\bar{\mu} c_p(\bar{T})}{Pr}, \tag{8}$$

where c_p is the heat capacity, Pr the Prandtl number and $\bar{\mu}$ the dynamic viscosity.

The appearing unknowns in the LES equations, the subgrid-scale (SGS) quantities, need to be modeled. The subgrid-scale turbulent viscosity ν_t has been modeled via the Wall Adapting Linear Eddy (WALE) model [7].
The equations are discretized by centered spatial schemes and explicit time schemes. Two different spatial schemes have been used: The second order finite volume Lax Wendroff (LW) scheme and a Finite-Element based Taylor-Galerkin (TTGC) low-dissipation scheme in a cell-vertex formulation. This explicit scheme is of third order accuracy in space and time. The time step is controled via the Courant-Friedrich-Lewy(CFL) condition for compressible flows:

$$CFL = \frac{(U + c)\Delta t}{\Delta x} \simeq 0.7, \tag{9}$$

with the grid cell size Δx and the minimal Δt in the whole domain. U and c are the local flow and sound velocities. Navier-Stokes characteristic boundary conditions are applied at the inlet and the outlet.

3.2. Solid solver

The conduction solver AVTP uses a Galerkin diffusion scheme, second order accurate with an explicit time advancement to solve the energy conservation:

$$\rho_s c_s \frac{\partial T(\mathbf{x}, t)}{\partial t} = -\frac{\partial q_i}{\partial x_i}, \tag{10}$$

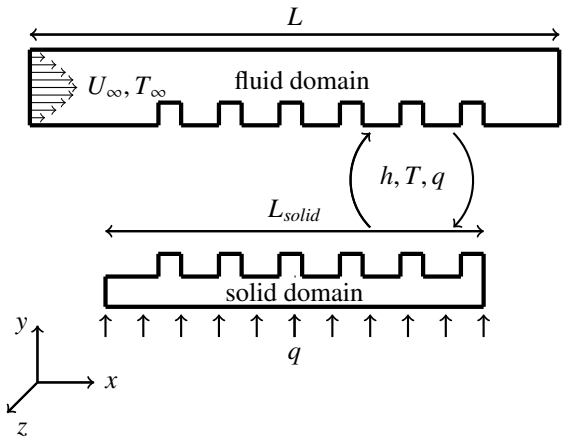

Figure 9: Sketch of the channel geometry.

with the temperature in the solid T, the solid density ρ_s, the heat capacity c_s and the heat flux q, given by Fourier's law of conduction:

$$q_i = -\lambda_s \frac{\partial T}{\partial x_i}. \tag{11}$$

4. Configuration and flow conditions

The applied configuration modeles the experimental facility of Cukurel, see [8] and [9], which was a simplified model of an internal rib-roughened turbine blade cooling channel. It was scaled up by a factor of 15 with respect ot real engine conditions, keeping the Reynolds number constant.
Figure 9 and tables 1, 2 and 3 show more details of the channel dimensions. The experimental facility consisted of three sectios: an inlet, a test and an outlet section from which the test section with its six ribs is fully represented by the configuration for the numerical simulations. The other two sections are represented in parts. The cross section dimensions are 75x75mm and the test section length is 1260mm. Since a compressible solver is used for the computations, the geometry was scaled down by a factor of 10 to increase the Mach number and reach faster convergence of the simulations.

5. Results

5.1. Adiabatic LES

Adiabatic computations were used for an evaluation of the created meshes and the used numerical model for the fluid domain. The results with respect to the aerodynamics were compared with the experimental data (iso-thermal) of Casarsa [10] [11], which are in good agreement as figures 15, 13, 16, 14 and 17 show. The secondary flow structures and the turbulence intensity are well represented by the computation.

Parameter	abbr.	Value
length	L	1597.5 mm
height, depth	H, d	75 mm
hydraulic diameter	D_h	75 mm
rib hight	h	22.5 mm
pitch	p/h	10
blockage ratio	h/D_h	0.3

Table 1: Channel characteristics.

Parameter	abbr.	Value
length	L_{solid}	1250 mm
height, depth	H_{solid}, d_{solid}	75 mm
thickness	t_{solid}	22.5 mm
material	AISI 304 Steel 1260	
conductivity	k	$16.2 \frac{W}{m^2}$

Table 2: Ribbed slab characteristics.

Parameter	abbr.	Value
flux under slab	q	$1167 W/m^2$
interface flux	q_w	$1153.8 W/m^2$
inflow temperature	T_∞	295.3K
Reynolds number	Re_{D_h}	40000
average heat transfer coeff.	$\overline{h}$	$36.5 W/m^2$

Table 3: Flow characteristics and boundary conditions.

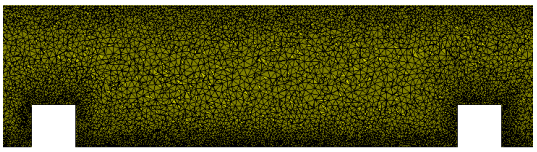

Figure 10: Mesh around two ribs in the fluid domain.

	M1	M2	M3
cells	3.53M	8M	10M
nodes	0.69M	1.5M	2M
prisms	no	yes	yes
mean y+	18.72	8	4.1
x+,z+	~ 1	~ 5	~ 5

Table 4: Used meshes. y+ is defined using the wall-normal distance y, the friction velocity u_τ the the wall shear stress τ_w as: $y+ = \frac{u_\tau y}{\nu}$. x+ and z+ are defined with the streamwise and spanwise mesh resolution.

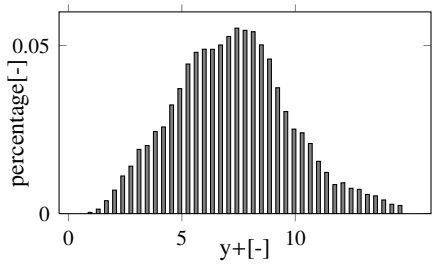

(a) M2

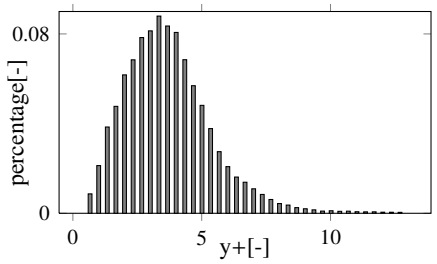

(b) M3

Figure 11: y+ value distribution around the ribs of the meshes. y+ is defined using the wall-normal distance y, the friction velocity u_τ the the wall shear stress τ_w as: $y+ = \frac{u_\tau y}{\nu}$.

5.2. *Convective LES*

For the convective computations, isothermal boundary conditions were applied around the ribs. The enhancement factor quantifies the increase of heat transfer in comparison with a correlation valid for flow in a smooth pipe at the same Reynolds number. It is defined as:

$$EF = \frac{Nu}{Nu_0}. \tag{12}$$

The Nussels number is defined as:

$$Nu = \frac{h \cdot D_h}{k_f}, \tag{13}$$

with the heat transfer coefficient h, the hydraulic diameter D_h and the fluid conductivity k_f . The Dittus-

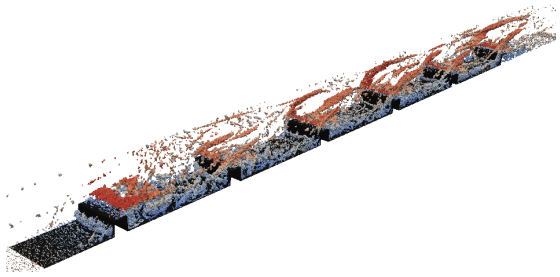

Figure 12: Secondary flow structures visualized via Q-criterion[12].

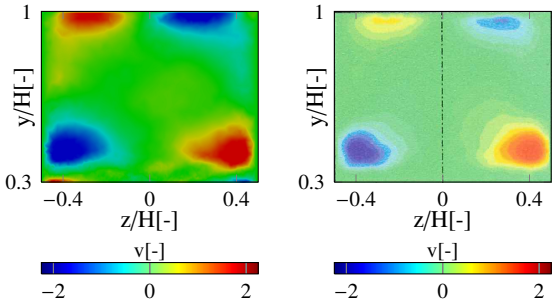

(a) LES (b) PIV measurement

Figure 13: Time averaged spanwise velocity component contour plot on top of the rib. Velocity component is non-dimensionalized with the maximal value for the respective velocity. The simulated channel (to increase the Mach number for the compressible solver AVBP) was scaled by a factor of 10 with respect to the experiments.

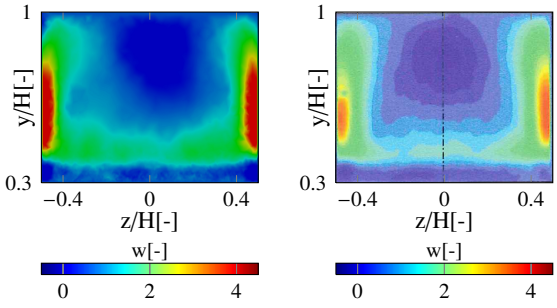

(a) LES (b) PIV measurement

Figure 14: Time averaged vertical velocity component contour plot on top of the rib. Velocity component is non-dimensionalized with the maximal value for the respective velocity. The simulated channel (to increase the Mach number for the compressible solver AVBP) was scaled by a factor of 10 with respect to the experiments

Boelter correlation gives the denominator for the enhancement factor and is defined as:

$$Nu_0 = 0.023 Re_{D_h}^{4/5} Pr^{0.4}. \tag{14}$$

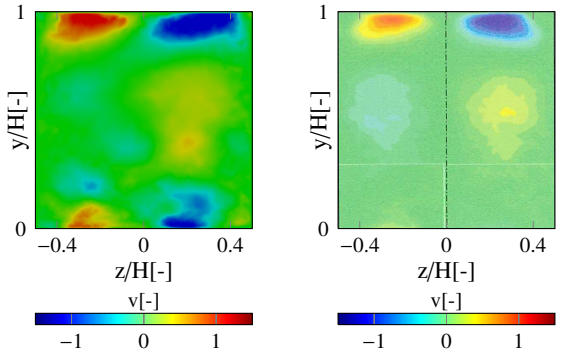

(a) LES (b) PIV measurement

Figure 15: Time averaged spanwise velocity component contour plot on the pitch. Velocity component is non-dimensionalized with the maximal value for the respective velocity. The simulated channel (to increase the Mach number for the compressible solver AVBP) was scaled by a factor of 10 with respect to the experiments

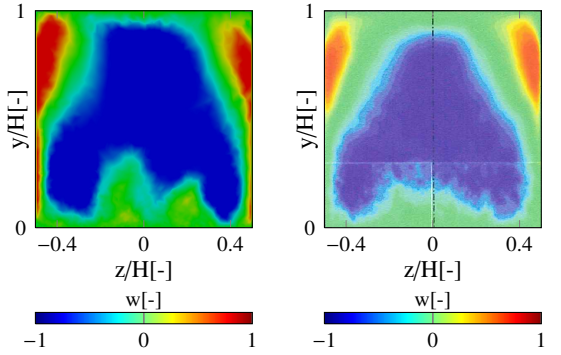

(a) LES (b) PIV measurement

Figure 16: Time averaged vertical velocity component contour plot on the pitch. Velocity component is non-dimensionalized with the maximal value for the respective velocity. The simulated channel (to increase the Mach number for the compressible solver AVBP) was scaled by a factor of 10 with respect to the experiments

The heat transfer coefficient h is defined as:

$$h = \frac{q}{T - T_\infty}. \tag{15}$$

T_∞ is defined here as the bulk temperature T_{bulk}, while T is the temperature at the wall. Figure 19 shows the enhancement factor around one rib of the channel, which is in a qualitatively fair agreement with the experimental result of [13]. The relative bulk flow temperature (or temperature ratio) $\frac{T_\infty}{\Delta T}$ was experimentally found to have only a small effect on the heat transfer [9] and it is assumed that the Nusselt number depends on rhe Reynolds number, the conductivity ratio

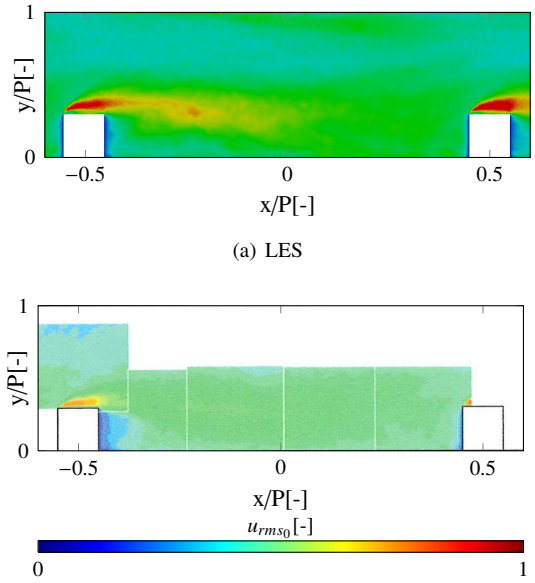

(a) LES

(b) PIV measurement

Figure 17: U_{rms} value around two ribs.

between fluid and solid and the Biot number:

$$Nu = f(Re, K, Bi). \tag{16}$$

Maffulli and He showed that a considerable effect of the temperature ratio on the heat transfer needs to be taken into account [14]. Figure 19 further shows the enhancement factor for three convective computations with different temperature ratios (inlet at ambiant temperature, interfaces varying with 300K, 400K and 500K). Yet, figure 18 shows that further grid refinement is required with the currently used solver AVBP.

5.3. Conjugate Heat Transfer and LES

Two major problems for conugate heat transfer computations exist, which ampify in conjunction with LES: First, the large time scale disparity between solid and fluid domain [15] makes a pure strong coupling solution strategy absolet. Second, it is well-known that for weak coupling strategies, stability problems occur. These stability problems depend on the specific weak coupling strategy(boundary conditions used, rate of exchange and the mesh size) and have been adressed by [3](confirmed by the numerical experiment presented in chapter 2), [16] and more recently [17], among others, and are current subject of research.

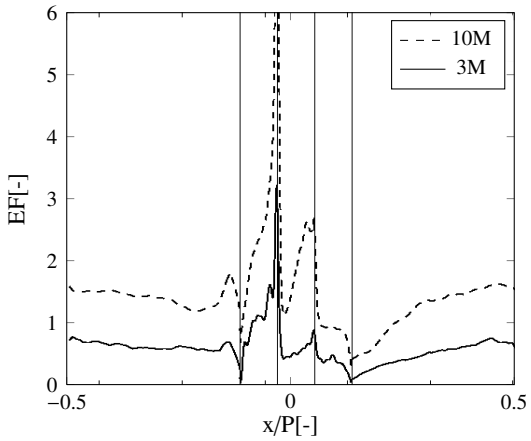

Figure 18: EF over one rib for convective computations. Figure shows results for two different used meshes (M1 and M3 with 3 and 10 million grid cells respectively).

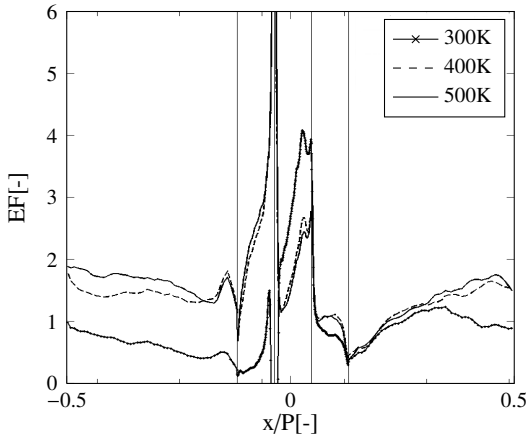

Figure 19: EF over one rib for convective computations. Figure shows results for three different temperature ratios or temperatures at the interface, the inlet temperature being at ambient conditions.

5.3.1. Loose coupling strategy

The loose coupling strategy resembles the coupling strategy detailed by Verstraete [3] for RANS computations. Boundary conditions are exchanged from one domain to another, if the solution is considered as converged. Since we apply an unsteady computation (LES) for the fluid part, convergence means a statistically converged state.
Knowing the stability properties of this weak coupling procedure for steady state simulation, we assume its validity also for statistically converged LES. Dealing with a Biot number of order unity, the TFFB and FFTB method disqualify for this coupling strategy. Mixed type boundary conditions using the heat transfer coefficient provide the advantage of an accelerated convergence using an appropriate vlaue for the heat transfer coefficient, obtained via convective computations.
For the cooling channel application, we used the hFTB method due to the solver preferances. By the time of the paper submission the loose coupled computations were not converged, yet, to reveal differences in terms of enancement factor for the conjugate case in comparison with the convective case.

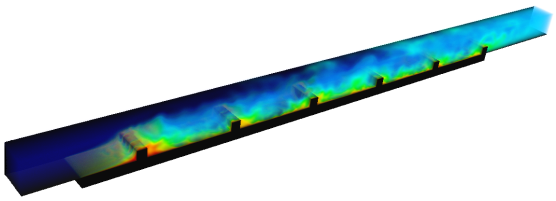

Figure 20: Flow around the ribs coloured by temperature (using volume rendering).

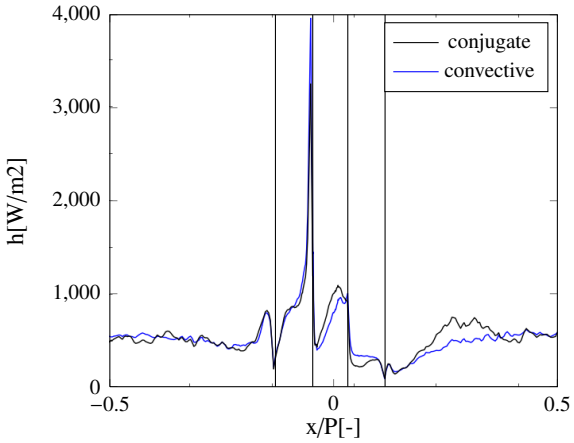

Figure 21: Heat transfer coefficient around one rib for two different computations.

5.3.2. Tight coupling strategy

The quasi-strong coupling strategy applied to the cooling channel was developed by [16] and further investigated by [18]. By the time of the paper submission the tight coupled computations show small differences in term of the heat transfer coefficient in comparison with the convective case (see figure 21).

Conclusions

We showed the suitability of the applied LES to capture the flow of a rib-roughened cooling channel, which is in good agreement with experimental results. Moreover, the heat transfer predictions for convective cases are in a fair agreement with experimental results, but still need further improvement of the meshes.
We observed the previously derived stability criterion, showing its validity for weak coupling procedures for LES. We applied the weak coupling strategy for the cooling channel and are currently applying a tight coupling strategy to be compared with each other in terms of quantitative results and computational efficiency.

Acknowledgments

The author is grateful to his Promotor Professor Wolfgang Schröder and supervisor Professor Tom Verstraete for the support and promotion of this doctoral research.
We would further like to thank Laurent Gicquel, Florent Duchaine, Dimitrios Papadopulous and Remy Fransen from CERFACS for their support and the valuable cooperation.
The research leading to these results has received funding from the European Community's Seventh Framework Programme (FP7, 2007-2013), PEOPLE programme, under the grant agreement No.FP7-290042(COPAGT project).

References

[1] J. Han, S. Dutta, S. Ekkad, Heat Transfer Cooling Technology, Taylor and Francis, Reading, MA, 2000.
[2] L. Perelmann, On conjugate problems of heat transfer, International Journal of Heat and Mass Transfer 3 (1961) 293–303.
[3] T. Verstraete, Multidisciplinary turbomachinery component optimization considering performance, stress and internal heat transfer, Ph.D. thesis, Ghent University and Von Karman Instititue for Fluid Dynamics (2008).
[4] T. Verstraete, Z. Alsalihi, R. A. V. den Braembussche, Numerical study of the heat transfer in micro gas turbines, ASME Journal of Turbomachinery 129 (2007) 835–841.
[5] V. Moureau, G. Latigue, Y. Sommerer, C. Angelberger, O. Colin, T. Poinsot, High-order methods for dns and les of compressible multi-component reacting flows on fixed and moving grids, Journal of Computational Physics 2 (2005) 710–736.
[6] M. Boileau, F. Duchaine, J.-C. Jouhaud, Y. Sommerer, Large-eddy simulation of heat transfer around a square cylinder using unstructured grids, AIAA JOURNAL 51 (2013) 372–385.
[7] F. Nicoud, F. Ducros, Subgrid-scale stress modelling based on the square of the velocity gradient., Flow Turb. Combust. 62 (1999) 183–200.
[8] B. Cukurel, Conjugate heat transfer investigation of a fixed rib roughened cooling passage., Ph.D. thesis, Purdue University and Von Karman Institute for Fluid Dynamics (2012).
[9] B. Cukurel, T. Arts, Local heat transfer dependency on thermal boundary condition in ribbed cooling channel geometries, ASME Journal of Heat Transfer 135 (2013) 101001–1–101001–11.
[10] L. Casarsa, Aerodynamic performance investigation of a fixed rib-roughened internal cooling passage, Ph.D. thesis, Universita Degli Studi Udine and Von Karman Instititue for Fluid Dynamics (2003).
[11] L. Casarsa, T. Arts, Experimental investigation of the aerothermal performance of a high blockage rib-roughened cooling channel, ASME Journal of Turbomachinery 127 (2005) 580–588.
[12] J. Hunt, A. Wray, P.Moin, Eddies, streams, and convergence zones in turbulent flows, Proceedings of the Summer Programm. Center for Turbulence Research.
[13] B. Cukurel, T. Arts, Film cooling extraction effects on the aero-thermal characteristics of rib-roughened cooling channel flow, ASME GT2012-68680.
[14] R. Maffulli, L. He, Wall temperature effects on heat transfer coefficient, Proceedings of ASME Expo 2013 GT2013.
[15] L.He, M. Oldfield, Unsteady conjugate heat transfer modeling, ASME Journal of Turbomachinery 133 (2011) 031022–1–12.
[16] F. Duchaine, A. Corpon, L. Pons, V. Moureau, F. Nicoud, T. Poinsot, Development and assessment of a coupled strategy for conjugate heat transfer with large eddy simulation: Application to a cooled turbine blade, International Journal of Heat and Fluid Flow 30 (2009) 1129–1141.
[17] M. Errera, B.Baque, A quasi-dynamic procedure for coupled thermal simulations, International Journal for Numerical Methods in Fluids 72 (2013) 1183–1206.
[18] S. Jaure, F. Duchaine, G. Staffelbach, L. Gicquel, Massively parallel conjugate heat transfer methods relying on large eddy simulation applied to an aeronautical combustor, Compuatational Science and Discovery 6.

Blade Tip Timing and Blade Tip Clearance Measurement System Based on Magnetoresistive Sensors

Roberto Tomassini

Turbomachinery and Propulsion Department, von Karman Institute for Fluid Dynamics, Belgium, roberto.tomassini@vki.ac.be

Supervisor: Jean-François Brouckaert

Associate Professor, Turbomachinery and Propulsion Department, von Karman Institute of Fluid Dynamics, Belgium, brouckaert@vki.ac.be

University Supervisor: Gianluca Rossi

Full Professor, Mechanical Engineering Department, University of Perugia, Italy, gianluca.rossi@unipg.it

The accurate control of the gap between static and rotating components is vital to preserve the mechanical integrity and ensure a correct functioning of any rotating machinery. Moreover, tip leakage above the airfoil tip results in relevant aerodynamic losses . One way to measure and monitoring blade tip gaps is by a Blade Tip Clearance (BTC) technique.
Another fundamental phenomenon to limit and monitoring in the turbomachines, is the vibration of the blades. For more than half a century, this has been performed by installing strain gauges on the blades and using telemetry to transmit the signals. The Blade Tip Timing (BTT) technique, (i.e. measuring the blade time of arrival from the casing at different angular locations with proximity sensors) is currently being adopted by all manufacturers as a replacement for the classical strain gauge technique because of its non-intrusive character.

In the frame of the present research investigation, a digital and an analogue magnetoresistive sensor for BTC and BTT measurement systems have been realized. The sensing element adopted is a Wheatstone bridge of permalloy elements. A preliminary characterization of the static and the dynamic response of the probes has been carried out in a dedicated calibration bench and in the VKI R2 compressor rig. The calibration curve for clearance measurement has been retrieved. The magnetoresistive sensors present high repeatability, low manufacturing costs and measurement accuracy in line with the main type of probes used in turbomachinery testing. The uncertainty analysis showed that running gaps can be measured at low speed within 0.021mm (20:1) at a working distance of 1mm. The magnetoresistive sensor has great potential for clearance and vibration measurements of ferromagnetic blades.

The challenge of this work concerns the development of a simultaneous BTC and BTT measurement system using the magnetoresistive probes. This PhD research project focuses on a detailed characterization of the static and dynamic sensors performance, further developments of the data processing algorithm and experimental investigations in the calibration bench and test rigs. Finally, comparisons with commercially available measurement systems and sensors, will give more accurate details of the performance.

Keywords:
Blade tip timing, blade tip clearance, non-intrusive vibration measurement system, turbomachinery testing, magnetoresistive sensor

OPTIMIZATION IN TURBOMACHINERY

Analysis and Consequences of the Separation/Transition Mechanisms of the Flow on a Modern Low-Pressure Gas Turbine Airfoil

Julien Clinckemaillie

Turbomachinery and Propulsion Department, von Karman Institute for Fluid Dynamics, Belgium, julien.clinckemaillie@vki.ac.be

Supervisor: Tony Arts

Professor and Head of Department, Turbomachinery and Propulsion Department, von Karman Institute for Fluid Dynamics, Belgium, arts@vki.ac.be

University Supervisor: Hervé Jeanmart

Professor, Institute of Mechanics, Materials and Civil Engineering, Université Catholique de Louvain, Belgium, herve.jeanmart@uclouvain.be

Modern commercial aero-engines are characterized by an ever-increasing bypass ratio which, in turn, requires the low-pressure turbine (LPT) to provide an increasingly higher specific power output in order to drive the large fan, without any efficiency penalty. At the same time, the actual trend to save weight and to reduce production and maintenance costs of aero-engines is translated in a reduction of the blade count per row and thus increased pitch-to-chord ratios. The combined effects of these requirements on the low-pressure turbine imply an increased aerodynamic load per blade, and lead to the development of very-high-lift and even ultra-high-lift airfoils. These are characterized by an increased velocity peak (almost near sonic conditions) on the suction side followed by a significant diffusion until the trailing edge. The resulting strong adverse pressure gradient along the rear part of the suction side can lead to a separation of the boundary layer, particularly under the low Reynolds number conditions which are germane to low-pressure turbines operating at cruising altitude. Separation bubbles cause a significant degradation of engine efficiency, particularly burst separation bubbles that fail to reattach, resulting in a major loss in aerodynamic efficiency and thrust. For large commercial turbofan engines, a loss in LPT efficiency of around 2% may occur between sea-level take-off conditions, when the Reynolds number value is of the order of $5\ 10^5$, and high-altitude cruise flight, where it reduces to $5\ 10^4$. Due to the low value of the cruise Reynolds number, a large part of the boundary layer developing around LPT blades may be laminar. The precise prediction of separation onset and transition development is therefore of utmost importance for the design of high-lift airfoils, where the strong initial acceleration tends to keep the suction side boundary layer laminar until past the velocity peak. If the subsequent diffusion is large enough, this laminar boundary layer can not withstand the strong adverse pressure gradient and separates from the blade surface. If transition occurs soon enough in the separated shear layer, the flow reattaches to the blade surface. Transition and separation are thus affecting each other, and parameters such as free-stream turbulence intensity, unsteady wake-boundary layer interactions and surface roughness are known to have a significant influence on these processes. Understanding the physics of these phenomena and how they influence each other, as well as learning how to predict them is therefore of crucial importance for the design of efficient low-pressure turbines and forms the main objective of this Ph.D research project. This study will be performed experimentally on a large linear cascade in the VKI S1/C high-speed wind tunnel, which allows an accurate reproduction of the operating conditions encountered in low-pressure turbines of modern aero-engines.

Keywords:
Turbomachinery, low-pressure turbine, transition, separation, bursting, unsteady interactions, surface roughness

NOISE AND AEROACOUSTICS

Development Of A High Fidelity Acoustic Simulation Platform For Detached Flows

Filip Baillien

Environmental and Applied Fluid Dynamics Department, von Karman Institute for Fluid Dynamics, Belgium, filip.baillien@vki.ac.be

Supervisor: Christophe Schram

Associate Professor, Environmental and Applied Fluid Dynamics Department, von Karman Institute for Fluid Dynamics, Belgium, christophe.schram@vki.ac.be.

Abstract

This paper shows the improvements to COOLFluiD to accurately predict sound generation through the coupling of a LES/DNS source region and a LEE propagation solvers. It covers improvements done and planned for the LES part and other tools developed to improve the computational speed of the platform. All improvements will be tested through two test cases presented in this paper.

Keywords: COOLFluiD, Residual Distribution Method, RDM, Coupling, Aeroacoustics, Tandem Cylinder, Corotating Vortices

1. Introduction

Current direct computational aeroacoustic simulations are limited by the computational cost required as it is bound by different timescales and different grid requirements. On one side the cost to simulate the turbulence and the forces generating sound is high due to the grid requirements posed by the solver and due to the unsteady nature of the problem. On the other side, the computational domain where the acoustic perturbation has to be analyzed is generally vast but, apart from the source region, quite linear. Solving therefore the whole domain with only a Large Eddy Simulation (LES) or a Direct Numerical Simulation (DNS) solver would be inefficient. A Linearized Euler Equations (LEE) solver on the other hand, is incapable of solving the non-linear source region due to its linear nature, but is well suited for the propagation region where the pressure waves expand linearly. A coupling between the two solvers, where the LEE can be effective to analyze and simulate the propagation region, while a LES/DNS solver analyzes the sound generation in the source region takes the best of the two solvers, so the combination can yield an efficient, yet accurate methodology. This hybrid technique generally requires to use two different software as most of the commercially available softwares do not have both tools available inside the same platform. The coupling between different codes always involves data I/O and storage, which increases the resources needed to perform a full aeroacoustic simulation. This work takes advantage of the potential of COOLFluiD, VKI's in-house simulation platform. COOLFluiD starts from the distinctive advantage of having both solvers available. This allows for cheap and easier communications between the two parts of the software. During this work, using COOLFluiD and the Residual Distribution Method(RDM), a faster yet accurate coupling will be implemented for aeroacoustic purposes. The Residual Distribution Method was chosen for its ability to provide accurate results with low dissipation, even when using a second order scheme. Moreover, RDM was designed to work on unstructured meshes making it a good candidate for complex geometries. This paper will show the idea behind the coupling and the theory of hybrid methods in section 2, and will then proceed with the brief summary of the main concepts of the RDM in section 3. In order to demonstrate and validate the proposed methodology, the two tandem cylinder test-case was chosen from the BANC (Benchmark problems for Aeroacoustics Noise Computations) database. This test case rep-

resents a simplified landing gear configuration with moderate Reynolds (Re) number. This is the first 3D LES test case attempted with the RDM solver, therefore several new implementations are needed to accomplish the task which are detailed in section 4. In order to make a parametric study on the different coupling techniques, a much smaller 2D test case of two co-rotating vortices was chosen. The general setup of this case is described in section 5. The paper will then conclude with a summary of the work done and expected in the future.

2. Governing equations and coupling technique

In order to numerically resolve aerodynamically generated noise productions one need to consider a time-dependent high fidelity computational tool due to the fact that noise generation is by nature a transient small perturbation non-linear phenomenon. In this work a compressible LES (and for limited problems DNS) solver is considered resolving the following governing equations:

$$\begin{aligned} \frac{\partial \overline{\rho}}{\partial t} + \frac{\partial \overline{\rho}\tilde{u}_j}{\partial x_j} &= 0 \\ \frac{\partial \overline{\rho}\tilde{u}_i}{\partial t} + \frac{\overline{\rho}\tilde{u}_i\tilde{u}_j}{\partial x_j} + \frac{\partial \overline{p}}{\partial x_i} + \frac{\partial \check{\sigma}_{ij}}{\partial x_j} &= \\ -\frac{\partial \tau_{ij}}{\partial x_j} + \frac{\partial}{\partial x_j}(\overline{\sigma}_{ij} - \check{\sigma}_i j) & \\ \check{E} = \frac{\overline{p}}{\gamma - 1} + \frac{1}{2}\overline{\rho}\tilde{u}_i\tilde{u}_i & \end{aligned} \tag{1}$$

Where $\overline{\rho}$, $\overline{p}$ and $\overline{\sigma}$ are scale high-pass filtered quantities, τ_{ij} is the residual stress tensor, $\tilde{u}$ is Favre filtered and $\check{E}$ is the computable energy.

In the present work the Linearized Euler Equations are considered for the propagation simulations. Compared to the acoustic analogies, LEE can handle inhomogeneous propagation domain while also taking into account refraction, reflections and scattering effects. The linearization of the equations takes place around the time averaged mean flow. Since the perturbations are small in most cases of acoustic wave propagation, this linearization can be done without neglecting any relevant flow physics. The equations used were derived by Bailly *et al.* [1] for inhomogeneous mean flow and are written in conservative form as:

$$\begin{aligned} \frac{\partial \rho'}{\partial t} + \frac{\partial}{\partial x_j}(\rho_0 u_j' + \rho' u_{0j}) + \{\frac{\partial}{\partial x_j}(\rho' u_j' + \overline{\rho' u_j'})\} &= 0 \\ \frac{\partial \rho_0 u_i'}{\partial t} + \frac{\partial}{\partial x_j}(\rho_0 u_i' u_{0j} + p'\delta_{ij}) + \frac{\partial u_{0i}}{\partial x_j}(\rho_0 u_j' + \rho' u_{0j}) + & \\ \{\frac{\partial \rho' u_i'}{\partial t} + \frac{\partial}{\partial x_j}(\rho' u_i' u_{0j} - \overline{\rho' u_i'} u_{0j}) + \frac{\partial u_{0i}}{\partial x_j}(\rho' u_j' - \overline{\rho' u_j'})\} & \\ = \{-\frac{\partial}{\partial x_j}(\rho u_i' u_j' - \overline{\rho u_i' u_j'})\} & \end{aligned} \tag{2}$$

$$\begin{aligned} \frac{\partial p'}{\partial t} + \frac{\partial}{\partial x_i}(\gamma p_0 u_i' + p' u_{0i}) + (\gamma - 1)(p' \frac{\partial u_{0i}}{\partial x_i} - u_i' \frac{\partial p_0}{\partial x_i}) & \\ + \{u_i' \frac{\partial p'}{\partial x_i} - \overline{u_i' \frac{\partial p'}{\partial x_i}} + \gamma(p' \frac{\partial u_i'}{\partial x_i} - \overline{p' \frac{\partial u_i'}{\partial x_i}})\} = 0 & \end{aligned}$$

Where ρ_0,u_0 and p_0 are the mean flow quantities, - are averaged quantities and ρ',u' and p' are the fluctuations.

To solve the test-cases, the computational domains will be split in two main regions: the LES region and the LEE region. Both solvers are implemented using the Residual Distribution Method (RDM) in COOLFluiD. The LES region will focus on the noise source region of the simulation since it is capable of accurately solving the turbulent fluctuations that generate the noise field. This process is viscous and highly non linear therefore the direct solution of the Navier-Stokes (NS) equations are needed. On the other hand, its complexity and its high grid requirements make it expensive and therefore not practical to be used also on the propagation domain. The LEE solver has opposite characteristics: since the vorticity structure in the source region is highly non-linear, it cannot be used for the source region. However, since the propagation region is a linear, it is perfectly suited for it. There are two ways to couple acoustic source field with noise propagation solver: the first by reconstructing the whole source field inside the propagation domain, and the second one by injecting the resolved variables through the boundary of the propagation domain. The first method is more demanding in terms of memory requirements as it requires to store the solution of the whole source domain with a frequency that will allow to avoid the truncation of some important frequencies. Thus, the storage cost varies depending on the size of the source domain mesh and on the sound frequency emitted by the source. There is small computational time penalty as well, as disk access is one of the slowest action in modern computing. Using the source reconstruction method, the LEE domain contains the source domain and the communication between the two solvers is one-way from the source domain to the propagation domain. The source reconstruction is done using the formula proposed by Bailly et al.[1]:

$$\vec{S} = \begin{bmatrix} 0 \\ S_i - \bar{S}_i \\ 0 \end{bmatrix} \tag{3}$$

With $S_i = -\frac{\partial \rho_0 u_i' u_j'}{\partial x_j}$.

This prompted for an improved coupling technique, which allows communication through the boundaries. This method, called Boundary Injection, allows to vastly reduce the memory requirements for the communication between the two solvers. Furthermore, if the coupling is done inside the same software, as in COOLFluiD[5] it is even possible and practical to execute this whole operation with no disk access just passing the data inside the program. Even though the boundary injection method is clearly superior to the other, both are used in this work for testing: the source reconstruction was needed in a previous work since all simulations were done with an incompressible solver. Since now all simulations are run using a compressible solver, the boundary injection method could be the sole used, but to assess the differences between the two couplings the source reconstruction is kept.

In case of the boundary injection method, care must be taken in the positioning of the communication boundary: it must be far enough from the source domain to avoid truncation of the source generation mechanism, but close enough to exclude mesh coarsening and boundary effects. Different values for the distance of the boundary from the source are therefore to be investigated to find the optimal configuration.

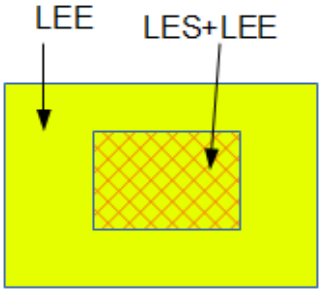

Figure 1: Coupling through source reconstruction

3. Residual Distribution Method

Given the flow physics under investigation the Residual Distribution Method was chosen as the preferred solution method for this work. Since the flow is unsteady, compressible and subsonic, with separation bubbles and recirculation, an accurate, robust and efficient method has to be chosen. The RDM, also

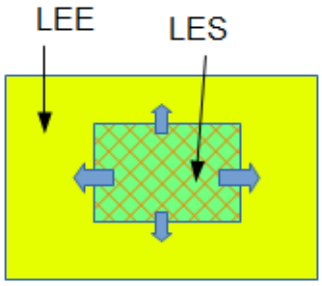

Figure 2: Coupling through boundary injection

known as the Fluctuation Splitting Method can be described as an hybrid between Finite Elements and Finite Volumes and has been proven to be accurate[2][3] and robust for aeroacoustic simulations. To analyze the unsteadiness of the flow, in this work the space-time method is used, which consists in considering time as an additional dimension of the domain. The implementation of the LEE solver has already been validated for aeroacoustic problems, so it is not detailed in this paper [4]. The multidimensional upwind LDA (Low Diffusion A) scheme introduce lower dissipation compared with other methods with the same order. Therefore, mainly this scheme is used throughout this work. The other scheme used in this work is the first order N-scheme which can achieve faster convergence than the LDA scheme. It is however more dissipative and will therefore only be used for initialization and where higher dissipation is actually beneficial like to avoid reflections from the domain boundaries. Finally, the RDM scheme allows easy and effective parallelization given its compact stencil on the nearest neighbors and is therefore usable on large test cases. A current limitation of the RDM scheme is that is limited to tetrahedral and triangular meshes. This is especially limiting when dealing with wall bounded flows where the mesh size normal to the wall is limited by the boundary layer and a non-homogeneous vertex distribution would lead to a more efficient simulation. The development of quad based elements is planned therefore, later within this PhD.

4. The Tandem Cylinder test-case

In order to validate the further developments and demonstrate the ability of RDM for aeroacoustic problems a well known benchmark test-case was chosen: the Tandem Cylinder which is described in the Benchmark problems for Aeroacoustics Noise Computations (BANC I). It is composed by two cylinders

aligned in stream-wise direction at a distance of 3.7 diameters. The two cylinders have the same diameter of 0.0515m, and are placed aligned in a stream with velocity 44m/s yielding a Re number of 0.166 million. This benchmark proved to be geometrical-wise simple yet flow-field-wise challenging and is therefore a good candidate to test the capabilities of the RDM solver for aeroacoustic problems in CF. This test-case is intrinsically unsteady, and could accurately be solved through an incompressible solver given its low flow velocity (Ma=0.128). However, given the aeroacoustic focus of this work, it will be solved using a compressible solver. The flow presents two separation bubbles behind each cylinder with the interaction of the first wake with the second cylinder generating.

Initial simulations were carried out in 2D in order to identify the missing tools necessary for this acoustic test-case. The current configuration for the 2D mesh includes a y+ of 0.9 with a domain that is 30x32 diameters. This yields a mesh of 230k elements which has a small memory requirement. The main limitation to the speed of this simulation comes from the small size elements in the boundary layer which limit the maximum time-step allowed by the past-shield condition of the RDM solver resulting about 5.E+5 time-steps for each flow pass-through. This represents a clear limitation that is the quad structure hopefully will solve. Lockard [10] suggests a minimum width of the domain of 3 diameters allowing the solver to generate the experimentally shown 3 dimensional vortices, though during the BANC, domain spans of up to 16 diameters have been analyzed showing that fluid quantities never get totally uncorrelated. The first setup used therefore consists of 3 diameters in order to allow assessing the requirements of the simulation and at the same time to limit the computational cost of the first simulations. The 3D simulation was limited to a smaller domain, 12x10 diameters and with a y+ of 10. This yields a mesh size of 2.2 million elements and can run with a bigger time-step though the boundary layer is not fully resolved. A mesh using y+=3 is ready to be used as soon as the flow fully develops in the coarser grid. The results from the coarse grid will be interpolated using the interpolation tool developed within this project and described in the next subsection. Mesh generation was done using both Gmsh and Gambit. Initial work was done using Gmsh which then proved not yet capable of generating the required meshes in 3D for CF. Multiple zones were created inside Gmsh and associate to one volume. When the simulation ran in COOLFluiD, it was possible to see that the different zones of the Gmsh mesh where not communicating properly inside CF leading to strong unphysical discontinuities in the solution, in particular between the first and the second region around the cylinder. It was therefore necessary to move to Gambit in 3D, which though lacking some capabilities of Gmsh, such as the ability to create a structured triangular mesh with high aspect ratio cells in the boundary layer as shown in figure 5, proved to be more stable and mature for the current task.

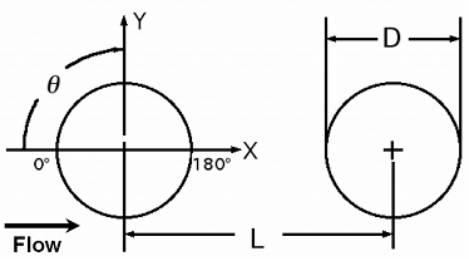

Figure 3: Schematic of tandem cylinder configuration

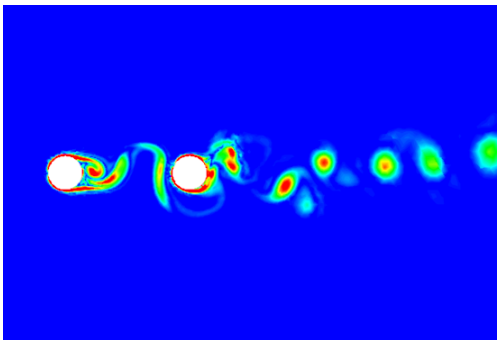

Figure 4: Vorticity profile from the 2D simulation

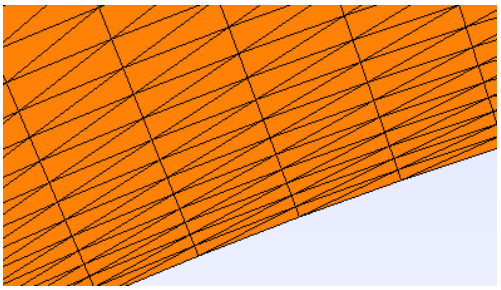

Figure 5: 2D Boundary layer with Gmsh

4.1. Related Activities

To improve the confidence in the results obtained with CF-RDS, and to achieve those results faster, two

new tools were developed and a profiling activity on CF was started. The tools are a Y+ post processor and an solution interpolation tool. The new Y+ post processor is implemented in the CF framework and is capable of analyzing, both in 2D and 3D. According to its definition Y+ is computed as:

$$y^+ \equiv \frac{u_* y}{\nu}$$

Where u_* is the friction velocity, y is the distance of the node from the wall and ν the kinematic viscosity of the fluid. The friction velocity is defined as

$$u_* \equiv \sqrt{\frac{\tau_\omega}{\rho}}$$

Where τ_ω is the wall shear stress which can be computed as:

$$\tau_\omega = \mu(\frac{\partial u}{\partial y})_{y=0}$$

Y+ can therefore be computed as

$$y^+ = \sqrt{\frac{(\frac{\partial u}{\partial y})_{y=0} y^2}{\nu}}$$

Where u is the flow velocity parallel to the wall and y the distance from the wall. Since the RDM implementation is only linear, $\frac{\partial u}{\partial y}$ can be linearized to u/y since the velocity at the wall is by definition null. The implemented y+ solver is therefore based on the following equation:

$$y^+ = \sqrt{\frac{uy}{\nu}}$$

This allows to make informed decisions about the mesh quality and the computational time.
The interpolation tool was developed to kick-start computational heavy simulations by restarting previous simulation done on a coarser and thus faster mesh. It initially used the nearest neighbor approach for quick development and first testing. It was sequentially expanded to use the more efficient and accurate bi-linear interpolation scheme. This allows 3D meshes of million elements to be interpolated in a matter of minutes. The tool works on both 2D and 3D meshes and the latest addition to it is the ability to extrapolate a 2D solution to a 3D domain, if the domain is a 3D extrusion of the 2D one. This feature was used for the 3D Tandem Cylinder testcase, with y+ of 10, from its 2D solution with y+ of 3 (10x the number of elements). The high computational cost of 3D LES-DNS simulations poses a challenge that is being met through the analysis of the efficiency of CF, through profiling. Two software are used for this purpose: Valgrind and TAU. Valgrind is a Free Software/Open Source instrumentation framework that can automatically detect many memory management and threading bugs, and profile programs in detail. TAU (Tuning and Analysis Utilities) Performance System ®is an international joint project registred by the State of Oregon. It can freely be downloaded from its web-page and is mainly focused at profiling code performance on parallel machines.

Initially, the Valgrind tool was used as it was readily available at VKI. The tool is extremely powerful as it allows a deep understanding of the computational costs of every single function and line of code in the profiled software. This for example allowed the identification of a small yet significant performance hit generated by the compiler: certain single lined functions, massively used were not inlined by the compiler. It was then possible to change this behavior by changing a compiler flag and this yielded an improvement of 5%. Unfortunately, Valgrind is particularly heavy as for even small cases (two thousand elements) for short computations (50 iterations) it requires long computations (about 1.5 hours). This prompted the study of TAU. This tool is capable of doing a similar work to Valgrind albeit at a much lower cost. The computational time of a test-case ran with TAU is of the same order of magnitude of a non-instrumented test-case : the same test-case that with Valgrind takes 1.5hours, in TAU takes 12 seconds.

5. The Corotating vortices test-case

While waiting for the source region of the Tandem Cylinder test-case to fully develop, a smaller test-case was chosen to test and validate the implementation of the coupling technique: two corotating vortices spinning in free field. This test case is $2D$ and is run in a fraction of the time it takes to run the tandem cylinder test-case. It represents a system of two spinning vortices in free field previously studied by many authors.[7][9][1][8] The aeroacoustic analogy noise source of this test case is a rotating quadrupole, and therefore generates one of the weakest basic aerodynamically generated noises. This represents a challenging test case that will allow a correct assessment of the capabilities of the proposed hybrid methodology. Furthermore, an analytical solution, which is the incompressible limit for this system, is

also available, allowing therefore a better accuracy assessment.

Following Bailly's[1] setup the vortices have the following initial distribution with no mean flow velocity:

Velocity	$V_\theta(r)$	$\frac{\Gamma r}{r_c^2+r^2}$
Distance between vortices	$2r_0$	3.6e-3
Angular frequency	$\omega = 2\pi f$	$\frac{\Gamma}{4\pi r_0^2}$
Period	T	$\frac{8\pi^2 r_0^2}{\Gamma}$
Mach	M_r	$\frac{\Gamma}{4\pi r_0 c_0}$
Re	$Re = \frac{\Gamma}{\nu}$	1.14E5

Table 1: Free field corotating vortices initial data[6]

The merging of the vortices can be devided into four distinct phases. They are associated with different sound emission levels and vortex behavior. In the first phase, the vortices just rotate around the central point. The vortices are clearly distinguishable and lose energy only due to diffusion. The duration of this phase is proportional to the Reynolds number. In the second phase, the merging of the two vortices begins. Advection of vorticity is the main contributor to the evolution of the system and the duration of the phase is mostly stable, independently from the Reynolds number. The third phase completes the merging. The main contributor to the evolution of the system is now diffusion of vorticity and its interaction with the rotation of the center makes the system axis-symmetric. In this phase, as with the first phase, the Reynolds number influences the duration of the phase. In the last phase, the newly formed vortex diffuses due to viscosity. At the same time, sound generation decreases. This source field is used both for source injection and coupling through the boundaries. First the same source region is considered as in the reference paper of Bailly *et al*[1]. A plot of the distance between the two vortices during the merging is shown in figure 6. It shows that for a long time the distance between the two vortices remains quite constant for a long period of time, until the two vortices abruptly merge after a adimentional time of $t^* = 7.1$.

6. Conclusion

This paper shows that the current work was done on mainly two fronts: on one side the improvements to the source region solver carried out with the aid of

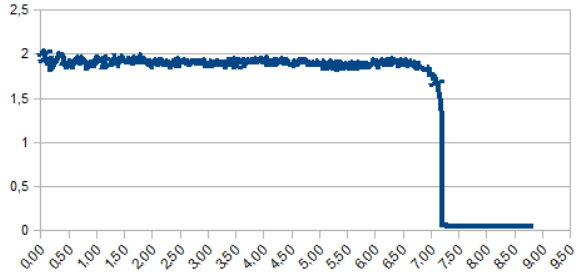

Figure 6: Plot of the distance between the two vortex cores

the Tandem Cylinder test-case, while on the other it presents the current and short term improvements that will be done on the coupling between LES/DNS and LEE through the co-rotating vortices test-case. Both test-cases will be used to verify the progress and validate the results.

In the coming months a parametric study will be performed with both the source reconstruction technique and the direct injection method with the help of the co-rotating vortices test-case. The results are planned to be presented in the next AIAA conference. An other objective is to further improve the capabilities of the noise source simulations and for that the implementation of quad based elements is considered.

Acknowlegments

The research leading to these results has received founding from the European Communitys Seventh Framework Programme (FP7, 2007-2013), PEOPLE programme, under the grant agreement No. FP7-289428 (ANADE project).

References

[1] C. Bailly, C. Bogey, and D. Juve. Computation of flow noise using source terms in linearized euler's equations. 6th AIAA/CEAS Aeroacoustic Conference, 2000. x, 112, 113, 119, 120, 122

[2] R. Abgrall and M. Mezine. Construction of second order accurate monotone and stable residual distribution schemes for unsteady flow problems. J. Comput. Phys, 188:1655, 2003. 33

[3] M. Ricchiuto, R. Abgrall, and H. Deconinck. Application of conservative residual distributive scheme to the solution of the shallow water equations on unstructured meshes. J. Comput. Phys., 222:287-331, 2007. 16, 18

[4] L.Koloszar, N. Villedieu and J.Anthoine. Residual Distribution Method for Aeroacoustics. AIAA Journal Vol 49. No 5 May 2011

[5] http://coolfluidsrv.vki.ac.be/trac/coolfluid

[6] P. Meunier, S. Le Dizes, and T. Leweke. Physics of vortex merging. C. R. Physique, pages 431-450, 2005. 116

[7] S. O. Koo and D. J. Lee. Numerical study of sound generation due to spinning vortex pair. AIAA Journal, 33, 1995. 112

[8] P. Moin, B. E. Mitchell, and S. Lele. Direct computation of the sound from a compressible co-rotating vortex pair. J. Fluid Mechanics, 285:181-202, 1995. 112

[9] C. Bogey. Calcul direct du bruit aerodynamic et validation de modeles acoustiques hybrides. PhD thesis, Ecole Central de Lyon, 2000. 112

[10] David P. Lockard, Mehdi R. Khorrami, Thomas F. Brooks. Tandem Cylinder Noise Predictions. 13th AIAA/CEAS Aeroacoustics Conference, May 23-25, Rome, Italy.

Tonal and Broadband Fan Noise Production and Propagation

Gabriele Grasso

Environmental and Applied Fluid Dynamics Department, von Karman Institute for Fluid Dynamics, Belgium, gabriele.grasso@vki.ac.be

Supervisor: Christophe Schram

Associate Professor, Aeronautics and Aerospace Department & Environmental and Applied Fluid Dynamics Department, von Karman Institute for Fluid Dynamics, Belgium, christophe.schram@vki.ac.be.

Keywords: Fan noise, computational aeroacoustics, hybrid methods, optimization, turbomachinery.

The reduction of aerodynamic noise is of increasing importance in many industrial applications. This is due to EU work regulations limiting the exposure to sound on the one hand, and an increasing worldwide competitive context on the other hand. Nowadays, the availability of computational resources allows to tackle this issue by performing numerical studies on geometries of industrial interest. In the field of rotating machinery, axial fans have been selected as case studies for this thesis, since they are primary sources of noise in duct or pipe systems. The fields of application include contra-rotating open rotors in the aeronautical field and low-speed fans in cooling and ventilation systems.

The purpose of this research is to develop numerical tools for predicting both the tonal and broadband components of noise produced by subsonic fans and to validate the algorithms with experimental data. Among the possibilities offered in the domain of Computational Aeroacoustics (CAA), hybrid methods based on the aeroacoustic analogy are a promising way to simulate high-Reynolds, low-Mach number problems. Hybrid CAA methods split the problem into three distinct parts: description of the flow field by means of CFD, modeling of the source of noise and computation of noise propagation. The source of noise can be reconstructed from the steady CFD data by means of a statistical method such as based on Amiet's theory for the simulation of broadband noise [1; 2]. Such low-order modeling approach presents low computational costs while yielding reasonably accurate results and is therefore suitable to be implemented in an optimization procedure.

A preliminary attempt to implement in an optimization procedure a newly developed model for the computation of tonal noise, due to the interaction of a blade with an incoming wake, has been performed. The contra-rotating fans of the VKI-L1 low-speed wind tunnel were taken as baseline configuration [3]. In this case, the wake-interaction noise model was based on a parallel gust formulation. A new version of the algorithm is currently under development, which takes into account the skewness of the gust when computing the source of noise and the effect of lean and sweep of the blades in the propagation model.

A four-bladed fan will be the second case study for this thesis. Its geometry has been provided by the Centre Technique des Industries Arauliques et Thermiques, Lyon, along with acoustic and blade surface pressure experimental data. In this case, the surface pressure spectrum will be reconstructed from RANS and scale-resolved simulations in order to compute the trailing-edge noise. Moreover, a model for the computation of noise due to the formation of tip-clearance vortexes will be developed and applied to this geometry.

A further objective of this thesis is to understand the issues related to the interaction between the components of a ventilation system by analysis of experimental data obtained in the IDEALVENT facility of VKI.

Acknowledgment. This PhD work is supported by the European Commission in the framework of the FP7 ITN project FLOWAIRS (Grant Agreement no 289352) and of the FP7 Collaborative Project RBF4AERO (Grant Agreement no 605396).

References

[1] R. K. Amiet, Acoustic radiation from an airfoil in a turbulent stream, Journal of Sound and Vibration 41 (4).

[2] R. K. Amiet, Noise due to turbulent flow past a trailing edge, Journal of Sound and Vibration 4 (3).

[3] G. Grasso, J. Christophe, C. Schram, T. Verstraete, Aerodynamic, aeroacoustic and structural optimization of a contra-rotating fan, in: Proceedings of the 15th International Symposium on Transport Phenomena and Dynamics of Rotating Machinery, ISROMAC-15.

Shock-Cells Noise Investigation on a Subsonic/Supersonic Coaxial Jet

Daniel Guariglia

Aeronautics and Aerospace Department, von Karman Institute for Fluid Dynamics, Belgium, daniel.guariglia@vki.ac.be

Supervisor: Christophe Schram

Associate Professor, Aeronautics and Aerospace Department & Environmental and Applied Fluid Dynamics Department, von Karman Institute for Fluid Dynamics, Belgium, christophe.schram@vki.ac.be

University Supervisor: Fulvio Stella

Associate Professor, Mechanical and Aerospace Engineering Depertment, Università di Roma "La Sapienza", Italy, fulvio@stella.dima.uniroma1.it

1. Introduction

This project is part of the Marie Curie Initial Training Network AeroTraNet2, focused on the investigation of shock-cell noise. This aeroacoustic mechanism is encountered in aeronautical engines working in off-design conditions, usually when the secondary flow of a turbofan is exhausted in under-expanded conditions. This leads to the formation of annular shock-cells as sketched in Figure 1.

The interaction between the coaxial jet shear layers and the annular shock-cell pattern leads to the production of broadband noise, which represents an environmental issue and a threat to passenger comfort. The aim of the study is to characterize the flow in different conditions in order to provide a phenomenological noise source model to be used by the aviation industry.

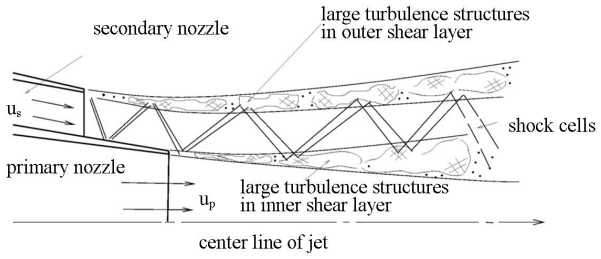

Figure 1: Sketch of the flow topology of shock-cells. Tam *et al* [1].

Tam *et al* [1] investigated a similar coaxial flow with microphones in the far field and they proposed two different mechanisms of sound generation. The first one is due to the interaction of the external shear layer with the shock-cells, which is directed mainly backward, while the inner shear layer generates a broadband noise that is convected by the supersonic flow and is thus directed mainly forward (Figure 2).

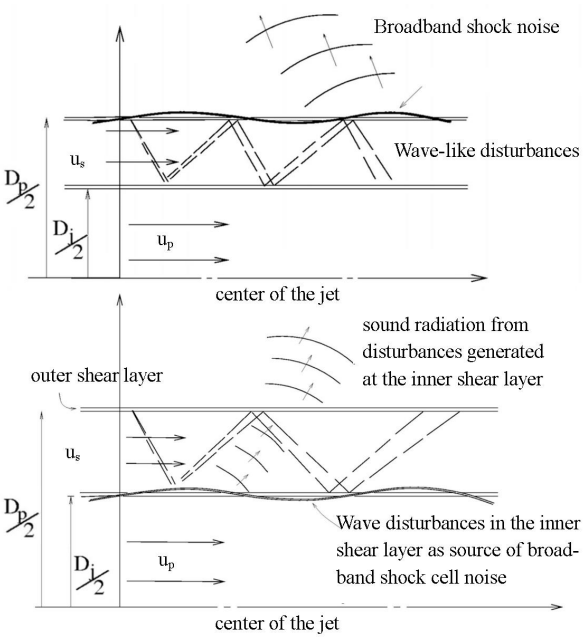

Figure 2: Wave-like disturbances in the outer and inner shear layer as source of broadband noise. Tam *et al* [1]

Our goal is to characterize the flow in different conditions using synchronized measurements of microphones, Schlieren, PIV and LDV. Intrusive measurements using hot wires and static probes are also considered.

2. Methodology

A feasibility study has been performed, leading to a preliminary design of the setup, defining also the test cases to investigate in agreement with the industrial partner Airbus. The target is to obtain a stable flow for a long enough test duration. Other constraints are the operability and safety of the facility, which should be operated by a single person.

To simplify the setup of the nozzle will have a conical shape, fixed geometry, and the core jet will be at the same total temperature of the secondary jet. The control parameter will be the *Fan Nozzle Pressure Ratio (FNPR)* and the *Core Nozzle Pressure Ratio (CNPR)*, defined as $p_0/p_{ambient}$ for the fan and the core respectively. The major points of interest are summarized in Table 1.

Table 1: Test conditions matrix

Test	$FNPR$	$CNPR$	M_{fan}	M_{core}	$\dot{m}_{tot}$ kg/s
1	2.450	1.675	1.21	0.89	1.09
2	2.500	1.720	1.22	0.91	1.11
3	2.400	1.626	1.19	0.86	1.06
4	2.350	1.589	1.18	0.84	1.04
5	2.250	1.518	1.14	0.80	0.99
6	2.150	1.450	1.11	0.75	0.94
7	2.050	1.385	1.07	0.70	0.90
8	2.000	1.353	1.05	0.67	0.87
9	1.800	1.235	0.96	0.56	0.77

These constraints resulted in a configuration that will use the 35 bar line of the VKI compressed air network operating in continuous for maximum 20 mins. Operative parameters will be the total pressure for the two lines set by two pilot controlled pressure regulators. To further increase flow steadiness and also to enhance seeding uniformity, a buffer tank (volume 350 l) is introduced upstream of the nozzle pressure lines, as shown in Figure 3.

2.1. Measurement techniques

Below we summarize the expected measurement techniques that we will apply to investigate the flow.

- **Schlieren.** This optical technique is relatively cheap and easy to implement. The aim is to have an insight of the flow field. Averaged and time resolved images will be used to validate the setup and to assess the axial-symmetry of the jet. Also the shock-wave patterns in different conditions will be easy to detect.

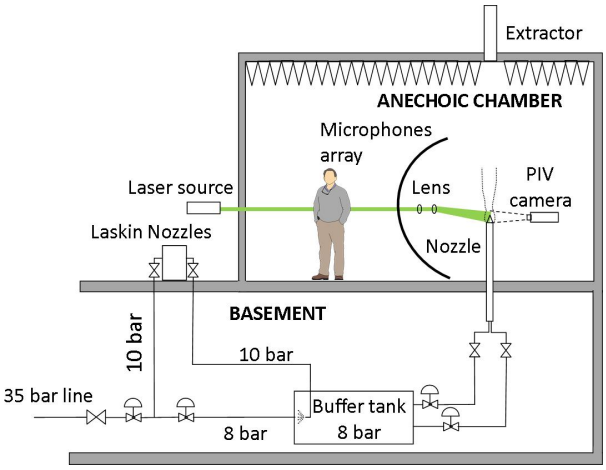

Figure 3: Sketch of the experimental facility.

- **Aerodynamic investigation.** We will use hot-wires and static pressure probes to have quantitative measurements inside the jet. Special care is necessary to avoid to disturb the flow field, especially in the shock-cells region. Contemporary use of Schlieren could be useful to verify the importance of the caused disturb.

- **Acoustic investigation.** Near and far field acoustic measurements will be used to capture the signature of the shock-cells noise, with expected frequencies up to 70 Khz. Synchronized use of the Schlieren technique with a high speed camera might be useful to recognize periodic variation in the shock-wave patterns that are referable to collected acoustic spectra .

- **PIV.** We will collect averaged PIV images at several conditions to characterize the flow field. The generated database will be used for validation of numerical studies by the partners of the project.

- **Synchronous PIV (or LDV) with microphones.** We will perform synchronous measurements with microphones to characterize the source of the noise. The data collected will be used for advanced post processing techniques such POD, Proper Orthogonal Decomposition, and LSE, Linear Stochastic Estimation.

3. Future plans

The next steps of this project will be the detailed design, the manufacturing and the assembly of the whole setup. We will also install a silencer for the dual flow to avoid noise contamination coming from the valves. Particular care will be put on the manufacturing of the nozzle, with the smallest achievable leap thickness, to avoid screech. The transverse for the microphones and for the LDV system will also be designed to achieve a good level of accuracy and efficiency.

Acknowledgments

I wish to acknowledge the European Commission for funding this project through the Marie Curie Grant Agreement ITN AeroTraNet2 as part of FP7 program, and the VKI Technical Drawing Office for the high level of accuracy and cooperation.

References

[1] C. Tam, N. Pastouchenko, K. Viswanathan, Broadband Shock-Cell Noise from Dual Stream Jets, in: Aeroacoustics Conferences, American Institute of Aeronautics and Astronautics, 2008.

[2] G. M. Carlomagno, T. Astarita, Slides from course of Gasdynamics, Università degli Studi di Napoli "Federico II" (2009).

[3] A. Jeronimo, Application of PIV to a Supersonic Jet, Project Report 2001-28, von Karman Institute (June 2001).

[4] S. Miller, P. Morris, The Prediction of Broadband Shock-Associated Noise from Dualstream and Rectangular Jets Using RANS CFD, in: Aeroacoustics Conferences, American Institute of Aeronautics and Astronautics, 2010.

[5] A. Savarese, P. Jordan, S. Girard, E. Collin, M. Porta, Y. Gervais, Experimental study of shock-cell noise in underexpanded supersonic jets, in: Aeroacoustics Conferences, American Institute of Aeronautics and Astronautics, 2013, pp. –.

[6] A. Kiran, Jet Noise: Aeroacoustic Distribution of a Subsonic Co-Axial Jet, Ph.D. thesis, University of Warwick (2008).

[7] K. Viswanathan, Instrumentation Considerations for Accurate Jet Noise Measurements, AIAA Journal 44 (6) (2006) 1137–1149.

Stochastic Modeling of Installation Effects in Environmental Control Systems

Ugur Karban

Environmental and Applied Fluid Dynamics Department, von Karman Institute for Fluid Dynamics, Belgium, ugur.karban@vki.ac.be

Supervisor: Christophe Schram

Associate Professor, Environmental and Applied Fluid Dynamics Department, von Karman Institute for Fluid Dynamics, Belgium, christophe.schram@vki.ac.be

Promotor: Wolfgang Polifke

Professor, Lehrstuhl für Thermodynamik, Germany, polifke@tum.de

Abstract

The aeroacoustic installation effects on a ducted tandem diaphragm are investigated experimentally and numerically. Two different numerical approaches are applied to estimate the noise prediction: a scale-resolved approach and a stochastic approach. A Helmholtz solver is used to calculate the noise propogation inside the duct for both approaches. Comparison data is provided via acoustic, PIV and hotwire measurements.

Keywords: aeroacoustics, stochastic approaches, SNGR, LES

1. Introduction

The motivation of this study is to investigate the aeroacoustic installation effects that take place in typical Environmental Control Systems (ECS) found in aircrafts. The focus is here placed on local singularities: isolated and tandem diaphragms. Flow restrictions are indeed implemented in complex ECS configurations in order to balance the mass flow rate between different branches of the ventilation network. To model this problem, we designed a simple case: a tandem diaphragm placed in a cylindrical duct (see Fig. 1.

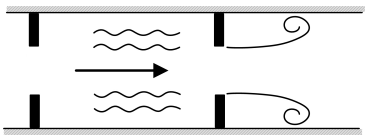

Figure 1: Schematic representation of the model problem. The first diaphragm is used as a turbulence generator, the second one as the main source for the noise generation

The upstream diaphragm induces a complex detached turbulent flow, which perturbations are then convected through the downstream diaphragm. This mechanism is known to generate significant extraneous noise, compared to the noise that would be emitted by the diaphragms if they were not interacting [1] Two different noise prediction methods are investigated in this study: scale-resolved and stochastic methods. In the scale-resolved approach, the pressure fluctuations on the diaphragm surfaces are computed using compressible Large Eddy Simulation (LES) in a first step. In a second step, these pressure data are given as an input of a Helmholtz solver using Boundary Element and Finite Element Methods [2]. The Stochastic Noise Generation and Radiation (SNGR) method, initiated by [3] and recently revisited by [4], is here applied to predict the extraneous noise level induced by the interaction between the two diaphragms. The stochastic method is used to generate a synthetic solenoidal velocity field, from which acoustic sources are computed and again used as the input of the Helmholtz solver.
On the experimental side, acoustic measurements have been carried out, highlighting significant installation effects. Noise propagated through the inlet of the duct is measured by two free-field microphones and flush-mounted microphone arrays. Particle Image

Velocimetry (PIV) and hotwire measurements provided two-dimensional, two-components validation data for the numerical approaches described above.
To understand the installation effects of a tandem diapragm located inside a duct, two configurations are investigated both numerically and experimentally:

1. Tandem diaphragm case: diaphragms apart from each other with an axial distance equal to two times the duct diameter.
2. Single diaphragm case: investigated to have a clear understanding of the effects of the second diaphragm in the tandem diaphragm case.

Diaphragm-to-duct ratio in diameter is set as 0.57 for all cases. For the tandem diaphragm case, the two diaphragms are separated from each other with a distance such that the flow interactions between the diaphragms dominated the noise field without facing any whistling. The frequency of interest of this study is restricted to the plane wave region not to deal with complex scattering mechanisms inside the duct.

2. Aeroacoustic Installation Effect: Experimental Analyses

The experimental rig for the duct flow test case is installed in the anechoic room of the von Karman Institute for Fluid Dynamics.The anechoic chamber, specifically designed for studying and certifying free and ducted fan noise, is split in two rooms, connected through acoustic dampers to an external blower that permits controlling the mass flow rate through the ducted diaphragms in this work. The duct is composed of modules corresponding to various flow obstructions and instrumented sections (static pressure probes, radial and azimuthal hot wire traversing system, microphone multi-ports, loudspeaker arrays). The modules are made of plexiglass to have optical access for the PIV measurements. An inlet bellmouth provides a clean inlet flow. The details of the setup is shown schematically in Fig. 3.

Experimental analyses are conducted in two phases: acoustic measurements and flow velocity measurements. In terms of the acoustic measurements, investigation of the aeroacoustic noise generation and propagation through outside-duct, and in-duct acoustic measurements are taken. As the flow velocity measurements, investigation of the flow field through PIV and hotwire measurements is performed. While determining flow velocity, there

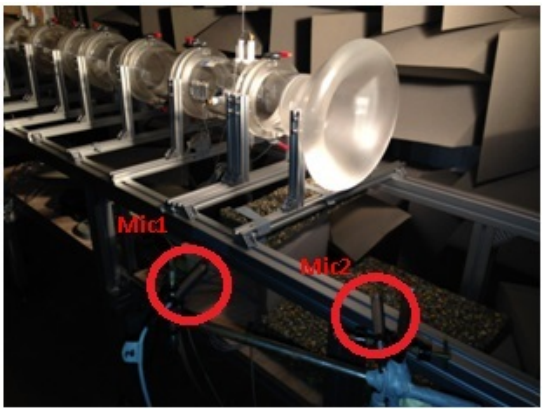

Figure 2: Duct system made of plexiglass

have been a compromise between the computational costs of the LES simulations and the measured noise levels. To determine minimum flow speed which will provide satisfactory increase in the noise levels as it is switched from single diaphragm to tandem diaphragm case, we performed some preliminary outside-duct acoustic measurements. Two free-field microphones both facing towards the center of the bellmouth are located at the positions depicted in Fig. 3.

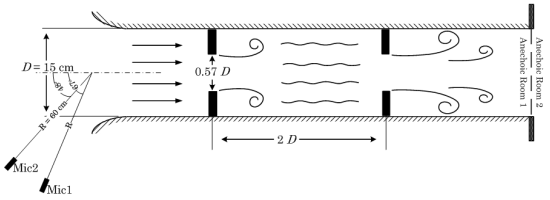

Figure 3: Schematic representation of the experimental setup for the outside-duct measurements

The outside-duct measurements revealed that it is possible to observe significant changes in the noise levels when swithced between different duct configurations with a bulk inflow velocity of $6m/s$. It can be seen in Fig. 4 that the background noise is at least 20 decibels (dB) lower than the noise measured with the single diaphragm in plane wave region which corresponds to the frequency range of interest. Adding the second diaphragm further increases the level of noise by about another $20dB$ for plane wave region, or $10dB$ when higher modes are propagative as well.

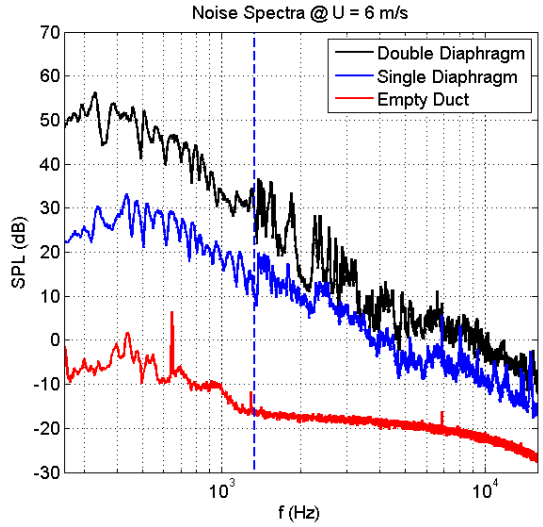

Figure 4: Noise spectra obtained from outside-duct acoustic duct measurememnts for different duct configurations. The vertical dashed line indicates the first cut-off frequency

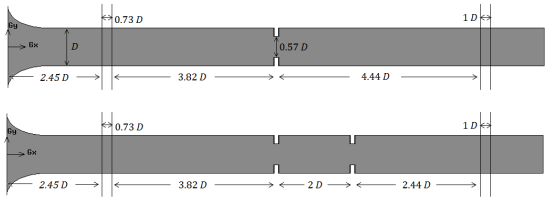

Figure 5: Microphone positions for in-duct acoustic measurements. The vertical line pairs located at the upstream and downstream of the diaphragm(s) indicate the cross-sections where the microphones installed. Four microphones evenly distributed in azimuthal direction are located at each cross-section.

For the in-duct acoustic measuremets, the rig is equiped with axial and azimuthal microphone arrays comprising eight microphones on each side of the diaphragm(s) modules, which are used to isolate the planar and first azimuthal modes radiated through the duct. For both the upstream and downstream parts of the diaphragm(s), two consecutive sections of microphone arrays are formed by putting four microphones on each section which are evenly distributed in azimuthal direction. The two sections are separated from each other by $0.73D$ and $1D$ distances in the upstream and downstream parts, respectively (see Fig. 5). The distances between the consecutive microphone array sections are selected large enough for the flow related noise contained in the microphone measurements to be uncorrelated. As a future work, the procedure developed by [5] for the projection of the acoustic field in the duct modes, using microphone arrays, will be followed to eliminate the uncorrelated turbulent noise and to identify the planar modes from the in-duct measurements. The results for the section closest to the inlet are presented in Fig. 6.

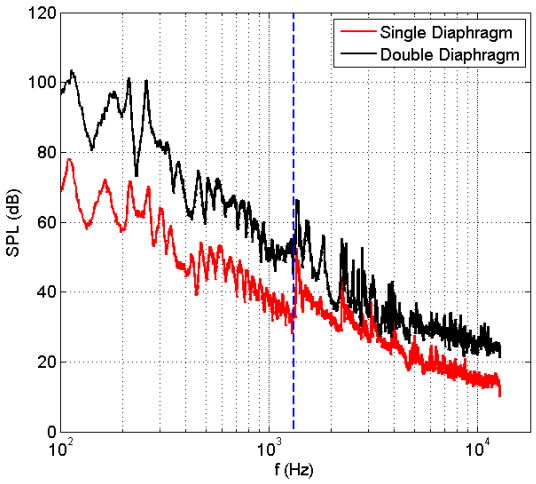

Figure 6: Noise spectrum obtained from inside-duct acoustic measurements for single and double diaphragm configurations. The vertical dashed line indicates the first cut-off frequency.

The validation of the numerical flow field is performed by dedicated PIV and hotwire measurements. PIV measurements are taken on the longitudinal symmetry plane of the duct in the upstream region close to the diaphragm for single diaphragm case, and upstream of the second diaphragm for the tandem diaphragm case using a pulsed laser at $5Hz$. The measurement window is $0.8D$ and $0.9D$ in the axial and radial directions, respectively. The hotwire measurements are taken at different cross-sections on the upstream and downstream of the diaphragm(s). A schematical illustration of these areas where the PIV and the hotwire measurements are taken can be seen in Fig. 7. The results of PIV, hotwire and in-duct acoustic measurements are presented in comparison with the numerical results in the following section.

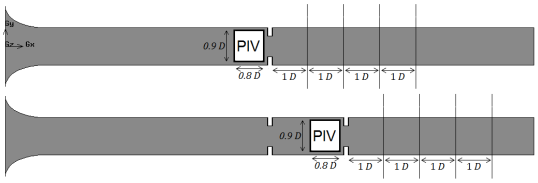

Figure 7: Measurement positions for PIV and hotwire. The white boxes and the vertical lines indicate the PIV measurements windows and hotwire scanning planes, respectively.

3. Flow realizations: Large Eddy Simulation (LES) and Reynolds Averaged Navier Stokes (RANS) computations

3.1. LES computations

The LES solver adopted in this work is AVBP [1], developed by CERFACS. This code solves the fully compressible Navier-Stokes equations on unstructured meshes. A second order Lax-Wendroff scheme and an explicit Euler scheme is selected to discretize the spatial and the temporal derivatives respectively. The time steps of the simulations is fixed after reaching the stationary flow condition, to afford a CFL number of 0.7. The latter let to achieve stable simulations while granting low acoustic dissipation and dispersion errors in the domain under analysis. The large turbulent eddies (compared to the mesh elements size) are resolved whereas the subgrid scales are resolved by means of the so called Wall-Attached-Layer-Eddy (WALE) model.

The computational mesh consists of 1.2×10^7 elements for the single diaphragm case whereas for the tandem diaphragms case 1.55×10^7 elements is utilized. Both meshes consists of hexahedral elements structured according to an O-grid topology around the diaphragm. The grid is refined in radial direction with elements of the order of the Taylor microscales. This choice let to resolve correctly the inertial turbulent scales whereas the viscous scales are handled as subgrid scales. In order to capture correctly the turbulent-generated noise, the boundary layer developed at the diaphragms is resolved. This is done by further refining the computational grid to have the first cell near the wall in the viscous sublayer, i.e. for a radial unit wall $r^+ = 5$.
The simulations are carried out assuring as less acoustic reflections as possible at the boundaries. Therefore boundary conditions adopted consists of a modified version of the Navier-Stokes Characteristic Boundary Conditions (NSCBCs) [6] based on the so called Plane Wave Masking method [7]. The wall boundary is described by an adiabatic no-slip condition. At the inlet a constant velocity profile of $U = 6m/s$ is assumed whereas at the outlet a constant standard pressure $P = 101325Pa$ is imposed.

3.2. RANS computations

RANS computations are performed for single and tandem diaphragm cases to be provided as a basis for the SNGR method using Ansys Fluent 15.0 solver.

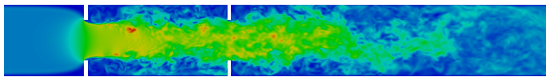

Figure 8: Instantaneous velocity field obtained from LES computation.

The *realizable* $k-\epsilon$ (RKE) model is selected as the turbulence model for the RANS computations. regarding similar works found in the literature where flow passing through a single diaphragm is investigated. In [8], RKE model shows good agreement in a ducted flow case passing through an diaphragm. The diaphragm-to-duct ratio in diameter and the Re number of the given work are 0.5 and 9×10^4 while they are 0.57 and 7×10^4 in our case, respectively. The computational meshes consist of hexahedrals with the total number of elements equal to 8×10^6 for the single diaphragm case and and 1×10^7 for the tandem diaphragm case. The inlet boundary condition is given as uniform flow with $U = 6m/s$.

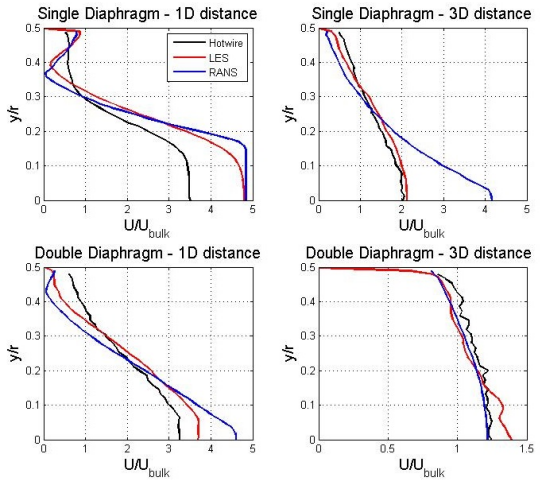

Figure 9: Comparison of the mean velocity profiles for single (top) and double (bottom) diaphragm cases. Figures on the left are measured at a distance of $1D$, figures on the right are measured at a distance of $3D$ downstream the diaphragm(s).

The bulk inflow velocity set for the PIV and hotwire measurements is $5.43m/s$ which is slightly lower than the ones used for the simulations and acoustical measurements. Looking at the mean velocities at different axial locations downstream the diaphragm(s) in Fig. 9, the velocity profiles obtained from LES computations and hotwire measurements matches better as further distance covered towards the downstream of the diaphragm, i.e. the velocity field is distributed more

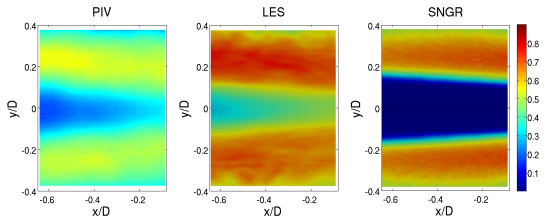

Figure 10: Turbulence intensity comparison between PIV (left), LES (center) and SNGR (right) for double diaphragm case. The horizontal axes of the plots corresponds to axial positions which are offseted to the second diaphragm.

homogeneuously. It can be seen that RANS method overestimates the length of the jet core in single diaphragm case although, in double diaphragm case, it manages to capture the same velocity profile with hotwire on the cross-section which is apart from the diaphragm with a $3D$ distance. Comparing the turbulence intensities calculated from PIV, LES and SNGR data for tandem diaphragm cases in Fig. 10, it can be seen that both numerical methods overestimates the turbulence generation.

4. Prediction approaches: LES based and SNGR

Two numerical approaches are compared for the investigation of the noise prediction problem. As the dominant sources for aeroacoustic noise generation, the pressure fluctuations on the walls of duct and diaphragm(s) are computed from LES and SNGR datasets. Later on, these fluctuation data are used as input to the Helmholtz solver mentioned above. The details of the two methods and the results obtained in comparison with acoustical measeurements are given in the following subsections.

4.1. LES approach

A compressible LES solver explained in detail in the previous section is used to obtain the pressure field and the dipoles on the boundaries of the domain are calculated using these unsteady pressure data. Being restricted to the plane wave region, only the surfaces having normals parallel to the longitudinal axis, i.e the direction propagation in this frequency range, are taken into account which basically correspond to the frontal and rear faces of the diaphragm(s).

Again being in the plane wave region, a further simplification is introduced by integrating these dipoles over the diaphragm surfaces to obtain a resultant point dipole which replaces the diaphragm itself (see Fig. 11). Results for this approach are presented at the end of the section.

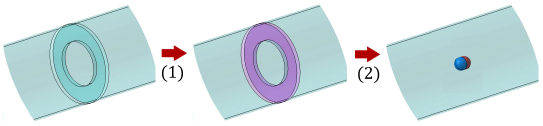

Figure 11: Procedure for calculating the noise sources in LES based method. First the dipoles on the faces of the diaphragm(s) perpendicular to the longitudinal axis are computed (1), and these distributed dipoles are summed up to a resultant point dipole which represents the effect of the diaphragm (2).

4.2. SNGR approach

The stochastic approach followed is the SNGR method, initially derived by [3] and revisited by [4]. The velocity field at the initial time is obtained by the superposition of spatial Fourier modes with weighted amplitudes yielding a target distribution of energy vs. wavenumbers:

$$\mathbf{u}_t(\mathbf{x},t) = 2\sum_{n=1}^{N} \hat{u}_n cos(\mathbf{k}_n(\mathbf{x}-u_c t)+\psi_n+\omega_n t)\sigma_n \quad (1)$$

where $\mathbf{k}_n$ is the wavevector whose magnitude gives the wavenumber, u_c is the convection velocity, and $\hat{u_n}$, ψ, and σ_n are the amplitude, phase and direction of the nth Fourier mode respectively. σ_n is defined on a plane normal to $\mathbf{k}_n$ to obtain a solenoidal velocity field (see Fig. 12.

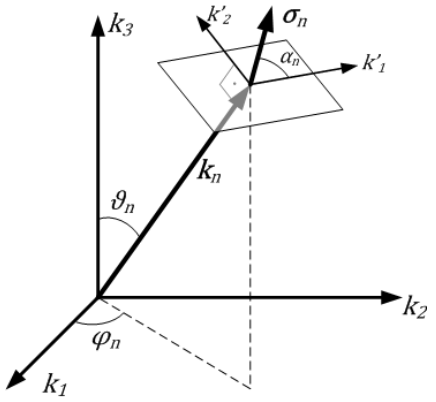

Figure 12: Geometric representation of a wave vector.

ω_n is a randomly selected phase bringing time-decorrelation to the synthesized fields. A normal distribution defined as a function of k wavenumber is used to obtain a random distribution for this frequency:

$$p(\omega) = \frac{1}{\omega_{on}\sqrt{2\pi}} e^{-\frac{(\omega-\omega_{on})^2}{2\omega_{on}^2}} \quad (2)$$

where the mean angular frequency of the nth mode $\omega_{on} = \sqrt{K}\, k_n$. In this work, the von Karman-Pao spectrum is used, which represents the energy spectrum for isotropic turbulence:

$$E(k) = \alpha \frac{2K/3}{k_e} \frac{(k/k_e)^4}{[1 + (k/k_e)^2]^{17/6}} e^{-2(\frac{k}{k_\eta})^2} \tag{3}$$

where K is the turbulent kinetic energy, k_e and k_η are the wavenumbers corresponding to the integral and Kolmogorov length scales; namely, k_e represents the length scales which contain the most kinetic energy and k_η is the Kolomogorov wavenumber. These scales are locally calculated by the following two equations which use the mean statistical properties of the flow as input;

$$k_\eta = \epsilon^{1/4} \nu^{-3/4} \tag{4}$$

$$k_e = \frac{9pi}{55} \frac{\alpha}{\Lambda} \tag{5}$$

where ν, ϵ and Λ correspond to the kinematic viscosity, dissipation rate and the integral length scale, respectively. The integral length scale is computed as follows;

$$\Lambda = f_L \frac{K^{-3/2}}{\epsilon} \tag{6}$$

The term α in Eq. 3 is a coefficient to scale the spectrum so that the integration of the spectrum along $(0, k)$ where $k \to \infty$ yields the turbulent kinetic energy. To have such an equality;

$$\alpha = \frac{4}{\sqrt{pi}} \frac{\Gamma(17/6)}{\Gamma(1/3)} \tag{7}$$

4.2.1. *Investigating a simple test case: Homogeneous Turbulence in a Cartesian Box*

The procedure is applied for a simple test flow where the flow velocity, turbulent kinetic energy and the dissipation rate is constant over a rectangular prismatic domain. Here the definition $K = 2/3u'^2$ is used to calculate the turbulent kinetic energy, however since k_n is a finite number, the energy calculated by integrating the von Karman-Pao energy spectrum (denoted as K_{eff} effective turbulent kinetic energy) is slightly less than this value. The ratio K_{eff}/K is found to be 0.966. The energy spectrum of the synthetic turbulent field is compared with the theoretical one in Figure 13.

The two-point correlations $f(r) = \overline{(u_1)_A (u_1)_B} / (u_1)_A^2$ and $g(r) = \overline{(u_2)_A (u_2)_B} / (u_2)_A^2$ have been obtained from the synthetic fields, and also space-time correlations are calculated using the expression

$$R(r, \tau) = \frac{\langle u_i(\mathbf{x}, t)\, u_i(\mathbf{x} + r\mathbf{e_1},\, t + \tau) \rangle}{\langle u_i(\mathbf{x}, t)^2} \tag{8}$$

where $\mathbf{e_1}$ represents the unit vector along the streamwise direction. This means that only longitudinal correlations are included in space-time correlation calculations. The effect of adding the de-correlating term $\omega_n t$ in Eq. 1 is assessed in Figure 15, by setting $\omega_n = 0$ (corresponding to frozen turbulence, left graph) or using the probability density function in Eq. 2 (right graph). Applying space-time correlation for the frozen field yields parallel contour lines over space-time separation domain, which slope is the convection velocity. When de-correlation is applied, elliptic curves are expected.

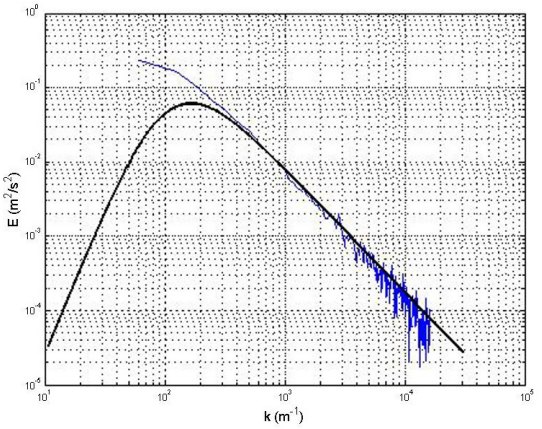

Figure 13: Energy spectrum of the synthetic turbulence: von Karman-Pao energy spectrum (black), synthesized energy spectrum (blue).

4.2.2. *Investigating the Single and Tandem Diaphragm Cases*

Once the basic statistical properties for the cartesian test case are satisfied, SNGR method is applied on the single and tandem diaphragm cases. Instead of using predefined constant values for turbulent kinetic energy, dissipation rate and the convection velocity, these data are taken from a RANS solution. Obtaining the RANS solutions, a synthetic turbulent velocity field is generated for both cases based on these RANS solutions following the procedure explained above.

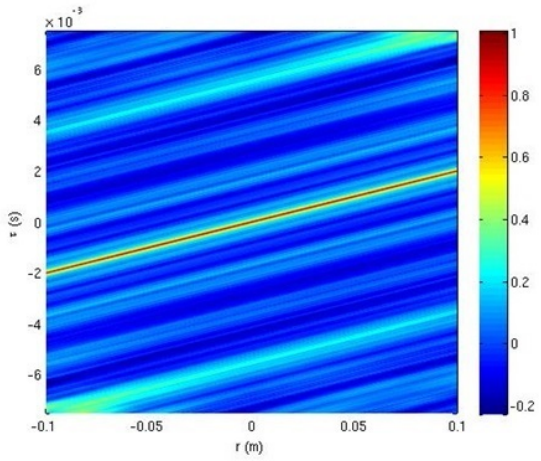

Figure 14: Space-time correlations for frozen turbulence.

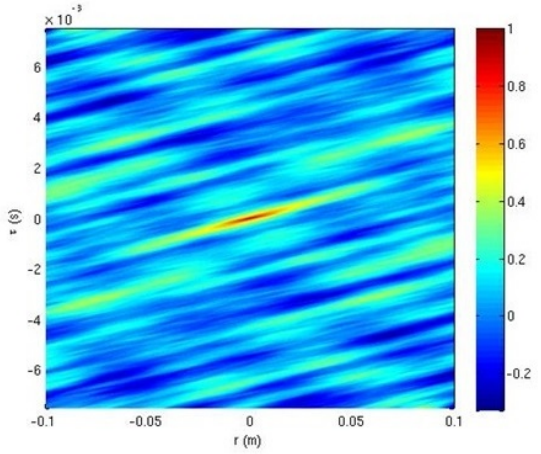

Figure 15: Space-time correlations for de-correlating turbulence.

The turbulent kinetic energy (TKE) distribution obtained from RANS and calculated from the synthesized field are compared in Fig. 15 and 16 for the single and tandem diaphragm cases, respectively. The given TKE distributions are normalized with respect to the dynamic pressure of the incoming flow. It can be seen that SNGR method is clearly capable of reproducing the TKE distribution over the domain. Using the synthetic turbulent velocity field, Lighthill stress tensor which is used as the noise source term is computed. Time-averaged distributions of these noise source terms computed using SNGR method are compared with the ones computed using LES method and PIV measurements in Fig. 17.

Noise Generation and Radiation

After obtaining the Lighthill stress terms, i.e.

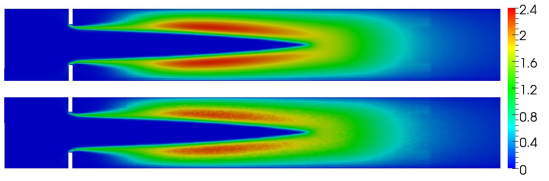

Figure 16: Comparison of the normalized TKE distributions for single diaphragm case obtained from RANS (top) and SNGR (bottom).

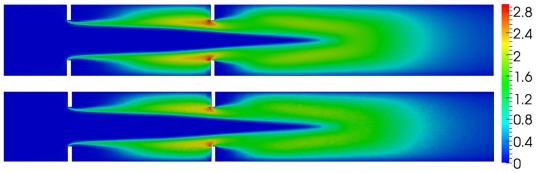

Figure 17: Comparison of the normalized TKE distributions for tandem diaphragm case obtained from RANS (top) and SNGR (bottom).

quadrupoles, the next step is to convert this data to pressure fluctuation data on the duct surfaces. Given a wave propagation for any variable φ;

$$\frac{\partial^2 \varphi}{\partial t^2} - c_0^2 \frac{\partial^2 \varphi}{\partial x_i^2} = 0 \tag{9}$$

and normalization parameters L for length scale, and τ for time scale so that $\tilde{t} \equiv t/\tau$ and $\tilde{x} \equiv x/L$, wave equation becomes;

$$\frac{\partial^2 \varphi}{\partial \tilde{x}_i^2} = \left(\frac{L}{c_0 \tau}\right)^2 \frac{\partial^2 \varphi}{\partial \tilde{t}^2} \tag{10}$$

where $L/(c_0\tau)$ is defined as Helmholtz number He. It can be easily seen that as $He \to 0$, eq. 10 reduces to;

$$\nabla^2 \varphi = 0 \tag{11}$$

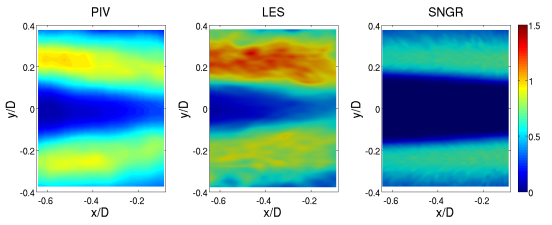

Figure 18: Axial component (Txx) of Lighthill stress tensor calculated using PIV (left), LES (center), SNGR (right) data for double diaphragm case. Turbulent velocities normalized with the bulk velocity are used.

which is the Laplace equation describing an incompressible irrotational flow. This brief analysis shows that, for small Helmholtz numbers; namely, acoustically compact regions, wave propagation equation reduces to incompressible potential flow equation. Therefore, given the source terms and using a wave equation solver, for instance a Helmholtz solver, it is possible to obtain an incompressible flow solution for an acoustically compact region. This solver has been used with success to simulate HVAC noise radiation [2] up to non-compact frequency range. The wavelength corresponding to the the first cut-off frequency is $0.25m$ which corresponds the same order of magnitude with the duct diameter. This let us to define an acoustically compact region downstream the diaphragm and upstream the second diaphragm for the tandem diaphragm case which is large enough to contain a certain amount of quadrupoles calculated using the SNGR method. Decreasing the number of quadrupoles introduced to the system to reduce the complexity, we grouped the quadrupoles inside the compact region and performed a volumetric summation of them to compute the resultant sources located at the volumetric centers of each group. Fig. 19, 20 and 21 schematically depict these concentrated sources as colored blocks where the actual position of the sources are defined as the volumetric center of these blocks.

Different cases investigated while performing noise estimation for the single and tandem diaphragm configurations are given as follows;

1. SNGR method with nearest quadrupole blocks downstream the diaphragm.
2. SNGR method with all the quadrupole blocks enclosing the entire flow domain.
3. LES based method with point dipoles replacing the diaphragm(s).

with a modeling level in decreasing order; namely, number of assumptions used in modeling is less.

The results of these three cases in comparison with the acoustical measurements are given in Fig. refsinglediap and reftandemdiap for the single and tandem diaphragm configurations, respectively. The noise spectra obtained using the LES method with the point dipoles, provided the best match with the measured spectra for both single and double diaphragm configurations although it significicantly underestimates the noise level for the frequencies lower than $40Hz$. The SNGR method with single section of quadrupole

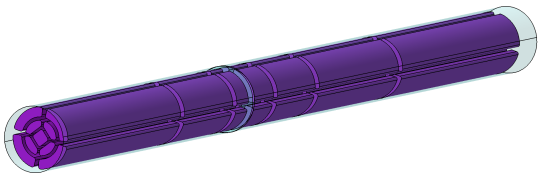

Figure 19: Blocks containing all the quadrupoles inside the flow domain for single diaphragm case. Sources contained by each block are summed and introduced as a concentrated source at the volumetric center of the block. The set for tandem diaphragm case is located downstream the second diaphragm.

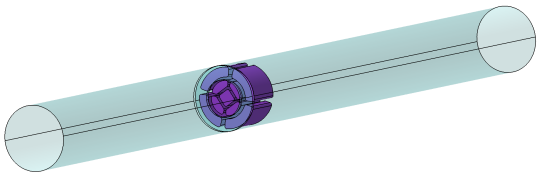

Figure 20: Quadrupole set selected downstream the diaphragm in an acoustically compact region with respect to the first cut-off frequency for single diaphragm case.

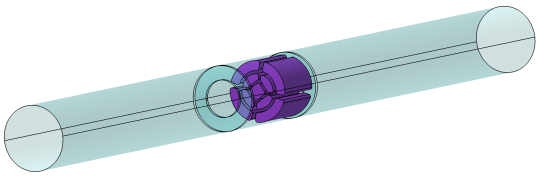

Figure 21: Quadrupole set selected upstream the diaphragm in an acoustically compact region with respect to the first cut-off frequency for tandem diaphragm case.

blocks yields spectra following the same pattern with LES method for lower frequencies. It appears that these methods require deeper investigation through numerous implementation which is set as the future goal.

5. Conclusions

Flow passing through a tandem diaphragm configuration placed in a duct is investigated both numerically and experimentally. The acoustic measurements indicates a clear predominance of the tandem diaphragm noise over the single diaphragm, particularly below the the first cut-off frequency. PIV and hotwire measurements are performed to provide validation data for numerical analyses. LES and RANS computations are performed to obtain a numerical solution for the flow field. LES provided a better representation of the flow field when compared

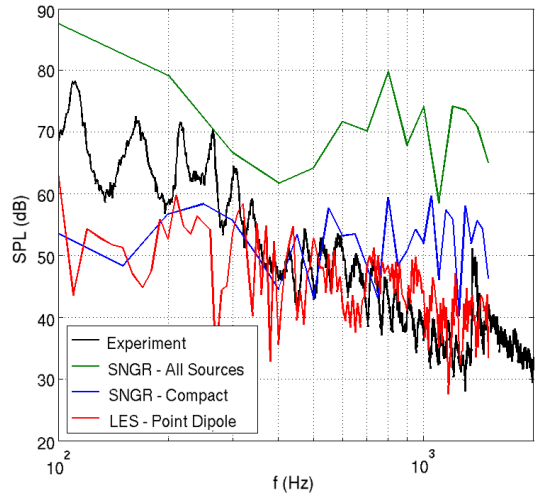

Figure 22: Noise spectra comparison for single diapragm case.

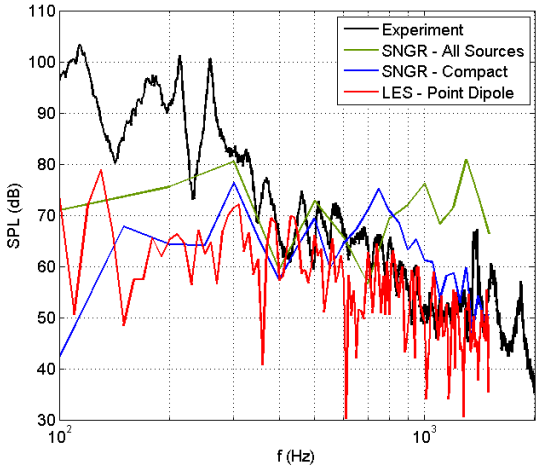

Figure 23: Noise spectra comparison for tandem diapragm case.

to the RANS.

The methodology to be used in the SNGR analyses for acoustic source definition and radiation provides reasonable time and space correlation properties in a generic cartesian volume, and is also capable of reproducing the turbulent kinetic energy distribution based on the RANS solution. Noise estimation is conducted using the two methods introduced: scale resolved and stochastic approaches. Some preliminary results are obtained which form a basis for further investigation.

References

[1] A. Sengissen, B. Caruelle, P. Souchotte, E. Jondeau and T. Poinsot, LES of Noise Induced by Flow Through Double Diaphragm System, no. 15th AIAA/CEAS Aeroacoustics Conference, Miami, 2009.

[2] P. Martinez-Lera, R. Hallez and H. Beriot, Computation of Sound in a Simplified HVAC Duct based on Aerodynamic Pressure, no. 18th AIAA/CEAS Aeroacoustics Conference, Colorado Spring, 2012.

[3] W. Bechara, C. Bailly and P. Lafon, Stochastic Approach to Noise Modeling for Free Turbulent Flows, AIAA Journal 32 (3).

[4] D. Casalino and M. Barbarino, A Stochastic Method for Airfoil Self-Noise Computation in Frequency-Domain, no. 16th AIAA/CEAS Aeroacoustics Conference, Stockholm, 2010.

[5] S. Sack, M. Abom, K. Kucukcoskun and C. Schram, Generation and Scattering of Acoustic Modes in Ducts with Flow, no. 20th AIAA/CEAS Aeroacoustics Conference, Atlanta, 2014.

[6] T. J. Poinsot and S. K . Lele, Boundary conditions for direct simulation of compressible viscous flows, Journal of Computational Physics 101 (1992) 104–129.

[7] W. Polifke, C. Wall and P. Moin, Partially reflecting and non-reflecting boundary conditions for simulation of compressible viscous flows, Journal of Computational Physics 213 (2006) 437–449.

[8] M. S. Shah, J. B. Joshi, A. S. Kalsi, C. S. R Prasad and D. S. Shukla, Analysis of flow through an orifice meter: CFD Simulation, Chemical Engineering Science 71 (2012) 300–309.

NUMERICAL APPROACH FOR HYPERSONIC AND PLASMA FLOWS

Multi-Fluid Modeling of Magnetic Reconnection in Astrophysical and Laboratory Plasmas

Alejandro Alvarez Laguna

Aeronautics and Aerospace Department, von Karman Institute for Fluid Dynamics, Belgium, alejandro.alvarez.laguna@vki.ac.be

Supervisor: Herman Deconinck

Professor and Dean of the Faculty, Aeronautics and Aerospace Department, von Karman Institute for Fluid Dynamics, Belgium, deconinck@vki.ac.be

University Supervisor: Stefaan Poedts

Professor, KU Leuven, Centrum voor mathematische Plasma-Astrofysica, stefaan.poedts@wis.kuleuven.be

Abstract

Improved models for characterizing collisional and reactive magnetized partially ionized plasma are essential to understand the phenomena taking place in astrophysical and laboratory plasmas. Particularly, scenarios where dissipative processes and thermo-chemical inequilibrium play an important role are beyond the classical single-fluid MHD representation. The multi-fluid models that consider each particle species as a separate fluid offer an alternative approach especially suitable for those situations. In the present work, a multi-fluid model considering two fluids, neutrals and charged species, is applied to simulate the magnetic reconnection taking place in the chromosphere.

Keywords: Magnetohydrodynamics (MHD), Magnetic Fields, Plasmas, Magnetic Reconnection, Sun: Atmosphere.

1. Introduction

The activity of the Sun has a great impact in our technology and ultimately in today's modern society that strongly depends on communications and satellite operations. From a global socio-economic perspective, the most important manifestations of solar activity are the solar wind and solar eruptions, i.e. solar flares and coronal mass ejection (CMEs). The unsteady but continuous emission of particles at high speed and temperature from the Sun into the space can hinder human activity at different levels. Satellite operations can be seriously affected by plasma ejected during solar storms, producing important damages or the loss of some of them, like the Telstar 401 that was short cut in January 1997. More recently, in 2003, a solar storm caused disruptions in the airplane routes and the CME affected several communication satellites (two were total loss). Also, when the high energetic charged particles ejected from the Sun reach our atmosphere can produce the so-called Geo-magnetically Induced Currents (GICs) that cause hazards in oil pipelines and power grid outages. An example of the latter is the magnetic storm that burned a $36 million transformer in New Jersey and left 6 million people more than 10 hours without electrical power in Quebec in winter conditions (March 1989). As a matter of fact, the cost of a severe space storm has been estimated to be trillions of dollars for the first year after the storm with recovery times of 4 to 10 years (an order of magnitude more than that of Hurricane Katrina) [1].

It is therefore necessary to improve the understanding and modeling of the phenomena taking place in the Sun for enhancing the tools used for the space weather forecasting and eventually reducing its risk on our technology. Magnetic reconnection is a process especially significant in space weather since it has been long considered as a mechanism for creating transient phenomena in magnetized plasma. It oc-

curs when oppositely directed magnetic field lines in conducting plasma merge due to diffusive processes producing a change of topology. The rearrangement of magnetic field lines produces a change of the magnetic flux that due to the finite conductivity creates a current sheet. In addition, the reconnection process causes a conversion of magnetic energy into kinetic and thermal energy, heating up the flow and accelerating it up to very high speed in very small timescales.

There are a wide variety of astrophysical scenarios in which the magnetic reconnection plays an important role. It is considered to be a likely mechanism to heat the corona to a few million degrees, still one of the biggest mysteries in Heliophysics [2]. Also, in CMEs and solar flares it is considered as a triggering mechanism which is present during the onset and early stages of the ejection [3]. In the Earths magnetosphere it is said to produce the plasma outflow at the magnetotail that is driven by the Earths magnetic field into the atmosphere producing the aurorae borealis and the GICs [4].

In the present work, we will focus on studying the magnetic reconnection in the Sun chromosphere, following the work presented in [5]. Observational data [6] have unveiled that the magnetic reconnection is the driver mechanism for the chromospheric jets and the spicules. The former can have timescales of 200-1000 s and current sheet length scales up to 5 Mm, producing outflows of 10 km/s. On the other hand, the spicules are smaller but faster phenomena, that last 10-600 s in length scales up to 1 Mm causing outflows up to 20-150 km/s [5].

The main goal of this study is the validation, throughout the comparison with the literature [5], of the numerical methods designed and implemented. Therefore, it can be considered as the starting point of a research that will be extended during the PhD. Future works will be targeted towards the improvement of magnetic reconnection models using multi-fluid description able to overcome the limitations of the standard single-fluid MHD. The ultimate goal is the development of efficient numerical tools that will be able to integrate the magnetic reconnection models in full-scale domains representing coronal mass ejections with improved fidelity.

2. Modeling of the magnetic reconnection

Magnetic reconnection is a process that happens as a result of a diffusive mechanism that produces a decay in the electrical conductivity of the plasma. The frozen-in constrain that holds in ideal plasmas (with infinite conductivity) is broken in a small region of width δ and length L. In this region, the magnetic field lines reconnect producing a rate of magnetic flux that results in the formation of a current sheet. Thus, the non-dimensional magnetic reconnection rate is defined [7] as follows:

$$M = \frac{d\Phi/dt}{v_A B_i} \tag{1}$$

where Φ is the magnetic flux per unit length in the direction perpendicular to the plane containing the current sheet , v_A is the Alfven speed and B_i is the magnetic field evaluated upstream of the current sheet.

Therefore, it is obvious to realize that the classical ideal MHD equations that consider the conductivity to be infinite are not able to tackle the physics involved in the reconnection. Nevertheless, the resistive singlefluid theory has developed analytical models for 2D steady magnetic reconnection. The Sweet-Parker model [8] proposes a non-dimensional reconnection rate of the form:

$$M = R_m^{-1/2} \tag{2}$$

where

$$R_m = v_A L/\eta \tag{3}$$

is called the Lundquist number, and η is the resistivity.

However, the model is unable to explain the fast energy released by the solar flares or in chromospheric jets and spicules, providing reconnection rates several orders of magnitude smaller.

On the other hand, the Petschek model [9] predicts faster reconnections suggesting geometry different from the Sweet-Parker one, Eq. 4. However, the model assumes explicitly or tacitly that resistivity gives the configuration setup. Because of this controversial issue, the Petschek model has been gradually thrown back [10].

$$M = \frac{\pi}{8 \ln(R_m)} \tag{4}$$

Therefore, it is necessary to consider alternative theories to model the reconnection. The multi-fluid models consider each particle species as a different fluid that interact among each other by means of collisions and chemical reactions, exchanging thus mass, momentum and energy in their interplay. Since the width of the diffusion region can be comparable to

the ion scales [4], therefore, the multi-fluid description are considered to capture diffusive effects that are completely neglected by the single-fluid theory.

In the literature, one can find several fluid closures accounting for the different behavior of the species of plasmas in presence of electromagnetic fields. Braginskii [11] derives a two-fluid formulation considering separate ions and electrons. In his seminal work, he proposes closures for the transport properties, accounting for the anisotropy introduced by the magnetic field. Similarly, Magin [12] proposes a multicomponent model separating heavy particles and electrons, treating the effect of the magnetic field on the transport properties. Most recently, Meier [13] has proposed a two-fluid model considering the charged particles and neutrals as separate fluids, considering both anisotropic effects in the plasma heat conduction due to the magnetic field and chemical reactions (ionization and recombination).

3. Governing Equations

The multi-fluid description used in the results shown hereafter is the model discussed in [13]. It is a two-fluid model that considers separately neutrals and charged species, i.e. hydrogen ions and electrons. The full set of equations considered comprises mass, momentum and total energy conservation for both fluids. The chemical reactions considered are electron impact ionization and radiative recombination. The excited states are not tracked, only an effective potential is assumed ϕ_{ion} for the ionization reaction. The plasma is assumed to be optically thin, so the radiation effects are completely lost from the system. Electrons are considered to be in thermal equilibrium with ions, allowing neutrals to be in non-LTE. Charge neutrality is assumed and the electrons inertia and viscosity is neglected. This simplifications yields the following system:

$$\frac{\partial \rho_i}{\partial t} + \nabla \cdot (\rho_i \vec{v}_i) = m_i(\Gamma_i^{ion} + \Gamma_i^{rec}), \tag{5}$$

$$\frac{\partial \rho_n}{\partial t} + \nabla \cdot (\rho_n \vec{v}_n) = m_n(\Gamma_n^{ion} + \Gamma_n^{rec}), \tag{6}$$

$$\frac{\partial \rho_i \vec{v}_i}{\partial t} + \nabla \cdot (\rho_i \vec{v}_i \vec{v}_i + p_i + p_e) = -\nabla \cdot (\pi_i) + \vec{j} \times \vec{B} + \vec{R}_i^{in} + \Gamma_i^{ion} m_i \vec{v}_n - \Gamma_n^{rec} m_i \vec{v}_i, \tag{7}$$

$$\frac{\partial \rho_n \vec{v}_n}{\partial t} + \nabla \cdot (\rho_n \vec{v}_n \vec{v}_n + p_n) = -\nabla \cdot (\pi_n) - \vec{R}_i^{in} - \Gamma_i^{ion} m_i \vec{v}_n + \Gamma_n^{rec} m_i \vec{v}_i, \tag{8}$$

$$\frac{\partial}{\partial t}\left(\varepsilon_i + \frac{p_e}{\gamma_e - 1}\right) + \nabla \cdot \left(\varepsilon_i \vec{v}_i + \frac{\gamma_e p_e}{\gamma_e - 1}\vec{v}_i + p_i \vec{v}_i\right) = -\nabla \cdot (\vec{v}_i \cdot \pi_i + \vec{q}_i + \vec{q}_e) + \vec{j} \cdot \vec{E} + \vec{v}_i \vec{R}_i^{in} + Q_i^{in} - \Gamma_n^{rec} \frac{1}{2} m_i v_i^2 - Q_n^{rec} + \Gamma_i^{ion}\left(\frac{1}{2} m_i v_n^2 - \phi_{ion}\right) + Q_i^{ion}, \tag{9}$$

$$\frac{\partial \varepsilon_n}{\partial t} + \nabla \cdot (\varepsilon_n \vec{v}_n + \vec{v}_n p_n) = -\nabla \cdot (\vec{v}_n \cdot \pi_n + \vec{q}_n) - \vec{v}_n \vec{R}_i^{in} + Q_n^{in} + \Gamma_n^{rec} \frac{1}{2} m_i v_i^2 + Q_n^{rec} - \Gamma_i^{ion} \frac{1}{2} m_i v_n^2 - Q_i^{ion} \tag{10}$$

Where the subindices i, e, n stand for ions, electrons and neutrals. The electrical current follows Ohm's law $\vec{E} + \vec{v}_i \times \vec{B} = \eta \vec{j}$ with the resistivity η assumed to be constant. The reaction rates Γ^{ion} and Γ^{rec} and the reaction energy production Q^{ion} and Q^{rec} are taken from [22] and [23]. The momentum and energy collisional terms $\vec{R}_\alpha^{\alpha\beta}$ and $Q_\alpha^{\alpha\beta}$ considered are discussed in [5]. Ions and neutrals viscosity stress tensor are assumed to be Newtonian, with constant viscosity. Neutrals heat conduction follows Fouriers law with constant thermal conductivity, whereas ions have anisotropic heat flux accounting for the effect of the magnetic field, described in [11]. The fluid are assumed to be perfect gases with $\gamma = 5/3$.

The electromagnetic influence is tackled with the Maxwell equations:

$$\frac{\partial \vec{B}}{\partial t} + \nabla \times \vec{E} = 0 \tag{11}$$

$$\frac{\partial \vec{E}}{\partial t} - c^2 \nabla \times \vec{B} = -\frac{\vec{j}}{\epsilon_0} \tag{12}$$

$$\nabla \cdot \vec{B} = 0 \tag{13}$$

$$\nabla \cdot \vec{E} = \frac{\rho_c}{\epsilon_0} \tag{14}$$

where ρ_c is the charge density that is assumed to be zero.

4. Numerical Modeling

4.1. Finite Volume Method

The results have been obtained using the FV solver for unstructured grids provided by the COOLFluiD platform [14]. The governing equations are written in conservative form, as follows:

$$\frac{d}{dt}\int_{\Omega_i}\mathbf{U}\,d\Omega+\oint_{\partial\Omega_i}\mathbf{F^c}\cdot\mathbf{n}\,d\Sigma=\oint_{\partial\Omega_i}\mathbf{F^d}\cdot\mathbf{n}\,d\Sigma+\int_{\Omega_i}\mathbf{S}\,d\Omega \tag{15}$$

The conservative form of Maxwell equations is found in [15]. The cell-centered FV discretization applies the integral conservation law to each cell, assuming the solution to be constant over the cell and storing the value at the centroid of it. In order to obtain second order accuracy in space, inverse-distance weighted least square reconstruction [16] is used. The multidimensional limiter of Venkatakhrisnan [17] is used to obtain oscillation free solutions. The discretization of the inviscid fluxes is explained hereafter.

4.2. Hyperbolic divergence cleaning for Maxwell equations

One of the biggest concerns in the development of a Maxwell solver is to satisfy the two divergence constrains Eq. 13 and Eq. 14 on the discrete level. The hyperbolic divergence cleaning method [19] is discussed to be an efficient way to enforce the constrains in Finite Volume solvers. Two lagrange multipliers ϕ and ψ are added in Maxwell equations as follows:

$$\frac{\partial\vec{B}}{\partial t}+\nabla\times\vec{E}+\gamma^2\nabla\Psi=0 \tag{16}$$

$$\frac{\partial\vec{E}}{\partial t}-c^2\nabla\times\vec{B}+\chi^2c^2\nabla\Phi=-\frac{\vec{j}}{\epsilon_0} \tag{17}$$

$$\frac{\partial\Psi}{\partial t}+c^2\nabla\cdot\vec{B}=0 \tag{18}$$

$$\frac{\partial\Phi}{\partial t}+\nabla\cdot\vec{E}=\frac{\rho_c}{\epsilon_0} \tag{19}$$

Artificial waves are introduced at speeds γc and χc that remove the errors in the fulfillment of the constrains. Therefore, the two scalar parameters γ and χ should be chosen to be ≥ 1.

4.3. Steger-warming scheme for Maxwell equations

The Steger-Warming scheme [18] splits the flux at the interface into positive and negative components based on the eigenvalue structure of the system as follows:

$$\mathbf{F^c}=\mathbf{A}_+\mathbf{U}^L+\mathbf{A}_-\mathbf{U}^R \tag{20}$$

where

$$\mathbf{A}=\frac{\partial\mathbf{F^c}}{\partial\mathbf{U}}=\mathbf{A}_-+\mathbf{A}_+\text{ and }\mathbf{A}_\pm=\mathbf{R}\Lambda_\pm\mathbf{R}^{-1} \tag{21}$$

where $\mathbf{R}$ is the matrix of right eigenvectors, $\Lambda_\pm$ the diagonal matrix of diagonal matrices with the positive and negative eigenvalues, $\mathbf{U}$ are the conservative variables. The discretization including the divergence cleaning method is discussed in [19]. The method is shown to work standalone and coupled with NS equations of a single conducting fluid [20].

4.4. AUSM scheme for fluid equations

AUSM-family schemes [21] split the inviscid flux of each fluid at the cell interface into the convective part and the pressure flux as follows:

$$\mathbf{F^c}=\mathbf{F^{conv}}+\mathbf{P} \tag{22}$$

with

$$\mathbf{F^{conv}}=\dot{m}\mathbf{\Psi}^{L/R} \tag{23}$$

$\dot{m}$ is the numerical mass flux at the interface and $\mathbf{\Psi}^{L/R}$ is a vector with the variables convected. The superindex L/R denotes that the values are taken from the left or the right neighboring cell to the cell interface as follows:

$$\mathbf{\Psi}=\begin{cases}(1,\ u,\ v,\ w,\ h)_L & \text{if } \dot{m}>0\\ (1,\ u,\ v,\ w,\ h)_R & \text{if } \dot{m}<0\end{cases} \tag{24}$$

The methods to compute the numerical mass flux $\dot{m}$ and the pressure $\mathbf{P}$ at the cell interface are discussed in [21] and [20].

4.5. Implicit time stepping

The resulting set of equations is a very stiff system since it has characteristic speeds ranging from the speed of light to the speed of sound of the different fluids. In order to deal with the strong time step requirements, implicit time stepping is used. The second-order accurate three-point Backward Euler is used:

$$\frac{3}{2}\mathbf{U}^{n+1}-2\mathbf{U}^n+\frac{1}{2}\mathbf{U}^{n-1}=\Delta t\,\mathbf{R}^{n+1} \tag{25}$$

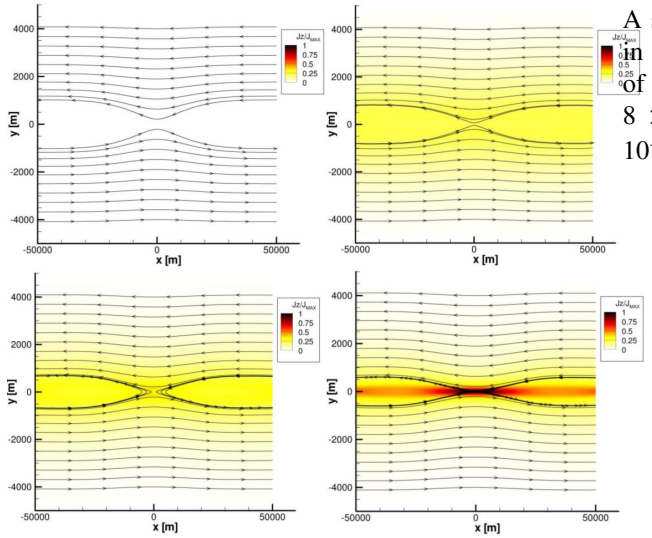

Figure 1: Evolution of the current sheet in the first seconds of simulation. Evolution of magnetic field lines and z-component of the electric current. Top: from left to right, $t = 0$ s and $t = 5$ s. Bottom: from left to right, $t = 10$ s and $t = 20$ s.

5. Results

The abovementioned model and numerical method are applied to reproduce a reconnection scenario under chromospheric conditions. The computational domain extends from -5×10^4 m to 5×10^4 m in the x direction and -5×10^3 m to -5×10^3 m in the y direction. Periodic boundary conditions are used in the x-direction and perfectly conducting boundaries in the y-direction. The simulation domain is divided into 182000 cells (1400×130). The mesh stretches in the center, where the reconnection takes place, up to sizes of the order of one meter, comparable to the neutral-ion collision mean free path.

The initial conditions are chosen to be similar to the middle chromospheric conditions estimated in the 1D model of the Sun [24]. The initial ion number density is $n_0 = 3.3 \times 10^{16} m^{-3}$ and the initial ionization level $n_i/(n_i + n_n) = 0.5\%$. The temperatures are set to 8750 K. A perturbation around the center in the temperature is imposed in order to create a pressure that balances the initial Lorentz force $T_i'(y) = 4366.49/\cosh^2(y/5000)$ K and $T_n'(y) = 5443.43/\cosh^2(y/5000)$ K. All the components of the velocity are set to zero excepting a small ions velocity in the vertical direction: $v_i(y) = 20.1 \tanh(y/5000)/\cosh^2(y/5000)$ m/s. The magnitude of the initial magnetic field is set to $1 \times 10^{-3} T$. A small perturbation around the center is introduced in order to obtain the reconnection in the center of the domain: $B_x = -1 \times 10^{-3} \tanh(y/5000) + 8 \times 10^{-9} y e^{-(x/20000)^2-(y/5000)^2}$ T and $B_y = -5 \times 10^{-10} x e^{-(x/20000)^2-(y/5000)^2}$ T.

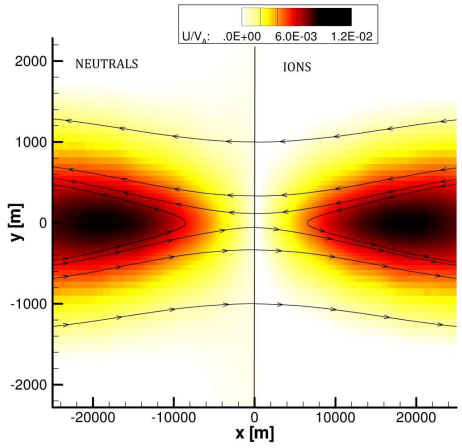

Figure 2: Horizontal velocity of neutrals and ions at $t = 20$ s. Non-dimensionalized with the value of the local Alfven speed outside the current sheet

.

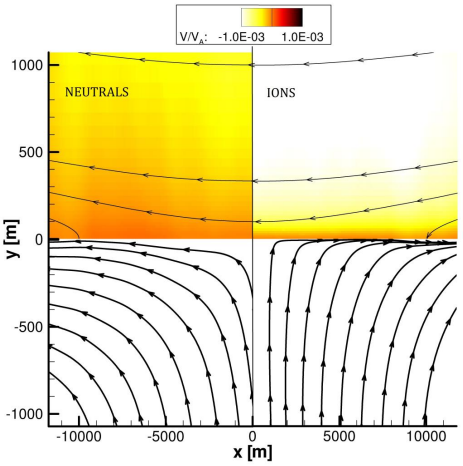

Figure 3: Vertical velocity and streamtraces of neutrals and ions at $t = 20$ s.

.

6. Conclusions

The first stages of a magnetic reconnection in the chromosphere have been simulated using a multi-fluid model considering two fluids, neutrals and charged particles. A current sheet is formed in the center of the domain, producing the acceleration of the ion fluid. The collisions drag the neutrals that have almost the same horizontal velocity, but much smaller vertical velocity. The results capture the phenomenology of the magnetic reconnection and agree with the literature. The numerical method, considering full set of Maxwell equations and using Finite Volume discretization is completely new. These results can be considered as the first steps that will be continued during the PhD targeted towards the study of the magnetic reconnection with multi-fluid models.

Acknowledgments

This research is funded through a fellowship provided by IWT (agentschap voor Innovatie door Wetenschap en Technologie). We would also like to thank Dr. Nagi N. Mansour for the supervision of this work at NASA Ames Research Center and Dr. Andrea Lani, COOLFluiD architect and advisor of this work.

References

[1] Committee on the Societal and Economic Impacts of Severe Space Weather Events, *Severe Space Weather Events Understanding Societal and Economic Impacts: A Workshop Report*, The National Academies Press, 2008.

[2] J. Birn and E. Priest, *Reconnection of Magnetic Fields*, Cambridge University Press, 2007.

[3] F. Zuccarello, *Data analysis and mathematical modeling of the initiation of coronal mass ejections*, PhD thesis, KU Leuven, 2012.

[4] M. Yamada, R. Kulsrud, and H. Ji, *Magnetic Reconnection*, Reviews of Modern Physics vol.82, 2010.

[5] J. E. Leake, V. Lukin, M. Linton and E. Meier, *Multi-fluid simulations of chromospheric magnetic reconnection*, ApJ. 760, 2012.

[6] K. Shibata et al., *Chromospheric Anemone Jets as Evidence of Ubiquitous Reconnection*, Science, Volume 318, Issue 5856, pp. 1591, 2008.

[7] K. Shibata and T. Magara, *Solar Flares: Magnetohydrodynamic Processes*, Living Rev. Solar Phys. 8, 2011.

[8] E. N. Parker, *Sweet's mechanism for merging magnetic fields in conducting fluids*, Geophysical research 62, No. 4, 509-520, 1957

[9] H. E. Petschek. *Magnetic Annihilation*. The Physics of Solar Flares, Proceedings of the AAS-NASA Symposium, October 1963

[10] D. Biskamp, *Magnetic Reconnection in Plasmas*, Cambridge University Press, 2005

[11] S. I. Braginskii, *Transport processes in a plasma*. Reviews of Plasma Physics, Volume 1., pp. 205 311. (1965)

[12] B. Graille , T. E. Magin , M. Massot, *Kinetic theory of plasmas. Translational Energy.* Mathematical Models and Methods in Applied Sciences, Vol. 19, 04 (2009) 527-599

[13] E. T. Meier, U. Shumlak, *A general nonlinear fluid model for reacting plasma-neutral mixtures.* Physics of Plasmas, Volume 19, Issue 7, pp. 072508-072508-11 (2012).

[14] A. Lani, *An object Oriented and high performmance platform for aerothermodynamics simulations*, PhD Thesis, von Karman Institute for Fluid Dynamics, 2009

[15] R. W. MacCormack. *Numerical Simulation of Aerodynamic Flow Including Induced Magnetic and Electric Fields.* In 39th AIAA Plasmadynamics and Lasers Conference, Seattle, June 2008.

[16] T. Barth. Aspects of unstructured grids and finite volume solvers for the euler and navier-stokes equations. 25th Computational Fluid Dynamics Lecture Series. Von Karman Institute, March 1994.

[17] V. Venkatakrishnan. *Convergence to steady state solutions of the euler equations on unstructured grids with limiters.* Journal of Computational Physics, 118:120130, 1995.

[18] J. Steger, R. F. Warming, *Flux vector splitting for the inviscid gas dynamic equations with application to finite difference methods*, J. Comp. Phys., Vol. 40, No. 2, pp. 263-293, 1981

[19] C.-D. Munz., P. Ommes, R. Schneider. *A three-dimensional finite-volume solver for the Maxwell equations with divergence cleaning on unstructured meshes*. Computer Physics Communications130, 83-117, December,1999.

[20] A. Alvarez, *Multi-Fluid MHD Development for Space Weather Modeling*, Research Master Report, von Karman Institute for Fluid Dynamics, June 2013.

[21] M. S. Liou, *A sequel to AUSM, part II: AUSM+ -up for all speeds.* J. Comp. Phys., 214:137170, 2006.

[22] G. S. Voronov, *A practical fit formula for ionization rate coefficients of atoms and ions by electron impact*, Atomic data nad nuclear data tables 65, 1-35, 1997

[23] B. M. Smirnov, *Physics of Atoms and Ions*, Springer-Verlag New York, Inc., 2003

[24] Vernazza, J. E., Avrett, E. H., Loeser, R., *Structure of the solar chromosphere. III. Models of the EUV brightness components of the quiet Sun*, ApJS45, 635-725, 1981

SPARK: Simplified Plasma Models based on Reduced Kinetics

Aurélie Bellemans

PhD candidate, Aeronautics and Aerospace Department, von Karman Institute for Fluid Dynamics, Belgium, aurelie.bellemans@vki.ac.be

Supervisor: Thierry Magin

Associate Professor, Aeronautics and Aerospace Department, von Karman Institute for Fluid Dynamics, Belgium, magin@vki.ac.be

University Supervisor: Alessandro Parente

Assistant Professor, Service dAéro-Thermo-Mécanique, Université Libre de Bruxelles, belgium, alessandro.parente@ulb.ac.be

Over the last 60 years many manned and unmanned exploration missions have been launched successfully from earth to space. When launching astronauts to space one aims to bring them back home safely, without having their spacecraft burn while re-entering our terrestrial atmosphere. The development of thermal protection systems for spacecraft is thus an important concern and requires the development of precise numerical engineering models to predict the heating during re-entry.

The modeling of high enthalpy and plasma flows is a complex multi-physical engineering problem because of the high degree of non-equilibrium in the composition of the various plasma components. Indeed, thermo-chemical non-equilibrium phenomena involve hundreds of reactions and thousands of species leading to expensive numer- ical simulations. As detailed multi-dimensional formulations are computationally expensive, one reduces either the dimensionality of the problem going from 3D to 1D or 0D expressions, or the physics by replacing detailed chemistry laws by simpler ones.

Fortunately, although complete models involve hundreds of species and thousands of reactions, only a small fraction of these play a major role in aerospace applications. This is due to the fact that many chemical processes have much shorter time scales than the typical transport time scale in the system, just as in combustion processes. As a result, the chemical composition lies on a so-called low dimensional manifold. This observation opens the way for the development of reduced chemical models using the same kind of techniques developed for combustion processes.

During this research project Principal Component Analysis (PCA) will be investigated as an application of a chemical reduction technique to plasma. PCA has been introduced recently as a mathematical method to retrieve the most active directions, or principal components, in a multivariate dataset by calculating the eigenvectors of the thermo-chemical state-space covariance matrix. Those eigenvectors form a low-dimensional basis on which the system is projected. Manifold Generated PCA (MG-PCA) uses PCA to reduce a physical model to a lower dimension. It allows for solving the transport equations for the principal variables only and reconstructs the remaining variables at each time step. Two different approaches of the method have been developed: a global one (MG-PCA) and a local one (MG-l-PCA). The local formulation divides the full dataset in clusters and applies MG-PCA on each of them. Different pre-processing techniques such as scaling and centering methods can be implemented and compared.

In a first instance the dynamics of highly reacting flows will be investigated in detail to understand the physics of non-equilibrium aero-thermodynamics. In a further step reduction techniques will be developed starting form detailed chemistry models such as multi-temperature and Collisional-Radiative (CR) models. The reduction will be applied on CR models for shock layer simulations and will be validated in a next step with ICP and flight data. Preliminary results have already been obtained by applying PCA on 1D shock tube simulations for argon plasma. The reduced model has been obtained by reducing the detailed collisional model for the argon excited levels. The model has been validated with UTIAS (University of Toronto, Institute for Aerospace Studies) shock tube experiments.

Non-Linear Extensions of Global Flow Stability Theory

Koen J. Groot

Aerodynamics (AWEP) Department, Delft University of Technology, The Netherlands, koengroot@tudelft.nl

Supervisors: Fabio Pinna and Olivier Chazot

Research Engineer, Aeronautics and Aerospace Department, von Karman Institute for Fluid Dynamics, Belgium, fabio.pinna@vki.ac.be

Professor, Aeronautics and Aerospace Department, von Karman Institute for Fluid Dynamics, Belgium, chazot@vki.ac.be

University Supervisor: Bas W. van Oudheusden

Associate Professor, Aerodynamics (AWEP) Department, Delft University of Technology, The Netherlands, b.w.vanoudheusden@tudelft.nl

University Promotor: Fulvio Scarano

Professor, Aerodynamics (AWEP) Department, Delft University of Technology, The Netherlands, f.scarano@tudelft.nl

Keywords: laminar-to-turbulent transition, e^N-method, BiGlobal, stability, bifurcation

1. Introduction

A plan is set up for a PhD project mainly performed at Delft University of Technology (TUD) in close collaboration with the Von Kármán Institute (VKI). The project focuses on the development of efficient methods to predict the inherently non-linear aerodynamic laminar-to-turbulent transition phenomenon.

Currently, the e^N-method based on Linear Stability Theory (LST) is the only feasible method to predict transition in design applications. LST equations, which in an incompressible flow can be rewritten into the Orr-Sommerfeld and Squire equations, govern the stability of perturbations that are inhomogeneous in a single spatial direction.

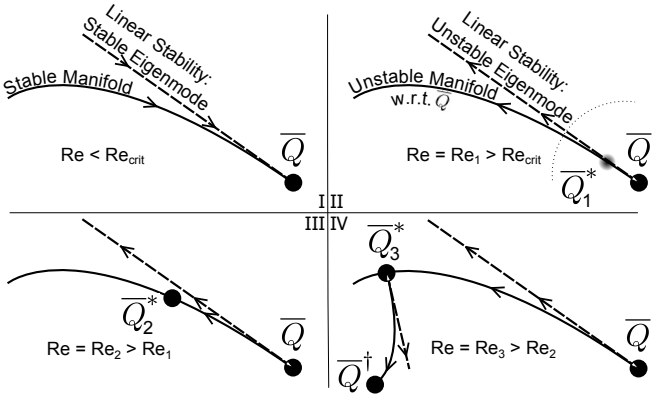

Figure 1: Illustration of an eigenvector, manifold and (twofold) bifurcation of the base flow $\overline{Q}$ in state space.

2. Linear Stability versus Bifurcations

The physical approximation in the linear stability methods (including also those considering higher-dimensional perturbations) can be illustrated using the state space representation in Fig. 1. In the linear stability case, one calculates eigenvectors and -values, which are equivalent to the shapes and the growth rates of resolved perturbations on a given base flow $\overline{Q}$. In Fig. 1, this information is given by the *straight* dashed lines originating in the base flow $\overline{Q}$ and the superimposed arrows, respectively. The critical Reynolds number Re_{crit} is defined to be the Reynolds number above which $\overline{Q}$ becomes linearly unstable, compare quadrants I and II in Fig. 1. In the non-linear case, strictly one must consider the more general equivalents of eigenvectors: the *generally curved* stable/unstable manifolds. It is assumed that somewhere along the unstable manifold a new base flow $\overline{Q}^*$ exists when $Re > Re_{crit}$. This new base flow *bifurcated* from $\overline{Q}$ at $Re = Re_{crit}$.

Basically, the linear stability methods approximate the unstable manifolds with their tangent manifolds around $\overline{Q}$. Whether this approximation is reasonable depends on the departure of the new base flow $\overline{Q}^*$ on the true manifolds from the positions on the tangents and thus on Re. The quadrants II and III of Fig. 1 show that this departure can become significant. Moreover, as shown in the fourth quadrant, the new base flow $\overline{Q}^*$ might bifurcate yielding a second new base flow $\overline{Q}^\dagger$. The flow might bifurcate several times more before it displays chaotic behaviour and, per definition, is tur-

bulent.

The linear stability methods applied on $\overline{Q}$ do not retrieve the secondary bifurcation. However, one could apply them on $\overline{Q}_3^*$ and show that this flow has an unstable eigenvector as shown in quadrant IV of Fig. 1. The latter approach is referred to as the secondary instability method, see Herbert [2]. Many other non-linear stability and bifurcation approaches are existent. Examples are weakly non-linear methods (see Stuart & Stewartson [5]), non-linear PSE (see Bertolotti *et al.* [1]) and continuation methods (see Seydel [4]).

3. Research Objectives & VESTA

The first objective of the current research is to set up a perspective of the possible performance of different stability and bifurcation methods in transition analysis and prediction in terms of yield and computational cost. Possible hybrid methods will be considered in the process. Another focus is the position of the tools currently present in the VKI Extensible Stability and Transition Analysis (VESTA) toolkit, initially developed by dr. F. Pinna [3], in this overview. Based on this assessment, the most promising method(s) will be selected, where the classical e^N-method and DNS can be seen to represent the far ends of the spectrum. All in all, the overview can be used to identify whether a competitor of the e^N-method exists and what the advantages are with respect to the sacrifices that have to be made when applying it. Thereafter, as a second objective, the selected method(s) will be implemented in VESTA and validated, preferably against existing experimental data.

An important feature of VESTA is its implicit methodology. All theory, e.g. in the form of stability equations, is derived, implemented and solved using linked extensible automatic tools. In this way, contributions of human-error in executing stability analyses are minimized as much as possible. In the candidate's master thesis these were demonstrated to be significant in published equations, for example. The fact that the tools are extensible implies that they can be extended to incorporate more general test cases rather easily. Currently, VESTA can perform stability analyses for a very broad speed range; from the incompressible to the high hypersonic regime. Furthermore, any kind of coordinate system is permitted, allowing the analysis of a curved geometry, although the overall geometry is restricted to a single (curved) rectangle.

Next to the primary PhD research, a secondary set of objectives is set up that focuses on the use of the BiGlobal stability tools currently present in VESTA, see Theofilis [6] for a review. Firstly, an objective is to provide the service to perform BiGlobal stability analyses on any provided mean flow, i.e. varying from PIV measurement to numerical datasets, in support of research at TUD and VKI. Secondly, some additional research is proposed to be done with respect to: first, seemingly "contaminated" developing Blasius base flows used in the literature, second, the structural changes of the continuous spectrum due to the consideration of a "quasi-developing" Blasius flow, third, the (possibly non-physical) influence of using Robin(-Gaster) conditions at the in- and outflow boundaries and, fourth, the potentially first consideration of the BiGlobal analysis of the compressible developing Blasius flow. The set-up of the developing Blasius flow problem is shown in Fig. 2.

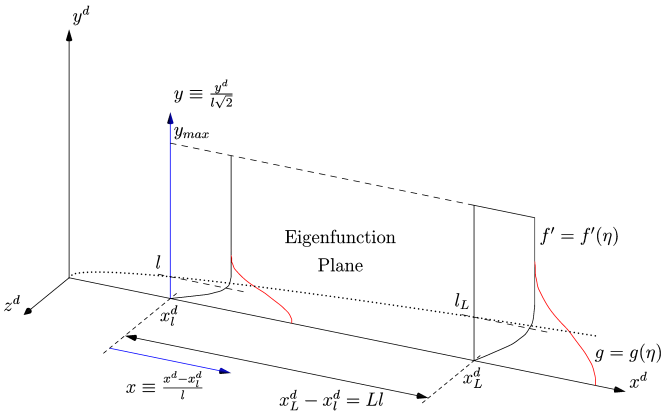

Figure 2: Developing Blasius flow: an overview.

References

[1] F.P. Bertolotti, Th. Herbert, and P.R. Spalart. Linear and nonlinear stability of the blasius boundary layer. *Journal of Fluid Mechanics*, 242:441–474, 1992.

[2] Th. Herbert. Secondary instability of boundary layers. *Annual Review of Fluid Mechanics*, 20:487–526, 1988.

[3] F. Pinna. *Numerical study of stability of flows from low to high Mach number*. PhD thesis, von Karman Institute for Fluid Dynamics & Universitá "La Sapienza" di Roma, 2012.

[4] R. Seydel. *Practical Bifurcation and Stability Analysis*. Springer Verlag, New York, ISBN: 978-1-4419-1739-3, 2010.

[5] K. Stewartson and J.T. Stuart. A non-linear instability theory for a wave system in plane poiseuille flow. *Journal of Fluid Mechanics*, 48(3):529–545, 1971.

[6] V. Theofilis. Global linear instability. *Annual Review of Fluid Mechanics*, 43:319–352, 2011.

DEVELOPMENT OF ADVANCED CFD AND OPTIMIZATION

Robust Multidisciplinary Optimization of Composite Fan Blades

Christopher Chahine

Turbomachinery and Propulsion Department, von Karman Institute for Fluid Dynamics, Belgium, christopher.chahine@vki.ac.be

Supervisor: Tom Verstraete

Assistant Professor, Turbomachinery and Propulsion Department, von Karman Institute for Fluid Dynamics, Belgium, tom.verstraete@vki.ac.be

Abstract

To achieve higher fuel efficiency, aero engine manufacturers develop turbofans with higher bypass ratio, which can only be achieved with larger (and heavier) fan sections. This makes weight reduction in fan components a major consideration and becomes a key driver for the use of composite materials in future engines. The design of composite fan blades is indisputably a multidisciplinary problem with a high level of interaction between the different disciplines. The goal of this PhD project is to use advanced numerical optimization techniques to assist the design of composite fan blades for minimal mass and state of the art efficiency while considering constraints from all relevant disciplines, including blade flutter, static stresses, noise, stall range, required pressure ratio at the operating point and other flight conditions, foreign object damage and manufacturing considerations.

Keywords: transonic fan blades, high bypass ratio turbofans, parametrization, multidisciplinary optimization, hot-to-cold transformation

1. Introduction

Weight reduction of turbofan engines is one of the main concerns of aero engine manufacturers in order to cut fuel burn. On average 30 per cent [1] of the total engine weight is added by the propulsor, which comprises the fan blades and related components such as the fan casing, disc and outlet guide vanes. Traditionally most parts of the propulsor are made of metallic materials; titanium alloys are nowadays the most common choice for the fan blades and the disc, while highly ductile steel, titanium, aluminium and magnesium are often used for main parts of the casing [2]. Significant weight savings can be achieved by replacing these metallic materials by fibre reinforced composite materials which are a mixture of very strong and stiff fibres carrying the major part of the load and a so called matrix material which holds together the fibres and distributes the load between them. Due to this property of the matrix material the strength of the composite can exceed the strength of the individual constituents [3]. For operating temperatures below 200°C [3] a widely used type of fibre reinforced composite material is carbon-fibre-reinforced plastic (CFRP). The density of CFRP is typically about 66% lower than the density of titanium, while providing a comparable strength [3]. The resulting strength to weight ratio makes these materials particularly attractive for the usage in turbofan engines.

Fan blades made of fibre reinforced composite materials are a key element for the weight reduction of the entire propulsor, since lighter fan blades allow the supporting structural components, including the disc, to become lighter. Additionally the fan casing can be reduced in weight as well since its task to contain the blades in case of a blade failure can be accomplished using less material than would be needed in the case of heavier metallic blades.

The design of composite fan blades is a multidisciplinary problem; e.g. composite blades tend to become thicker than hollow metallic ones in order to meet the structural performance targets but this affects the aerodynamic performance (efficiency). Moreover, unlike metals, composite materials introduce the possibility to be optimized by specifically tailoring their characteristics, e.g. fibre orientations, constituent materials, ply thicknesses and ply stacking sequence, for a particular application. This introduces a high poten-

tial for innovative designs, but on the other hand adds considerable complexity to the design space. The goal of this PhD project is to extend and apply existing numerical optimization methods to effectively assist the design of composite fan blades for minimal mass and state of the art aerodynamic efficiency. Constraints from all relevant disciplines will be considered, including blade flutter, static stresses, noise, stall range, required pressure ratio at the operating point and other flight conditions, foreign object damage and manufacturing considerations.

Changing operation conditions and manufacturing tolerances can have an adverse influence on the fan's performance. Particularly optimized designs often show rapid performance degradation upon minor parameter changes, which needs to be avoided in order to guarantee reliable operation over the entire lifetime of the fan. Therefore, the probable parameter changes need to be taken into account in the design process. In this project this aspect will be addressed by making use of methods for robust optimization, which take into account the uncertainties of design variables and their influence on the performance.

In this paper a summary of the work performed in the first year of the project is given. In Section 2 the fan blade parametrization is introduced, followed by a presentation of an automatic method to generate a parametrized fan blade from a through-flow code in Section 3. Subsequently, the automatic generation of a CAD model of the fan is presented in Section 4. In Section 5 an automatic cold geometry generation procedure is explained. Finally, the currently established evaluation chain for a multidisciplinary optimization framework is discussed in Section 6.

2. Fan blade parametrization

2.1. Camber surface parametrization

A schematic showing the camber surface parametrization of a fan blade can be seen in Fig. 1. The camber surface parametrization used here is partly based on previous methods developed at the von Karman Institute [4] and has been further developed in the framework of this project. The camber surface can be considered as the mean surface of the blade, running from the leading edge to the trailing edge, and having at every point an equal minimum distance to the suction side and the pressure side surfaces. Several *camber lines*, each defined on a specific spanwise position (span $\in$ [0,1], 0 at the hub and 1 at the tip), define the camber surface's shape.

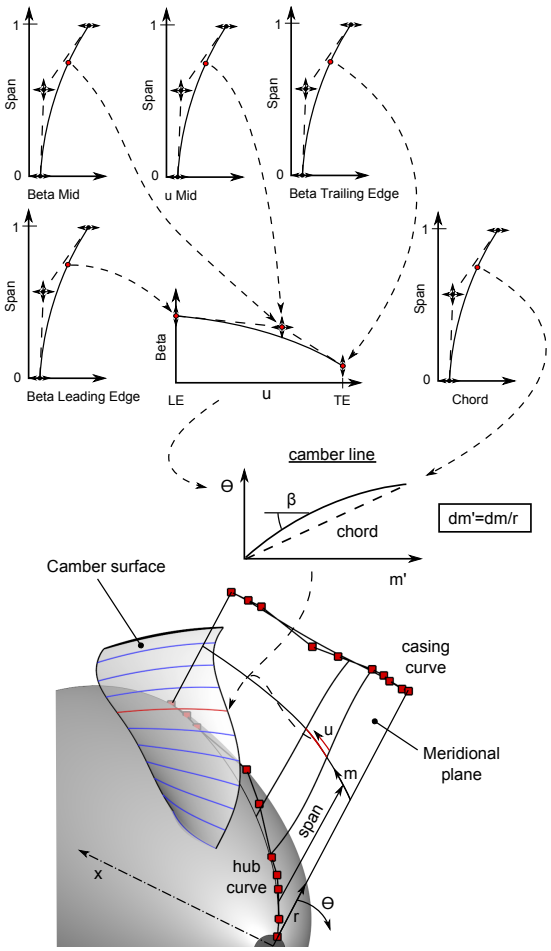

Figure 1: Parametrization of the camber surface.

In order to construct the camber surface, the meridional flow path needs to be defined first. The meridional plane is defined by the axial coordinate x as abscissa and the radius r as ordinate, as shown in Fig. 1. Parametric B-Spline curves are used for the definition of the hub and casing contour. The control points of the B-Spline curves are shown as red rectangles in Fig. 1. By modifying the control point coordinates in the meridional plane, the contour of the hub and shroud curves can be changed. The hub and casing surfaces are generated by creating a surface of revolution around the x-axis for each of the curves.

For the construction of a single camber line, a blade metal angle distribution from leading to trailing edge $\beta(u)$ (with $u \in [0,1]$ being the non-dimensional meridional length, 0 at the leading edge and 1 at the trailing edge) and a chord length need to be specified (Fig. 1).

In conventional parametrization methods, the user directly defines the parameters needed for the generation of each spanwise camber line. In the present work a different approach is used, in which the blade angle distributions and the chord length are defined as continuous curves over the blade span. In contrast to the conventional method, this parametrization guarantees a smooth spanwise evolution of the blade angles and furthermore allows the parameters to be directly linked to the output from two-dimensional throughflow codes, as will be further detailed in section 3. In total four B-Spline curves are used for the definition of the spanwise blade angle distributions; three curves are needed for the specification of blade angles at the leading edge, trailing edge and a mid point while one additional curve defines the local position of the mid point in non-dimensional meridional length u. A fifth B-Spline curve is introduced for the specification of the spanwise chord length distribution. The number of control points of these B-Splines, their coordinates and the knot vectors are parameters which can be specified by the user in order to define and modify the geometry. By extracting the values from the angle distributions at an arbitrary spanwise position, the control point coordinates of a two-dimensional second order Bézier curve are given defining the blade metal angle distribution from the leading to the trailing edge. The fact that the meridional stream line with arc length m can be arbitrarily curved introduces the requirement of generating the camber line in different mathematical spaces. By integration of the blade angle distribution a two-dimensional camber line is constructed in (m',θ) space, with dm' being the differential arc length dm at span s normalized with respect to the radius r ($dm' = dm/r$), see Fig. 1. The space defined in (m',θ) coordinates is angle preserving with respect to the three-dimensional (x, r, θ) space, therefore allowing the definition of critical blade angle properties, including the conformal generation of the camber lines. Subsequently, the two-dimensional camber line is scaled to the desired chord length which is extracted from the spanwise parametrization.

With knowledge of the meridional curve at a specific spanwise position, the camber line can be transformed to a three-dimensional curve in Cartesian coordinates. In order to avoid bending moments in the blade resulting from centrifugal forces, the camber lines are positioned relative to each other in such a way that the center of gravity of each two-dimensional spanwise blade section is lying on a radial stacking axis whereas the axial coordinate of this axis is an additional parameter to be defined by the user, see Fig. 2.

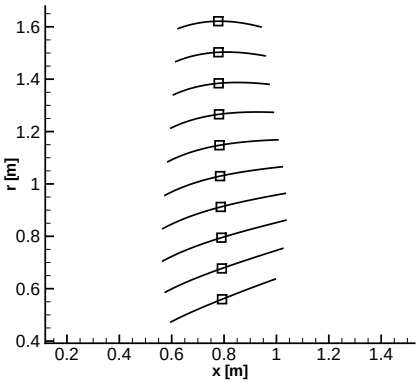

Figure 2: Meridional view showing the initial radial stacking of camber lines through the center of gravity of the associated two-dimensional blade section. Gravity centers are shown as rectangles.

This radial stacking of two-dimensional cross sections involves operations like the interpolation of spanwise thickness distributions and multiple coordinate transformations. A detailed explanation of this procedure will therefore not be given here.

The camber surface is finally created by lofting a surface through all previously generated three-dimensional camber lines.

2.2. Lean and sweep

Especially in transonic and supersonic compressors and fans it can prove beneficial for the aerodynamic performance to deviate from the purely radial stacking of blade profiles as presented above. The idea behind this is to influence the relative position of the leading edge shock with respect to the incident flow so that the component of Mach number perpendicular to the shock, and hence the shock loss, is reduced [5]. The way this is usually done is by introducing a certain amount of *lean* and *sweep*. However, although the terms lean and sweep are widely used, the definitions vary in the literature. Therefore, to avoid misconception, Fig. 3 shows the definitions of lean and sweep used in this work. As can be seen on the left hand side of the figure, lean and sweep are both parametrized by two-dimensional B-Spline curves over the blade span. The upper part of Fig. 3 shows the definition of sweep. Sweep is defined by a translation of the camber line along the chord line, being positive when moved towards the trailing edge. The upper right hand side shows how positive sweep of the tip section would affect a typical shape of a fan blade. Lean is defined as

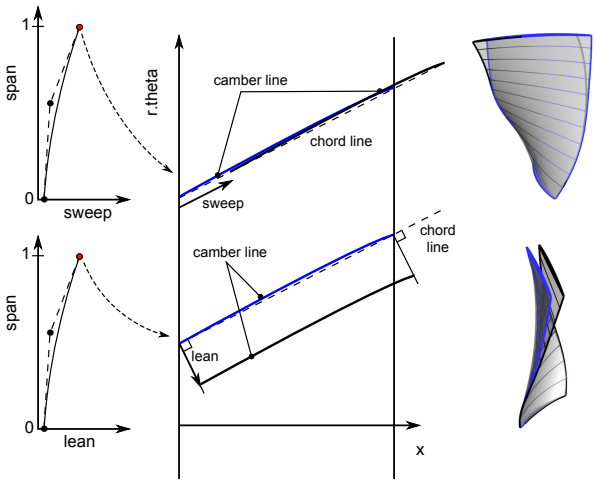

Figure 3: Definition of lean and sweep.

a translation of the camber line perpendicular to the chord line, as shown in the lower part of Fig. 3, being positive when moved in the direction of rotation. The effect of positive lean of the tip section on the blade can be seen in the lower right corner of the figure.

2.3. Thickness

The last step required to generate the suction and pressure side surfaces of the blade is the application of a thickness to the camber surface. The blade thickness is parametrized by B-Spline curves at several spanwise positions, usually at hub and tip, see Fig. 4. By adding the thickness perpendicular to the camber surface the final blade shape is obtained, as shown schematically on the right hand side of Fig. 4.

3. Generation of initial blade parameters

With the parametrization being established as presented in the previous section, a blade geometry can be generally created by defining all required parameters manually. However, a preliminary design is usually existing, coming from two-dimensional through-flow codes. The task is then to find the parameters which best match the geometry at hand. Considering the many parameters that need specification, doing this manually can be a very time consuming and error prone process.

To facilitate the process of generating the full set of parameters for a given blade design coming from a through-flow calculation, this task has been automatized in the VKI in-house through-flow code ACPreDesign. The code was augmented with a functionality which generates and exports the entire set of parameters consistent with the parametrization presented above.

A comparison between a geometry resulting from ACPreDesign, and the parametrized representation is shown in Fig. 5 for the spanwise blade angle and chord length distributions. However, the entire set of parameters needed for the generation of a blade is generated in ACPreDesign, including the meridional flow path and the thickness distributions.

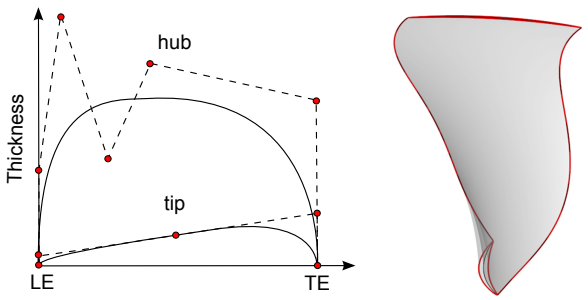

Figure 4: Construction of the final blade shape by adding a thickness distribution to the camber surface.

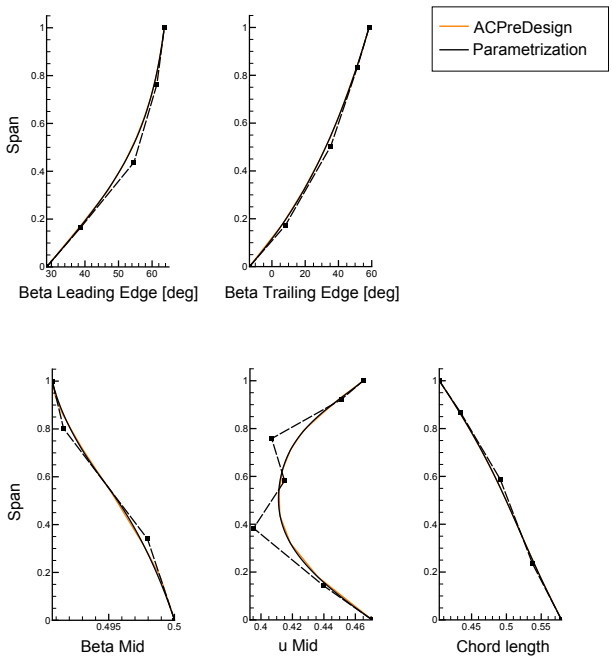

Figure 5: Generation of parametric curves from ACPreDesign.

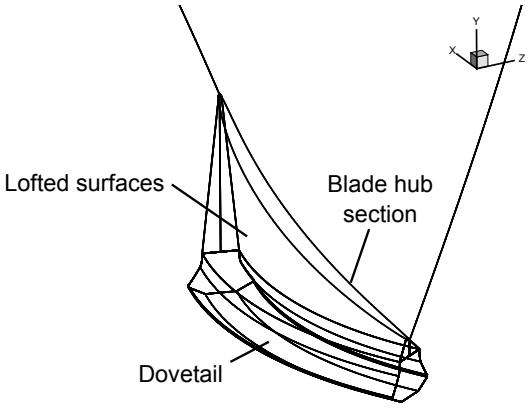

Figure 6: Dovetail with blade attachment.

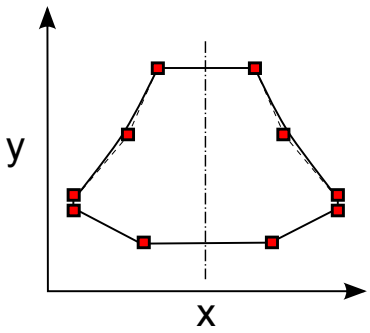

Figure 7: Parametrization of the dovetail cross section.

4. Solid blade modeling and CAD export

The parametrization given above defines the blade geometry from hub to tip and the end wall contours, thereby allowing to specify the computational domain for CFD computations. However, for structural evaluations the blade geometry is still incomplete. The essential part missing is the blade root, which is the structural connection between the blade and a supporting disk. For modern fan blades, this connection is established by a so-called dovetail, see Fig. 6. The dovetail root typically slides into a slot in the disk which holds the fan in place while the disk is rotating.

In the framework of this project, a parametrization and geometry generation of a dovetail has been developed. The geometry is defined by a dovetail cross section which is parametrized by Bézier curves as shown in Fig. 7. The dovetail geometry is generated by rotating the cross section around a rotational axis in (x,y,z) space, which is automatically positioned such that the dovetail best matches the camber line at the hub section of the blade. Once the dovetail is generated, a smooth connection to the hub section of the blade is established by lofted surfaces, see Fig. 6.

The resulting CAD model of the entire fan blade can be exported as STEP file for visualization in a CAD program or used for subsequent structural performance evaluations. Fig. 8 shows an example of an exported CAD model of the entire fan blade.

5. Automatic cold geometry generation

The parametrized geometry as described in section 2 defines the geometry under operating conditions, e.g. at cruise speed of the aircraft, and as such defines the desired aerodynamic shape of the fan blade at the design operating point. Static loads acting on the fan during operation (with the main part being due to centrifugal forces) result in a deformation of its shape, therefore leading to a different shape between operating conditions and rest. Modern high bypass ratio fan blades can have tip diameters of 3 meters and more, low hub-to-tip ratios in the range of 0.35 to 0.4 and highly three-dimensional blade designs (with lean and/or sweep applied, see section 2.2). The deformations encountered between rest and design rotational speed in such geometries can be in the range of millimeters, often associated with an untwist of the blade shape. Therefore, if a structural analysis is to be performed, one first needs to find the geometry at rest, which, under static loads at the design operating point, matches the desired aerodynamic shape of the blade as close as possible. The blade geometry at rest is the geometry which is manufactured and is often referred to as “cold” geometry of the blade. Usually, the task of finding a cold geometry is the first task a

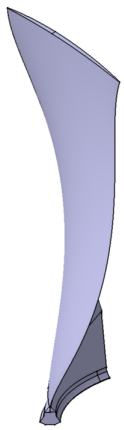

Figure 8: CAD model of a fan blade with dovetail.

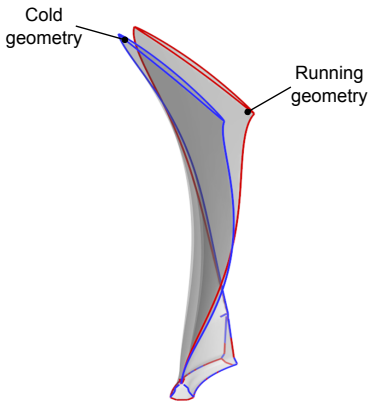

Figure 9: Comparison of a running blade geometry (red edges) with its counterpart at rest (blue edges).

human stress designer needs to do before attempting a structural analysis. An approach often adopted is based on an iterative technique [6] which lends itself to automatization and has therefore been implemented in this work. Following explanation outlines the main steps of the method: in a first step, the solid geometry at operating conditions is meshed and a static non-linear geometric FEM computation is performed with the centrifugal forces being applied. The mesh generated during this step is used as a reference mesh for the following part of the procedure, since it represents the desired geometry at the design operating point. Subsequently, the displacement field resulting from the FEM computation is subtracted from the initial mesh which results in a first guess for the mesh of the cold geometry. Another FEM computation is then performed with this new mesh, and the resulting deformed shape is compared to the reference mesh. The difference between these two meshes is then again subtracted from the current mesh of the cold geometry to generate a better guess for the cold geometry. This loop is repeated until the maximum difference between the deformed cold mesh and the reference mesh falls below a specified limit. Since the computation of the cold mesh can be computationally expensive, this limit needs to be specified with care. For the computations performed in this work, the limit was set to 0.5 millimeters, which was found to be a reasonable compromise between accuracy and computational cost. Fig. 9 shows a comparison of a fan geometry at operating conditions and its counterpart at rest. In this case 11 iterations were needed for the generation of the cold geometry. The difference between the two geometries is apparent in the figure.

The implemented method allowed to investigate the impact of neglecting the cold geometry generation in a static structural FEM analysis, i.e. if the analysis is performed for the running geometry instead of the geometry at rest. Of particular interest in such an analysis are the von Mises stresses in the blade. It has been found for different geometries that errors of 10% in the maximum von Mises stresses are not unusual (which translates to about 80 MPa of absolute error for a typical titanium fan blade). This is a not negligible amount for any stress analysis, therefore justifying the additional computational cost that is invested in the generation of the cold geometry.

6. Evaluation chain for multidisciplinary optimization

The methods presented in the preceding sections of this paper have been implemented into the VKI in-house optimization system CADO [7; 8], see Fig. 10, in order to allow them to be used in a multidisciplinary optimization framework. The main changes made to the system concern the high-fidelity evaluation part (left hand side of Fig. 10). As can be seen in the figure, the geometry generation can be assisted by the preliminary through-flow code ACPreDesign, as discussed in Section 3. The geometry is then passed on to the high-fidelity evaluation by Computational Fluid Dynamics (CFD) and Computational Structural Mechanics (CSM). The commercial 3D RANS solver Numeca FINE/Turbo is used for the aerodynamic performance evaluation of a design. The structural evaluation consists of three main parts: the mesh generation of the cold geometry (see section 5), a vibration analysis and a static stress analysis. The vibrations and static stresses are analyzed with the open-source

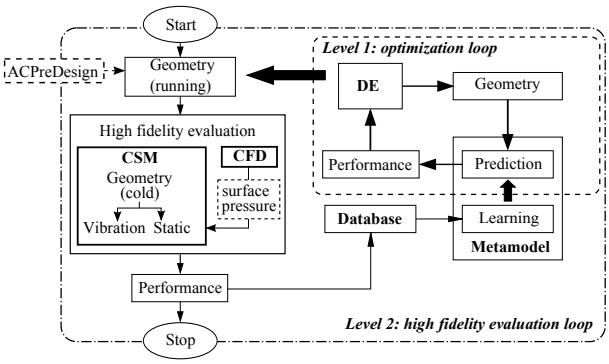

Figure 10: Flow chart of the VKI optimization system.

finite element solver CalculiX [9]. Within the framework of this project, a vibration model has been developed which allows to characterize the vibration response of a fan blade to multiple excitation sources (e.g. struts, vanes, unbalance, cross-wind) in order to avoid dangerous resonance within its operating range. The static stress analysis is performed in order to ensure that the stresses in the fan do not exceed the allowable material limits during operation. Centrifugal and aerodynamic loads are applied to the fan, the latter represented by the static pressure distribution on the pressure and suction side surfaces of the blade. These pressure distributions are extracted from the results of the CFD computation and interpolated onto the FEM mesh. Since the static loads result in relatively large displacements of the fan blade, the stresses are computed using non-linear geometric analyses.

7. Conclusion

This paper summarizes the results of some key developments performed in the first year of the project, such as the development of a fan blade parametrization, a method for the automatic generation of the parametrized blade from a two-dimensional throughflow code, a procedure for the automatic cold geometry generation and the implementation of these techniques into the evaluation chain of the VKI in-house optimization code CADO. The focus during this first project year was to establish a basis for the following more complex evaluations that are planned to be implemented in the second project year, including composite optimization.

Acknowledgments

The research leading to these results has received funding from the European Union Seventh Framework Programme (FP7/2007-2013) under grant agreement no [316394].

References

[1] D. Johnson and G. V. Brown, Power Requirements Determined for High-Power-Density Electric Motors for Electric Aircraft Propulsion, in: Research and Technology, no. NASA/TM-2005-213419.

[2] W. Smarsly, Aero Engine Materials Part 1, in: International Workshop on Aero Engines, MTU Aero Engines GmbH, 2007.

[3] Z. Guerdal, R. T. Haftka, P. Hajela, Design and Optimization of Laminated Composite Materials, John Wiley and Sons, Inc., 1999.

[4] M. Joly and T. Verstraete and G. Paniagua, Full Design of a Highly Loaded and Compact Contra-Rotating Fan Using Multidisciplinary Evolutionary Optimization, in: Proceedings of ASME Turbo Expo 2013, no. GT2013-94433, San Antonio, Texas, USA, 2013.

[5] J. D. Denton and L. Xu, The Effects of Lean and Sweep on Transonic Fan Performance, in: Proceedings of ASME Turbo Expo 2002, no. GT2002-30327, Amsterdam, The Netherlands, 2002.

[6] E. Seinturier, Forced Response Computation for Bladed Disks - Industrial Practices and Advanced Methods, in: Structural Design of Aircraft Engines: Key Objectives and Techniques, no. VKI LS 2008-05, Rhode-St-Genèse, Belgium, 2008.

[7] S. Pierret, Designing Turbomachinery Blades by Means of the Function Approximation Concept Based on Artificial Neural Network, Genetic Algorithm and the Navier-Stokes Equations, Ph.D. thesis, Faculté Polytechnique de Mons (1999).

[8] T. Verstraete, Multidisciplinary Turbomachinery Component Optimization Considering Performance, Stress, and Internal Heat Transfer, Ph.D. thesis, University of Gent (2008).

[9] G. Dhondt, K. Wittig, A Free Software Three-Dimensional Structural Finite Element Program, www.calculix.de, Tech. rep. (1998).

Efficient High Performance Computing Techniques for Multi-disciplinary Optimisation

Mohamed Hassanine Aissa

Turbomachinery and Propulsion Department, von Karman Institute for Fluid Dynamics, Belgium, aissa@vki.ac.be

Supervisor: Tom Verstraete

Assistant Professor, Turbomachinery and Propulsion Department, von Karman Institute for Fluid Dynamics, Belgium, tom.verstraete@vki.ac.be

Abstract

The multidisciplinary design optimization (MDO) of turbomachinery components relies nowadays on performance estimations through simulation tools. These tools have to include mainly: aerodynamical, structural and thermodynamical considerations. The accuracy of the multidisciplinary aspect requires a high computational power available nowadays only by High-Performance-Computing systems (HPC).
One of the newest HPC hardware and most powerful shared-memory systems is Graphics processing Unit (GPU). Its actual widespread is encouraged by a higher computational power and limited by a different hardware architecture compared to conventional Central Processing Units (CPU). The aim of this work is therefore to utilize the GPU computational power to develop and validate one of the firsts viable GPU code for multidisciplinary design optimization on turbomachinery application. The current step is to boost the time consuming CFD solver - Euler and Navier-Stokes - of the in-house MDO system by adapting it for GPU. A second target envelops a larger use of GPU on the MDO algorithm. Preliminary results have been achieved with the verification and porting to GPU of the Euler version of the in-house CFD solver with explicit time stepping. The GPU saved 15% of the simulation run-time. The preexisting CPU-based Navier-Stokes solver has been validated against the VKI LS89 turbine guide vane. These first results pave the way for the porting and optimization of the full CFD simulation and therefore achieving better overall speedups.

Keywords: Multidisciplinary design optimization, graphics processing units, RANS Navier-stokes , Turbomachinery, LS89 turbine , GAMM test case,

1. Introduction

Multidisciplinary Design Optimization (MDO) is a key technology in the further improvement of the energy efficiency of aero engines. Turbomachinery design is highly based on multidisciplinarity. Structural analysis, aerodynamics and heat transfer are some of the essential disciplines to be coupled in the design process in order to achieve a global, constrained design optimality. The flow equations are solved to find the structural load. This load acts on the blades and influences their shape, thus altering again the flow equations.

Most of internal flows in turbomachinery applications are related to viscosity and turbulence. To simulate such a flow solving the Euler equations is not accurate enough. Theses equations are indeed able to capture shocks but neglects viscous effects. In order to resolve boundary layer occurring on the hub, shroud and on blades the full Navier-Stokes equations have to be solved. Solving the full Navier-Stokes equation requires a very high computational power even for low Reynolds number. Therefore some methods have been developed that models the turbulence or only part of its scales. Reynolds-Averaged Navier-Stokes approaches models all scales of turbulence. Large Eddy Simulation solves the low frequency part and models the rest. Direct Numerical Simulation solves all turbulence but the computational power required is scaling as Re^3[1] which stay beyond the today computing power.

In order to increase the time performance even RANS equations are run on High Performance systems. The GPU constitutes one of the most powerful shared-memory systems with hundreds of cores and is therefore a new alternative in HPC.

Graphics Processing Units (GPU) have been used from the eighties to display data on screen. As their function was clear and predefined the users had no control on the procedure of data preparation and displaying. The concept was based on a closed *graphic pipeline*. A multitude of small computation units calculate simultaneously the right color of pixels using information send by the Central Processing Unit.

With the evolution of GPU techniques users had more and more possibilities to control the running functions on the pipeline. With the appearance of CUDA-enabled GPUs in 2007 [2] the users started to write their own function on GPUs with a C-similar programming language called CUDA C [3].
Scientists showed indeed interests on GPU even before a comfortable programming language like CUDA appeared. They translated their CFD problems into graphics functions to have the GPU solving them in parallel. This interest for GPU is motivated by the relatively high computational power of GPUs. The large number of computation units (CUDA cores) is able to compute CFD variables of a numerical cell inside a grid analogous to a pixel inside a picture. GPU designers are increasing the number of CUDA cores and the interest is much bigger since the programming burden is reduced.

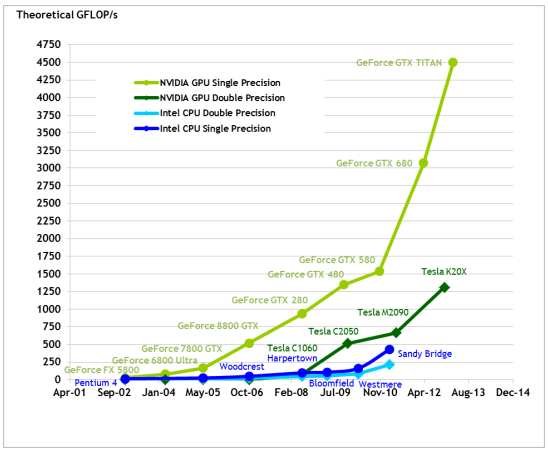

Figure 1: Floating-Point Operations per Second for the CPU and GPU

The computational power is measured on float operation per second (FLOPs). Figure 1 taken from the CUDA programming guide [3] shows the fast increasing gap on computational power between CPUs and GPUs over last decade on single and double precision.

GPU-cores are indeed very efficient for intensive arithmetical operation but present a weakness when it comes to data transfers. The GPU code has therefore to cope with the memory bandwidth as a bottle neck following a new programming approach. The challenge is then to write traditional sequential algorithms in a parallel way giving different cores the possibility to compute simultaneously.

This paper focus on the presentation of the MDO system CADO host of all optimization efforts related to this work and the CFD simulation of the CADO system to be optimized. Preliminary results are also presented.

2. Multidisciplininary Design Optimization

2.1. Optimization Algorithm

The multidisciplinary optimization tool CADO [4] developed at the Von Karman Institute for Fluid Dynamics (VKI) is conceived to improve the performance of turbomachinery components. The CADO algorithm presented in figure 2 involves a high fidelity performance evaluation based on computational fluid dynamics analysis (CFD) and Computational Solid Mechanics analysis (CSM). A metamodel assisted low-fidelity performance estimation reduces the computational costs and accelerates the design optimization process. The CFD analysis, performed in the actual version by commercial packages, takes much longer than the CSM analysis. Therefore the focus is on the optimization of the CFD simulation runtime. The saved run-time could decrease the computation costs or serves to perform more designs analysis and so increase the accuracy of the optimization algorithm.

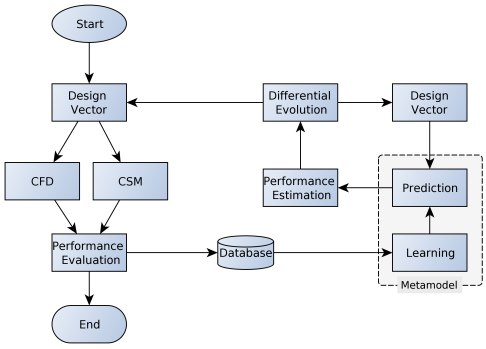

Figure 2: VKI optimization Algorithm (CADO)

GPUs have been already used to accelerate CFD simulation. Pullan et. al[5] used this hardware to accelerate a turbomachinery code having an over all speedup of one order of magnitude. Wang et Al. adapted his high-order accurate CFD method to GPU accomplishing a maximum speed up of 70x against single CPU core [6].

As a first step in the optimization of the CFD simulation an Euler-solver has been rewritten with CUDA C and so adapted for GPU. The CPU-based and the GPU-based Euler-solvers have been kept working side to side during the developing process to ensure the same output of both solvers given the same initialization data. The exact behavior of both solver has been verified automatically. The function per function porting of the CPU code relied on the *verification* of each ported piece of code against the CPU-based one.

A wider use of GPU on CADO is to be investigated. Running the metamodel on GPU with single precision could boost the process since GPU have an optimized hardware and function sets for single precision arithmetic[3]. New MDO algorithm are also to be investigated.

2.2. Flow Analysis

The flows considered in turbomachinery are viscous and turbulent.

2.2.1. Governing equations

The conservative integral form of the governing equations for internal flow in turbomachinery [1] are :

$$\frac{\partial}{\partial t}\int_\Omega \vec{W} d\Omega + \oint_{\partial\Omega} (\vec{F_c} - \vec{F_v}) dS = \int_\Omega \vec{Q} d\Omega \qquad (1)$$

where the conservative variable vector $\vec{W}$ consist of those components in three dimensions:

$$\vec{W} = \begin{bmatrix} \rho \\ \rho u \\ \rho v \\ \rho w \\ \rho E \end{bmatrix} \qquad (2)$$

and the convective flux vector is defined as follows:

$$\vec{F_c} = \begin{bmatrix} \rho V \\ \rho u V + n_x p \\ \rho v V + n_y p \\ \rho w V + n_z p \\ \rho H V \end{bmatrix} \qquad (3)$$

With following *contravariant velocity* definition:

$$V \equiv \vec{v} \cdot \vec{n} = n_x u + n_y v + n_z w \qquad (4)$$

and the viscous flux is

$$\vec{F_v} = \begin{bmatrix} 0 \\ n_x\tau_{xx} + n_y\tau_{xy} + n_z\tau_{xz} \\ n_x\tau_{yx} + n_y\tau_{yy} + n_z\tau_{yz} \\ n_x\tau_{zx} + n_y\tau_{zy} + n_z\tau_{zz} \\ n_x\Theta_x + n_y\Theta_y + n_z\Theta_z \end{bmatrix} \qquad (5)$$

where

$$\begin{aligned} \Theta_x &= u\tau_{xx} + v\tau_{xy} + w\tau_{xz} + k\frac{\partial T}{\partial x} \\ \Theta_y &= u\tau_{yx} + v\tau_{yy} + w\tau_{yz} + k\frac{\partial T}{\partial y} \\ \Theta_z &= u\tau_{zx} + v\tau_{zy} + w\tau_{zz} + k\frac{\partial T}{\partial z} \end{aligned} \qquad (6)$$

and the viscous stress tensor τ after application of stokes hypothesis ($\lambda + \frac{2}{3}\mu = 0$) reads in tensor notation:

$$\begin{aligned} \tau_{ii} &= 2\mu\left(\frac{\partial v_i}{\partial x_i} - \frac{1}{3} div\vec{v}\right) \\ \tau_{ij} &= \tau_{ji} = \mu\left(\frac{\partial v_i}{\partial x_j} + \frac{\partial v_j}{\partial x_i}\right) \end{aligned} \qquad (7)$$

with following source term Q:

$$\vec{Q} = \begin{bmatrix} 0 \\ \rho f_{e,x} \\ \rho f_{e,y} \\ \rho f_{e,z} \\ \rho \vec{f_e} \cdot \vec{v} + \dot{q}_h \end{bmatrix} \qquad (8)$$

In absence of external force and in non-rotating system the source term is equal to zero. In a rotating frame of reference the Coriolis and centrifugal forces have effects on the source term. The appropriate formulation in this case is to be found in [1].

2.2.2. Turbulence Modeling

An MDO systems requires a large number of designs evaluation partly by means of flow simulations to achieve an improved design. The time and memory consuming DNS and LES methods are therefore out of reach of actual MDO systems. In the Reynolds-Averaged Navier-Stokes equation (RANS) the turbulence is however fully modeled. The time efficient RANS equations are consequently widely used on MDO systems. To account for turbulence the in-house Navier-Stokes equations solver uses a modified version [7] of SpalartAllmaras (SA) one-equation turbulence model [8; 9]. The SA Model is based on a linear eddy viscosity. It defines the turbulent viscosity (eddy viscosity) as:

$$\mu_T = \rho\tilde{\nu} f_{v1} \quad f_{v1} = \frac{\chi^3}{\chi^3 + c_{v1}^3} \quad \chi = \frac{\tilde{\nu}}{\nu} \tag{9}$$

the fully turbulent version of the transport equation for the variable $\tilde{\nu}$ is

$$\begin{aligned} \frac{D\tilde{\nu}}{Dt} &= \underbrace{c_{b1}\tilde{S}\tilde{\nu}}_{\text{production}} \\ &+ \underbrace{\frac{1}{\sigma}\{\nabla\cdot[(\tilde{\nu}+\nu)\nabla\tilde{\nu}] + c_{b2}(\nabla\tilde{\nu})^2\}}_{\text{diffusion}} \\ &- \underbrace{c_{w1} f_w(r)\left(\frac{\tilde{\nu}}{d}\right)^2}_{\text{destruction}} \end{aligned} \tag{10}$$

Full details about the used modified Spalart-Allmaras model can be found in [7].

The SA model is linked to the Navier-Stokes equation by the extension of the dynamic viscosity μ on equation 7 [1]:

$$\mu = \underbrace{\mu_L}_{\text{laminar viscosity}} + \underbrace{\mu_T}_{\text{turbulent viscosity}} \tag{11}$$

3. Results

The first result concerns the verification and porting for GPU of the in-house CFD solver for inviscid Euler-governed flows using the GAMM circular bump testcase [10]. The second result is the validation of in-house CPU-based solver for turbulent viscous flows against the VKI turbine inlet guide vane testcase [11].

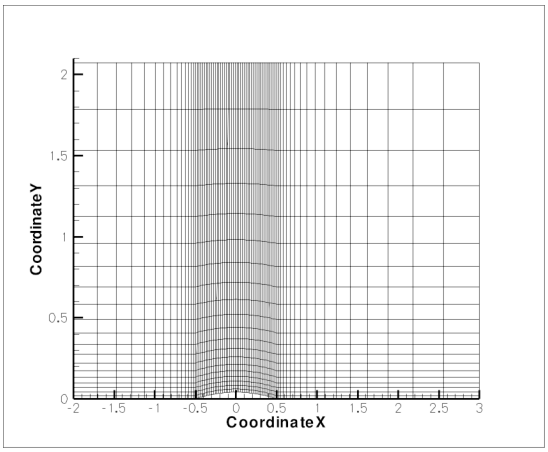

Figure 3: 72x21 Mesh of the GAMM [10] test case

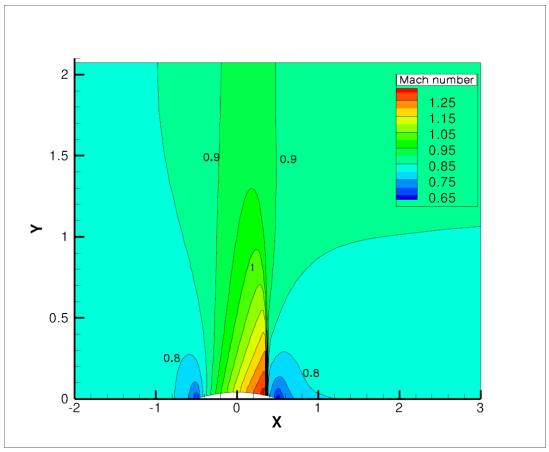

Figure 4: Mach contours for output isentropic Mach number of 0.85

3.1. GAMM circular arc "bump"

The test case is an internal transonic flow through a parallel channel having a 4.2 % thick circular bump on the lower wall as shown in Figure 3. The boundary condition concerns the exit pressure giving an isentropic Mach number of 0.85. The Mach number contours presented in figure 4 shows a supersonic pocket on trailing edge of the bump ended by a normal shock. The solver uses a central scheme for the space discretization. For the sake of verification the same test case with same setting is run by Numeca FineTurbo CFD solver with Spalart Allmaras turbulence model. Comparison of the pressure coefficient c_p of both simulations is shown in figure 5. The two distributions are very close and predict the shock at the same position on the bump. The Numeca solver predicts however a higher pre-shock Mach number.

Starting from a low level of complexity the performance of the ported Euler equations solver has been measured on this test case. A relative small speedup of 1.15 has been achieved, which is a reasonable start for a GPU program not making use of most of the GPU optimization techniques.

Table 1: Performance comparison on GAMM inviscid testcase

Hardware	Number of cores	Memory Bandwidth [GB/s]	Speedup
Xeon(R) E3	1	25.6	1
Tesla C2070	448	144	0.6
Geforce 780	2304	288.4	1.15

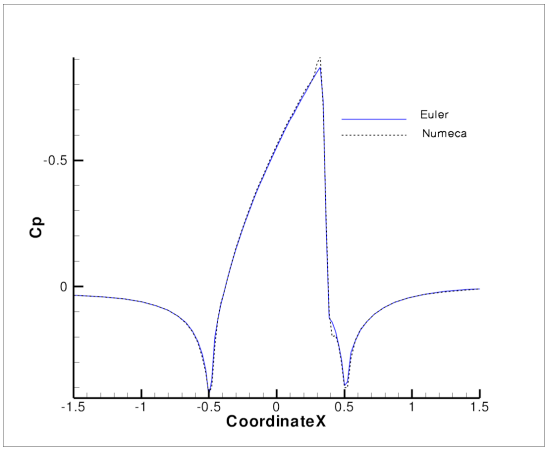

Figure 5: Cp distribution along the channel lower wall for different solvers (M2i=0.85)

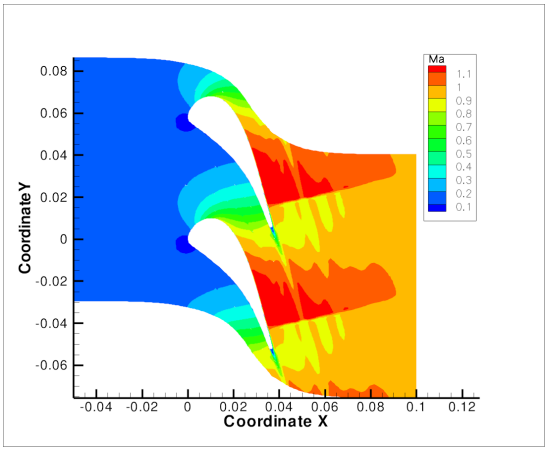

Figure 7: Mach contours of the transonic LS89 [11] turbine guide vane test case

3.2. *LS89 Transonic Turbine Guide Vane*

Figure 6 shows the multi-block mesh used on the testcase. An O-mesh block with small near wall cell width surrounds the turbine guide vane profile for a better resolution of the boundary layer.

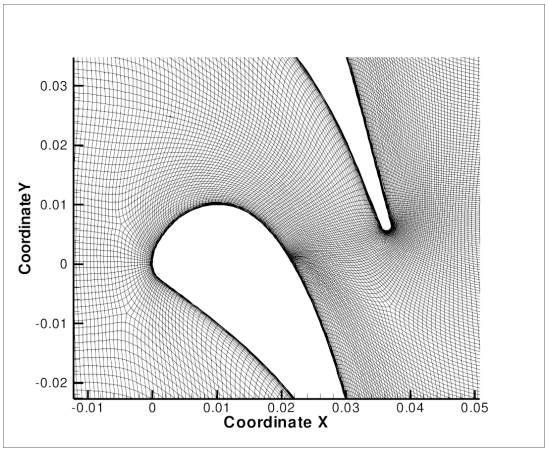

Figure 6: Multiblock Mesh of the LS89 VKI turbine guide Vane cascade [11]

The boundary condition concerns the exit isentropic Mach number, which leads to a subsonic or a transonic testcase. Figure 7 shows the Mach number contours of the transonic testcase revealing a normal shock occurring on the suction side of the profile.

The isentropic Mach number is computed from local static pressure using a constant total pressure equal to the inlet total pressure. The isentropic Mach number is obtained by following equation:

$$M_{is} = \sqrt{\frac{2}{\gamma - 1}((\frac{p_0}{p})^{\frac{\gamma-1}{\gamma}} - 1)} \qquad (12)$$

For the validation, numerical isentropic Mach number has been compared to the experimental one. Figure 8 and 9 shows the turbine blade surface isentropic Mach number distributions of the experiment and the numerical calculation with a subsonic and a transonic exit isentropic Mach number. The calculation results are in a fair agreement with the experimental data although the transonic case is better resolved

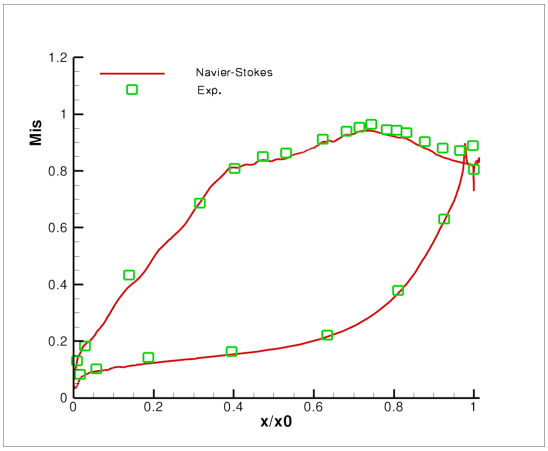

Figure 8: Mach-number distribution on LS89 turbine subsonic case : M_{is}=0.84 and P_{01}= 1.435 bar

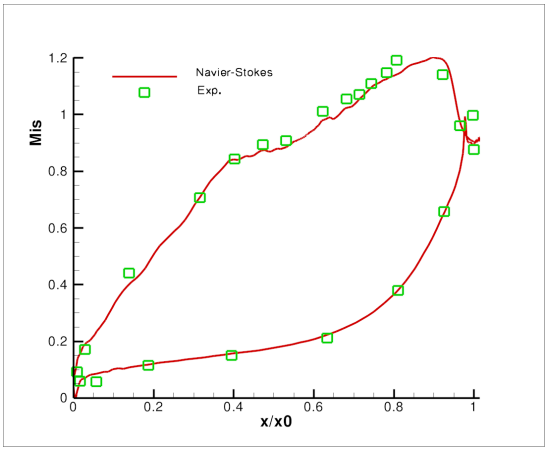

Figure 9: Mach-number distribution on LS89 turbine subsonic case : M_{is}=1.02 P_{01}= 1.605 bar

4. Conclusion

This work showed the progress of the development toward a GPU-based multidisciplinary design optimization system. The focus is on the CFD solver of the MDO system. First performance optimization of 15% are performed on Euler-governed flows. The validated CPU version of the Navier-stokes solver will be ported and a wide variety of GPU optimization techniques will be used to achieve an interesting speedup able to compete with the implicit version of the same in-house flow solver. The acceleration of the CPU solver using multigrid techniques will be performed for a mature performance comparison with future GPU-version. The multigrid acceleration technic will be investigated on GPU also as it showed benefits on GPU clusters [12; 13].

Acknowledgments

This research activity is funded by a Marie Curie Action as part of the European union's Framework 7 research program (AMEDEO :Project No. 316394). This work is using the CPU-based Solver of Dipl.-Ing. Lasse Müller

References

[1] J. Blazek, Computational Fluid Dynamics:Principles and Applications, Elsevier, 2001.

[2] E. Lindholm , J. Nickolls, S. Oberman and J. Montrym , Nvidia Tesla: a Unified Graphics and Computing Architecture, Micro, IEEE 28 (2) (2008) 39–55.

[3] Nvidia, CUDA C Programming Guide, PG-02829-n 001 v5.5, 2013.

[4] Verstraete T., CADO: a computer aided design and optimization tool for turbomachinery applications, 2nd International Conference on Engineering Optimization.

[5] Brandvik, Tobias and Pullan, Graham , An Accelerated 3D NavierStokes Solver for Flows in Turbomachines, Journal of Turbomachinery 133 (2).

[6] B. Zimmerman and Z.J. Wang , The Efficient Implementation of Correction Procedure Via Reconstruction with GPU Computing, AIAA 2013-2692.

[7] J. R. Edwards and S. Chandra, Comparison of Eddy Viscosity-Transport Turbulence Models for Three-Dimensional, Shock-Separated Flowfields, AIAA Journal.

[8] Spalart P. R. and Allmaras S. R., A one-equation turbulence model for aerodynamic flows, AIAA-Paper 92-0439.

[9] Allmaras S. R., Johnson F. T. and Spalart P. R., Modifications and Clarifications for the Implementation of the Spalart-Allmaras Turbulence Model, ICCFD7-1902.

[10] A. Rizzi and H. Viviand, Numerical Methods for the Computation of Inviscid Transonic Flows with Shock Waves, Notes on Numerical Fluid Mechanics (3).

[11] T. Arts, M. Lambert de Rouvroit and A.W. Rutherford, Aerothermal Investigation of a highly loaded transonic linear Turbine Guide Vane Cascade, TN 174, von Karman Institute for Fluid Dynamics (1990).

[12] D. Göddeke, Fast and accurate finite-element multigrid solvers for PDE simulations on GPU clusters, Ph.D. thesis, Technische Universität Dortmund, Fakultät für Mathematik (May 2010).

[13] D. Goddeke, R. Strzodka, J. Mohd-Yusof, P. McCormick, H. Wobker, C. Becker, S. Turek, Using gpus to improve multigrid solver performance on a cluster, Int. J. Comput. Sci. Eng. 4 (1) (2008) 36–55.

Numerical Investigation of Inlet Distortion on the Stall Inception of a Radial Compressor

Stefano Vagnoli

Turbomachinery Department, von Karman Institute for Fluid Dynamics, Belgium, stefano.vagnoli@vki.ac.be

Supervisor: Tom Verstraete

Assistant Professor, Turbomachinery Department, von Karman Institute for Fluid Dynamics, Belgium, tom.verstraete@vki.ac.be

University Supervisor: Francesco Martelli

Professor, Mechanical Engineering, University of Florence, Italy, francesco.martelli@unifi.it

Abstract

In this paper unsteady CFD computations are used to study the stability and the rotating stall inception of a transonic radial compressor, considering two different configurations influencing the inlet flow.
The influence on the stability limit of an elbow installed in front of the compressor is analyzed by means of unsteady RANS simulations and compared to an undistorted flow resulting from a straight inlet.
All simulations are done modeling the whole annulus of the radial machine, using high performance computing, in order to take into account the non-periodic phenomena leading to stall inception. The mechanisms leading to flow separation in the low mass flow regime are studied, pointing out how they are influenced by the unsteady interactions between the tip leakage vortices and the distorted flow field resulting from the inlet elbow.

Keywords: Radial compressor, stall, URANS, inlet distortion

1. Introduction

An efficient design of radial compressors is closely linked to the prediction of the stall limit and the improvement of the operating range. To this sense, it is important to understand how the transition to stall takes place, and which technical solutions can be implemented to enhance the stability of the machines working close to stall.
Today the design of efficient and stable compression systems becomes increasingly more challenging considering that more compact solutions are required, resulting from strict limits on the encumbrances and weight. Because of this, bent pipes are often installed in the proximity of the compressor inlet, forcing the impeller to operate with a nonuniform inlet flow, which will affect the performance and the stall limit.
A first structured classification of the main stall inception mechanisms for compressors can be attributed to Camp and Day [1]. In this work, the authors clearly identify two kinds of stall inception. The modal stall is given by a circumferential oscillation taking place close to the peak of the pressure rise characteristic, which leads to an abrupt massive separation of a large part of the annulus. The spike stall inception, on the other hand, is a progressive phenomenon beginning with a flow separation in one particular blade, usually limited to the tip region, which leads to the development of one or more rotating stall cells. A progressive stall inception due to a partial flow separation at the tip of the radial compressor inducer is also pointed out by Frigne and Van den Braembussche [2] who define this kind of stall as Progressive Impeller Rotating Stall (PIRS).
For centrifugal compressors, it is not as trivial to identify the occurrence of stall as in axial compressors. This is particularly due to the fact that in radial impellers the presence of stalled profiles is often indicated by an increase of noise only, without an abrupt change of performance [3], since the centrifugal effect is always predominant on the aerodynamic one.

For unshrouded transonic compressors, one of the most important initiators of rotating stall is the interaction between the tip clearance vortex and the main flow [4; 5; 6]. It is generally agreed that at the stall limit the interface between incoming and tip flow lines up with the leading edge of the blades [5]. Based on that, methods to increase the stall limit by means of casing treatment of the shroud have been often proposed and analyzed [7].
Because of the intrinsically time-dependent nature of the stall itself, it is not trivial to reproduce the rotating stall inception by means of CFD: an unsteady approach shall be used, and the whole annulus of the compressor has to be analyzed, to take into account the non-periodic time-dependent nature of the phenomenon. Such kind of approach is highly time consuming, and has become possible in the recent years only, thanks to an increased computational power.
Few studies can be found in literature with the aim to numerically reproduce the rotating stall, mainly related to axial compressors [4; 8; 9; 10]. This emphasizes a lack of similar studies applied on centrifugal compressor.
Chen [4] and Gourdain [10] compare numerical results with experiments for axial compressors in stall. Despite a close prevision of the operative point at the stall inception limit, differences between CFD and experiments are observed in terms of representation of number and velocity of stall cells. To explain this, Gourdain points out a possible influence of the whole experimental set-up on the stall development.
Another element that could heavily influence the rotating stall inception is the non-uniformity of the flow entering the compressor. This can be due to for example bended pipes installed really close to the inlet, because of strict space constraints to be taken into account during the design of many applications.
For radial compressors, Engeda et al. indicated a lack in literature about inlet distortion effects [11]. Ariga et al [12] studied the influence of different types of total pressure inlet distortions experimentally, comparing the performance of the impeller with distorted and undistorted inlet flow. The degradation of the performance due to nonuniformities becomes more remarkable at high mass flow, while little effect is noticed at lower mass flow, as also confirmed by other authors [13]. Moreover, Ariga states that under some circumstance the surge margin can be even slightly increased by imposing a circumferential perturbation.
From a numerical point of view, Kim et al. [14] investigate three different bends with the aim to reduce the nonuniformity at the impeller inlet and to improve the performance of the machine. In this case, CFD is only used to design the inlet duct, but the effect on the radial compressor itself is not investigated. Sheoran et al. [15] studied the effect of standard configurations of flow distortion at the inlet of an axial machine. For this purpose, a steady RANS approach is used, coupling the impeller and the static parts by frozen rotor interfaces.
The aim of the current paper is to analyze in detail the transition to stall of a transonic radial compressor through numerical simulations. The influence of a bent pipe and of a straight inlet installed upstream the impeller is investigated by means of coupled unsteady RANS simulations of the inlet duct and the radial compressor. A full annulus model of the compressor is used to take in account the non-periodic nature of the rotating stall.

2. The Flow Solver and Numerical Model

2.1. The Flow solver

In the present work, the commercial software FINE/TURBO has been used to solve both steady and unsteady compressible Reynolds-Averaged Navier-Stokes (URANS) equations. This is a second order cell-centered finite volume solver for structured multiblock meshes.
For the Unsteady RANS simulations 405 time steps are used to model one rotation of the compressor. The solution for every time step is obtained by means of 100 internal iterations, using the 4th order Jameson's time scheme.

2.2. Analyzed Geometry

The geometry used in this investigation is shown in Fig.1(a). It is a transonic radial compressor, whose shape has been optimized at the von Karman Institute of Fluid Dynamics. The geometry consists of an unshrouded impeller with 9 main and 9 splitter blades, and a vaneless diffuser. The main design parameters are shown in table 1.
Two different configurations for the flow at the inlet have been considered. In the first case, a straight pipe is modeled, whilst in the second case a 90° bent section is imposed upstream of the impeller. Dimensions of the bent pipe are shown in Fig.1(b).

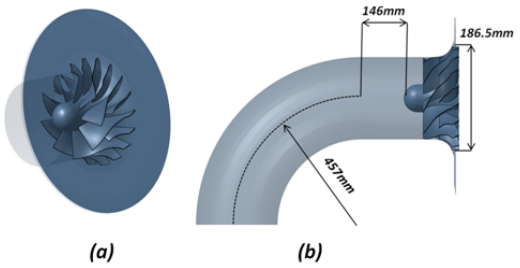

Figure 1: (a) Geometry of the radial transonic compressor analyzed. (b) Bent pipe considered for the analysis.

Table 1: Design parameters for the centrifugal compressor in study.

PARAMETER	DESIGN VALUE
Design massflow	10.84 (kg/s)
π_{TT} design	3.87 (-)
η_{TT} design	0.845 (-)
Rotation velocity	24800 (RPM)
Matip (based on ωr_{tip})	1.11 (-)
Number of main blades	9
Impeller exit radius	186.5 (mm)
Clearance (% of span at LE)	1%

2.3. Numerical Setup

The mesh representing the full annulus of the radial compressor is composed by 25 x 10^6 nodes, maintaining the $y+$ at wall around 20 to permit a correct application of wall models. A detail for one blade passage is shown in Fig.2. 16 elements have been used in radial direction to correctly reproduce the flow at the tip.

At the inlet, standard RANS boundary conditions

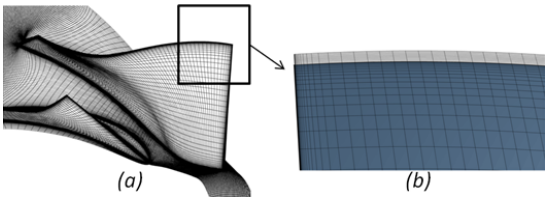

Figure 2: Detail of the mesh for one blade passage (a) and detail of the tip clearance mesh (b).

such as uniform total pressure, uniform total temperature and the velocity direction are assigned for all cases.

The outlet boundary condition needs to be discussed in detail. When the compressor is modeled alone, it is important to avoid the inception of a large surge cycle, which cannot be represented without taking into account the whole compression system. Imposing a constant pressure at the compressor outlet, the static stability condition for the system cannot be satisfied on the part of the characteristic curve which has a positive slope, according to the lumped parameter theory introduced by Greitzer [16]. This means that a surge cycle will be initialized in this part of the curve. Because of this, a constant pressure boundary can be used for a preliminary analysis only, to get useful information on the very first stall inception mechanisms [4; 5; 9]. Such information has to be extracted with care, since the further stall cell development will be strongly influenced by the surge.

A proper boundary condition to get stable rotating stall configurations without surge inception requires an increase of the static stability limit, and this can be achieved using a relation between mass flow and pressure with one degree of freedom, as shown in equation 1.

$$p_{out} = p_0 + \kappa \cdot \dot{m} \tag{1}$$

In this case, the equation represents the effect of a valve installed at the compressor outlet. The parameter κ is the throttle setting, and an increase of this value represents the closure of the throttle itself.

It is worthwhile to note that such a boundary condition does not introduce any further inertial effect for the outlet flow, representing a fully resistive system for the electrical analogy. This means that, according to Greitzers analysis, the dynamic stability limit will be similar to the static one.

Before studying the flow close to stall with an unsteady RANS, a first estimate of the stability limit of the machine is made by means of steady simulations, using a frozen rotor approach. The last stable operating point is identified by gradually closing the numerical throttle until convergence can no longer be obtained. At this point, unsteady simulations are initialized introducing a sliding mesh interface in between the static inlet and the compressor.

3. Detection of the Stall Inception Mechanisms: Configuration in Surge

A preliminary study has been conducted imposing a constant outlet pressure, with the purpose to analyze which are the first stall inception mechanisms for the machine. This information would then be useful to eventually detect these unsteady phenomena for the

stabilized solutions obtained with the boundary condition described by equation 1.

Fig.3 shows the entropy field at 98% of the span at the last stable operating point for this set up. The flow field is already in good agreement with the Vo criterion [5] for the stability limit, since the entropy peak, corresponding to the interaction between main flow and tip vortex, is lined up with the blade passage inlet.

To get a first unsteady solution of the flow, a time-

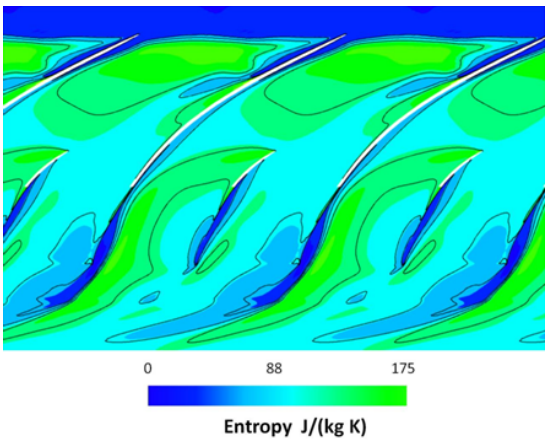

Figure 3: Entropy field at the last stable RANS steady solution detected with constant outlet pressure .

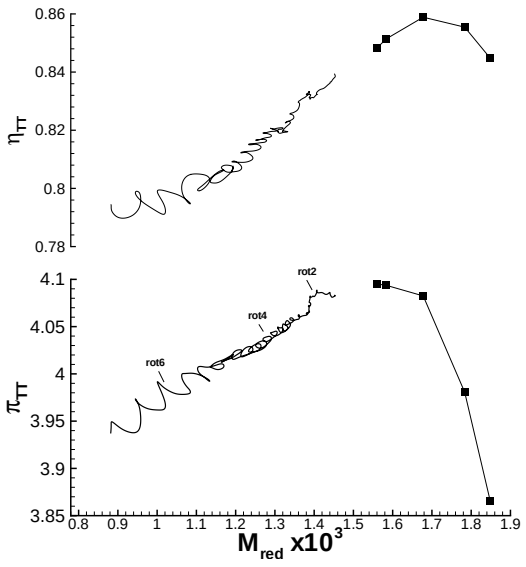

Figure 4: Overal performance of the compressor during stall at high fixed outlet pressure: total to total pressure ratio (lower part) and total to total efficiency (higher part).

dependent simulation is performed using the last stable boundary condition detected by the steady computations. After that, the fixed outlet pressure is progressively increased by 1% during a transient lasting two rotations.

The global performance detected during the time dependent analysis, shown in Fig. 4, depicts a decay of efficiency and pressure ratio. Strong fluctuations are clearly visible here after τ_{rot}=6, describing a strengthening of the unsteadiness due to rotating stall induced by the surge cycle.

Fig. 5 shows the entropy field in a plane perpendic-

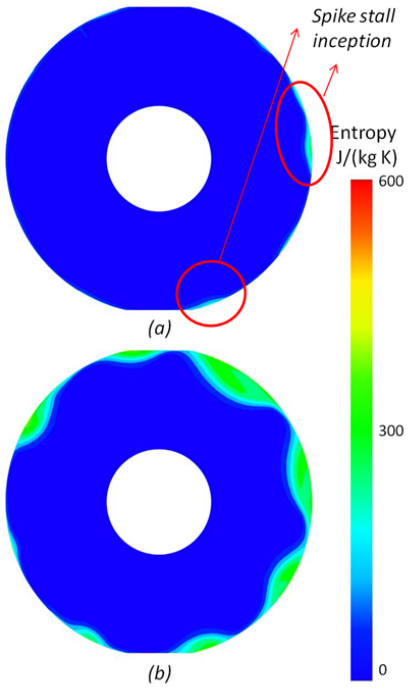

Figure 5: Entropy field on the surface at z/c_{main}=0.12 for τ_{rot}=5.5 (a) and τ_{rot}=6.5 (b).

ular to the streamlines, taken at z/c_{main} = -0.12 from the blade leading edge, between τ_{rot} 5.5 and 7.5. At the first time instant, two small sections of the passage close to the casing are characterized by an higher entropy value, having the clear shape of a spike-type disturbance taking place at the tip of two blades. Such disturbances lead then to the inception of the stall cells, which are strongly influenced by the surge cycle, and because of that they will not be further discussed.

To represent the first unsteady mechanisms inside the impeller, Fig. 6 represents the entropy field at 85% of span.

Already at τ_{rot}=2 the entropy field is not uniform among the passages, showing a high entropy flow completely covering the suction side of few blades only, for which the blockage is higher.
Fig. 7 represents a detail of flow streamlines at tip at τ_{rot}=2. The tip vortex, marked in red, breaks down mixing with the main flow. Such interaction is responsible of the formation of an area of high entropy at the center of the blade passage, which deviates the entering streamlines, locally increasing the blockage.
The non-uniform entropy field depicted in Fig. 6 at τ_{rot}=2 is due to the non uniform effect of the blockage among channels, generated by the tip vortex fluctuating in time, as will be clarified in the next sections. This creates two primordial stall cells evolving towards a global separation of the flow at the blade tip at τ_{rot}=4 and then to the formation of the stall cells.

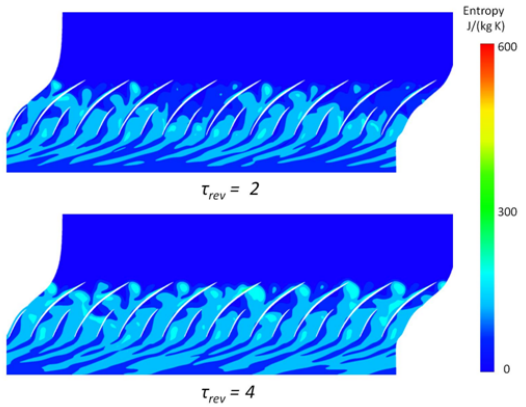

Figure 6: Entropy field at 85% span for rotation 2 and 4 at high fixed outlet pressure.

4. Analysis of the Stability Limit for the Configurations with Straight and Bent Pipe

Based on the results obtained from the previous analysis, attention will be focused in particular on the entropy field at the compressor tip and its evolution in time, to detect the interaction between tip and main flow.
Stabilized points have been obtained using the outlet boundary condition defined by equation 1. Values for κ are shown in teble 2.

4.1. Centrifugal Compressor With Straight Inlet

For the configuration with straight inlet, the three operating points shown in Table 2 have been progressively analyzed with an unsteady approach. Before this, the characteristic curve close to stall has been reproduced using a steady RANS approach and equation 1 for the outlet, varying the value of κ. The last stable boundary condition has been used to initialize a first unsteady simulation.
The global performance of the compressor over time is plotted in Fig. 8. For the URANS simulations, values over time from rotation 3 are considered. At the last stable RANS operating condition the characteristic curve has a clear positive slope. Moreover, a different performance estimate between steady and time-dependent solutions at the same massflow is depicted. In this part of the curve, performances are strongly influenced by the unsteady interaction of tip vortex, main flow and shock at the tip, and the different values obtained can be related to the more accurate unsteady reproduction of such phenomenon.

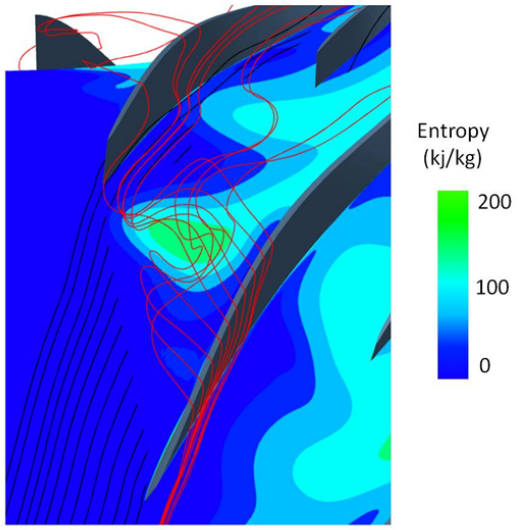

Figure 7: Detail of the stream vortex main flow interaction at tip and its effect on the entropy field at 85% span.

Table 2: Values for k for the different cases analyzed according to equation 1.

COMPRESSOR WITH STRAIGHT PIPE	COMPRESSOR WITH BENT PIPE
CASE 1 (C1) : k = 3100	CASE 4 (C4) : k = 3000
CASE 2 (C2) : k = 3250	CASE 5 (C5) : k = 3150
CASE 3 (C3) : k = 3400	CASE 6 (C6) : k = 3300

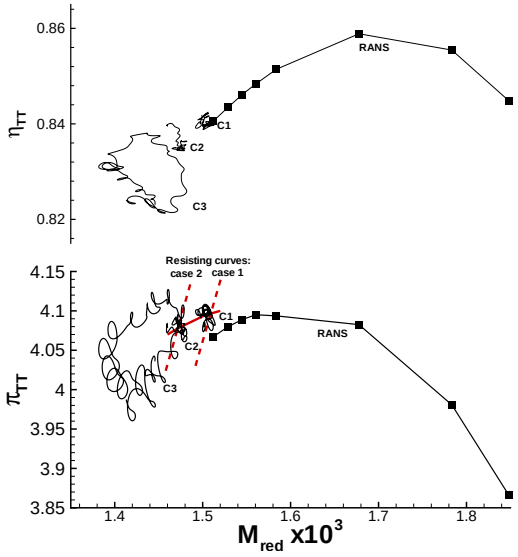

Figure 8: Overal performance of the compressor for cases 1, 2 and 3: total to total pressure ratio (lower part) and total to total efficiency (higher part) together with RANS results for higher massflow operating points. The compressor curve (in red) respects the stability limit imposed by the resisting curves (in dotted red) for cases 1 and 2.

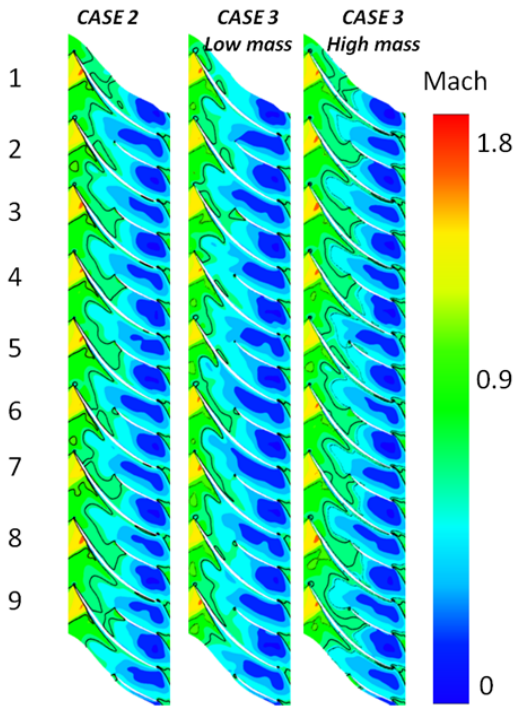

Figure 9: Blade to blade relative Mach number at 85% of blade span.

Cases 1 and 2 show an unsteady high frequency fluctuation of performance in time around a well defined average value, leading to quasi stable solutions. The intersection between the throttle and the compressor curve clearly shows that operative points 1 and 2 respect the stability limit (the local tangent of the throttle curve is still higher than the one of the compressor). Since the dynamic stability limit is similar to the static one for such configuration, an inception of surge is not expected in these points.

Case 3, on the other hand, shows a large periodic fluctuation which continues also for τ_{rot} beyond 10. This is related to a cycle of hysteresis caused by surge of the analyzed configuration. The small volume represented by the computational domain composed by rotor, bladeless diffuser and pipe leads to a relatively high frequency fluctuation for the phenomenon, estimated to be around 135Hz based on the frequency of the fluctuation of the entering and exiting massflow.
Fig.9 shows the impeller relative Mach field at 85% span for the last quasi-stable URANS case at τ_{rot}=5, and for condition 3 at the highest and lowest massflow during the surge cycle. The low mach zone at the impeller outlet is due to the jet-wake effect, while the flow on the suction side of the inducer is dominated by a shock wave.
A low Mach number area can also be noticed at the suction side of blades along the inducer, representing a zone of higher blockage due to flow separation generated by the interaction of the shock wave with the boundary layer. The separated low velocity flow is merging with the wake and affects a high part of the blade passage at tip, which increases with decreasing massflow. Despite the separation along the profiles, an abruptly unstable condition due to profile stall is not obtained, because of the much higher contribution of the centrifugal force in the pressure rise. Strong performance variation compared to the stable solutions are detected for the configuration in surge only.
Fig.10 shows the entropy field at 85% span for the same cases. The lower massflow configurations present an area of high entropy on the blade suction side involving the whole inducer, showing a thickened boundary layer just upstream of the shock. The non uniform entropy field in the middle of the passage represents a mixing between main flow and tip vortex which is fluctuating in time, similarly to what is described in the previous section.
To better understand the interaction between the time dependent tip vortex and the main flow, a detail of the relative Mach and pressure field at 92% of span for

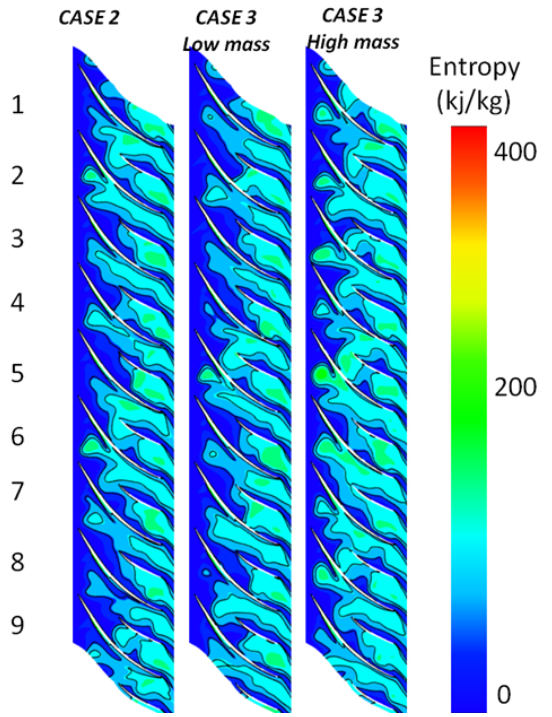

Figure 10: Blade to blade entropy field at 85% of blade span.

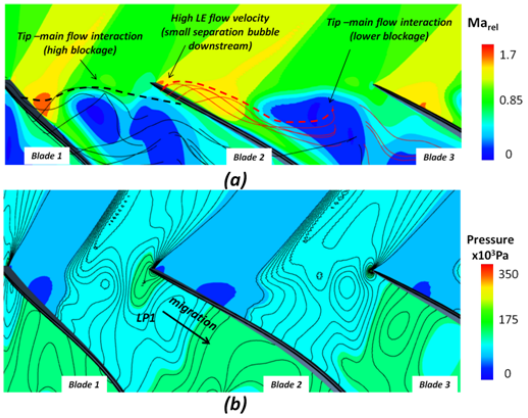

Figure 11: Relative Mach (a) and Pressure field (b) at 92% of span for case 2 at time = t_0. The tip flow of passage 1 is represented in black, while the one of passage 2 is in red.

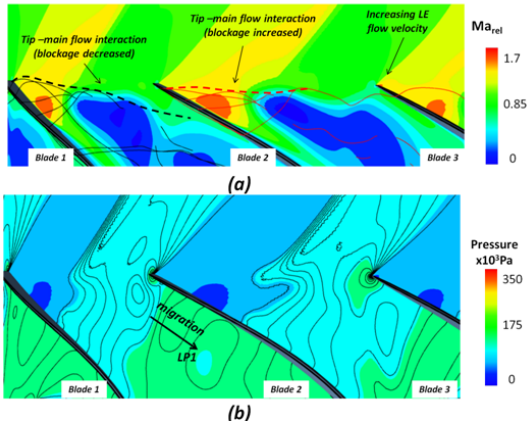

Figure 12: Relative Mach (a) and Pressure field (b) at 92% of span for case 2 at time = $t_0 + \tau_{rot}/8$. The low pressure area migration is indicated.

case 2 is shown in Fig.11 for a reference time t_0, whilst the same fields are shown in Fig. 13 for the time $t_0 + \tau_{rot}/8$.

According to Fig.11(a), blade 1 is highly loaded and characterized by a strong over tip flow. This interacts with the pressure side of blade 2, generating the low pressure area indicated as LP1 in Fig.11(b). The low pressure area is preceded by a higher pressure section, which indicates blockage of the entering main flow. Consequently, the flow velocity at the leading edge of blade 2 increases, leading to the formation of a small separation bubble on the suction side.

This effect, together with the low pressure area on the pressure side, decreases the tip load close to the leading edge of blade 2, generating a weak clearance vortex above the blade itself which does not interact with blade 3.

The pressure field at time $t_0+\tau_{rot}/8$ in Fig.12 (b) shows a migration of LP1 downstream: this leads to a decreasing flow blockage within the passage, restoring the correct blade load at leading edge of blade 2. Its clearance flow tends then to increase, interacting with the pressure side of blade 3 and leading to a variation of blade load (and consequently of tip flow intensity). Such unsteady interaction, schematized in Fig.13, generates the fluctuating tip vortex observed. The frequency of the tip vortex fluctuation at the last quasi stable condition has been estimated to be around 2100Hz. The higher intensity blockage due to the mixing is organized in eight cells propagating within the annulus with an absolute velocity equal to 36% of the compressor rotation velocity.

This phenomenon has been also pointed out by Yamada et al. [17] analyzing the flow field of an axial transonic compressor. For radial compressors with vaneless diffuser, the authors assume that the observed phenomenon correspond to MIRS (Mild Impeller Rotating Stall) as described by Frigne and Van Den Baenbussche [2]. Due to the limited measurement capabilities of that time, limited explanation could be

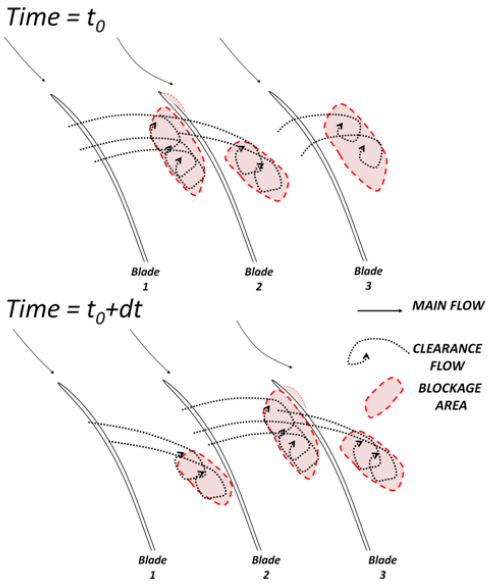

Figure 13: Scheme of the generation of the unsteady tip vortex interacting with the adjacent blades.

given for this.

Fig.14 points out the averaged Fast Fourier Transform performed on the pressure signal taken by three numerical probes placed on the relative frame of reference in the diffuser at r/r_{imp} = 1.2 and 98% of span, and equally spaced in tangential direction. The relative frame of reference has been chosen to directly filter the effect of the blade passing on pressure fluctuations. Detailed data cannot be forcedly achieved in these cases because of the small time window simulated.

The result is strongly influenced by the tip flow unsteadiness. For case 1 and case 2, a peak for pressure fluctuations at φ_{rot}= 5 is detected, and this value fits very well with the calculated vortex frequency (considering that φ_{rot} in the relative frame of reference is equal to the number of cell multiplied by their relative velocity, equal in this case to about the 87% of the compressor speed). The tonal contribution is less visible for case 2, this can be linked to the poor frequency resolution.

We can conclude that despite the fact that the averaged performance is not strongly affected by tip separation, the frequency spectrum produced by the compressor will be characterized by a clear tonal contribution.

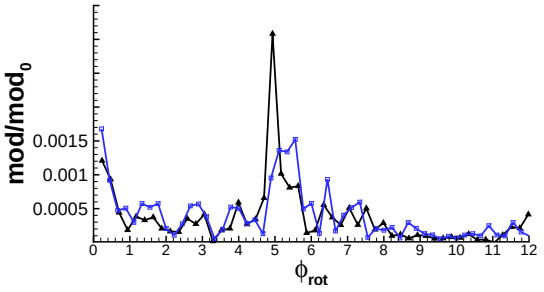

Figure 14: Fast Fourier Transform of pressure field detected on the relative frame of reference for cases 1 and 2.

4.2. *Centrifugal Compressor With Bent Pipe*

The viscous flow field at the outlet of the analyzed bent pipe can be described by Fig. 15, where isolines of the axial component of velocity field for near stall condition are depicted at a distance z/c_{main}=- 0.12 from the leading edge of blades. Together with this, the geometrical angle δ used in this paper to describe the flow is also shown for later reference. At δ = 0°, where a strong increase in axial velocity should be expected for a potential flow, a low momentum zone is present indicating a separation.

The typical secondary flows generated along the elbow will lead then to positive incidence for blades located at negative δ angles, and positive incidence for blades located at positive δ. Similar to the previous configuration, three different conditions are analyzed, with κ values (as per equation 1) shown in Table 2.

The performance is plotted in Fig.16, starting from

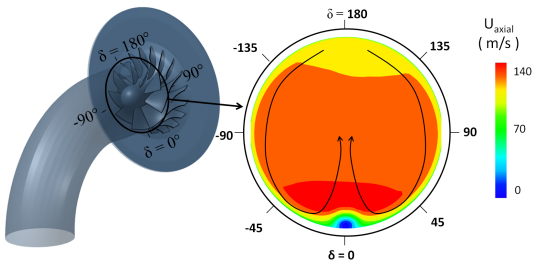

Figure 15: Detail of the flow field at outlet of the bent pipe.

4 rotations onwards to avoid the transient, which is longer than the previous case because of the increased dimension of the domain. Values are then compared to the ones obtained with straight pipe in Fig.17, where the time-average is plotted for the URANS simulation, to make the graph more clear. The inception of a large surge cycle is noticed for case 6, characterized by a fluctuation of lower frequency compared to

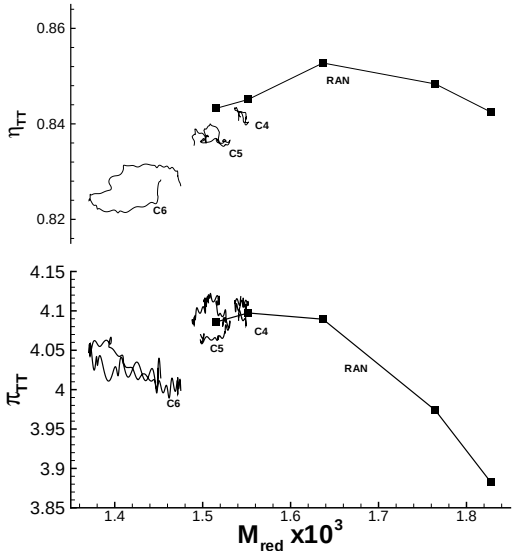

Figure 16: Overal performances of the compressor for cases 4, 5 and 6: total to total pressure ratio (lower part) and total to total efficiency (higher part) together with RANS results for higher massflow operating points.

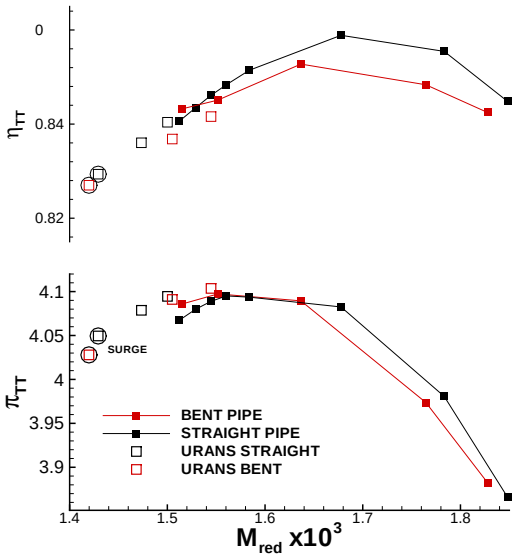

Figure 17: Comparison between averaged results for the straight and bent pipe in terms of total to total pressure ratio (lower part) and total to total efficiency (higher part).

case 4 due to the higher volume of the domain which includes bent pipe. The surge frequency can be estimated in this case to be around 57 Hz. Case 5 shows also a fluctuation of inlet massflow, but it is of limited amplitude compared with the typical configuration in surge, and decreasing with time. Because of this, it has been considered as the effect of a transient stabilizing with time.

Cases 4 and 5 show a lower average efficiency compared to the one obtained for the straight pipe, due to the flow separation in the elbow. Despite this, performance in terms of average pressure ratio is similar, strengthening the consideration that the compressor in study is not significantly affected by different aerodynamic configurations of the flow close to stall, because of the high centrifugal contribution to compression. A stronger effect due to the bent is depicted by the steady results at higher massflow instead, confirming what experimentally observed by Ariga et al. [12].

Fig.18 shows the relative entropy field at 85% of span for case 5, for values at higher and lower massflow for the large surge cycle (case 6), and the design condition computed with the steady frozen rotor approach. As expected, the structure of the flow within the inducer is completely different from the case with straight pipe: separation on the blade suction side is noticed limited to passages interacting with the recirculating flow at the pipe outlet, between δ equal to +45° and -45° (see Fig.15). In this case in fact, a strong incidence on the profile is obtained leading to flow separation on the suction side. As soon as the blade continues beyond -45°, the flow reattaches.

In the area around δ= 0°, the tip vortex main flow interaction is stronger and aligned to the leading edge of blades, increasing the blockage at tip in an unsteady manner according to the mechanisms previously described. On the contrary, the tip vortex - main flow interacting area appears to be within the channel for δ close to 180°, which is typical for non stalled passages according to the Vo criterion.

Fig.19 shows the instantaneous incidence of the flow on the leading edge of the nine blades of the compressor at 85% span for case 1 and 5, which are characterized by a similar value of massflow. The incidence of the flow has been evaluated considering the circumference at the required radius at a distance z/c_{main}=-0.06 from the blades. The circumference has been then splitted in nine equal arcs, each representing the flow interacting with a specific blade, and the incidence has been spatially averaged along such sections.

When the bent pipe is installed in front of the compressor, the strong effect of the recirculation entering the blade passages at δ= 0° is clearly shown by the high incidence on the profile in that position, leading the flow to separate. A lower incidence compared to the configuration with straight inlet is depicted for all the other channels, due to the increase of the average

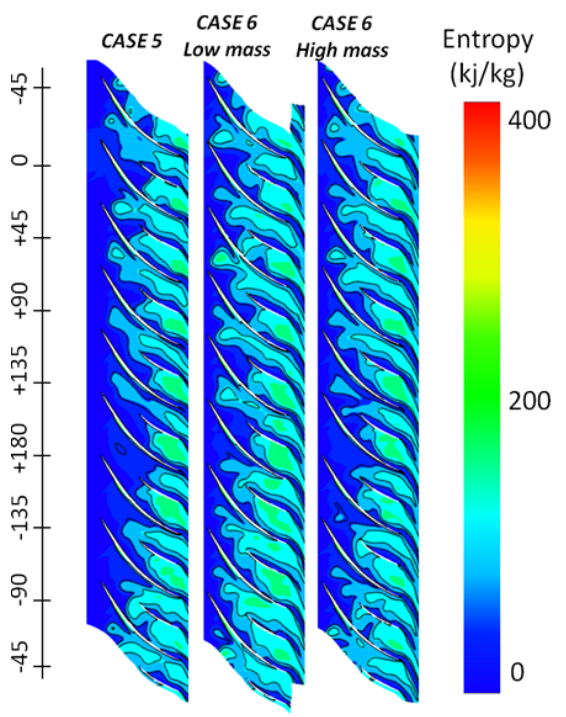

Figure 18: Blade to blade entropy field at 85% of blade span for cases with bent pipe.

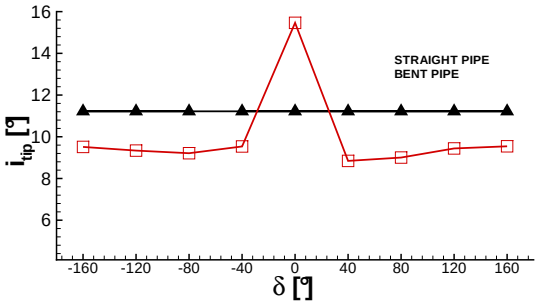

Figure 19: Calculated incidence of the flow on blade leading edge at 85% span for case 1 (straight pipe) and case 5 (bent pipe).

velocity, consequently to the blockage taking place at the bent pipe outlet for δ= 0°. The lower incidence in this area is consistent with the observation of a flow reattaching after δ= -45°. The effect of secondary flows on incidence is limited compared to the one of the separated flow at δ = 0°, and can be recognized in a slightly higher value for blades at negative δ, compared to the ones at positive δ. Because of this, no noticeable influence on the flow field within the passage is expected due to secondary flows.

5. Conclusions

A study on rotating stall inception based on a numerical unsteady approach analyzing the full annulus of a radial compressor has been presented, with the purpose to point out the influence of a bent pipe placed in front of the compressor inlet.
The approach has been applied first to the case with straight pipe imposing a constant pressure value at the outlet of the domain. In this case, a large surge cycle appears, and eight fully developed stall cells are reproduced by the simulation for the compressor after 6.5 rotations, merging together afterwards. The very first mechanisms leading to stall inception are linked to a limited unsteady flow separation at blade tip, influenced by the fluctuation of tip vortex.
In order to analyze the behavior of the compressor working in points close to stability limit without surge inception, a more dynamically stable boundary condition has been employed. The flow field shows clear differences in this case between the configuration with straight inlet and with bent pipe.
For the first case, a separated flow is detected at the tip of all blades. An unsteady interaction of the tip vortex and the main flow has been observed, leading to a pressure fluctuation and an unsteady circumferentially non-uniform blockage among passages limited to the tip, organized in 8 cells rotating at 36% of rotor speed.
For the configuration with a bent pipe the flow separates along the elbow, creating an area of blockage at the pipe outlet limited to a small portion of the passage close to the shroud. Because of that, the incidence increases at tip of blades interacting with the low-momentum flow, leading to separation on the suction side. The flow then reattaches when the higher momentum flow interacts with the blade. By further decreasing the massflow to lower values, a surge cycle develops for both configurations before detecting a typical flow field with completely developed stall cells.
No noticeable difference are then observed between the two different configurations in terms of performance at the stability limit, despite the different flow field inside the machine. The reason for this is that the centrifugal effect on the compression is dominating the aerodynamic one. The steady analysis with frozen rotor approach shows a higher influence of the pipe on performance for higher massflow values, with a clear reduction of pressure ratio and effectiveness for the configuration with bent inlet.

Acknowledgments

The research has received funding from the European Communitys Seventh Framework Programme (FP7, 2007-2013), People programme, under the grant agreement No.FP7-290042 (COPA-GT project).

Nomenclature

Mred	= Reduced massflow
Ma	= Mach number
i	= Incidence
$\dot{m}$	=Mass flow
mod/mod_0	= Modulus over modulus at zero frequency
c	= Chord length at 50% span.
f	= Frequency
p	= Pressure
r	= Radius
t	= Time
z	= Axial direction

Greek symbols

β	= Pressure ratio
δ	= Geometric angle at the pipe outlet
η	= Effectiveness
τ_{rot}	= Time over time of a rotor revolution
φ_{rot}	= Frequency over frequency of rotations
ω	= Rotation velocity

Subscripts

0	= Referred to ambient
imp	= Impeller
main	= Main blade
rot	= Rotations
tip	= Referred to tip
TT	= Total to - total

References

[1] Camp, T. R., Day, I. J., A Study of Spike and Modal Stall Phenomena in a Low-Speed Axial Compressor, ASME Journal of Turbomachinery 120 (1998) 393–401.

[2] Frigne, P., Van den Braenbussche, R. A., Distinction between Types of Impeller and Diffuser Rotating Stall in Centrifugal Compressors with Vaneless Diffuser, ASME Journal of Engineering for Gas Turbines and Power 106 (1984) 468–474.

[3] J. D. Anderson, Compressor Aerodynamics, Longman, Essex, U.K, 1989.

[4] Chen, J. P., Hathaway, M. D., Herrick, G. P., Prestall Behavior of a Transonic Axial Compressor Stage via Time-Accurate Numerical Simulations, ASME Journal of Turbomachinery 130 (4).

[5] Vo, H. D., Role of Tip Clearance Flow on Axial Compressor Stability, Ph.D. thesis, Massachusetts Institute of Technology (2001).

[6] Hah, C., Rabe, D. C., Wadia, A.R., Role of Tip-Leakage Vortices and Passage Shock in Stall Inception in a Swept Transonic Compressor Rotor, no. Proceedings of ASME Turbo Expo 2004: power for land, sea and air. , Vienna, Austria, 2004.

[7] Nolan, S., Effect of Radial Transport on Compressor Tip Clearance Flow Structures and Enhancement of Stable Flow Range, Ph.D. thesis, Massachusetts Institute of Technology (2005).

[8] Niazi, S., Numerical Simulation of Rotating Stall and Surge Alleviation in Axial Compressors, Ph.D. thesis, Georgia Institute of Technology (2000).

[9] Hathaway, M. D., Herrick, G., Chen, J., Webster, R., A Time Accurate Unsteady Simulation of the Stall Inception Process in the Compression System of a US Army Helicopter Gas Turbine Engine, no. Proceedings of the DoD Users Group Conference , Washington, DC, USA, 2004.

[10] Gourdain, N., Burguburu, S., Leboeuf, F., Michon, G.J., Simulation of Rotating Stall in a Whole Stage of an Axial Compressor, Journal of Computers & Fluids 39.

[11] Engeda, A., Kim, Y. , Aungier, R., Direnzi, G., The Inlet Flow Structure of a Centrifugal Compressor Stage and Its Influence on the Compressor Performance, ASME Journal of Fluids Engineering 125 (2003) 779–785.

[12] Ariga, I., Masuda, S., Ookita, A., Inducer Stall in a Centrifugal Compressor with Inlet Distortion, ASME Journal of Turbomachinery 109 (1987) 27–35.

[13] Leilei, W., Ce, Y., Ben, Z., Dazhong, L, Chaochen, M., Du L., The change of the inlet geometry of a centrifugal compressor stage and its influence on the compressor performance, Journal of Thermal Science 22 (3) (2013) 197–208.

[14] Kim, Y., Engeda, A., Aungier, R., Direnzi, G., The Influence of Inlet Flow Distortion on the Performance of a Centrifugal Compressor and the Development of an Improved Inlet using Numerical Simulations, Journal of Power and Energy 215 (2001) 1–16.

[15] Sheoran, Y., Bouldin, B., Murali Krishnan, P., Compressor Performance and Operability in Swirl Distortion, ASME Journal of Turbomachinery 134 (4).

[16] Greitzer, E.M., The Stability of Pumping Systems The 1980 Freeman Scholar Lecture, Journal of Fluid Engineering 103 (1981) 193–235.

[17] Yamada, K., Funazaki, K., Sazaki, H., Numerical Investigation on Relation Between Unsteady Behavior of Tip Leakage Vortex and Rotating Disturbance in a Transonic Axial Compressor Rotor, no. Proceedings of ASME Turbo Expo 2008: power for land, sea and air, Berlin, Germany, 2008.

Residual Distribution Schemes With Variable Distribution Coefficients

Martin Vymazal

Aeronautics and Aerospace Department, von Karman Institute for Fluid Dynamics, Belgium, mymail@vki.ac.be

Supervisor: Herman Deconinck

Professor, Aeronautics and Aerospace Department, von Karman Institute for Fluid Dynamics, Belgium, deconinck@vki.ac.be.

University Supervisor: Chris Lacor

Professor, Department of Mechanical Engineering, Faculty of Applied Sciences, Vrije Universiteit Brussel, Chris.Lacor@vub.ac.be.

Abstract

Residual distribution schemes are discussed in the context of higher order spatial discretization for hyperbolic conservation laws. The discrete solution is approximated by a finite element space based on triangular Lagrangian P_k elements. A natural subtriangulation of these elements allows the reuse of simple distribution formula previously developed for linear P_1 triangles. Curved elements with piecewise quadratic and cubic approximation of the boundaries of the domain are considered.

Since this methodology is difficult to extend in three space dimensions, a new variant of RD scheme is proposed in the second part. This particular formulation avoids the sub–triangulation procedure and allows straightforward extension to quadrilateral elements and to three dimensions.

Keywords: residual distribution, multidimensional upwind, high order, curvilinear geometry

1. Introduction

The present work follows a Residual Distribution approach [1; 2; 3], which is close to continuous finite element methods, but allows the use of a maximum principle to construct nonlinear monotonicity preserving and truely multidimensional stabilizations. In previous papers [4] we have exploited the close relation with continuous finite element discretizations to present a class of higher order residual distribution methods defined on P_k Lagrangian triangular finite elements. Here we focus on the use of curved elements to allow for a higher order representation of the boundaries of the domain, using sub- or isoparametric transformation from physical space to a Cartesian parent element.

2. Notations

We consider the steady state solution of a conservation law on a two–dimensional spatial domain Ω:

$$\frac{\partial \boldsymbol{u}}{\partial t} + \nabla \cdot \boldsymbol{\mathcal{F}} = 0 \quad \forall (x, y) \in \Omega \subset \mathbb{R}^2, \quad \forall t \geq 0, \quad (1)$$

where $\boldsymbol{u}$ is the vector of conserved variables and $\boldsymbol{\mathcal{F}}$ is the inviscid flux vector, $\boldsymbol{\mathcal{F}}(\boldsymbol{u}) = (\mathbf{f}(\boldsymbol{u}), \mathbf{g}(\boldsymbol{u}))$. We denote by $\mathcal{T}_{h,k}$ a triangulation of the domain Ω, whereby each triangular element T of the triangulation $\mathcal{T}_{h,k}$ is a Lagrangian P_k finite element equipped with $K = \frac{(k+1)(k+2)}{2}$ degrees of freedom.

In the simplest case the geometry of the P_k triangle is considered to be linear, defined by its three corner nodes. Hence, the intermediate nodes on the boundary of the element are all located on the straight edges and therefore the boundary of the domain Ω is approximated by a polygone. Such a discretization will be denoted as a P_1P_k discretization (P_1 for geometry and P_k for the solution).

We work with elements whose edges are described by second- and third- order polynomials. Elements with quadratic geometry will be denoted as P_2P_k elements (P_2 for geometry and P_k for the solution). P_2P_2 elements are called isoparametric, while P_2P_k with $k > 2$ are called subparametric elements. The notation for P_3 elements is analogous.

The geometry of the curvilinear P_2 (P_3) element is

transformed to a parent element in ξ–η space. In our

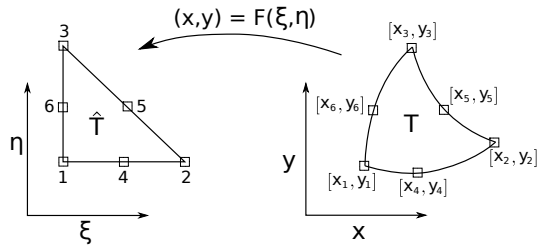

Figure 1: Transformation of triangle geometry from physical to reference space using Lagrange shape functions

case, we define $\mathbf{F}(\xi, \eta)$ from figure (1) as isoparametric mapping

$$\begin{bmatrix} x(\xi,\eta) \\ y(\xi,\eta) \end{bmatrix} = \sum_{i=1}^{N} \varphi_i^{h,k}(\xi,\eta) \cdot \begin{bmatrix} x_i \\ y_i \end{bmatrix} \tag{2}$$

where N is the number of degrees of freedom of P_2 or P_3 triangle, respectively. The number k refers to the order of shape functions φ_i and x_i, y_i denote the nodal coordinates of the triangle.

3. Residual Distribution method

For any triangulation $\mathcal{T}^{h,k}$ the cell residual for a given triangle is defined as the integral over the triangle of the spatial operator:

$$\begin{aligned} \phi^T &= \int_T \nabla \mathcal{F}(u^{h,k})\, d\Omega = \oint_{\partial T} \mathcal{F}(u^{h,k}) \cdot \vec{n}\, dl \\ &= \sum_{s=0}^{N_s} \int_{T_s} \vec{a}(u^{h,k}) \cdot \nabla u^{h,k}\, dx\, dy \\ &\quad (N_s \ldots \text{number of sub–elements}) \end{aligned} \tag{3}$$

where we have used the expression for the Jacobian of the flux $\mathcal{F}(u)$ in (1),

$$\vec{a}(u) = \frac{\partial \mathcal{F}(u)}{\partial u} = \left(\frac{\partial f_1(u)}{\partial u}, \frac{\partial f_2(u)}{\partial u} \right) \tag{4}$$

We can also construct the residual over each P_1 sub-element of $\mathcal{T}^{h,k}$

$$\phi^{T_s} = \oint_{\partial T_s} \mathcal{F}(u^{h,k}) \cdot \vec{n}\, dl \tag{5a}$$

$$= \int_{T_s} \vec{a}(u^{h,k}) \cdot \nabla u^{h,k}\, dx\, dy \equiv \vec{a}^* \cdot \int_{T_s} \nabla u^{h,k}\, dx\, dy \tag{5b}$$

with $\vec{a}^*$ a properly defined local average of $\vec{a}(u)$ over the sub-triangle such that conservation is preserved [5]. The existence of such local average for general nonlinear conservation law is not guaranteed, but in case of the conservation law (1) applied to the Euler equations considered in this work, a conservative linearisation is possible under the assumption that the vector of Roe variables changes linearly in each cell.

The basic idea of the residual distribution (RD) method consists of distributing fractions of this cell residual to the three nodes of the element T. The fraction sent to node $i \in T$ is denoted ϕ_i and we require

$$\sum_{i \in T} \phi_i = \phi^T \tag{6}$$

This requirement can be written in terms of *distribution coefficients* β_i which for consistency sum to unity

$$\sum_{i \in T} \beta_i = 1, \qquad \beta_i = \frac{\phi_i}{\phi^T} \tag{7}$$

After assembling all contributions in the nodes, the nodal equation for node i reads, with $\mathcal{D}_i$ the set of all triangles that share node i:

$$\sum_{T \in \mathcal{D}_i} \phi_i = 0 \tag{8}$$

Since the distribution is restricted to the nodes of the triangle itself, the stencil of the scheme remains compact. This equation can be solved by embedding in a pseudo–time iteration, i.e. by finding a steady state solution of

$$|S_i| \frac{du_i}{d\tau} + \sum_{T \in \mathcal{D}_i} \phi_i^T = 0, \tag{9}$$

where $|S_i|$ is the area of median dual cell.

3.1. Residual Distribution schemes on P_1 elements

For a given P_1 (both solution and geometry) triangle we consider the set of normal vectors $\{\vec{n}_j\}_{j \in T}$, defined by the inward normals to the edges of T facing each node $j \in T$ (see figure 2 left). The norm of $\vec{n}_i$ is equal to the length of the edge. Let us define the upwind parameter

$$k_j = \frac{1}{2} \vec{a}^* \cdot \vec{n}_j \quad \text{implying} \quad \sum_{i \in T_s} k_i = 0 \tag{10}$$

In this case, using a conservative linearisation (eq. 5b, 10), we can express the cell residual as follows:

$$\phi^T = \oint_{\partial T} \mathcal{F}(u^{h,1}) \cdot \vec{n}\, dl = \int_T \nabla \mathcal{F}(u^{h,1})\, d\Omega = \sum_{i \in T} k_i u_i \tag{11}$$

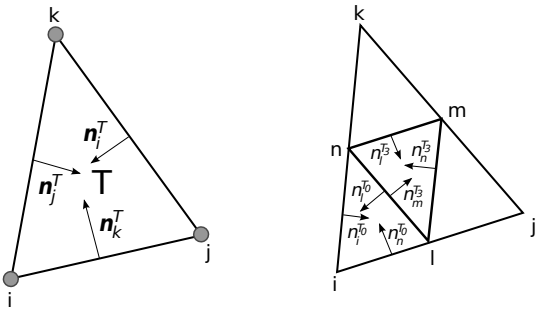

Figure 2: Definition of the normal vectors $\vec{n}_i$ in P_1 and P_2 elements

When all contributions for a given node are assembled, we end up with the following system of nodal equations, similar to equation (9), to be solved using explicit or implicit pseudo-time iterations. For example, using forward Euler method, we get:

$$|S_i|\frac{u_i^{n+1}-u_i^n}{\Delta\tau}+\sum_{T_s,\ i\in T_s}\phi_{i,n}^{T_s}=0 \tag{12}$$

Many distribution schemes (defining the split residuals ϕ_i) for P_1 elements have been developed in the past [4; 6; 7]. A particular class satisfies a multidimensional upwinding property (MU). Such distributions satisfy the requirement that a node in a triangle does not receive a contribution if its opposed face is an outflow face. The condition is easily imposed by requiring $\phi_i = 0$ whenever $k_i < 0$. Within this work, we limited ourselves to the use of the LDA (Low Diffusion A) scheme. Denoting by k_i^+ and k_i^- the positive and negative part of the upwind parameter, $k^\pm = \frac{k\pm|k|}{2}$, the distribution coefficients of the LDA scheme can be written as

$$\beta_i^{LDA}=\frac{k_i^+}{\sum_{m=1}^3 k_m^+} \tag{13}$$

This scheme is of order $O(k+1)$ (k being the order of interpolating polynomial), but not strictly monotone. We refer the reader interested in detailed description of the LDA scheme to other literature [1; 8; 4; 6; 9].

3.2. Residual distribution schemes on P_1P_k elements

Consider now the extension of multidimensional upwind (MU) schemes to high order P_1P_k elements. We will assume that the inward normals $\vec{n}_j$'s are defined on the local P_1 sub-elements $T_s \in T$, as shown on figure 2 (right) for $k = 2$. Note that if we consider a P_1P_k element (P_k element for the solution but only P_1 triangles for the geometry, defined by the 3 corner nodes), the inward normals of the sub-elements can be deduced easily from the ones of the parent element by a simple rescaling. We compute the residual on each sub-element:

$$\phi^{T_s}=\int_{T_s}\nabla\mathcal{F}(u^{h,k})\,d\Omega=\oint_{\partial T_s}\mathcal{F}(u^{h,k})\cdot\hat{n}\,dl \tag{14}$$

Then, this residual is distributed to the 3 nodes of the sub-element, using the LDA distribution scheme (13) developed for P_1 triangles:

$$\phi_i^{T_s,LDA}=\beta_i\phi^{T_s} \tag{15}$$

The linearization used to compute the parameters k_i can be based on any linearized state over the sub-triangle, without affecting accuracy nor conservation.

Remark. *This is not the only strategy to achieve residual distribution schemes on P_k elements. In particular, we refer to Lax Friedrichs distribution schemes of Abgrall and collaborators [10], [11]. In this case the residual is computed on the complete P_k element and then distributed to the N nodes of the element without making use of a sub-triangulation.*

3.3. Curvilinear P_2P_k and P_3P_k elements

We consider elements where the geometry is either piecewise quadratic or cubic. The geometry and numerical solution can be discretized independently so in general the solution can have any order k. However, we focus on isoparametric (P_2P_2 or P_3P_3) high–order elements.

To ensure conservation of fluxes, we compute the sub-element residual from equation (14) as a contour integral:

$$\phi^{T_s}=\oint_{\partial T_s}\mathcal{F}(u^{h,k})\cdot\vec{n}\,dl \tag{16}$$

The boundary ∂T_s is described by transformation (2). For every face on ∂T_s, this transformation is a function of only one parameter ζ:

$$\begin{aligned}x&=x(\zeta)\\ y&=y(\zeta)\end{aligned} \tag{17}$$

We integrate numerical the fluxes of (16) using Gauss quadrature: 3 points per face f of the sub–element for P_2 and 5 points for P_3:

$$\oint_f\mathcal{F}(u^{h,k})\cdot\vec{n}\,dl\simeq\sum_{q=1}^{N}w_q[\mathcal{F}(u_q)\cdot\vec{n}_q]J_q, \tag{18}$$

$$J_q=\sqrt{\dot{x}^2(\zeta_q)+\dot{y}^2(\zeta_q)} \tag{19}$$

where J_q is the Jacobian of transformation (17) at quadrature point q. We use the transformation also to compute the normal $\vec{n}_q$.

The integral over f in equation (18) is approximated:

- by three-point Gauss quadrature for each face of P_1P_1 triangle
- by the same quadrature for each face of each *sub–triangle* in the case of P_1P_2 and P_2P_2 elements
- by five–point Gauss quadrature on each sub–face of the P_3P_3 element

The quadrature nodes and weights on the biunit interval are given in table 1.

	Quadrature points	*Weights*
P_1P_1, $P_{1(2)}P_2$	0.0	$\frac{8}{9}$
	$\pm\sqrt{\frac{3}{5}}$	$\frac{5}{9}$
P_3P_3	0.0	0.5688888889
	±0.5384693101	0.4786286705
	±0.9061798459	0.2369268850

Table 1: Gauss quadrature used to approximate the residuals $\phi^{T,in}$.

3.4. Subsonic flow around a cylinder

We present results for a test case with stagnation point, namely the flow around a circular cylinder at $M_\infty = 0.38$. We consider four O–meshes with 16×5 (M1), 32×9 (M2), 64×17 (M3) and 128×33 (M4) points as described in [12]. The first number indicates the number of nodes in the circular direction of the mesh, the second number refers to the number of nodes in the radial direction (figure 3). The radii of the circles in each mesh follow a geometric series

$$r_j = r_0\left(1 + \frac{2\pi}{128}\sum_{k=0}^{j-1}\alpha^k\right),\ j = 1, 2, \ldots 32, \qquad (20)$$

where $\alpha = 1.1648336$ and $r_0 = 0.5$ is the radius of the cylinder. The farfield boundary is located at 20 diameters from the center. To have the same number of degrees of freedom and make a fair comparison between the P_1P_1 and P_2P_2 schemes, we create a P_1 sub-triangulation of each P_2 triangle. The P_3P_3 meshes were created independently such that the number of *elements* is equal for P_1P_2, P_2P_2 and P_3P_3 meshes. We plot the P_1 solutions on all four meshes

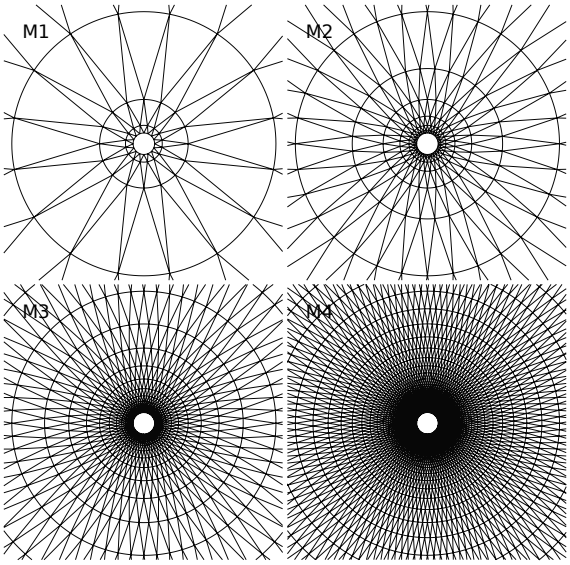

Figure 3: 16×5, 32×9, 64×17 and 128×33 meshes for subsonic cylinder test case.

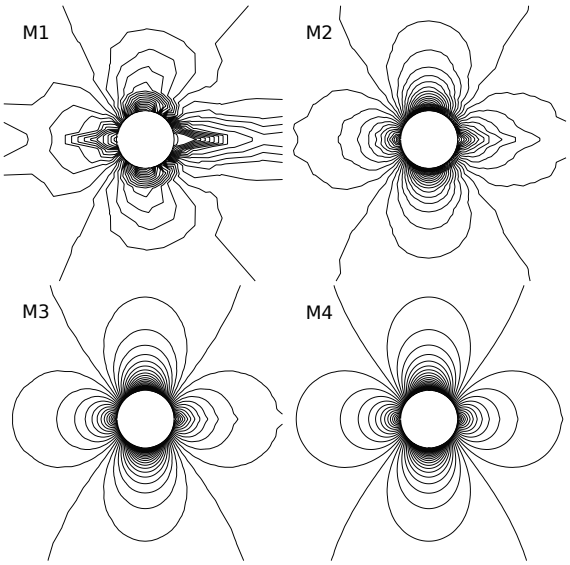

Figure 4: Mach isolines plotted for Ma $\in \langle 0, 1\rangle$, $\Delta Ma = 0.025$ on mesh with P_1P_1 elements.

(figure 4). Higher–order solution is shown in figure 5 for M2 and M3. Figure 6 presents the pressure coefficient on the cylinder wall and the entropy deviation on mesh M1. We measure the rate of convergence again by computing the relative decrease of the L_2 norm of entropy error Σ as the mesh is refined. The measured order is reported in figure 7. We did not include the entropy error on M1 in the computation of the convergence order of P_1P_2 discretization, since

this error is very large (all values are listed table 2). As a result, the convergence rate measured on all four meshes seems to be very high due to rapid decrease of the entropy error as the element size becomes small compared to the curvature of the cylinder.

		P_1P_1	P_1P_2
Mesh	NDOF	$\|\|\Sigma\|\|_{L_2}$	$\|\|\Sigma\|\|_{L_2}$
M1	288	4.87E -02	6.03E-02
M2	1088	7.64E -03	1.78E-03
M3	4224	1.13E -03	1.57E-04
M4	16640	1.78E -04	2.04E-05
Order		*1.99*	*3.05*

		P_2P_2	P_3P_3
Mesh	NDOF	$\|\|\Sigma\|\|_{L_2}$	$\|\|\Sigma\|\|_{L_2}$
M1	624	1.00E-02	1.46E-03
M2	2400	1.78E-03	5.62E-05
M3	9408	1.27E-04	5.35E-06
M4	37248	2.76E-05	5.33E-07
Order		*2.98*	*3.84*

Table 2: L_2 norm of entropy error (Σ): subsonic cylinder test case.

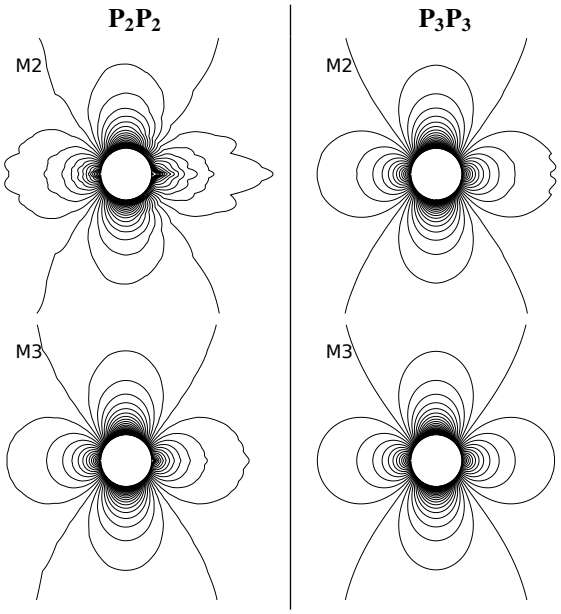

Figure 5: Mach number isolines plotted for $Ma \in \langle 0, 1\rangle$, $\Delta Ma = 0.025$ on meshes M_2 and M_3. Left: P_2 elements, right: P_3 elements.

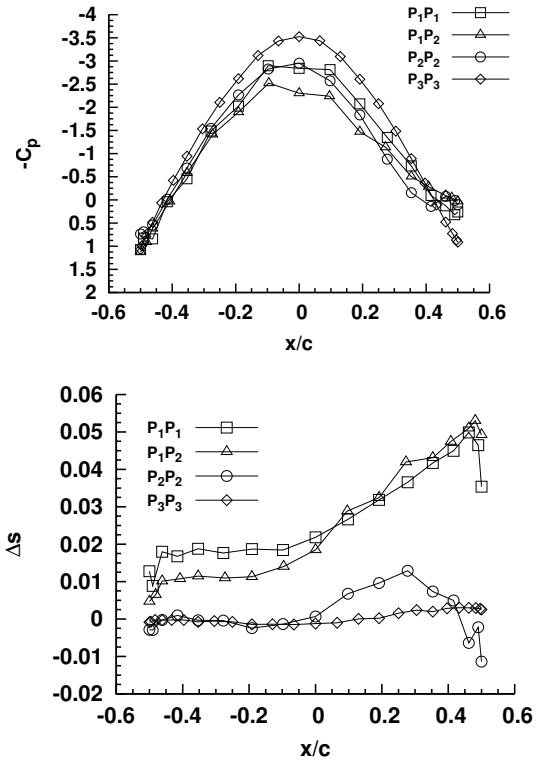

Figure 6: Pressure coefficient (left) and entropy deviation $s - s_{in}$ (right) on the cylinder wall on mesh M1

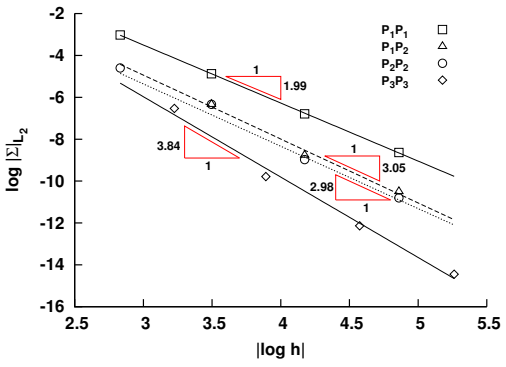

Figure 7: Subsonic cylinder test case; L_2 norm of the entropy error as a function of the mesh size h.

4. Residual distribution schemes with variable distribution coefficient

We consider a linear differential problem

$$\mathcal{L}u = f,$$

with for example $\mathcal{L} = \boldsymbol{\lambda} \cdot \nabla$ or $\mathcal{L} = \boldsymbol{\lambda} \cdot \nabla - \nu\Delta$. The numerical solution $u^{h,k}$, is a FE representation polynomial of the discrete solution:

$$u_h = \sum_{T \in \text{mesh}} \sum_{j \in T} \varphi_j u_j^{h,k}$$

When $k = 1$ ($u^{h,k}$ is a linear polynomial), RDS proceeds as follows

1. *Compute residual:*

$$\begin{aligned} \Phi^T &= \int_T \mathcal{L}u^h dX = \sum_{j \in T} \left(\int_T \mathcal{L}\varphi_j \, dX \right) u_j \qquad (21) \\ &= \sum_{j \in T} u_j \int_T k_j \, dX \end{aligned}$$

   defining k_j as

$$k_j = \mathcal{L}\varphi_j$$

2. *Distribution:* achieved eventually via the definition of coefficients $\beta_i^T = \beta_i^T(\{k_j\}_{j \in T}, u_h, \boldsymbol{\lambda}, h, \Phi^T)$
3. *Assembly/resolution:* obtain the values $\{u_j\}_{j \in \text{mesh}}$ as a solution of $\sum_{T | j \in T} \beta_j^T \Phi^T = 0$

In the linear case the derivatives of the basis functions are constants. This allows the following reinterpretation of the above scheme as a Petrov–Galerkin scheme with particular test functions.

1. Definition of the test function β:

$$k_j = \mathcal{L}\varphi_j, \quad \beta_j(x) = \beta_j^T(\{k_j\}_{j \in T}, u_h, \boldsymbol{\lambda}, h, r^T) \quad \text{with } r^T = \mathcal{L}u_h|_T$$

2. Integrate: $\Phi_i^T = \int_T \beta_i(x) r^T$
3. Assembly/resolution: get the values $\{u_j\}_{j \in \text{mesh}}$ by solving $0 = \sum_{T | j \in T} \Phi_i^T = \sum_{T | j \in T} \int_T \beta_i(x) r^K$

Since all the known definitions of β_i^T depend on the definition of k_j (i.e. on the derivatives of the shape functions), the two schemes are identical in the P^1 case. The schemes are not the same anymore for P^k interpolation, $k > 1$.

4.1. Conservation issues

In case we need apply the method to nonlinear conservation law

$$\nabla \cdot \boldsymbol{\mathcal{F}} = 0$$

a necessary condition for the scheme to converge to some weak solution is that

$$\sum_{j \in K} \varphi_j = \oint_{\partial K} \boldsymbol{\mathcal{F}}(u^{h,k}) \cdot \boldsymbol{n}$$

is satisfied for some approximation of the *physical* flux $\boldsymbol{\mathcal{F}}$ which is continuous across element edges. One possible approach to satisfy this requirement is a suitable volume integration.

Suppose that the flux is approximated by Finite Element shape functions φ^F:

$$\boldsymbol{\mathcal{F}}(u^{h,k}) = \sum_{j \in K} \boldsymbol{\mathcal{F}}_j(u^{h,k}) \varphi_j^F \qquad (22)$$

The Finite Element space which interpolates the discrete flux need not be the same as the Finite Element space used for the solution variable. However, it should be richer to account for the nonlinearity of the flux $\boldsymbol{\mathcal{F}} = \boldsymbol{\mathcal{F}}(u)$. Assuming the continuity of the flux function, the following relation is satisfied for exact integration

$$\int_K \nabla \cdot \boldsymbol{\mathcal{F}}(u^{h,k}) = \oint_K \boldsymbol{\mathcal{F}}(u^{h,k}) \cdot \boldsymbol{n}$$

Since the flux is interpolated as described in equation (22), the following identity holds

$$\begin{aligned} \int_K \nabla \cdot \boldsymbol{\mathcal{F}}(u^{h,k}) &= \sum_{j \in K} \boldsymbol{\mathcal{F}}_j(u^{h,k}) \cdot \int_K \nabla \varphi_j^F \\ &= \sum_{j \in K} \boldsymbol{\mathcal{F}}_j(u^{h,k}) \cdot \sum_{q \in K} |K| w_q \nabla \varphi_j^F(x_q) \end{aligned}$$

The quadrature points x_q and weights w_q are chosen such that the gradients of flux shape functions are integrated exactly. The nodal residual is then evaluated as

$$\int_K \beta_i(x) \nabla \cdot \boldsymbol{\mathcal{F}}(u^{h,k}) = \sum_{j \in K} \sum_{q \in K} |K| w_q \beta_i(x_q) \boldsymbol{\mathcal{F}}_j(u^{h,k}) \cdot \nabla \varphi_j^F(x_q)$$

4.2. Advantages of RD formulation with variable β

The RD schemes with variable distribution coefficient β work without any substantial modification not only on simplex elements, but also on tensor-product

elements (quadrilaterals in 2D). The construction of sub–elements used previously for the RD method becomes an important issue as the polynomial order of the underlying FE interpolation space becomes high (number of quadrature points per element quickly increases) and as we go to three dimensions (division into sub–elements becomes rather complex to implement in computer codes).

The generic formulation (21) avoids these problems and at the same time, it preserves the upwind nature of the original formulation of the RD schemes.

4.3. Examples of schemes

LDA

For the LDA scheme, we set

$$k_i = L\varphi_i = \boldsymbol{\lambda} \cdot \nabla \varphi_i, \qquad \beta_i^T = \frac{k_i^+}{\sum\limits_{j \in T} k_j^+}$$

and the nodal residual becomes

$$\Phi_i^T = \int\limits_T \frac{(L\varphi_i)^+}{\sum\limits_{j \in T} (L\varphi_j)^+} Lu_h \, dX$$

SUPG

Using the notation above, the SUPG residual can be written as

$$\Phi_i^T = \int\limits_T (\varphi_i + \tau L\varphi_i) Lu_h \, dX$$

with the upwind stabilization parameter $\tau = (\sum\limits_{i \in T} k_i^+)^{-1}$.

5. Scalar advection test case

Given a rectangular domain, we consider a steady advection equation

$$\lambda \cdot \nabla u = 0 \text{ with } \boldsymbol{\lambda} = (y, -x)$$

A cosinus profile is imposed at the inlet. The advection field is supposed to rotate this profile in the direction indicated in figure 8. The solution obtained with the LDA and SUPG schemes on a mesh consisting of P_2 triangles is depicted in figure 9.

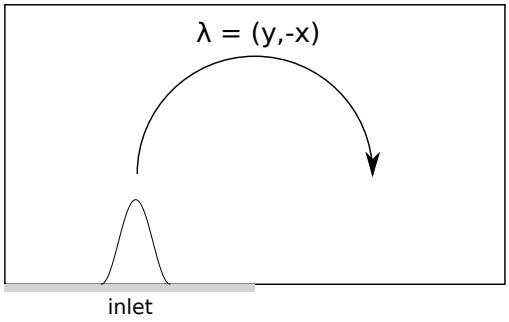

Figure 8: Setup for linear advection test case

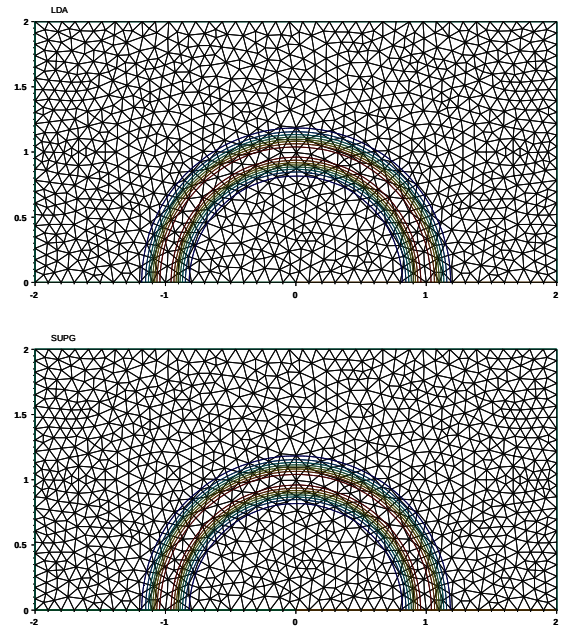

Figure 9: Linear advection test case - isolines of solution obtained with the LDA (top) and SUPG (bottom) schemes

6. Euler 2D test case

The extension of the scheme to a (nonlinear) system of equations was tested on a simple test case for Euler equations in 2D dimensions. Two supersonic states $\mathbf{u}_{L/R} = (\rho, \rho u, \rho v, E)_{L,R}$ are prescribed at the left and right half of the inlet (inlet boundary condition), and also in the left and right half of the whole domain as initial conditions (see figure 10). This test case was chosen because it does not require wall boundary condition, which are not implemented at this moment. The solution eventually forms an expansion fan (figure 11).

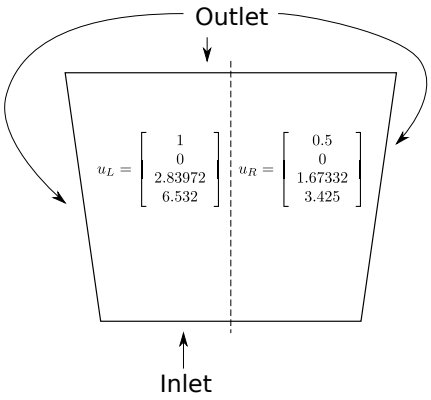

Figure 10: Initial and boundary conditions for the Euler 2D test case

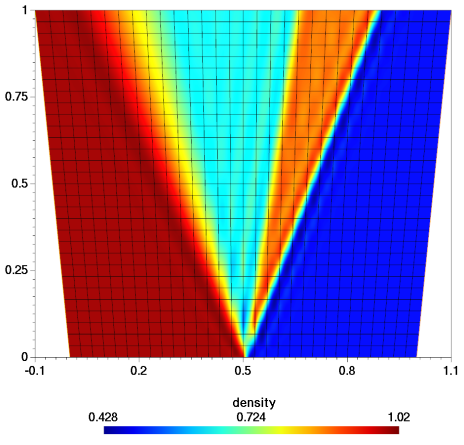

Figure 11: Solution of the Euler test case with LDA scheme on Q_2 elements

Acknowledgments

The presented results were obtained in collaboration with Tiago Quintino, Mario Ricchiuto and Nadège Villedieu. The construction of residual distribution schemes with variable β-coefficients as described in section 4 is due to an original idea of Mario Ricchiuto.

References

[1] H. Deconinck, R. Abgrall, Introduction to residual distribution methods, VKI Lecture Series, Comput. Fluid Dynam., 2005.

[2] M. Ricchiuto, N. Villedieu, R. Abgrall, H. Deconinck, On uniformly high–order accurate residual distribution schemes for advection-diffusion, J. Comput. Appl. Math. 215 (2008) 547–556.

[3] H. Deconinck, K. Sermeus, R. Abgrall, Status of multidimensional upwind residual distribution schemes and applications in aeronautics, AIAA paper 2000-2328, AIAA CFD Conference, Denver (USA), June 2000.

[4] M. Ricchiuto, N. Villedieu, R. Abgrall, H. Deconinck, High–order residual distribution schemes: discontinuity capturing crosswind and extension to advection–diffusion, VKI Lecture Series, Comput. Fluid Dynam., 2005.

[5] H. Deconinck, P. L. Roe, R. Struijs, A multidimensional generalization of Roe's difference splitter for the Euler equations, Computers and Fluids 22(2/3) (1993) 215–222.

[6] H. Paillere, Multidimensional upwind residual distribution schemes for the Euler and Navier–Stokes equations on unstructured grids, Ph.D. thesis, Von Karman Institute for Fluid Dynamics and Université Libre de Bruxelles, Faculté des Sciences Appliquées (1995).

[7] E. van der Weide, H. Deconinck, Positive matrix distribution schemes for hyperbolic systems, with application to the Euler equations, Computational Fluid Dynamics (1996) 747–753.

[8] E. van der Weide, Compressible flow simulation on unstructured grids using multi–dimensional upwind schemes, Ph.D. thesis, Von Karman Institute for Fluid Dynamics and TU Delft (1998).

[9] N. Villedieu, T. Quintino, M. Vymazal, H. Deconinck, High-order residual distribution schemes: Unsteady and viscous terms, 35th Computational Fluid Dynamics Lecture Series, VKI/ADIGMA Course on High order Discretization Methods, Von Karman Institute for Fluid Dynamics, 2008.

[10] R. Abgrall, A. Lerat, M. Ricchiuto, C. Tavé, A simple construction of very high order non-oscillatory compact schemes on unstructured meshes, Computers and Fluids 38(7) (2009) 1314–1323.

[11] R. Abgrall, Residual distribution schemes: Current status and future trends, Computers and Fluids 35(7) (2006) 641–669.

[12] F. Bassi, S. Rebay, High–order accurate discontinuous finite element solution of the 2D Euler equations, J. Comput. Phys. 138 (1997) 251–285.

ABLATION

Recession and Boundary Layer Characterization of Carbon-Phenolic Ablation in Plasma Flows

Bernd Helber

Aeronautics and Aerospace Department, von Karman Institute for Fluid Dynamics, Belgium, helber@vki.ac.be
Department of Electrochemical and Surface Engineering, Vrije Universiteit Brussel

Supervisor: Thierry Magin

Associate Professor, Aeronautics and Aerospace Department, von Karman Institute for Fluid Dynamics, Belgium, magin@vki.ac.be

Promotor: Annick Hubin

Professor, Department of Electrochemical and Surface Engineering, Vrije Universiteit Brussel, Belgium, anhubin@vub.ac.be

Abstract

An important effort in theoretical, numerical, and experimental investigation is required to understand the complex material response of a new class of ablators under sever re-entry conditions. Ablation experiments have been performed in the VKI Plasmatron focusing on low density carbon-phenolic materials to investigate the ablating behavior in different flow conditions, in particular, their recession rates and the transport phenomena in the boundary layer. The experiments indicated a transition from reactive controlled to diffusion limited ablation regime, based on in-situ recession measurements. The reactive boundary layer was investigated by means of three optical emission spectrometers, synchronized with a high-speed camera to determine the probing locations respective to the ablating surface. This enabled reconstruction of the CN violet system emission profile within the boundary layer. A stagnation line description with ablative boundary condition, together with the Specair radiation tool, was then used to produce numerically estimated emission profiles. Emission intensities were in the same order of magnitude compared to the experimental data although a very simplified approach was used.

Keywords: ablation, plasma flows, gas-surface interaction, emission spectroscopy, radiation

1. Introduction

Future space exploration missions, such as sample returns from Mars and asteroids at very high re-entry speeds, will use ablative materials for the thermal protection system (TPS) to shield the spacecraft against the severe heating during re-entry. Ablative heat shields are able to dissipate high heat fluxes through chemical and physical decomposition, transforming the thermal energy into mass loss and recession, whilst the remaining solid material insulates the vehicle substructure [1; 2].

To achieve high performance characteristics of ablative materials, mostly composites are used, providing a pyrolyzing, ablating, and insulating material at low weight with reasonable mechanical properties due to a carbon-fiber preform. A new generation of low density carbon/resin composite ablators is currently being developed, made of a carbon fiber preform impregnated with phenolic resin. Examples are phenolic-impregnated carbon ablator (PICA) [3] and ASTERM [4], developed for high-speed entry missions.

Selection and sizing of the thermal protection material (TPM) are the two key performance parameters in TPS design and prediction inaccuracies can be fatal for the crew or the success of robotic missions. The prediction tools for ablative TPS design are still inherited from the Apollo program [5; 6] and new high fidelity material response models are proposed [7] in order to take into account the porous micro-structure of the new class materials. Our study is oriented towards the effects of material degradation through pyrolysis and ablation in various air and nitrogen plasma

flow conditions in the VKI Plasmatron facility. A high speed camera coupled with three emission spectrometers was used to observe and track outgassing species, which are ejected into the boundary layer from the material. The emission spectrometer enabled a spatial and temporal resolution of various species originating from internal pyrolysis and gas-surface interaction [8]. The high speed camera was used to determine probing distances of the adjoin spectrometers respective to the ablating surface. The materials used for this study were carbon fiber preform, AQ61, and ASTERM provided by EADS Astrium.

The materials were tested at heat fluxes of $1.0 - 3.0\,\mathrm{MW/m^2}$ at various pressure levels ranging from 1.5 kPa to 20 kPa . The paper is organized according to the following objectives:

- Review of the ablation process of charring materials (section 2)
- Description of the VKI Plasmatron facility, experimental methods, test conditions and stagnation line description with an ablative boundary condition (section 3).
- Recession analysis (section 4.1).
- Surface emissivity measurements (section 4.2).
- Analysis of emission profiles in the boundary layer and comparison to numerical estimates (section 4.3).
- Conclusions and perspectives (section 5).

2. Ablation of charring materials

The processes through which ablators are able to accommodate high heat fluxes are balanced between surface radiation, phase transitions (melting, sublimation) as well as chemical reactions (charring, oxidation) on the surface and inside the material. To achieve high performance characteristics of ablative materials, mostly composite materials are used for the ablative heat shield. When subjected to increasing temperature, the virgin material successively transforms following two mechanisms (Fig. 1):

a) During ***pyrolysis*** the phenolic resin is progressively carbonized into a low density, porous char and loses around 50% of its mass producing pyrolysis gases by vaporization. The pyrolysis gases are transported out of the material by diffusion and convection, and exhaust into the boundary layer, providing a further barrier for the heat exchange (blowing), and undergo additional chemical reactions, consuming more heat. Making use of polymers such as phenolic resins for the matrix of the composite takes advantage of their endothermic degradation nature, thereby absorbing energy, and serving as a binder for the other components [9].

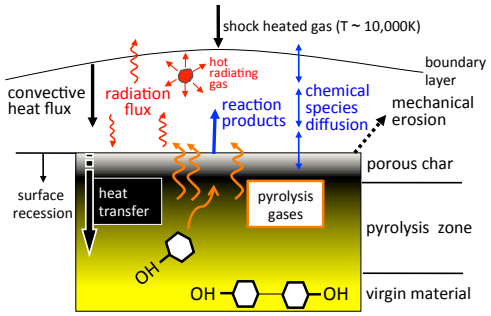

Figure 1: Ablation and pyrolysis processes of a charring material

b) ***Ablation*** of the char layer (composed of the carbonized resin and the remaining carbon fibers) is then promoted by heterogeneous chemical reactions, phase change and mechanical erosion (e.g. spallation), altogether leading to recession of the material. The rate at which an ablator recesses is a consequence of its prevention of heat conduction and strongly coupled to the aerothermal conditions it encounters. In other words, the material will primarily respond with a higher ablation rate to increased heating whilst the heat conducted to the bondline will stay constant. This illustrates the great importance of material response models to accurately predict recession of the material. However, due to lacking good experimental data, this quantity remains as one of the largest uncertainties in material response analysis [10].

3. Methodology for ablation characterization

To enable a proper design of heat shields based on porous, low-density composite ablators, a complete experimental analysis with parallel modeling is necessary. The following phenomena have to be analyzed and described accurately: **finite-rate chemistry** for pyrolysis gas, **transport phenomena in porous medium** as well as in the **boundary layer**, and **volume ablation** with a possible ablation zone (microscopic description of the porous medium).

3.1. Materials of investigation

We propose a testing strategy for ablative material characterization starting with experimental characterization of the fiber preform compound, followed by fully developed ablators. The tested materials are described below:

3.1.1. Carbon fiber preform (Mersen Scotland Ltd.)

The bulk material of carbon preform was provided by Mersen Scotland Holytown Ltd. (CALCARB CBCF 18-2000) and machined in-house to hemispherical test samples of radius 25 mm and 45 mm length. The CBCF preform is a short fiber insulation originating from rayon, the short cut carbon fibers are interconnected in a fully carbonized matrix produced of phenolic resin. The carbon preform compound then consists of randomly oriented carbon fibers with a density typically ranging between $180 - 210\,\mathrm{kg/m^3}$ and a porosity of 90%. This material is very similar to the basic material used for production of cabonphenolics such as ASTERM and PICA and was previously tested at VKI [11].

3.1.2. ASTERM (EADS Astrium ST)

The ASTERM material is manufactured by impregnating a rigid graphite felt similar to the above carbon preform with phenolic resin, which is followed by a polymerisation process and final machining [4]. This approach significantly reduces the manufacturing effort and allows a large scale production. The manufacturing approach allows a large range of final material densities, from $240 - 550\,\mathrm{kg/m^3}$.

3.1.3. AQ61 (EADS Astrium ST)

AQ61 is a basic ablative material previously developed by EADS Astrium, which represents a low density carbon-phenolic material manufactured by impregnating large pieces of carbon felts compressed to the right density during the impregnation process [4].

3.2. Inductively-coupled Plasmatron facility

The Plasmatron facility has been used for all the experiments carried out in this study. It is extensively utilized at the von Karman Institute for Fluid Dynamics for the reproduction of the aero-thermodynamic environment of re-entry plasma flows, creating a high-enthalpy, highly dissociated subsonic gas flow[12]. The facility is equipped with a 160 mm diameter ICP (Inductively Coupled Plasma) torch powered by a high frequency, high power, high voltage (400 kHz, 1.2 MW, 2 kV) generator (MOS technology). In order to achieve heat fluxes higher than $\sim 5\,\mathrm{MW/m^2}$, a converging nozzle can be attached to the torch of the Plasmatron (not performed for this work). As the gas is heated by induction through a coil, the advantages of ICP torches are the high purity of the plasma flows produced, due to the absence of electrodes and their associated erosion. With its 1.2MW inductively coupled plasma generator, the VKI Plasmatron facility is the most powerful of its kind in the world. An overview of the facility and the complete experimental setup for free-stream and in-situ ablation measurements can be found in Figure 2, as reviewed below.

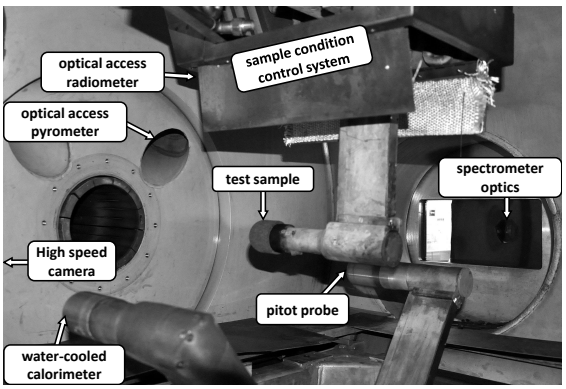

Figure 2: Experimental setup in the VKI Plasmatron facility with free-stream characterization techniques (heat flux probe, pressure probe) and measurement techniques for ablation characterization.

A 50 mm diameter copper water-cooled probe, mounting a copper calorimeter in the center of the front face, is used for the calibration of plasma flow conditions. The cold wall (~350 K) stagnation point heat flux is determined by the cooling water mass flow, controlled by a calibrated rotameter, and the inlet/outlet temperature difference, measured by two type-E thermocouples. A Teflon© insulator is inserted between the calorimeter and the probe's wall in order to have side adiabatic conditions. Both the probe and calorimeter have copper surfaces which are high catalytic to nitrogen and oxygen atoms recombination. The heat flux can be measured with ±10% accuracy. A water-cooled Pitot probe is used to perform stagnation pressure measurements. The pressure line is connected to a Validyne variable reluctance pressure transducer and a voltage demodulator amplifies the output. Beside the calorimeter and dynamic pressure probe for free-stream characterization, the measurement techniques included temperature measurements (two-color pyrometer, IR-radiation-thermometry and thermocouples), emission

spectroscopy and high speed camera imaging. Validyne and amplifier are calibrated prior to the test by means of a Betz water manometer, leading to an uncertainty of ±0.2%. The Plasmatron chamber is also equipped with an absolute pressure transducer that measures the static pressure with ±2Pa accuracy. The probes are mounted inside the Plasmatron test chamber at 0.445 m distance from the ICP torch exit.

Surface temperature measurements were carried out using a two-color Raytek Marathon MR1S-C pyrometer (0.75 - 1.1 µm), with a temperature range from 1300 K to 3300 K. Measurements in two narrow wavelength bands under the assumption of a wavelength independent emissivity allow temperature estimations neglecting the emissivity. A detailed description of this technique can be found in literature [13].

3.3. Spatially resolved boundary layer emission

Temporally and spatially resolved emission spectroscopy enabled measurements of erosion products and erosion rates as a function of the plasma parameters in front of the test specimen. This work used three Ocean Optics HR4000 spectrometers, which cover a wide wavelength range (200nm-1000nm) within one single acquisition and a minimum integration time of 5ms. The optical diagnostic bench consisted of a light collection system, optical fibers and the three spectrometers, synchronized with a high-speed-camera (Fig. 3).

The light emitted by the plasma was collected through a variable aperture and focused by a plano-convex, uncoated fused silica lens (LA4745, 750 mm focal length) via two mirrors on the entry of three optical fibers (Ocean Optics QP600-2-SR/BX, 600 ± 10 µm core diameter).

The optical fibers were characterized by an optimized numerical aperture to match the entrance slit of the spectrometer. The optical path was aligned perpendicular to the flow and tangential to the test sample surface. Three small probing volumes with variable distances (by the magnification and arrangement of the fibers) along the stagnation line through the boundary layer were imaged onto the three optical fibers. The magnification of the optical system was set to 3 resulting in a distance between each probing volume of $\Delta d = 2$ mm.

Each optical signal was lead to a HR4000 spectrometer, which covers a broad spectrum in the desired range (200-1100 nm), suitable to rapidly determine radiating transitions of excited atoms and main molecular bands. All optical components operated in the HR4000 spectrometer wavelength range. The

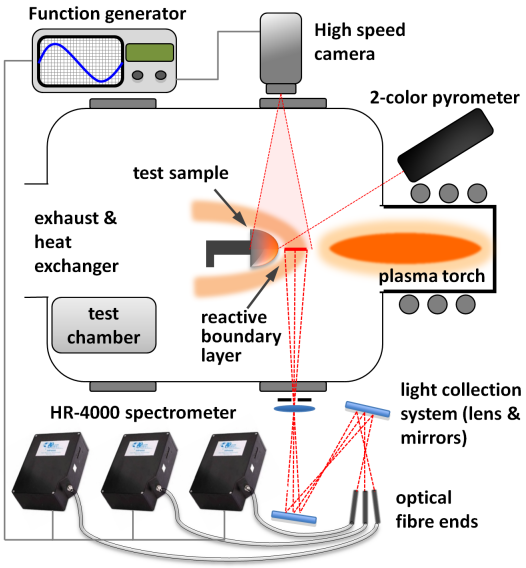

Figure 3: Schematic view of the VKI Plasmatron showing the optical paths of three adjoin spectrometeres perpendicular to the plasma flow ahead of the ablating sample (sample position: 445mm from plasma jet exit)

fixed entrance slit width of 5µm and a 300 groove/mm grating lead to a typical resolution of approximately 0.7 nm (Full Width Half Maximum (FWHM)), as was determined by a low pressure Hg lamp (Oriel 6060).

The spectrometers were triggered with an acquisition frequency of $f_s = 4$ Hz to analyze the temporal erosion products evolution. The integration time was adjusted for each test to prevent saturation of the CCD detector, averaging the acquired spectrum during the integration period.

The optical diagnostic bench (aperture, lens, mirrors and fibers) was mounted on a movable holding system, which enabled horizontal movements to be able to adjust the line of sight. The positioning of the three probing volumes was checked and adjusted before each experiment using a laser beam, which was sent through the optics and located ahead of the stagnation point of the sample.

Calibration of the whole system consisting of the light collection mechanism and spectrometer efficiencies in [W/m^2.sr.nm] was performed between 350nm and 900nm by placing a tungsten ribbon lamp (OSRAM WI 17G) in the focus of the collection optics inside the test chamber. As the spectrometer response of the calibration lamp below 350nm is too low, calibrated spectra are only reported within the range 350-900nm. Plotted spectra below 350nm (e.g. of OH and NH emission) are shown in arbitrary units.

Calibrated emission spectra recorded by the three

adjoin spectrometers in air plasma free-stream are presented in Fig 4. All three signals coincided very well for the full spectral range where the calibration was performed (350-900 nm) and suggest a sufficient intensity calibration to enable quantitative comparison of the three emission signals.

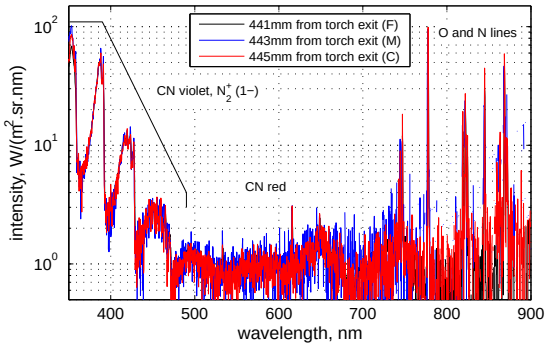

Figure 4: Calibrated free-stream emission recorded by three adjoin spectrometers along jet center line coincide well representing sufficient intensity calibration (20 kPa, 3 MW/m^2).

In order to determine the varying distances of the spectrometer probing volumes from the recessing surface, a high speed camera was used, synchronized with the emission spectrometers. The Vision Research Phantom 7.1 CMOS high-speed camera (HSC) provides the possibility of using short exposure times (2µs) to capture images at high sampling frequencies. Such short exposure times are required as the very bright surface during material ablation can lead to saturation of the CCD sensor of normal cameras. High-speed imaging also enables in-situ, non-intrusive determination of the surface recession. The accuracy of this method depends on the resolution of the HSC and the successive conversion of pixel into millimeters. A surface detection uncertainty of one pixel lead to a recession uncertainty of $\delta HSC = \pm 0.1$ mm. The bright surface was extracted from the original image by adjusting dark-white contrasts and applying edge detection filters.

3.4. Test procedures and conditions

Two test gases have been used, air and nitrogen, in order to restrict the number of chemical reactions. The mass flow was kept at $\dot{m} = 16$ g/s. The duration of each test was chosen in order to maintain a constant heat load on the samples for all test cases. The actual duration of the ablation test was determined from the high-speed-camera images. For the results presented throughout this paper, the time indication $t = 0$ s corresponds to the injection of the test sample into the plasma flow. Plasmatron test conditions providing test gas, static and dynamic pressure, cold wall heat flux, test time and surface temperature are listed in Table 1.

3.5. Stagnation line code with ablative boundary condition

During the Apollo program, engineers made a start on the design of numerical models for prediction of the complex gas surface interaction of TPMs. Those models, developed for dense ablative materials, are inspired from Kendall et al. published in 1968 [5; 14]. They rest on major assumptions and describe ablation as a surface phenomenon occurring on a homogeneous, dense material assuming equilibrium or finite-rate chemistry in a control volume close to the wall. The coupling strategy with the flow environment is based on considering a thin control volume where the gas-surface interactions occur and where mass balance and equilibrium chemistry are satisfied. By this, the interaction of material and flow codes are approximated through the use of heat and mass transfer coefficients.

New efforts on numerical modeling for the material response of carbon composite ablators have been initiated at the VKI [15; 16]. As part of the coupling between the flow field and the material, an ablative boundary condition has been added to a stagnation line description in order to model the gas-surface interaction of carbonaceous materials [17]. Output of this procedure are mole fractions and temperatures along the stagnation line in the reactive boundary layer, as well as the recession of the material under different flow conditions. In section 4.3, experimentally obtained boundary layer radiation profiles are compared to numerical data coming from the boundary layer description. This was done by using the data of the stagnation line code as input values to calculate theoretical spectra using the Specair tool [18].

As the recorded spectroscopic data are line-of-sight measurements in the reactive boundary layer (Fig. 3), the slab width used by Specair had to be approximated to allow a quantitative comparison. A simple procedure has been applied to obtain the numerical emission profiles, which is described below and illustrated in Fig. 5:

1. the boundary layer thickness δ was determined from subsonic Plasmatron flow-field simulations using a Navier-Stokes-Solver, characterizing the boundary layer geometry around the test sample under LTE and axisymmetric flow assumption [19; 20],

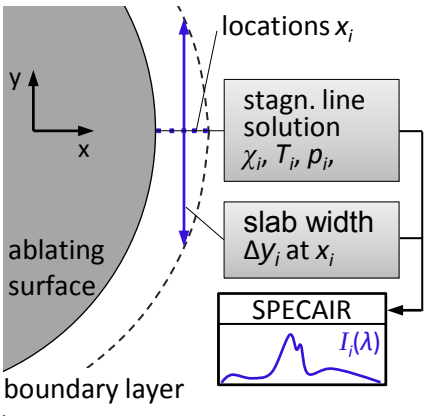

Figure 5: Application of stagnation line computation with ablative boundary condition for synthetic spectra generation using Specair.

2. the stagnation line boundary layer was split into multiple increments at distance x_i from the ablating surface,
3. mole fractions and temperature for each location x_i were taken from the stagnation line solution,
4. the slab width Δy_i (optical path of the spectrometer) was approximated as the chord of a circular segment:

$$\Delta y_i = 2\sqrt{(r+\delta)^2 - ((r+\delta) - (\delta - x_i))^2} \quad (1)$$

This formulation is based on the very strong assumption that mole fractions and temperatures do not change within the approximated slab width.

4. Results and discussion

4.1. Recession analysis and gas-surface interaction

A recession analysis of carbon preform (a) and AQ61 (b) ablation is plotted in Fig. 6 for cold wall heat fluxes of 1 & 3 MW/m^2, and pressures of 1.5 & 20 kPa. The surface recession rate was determined from the slope of a linear curve fit. The first 10 s of the test were neglected for the fitting procedure in order to ensure a steady ablation behavior and to disregard the first seconds during which the sample is being heated.

In all cases, a linear fit could well represent recession of the surface. In the case of the carbon preform, recession rates did not vary much for the different test conditions, represented by parallel slopes for test cases P1-P6. The slope of test case P0 at 1724 K was slightly smaller compared to the others. The reason for this might be a reaction controlled ablation regime at this temperature, whereas tests P1-P6

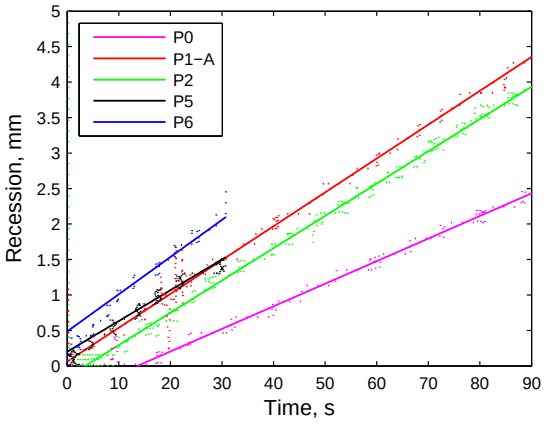

(a)

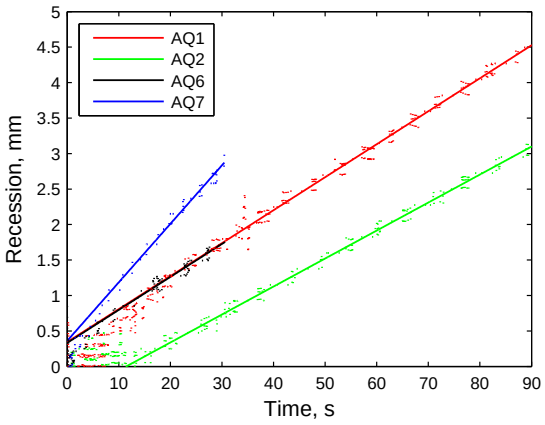

(b)

Figure 6: High-speed camera recession measurements of carbon preform (a) and AQ61 (b) ablation in various heat flux and pressure conditions; dotted lines indicate the HSC measurement and full lines represent a linear curve fit.

were controlled by diffusion of oxygen in the boundary layer. Hence, a temperature change of 700 K between P1/P2 and P5/P6 did not have much effect on the ablation rate.

This is further evident in a comparison of the recession rates including their uncertainties as plotted in Fig. 7 for increasing surface temperature and different pressures. The uncertainties of the recession measurements were estimated using the RMSE of the linear fit divided by the test time. Above 2000 K, the surface temperature did not influence much the recession rates except the outlier AQ7 at 200 mbar. Due to a diffusion limited ablation, all oxygen is consumed at the surface and a temperature increase does not result in an increasing consumption of the carbonaceous material.

As can be found in table 1, tests in nitrogen did not

Table 1: Plasmatron test conditions: test case reference (Carbon Preform (P), AQ61 (AQ), ASTERM (AS), followed by target heat flux in MW/m^2 and target chamber pressure in mbar), test gas, static pressure p_s, dynamic pressure p_d, electrical power, mean cold wall heat flux $\dot{q}_{cw}$, exposure time & surface temperature T_S, recession rate $\dot{r}$, and mass loss $\dot{m}$.

test #	gas	p_s, kPa	p_d, Pa	P, kW	$\dot{q}_{cw}$, MW/m^2	t, s	T_S, K	$\dot{r}$, µm/s	$\dot{m}$, mg/s
P0	air	1.5	60	109	312	90.5	1724	31.8	30.0
P1-A	air	1.5	141	166	1.019	91.0	2180	47.7	48.2
P1-B	air	1.5	190	204	1.025	90.3	2347	53.6	53.0
P2	air	20	-	188	1.050	91.2	2020	45.5	53.2
P5	air	1.5	342	365	3.074	30.7	2848	43.4	69.8
P6	air	20	48	321	2.962	30.8	2783	52.4	74.6
P3	N_2	1.5	124	154	1.057	90.7	2030	0	3.47
P4	N_2	1.5	285	350	3.149	31.2	2644	7	8.42
AQ1	air	1.5	135	161	1.023	90.4	2167	46.5	63.6
AQ3	air	10	17.0	181	1.038	90.4	2134	46.3	54.1
AQ2	air	20	6.20	158	1.026	90.3	1890	39.4	40.2
AQ6	air	1.5	400	400	2.994	30.0	2884	46.5	132
AQ7	air	20	57.0	356	3.058	30.0	2906	82.5	124
AQ4	N_2	1.5	131	177	0.997	90.5	2017	5	26.2
AQ5	N_2	10	13.4	213	1.017	90.0	2051	6	20.2
AQ8	N_2	1.5	263	354	3.034	30.4	2612	21	74.6

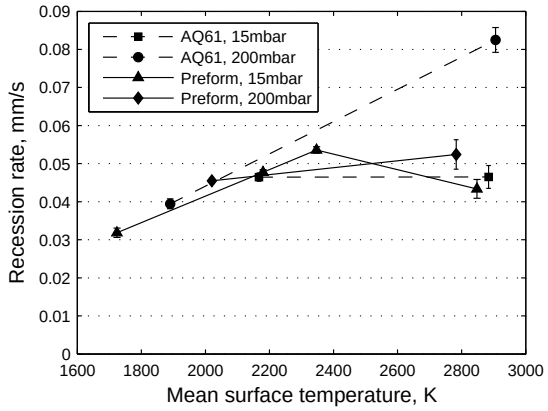

Figure 7: Influence of test chamber static pressure on recession rates of AQ61 & Preform (1 MW/m^2).

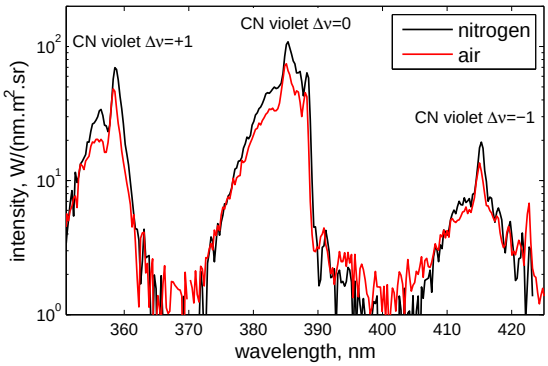

Figure 8: CN violet emission signal during air and nitrogen ablation recorded at the stagnation point at 3MW/m^2, 1.5 kPa.

result in significant recession for any of the samples. Although nitridation does not cause much recession of the surface, production of gaseous CN has a significant contribution to the overall radiative heat flux of fast re-entry vehicles [21]. Many experiments in the past were dedicated to the effects of oxygen as a main driver for carbon heat-shield recession, but the nitridation reaction $C_s + N \rightarrow CN$ on a solid (s) carbon surface is still weakly understood. Nitridation coefficients available in the literature differ by several orders of magnitude [22; 23]. Reactive collisions that may produce or lead to an electronically excited CN (B) state still lack sufficient information [24].

In the case of an oxidizing carbon surface the homogeneous reaction

$$CO + N \rightleftharpoons CN + O \qquad (2)$$

may lead to CN production [25]. But strong CN emission was recorded during tests in air as well as in nitrogen plasmas as can be seen in Fig. 8, omitting reaction (2). Recombination reactions in the boundary layer with atomic nitrogen are very unlikely, as no atomic or molecular carbon was measured during any ablation test in nitrogen, confirming the wall origin of CN. The high degree of nitrogen dissociation in all test conditions supports the assumption of nitridation at the wall, but atomic nitrogen is also highly subjected to recombination reactions, forming N_2 at

the surface. It is not an easy task to determine the so-called recombination efficiency of carbon ablator surfaces, which will be the subject of future work. Comparisons with numerical data could help to investigate the recombination efficiency of ablating surfaces, as a high recombination rate will also lead to an increasing wall heat flux due to the released energy.

Previous emission spectroscopy measurements carried out by Boubert and Vervisch [26] have shown strong CN formation on a carbon surface in nitrogen and carbon dioxide plasmas. CN production might be caused by dissociative adsorption of highly vibrationally excited N_2, induced by high temperatures, creating reactive sites N_w at the surface:

$$N_2(X, \upsilon) + w + w \rightarrow N_w + N_w \tag{3}$$

$$C_w + N_w \rightarrow CN \tag{4}$$

If nitrogen experiences a high recombination at the surface, reactions (3)-(4) are possible candidates to create the cyanogen radical. In air plasma, excitation of the CN(B) state can be a result of collisions with highly vibrationally excited CO molecules:

$$CN(X) + CO(X, \upsilon \geq 11) \rightarrow CN(B) + CO \tag{5}$$

However, from the measurements in nitrogen it seemed that excitation of CN(B) was not test gas dependent, and we envisage excitation transfer with molecular nitrogen to explain the strong CN(B) emission [26]:

$$CN(X) + N_2(X, \upsilon \geq 11) \rightarrow CN(B) + N_2 \tag{6}$$

4.2. Surface radiation and emissivity

In order to have the distribution of temperature over the sample surface, one of the tests, P0 at 0.3 MW/m^2 and 1.5 kPa, was observed by an infrared (IR) camera (ThermaCAM® SC3000).

The camera records the radiance of an object in the wavelength range of 8-9 µm with a saturation limit of 1770 K. The instrument was calibrated after the experiment with the same window (KRS-5) as used in the plasma tunnel. From the combined measurements of infrared camera (8-9 µm) and two-color pyrometer (0.75-1.1 µm) it is possible to calculate the emissivity of the emitting surface:

$$\varepsilon_{8-9\mu m,T} = \frac{W_{8-9\mu m,T}}{W^{bb}_{8-9\mu m,T}} \tag{7}$$

the index ^{bb} stands for the black body radiance at temperature T, calculated from the emissivity independent two-color pyrometer measurements. This procedure yielded an emissivity $\varepsilon = 0.9$ for test case P0.

This value was compared to the spectral radiation recorded by the spectrometer at the surface. Some data are available were the closest spectrometer to the test sample was pointing at the hot surface during the first test seconds. The two-color pyrometer surface temprature was used to compute Planck's curve at the wavelength of interest:

$$B_\lambda(T) = \frac{2hc^2}{\lambda^5} \frac{1}{e^{\frac{hc}{\lambda k_B T}} - 1} \tag{8}$$

where B denotes the spectral radiance, T its absolute temperature, k_B the Boltzmann constant, h the Planck constant, and c the speed of light in air. For comparison to experimental data $B_\lambda(T)$ was then multiplied with the emissivity $\varepsilon_{8-9\mu m,T}$.

The resulting Planck curves of this approach as well as the experimentally obtained data of P0 and P5 are plotted in Fig. 9.

We used the estimated emissivity of $\varepsilon = 0.9$ and the surface temperature measured with the two-color pyrometer as baseline. In the test case P0, we found a difference between the calculated Planck distribution and the measured observation. Even a higher emissivity of $\varepsilon = 0.95$ did not help to shift the Planck curve inside the estimated confidence bounds of 90%. However, a slight surface temperature increase of 20 K (~1%, well in the range of the measurement uncertainty) allowed both calculated Planck curves to lie inside the confidence levels, with that one of $\varepsilon = 0.95$ even lying on the fitted data.

In the higher surface temperature case P5, no modulation of the surface temperature was needed to adjust the calculated Planck distribution. A Planck curve calculated with an emissivity of $\varepsilon = 0.95$ agreed well with the fitted data. The previously estimated emissivity of $\varepsilon = 0.9$ lead also in this case to a slightly too low Planck distribution.

Note the different scales of measured intensity for the different cases as well as the apparent CN violet radiation. In general it seems that emissivities are beyond $\varepsilon = 0.9$, but the radiation coming from the gas phase and especially, highly radiating ablation products, might lead to an over-estimation of this value as they may contribute to the measured Planck radiation.

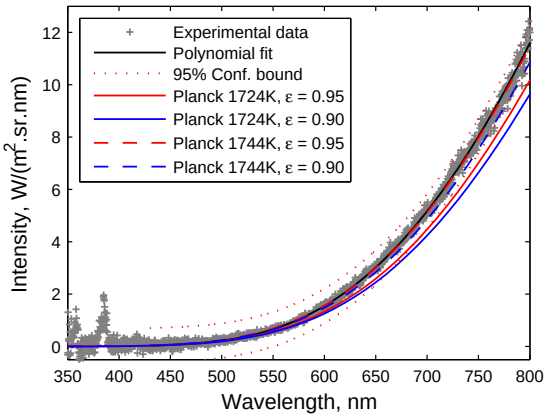

(a) P0: 1724 K, 1.5 kPa

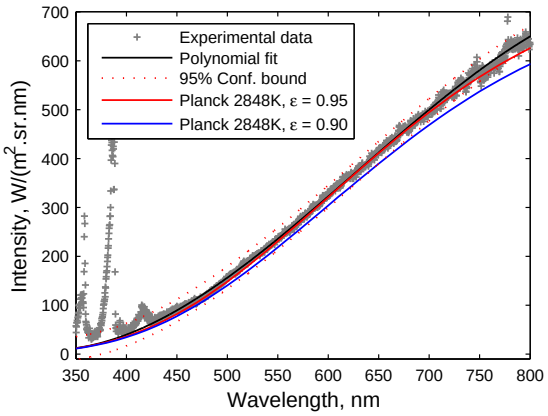

(b) P5: 2848 K, 1.5 kPa

Figure 9: Surface radiation recorded by emission spectrometer and computed Planck curves for comparison based on varying emissivities and surface temperatures.

4.3. *Boundary layer emission and comparison with numerical code*

As introduced in section 3 we used the temporal CN violet system emission to obtain a spatial profile of molecular emission in the boundary layer. The CN violet emission signal $\epsilon(\lambda)$ of the $\Delta\nu = 0$ sequence (370-390nm) was integrated with respect to the wavelength for each individual spectrum at time step t:

$$I_{CN}^{(t)} = \int_{370nm}^{390nm} \epsilon(\lambda) d\lambda \qquad (9)$$

An example of CN violet emission indicating the integration range for the $\Delta\nu = 0$ sequence is shown in Fig. 10.

The resulting temporally and spatially resolved emission profiles of the three spectrometers can be found in Figure 11. Spectrometer 1 was pointing at the ablating surface for the first 1 s of the test during

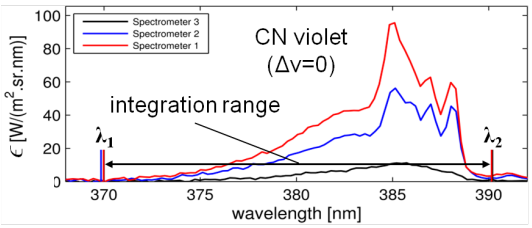

Figure 10: Integration range of emission signal $\epsilon(\lambda)$ for CN violet $\Delta\nu = 0$ sequence.

which the CN emission increased until the maximum was reached just when the recessing surface passed the spectrometer's probing volume.

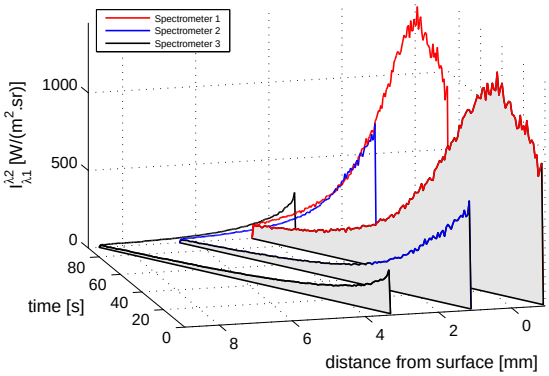

Figure 11: 3D plot illustrating CN violet bandhead ($\Delta\nu = 0$) emission over time and distance from sample surface along the stagnation line (1 MW/m^2, 1.5 kPa).

Good agreement of all three spectrometer responses can be observed for the test in the time-distance plane, supporting the assumption of a steady state ablation behaviour of the material.

The resulting spatial emission profiles along the stagnation line in front of preform test samples for all tests in air plasma are shown in Fig. 12 and 14. The two tests presented in Fig. 12 have been performed at the same conditions and both emission profiles agree well in terms of intensity and shape. If we define the inflection point of the emission profile as a finite thickness for comparison of the different profiles, the location of this inflection point is almost identical for the two tests, roughly located 1 mm in front of the test sample.

In the following, Fig. 13 and Fig. 14 present similar profiles for tests at higher pressure (20 kPa) and higher heat flux (3 MW/m^2). In addition, a comparison with profiles obtained from the stagnation line description is made.

In the case of 200 mbar, the maximum intensity was recorded further upstream the boundary layer, with the

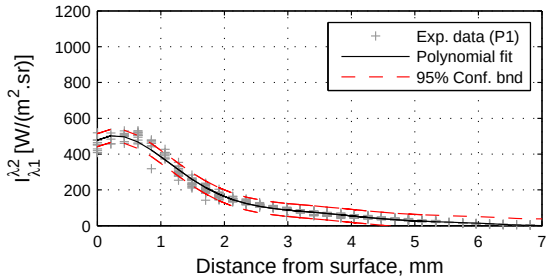

(a) P1-A: 2180 K, 1.5 kPa

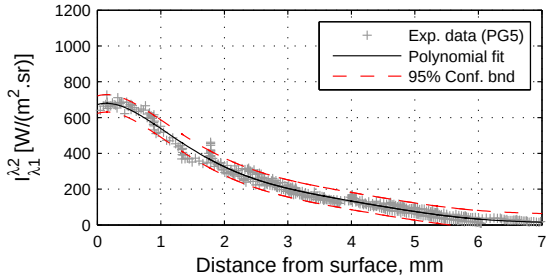

(b) P1-B: 2347 K, 1.5 kPa

Figure 12: Spatial emission profiles obtained from CN violet radiation along the stagnation line of carbon preform test samples (1 MW/m^2, 1.5 kPa).

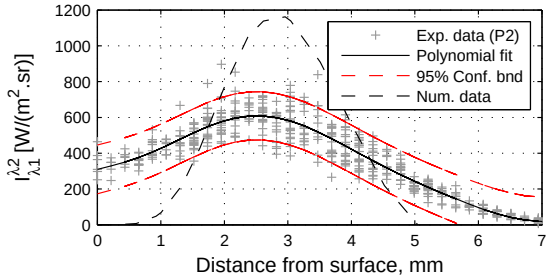

Figure 13: Spatial emission profiles obtained from CN violet radiation along the stagnation line of carbon preform test sample (P2: 2020 K at 1 MW/m^2, 20 kPa).

inflection point now roughly located 4 mm ahead of the surface. A similar behavior was predicted by the numerical method, although emission intensities do not agree well with the experimental values. The stagnation line description with ablative boundary condition did not account for nitridation at the wall, represented by an emission intensity close to zero. Further in the boundary layer, CN was then most probably created following eq. 2.

At higher heat flux (Fig. 14), emission intensities were one order of magnitude higher, what was also represented by the numerical data. Further, at high pressure, maximum emission intensity and inflection point of the emission profile were closer to the surface.

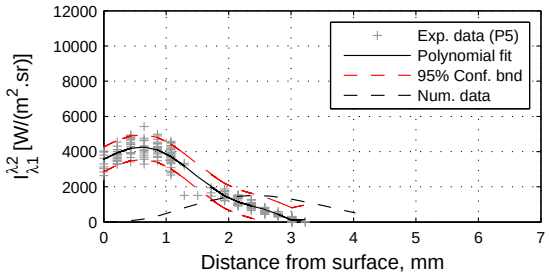

(a) P5: 2848 K, 1.5 kPa

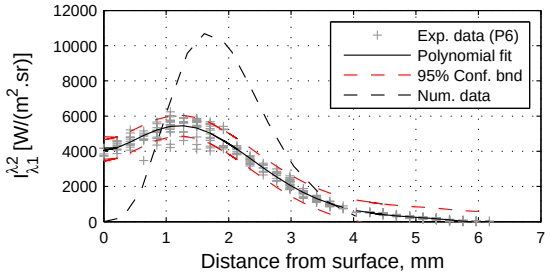

(b) P6: 2783 K, 20 kPa

Figure 14: Spatial emission profiles obtained from CN violet radiation along the stagnation line of carbon preform test samples including comparison to numerical model (3 MW/m^2, 1.5 & 20 kPa).

The numerical model showed the same trend.

It has to be pointed out that the numerical model for the ablation computations as well as the procedure to rebuild emission profiles from simulated CN violet spectra are very simplified at this stage. The functionality of nitrogen recombination at the wall as well as nitridation reactions are being implemented at the moment.

5. Concluding remarks and perspective

5.1. Summary

To enable proper design of ablative heat shields, experimental analysis with parallel modeling is mandatory. We want to investigate the influence of the test environment on the surface recession rate, the pyrolysis gas chemistry, and transport phenomena in the boundary layer. With this work we started a closer study of the ablative behavior of a non-pyrolizing carbon preform and the carbon-phenolic ablator AQ61. This was done by observing in-situ recession rates of the two materials, the radiance of the surface for emissivity estimations, and spatial molecular radiation profiles in the boundary layer, which were finally compared to a numerical approach.

Recession rates were obtained by a linear curve fit of in-situ high-speed camera measurements. In

the case of carbon preform and surface temperatures above 2000 K, recession rates were most likely in a diffusion limited ablation regime, where the temperature of the material does not have much effect on the ablation rate. At lower temperature, the results suggest a transitional regime, where reaction rate controlled ablation changes into diffusion limited ablation.

Emissivities of the material for a low and high surface temperature condition spanned between $\varepsilon_{8-9\mu m} = 0.9 - 0.95$. The in-band emissivity was estimated during one dedicated experiment using an infrared camera in the range $8 - 9\mu$m. Computed Planck curves were then compared to spectral radiation measurements of the surface by one of the emission spectrometers.

The reactive boundary layer in front of the ablative sample was investigated by means of three optical emission spectrometers. Emission intensities of the cyanogen molecule correlated well for several test cases when reaching identical probing distances from the ablating surface. This enabled reconstruction of the CN violet system emission profile within the boundary layer. A stagnation line description with ablative boundary condition, together with the Specair radiation tool, was then used to produce numerically estimated emission profiles as comparison. Although a reduced numerical model was used in combination with a very simplified approach to compute the boundary layer emission, emission intensities were in the same order of magnitude compared to the experimental data. Furthermore, the model was able to predict the location of the maximum emission in a high pressure environment, changing from 2.5 mm-1.5 mm when heat flux was tripled.

5.2. Future work and collaborations

A strong emphasis on detailed characterization of the different materials is planned for the future. For example, a Thermogravimetric analysis (TGA) and Differential scanning calorimetry (DSC) measurements will be undertaken shortly at the VKI. This goes along with Scanning Electron Microscopy (SEM) imaging to examine the ablated fibers and char layer of the material.

Further interest is on the effect of fiber directions (with the grain / through the grain) of the fiber preform and a preliminary test campaign was already performed to research into this aspect, the results are still to be evaluated.

The experiments in this paper did not exceed heat fluxes of $3\,\mathrm{MW/m^2}$, resulting in surface temperatures below 3000 K and therefore, were not sufficiently high to reach a carbon sublimation regime of the ablator. The capability of Plasmatron to reach heat fluxes exceeding $10\,\mathrm{MW/m^2}$, representative of high-speed reentry missions on Earth, was recently achieved [27], and material tests will soon be undertaken in this new condition.

Finally, the stagnation line description with ablative boundary condition will be extended in collaboration at the VKI in order to account for pyrolysis outgassing of the material, with mixing products in the boundary layer. In this paper, we showed a comparison of the numerical model for surface ablation of the non-pyrolyzing carbon fiber preform. The next step will be to compare similar results of ablation rates and boundary layer chemistry with the updated numerical model. This will be followed by Uncertainty Quantification methods to estimate the influence of uncertain parameters on the physical system.

Acknowledgements

We gratefully acknowledge EADS Astrium Space Transportation for providing the test material, in particular Jean-Marc Bouilly for scientific discussion. Mersen Scotland Holytown Ltd. is acknowledged for providing the preform material as well as informative support. The research of B. H. is supported by a fellowship of the Agency for Innovation by Science and Technology (IWT, dossier #111529) in Flanders, and research of T.M. by the European Research Council Starting Grant #259354. Pascal Collin is acknowledged for his valuable help as Plasmatron operator.

References

[1] G. Sutton, The initial development of ablation heat protection: An historical perspective, J. Spacecraft Rock. 19 (1) (1982) 3–11.

[2] B. Laub, E. Venkatapathy, Thermal protection system technology and facility needs for demanding future planetary missions, in: International Workshop on Planetary Probe Atmospheric Entry and Descent Trajectory Analysis and Science, 2003.

[3] H. Tran, Development of lightweight ceramic ablators and arc jet test results, in: NASA TM-108798, 1994.

[4] H. Ritter, P. Portela, K. Keller, J.-M. Bouilly, S. Burnage, Development of a European Ablative Material for Heatshields of Sample Return Missions, in: 6th European Workshop on TPS and Hot structures, Stuttgart, Germany, 1-3 April 2009.

[5] R. Kendall, E. Bartlett, R. Rindal, C. Moyer, An analysis of the coupled chemically reacting boundary layer and charring ablator: Part i, NASA CR 1060, NASA (1968).

[6] F. Milos, Y.-K. Chen, Comprehensive model for multicomponent ablation thermochemistry, in: AIAA 1997-0141, Reno, NV, USA, 1997.

[7] J. Lachaud, I. Cozmuta, N. Mansour, Multiscale approach to ablation modeling of phenolic impregnated carbon ablators, J. Spacecraft Rock. 47 (6) (2010) 910–921.
[8] B. Helber, O. Chazot, T. Magin, A. Hubin, Space and Time-Resolved Emission Spectroscopy of Carbon Phenolic Ablation in Air and Nitrogen Plasmas, in: AIAA paper 2013-2770, 2013.
[9] L. Torre, J. Kenny, A. Maffezzoli, Degradation behaviour of a composite material for thermal protection systems Part I - Experimental characterization, J. Mater. Sci. 33 (1998) 3137–3143.
[10] Cozmuta, I. and Wright, M. J. and Willcockson, W. H., Defining Ablative Thermal Protection System Margins for Planetary Entry Vehicles, in: AIAA 2011-3757, 2011.
[11] B. Helber, O. Chazot, T. Magin, A. Hubin, Ablation of carbon preform in the VKI Plasmatron, in: AIAA paper 2012-2876, 2012.
[12] B. Bottin, O. Chazot, M. Carbonaro, V. van der Haegen, S. Paris, The vki plasmatron characteristics and performance, in: RTO AVT Course on Measurement Techniques for High Enthalpy and Plasma Flows, published in RTO EN-8, Belgium, 1999.
[13] A. Gülhan, Application of pyrometry and ir-thermography to high surface temperature measurements, in: RTO AVT Course on Measurement Techniques for High Enthalpy and Plasma Flows, Belgium, 1999.
[14] C. Moyer, R. Rindal, An analysis of the coupled chemically reacting boundary layer and charring ablator: Part II, NASA CR 1061, NASA (1968).
[15] P. Schrooyen, T. E. Magin, P. Chatelain, Development of a Numerical Simulation Tool for the Aerothermal Flow through an Ablative Thermal Protection System for Atmopheric Entry, in: Review of the VKI Doctoral Research 2012-2013, von Karman Institute for Fluid Dynamics, 2013.
[16] J. B. Scoggins, T. Magin, A. Soufiani, Development of MUTATION++: MUlticomponent Thermodynamics And Transport properties for IONized gases library in C++, in: Review of the VKI Doctoral Research 2012-2013, von Karman Institute for Fluid Dynamics, 2013.
[17] A. Turchi, M. Pietro, T. E. Magin, Ablation modeling with forward uncertainty analysis in Plasmatron acility, in: BOQUSE 2013, International Workshop on Uncertainty Quantification in fluids simulation, 16-18 December, Bordeaux, France, 2013.
[18] C. Laux, Radiation and Nonequilibrium Collisional-Radiative Models, in: Fletcher, D., and Charbonnier, J.M., and Sarma, G.S.R., and Magin, T. (Ed.), Physico-Chemical Modeling of High Enthalpy and Plasma Flows, von Karman Institute Lecture Series 2002-07, 2002.
[19] G. Degrez, D. P. Vanden Abeele, P. F. Barbante, B. Bottin, Numerical simulation of inductively coupled plasma flows under chemical non-equilibrium, Int. J. Numer. Meth. Heat. Fluid Flow 14 (4) (2004) 538–558.
[20] D. Vanden Abeele, G. Degrez, Efficient computational model for inductive plasmas flows, AIAA J. 38 (2) (2000) 234–242.
[21] A. Martin, E. D. Farbar, I. D. Boyd, Numerical modeling of the CN spectral emission of the Stardust re-entry vehicle, in: AIAA 2011-3125, Honolulu, HI, USA, 2011.
[22] C. Park, D. Bogdanoff, Shock tube measurement of coefficient of reaction of nitrogen atoms with solid carbon: Preliminary results, in: AIAA 2003-158, Reno, NV, USA, 2003.
[23] T. Suzuki, K. Fujita, K. Ando, T. Sakai, Experimental Study of Graphite Ablation in Nitrogen Flow, Journal of T 22 (3) (2008) 382 – 389.
[24] D. Bose, M. Wright, D. Bogdanoff, G. Raiche, J. Allen, G.A., Modeling and experimental validation of cn radiation behind a strong shock wave, in: AIAA 2005-0768, Reno, NV, USA, 2005.
[25] S. Andersson, N. Markovic, G. Nyman, Computational Studies of the Kinetics of the C + NO and O + CN Reactions, J. Phys. Chem. A 107 (2003) 5439–5447.
[26] P. Boubert, P. Vervisch, CN spectroscopy and physicochemistry in the boundary layer of a C/SiC tile in a low pressure nitrogen/carbon dioxide plasma ow, J. Chem. Phys 112 (23) (2000) 10482–10490.
[27] D. Guariglia, Boundary Layer Investigation in Plasmatron at High Heat Flux Conditions for High Speed Re-entry Missions, Master's thesis, VKI PR 2013-04 (2013).

Development of a Numerical Simulation Tool for the Aerothermal Flow through an Ablative Thermal Protection System for Atmospheric Entry

Pierre Schrooyen

Aeronautics and Aerospace Department, von Karman Institute for Fluid Dynamics, Belgium, pierre.schrooyen@vki.ac.be

Supervisor: Thierry Magin

Associate Professor, Aeronautics and Aerospace Department, von Karman Institute for Fluid Dynamics, Belgium, magin@vki.ac.be

Promotor: Philippe Chatelain

Assistant Professor, Institute of Mechanics, Materials and Civil Engineering, Université Catholique de Louvain, philippe.chatelain@uclouvain.be

Abstract

The interaction between the flow in the free stream and the ablation is one of the phenomena that leads to difficulties in heat-flux prediction during atmospheric entries. The objective of this work is to develop a computational tool based on a high-order discontinuous Galerkin method, that simulates and models both the flow and wall phenomena in a unified approach. This paper presents the continuum approach developed to go progressively from a plain fluid region to a porous medium. Numerical results to verify and validate the methodology are presented for cases without recession.

Keywords: atmospheric entry, thermal protection system, ablation, discontinuous Galerkin.

1. Introduction

The atmospheric entry of spacecraft presents several challenges in simulating the aerothermal flow around the heat shield. For instance, predicting an accurate heat-flux is a complex task, especially regarding the complex gas-surface interaction on the thermal protection material. These challenges are enhanced at higher entry velocities, typical of new missions, such as samples return from Mars or asteroids, for which ablative materials are used [1]. Requirements concerning mass efficiency for missions with very high entry velocities have led to the development of new class of light carbon composite ablators. New physico-chemical models and computational methods need to be developed to understand the material response of these new ablators in a hypersonic flow.

The components of these ablative materials are carbon fibers and a matrix of phenolic resin. During atmospheric entry, a part of the heat flux is transferred inside the heat shield, leading to a gradual temperature increase of the material and to its transformation. The resin will pyrolyse and produce gases which are going to be transported out of the material to the free stream and will thicken the boundary layer. Close to the surface, the gases of the boundary layer can penetrate the heat shield because of its high porosity and erode the remaining carbonized phenolic resin and carbon fibers until these completely vanish [2]. The thin layer of the heat shield close to the surface will therefore interact with the flow in the boundary layer. Among those interactions, pyrolysis and ablation generate a mass flow and a surface roughness that interact with the flow in the boundary layer [3]. Such perturbations can trigger transition of the flow from laminar to turbulent, leading to a strong increase of the convective heat-flux [4]. This interaction between the type of flow and the roughness is illustrated in Fig. 1.

To simulate the phenomena in these zones, the common strategy proposed by Kendall et al [5] is

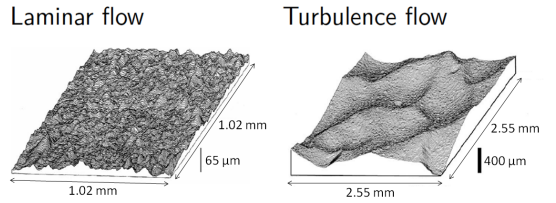

Figure 1: Surface topographies of polycrystalline graphite samples ablated under different flow regimes [3].

to solve the flow field and the material response independently and couple them using boundary conditions on the mass flux and heat fluxes. Using this formulation, the interaction previously discussed can not be captured. The objective of this project is to propose a combined simulation and modeling of the flow and wall phenomena by means of a computational approach that can go seamlessly from a compressible flow to a porous medium.

Previous work [6] has studied the in-depth thermal response of such material to high enthalpy flow in 1D. This paper reviews the efforts undertaken during the last year of doctoral activities. It deals with the interaction between the flow in the boundary layer and the ablative porous medium. The first part focuses on the general methodology. The continuum approach to treat a porous medium is presented and the constitutive equations are derived. The technique used to treat the moving interface region between the flow and the receding material is also described. Numerical results to verify and validate the approach are shown in the second part of this paper.

2. Methodology

The objective of this work is to develop a computational tool that simulates and models the flow and wall phenomena in a unified approach. This is implemented within the research code Argo [7] which is shortly described in the first part of this section. In this work, a continuum approach to treat the homogeneous porous medium is developed. The Navier-Stokes (NS) equations, valid in the fluid phase, are spatially smoothed to be valid everywhere. Therefore, an averaged macroscopic flow field can be computed in the porous medium. The Volume Averaged Navier-Stokes (VANS) set of equations for multi-species flow is summarized in the second part of this section. For exhaustive derivation, readers are referred to Whitaker [8], Drew and Passman [9] or Ganesan [10] to only cite a few. Finally, the technique to treat the heterogeneous transition layer between the clear fluid and the receding porous media is investigated.

2.1. Numerical tool

The multi-dimensional numerical tool is implemented within the research code Argo based on a high-order discontinuous Galerkin method (DGM). This type of discretization was introduced back in 1973 by Reed and Hill [11] to solve neutron transport problems. DGM cumulates the advantages of finite volume and finite element methods. The advantage lies in their accuracy on unstructured meshes, computational efficiency and scalability due to the locality of data and operations [12].

This type of discretization is a particular class of *Finite Elements Methods (FEM)*. Consider a general convection-diffusion problem, with solution $\tilde{u}$

$$\mathcal{L}(\tilde{u}) = \frac{\partial \tilde{u}}{\partial t} + \nabla \cdot (F(\tilde{u})) + \nabla \cdot (\mu(\nabla \tilde{u})) = 0. \quad (1)$$

First of all, the solution is approximated by a function $u \approx \tilde{u}$ in a given functional space $\mathcal{V}$, as a linear combination of the *shape functions* N_i, which form a base for $\mathcal{V}$

$$u = \sum_{i=0}^{p} U_i N_i. \quad (2)$$

The functional space is composed of polynomials of order p in the interior of each cell. Unlike for classical FEM, no continuity of the functions is required across the interfaces. In this case N_i are elementwise Lagrange polynomials. The expansion weights U_i are found by requiring the residual to vanish locally in a Galerkin sense:

$$\int_\Omega v\mathcal{L}(u) = 0, \ \forall \ v \ \in \ \mathcal{V} \quad (3)$$

and as usual in FEM the required regularity of the functions v is decreased by partially integrating this equation. Due to the discontinuity of the interpolatory and test functions, element interface contributions need to be added to the residual of the variational problem, which are absent for continuous FEM. The discretization of those terms in the convective part is done by an appropriate Riemann solver or a monotone flux like in classical finite volume methods [7]. In this implementation, a Lax-Friedrich scheme was chosen to compute the cell flux balances over the boundaries of an element. In contrast to the discretization of the convective terms, many alternatives exist for the

discretization of the diffusion terms, an overview and comparison can be found in Arnold et al. [13]. Within this work, the interior penalty method proposed in particular by Riviere [14] to solve parabolic problems in porous media has been chosen. A weak formulation that uses these two techniques for the convective and diffusive parts can then be expressed as

$$a(u, v) = 0 \ , \ \forall \ v \ in \ \mathcal{V} \tag{4}$$

with

$$\begin{aligned} a(u,v) = & \\ \sum_{\Omega_e \in \Omega} \int_{\Omega_e} \nabla v \cdot F(u) \, d\Omega_e - \sum_{I_i \in I} \oint_{I_i} [\![v]\!] \mathcal{H}(u^+, u^-, \mathbf{n}) \, dS & \\ - \sum_{\Omega_e \in \Omega} \int_{\Omega_e} (\nabla v) \cdot (\mu \nabla u) \, d\Omega_e + \sum_{I_i \in I} \oint_{I_i} \{\!\{\mu \nabla u\}\!\} [\![v]\!] \, dS & \\ + \theta \sum_{I_i \in I} \oint_{I_i} \{\!\{\mu \nabla v\}\!\} [\![u]\!] \, dS - \alpha \sum_{I_i \in I} \oint_{I_i} [\![v]\!] [\![u]\!] \, dS, & \end{aligned} \tag{5}$$

where Ω_e are the elements and I_i are interfaces between adjacent elements. On the latter, the jump and average *trace operators* are defined respectively by

$$[\![a]\!] = a^- n^- + a^+ n^+ \tag{6}$$

$$\{\!\{a\}\!\} = \frac{1}{2}(a^- + a^+). \tag{7}$$

Finally, $\mathcal{H}$ is the interface flux, for which a Riemann solver for the convective problem is used. The first and third terms of the right hand side of Eq.(5) are volume contributions for the convective and diffusive terms respectively which are common with the classical continuous Galerkin FEM (CGFEM). The remaining terms, absent in CGFEM, can be considered as internal boundary conditions that couple the element with its neighbors. These are implemented for the convective terms using an (approximate) Riemann solver for the convective problem, while terms 4 through 6 implement a Nitsche type weak Dirichlet condition for the diffusive part. In this approach, called *interior penalty*, the parameter θ can in principle be chosen freely without impacting on consistency, while the interior penalty parameter α needs to be above a certain critical value to ensure stability. In practice, the *symmetric IP (SIP)* with $\theta = 1$ is chosen due to superior convergence. Another useful variant is the *non-symmetric IP (NIP)* due to the relaxed requirements on α, since in this case only positivity of α is required.

The Argo platform possesses already a formalism to treat convection, diffusion reaction problem in an implicit way. During the last year, the approach to treat multi-components flow through porous media was implemented.

2.2. Volume Averaged Navier-Stokes equations

Volume averaging is a method to derive rigorously continuum equations in case of multiphase systems. Within this work, the system is composed of two phases, the solid matrix and the fluid phase (see figure 2).

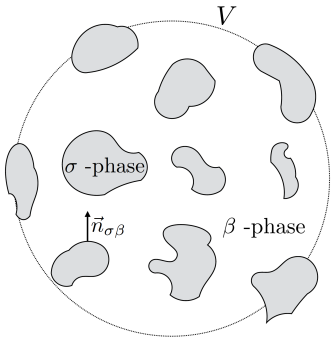

Figure 2: Volume averaging for the porous medium

The pores of the medium are filled with a fluid phase β and σ represents the solid phase. A elementary volume V is therefore composed of V_β and V_σ, and the volume fraction of each phase is defined as

$$\epsilon_\beta = \frac{V_\beta}{V} \ , \ \epsilon_\sigma = \frac{V_\sigma}{V}. \tag{8}$$

The volume fraction of the fluid phase is usually called the porosity or the void fraction. The superficial average of a quantity α

$$\langle \alpha \rangle_s = \langle \alpha \rangle \ = \ \frac{1}{V} \int_{V_\gamma} \alpha \, dV, \tag{9}$$

has to be distinguished from the intrinsic average on a phase γ,

$$\langle \alpha \rangle_\gamma = \frac{1}{V_\gamma} \int_{V_\gamma} \alpha dV. \tag{10}$$

The two averages are linked by the volume fraction:

$$\langle \alpha \rangle_s = \epsilon_\gamma \langle \alpha \rangle_\gamma. \tag{11}$$

In order to derive the VANS equations, the volume average of derivative has to be related to the derivative of volume averaged quantity. The theorem of local volume averaging is

$$\langle \nabla \cdot \alpha \rangle = \nabla \cdot (\langle \alpha \rangle) + \frac{1}{V} \oint_{\partial \Omega_\beta} \alpha \cdot n_{\beta\sigma} \, dS \ , \qquad (12)$$

$$\langle \frac{\partial \alpha}{\partial t} \rangle = \frac{\partial \langle \alpha \rangle}{\partial t} - \frac{1}{V} \oint_{\partial \Omega_\beta} (\alpha w) \cdot n_{\beta\sigma} \, dS \ , \qquad (13)$$

where equation (13) comes from the Reynolds transport theorem. Using volume averaging, the value of a quantity α can be expressed as

$$\alpha = \langle \alpha \rangle + \alpha'. \qquad (14)$$

We will assume that the elementary volume used for the average is such that

$$\langle \langle \alpha \rangle \rangle = \langle \alpha \rangle \text{ , and } \langle \alpha' \rangle = 0 \qquad (15)$$

are satisfied. Hence the mean of the product can be written

$$\begin{aligned} \langle \alpha\beta \rangle = \langle \langle \alpha \rangle \langle \beta \rangle \rangle + \langle \alpha' \langle \beta \rangle \rangle + \langle \langle \alpha \rangle \beta' \rangle + \langle \alpha' \beta' \rangle \\ = \langle \alpha \rangle \langle \beta \rangle + \langle \alpha' \beta' \rangle. \end{aligned} \qquad (16)$$

The constitution laws for mass, momentum and energy are described hereafter and the assumptions are summarized.

2.2.1. Mass conservation law

The mass conservation law is averaged for each species in the gaseous phase accounting for species diffusivity and heterogeneous reaction at the surface of the solid matrix. In the case of material recession, a mass balance for the solid phase is added to the system of equations to track the evolution of the porosity. The solid phase is assumed rigid and the mass loss will occur at the surface of the solid particles. Applying the volume averaging theory, the mass conservation equation can be expressed as:

$$\frac{\partial \langle \rho_i \rangle}{\partial t} + \nabla \cdot (\langle \rho_i u \rangle) = \nabla \cdot \Big((D_{eff} + D_{disp}) \nabla \langle \rho_i \rangle_\beta \Big) + \omega_h, \qquad (17)$$

where $\langle \rho_i \rangle$ is the superficial average over the small elementary volume ($\langle \rho_i \rangle = \epsilon_\beta \langle \rho_i \rangle_\beta$), ω_h is the heterogeneous source term, D_{eff} is the effective diffusion coefficient and D_{disp} is the hydrodynamic dispersion. The effective diffusivity will depend on the void fraction and the tortuosity (η) of the inner porous medium

$$D_{eff} = \frac{\epsilon_\beta}{\eta} D_{ref}. \qquad (18)$$

The dispersive effect will only be important if the Peclet number based on the pore size is larger than one [8]. According to Lachaud [15], for the ablation of carbon fibers the Peclet number is smaller than unity leading to a negligible dispersive effect.

2.2.2. Momemtum conservation law

The volume averaging theory can be applied on each term of the momentum equation.

$$\langle \frac{\partial (\rho \boldsymbol{u})}{\partial t} \rangle = \frac{1}{V} \frac{\partial (\int_V \rho \boldsymbol{u} \, dV)}{\partial t} + \frac{1}{V} \oint_{\partial V} \rho u (u - u^*) \cdot n \, dS, \qquad (19)$$

$$\langle \nabla \cdot \rho \boldsymbol{u} \rangle = \nabla \cdot (\epsilon_\beta \langle \rho \rangle_\beta \langle u \rangle_\beta \langle u \rangle_\beta) + \nabla \cdot \langle \rho' u' u' \rangle, \qquad (20)$$

$$\langle \nabla \cdot \sigma \rangle = -\epsilon_\beta \nabla \langle p \rangle_\beta + \nabla \cdot \langle \tau \rangle + \frac{1}{V} \oint_{\partial V} (-p' + \tau) \cdot n \, dS, \qquad (21)$$

where $\langle p \rangle_\beta$ is the pressure inside the fluid phase, u^* is the recession velocity of the solid phase, prime quantity are deviations and τ is the viscous stress tensor. The surface integrals terms in eq: 19 and 21 as well as the dispersive term in eq: 20 have to be modeled to close the system of equations. In eq:19, the last term represents the exchange of momentum due to volume change. The second surface integral (eq: 21) is a drag term imposed by the presence of the solid phase in the porous medium. Whitaker [8] has shown that the drag force can be modeled by

$$F = \frac{-\mu}{\kappa} \epsilon_\beta^2 \langle u \rangle_\beta. \qquad (22)$$

This model is only valid if the Reynolds number based on the length of a pore is sufficiently small such as the inertial term can be neglected. Assuming incompressible flow, Darcy's law can be retrieved at steady state:

$$\nabla p = \frac{-\mu}{\kappa} \epsilon_\beta \langle u \rangle_\beta = \frac{-\mu}{\kappa} \langle u \rangle. \qquad (23)$$

Breugem [16] has shown that the correlation between the deviations is often negligible with respect to the drag force term. The exchange of momentum due to volume change will also be neglected in the case of fibers ablation because it can be shown that Darcy's term will be predominant. This leads to

$$\begin{aligned} \frac{\partial (\langle \rho \boldsymbol{u} \rangle)}{\partial t} + \nabla \cdot (\epsilon_\beta \langle \rho \rangle_\beta \langle u \rangle_\beta \langle u \rangle_\beta) \\ = -\epsilon_\beta \nabla \langle p \rangle_\beta + \nabla \cdot \langle \tau \rangle + F. \end{aligned} \qquad (24)$$

2.2.3. Energy conservation law

For the energy equation, thermal equilibrium between the two phases is assumed. Therefore only one equation is used for both phases:

$$\frac{\partial\langle\rho E_{tot}\rangle}{\partial t}+\nabla\cdot\left(\epsilon_\beta\langle\rho\rangle_\beta\langle H\rangle_\beta\langle u\rangle_\beta\right) = \nabla\cdot k_{eff}\nabla T+\nabla\cdot(\langle\sigma\cdot u\rangle), \tag{25}$$

where the total energy is composed of the energy of the solid phase and the energy of the fluid phase

$$\langle\rho E_{tot}\rangle = \epsilon_\beta\left(\langle\rho\rangle_\beta(\langle e\rangle_\beta+0.5\langle u\rangle_\beta^2)\right)+\epsilon_\sigma\langle\rho\rangle_\sigma\langle e\rangle_\sigma, \tag{26}$$

with H being the enthalpy of the gaseous phase, σ is the stress tensor and k_{eff} is an effective conductivity inside the porous medium.

2.3. Modeling the interface area

The hypothesis made to derive this system of equations assumes that the porosity is constant in the small averaging volume. This is no longer valid in the interface region between a porous medium and a plain fluid domain. To treat this interface, the two existing main methods either use a jump condition to correct the approximation of the closure model in the interface region ([16], [17]) or use a variable permeability/porosity in a part of the domain ([18] and [19]). In the case of a flow field over an ablative material, this interface area will move due to recession. Therefore, an *interface tracking* or an *interface capturing* method has to be used to follow the moving boundary.

Since most material codes solve independently the flow field and the material response, they still use a moving mesh technique proposed by Rindal [20]. This *interface tracking* technique presents many limitations for multidimensional problems, since the mesh movement can seriously degrade mesh quality in cases of non-uniform material recession. Remeshing can be time consuming and quite complex depending on the shape of the interface. Therefore, it is proposed to use an *interface capturing* technique, which does not require the meshes to follow the interface.

Many interface capturing methods have been developed for the finite element method. With respect to the numerical evaluation of the discretized equations, these methods can be roughly divided in *diffuse* and *sharp interface capturing* methods. Diffuse techniques, such as the *immersed boundary method* proposed by Peskin [21] , smooth the discontinuity over a transition region. Due to this regularization, the method obviously is easy to implement, but on the other hand it implies the loss of accuracy near the surface. Sharp interface methods locally modify the stencil of the numerical scheme, and can thereby - in theory - keep the convergence order of the method even near the interface region. Of the several variants in this last category, both the *immersed interface finite element (IFEM)* technique and the *eXtended Finite Element Method (XFEM)* were investigated.

During the past year, the coupling of extended Finite Element Method and DGM has demonstrated the capabilities of such method to achieve high order accuracy for problem with moving boundaries in one dimension. This method was preferred to immersed interface method because of its relatively ease of extension to multi-dimensional problems and its capability to achieve high order accuracy. The results of such implementation in 1D can be found in the AIAA paper [22]. However, applying XFEM to DGM raises different issues mainly related to the discontinuous character of XFEM (enrichment strategy, numerical and temporal integration) which are even more complex for multi-dimensional problems. In addition, for the enrichment strategy, a level-set method has to be used to track the interface. Using a level-set method implies different challenges, for example, the reinitialization of the level-set function to ensure the distance property or the extension of the velocity field known only at the interface. Therefore, in a first attempt, a diffuse approach is used and the position of the porous medium is deduced implicitly by the evolution of the solid mass density.

A normalized hyperbolic tangent function is used to smooth the initial solid volume fraction on the grid

$$H(\phi) = \tanh\left(\frac{\pi\phi}{\epsilon_\phi}\right), \tag{27}$$

where ϕ is the initial distance function from the porous medium and ϵ_ϕ is the double grid distance on which the quantity is smoothed. Following the work of Pochet [23], the smoothing distance has to be at least equal to

$$\epsilon_\phi = 1.5\frac{h}{p}, \tag{28}$$

h being the mesh size and p the interpolation order. The effect of the smoothing distance are investigated in the second part of this paper (see Section 3).

Since a diffuse interface capturing method is chosen, it is not possible to use the jump condition to correct what is happening in the interface region. Instead, the permeability will vary from the constant value in the homogeneous porous medium to infinity in the plain fluid region. There is no general relationship between the porosity and the permeability and theses models assume usually that the porous medium is homogeneous. However, the model of Carman-Kozeny [24] will be used to link the local porosity and the permeability. This semi-heuristic model is based on the concept of hydraulic radius and leads to a permeability which depends on the porosity, the tortuosity and the specific surface area

$$\kappa^{-1} = \frac{A_0^2(1-\epsilon_\beta)^2 k_k}{\epsilon_\beta^3}. \tag{29}$$

where k_k is directly proportional to the tortuosity and the proportional constant depends on the shape of the solid matrix. The specific surface (A_0) is defined as

$$A_0 = \frac{A_{fs}}{V_s}, \tag{30}$$

where A_{fs} and V_s are respectively the contact surface of the solid matrix with the fluid phase and the volume of the solid phase. Using this model, even in the heterogeneous interface region, the permeability will be adapted implicitly in case of recession.

3. Numerical test cases

This section presents the different test cases that have been used to verify the approach and the implementation inside the Argo code. For the two first test cases, only one species is considered. The last test case shows preliminary results for the multi-components solver and the coupling of Argo with a thermodynamic and transport property library.

3.1. Channel Flow with a porous plug

This test case studies a channel flow with a porous plug filling half of the domain (see Fig. 3). In this case, the flow is normal to the interface hence the pressure gradient will be substantially higher in the porous region while the averaged velocity is expected to be of the same order of magnitude. A uniform velocity profile of 0.1 $[m/s]$ is used for the left boundary condition and a pressure outlet of $1e^4$ $[Pa]$ for the right part of the domain while periodic conditions have been imposed on the top and bottom part of the channel to

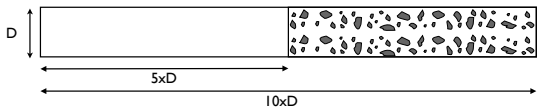

Figure 3: Porous plug test case. The height of the channel used is $D = 22e^{-3}$ $[m]$ The porous medium is characterized by a $\epsilon = 0.875$ and $\kappa = 1e^{-8}$ $[m^2]$. The fluid viscosity is $\mu = 1.5e^{-5}$ $[m^2/s]$.

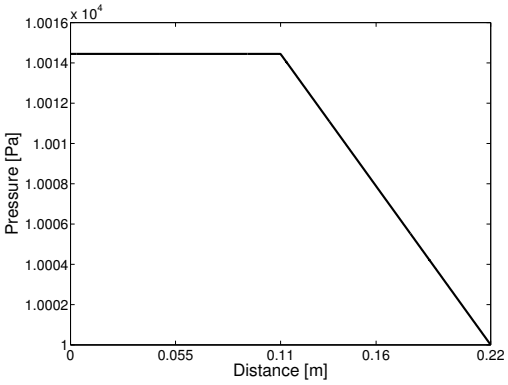

Figure 4: Porous plug test case. Pressure profile along the channel.

retrieve one dimensional Darcy's law. The resulting pressure profile is shown in Fig. 4.

As expected, the pressure drop is linear inside the porous medium and the difference in pressure at steady state matches Darcy's law with an error of 0.05%

$$\Delta P_{Darcy} = L \cdot \frac{\mu}{\kappa} \cdot \langle u \rangle_s = 14.4375\ [Pa] \tag{31}$$

$$\Delta P_{Argo} = 14.4454\ [Pa]. \tag{32}$$

3.2. Channel Flow with a porous slab

This test case studies a channel flow with a porous slab (see Fig. 5). A parabolic velocity profile is imposed at the left boundary, while the outlet pressure is given for the right boundary. The upper and lower part of the domain are modeled as non-slip walls.

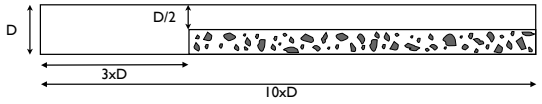

Figure 5: Porous slab test case. The height of the channel used is $D = 22e^{-3}$ $[m]$ The porous medium is characterized by a $\epsilon = 0.875$ and $\kappa = 0.132 d_p^2$ $[m^2]$ where $d_p = 0.0625D/2$ $[m]$. The fluid viscosity is $\mu = 1.5e^{-5}$ $[m^2/s]$.

For parallel flows, the behavior of the velocity and pressure gradient is opposite to what was expected for Section 3.1. The averaged velocity is substantially larger in the plain fluid region while the pressure gradient is almost constant. For a laminar case, an analytical solution for a steady-state fully developed flow can be found by solving independently what is happening in the flow region and in the porous medium. These two solutions are coupled by using an interface condition such as the Ochoa-Tapia-Whitaker condition which has shown good agreements with experiments [19]. This condition forces the continuity of the superficial velocity at the interface and a jump in the viscous stress:

$$\langle u \rangle_{interface} = U_i \tag{33}$$

$$\mu \frac{d\langle u \rangle_p}{dy} - \mu \frac{d\langle u \rangle_f}{dy} = \mu \frac{\beta_t}{\sqrt{\kappa}} U_i \tag{34}$$

where, $\langle u \rangle_f$ and $\langle u \rangle_p$ are respectively the velocity in the pure fluid region and averaged velocity in the porous region, U_i is the interfacial velocity and β_t is a parameter that has to be determined. The derivation of such analytical solution can be found in [16] or [25] for other types of interface conditions. In addition to the good agreement of such method to experiments, this solution matches a Direct Numerical Simulation (DNS) computed by Breugem [16]. In this DNS, the porous medium is modeled by a grid of squares (see Fig. 6). The Navier-Stokes equations are solved in the whole domain using an immersed boundary method to account for the obstacles. Using volume averaging theory, the closure parameters for the analytical model can be found such that solutions are comparable. The results for the channel computation in DNS overlap almost entirely the approximate analytical solution with a small discrepancy in the interface region [16]. The velocity profile seems to be underestimated in the interface region by the two domains approach.

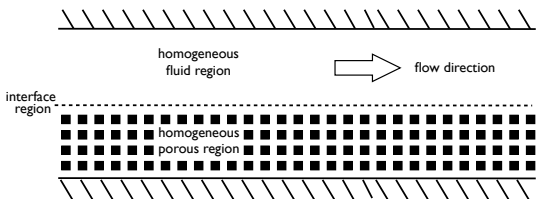

Figure 6: Porous slab test case. The permeable wall is modeled by a grid of squares of length d_p.

The parameters for the run are summarized in Table 1. The results for the variable permeability approach developed inside Argo are compared with the analytical approach in Fig: 7.

Table 1: Parameters for the run

Test	*Value*	*Units*
Re_{dp}	1	$[-]$
dp	0.0625 H	$[m]$
κ	0.132 dp^2	$[m^{-2}]$
ϵ_ϕ	$1e^{-4}$	[m]
P	1e-4	$[Pa]$

The solutions are close but do no match exactly. First, it can be noticed that the interface thickness chosen will influence the velocity profile in the interface region itself. Secondly, the discrepancy in the fluid part can also be explained by phenomena occurring in the interface region. Indeed, changing the skin friction at the permeable wall will influence the flow in the free fluid region. Subsequently, if the velocity at the interface is smaller, the mass flow rate will be higher than expected in the plain fluid region and the peak will be located nearer the center of the channel.

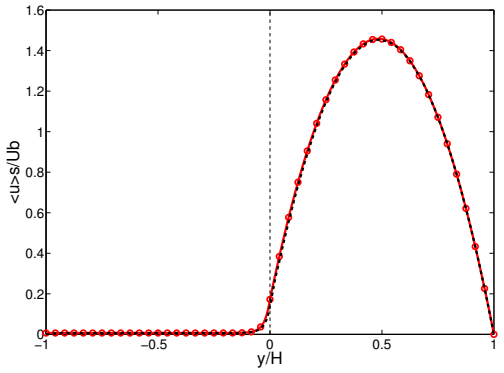

Figure 7: Channel flow over a permeable wall. Comparison between the analytical averaged velocity profile (plain dotted line) computed assuming OTW condition with $\beta_t = 0.91$ given by the DNS of Breugem [16] and the Argo results (dashed line).

Refining the grid close to the interface and reducing the acceptable distance of smoothing (ϵ_ϕ) will give results that converge towards the analytical solution. A zoom on the solution close to the interface for three smoothing distances on the same grid is shown in

Fig 8. It can be observed that with this model for the permeability, a larger smoothing distance will lead to a lower velocity at the interface and a peak in the fluid region slightly shifted towards the center.

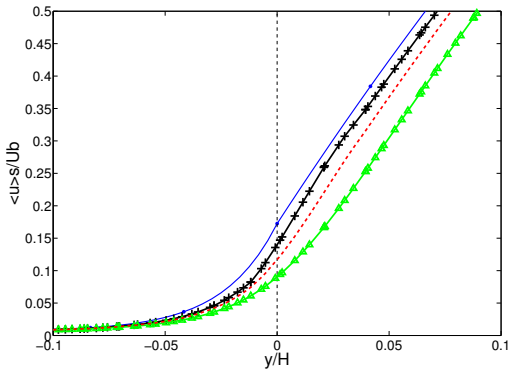

Figure 8: Channel flow over a permeable wall. Comparison of velocity profiles close to the interface for different smoothing distance on the same mesh. The plain dotted line is the analytical solution using two domains approach, the crossed line, dashed line and the one with triangles are respectively for $\epsilon_\phi = 1e^{-4}$, $5e^{-4}$ and $1e^{-3}$.

Reducing the distance of smoothing might lead to spurious non-physical overshoot for the void fraction due to the high-order approximation. This effect does not only depend on ϵ_ϕ but also on the relative position of the interface on the unstructured mesh. This spurious overshoot in the interface region is shown in Fig. 9.

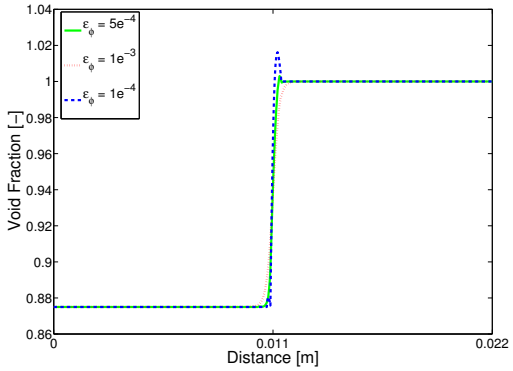

Figure 9: Void fraction profile along the height of the channel. Influence of the smoothing distance on the void fraction.

3.3. Multi-components flow

In order to model the heterogeneous reactions in the interface region, different species need to be tracked in the flow field. The current Argo solver has been extended to multi-species flows and coupled with the thermodynamic and transport library Mutation++ developed at the von Karman Institute by J.B. Scoggins [26]. The dissociation of O_2 in a 0D reactor is used to verify the implementation of the source term and the coupling with Mutation++ (see Fig 10). The initial temperature is 5000 $[K]$, the initial composition is 100% of O_2 with a density of $2.85e^{-4}$ $[kg/m^3]$. The results are compared with a 0D code provided as an example with the distribution of Mutation++.

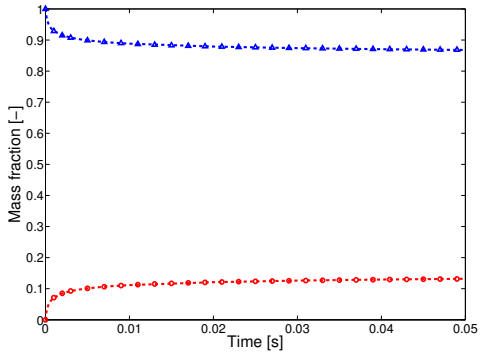

Figure 10: Oxygen dissociation. Comparison of results from a code given in the distribution of Mutation++ and Argo. The (red) dotted points are the mass fraction of O for different times while the (blue) triangles represent the mass fraction of O_2 computed with Argo. The dashed lines are the results of the software furnished with Mutation++.

4. Perspectives and future work

Currently, the work is focused on the coupling between the multi-species solver implemented and the volume averaging approach developed to account for the presence of an ablative material. A number of issues related to the stiffness of the heterogeneous source term and to the use of a compressible solver to simulate low Mach number flows are currently investigated. The numerical simulation of an experiment conducted by F. Panerai et al at Nasa Ames is one of the step that will allow to validate this approach. For this experiment, a fiber form plug is inserted inside the sidearm reactor facility [27] and is ablated. The model for the mechanisms of fibers ablation is given by J. Lachaud [15]. The results will also be compared with numerical simulations performed by Martin [28]. The reproduction of such test case will validate the approach followed to treat the interaction between the multi-component flows and the porous medium.

5. Conclusion

During the past year, the effort has been dedicated to the methodology to treat both a receding porous phase and a fluid flow inside the same domain of computation. Different methods have been investigated and implemented in 1D. The extended Finite Element Method coupled with the Discontinuous Galerkin discretization has demonstrated promising capabilities to treat the discontinuity between the two domains in a sharp way. However, due to the challenge of such method to be extended to 2D/3D, a diffuse method was first chosen. The continuum approach developed and implemented inside the Argo code has been verified against analytical solutions and has been compared with direct numerical simulations. The multi-dimensional tool has been coupled with Mutation++ and has been extended to treat multi-component flows.

Acknowledgments

The first author would like to acknowledge continuous support from K. Hillewaert and the Argo team from Cenaero in the development of the numerical tool. The first author would like to thank N. Mansour (Nasa Ames Research Center), for hosting him during summer 2013 at Nasa Ames Research Center. Fruitful discussions with F. Panerai (Nasa Ames) on the different test cases are gratefully acknowledged. The first author acknowledges support through a fellowship from the “Fond pour la formation à la Recherche dans l’Industrie et dans l’Agriculture ”.

References

[1] J. Dec, R. Braun, B. Laub, Ablative thermal response analysis using the finite element method, Journal of thermophysics and heat transfer 26(2) (2012) 201–212.

[2] J. Lachaud and N. M. Mansour , Microscopic scale simulation of the ablation of fibrous materials, no. 48th AIAA Aerospace Sciences Meeting and Exhibit, Orlando, FL, 2013.

[3] G. Vignoles, J. Lachaud, Y. Aspa, J. Goyhénèche, Ablation of carbon-based materials: Multiscale roughness modelling, Composites Science and Technology 69 (2008) 1470–1477.

[4] R. Crocker, Y. Dubief, Numerical study of turbulence over a receding wall by controlled and thermal ablation, in: Proceedings of the Summer Program 2010, Center for Turbulence Research, Stanford, USA, 2010.

[5] E. P. Bartlett, R. M. Kendall, C. B. Moyer, R. A. Rindal, An analysis of the coupled chemically reacting boundary layer and charring ablator, part 1 summary report, Contractor Report CR-1060, NASA (June 1968).

[6] P. Schrooyen and T.E. Magin and P. Chatelain , Development of a Numerical Simulation Tool for the Aerothermal Flow through an Ablative Thermal Protection System for Atmospheric Entry, no. VKI PhD Symposium, Sint-Genesius Rode, Belgium, 2013.

[7] K. Hillewaert, Development of the discontinuous Galerkin method for large scale/high-resolution CFD and acoustics in industrial geometries, Ph.D. thesis, Universite catholique de Louvain (2013).

[8] S. Whitaker, The Method of Volume Averaging, Kluwer Academic Publishers, Dordrecht, The Netherlands, 1999.

[9] D. Drew, S. Passman, Theory of Multicomponent Fluids , Springer, New York, 1999.

[10] S. Ganesan and D.R. Poirier, Conservation of Mass and Momentum for the Flow of Interdendritic Liquid during Solidification, Metallurgical transactions 21 (B) (1990) 173–181.

[11] W. Reed, T. Hill, Triangular mesh methods for the neutron transport equation, Contractor Report LA-UR-73-479, Los Alamos Scientific Laboratory (June 1973).

[12] B. Cockburn, G. Karniadakis, C.-W. Shu, The development of discontinuous Galerkin methods, in: B. Cockburn, G. E. Karniadakis, C.-W. Shu (Eds.), Discontinuous Galerkin Methods, Springer, 2000, pp. 3–50.

[13] D. Arnold, F. Brezzi, B. Cockburn, M. L.D., Unified analysis of discontinuous galerkin methods for elliptic problems, SIAM Journal Numerical Analysis 39(5) (2001) 1749–1779.

[14] B. Riviere, Discontinuous Galerkin Methods for Solving Elliptic and Parabolic Equations - Theory and Implementation, Society for Industrial and Applied Mathematics, 2008.

[15] J. Lachaud and N. M. Mansour and A. Ceballos and D. Pejakovic and L. Zhang and J. Marschall , Validation of a volume-averaged fiber-scale model for the oxidation of a carbon-fiber preform, no. 42nd AIAA Thermophysics Conference, Honolulu, Hawaii, 2011.

[16] W.P. Breugem, The influence of wall permeability on laminar and turbulent flows, Ph.D. thesis, Technishe Universiteit Delft (2005).

[17] M. Moesner and R. Radespiel , Numerical Simulation of Turbulent Flow over Porous Media, no. 21st AIAA Computational Fluid Dynamics Conference, San Diego, CA, 2013.

[18] M.Sahraoui and M. Kaviany, Slip and no-slip velocity boundary conditions at interface of porous, plain media, International Journal of Heat and Mass Transfer 35 (1992) 927–943.

[19] J.A. Ochoa-Tapia and S. Whitaker, Momentum transfer at the boundary between a porous medium and a homogeneous fluid-II. Comparison with experiment, International Journal of Heat and Mass Transfer 38 (1995) 2647–2655.

[20] C. B. Moyer, R. A. Rindal, An analysis of the coupled chemically reacting boundary layer and charring ablator. part 2 - finite difference solution for the in-depth response of charring materials considering surface chemical and energy balances, Contractor Report CR-1061, NASA (June 1968).

[21] C. Peskin, Numerical analysis of blood flow in the heart, Journal of Computational Physics 25 (1977) 220–252.

[22] P. Schrooyen and K. Hillewaert and T.E. Magin and P. Chatelain , Discontinuous Galerkin discretization coupled with sharp interface method for ablative materials, no. 21st AIAA Computational Fluid Dynamics Conference, San Diego, CA, 2013.

[23] F. Pochet and K. Hillewaert and P. Geuzaine and J.-F. Remacle and E. Marchandise, A 3D strongly coupled implicit discontinuous Galerkin level-set based method for modeling two-phase flows, Computers and Fluids 87 (25) (2013) 144–155.

[24] F. Dullien, Porous Media: Fluid Transport and Pore Structure, Academic Press, San Diego, 1991.

[25] M. Kaviany, Principles of Heat Transfer in Porous Media, Springer, New York, 1999.

[26] J.B. Scoggins , Development of multiphysics numerical methods to study coupled flow, radiation, and ablation phenomena for planetary entry vehicle, no. VKI PhD Symposium, Sint-

Genesius Rode, Belgium, 2013.
[27] F. Panerai and A. Martin and N.N. Mansour and S. Sepka and J. Lachaud, Flow tube Oxidation Experiments on the Carbon Preform of PICA, no. 44th AIAA Thermophysics Conference, San Diego, CA, 2013.
[28] A. Martin, Volume Averaged modeling of the oxidation of porous carbon fiber material, no. 44th AIAA Thermophysics Conference, San Diego, CA, 2013.

An Extension of the Gibbs Function Continuation Method for Linearly Constrained Multiphase Equilibria

James B. Scoggins

Aeronautics and Aerospace Department, von Karman Institute for Fluid Dynamics, Belgium, james.scoggins@vki.ac.be

Supervisor: Thierry Magin

Associate Professor, Aeronautics and Aerospace Department, von Karman Institute for Fluid Dynamics, Belgium, magin@vki.ac.be
Laboratoire d'Énergétique Moléculaire et Macroscopique, Combustion (EM2C), École Centrale Paris, France

University Supervisor: Anouar Soufiani

Research Head, Laboratoire d'Énergétique Moléculaire et Macroscopique, Combustion (EM2C), École Centrale Paris, France

Abstract

A novel method for solving linearly constrained, multiphase phase, chemical equilibrium problems is developed based on the single phase Gibbs function continuation method. The robustness and accuracy of the method is discussed and several results which clearly demonstrate the discussion topics are provided.

Keywords: chemical equilibria, multiphase, constrained equilibrium, Gibbs function continuation

1. Introduction

The efficient computation of multiphase, constrained equilibrium compositions is an important topic for a wide range of applications including combustion, aerospace engineering, plasma dynamics, and thermal protection system design. For a detailed history and list of applications, the reader is referred to the treatise by van Zeggeren and Storey [1].

Prior to 1958, the equilibrium constant formulation was primarily used to compute equilibrium compositions for ideal, gas phase mixtures [2]. The equilibrium constant formulation works by assigning formation reactions to each species based on a set of base or component species which are chosen *a priori* for the given reaction system. Kuo [2] cites several disadvantages that hindered researches using this method including difficulties in extending the method to non ideal equations of state, testing for the presence of condensed species and numerical complications with the use of component species. Perhaps most importantly, the equilibrium constant formulation requires the list of formation reactions to be specified, making a general treatment of any chemical system difficult.

In 1958, White, Johnson, and Dantzig [3] introduced the concept of free-energy minimization and proposed a numerical solution technique using the method of steepest decent. White [4] later elaborated on the advantages of free-energy minimization and the use of element potentials in the solution of equilibrium compositions, including the possibility to treat any general chemical system without the necessity of specifying the formation reactions. In addition, the use of element potentials allowed for the solution of linear systems whose size scaled with the number of elements, not species, present in the mixture. This fact alone offers a significant computational advantage when considering large chemical systems.

Today, both the equilibrium constant formulation and the free-energy minimization methods are widely used. Most commercial and general purpose research codes implement various numerical methods for solving the free-energy minimization problem, however the equilibrium constant formulation is still used in certain applications [5]. Perhaps one of the most widely used equilibrium codes today is the Stanford-JANAF (STANJAN) code by Reynolds [6] who popularized the element potential method for constrained Gibbs free-energy minimization by developing a numerical solution procedure to the minimiza-

tion problem which solves the so-called "dual problem." Part of the success of the STANJAN method lies in its powerful initialization and preconditioning procedures which help make STANJAN extremely robust for most problems. The Chemical Equilibrium with Applications (CEA) code developed by Gordon and McBride [7, 8] is also used heavily, helped by the overwhelming success of the detailed thermodynamic database developed at NASA Glenn Research Center, which it employs.

Bishnu *et al.* [9] added the ability to include general linear constraints on the equilibrium solutions to both STANJAN and CEA. Linear constraints are often used in Rate Controlled Chemical Equilibrium (RCCE) calculations - a process designed to significantly reduce the computational effort to simulate the time history of a kinetic system which can be described as a series of pseudo-equilibrium compositions. It was found under certain conditions that both the constrained versions of STANJAN and CEA could fail to converge to a solution. In general, these situations arise when the linear constraints force the equilibrium composition near the boundary of the feasible region imposed by the hyperplane defined by the constraints.

In an effort to provide a provably robust equilibrium solver, Pope [10, 11] developed the Gibbs Function Continuation (GFC) method which solves the element potential equations for a single phase, ideal gas mixture under general linear constraints. The purpose of this paper is to extend Pope's GFC method to multiphase mixtures. An attempt is also made to formulate the continuation method in a manner which is easier to understand and implement than the original GFC method. Additionally, a unique method of determining the analytically derived partial derivatives of the equilibrium mole fractions versus temperature and pressure is shown which can greatly speedup numerical routines relying on finite-difference calculations to compute equilibrium properties such as the specific heat or sound speed of the a mixture in equilibrium.

2. Constrained Chemical Equilibrium

Consider a chemical system composed of any number of ideal phases. The set of indices which denote all species in this system is $\mathcal{S} = \left\{1, \ldots, n^{\mathcal{S}}\right\} = \cup_{m\in\mathcal{P}}\mathcal{S}_m$ where $n^{\mathcal{S}}$ is the total number of species considered, $\mathcal{P} = \left\{1, \ldots, n^{\mathcal{P}}\right\}$ is the set of phase indices with $n^{\mathcal{P}}$ the number of phases, and $\mathcal{S}_m$ denotes the set of species indices belonging to phase m. Note that a species may only belong to a single phase. Since all phases are ideal, the normalized Gibbs function for this system is

$$\tilde{G} = \frac{G}{RT} = \sum_{j\in\mathcal{S}} \left(\tilde{g}_j(T,p) + \ln N_j - \ln \bar{N}_{p_j}\right) N_j, \quad (1)$$

where N_j is the number of moles of species j and $\tilde{g}_j(T,p)$ is the non-dimensional Gibbs function of pure species j at the system temperature and pressure, R is the molar universal gas constant, and $\bar{N}_{p_j}$ is the phase moles for the phase to which species j belongs.

$$\bar{N}_{p_j} = \sum_{k\in\mathcal{P}_{p_j}} N_k, \quad \forall\ j \in \mathcal{S} \quad (2)$$

The subscript $p_j \in \mathcal{P}\ \forall\ j \in \mathcal{S}$ is used to denote *the phase index to which the species index, j, belongs*. The non-dimensional Gibbs function for a pure species j is given by

$$\tilde{g}_j(T,p) = \frac{H_j^\circ(T)}{RT} - \frac{S_j^\circ(T)}{R} + \begin{cases} \ln \frac{p}{p^\circ}, & j \in \text{gas phase} \\ 0, & \text{otherwise} \end{cases}, \quad (3)$$

where H_j° and S° are the molar enthalpy and entropy, respectively, for pure species j evaluated at the standard state pressure p°.

The total moles of atoms of each element i in the system, c_i^{e}, can be computed from the simple elemental mass balance relation

$$\sum_{j\in\mathcal{S}} B_{ji}^{\mathrm{e}} N_j = c_i^{\mathrm{e}} \quad \forall\ i \in \mathcal{E}, \quad (4)$$

where B_{ji}^{e} is equal to the number of i atoms belonging to species j and $\mathcal{E} = \{1, \ldots, n^{\mathcal{E}}\}$ is simply the set of all element indices. It is often useful to impose other constraints on the system. Therefore, we consider any general linear constraints on the number of moles of each species.

$$\sum_{j\in\mathcal{S}} B_{ji}^{\mathrm{g}} N_j = c_i^{\mathrm{g}} \quad \forall\ i \in \mathcal{G} = \{1, \ldots, n^{\mathcal{G}}\} \quad (5)$$

Therefore, using matrix notation, the total constraints imposed on the composition are given as

$$B^T N = c, \quad (6)$$

where

$$B \in \mathbb{R}^{n^{\mathcal{S}}\times n^C} = \begin{bmatrix} B^{\mathrm{e}} & B^{\mathrm{g}} \end{bmatrix}, \quad c \in \mathbb{R}^{n^C} = \begin{bmatrix} c^{\mathrm{e}} \\ c^{\mathrm{g}} \end{bmatrix}, \quad (7)$$

and $n^C = n^{\mathcal{E}} + n^{\mathcal{G}}$ are total number of linear constraints. For a given B, c, and a fixed temperature and pressure, the equilibrium composition for the system is the one which minimizes $\tilde{G}$ while satisfying the linear constraints in Eq. (6).

3. Element Potentials

The Lagrange multiplier method is a well known technique for solving constrained minimization problems and will be used here. To begin, the Gibbs function and mass balance constraints are combined in the Lagrange function, L, which is written as

$$\begin{aligned} L &= \tilde{G} - \sum_{i\in C} \lambda_i \left(\sum_{j\in S} B_{ji} N_j - c_i \right) \\ &= \sum_{j\in S} N_j \left(\tilde{g}_j + \ln N_j - \ln \bar{N}_{p_j} \right) - \sum_{i\in C} \lambda_i \left(\sum_{j\in S} B_{ji} N_j - c_i \right). \end{aligned} \tag{8}$$

Here, λ_i are called Lagrange multipliers or constraint potentials. Because they apply the elemental mass balance constraint, they are often referred to as the element potentials for Gibbs free-energy minimization problems. The solution to the constrained minimization problem is found by differentiating the Lagrange function and setting the result equal to zero.

$$\begin{aligned} dL = &\sum_{j\in S} \left(\tilde{g}_j + 1 + \ln N_j - \ln \bar{N}_{p_j} + \sum_{i\in C} \lambda_i B_{ji} \right) dN_j \\ &- \sum_{j\in S} \frac{N_j}{\bar{N}_{p_j}} d\bar{N}_{p_j} - \sum_{i\in C} \left(\sum_{j\in S} B_{ji} N_j - c_i \right) d\lambda_i = 0 \end{aligned} \tag{9}$$

The term multiplying $d\lambda_i$ is simply the constraint equation which is satisfied at equilibrium and is thus zero. From Eq. (2) it also evident that

$$\begin{aligned} \sum_{j\in S} dN_j - \sum_{j\in S} \frac{N_j}{\bar{N}_{p_j}} d\bar{N}_{p_j} = \\ \sum_{m\in \mathcal{P}} \left(d\bar{N}_m - \frac{1}{\bar{N}_m} \sum_{j\in S_m} N_j d\bar{N}_m \right) = 0. \end{aligned} \tag{10}$$

Furthermore, dN_j may be positive or negative and does not depend on the term multiplying it. Therefore, the differential of the Lagrange function requires that all multipliers in the first summation be zero resulting in the following n^S equations

$$N_j = \bar{N}_{p_j} \exp\left(-\tilde{g}_j + \sum_{i\in C} \lambda_i B_{ji} \right), \quad \forall\ j \in \mathcal{S}. \tag{11}$$

The equations in Eq. (11) are called the Element Potential Equations [6]. Note that when written in terms of species mole fractions, $x_j = N_j/\bar{N}_{p_j}$, the n^C element potentials, λ_i, completely define the equilibrium composition for a fixed temperature and pressure. Physically, they represent an amount of Gibbs free-energy associated with each element at equilibrium. The substitution of Eq. (11) into Eqs. (2) and (6) leads to a nonlinear system of $n^C + n^{\mathcal{P}}$ equations and as many unknowns ($\bar{N}_m, \lambda_i$).

4. Coordinate Transformation and Matrix-Vector Representation

The proceeding sections make use of a coordinate transformation which simplifies the development of the multiphase Gibbs function continuation method. This transformation is similar to the one made by Pope in the original development of the single-phase method. Instead of dealing directly with species moles, it is convenient to instead use the square-root of the species moles

$$y_i \equiv \sqrt{N_i}. \tag{12}$$

Using Eq. (11), the vector $\boldsymbol{y} \in \mathbb{R}^{n^S}$ may be expressed in matrix-vector notation as a function of the element potential vector, $\boldsymbol{\lambda} \in \mathbb{R}^{n^C}$, and phase mole vector $\bar{\boldsymbol{N}} \in \mathbb{R}^{n^{\mathcal{P}}}$ by

$$\boldsymbol{y} = \exp\left(-\tilde{\boldsymbol{g}} + \mathbf{B}\boldsymbol{\lambda} + \mathbf{P} \ln \bar{\boldsymbol{N}} \right)^{\frac{1}{2}}, \tag{13}$$

where the matrix $\mathbf{P} \in \mathbb{R}^{n^S \times n^{\mathcal{P}}}$ is simply

$$P_{jm} \equiv \delta_{mp_j}. \tag{14}$$

Here, the exponential and square-root operators act element wise on the vector in parenthesis. Finally, the matrices $\mathbf{H} \in \mathbb{R}^{n^S \times n^C}$ and $\mathbf{Y} \in \mathbb{R}^{n^S \times n^S}$ are defined as

$$\mathbf{H} \equiv \mathbf{YB}, \quad \mathbf{Y} \equiv \operatorname{diag}(\boldsymbol{y}). \tag{15}$$

Using the above notation, the constrained chemical equilibrium problem defined in Eqs. (2) and (6) may be written as

$$\mathbf{H}^T \boldsymbol{y} - \boldsymbol{c} = 0 \tag{16}$$

$$(\mathbf{YP})^T \boldsymbol{y} - \bar{\boldsymbol{N}} = 0 \tag{17}$$

5. Multiphase Gibbs Function Continuation

Newton's method, or a variant thereof, is the most common method for solving nonlinear equations such as Eqns. (16) and (17). In general, the convergence of Newton's method for a nonlinear system, $\boldsymbol{F}(\boldsymbol{x}) = 0$,

is dependent entirely on the initial guess for the solution. In fact, quadratic convergence is only guaranteed when the initial guess, $\boldsymbol{x}_0$, is close enough to the real solution, $\boldsymbol{x}^*$, to satisfy the condition

$$\|\boldsymbol{x}_0 - \boldsymbol{x}^*\|_2 < \frac{\|\mathbf{F}'(\boldsymbol{x}^*)\|_2}{\gamma\kappa(\mathbf{F}'(\boldsymbol{x}_0))}, \tag{18}$$

where $\mathbf{F}'(\boldsymbol{x})$ is the system Jacobian evaluated at $\boldsymbol{x}$, γ is the Lipschitz constant for $\boldsymbol{F}$, and $\kappa(\mathbf{F}'(\boldsymbol{x}))$ is the condition number of $\mathbf{F}'(\boldsymbol{x})$. The condition number is a measure of how close a matrix is to being singular, increasing to infinity when the matrix is singular. Thus, as the Jacobian of the system approaches a singular matrix, the corresponding bound on the initial guess's proximity to the actual solution becomes nearly zero. For the equilibrium problem of Eqns. (16) and (17), situations often arise in which the system Jacobian approaches a singular matrix causing the Newton convergence to stagnate.

The MPGFC method avoids the above difficulties by converting Eqns. (16) and (17) into an initial value problem which may be integrated robustly through the use of a continuation parameter. To explain this more clearly, the multiphase residual vector, $\boldsymbol{R}$ is formally expressed as a function of $\boldsymbol{\lambda}$ and $\ln \bar{\boldsymbol{N}}$,

$$\boldsymbol{R}\left(\boldsymbol{\lambda}, \ln \bar{\boldsymbol{N}}\right) = \begin{bmatrix} \mathbf{H}^T \boldsymbol{y} - \boldsymbol{c} \\ (\mathbf{YP})^T \boldsymbol{y} - \bar{\boldsymbol{N}} \end{bmatrix}. \tag{19}$$

For a $\tilde{g}^* \equiv \tilde{g}(T, p)$, the equation

$$\boldsymbol{R} = 0 \tag{20}$$

implicitly defines an equilibrium point denoted as $(\boldsymbol{\lambda}^*, \ln \bar{\boldsymbol{N}}^*)$. The solution of this nonlinear system, based on a fixed Gibbs energy vector, via Newton's method is not guaranteed to succeed based on the arguments made above. If however, the Gibbs energy vector is allowed to vary linearly versus a continuation parameter s as in

$$\tilde{\boldsymbol{g}}(s) = \tilde{g}(0) + s\left[\tilde{\boldsymbol{g}}^* - \tilde{\boldsymbol{g}}(0)\right], \tag{21}$$

where $\tilde{\boldsymbol{g}}(0)$ denotes $\tilde{\boldsymbol{g}}$ at $s = 0$, then Eq. (20) implicitly defines a path of pseudo-equilibrium points $(\boldsymbol{\lambda}(s), \ln \bar{\boldsymbol{N}}(s))$ which is parameterized by s. Given a set of initial values of $\tilde{\boldsymbol{g}}(0)$, $\boldsymbol{\lambda}(0)$, and $\bar{\boldsymbol{N}}(0)$ which satisfy Eq. (20), the equilibrium point $(\boldsymbol{\lambda}^*, \ln \bar{\boldsymbol{N}}^*)$ can be determined by tracing the path of pseudo-equilibrium points from $s = 0$ to $s = 1$, at which point $\tilde{\boldsymbol{g}} = \tilde{\boldsymbol{g}}^*$.

$$\begin{bmatrix} \boldsymbol{\lambda}^* \\ \bar{\boldsymbol{N}}^* \end{bmatrix} = \int_0^1 \frac{d}{ds} \begin{bmatrix} \boldsymbol{\lambda} \\ \ln \bar{\boldsymbol{N}} \end{bmatrix} ds + \begin{bmatrix} \boldsymbol{\lambda}(0) \\ \ln \bar{\boldsymbol{N}}(0) \end{bmatrix} \tag{22}$$

In its most basic form, the MPGFC method computes the equilibrium point, $(\boldsymbol{\lambda}^*, \ln \bar{\boldsymbol{N}}^*)$, by numerically integrating $d\boldsymbol{\lambda}/ds$ and $d \ln \bar{\boldsymbol{N}}/ds$ forward from $s = 0$ to $s = 1$ using a simple Euler integration scheme. The derivatives, $d\boldsymbol{\lambda}/ds$ and $d \ln \bar{\boldsymbol{N}}/ds$, can be computed robustly by exploiting a feature of least-squares solutions. Further improvements to the efficiency and global accuracy of the method are obtained by using an adaptive step-size, Δs, as well as Newton's method when possible to reduce errors in the numerical integration. Of course, as always, the devil is in the details which are explained in the proceeding subsections.

5.1. Initial Conditions

The initial conditions, $\tilde{\boldsymbol{g}}(0)$, $\boldsymbol{\lambda}(0)$, and $\bar{\boldsymbol{N}}(0)$, are determined such that Eq. (20) is satisfied. Specifically, initial values of the species moles are determined by a linear combination of the Max-Min and Min-G compositions which are described in Appendix A,

$$\boldsymbol{N}(0) = \boldsymbol{N}_{\text{min-g}}(1 - \alpha) + \boldsymbol{N}_{\text{max-min}}\alpha, \tag{23}$$

where α is a small number such as $\alpha = 0.01$. This method does a good job of predicting the major species and ensures that species moles are strictly positive while satisfying the mass balance equations. The initial phase moles are then determined directly by summing the moles in each phase.

$$\ln \bar{\boldsymbol{N}}(0) = \ln\left(\mathbf{P}^T \boldsymbol{N}(0)\right) \tag{24}$$

The initial element potentials are computed via a least-squares solution of the element potential equation using the Gibbs energy vector, $\tilde{g}^*$.

$$\boldsymbol{\lambda}(0) = \arg\min_{\boldsymbol{\lambda}} \|\mathbf{B}\boldsymbol{\lambda} - \ln \boldsymbol{x}(0) - \tilde{\boldsymbol{g}}^*\|_2 \tag{25}$$

Finally, the initial Gibbs energy vector is chosen such that Eq. (13) is satisfied.

$$\tilde{\boldsymbol{g}}(0) = -\ln \boldsymbol{N}(0) + \ln \bar{\boldsymbol{N}}(0) + B\boldsymbol{\lambda}(0) \tag{26}$$

5.2. Computing $d\boldsymbol{\lambda}/ds$ and $d \ln \bar{\boldsymbol{N}}/ds$

The derivatives, $d\boldsymbol{\lambda}/ds$ and $d \ln \bar{\boldsymbol{N}}/ds$ can be obtained from the implicit relations found when the residual equation (Eq. (20)) is differentiated with respect to s.

$$\frac{d\boldsymbol{R}}{ds} = \frac{d}{ds} \begin{bmatrix} \mathbf{H}^T \mathbf{Y} \\ (\mathbf{YP})^T \boldsymbol{y} - \bar{\boldsymbol{N}} \end{bmatrix} = 0. \tag{27}$$

Differentiating the mass balance relation yields the first implicit relationship for $d\boldsymbol{\lambda}/ds$ and $d\ln\bar{\boldsymbol{N}}/ds$

$$\begin{aligned}\frac{d}{ds}\left(\mathbf{H}^T\boldsymbol{y}\right) &= \mathbf{H}^T\left(\mathbf{H}\frac{d\boldsymbol{\lambda}}{ds} - \mathbf{Y}\frac{d\tilde{\boldsymbol{g}}}{ds} + \mathbf{YP}\frac{d}{ds}(\ln\bar{\boldsymbol{N}})\right) \\ &= 0\end{aligned} \tag{28}$$

The derivative vector, $d\boldsymbol{\lambda}/ds$, is then taken to be

$$\frac{d\boldsymbol{\lambda}}{ds} = \dot{\boldsymbol{\lambda}}^g - \dot{\boldsymbol{\Lambda}}^{\mathbf{y}}\frac{d}{ds}(\ln\bar{\boldsymbol{N}}) \tag{29}$$

where $\dot{\boldsymbol{\lambda}}^{\boldsymbol{g}}$ and $\dot{\boldsymbol{\Lambda}}^{\boldsymbol{y}}$ are obtained via the minimum-norm solutions to the following least-squares problems

$$\begin{aligned}\dot{\boldsymbol{\lambda}}^g &= \arg\min_{\dot{\boldsymbol{\lambda}}}\left\|\mathbf{H}\dot{\boldsymbol{\lambda}} - \mathbf{Y}\frac{d\tilde{\boldsymbol{g}}}{ds}\right\|_2 \\ \dot{\boldsymbol{\Lambda}}^{\mathbf{y}} &= \arg\min_{\dot{\boldsymbol{\Lambda}}}\left\|\mathbf{H}\dot{\boldsymbol{\Lambda}} - \mathbf{YP}\right\|_2.\end{aligned} \tag{30}$$

It is a general property of least-squares problems that the residual is in the null-space of the coefficient matrix transposed. Therefore, from the definitions of $\dot{\boldsymbol{\lambda}}^g$ and $\dot{\boldsymbol{\Lambda}}^{\mathbf{y}}$ we have,

$$\begin{aligned}\mathbf{H}\left(\dot{\boldsymbol{\lambda}}^g - \dot{\boldsymbol{\Lambda}}^{\mathbf{y}}\frac{d}{ds}(\ln\bar{\boldsymbol{N}})\right) - \mathbf{Y}\frac{d\tilde{\boldsymbol{g}}}{ds} + \mathbf{YP}\frac{d}{ds}(\ln\bar{\boldsymbol{N}}) \\ \in \operatorname{null}\left(\mathbf{H}^T\right),\end{aligned} \tag{31}$$

regardless of the choice of derivative vector $d\ln\bar{\boldsymbol{N}}/ds$, thus satisfying Eq. (28). Furthermore, the least-squares solutions may always be obtained using the singular value decomposition of $\mathbf{H}$, even when $\mathbf{H}$ is rank deficient.

The phase moles derivatives, $d\ln\bar{\boldsymbol{N}}/ds$, are determined from the second implicit relation defined in Eq. (27), namely

$$\begin{aligned}\frac{d}{ds}\left(\mathbf{P}^T\mathbf{Y}\boldsymbol{y} - \bar{\boldsymbol{N}}\right) = \\ \mathbf{P}^T\mathbf{Y}\left(\mathbf{YP}\frac{d}{ds}(\ln\bar{\boldsymbol{N}}) - \mathbf{Y}\frac{d\tilde{\boldsymbol{g}}}{ds} + \mathbf{H}\frac{d\boldsymbol{\lambda}}{ds}\right) - \frac{d\bar{\boldsymbol{N}}}{ds} = 0\end{aligned} \tag{32}$$

Making use of the following relationship for $d\ln\bar{\boldsymbol{N}}/ds$ when the residual is zero,

$$\frac{d}{ds}(\ln\bar{\boldsymbol{N}}) = \operatorname{diag}(\bar{\boldsymbol{N}})^{-1}\frac{d\bar{\boldsymbol{N}}}{ds} = \left(\mathbf{P}^T\mathbf{Y}^2\mathbf{P}\right)^{-1}\frac{d\bar{\boldsymbol{N}}}{ds}, \tag{33}$$

and substituting Eq. (29), the following linear system is derived for the phase mole derivatives.

$$\mathbf{P}^T\mathbf{YH}\dot{\boldsymbol{\Lambda}}^{\mathbf{y}}\frac{d}{ds}(\ln\bar{\boldsymbol{N}}) = \mathbf{P}^T\mathbf{Y}\left(\mathbf{H}\dot{\boldsymbol{\lambda}}^g - \mathbf{Y}\frac{d\tilde{\boldsymbol{g}}}{ds}\right) \tag{34}$$

It can be shown that the above system is nonsingular when the phase moles of each phase are non-zero. With a careful treatment of nearly empty phases, this system can be solved in a robust manor. However, this discussion is beyond the scope of this report, the details of this procedure will not be given. It is sufficient to note simply that the derivatives $d\boldsymbol{\lambda}/ds$ and $d\ln\bar{\boldsymbol{N}}/ds$ can be determined in a fully robust way allowing for a completely stable algorithm to be developed.

5.3. Newton's Method

As the Euler integration scheme approximates the pseudo-equilibrium path in a linear manor, errors may accumulate during the course of the numerical integration. Therefore, after each new solution is obtained in the numerical integration of Eq. (22), Newton's method is used to attempt to reduce the residual below a specified global error tolerance for the fixed value of s (fixed $\tilde{\boldsymbol{g}}$). Newton's method corresponds to solving the following linear system for successive updates in the pseudo-equilibrium solution.

$$\begin{bmatrix}\mathbf{H}^T\mathbf{H} & \mathbf{H}^T\mathbf{YP} \\ \mathbf{P}^T\mathbf{YH} & \mathbf{P}^T\mathbf{Y}^2\mathbf{P} - \operatorname{diag}\left(\bar{\boldsymbol{N}}\right)\end{bmatrix}\begin{bmatrix}\Delta\boldsymbol{\lambda} \\ \Delta\ln\bar{\boldsymbol{N}}\end{bmatrix} = -\boldsymbol{R} \tag{35}$$

In some situations the above system will be singular and it will be impossible to converge the solution further after taking a continuation step. For these cases, Newton's method is abandoned and the residual is reduced by reducing the step-size used for the numerical integration and retaking the step.

6. Solution Algorithm

The previous section detailed the mathematical basis for the MPFGC method. In order to create an efficient and robust equilibrium solver however, several algorithmic details must be developed. An overview of the full MPFGC algorithm is presented in this section.

Given a fixed temperature, pressure, and constraint vector, the initial moles of each species and the corresponding solution quantities are determined using Eqns. (23) through (26). Following initialization, the proceeding steps are used to compute the integral in Eq. (22).

1. Begin with $s = 0$, $\Delta s = 1$, and set the solution vector to the initial conditions.

2. Compute the tangent vector of the pseudo-equilibrium path, $[d\boldsymbol{\lambda}/ds, d\ln\bar{\boldsymbol{N}}/ds]^T$ at point s using the current solution and Gibbs energy vector from Eqns. (29), (30), and (34).
3. Next, integrate the solution forward along the pseudo-equilibrium path with an Euler integration over Δs.

$$\begin{bmatrix}\boldsymbol{\lambda}\\ \ln\bar{\boldsymbol{N}}\end{bmatrix}^{k+1} = \begin{bmatrix}\boldsymbol{\lambda}\\ \ln\bar{\boldsymbol{N}}\end{bmatrix}^{k} + \frac{d}{ds}\begin{bmatrix}\boldsymbol{\lambda}\\ \ln\bar{\boldsymbol{N}}\end{bmatrix}^{k}\Delta s \tag{36}$$

   The Gibbs energy vector is also updated via Eq. (21) at $s + \Delta s$.
4. Newton's method is then used to reduce the residual vector below a specified tolerance, ϵ_{abs}, at for the solution at $s + \Delta s$, using Eq. (35). The Newton iterations are stopped when either the iterations converge, a maximum number of iterations is reached, or if at any point in the iteration the residual norm increases above the previous residual norm.
5. Following the Newton iterations, the new solution vector is tested against the following criteria.

$$\left\|R^{k+1}\right\|_2 \leq (1+\epsilon_{\text{rel}})\left\|R^{k}\right\|_2 \tag{37}$$

   If the above inequality holds true, then the step $k+1$ is accepted and the solution is updated accordingly, $s = s + \Delta s$, and the step-size Δs is updated via

$$\Delta s = \min(s-1,\ 2\Delta s). \tag{38}$$

   Otherwise, the solution is not updated and Δs is reduced by a factor of 2 and the algorithm continues at Step 3.
6. Finally, if $s = 1$ after the above step, then the solution vector corresponds to desired solution. If not, the solution procedure is continued starting from Step 2.

There are several aspects of the above algorithm which are worth elaborating on. It should be noted that while the Newton iteration procedure attempts to bring the residual below an absolute tolerance, ϵ_{abs}, the step is accepted as long as Eq. (37) is valid for some small ϵ_{rel}. This procedure is done in order to allow the integration to proceed for a small enough Δs even when then Newton method cannot converge the solution further. Typically, if such a situation is encountered, allowing the solution to proceed forward will eventually allow Newton to converge and maintain an acceptable error tolerance on the solution.

Another important thing to note is the choice of solution variable $\ln\bar{\boldsymbol{N}}$ as opposed to simply $\bar{\boldsymbol{N}}$. This has two benefits. The first is that the algebra necessary to develop this method is simpler to work out with this choice of variable. The second and more important reason is that this choice automatically guarantees that the phase moles are strictly positive which further guarantees the species moles are strictly positive as well.

7. Results and Discussion

Two results are shown which briefly demonstrate the convergence of the method. As previously mentioned in the introduction, Bishnu [9] developed a linearly constrained version of the CEA and STANJAN codes and performed several numerical experiments to judge the overall robustness of the two methods with constraints in addition to the mass balance constraints. One such set of calculations used a simple 8-species H_2O mixture comprised of H, O, OH, H_2, O_2, H_2O, HO_2, and H_2O_2 in which the total moles of the mixture were constrained. This constraint may be written as

$$\sum_{j\in\mathcal{S}} N_j = N_{\text{mix}} \tag{39}$$

If the elemental moles of H and O are constrained to be 4 and 2 respectively, then the above constraint on the total moles of the mixture limits the feasible region of equilibrium solutions to $2 \leq N_{\text{mix}} \leq 6$. On the boundaries of this feasible region, the species moles are determined completely by the constraints themselves: at $N_{\text{mix}} = 2$, $N_{\text{H}_2\text{O}} = 2$ while all other species are zero, and at $N_{\text{mix}} = 6$, $N_{\text{H}} = 4$ and $N_{\text{O}} = 2$ with the other species zero. Bishnu found that at these boundaries, CEA failed to converge to a solution with a temperature and pressure of 1000 K and 1 atm respectively.

Fig. (1) shows the equilibrium mole fractions obtained using the MPGFC method for this H_2O mixture at the 1000 K and 1 atm with the mixture moles constrained over the span of the feasible region. It is clear from the figure that the MPGFC method can successfully solve the equilibrium solution even at the boundaries of the feasible region. Perhaps more importantly, the method also detects when the constraints have no feasible region as a result of the Simplex algorithm to obtain the initial solution.

In many fields, multiphase equilibrium solutions are used to make engineering calculations or to understand complex chemical processes. As an example

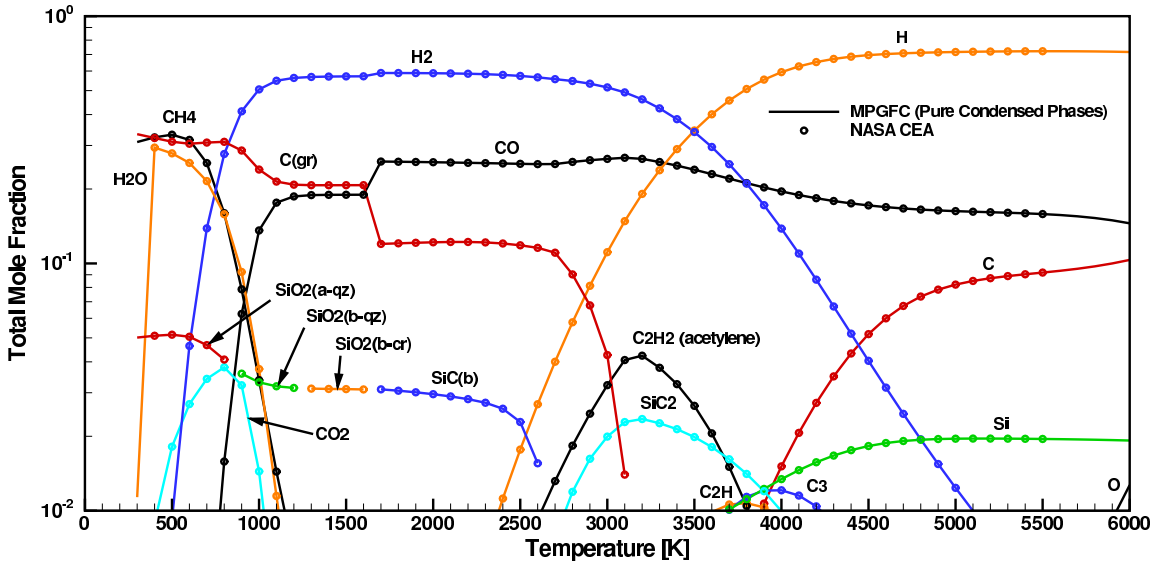

Figure 2: Phenol-Silicon mixture composition.

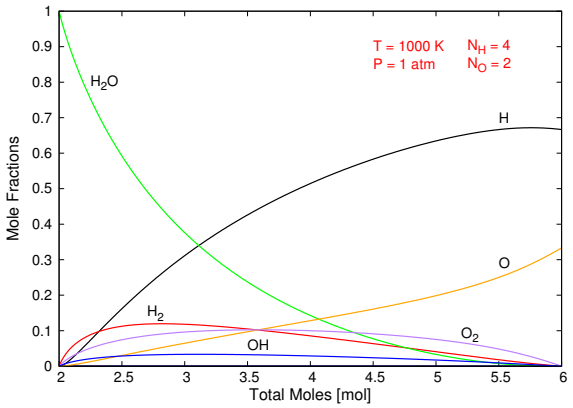

Figure 1: Water mixture composed of 4 moles of H and 2 moles of O at 1000 K and 1 atm with total number of moles constrained between the limits of 2 and 6 moles.

of a multiphase problem, a calculation has been performed with a Silicon-Phenolic mixture which is typically studied to understand complex ablation phenomena occurring at the surface of some ablator materials during atmospheric entry. Fig. (2) shows the results of a calculation with the complex $Si{-}C_6H_5OH$ mixture. The thermodynamic data used was directly taken from the CEA thermodynamic database such that a direct comparison could be made between the CEA method and the MPGFC algorithm. Because CEA treats all condensed phases as pure phases, each condensed phase was treated separately in the MPGFC calculation (though the algorithm described here can be used on any general set of ideal phases). It is clear from Fig. (2) that the results obtained with the MPGFC method compare exactly with those obtained using CEA. It should also be noted that CEA was not able to converge for a temperature of 300 K due to its poor initial estimate of the solution. Therefore, the CEA solution begins at 400 K in Fig. (2).

One interesting feature of the solution is how the solid silicon-oxide transforms between each of its 3 stable forms. Due to the pure condensed phase assumption, there is a discontinuity in the mole fractions at around 1700 K when it becomes more preferential for the Si to combine with C to form solid SiC rather than combining with O to form solid SiO_2 in its β-crystalline state. The carbon need to form SiC is taken from the graphite when this change occurs, causing a steep drop in the graphite mole fraction at 1700 K.

8. Concluding Remarks

The MPGFC method is a reliable and robust algorithm for computing linearly constrained, multiphase, chemical equilibrium solutions. In order to extend the single phase GFC method to include multiple phases,

a new system of equations was introduced to compute the tangent vector of the pseudo-equilibrium path. In addition, the Newton's method must be modified to account for the update in the phase moles vector. With changes, it can be shown that the multiphase method can maintain the robustness features of the single phase method. In fact, while it is not shown here, the single phase case is easily obtained when on one phase is considered in the MPGFC method. Thus, the single phase GFC method is simply a special case of the MPGFC method.

Acknowledgments

This research is funded through a Fellowship provided by the European Research Council Starting Grant #259354: "*Multiphysics models and simulations for reacting and plasma flows applied to the space exploration program.*"

References

[1] F. V. Zeggeren, S. H. Storey, The Computation of Chemical Equilibria, Cambridge at the University Press, 1970.
[2] K. K. Kuo, Principles of Combustion, second edition Edition, John Wiley and Sons, Inc, 2005.
[3] W. B. White, S. M. Johnson, G. B. Dantiz, Chemical equilibrium in complex mixtures, Journal of Chemical Physics 28 (5) (1958) 751–755.
[4] W. B. White, Numerical determination of chemical equilibrium and the partitioning of free energy, Journal of Chemical Physics 46 (11) (1967) 4171–4175.
[5] F. S. Milos, Y.-K. Chen, Comprehensive model for multicomponent ablation thermochemistry, AIAA, Aerospace Sciences Meeting and Exhibit.
[6] W. C. Reynolds, The element potential method for chemical equilibrium analysis: implementation in the interactive program stanjan version 3, Tech. rep., Department of Mechanical Engineering, Stanford University (January 1986).
[7] S. Gordon, B. J. McBride, Computer program for calculations of complex chemical equilibrium compositions and aplications: Part 1. analysis, RP 1311, NASA (October 1994).
[8] B. J. McBride, S. Gordon, Computer program for calculations of complex chemical equilibrium compositions and aplications: Part 2. users manual and program description, RP 1311, NASA (June 1996).
[9] P. S. Bishnu, D. Hamiroune, M. Metghalchi, J. C. Keck, Contrained-equilibrium calculations for chemical systems subject to generalized linear constraints using the nasa and stanjan equilibrium programs, Combustion Theory and Modelling 1 (1997) 295–312.
[10] S. B. Pope, The computation of constrained and unconstrained equilibrium compositions of ideal gas mixtures using gibbs function continuation, FDA 03-02 (December 2003).
[11] S. B. Pope, Gibbs function continuation for the stable computation of chemical equilibrium, Combustion and Flame 139 (2004) 222–226.

Appendix A. Linear Programming

Linear programming (LP) is a subset of optimization referring to a class of mathematical algorithms which maximize a linear function

$$\max_{\boldsymbol{x}} \boldsymbol{f}^T \boldsymbol{x}, \quad \boldsymbol{f}, \boldsymbol{x} \in \mathbb{R}^n, \tag{A.1}$$

under a general set of linear inequality and equality constraints

$$\begin{aligned} \mathbf{A}\boldsymbol{x} &\leq \boldsymbol{a}, \quad \mathbf{A} \in \mathbb{R}^{m_{\text{le}} \times n}, \quad \boldsymbol{a} \in \mathbb{R}^{m_{\text{le}}} \\ \mathbf{B}\boldsymbol{x} &\geq \boldsymbol{b}, \quad \mathbf{B} \in \mathbb{R}^{m_{\text{ge}} \times n}, \quad \boldsymbol{b} \in \mathbb{R}^{m_{\text{ge}}} \\ \mathbf{C}\boldsymbol{x} &= \boldsymbol{c}, \quad \mathbf{C} \in \mathbb{R}^{m_{\text{eq}} \times n}, \quad \boldsymbol{c} \in \mathbb{R}^{m_{\text{eq}}} \end{aligned} \tag{A.2}$$

and positivity condition

$$\boldsymbol{x} \geq 0. \tag{A.3}$$

The $m = m_{\text{le}} + m_{\text{ge}} + m_{\text{eq}}$ constraints in Eq. (A.2) define a convex polyhedron which represents the feasible region for the solution of $\boldsymbol{x}$. Note that equality constraints reduce the dimensionality of the solution by projecting the feasible region onto hyperplanes of smaller dimension.

LP problems may be solved using the Simplex algorithm. Several texts describe the Simplex algorithm in detail, therefore it will not be described here.

Appendix A.1. The Max-Min Composition

The max-min composition is defined as the composition which maximizes the minimum species moles while satisfying the mass balance constraints. This is easily formulated as an LP problem using the notation above where

$$\boldsymbol{f} = \begin{bmatrix} 0 \\ 1 \end{bmatrix}, \quad \boldsymbol{x} = \begin{bmatrix} \boldsymbol{N} \\ N_{\min} \end{bmatrix},$$

and the constraints are formulated as

$$\begin{bmatrix} \mathbf{I}_{n^S+1} & -\mathbf{1} \end{bmatrix} \boldsymbol{x} \geq 0, \quad \begin{bmatrix} \mathbf{B}^T & 0 \end{bmatrix} \boldsymbol{x} = \boldsymbol{c}.$$

Appendix A.2. The Min-G Composition

The Min-G composition is the composition which minimizes the sum of species Gibbs energies (Eq. (1) without including the species mole fraction term). Therefore, the Min-G composition can be represented as an LP problem where

$$\boldsymbol{f} = -\tilde{\boldsymbol{g}}, \quad \boldsymbol{x} = \boldsymbol{N},$$

under the constraints

$$\mathbf{B}^T \boldsymbol{x} = \boldsymbol{c}.$$

This composition will have at most n^C non-zero species which will approximate the minimum of Eq. (1) and satisfy the mass balance constraints.

GROUND AND FLIGHT EXPERIMENTS

Uncertainty Quantification of the Orbital Lifetime of a LEO Spacecraft

Lamberto Dell'Elce

University of Liège, Aerospace and Mechanical Engineering Department, Belgium, lamberto.dellelce@vki.ac.be

Supervisor: Thierry Magin

Associate Professor, Aeronautics and Aerospace Department, von Karman Institute for Fluid Dynamics, Belgium, thierry.magin@vki.ac.be

University Supervisor: Gaëtan Kerschen

Professor, University of Liège, Aerospace and Mechanical Engineering Department, Belgium, g.kerschen@ulg.ac.be

Abstract

Orbital lifetime estimation is a problem of great timeliness and importance in astrodynamics. In view of the stochastic nature of the thermosphere and of the complexity of drag modeling, any deterministic assessment of orbital lifetime is likely to be bound to failure. This is why the present paper performs uncertainty quantification of satellite orbital lifetime estimation. Uncertainties in the initial state of the satellite and in the atmospheric drag force, as well as uncertainties introduced by modeling limitations associated with atmospheric density models, are considered. Mathematical statistics methods in conjunction with mechanical modeling considerations are used to infer the probabilistic characterization of these uncertainties from experimental data and atmospheric density models. Monte Carlo propagation is then exploited to achieve a probabilistic description of the orbital lifetime.

Keywords: Uncertainty quantification, low-Earth orbits, orbital lifetime, QB50

1. A brief overview of my PhD thesis

The last ten years have seen the emergence of nanosatellites with a mass comprised between 1 and 10 kilograms. Space has become more accessible, both in terms of development costs and launch opportunities. In addition, these small satellites pave the way for scientific missions that are complementary to those of larger satellites. This is precisely the case of the QB50 constellation, a network of 50 nanosatellites that will study in situ the lower thermosphere [1].

Because nanosatellites have very limited maneuvering capabilities, the objective of the research is to exploit residual atmospheric drag to perform propellantless rendez-vous and formation flying between QARMAN, the QB50's spacecraft developed at the Von Karman Institute, and another satellite of the constellation. For this purpose, the level of aerodynamic drag of QARMAN will be modified by imposing its attitude, in order to create a differential force with respect to the target.

Targeting autonomous rendez-vous and formation flying, the main contribution of the thesis will be the introduction of a novel and efficient control method of the active spacecraft's attitude. Because the space environment is difficult to model and predict, uncertainty characterization and propagation in low-Earth orbit (LEO) is a significant part of the research. For this reason, this paper discusses a study on the uncertainty quantification of the orbital lifetime of a LEO spacecraft.

2. Introduction

The continuing growth of space debris is a problem of great concern to the astrodynamics community. Most national space agencies and the Inter-Agency Space Debris Coordination Committee (IDAC) now firmly accept a maximum orbital lifetime [2]. Specifically, spacecraft must now be able to deorbit within 25 years from protected regions, namely, from LEO and geostationary orbits (GEO). Spacecraft most often exploit chemical propulsion for this purpose, although novel deorbiting strategies, including electrical propulsion, solar sails, and tethers, are currently

being investigated as well. In other cases, proving through supporting long-term orbit propagations that the natural orbital decay of the spacecraft requires less time than the prescribed 25-year limit may suffice to satisfy the requirement. In this context, the design and optimization of deorbiting strategies require reliable orbital lifetime estimation.

However, owing to various experimental and modeling limitations, various parametric uncertainties and modeling errors impede accurate orbital lifetime estimation. For example, Oltrogge and Leveque [3] provide the variability of three different lifetime estimation tools in the analysis of orbital decay of CubeSats. Variations of the order of 50% were observed between predicted and observed lifetime.

Dominant sources of parametric uncertainties and modeling errors in orbital lifetime estimation include uncertainties in drag modeling, in the initial states, and in physical properties of the satellite. All these uncertainties exist for every mission, but their relative importance is case-dependent.

The first step of this study involves using methods from mathematical statistics in conjunction with mechanical modeling considerations to characterize the uncertainties involved in the orbital lifetime estimation problem as one or more random variables. The second step is to map this probabilistic characterization of inputs through the orbital propagator into a probabilistic characterization of the orbital lifetime; this is achieved through Monte Carlo propagation.

To illustrate the proposed methodology, the standard two-unit (2U) CubeSat of the QB50 constellation [1] proposed by the von Karman Institute for Fluid Dynamics in Belgium is considered. This case study is particularly relevant for two reasons. First, the objective of the constellation is to study in situ the spatial and temporal variations in the lower thermosphere. The initial circular orbit will have an altitude of 320 km where atmospheric drag, one of the dominant uncertainty sources in astrodynamics, is significant. Second, it is a real-life mission that should be launched in mid-2015[1]; hence, the results described here can be useful not only to the astrodynamics community but also to the CubeSat developers. The simulation parameters are summarized in Table 1.

The remainder of this paper is organized as follows. Firstly, the modeling assumptions are detailed and the dominant sources of uncertainty are identified.

[1] We note that the new orbital altitude of QB50 is 380 km and the launch is scheduled for the early 2016. However, the computations of this work were performed with the old data.

Table 1: Nominal parameters for the simulations.

	Variable	Value
Initial conditions	Initial altitude	320 km
	Eccentricity	0
	Orbital inclination	79 deg
	Launch date	April 2015
Spacecraft properties	Mass	2 kg
	Size	0.2 m × 0.1 m × 0.1 m

Two stochastic methods for uncertainty characterization are then introduced. Subsequently, the characterization of the uncertainties in the initial conditions and in the drag force is carried out. Finally, the results of the propagation of the uncertainties obtained in the test case are discussed.

3. Modeling assumptions and uncertainty source identification

The motion of the center of gravity of a non-propelled Earth orbiting spacecraft is governed by Newton's second law

$$\ddot{\mathbf{r}} = -\frac{\nu}{r^3}\mathbf{r} + \mathbf{f}_{pert}\left(\mathbf{r}, \dot{\mathbf{r}}, t, \mathbf{p}, \mathbf{q}\right), \tag{1}$$

with the following initial conditions

$$\begin{aligned} \mathbf{r}\left(t_0\right) &= \mathbf{r}_0, \\ \dot{\mathbf{r}}\left(t_0\right) &= \dot{\mathbf{r}}_0; \end{aligned} \tag{2}$$

here, $\mathbf{r}$ is the spacecraft position vector in an Earth-centered inertial frame (ECI), $\nu = 3.986 \cdot 10^{14}\,\mathrm{m^3 s^{-2}}$ is the Earth's gravitational constant, $\mathbf{r}_0$ and $\dot{\mathbf{r}}_0$ are the initial position and velocity vectors, respectively, and $\mathbf{f}_{pert}$ is the perturbing force per unit mass, which is a function of parameters $\mathbf{p}(t)$ and of the spacecraft attitude $\mathbf{q}(t)$.

The gravitational constant is known with high accuracy, $\nu = 3.986 \cdot 10^{14}\,\mathrm{m^3 s^{-2}} \pm 8 \cdot 10^{5}\,\mathrm{m^3 s^{-2}}$; hence, it is supposed to be deterministic in this work. Thus, the uncertainties in the spacecraft dynamics, and, in particular, in the orbital lifetime, originate from the initial conditions and the perturbing forces, as shown in Figure 1. These forces for a LEO spacecraft are due to the gravitational perturbations, i.e., non-spherical harmonics of the Earth's gravity field and third-body disturbances of sun and moon, $\mathbf{f}_g$, to the atmospheric drag $\mathbf{f}_d$, and to the solar radiation pressure (SRP) $\mathbf{f}_{SRP}$; hence, $\mathbf{f}_{pert} \simeq \mathbf{f}_g + \mathbf{f}_d + \mathbf{f}_{SRP}$.

Both the Earth's gravitational attraction and third-body perturbations are considered as deterministic quantities in this study because they can be modeled

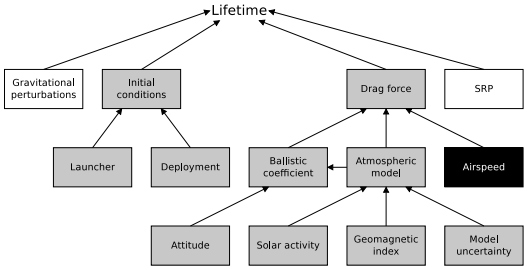

Figure 1: Schematic representation of uncertainty quantification of orbital lifetime in LEO. White box: deterministic modeling, gray box: stochastic modeling, black box: unmodeled dynamics.

with extremely high accuracy. Concerning the Earth's attraction, Fraysse *et al.* [4] reported that it is sufficient to include zonal harmonics up to J_4 for lifetime estimation[2]. The modeling of the perturbing force due to SRP is a challenging and demanding task. However, SRP can usually be neglected for low altitudes and it is also considered deterministic in this work. We therefore assume in the context of this study that *only the perturbations due to atmospheric drag play an important role for UQ of orbital lifetime estimation*. Besides the large magnitude of drag perturbations in LEO, this assumption is supported by the fact that drag is uncertain in nature and does not exhibit any relevant compensation throughout one orbit, i.e., it is responsible for a monotonic decrease of the semi-major axis.

The popular Runge-Kutta 8(7) [5] is exploited as numerical integrator for orbital propagation. To reduce the computational burden, we select a relative precision of 10^{-9}, which provides an error of 10^{-2} % with respect to a precision of 10^{-13}.

4. Stochastic methods for uncertainty characterization

Within a probabilistic UQ framework, the objective of characterization is to model the sources of uncertainty involved in the problem under study as one or more random variables X with values in the support $\mathcal{I}_X$. This requires that an adequate probability distribution, or, if X is continuous, its probability density function (PDF), $p_X : \mathcal{I}_X \to \mathbb{R}^+$, be assigned to these random variables. The information available for obtaining this distribution typically consists of one or more of the following sources. First, various types of experimental data can be available. Next, there can be mechanical laws that impose constraints on the values that the random variables may take (for example, mechanical laws can require that an uncertain atmospheric density be positive); these constraints act as sources of information because the inferred probability distribution must assign a vanishing probability to those values of the random variables that do not satisfy these constraints. Finally, various other sources can contribute information, for example, in the form of nominal values.

Methods from mathematical statistics are most often used in conjunction with mechanical modeling considerations to infer a characterization of uncertainties from the available information. Providing an exhaustive account of all available methods from mathematical statistics is beyond the scope of this paper; instead, we confine ourselves to a succinct presentation of two of the fundamental methods.

It is common practice in statistics to use uppercase letters to denote random variables; by contrast, lowercase letters indicate deterministic variables. We use this system of notation in this section, which focuses on the mathematical aspects. However, this rule is not respected elsewhere in the paper, when dealing with physical variables.

4.1. Maximum likelihood estimation

The first method involves selecting an adequate 'labeled' probability distribution, followed by inferring suitable values for its parameters from data, for example, by using the method of maximum likelihood (MLE). By labeled probability distribution we mean Gaussian, uniform, and other probability distributions given in catalogs in the literature. Consider a set of n samples $x_1, \ldots, x_n$ of a random variable X and a PDF $p_X(x; \vartheta_1, \ldots, \vartheta_d)$, where $\vartheta_1, \ldots, \vartheta_d$ are the parameters defining the distribution, e.g., the mean and the standard deviation for the normal distribution. According to the maximum likelihood method, the d parameters of the PDF have to be chosen such that they are consistent, e.g., they have a positive standard deviation,

[2] Special cases may require a more complete modeling of the perturbing agents. For instance, if sectorial perturbations have very little influence on long-term propagations in LEO, we note that some special orbits could require a more detailed modeling of the gravity field, e.g., it is recommended to include zonal harmonics up to J_{15} for orbits with inclination close to 63.4deg.

and maximize the likelihood function

$$\mathcal{L}(\vartheta_1, ..., \vartheta_d) = \prod_{j=1}^{n} p_X(x_j; \vartheta_1, ..., \vartheta_d) \tag{3}$$

In practice, the logarithm of the likelihood function is generally considered as the objective function in order to reduce numerical errors due to the product of small numbers.

Care should be taken to select a labeled PDF that is consistent with the physical constraints; for example, the Gaussian probability distribution should not be selected to characterize an uncertain atmospheric density because its support is the whole real line and its selection would thus lead to the assignment of a non-vanishing probability to negative values.

4.2. Maximum entropy

If no adequate labeled probability distribution is available, the possibility of constructing a new adequate one can be considered, using, for example, the maximum entropy principle [6]. The maximum entropy principle states that the probability distribution with the largest entropy should be selected from among those that are consistent with the available information. The entropy of a continuous random variable X with PDF $p_X(x)$ and support $\mathcal{I}_X$ is defined as

$$s_X = -\int_{\mathcal{I}_X} p_X(x) \log p_X(x)\, dx. \tag{4}$$

For most of the sources of uncertainty that we characterize using the principle of maximum entropy, the probability distribution is obtained as the one that maximizes entropy,

$$\max_{p_X} s_X(p_X), \tag{5}$$

from among those that are consistent with available information of the following form

$$\begin{aligned} \int_{\mathcal{I}_X} p_X(x)\, dx - 1 &= 0, \\ \int_{\mathcal{I}_X} x\, p_X(x)\, dx - \mu_X &= 0, \\ \int_{\mathcal{I}_X} (x-\mu_X)^2\, p_X(x)\, dx - \sigma_X^2 &= 0; \end{aligned} \tag{6}$$

here $\mathcal{I}_X = [x_{min}, x_{max}]$, μ_X and σ_X are a given support, a given mean, and a given standard deviation, respectively. The exact analytical solution to this constrained optimization problem can be obtained using Lagrange multipliers, and it is the truncated Gaussian distribution with support $\mathcal{I}_X$ and with second-order statistical descriptors μ_X and σ_X [3].

For more general applications of the maximum entropy principle, the numerical solution of the problem is an alternative. An interesting approach that is particularly suitable for high-dimensional problems was proposed by Soize [7].

5. Uncertainty characterization of initial conditions

As anticipated in the previous sections, the two main sources of uncertainties considered in the present study are those in the initial states and atmospheric drag. Uncertainty characterization of the initial states is strongly related to the current status of the mission. Two scenarios may occur:

- The spacecraft is in orbit. The uncertainty in the initial states depends on measured data, while the initial epoch can generally be considered as deterministic. Two-line elements (TLEs) and GPS are two common measurement techniques. The former is responsible for wider dispersion than the latter, but it is often the only option available for debris and nanosatellites. Relevant work on TLEs uncertainty was performed by Vallado [8] and Flohrer *et al.* [9], whereas the exploitation of GPS-based data is reported in [10].

- The mission is still in a design phase, which is the scenario studied in this paper. In this case, uncertainty in the initial states is related to the launch vehicle injection accuracy and to the deployment strategy. The set of nominal initial conditions may also not be fully defined, e.g., the initial right ascension of the ascending node (RAAN) may be unknown.

For the QB50 network, the reference initial conditions before the deployment are $h_{0,l}^{ref} = 320\ km$, $i_{0,l}^{ref} = 79\,\text{deg}$, and $e_{0,l}^{ref} = 0$ [1], where $h_{0,l}^{ref}$, $i_{0,l}^{ref}$ and $e_{0,l}^{ref}$ are the initial altitude above the equatorial radius, the orbital inclination, and the eccentricity, respectively. Keplerian elements are used for orbit parametrization because the true anomaly is the only

[3] We stress that these are the second-order descriptors of the actual PDF, i.e., the truncated normal distribution, and not of the associated unbounded normal distribution.

fast variable in this parameter set. Mean elements, instead of osculating elements, are considered to avoid an important sensitivity of the lifetime with respect to the initial anomaly resulting from short-period variations of the semi-major axis. Doing so, we can remove the initial anomaly from the uncertainty sources. Since the reference orbit is circular, the characterization of the initial argument of perigee (AoP) is not relevant either. As no information is available yet, the initial RAAN is modeled as an aleatory variable with uniform uncertainty between 0 and 360 deg, in accordance with the maximum entropy principle.

The uncertainty in $h_{0,l}$, $i_{0,l}$, and $e_{0,l}$ depends on the accuracy of the launcher. Standard deviations of the Keplerian elements consistent with the performance of current launchers used for LEO are considered, namely, $\sigma_h = 2.5\ km$, $\sigma_i = 0.03$ deg, and $\sigma_e = 3.5 \cdot 10^{-4}$. These three variables are supposed to be independent because no information about their correlation is usually provided, and univariate PDFs are constructed in the following.

The initial altitude of the spacecraft is a non-negative random variable, so that its support is $\mathbb{R}^+$. The mean and standard deviation of the PDF are constrained to be equal to the nominal values $h_{0,l}^{ref}$ and σ_h, respectively. Thus, according to the maximum entropy principle, $h_{0,l}$ is modeled as a truncated Gaussian distribution with support $\mathbb{R}^+$ and with the imposed second-order descriptors. A similar problem is solved for the initial orbital eccentricity and inclination. For these variables the support is $[0, 1]$ and $\mathbb{R}$, respectively.

The initial date t_0 is the last parameter necessary to fully define the initial state right before the deployment of the constellation. The launch is foreseen for April 2015 [1]. However, because of the frequent delays in space missions, t_0 is modeled as a uniform random variable between April 1, 2015 and April 1, 2016. A wider launch window is not necessary, since the long-term variations in the atmospheric models are not considered herein.

A second source of uncertainty for the initial conditions is the deployment of the QB50 constellation. Even though the exact strategy for deployment is still unknown, the nanosatellites will be ejected thanks to a spring-loaded pusher plate with an ejection velocity between 1 and 1.5 $m.s^{-1}$. Though negligible with respect to the orbital speed, the ejection velocity may be responsible for uncertainties of the order of launcher accuracy. For example, an ejection velocity in the flight direction leads to an increment of the semi-major axis of 2.6 km, which is larger than σ_h. Therefore, the ejection velocity is modeled by three uniform random variables, v_{ej}, Θ, and χ, representing the norm of the ejection velocity and the spherical angles in an ECI frame. Their support is $[1.0, 1.5]$ ms^{-1}, $[0, 360]$ deg, $[-90, 90]$ deg, respectively.

6. Uncertainty characterization of atmospheric drag

The second main source of uncertainty considered in this paper is the atmospheric drag. The drag force per unit of mass is computed using the empirical equation

$$\mathbf{f}_d = -\frac{1}{2} C_b \rho v_{TAS} \mathbf{v}_{TAS} \tag{7}$$

where C_b, ρ, $\mathbf{v}_{TAS}$ and v_{TAS} are the ballistic coefficient, the atmospheric density, the true airspeed (TAS), and its modulus, respectively. According to Vallado [11], all the terms involved in Equation 7 and the equation itself are affected by uncertainties.

In this paper, the TAS is calculated using the assumption of a co-rotating atmosphere. This means that we do not consider the upper-thermosphere winds, which can be in the order of some hundreds of meter per second [12]. However, the basic dynamics of the wind involves a movement from daylight to night-time, which approximately results in a compensation of their effects throughout one orbit. The thermospheric cooling trend [13] is also ignored herein.

We stress that the drag force is just one component of the aerodynamic force. Lift and side forces are also considered in our simulations.

6.1. Atmospheric model

The dominant uncertainty source in the drag estimation is the atmospheric density. One of the most advanced atmospheric models is NRLMSISE-00 [14], which is a global empirical model developed by the US naval research laboratory (NRL). Two important inputs of the model are the daily and 81-day averaged radio flux indices, $F_{10.7}$ and $\bar{F}_{10.7}$. The 3-hour geomagnetic index, a_p, is another input of the model, but, for long-period propagations, its daily average, A_p, can be exploited. The other inputs required by NRLMSISE-00 are the position of the spacecraft and the julian date, which are computed throughout the numerical integration of the equations of motion. Although they depend on random variables, e.g., $JD(t) = t + t_0$, they are not primary sources of uncertainty. Given these inputs, NRLMSISE-00 is able to estimate the number densities of helium, atomic

and molecular oxygen, atomic and molecular nitrogen, argon, and hydrogen, together with the local atmospheric temperature. The total mass density is deduced directly from these outputs.

6.1.1. *Solar and geomagnetic proxies.*

Correlation between gas density and space weather proxies, e.g., solar radio flux and geomagnetic index, is crucial in the development of an atmospheric model. The sensitivity of the orbital lifetime with respect to these variables is very substantial [15].

The consideration of time-varying series complicates the uncertainty propagation because the problem belongs to the family of stochastic differential equations (SDE). As an alternative for use in orbital lifetime estimation, Fraysse *et al.* introduced the concept of *constant equivalent solar activity* [4]. The idea is to consider a constant solar flux and geomagnetic index throughout the propagation. This technique is particularly interesting for very long propagations in the order of one or several solar cycles.

In this work, we propose another approach to the problem. It is also based upon the idea of using an effective solar activity, but it is more suitable for propagations of the order of a fraction of the solar cycle. Instead of a deterministic effective solar activity, we consider a random effective solar activity.

$F_{10.7}$, $\bar{F}_{10.7}$ and A_p are considered herein as three different stochastic random variables that are constant during a single simulation. They are characterized using the data measured over the last 50 years provided by the Celestrack database. Bearing in mind that QB50 has a lifetime of a few months and that the launch window is [April 2015, April 2016], the portion of the solar cycle between [October 2014, October 2016] is considered to be conservative. Thus, only the data of the previous cycles that correspond to the same portion of the solar cycle are exploited for uncertainty characterization. Because of the important variations in correspondence of the solar maxima and of the variability in the period of the solar activity, the identification of the selected data set is achieved by identifying the minima of the solar flux curve smoothed by a moving-average filter of 2-year width. These minima are then used to define a dimensionless position between two consecutive minima of the solar cycle. This process is illustrated for the daily solar flux in Figure 2; a similar process can be carried out for $\bar{F}_{10.7}$ and A_p. The data in the shaded windows are retained for uncertainty characterization of the solar weather proxies.

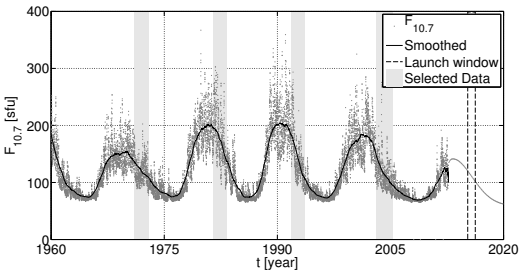

Figure 2: Observed daily solar activity.

To account for statistical dependence, $F_{10.7}$, $\bar{F}_{10.7}$ and A_P are modeled by the following Gaussian copula

$$\left.\begin{matrix} Z_1 \\ Z_2 \\ Z_3 \end{matrix}\right\} \xrightarrow{\text{chol}(C)} \left\{\begin{matrix} \Xi_1 \xrightarrow{c_N(\xi_1)} U_1 \xrightarrow{\mathcal{F}^{-1}_{F_{10.7}}\left(u_1;\boldsymbol{\vartheta}_{F_{10.7}}\right)} F_{10.7} \\ \Xi_2 \xrightarrow{c_N(\xi_2)} U_2 \xrightarrow{\mathcal{F}^{-1}_{F_{10.7}}\left(u_2;\boldsymbol{\vartheta}_{F_{10.7}}\right)} \bar{F}_{10.7} \\ \Xi_3 \xrightarrow{c_N(\xi_3)} U_3 \xrightarrow{\mathcal{F}^{-1}_{A_p}\left(u_3;\boldsymbol{\vartheta}_{A_p}\right)} A_p \end{matrix}\right. ; \tag{8}$$

here

- Z_1, Z_2, and Z_3 are independent standard Gaussian random variables,
- Ξ_1, Ξ_2, and Ξ_3 are correlated standard Gaussian random variables; $\text{chol}\,(C)$ is the Cholesky decomposition of their correlation matrix. It yields $[\Xi_1, \Xi_2, \Xi_3] = [Z_1, Z_2, Z_3]\,\text{chol}\,(C)$,
- U_1, U_2, and U_3 are correlated uniform random variables with support $[0, 1]$,
- $\mathcal{F}_{(\cdot)}$ is the cumulative distribution function (CDF) of the marginal distribution that is chosen to fit the model, and $\boldsymbol{\vartheta}_{(\cdot)}$ is the vector of parameters defining the distribution.

The identification of the parameters of the statistical model is achieved by means of the MLE. The design variables of the MLE problem are the parameters of the marginal PDFs and the 3 off-diagonal elements of the correlation matrix.

Physical constraints impose that the chosen distributions of the solar flux indices are defined on $\mathbb{R}^+$, whereas the support of the geomagnetic indicator is $[0, 400]$.

Several labeled PDFs and non-parametric histogram distributions were tested to model the

marginal PDFs. On the one hand, labeled distributions are interesting because the resulting model can be tuned with a very limited number of parameters. On the other hand, histogram distributions are able to represent with the highest fidelity the statistical content of the dataset, but several parameters are necessary to tune the model, i.e., the heights of each bin.

Among the different labeled distributions we tested, beta distributions generated the maximum likelihood. However, the histogram model performed better. This result is illustrated in Figure 3, which presents the beta and histogram marginal PDFs for the three variables. If the distributions of $F_{10.7}$ and A_p appear to be sufficiently well fitted by the beta distributions, this is not the case for $\bar{F}_{10.7}$, and histogram distributions for the marginal PDFs are retained.

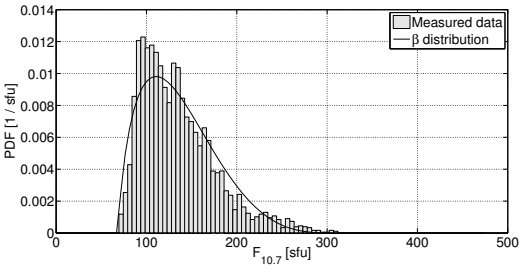

(a) Daily $F_{10.7}$

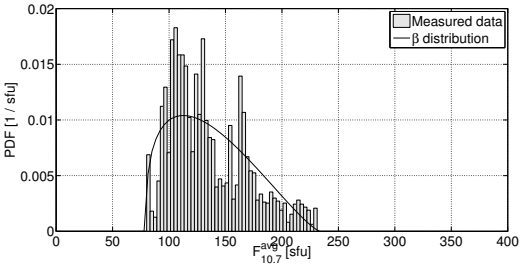

(b) 81-day averaged $F_{10.7}$

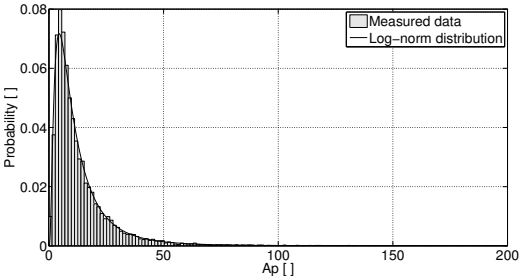

(c) Geomagnetic activity A_p

Figure 3: Distributions of the geomagnetic and solar activity proxies (maximum likelihood).

6.1.2. Model uncertainty.

Targeting practicality and efficient numerical computation, the most popular atmospheric models exploit a limited number of proxies to take the correlation between density and stochastic processes into account. This is why the uncertainty characterization of the density should also consider the uncertainty related to the discrepancy of the model with respect to reality. For instance, Scholtz *et al.* compared the atmospheric densities given by different models including NRLMSISE-00, DTM-2009, JB-2008 and GITM [16]. They observed deviations in the order of 50% considering the same environmental conditions.

Picone *et al.* [17] performed a statistical analysis between the NRLMSISE-00 model and experimental data. They tabulated the biases and standard deviations of the gas composition and temperature for different ranges of altitudes, for in-situ and ground based measurements, and for quiet ($Ap \leq 10$), active ($A_p \geq 50$) and all geomagnetic conditions. Biases for number density of gas species n_j and for the temperature T are defined as

$$\beta_{n_j}^{(k)} = \exp\left[\mathrm{E}\left(\log \frac{n_j^{(data,k)}}{n_j^{(model)}}\right)\right] - 1, \quad (9)$$

$$\beta_{T}^{(k)} = \mathrm{E}\left(T^{(data,k)} - T^{(model)}\right), \quad (10)$$

respectively. Superscripts *model* and *data* correspond to the outputs of the NRLMSISE-00 model and experimental data, respectively. E[•] denotes the expectation operator with respect to the different measurements within a single dataset, k. The corresponding

standard deviations are

$$\sigma_{n_j}^{(k)} = \sqrt{\mathrm{E}\left(\log^2 \frac{n_j^{(data,k)}}{n_j^{(model)}}\right) - \log^2\left(\beta_{n_j}^{(k)} + 1\right)}, \quad (11)$$

$$\sigma_T^{(k)} = \sqrt{\mathrm{E}\left(\left(T^{(data,k)} - T^{(model)}\right)^2\right) - \beta_T^{(k)\,2}}. \quad (12)$$

In what follows, the measurements for all levels of geomagnetic activity in the altitude range $[200, 400]$ km are considered[4]. To account for this variability, we define random variables, denoted η_{n_j} and η_T, for each of the outputs of NRLMSISE-00 such that the corrected atmospheric properties are given by

$$n_j = n_j^{(model)} \exp\left(\eta_{n_j}\right), \quad (13)$$

$$T = T^{(model)} + \eta_T. \quad (14)$$

These random variables are considered constant throughout a single orbit propagation.

They are characterized using the maximum entropy principle in the following. Because the available information is given in terms of the bias and standard deviation and because their support is $\mathbb{R}$, the random variables η_{n_j} are characterized by a normal distribution with second order descriptors

$$\mu_{n_j} = \mathrm{E}\left(\log\left(1 + \beta_{n_j}^{(k)}\right)\right), \quad (15)$$

$$\sigma_{n_j} = \sqrt{\mathrm{E}\left(\sigma_{n_j}^{(k)\,2} + \mu_{n_j}^{(k)\,2}\right) - \mu_{n_j}^2}; \quad (16)$$

here the expectation operator is with respect to the different datasets.

For the random variable η_T, non-negativity of the temperatures must be enforced, i.e., $\mathcal{I}_{\eta_T} = [-T, \infty)$. The resulting distribution depends on the temperature T and no feasible solution exists for $T < -\beta_T$, β_T being the mean value of $\beta_T^{(k)}$ across the different datasets. In practice, however, this temperature range is not physically meaningful; it is never reached using the NRLMSISE-00 model. The resulting distribution is a truncated Gaussian with left bound equal to $-T$ and second-order descriptors β_T and σ_T. We note that the distributions converge to the unbounded normal distribution for $T \gg -\beta_T + 3\sigma_T$.

The obtained second order statistical descriptors of η_{n_j} and η_T are listed in Table 2.

Table 2: Global biases and standard deviations of the model correction factors of the outputs of NRLMSISE-00 for all levels of geomagnetic activity and an altitude range of $[200, 400]$km.

Output	Mean	Std
Temperature (K)	-27.9	121.2
Helium (%)	8.0	34.7
Total oxygen (%)	1.6	25.4
Molecular nitrogen (%)	-1.1	35.9
Argon (%)	18.6	52.0
Hydrogen (%)	4.0	31.4
Atomic nitrogen (%)	-15.7	53.0

6.2. *Ballistic Coefficient*

The computation of the ballistic coefficient

$$C_b = \frac{C_d\, A_{ref}}{m} \quad (17)$$

where C_d, A_{ref}, and m are the dimensionless drag coefficient, the reference surface, and the mass of the spacecraft, respectively, is a very challenging and important problem for LEO propagation.

A large body of literature on the determination of the drag coefficient is available, see, e.g., [18; 19]. For complex satellite geometries, direct simulation Monte Carlo (DSMC), which uses probabilistic Monte Carlo simulations to solve Boltzmann's equation for finite Knudsen number fluid flows, is arguably the only way of computing this coefficient. However, this technique is extremely computationally intensive and does not lend itself to uncertainty quantification. For simple geometries such as a CubeSat, semi-empirical analytic methods relying on the decomposition into elementary panels provide an accurate and computationally-effective alternative. The semi-analytic method considered in this work is based upon the research of Sentman [20] and Cook [21] and upon more recent contributions. The method is efficiently summarized in E. Doornbos's PhD dissertation [12].

According to this theory, the drag coefficient is determined as a function of the atmospheric conditions, i.e., gas composition and external temperature, of the physical properties of the spacecraft, i.e., the mass and geometry, of the wall temperature T_w, of the gas-surface interaction, and of its attitude, i.e.,

$$C_b = C_b\left(n_j, T, m, geometry, T_w, \alpha, \delta, \epsilon\right), \quad (18)$$

where α, δ, and ϵ are the energy flux accommodation coefficient, the angle of attack[5], and the roll angle, re-

[4] This is where most of the lifetime will be spent in our test case. The residual lifetime below 200km is in the order of one day.

[5] For a 2U CubeSat it is defined as the angle between the long axis and the TAS direction.

spectively. The accommodation coefficient is an indicator of the gas-surface interaction. It determines whether the reflected particles retain their mean kinetic energy (for $\alpha = 0$) or they acquire the spacecraft wall temperature T_w (for $\alpha = 1$) [12]. This model was used in our orbital propagator to compute the ballistic coefficient at every time step.

The numerical simulations we carried out pointed out that the sensitivity with respect to the wall temperature is extremely small. We therefore consider it as deterministic with $T_w = 300\,\mathrm{K}$. For the energy accomodation coefficient, to our knowledge, data for its stochastic characterization are not available, and we model it as a function of the Oxygen concentration such that $\alpha = 5.10^{-7} n_O T (1 + 10^{-7} n_O T)^{-1}$, as suggested by Pilinsky [22].

The main contribution to uncertainty depends on the outputs of the atmospheric model, which were already characterized in the previous section. Another contribution is spacecraft attitude. The requirements for a standard QB50 spacecraft impose that the angle of attack δ be smaller than 5 deg with 3-σ confidence [23]. There is no requirement on the roll angle ϵ. According to the maximum entropy principle, the attitude angles δ and ϵ are modeled as a Gaussian random variable with zero mean and a standard deviation of $\frac{5}{3}$ deg, and a uniform random variable with values in $[0, 360]$ deg, respectively.

7. Uncertainty propagation

The mapping $y = g(\mathbf{x})$ is considered for which the stochastic input vector $\mathbf{x}$ and the (scalar) variable of interest (VoI) y are defined on the supports $\mathcal{I}_{\mathbf{X}}$ and $\mathcal{I}_Y$, respectively. MC propagation is a means of quantifying uncertainty in the VoI by mapping uncertainties in the inputs through the model $g(\cdot)$. The generation of a set of N realizations $\mathbf{x}_1, \mathbf{x}_2, \ldots, \mathbf{x}_N$ of the stochastic vector $\mathbf{X}$ according to the joint PDF of its elements is the first step of the MC propagation.

The direct evaluation of the mapping for each generated sample leads to N samples of the VoI from which statistics can be computed. Specifically, the second-order descriptors are given by

$$\mu_Y^{(N)} = \frac{1}{N} \sum_{j=1}^{N} y_j, \tag{19}$$

$$\sigma_Y^{(N)} = \frac{1}{N} \sum_{j=1}^{N} \left(y_j - \mu_Y^{(N)} \right)^2. \tag{20}$$

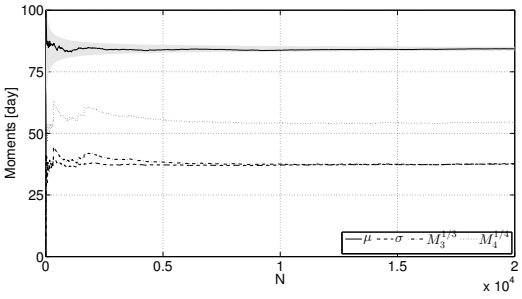

Figure 4: Convergence of the statistical descriptors of orbital lifetime (MC propagation). The envelope of the shaded area is determined using the bounds $\mu_Y \pm 3\frac{\sigma_Y}{\sqrt{N}}$

.

The convergence and rate of convergence of MC propagation are ensured by the law of large numbers and the central limit theorem under limited assumptions. If the mean value μ_Y of the VoI exists, the law of large numbers states that the sample mean $\mu_Y^{(N)}$ converges almost surely to μ_Y as N increases. If the standard deviation σ_Y of the VoI exists and if Lindeberg's condition is satisfied, the central limit theorem states that the error $\mu_Y^{(N)} - \mu_Y$ is a normally distributed random variable with zero mean and standard deviation $\frac{\sigma_Y}{\sqrt{N}}$.

The MC algorithm was used to compute the orbital lifetime of one nanosatellite of the QB50 constellation considering the uncertainty sources discussed the previous sections and summarized in Table 3. Figure 4 shows that 20000 evaluations were necessary for achieving the convergence of the mean value within ± 1 day with a confidence level of 3σ. The convergence of the higher-order statistical descriptors is also depicted in this figure. Because a single orbital propagation lasts 10 minutes on average, the complete propagation was run on a computer cluster thanks to the parallelization capabilities of the DAKOTA software [24]; it resulted in an accumulated computational burden of 139 days.

Histogram distributions and kernel density evaluations [25] were then implemented to derive a non-parametric representation of the PDF of orbital lifetime. They are presented in Figure 5. Very useful information can be inferred from Figures 4 and 5:

- The mean orbital lifetime is 84.3 days, which is somewhat smaller than the desired lifetime of 3

Table 3: Summary of uncertainty characterization.

Variable	Symbol	Units	Stochastic modeling
Launch date	t_0	day	Uniform in [1/04/2015, 1/04/2016].
Initial altitude (before injection)	$h_{0,I}$	km	Truncated Gaussian [0, +∞), 320km mean, 2.5km std
Initial inclination (before injection)	$i_{0,I}$	deg	Normal with 89deg mean and 0.03deg std
Initial eccentricity (before injection)	$e_{0,I}$	-	Truncated Gaussian [0, +∞), 0 mean, $3.5 \cdot 10^{-4}$ std
Initial RAAN (before injection)	$\Omega_{0,I}$	deg	Uniform in [0, 360]deg
Ejection velocity (norm)	v_{ej}	m/s	Uniform in [1, 1.5]ms^{-1}
Ejection velocity (1st spherical angle)	Θ	deg	Uniform in [0, 360]deg
Ejection velocity (2nd spherical angle)	χ	deg	Uniform in [−90, 90]deg
Daily solar activity	$F_{10.7}$	sfu	Histogram distribution (Figure 3(a))
81-day averaged solar activity	$\bar{F}_{10.7}$	sfu	Histogram distribution (Figure 3(b))
Geomagnetic index	A_p	-	Histogram distribution (Figure 3(c))
Model error of the *j-th* number density	η_{n_j}	-	Gaussian with parameters listed in Table 2
Model error of the temperarure	η_T	K	Truncated Gaussian, temperature dependent
Angle of attack	δ	deg	Gaussian with 0deg mean and 5/3deg std
Roll angle	ϵ	deg	Uniform in [0, 360]deg

Variables	Correlation [%]
$F_{10.7}$ and $\bar{F}_{10.7}$	86
$F_{10.7}$ and A_P	14
$\bar{F}_{10.7}$ and A_P	13

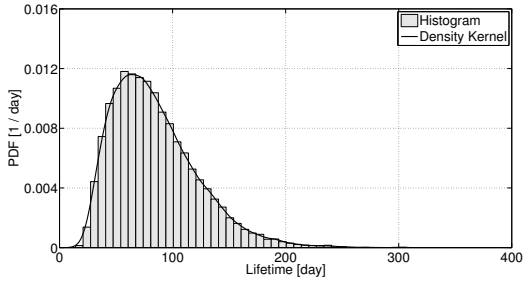

Figure 5: Histogram and kernel density estimations of the PDF of the orbital lifetime (MC propagation).

months. We note that the mean does not correspond to the peak of the distribution because the PDF is characterized by a non-negligible (positive) skewness.

- The standard deviation amounts to 37.5 days, which results in standard deviation to mean ratio of about 0.45. This reflects a substantial, but expected, variability of orbital lifetime that invalidates any deterministic estimation of this quantity.

- The lifetime can be as short as 14 days and as long as 347 days depending on the considered input sample. The minimum and maximum lifetime correspond to an initial altitude h of 316 and 322 km and a daily radio flux $F_{10.7}$ of 72 and 273 sfu, respectively.

Figure 6 depicts the complementary cumulative distribution function (CCDF) of orbital lifetime. It shows that there is a 6% probability to have a lifetime of 150 days of more. Conversely, there is a non-negligible probability, i.e., 18 %, to have a lifetime shorter than 50 days, which may compromise the success of the mission.

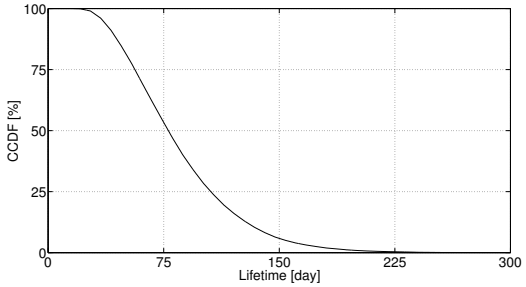

Figure 6: Complementary cumulative distribution function of orbital lifetime (MC propagation).

8. Conclusion

The present study performed a probabilistic characterization and propagation of the dominant sources of uncertainty involved in the lifetime estimation of low-altitude satellites. The developments were illustrated using one CubeSat of the QB50 constellation. Uncertainties in the initial state of the satellite and in the atmospheric drag force, as well as uncertainties that may be introduced by atmospheric density models, were considered.

Future improvements of the characterization should consider thermospherical winds, the correlation of the atmospheric temperature with solar activity and the characterization of the initial states measures through TLEs or GPS data. Provided that sufficient information is available, the proposed methodology could also be extended to other quantities of interest, such as, for instance, the solar radiation pressure.

Concerning the uncertainty propagation and analysis of the results, efficient propagation techniques like polynomial chaos should be considered to drastically reduce the computational burden, while stochastic sensitivity analysis could provide with relevant insight into the impact that every input uncertainty source have on the orbital lifetime.

Acknowledgment

The author Lamberto Dell'Elce would like to acknowledge the Belgian National Fund for Scientific Research for its financial support (FRIA fellowship).

This work was performed in the framework of the ESA project *"Uncertainty quantification for aerospace application"* (Grant manager: D. Giordano, European Space Agency; Principal investigator: T. Magin, von Karman Institute for Fluid Dynamics).

References

[1] Muylaert, J., *et al.*, "QB50: An International Network of 50 Cubesats for Multi-Point, In-Situ Measurements in the Lower Thermosphere and for Re-Entry Research", Proceedings of the ESA Atmospheric Science Conference, Barcelona, Spain, 2009.

[2] "IADC Space Debris Mitigation Guidelines", 40th Session of the Scientific and Technical Subcommittee of the United Nations Committee on Peaceful Uses of Outer Space, A/AC.105/C.1/L.260, Vienna, Austria, 2003.

[3] Oltrogge, D. and Leveque, K., "An Evauation of CubeSat Orbital Decay", Proceedings of the 25th Annual AIAA/USU Conference on Small Satellites, Logan, USA, 2011.

[4] Fraysse, H., *et al.*, "Long Term Orbit Propagation Techniques Developed in the Frame of the French Space Act", Proceedings of the 22nd International Symposium on Space Flight Dynamics, San Jose dos Campos, Brazil, 2011.

[5] Montenbruck, O., and Gill, E., "Satellite Orbits. Models, Methods, Applications", Springer, 2005.

[6] Shannon, C., "A Mathematical Theory of Communication", Bell System Technical Journal 27, 379-423, 1948.

[7] Soize, C., "Construction of probability distributions in high dimension using the maximum entropy principle: Applications to stochastic processes, random fields and random matrices", International Journal for Numerical Methods in Engineering 76.10, 1583-1611, 2008.

[8] Vallado, D.A., "Verifying Observational Data for Real-World Space Situational Awareness", Proceedings of the AAS/AIAA Astrodynamics Specialist Conference, Girdwood, USA, 2011.

[9] Flohrer, T., Krag, H., and Klinkrad, H., "Assessment and Categorization of TLE Orbit Errors for the US SSN Catalogue", Proceedings of the Advanced Maui Optical and Space Surveillance Technologies Conference, Maui, USA, 2008.

[10] Xu, G., "GPS: Theory, Algorithms and Applications", Springer, 2003.

[11] Vallado, D.A., and Finkleman, D., "A Critical Assessment of Satellite Drag and Atmospheric Density Modeling", Proceedings of the AIAA/AAS Astrodynamics Specialist Conference, Honolulu, USA, 2008.

[12] Doornbos, E., "Thermospheric Density and Wind Determination from Satellite Dynamics", Springer, Series: Springer Theses, 2012.

[13] Emmert, J.T., Picone, J.M., and Meier, R.R., "Thermospheric Global Average Density Trends, 1967–2007, Derived from Orbits of 5000 Near-Earth Objects", Geophysical Research Letters 35, 2008.

[14]

[15] Naasz, B.J., Berry, K., and Schatten, K., "Orbit Decay Prediction Sensitivity to Solar Flux Variations", Proceedings of the AAS/AIAA Space Flight Mechanics Conference, Mackinac, USA, 2007.

[16] Scholz, T., Asma, C.O., and Aruliah, A., "Recommended Set of Models and Input Parameters for the Simulations of Orbital Dynamics of the QB50 CubeSats", Proceedings of the 5th International Conference on Astrodynamics Tools and Techniques, Noordwijk, The Netherlands, 2012.

[17] Picone, J.M., Hedin, A.E., Drob, D.P., and Aikin, A.C., "NRLMSISE-00 Empirical Model of the Atmosphere: Statistical Comparisons and Scientific Issues", Journal of Geophysical Research: Space Physics 107, 2002.

[18] Storz, M.F., Bowman, B.R., Branson, J.I., Casali, S.J., and Tobiska, W.K., "High Accuracy Satellite Drag Model (HASDM),", Advances in Space Research 36, 2497-2505, 2005.

[19] Marcos, F.A., "New Satellite Drag Modeling Capabilities", Proceedings of the 44th AIAA Aerospace Sciences Meeting and Exhibit, Reno, USA, 2006.

[20] Sentman, L.H., "Free Molecule Flow Theory and its Application to the Determination of Aerodynamic Forces", Technical Report LMSC-448514, Lockheed Missiles & Space Company, 1961.

[21] Cook, G.E., "Satellite Drag Coefficients", Planetary and Space Science 13, 929–946, 1965.

[22] Pilinski, M.D., Argrow, B.M., and Palo, S.E., "Semiempirical Model for Satellite Energy-Accommodation Coefficients", Journal of Spacecraft and Rockets 47, 951-956, 2010.

[23] "Call for CubeSat Proposals for QB50", Von Karman Institute for Fluid Dynamics, 2012.

[24] Adams, B.M., *et al.*, "DAKOTA, A Multilevel Parallel Object-Oriented Framework for Design Optimization, Parameter Estimation, Uncertainty Quantification, and Sensitivity Analysis", Version 5.2 Reference Manual, Sandia National Laboratories, 2011.

[25] Rosenblatt, M., “Remarks on Some Nonparametric Estimates of a Density Function,” Annals of Mathematical Statistics 27, 832-837, 1956.

Natural Boundary Layer Transition on a 7 Degree Half-angle Cone at Large Hypersonic Mach Numbers

Guillaume Grossir

Aeronautics and Aerospace Department, von Karman Institute for Fluid Dynamics, Belgium, grossir@vki.ac.be

Supervisor: Olivier Chazot

Professor and Head of the Aeronautics and Aerospace Department, von Karman Institute for Fluid Dynamics, Belgium, chazot@vki.ac.be

University Supervisor: Herman Deconinck

Professor, Université Libre de Bruxelles, Belgium, deconinck@ulb.ac.be

Abstract

Hypersonic boundary layer transition experiments are performed in the Mach 11 Longshot wind tunnel on an 800 mm long 7 ° half-angle cone with various nosetip radii. Instrumentation includes flush-mounted fast-response thermocouples and pressure sensors. An overview of the results is reported and includes Schlieren flow visualization of the instabilities. Results suggests the dominance of second mode waves in the transition process for such large hypersonic Mach numbers.

Keywords: Hypersonic, boundary layer, transition, cone, second mode instabilities, Schlieren, wavelet analysis.

Nomenclature

Symbols

c	specific heat, J/(kg.K)
C_H	Stanton number, -
f	frequency, kHz
h	enthalpy, J/kg
k	thermal conductivity, W/(m.K)
M	Mach number, -
p	flow pressure, Pa
$\dot{q}$	wall heat flux, W/m^2
Ra	roughness height arithmetic mean value, μm
Re	Reynolds number, -
r_N	nosetip radius, mm
s	distance measured along the conical surface
t	time, ms
T	temperature, K
u	velocity, m/s
δ	boundary layer thickness, mm
γ_b	bandwidth/variance of the Morlet wavelet
γ_c	center frequency of the Morlet wavelet
λ	wavelength, mm
ρ	density, kg/m^3
σ	standard deviation

Subscripts/Superscripts

0	stagnation condition
c	convection
e	at the boundary layer edge
w	at the wall
∞	free-stream value

1. Introduction

Boundary layer transition is a critical phenomenon at hypersonic Mach numbers for several reasons. The increase of the wall heat fluxes (up to an order of magnitude larger) is probably the most critical consequence [1; 2] and this has driven a large number of studies aiming at predicting the transition location in such high-speed flows. Nevertheless, the complexity of the phenomenon is still associated to large uncertainties in the current predictions. This has lead to the conservative design of thermal protecting systems for reentry vehicles which is therefore detrimental to the

scientific payloads. Additional investigations are still required to evaluate the influence on the transition location of various parameters such as the local Mach number or the nosetip bluntness.

Numerous transition experiments have been performed on different geometries since the sixties, either in flight or in wind tunnels. Initial investigations were essentially focusing on the determination of the transition location and the extension of the transition region, for instance by using thermocouples along a surface and determining the minimum and maximum wall heat flux locations. Measurements on conical geometries within air or nitrogen flows have for instance been reported in Refs. [3; 4; 5; 6] for Mach numbers larger than 10. They have demonstrated the importance of the bluntness effect for the stabilization of the boundary layer and evidenced a strong unit Reynolds number dependence effect. However, the limitations of the instrumentation techniques used at that time did not allow to characterize the hypersonic boundary layer disturbances.

More recent studies have sought for the mechanisms responsible for the transition, which required the ability to measure boundary layer disturbances. This has been achieved thanks to the improved bandwidth of the measurements techniques (several hundreds of kilohertz are typically required), using hot-wires [7; 8; 9], pressure sensors [10; 11; 12; 13; 14] or heat flux sensors [15; 16]. These investigations at hypersonic Mach numbers between 6 and 8, have shown the dominance of the so-called second mode of instabilities on conical geometries. This confirms the earlier Linear Stability Theory results of Mack [17; 18] who predicted the amplification of an inviscid mode distinct from the one responsible for transition at lower speeds. However, only few studies have extended these investigations to larger Mach numbers while keeping low enthalpy levels. This is a desirable step to isolate the importance of the Mach number on the transition process.

Experiments reported in Refs. [19; 20; 21] have recently succeeded to measure instability waves along 7 ° half-angle cones in different hypersonic wind tunnels between Mach 10 and 14. Boundary layer perturbations along the cone were identified as second mode instability waves and were associated with a large intermittency factor (varying between 0 and 1 and representing the fraction of time a boundary layer is turbulent at a given location [22]). Instabilities were detected in both linear and non-linear stages of their growth and a fully turbulent flow could be obtained for some test conditions. Additional characterization of the flow perturbations is nevertheless desirable to improve the understanding of the transition mechanisms and benefit numerical models.

Similar measurements can potentially be obtained in the VKI Longshot wind tunnel. Such experimental data would contribute to the characterization of the dominant disturbances for such large Mach numbers.

An overview of the transition measurements obtained on a conical model in the Longshot wind tunnel will be presented in this paper. At first, the experimental setup is described. Then, measured wall heat fluxes are compared to numerical predictions and allow to determine the transition onset location and its extension for various conical geometries. Slight nosetip bluntness is shown to delay the onset of transition significantly. Wavelet analysis of the wall pressure fluctuations reveals a large number of wave packets whose most amplified frequencies and convection velocities are determined. Finally, a novel flow visualization technique allows to observe the structure of the disturbances and their breakdown into turbulence.

2. Experimental setup

2.1. Wind tunnel

Experiments are performed in the Longshot hypersonic facility of the von Karman Institute. This conventional wind tunnel is based on the principle of a gun tunnel and allows to reach large Reynolds numbers with a free-stream Mach number about 11 with the nozzle currently used. It has been described recently in details in Ref. [23] and a characterization of the nozzle flow is reported in Ref. [24]. The axisymmetric nozzle produces a flow with a uniformity of $\sigma = \pm 3.5\%$ within its inviscid core.

The free-stream conditions are determined using two distinct probes located in the test section. The first one is hemispherical with a diameter of 25.4 mm. It measures the stagnation point heat flux and the stagnation point pressure. These measurements allow to determine the free-stream total enthalpy based on the equation of Fay-Riddell [25]. The second one is a slender probe used to measure the free-stream static pressure. The relevant technical details and the operation of this static pressure probe have been reported in Ref. [23]. Most of the free-stream conditions are then determined according to the rebuilding procedure presented in Ref. [23].

2.2. Conical model

2.2.1. Characteristics

The model selected for transition studies is a 7° half-angle cone with a length of 800 mm.

Such a axisymmetric geometry is rather simple and preferred to a flat plate for numerous reasons: side effects polluting the natural transition are avoided; long models can be used, hence achieving large local Reynolds number; no streamwise curvature effects introducing Görtler vortices; easily modeled numerically; and widely studied at lower Mach numbers.

The cone is split in two lateral shells as shown in Fig. 1, each divided in three longitudinal sections due to manufacturing constrains and to ease the access to instrumentation. These different sections have been assembled together prior to the final surface machining giving an accurate cone angle. This also ensures a good surface quality and minimizes the eventual steps between the different junctions. The final surface quality is characterized by $Ra < 3.2\,\mu$m. Exchangeable nosetips ranging from 0.05 mm to 10 mm radii can be mounted on the model and are illustrated in Fig. 2. Noses are made of stainless steel to resist the large stagnation point heat fluxes applied to the model. The downstream sections are manufactured out of Aluminum.

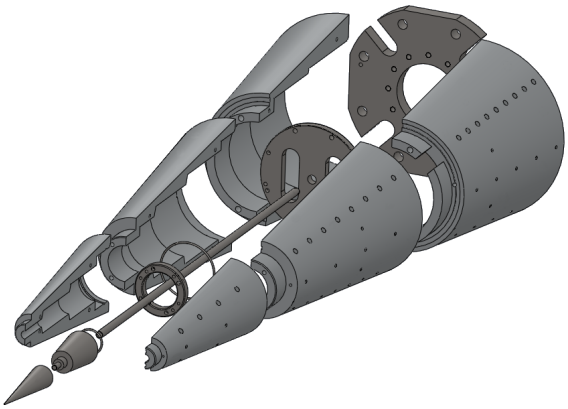

Figure 1: Exploded view of the 7° half-angle cone

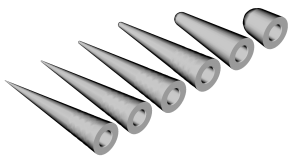

Figure 2: Exchangeable nosetips (0.05 mm, 0.2 mm, 0.75 mm, 1.75 mm, 4.75 mm and 10 mm radii)

2.2.2. Instrumentation

Only one side of the cone is instrumented along three main generatrix. The instrumentation includes 21 streamwise fast response thermocouples, 7 streamwise piezoresistive Kulite XCE-093-5psi pressure sensors, and 8 piezoelectric pressure sensors PCB 132A31 at various locations as illustrated in Fig. 3.

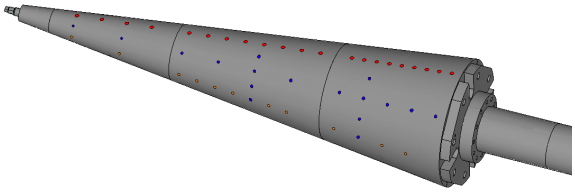

Figure 3: Instrumentation locations along the cone (thermocouples ●, Kulite pressure sensors ●, PCB pressure sensors ●)

Type-E thermocouples are manufactured by the Shock Wave Laboratory of the RWTH Aachen University [26]. They are composed of a small pin of Constantan and an outer cylinder of Chromel, electrically isolated by a 10 μm thick layer. The active junction of each thermocouple is obtained by grinding its front surface to locally bypass the electrical insulation. The small mass of the active thermal junction ensures response times of few microseconds particularly suited for the study of hypersonic flows in short duration tunnels. The small diameter of the active junction is 0.5 mm and ensures a localized measurement. Thermocouples elements are shaped and polished to fit the conical surface. The wall temperature history $T_w(t)$ measured during an experiment is integrated numerically according to eq. 1 to yield the surface heat flux $\dot{q}_w$ [27].

$$\dot{q}_w(t_j) = 2\frac{\sqrt{\rho c k}}{\sqrt{\pi}} \sum_{i=1}^{j} \frac{T_w(t_i) - T_w(t_{i-1})}{\sqrt{t_j - t_i} + \sqrt{t_j - t_{i-1}}} \qquad (1)$$

It is based on the assumption of a 1-dimensional heat flux into a semi-infinite body of uniform constant thermal properties ρck. The thermal properties of the thermocouples are determined by the manufacturer and stated with a standard deviation of $\sigma = \pm 3\%$. Each thermocouple is mounted within a 6 mm diameter Chromel insert so that lateral heat conduction, with the surrounding Aluminum during the whole test duration, is negligible and the 1-dimensional heat flux assumption is satisfied. Thermocouple signals

are amplified by a Fylde FE-351-UA universal amplifier which also low-pass filters the measurements at 10 kHz. The calibration law of the thermocouples is obtained according to reference tables for type-E thermocouples.

Kulite XCE-093-5psi absolute pressure sensors are used to measure the wall pressure along the cone and evaluate the magnitude of viscous effects. They can also be used to confirm the free-stream Mach number independently of the measurements obtained with the free-stream static pressure probe. Their range has been selected to meet the requirements of the small wall pressure to be measured. Sensors are equipped with a screen which limits their bandwidth to about 150 kHz. They are mounted flush to the surface. In-house bridge conditioners are used to supply the sensors with a constant 10 V excitation and the output signals are amplified using Fylde FE-351-UA universal amplifiers with a 100 kHz low-pass filter.

The piezoelectric pressure sensors PCB 132A31 are used to measure the pressure fluctuations along the cone. They have a low-frequency cut-off at 11 kHz according to specifications from the manufacturer. Sensors are flush mounted to the conical surface and were arranged in the streamwise direction for the present tests. Sensors are connected to a PCB 482C05 signal conditioner and the output signals are amplified by 100 using an in-house 6 poles Butterworth low-pass filter set at 900 kHz. The calibration laws used for the sensors are the ones issued by the manufacturer.

All sensors are held in position from the inner parts of the cone in order to minimize the disturbances introduced at the surface.

2.3. Data acquisition

Experimental data were acquired at 500 kS/s using a National Instruments 16-bit PXI-6123 module mounted on a PXI-1045 chassis. PCB sensors were sampled at 2500 kS/s using a 14-bit PXI-6133 module.

The reference time $t = 0$ is arbitrarily chosen after each test as the time when the measured test section stagnation pressure reaches half of its peak amplitude.

2.4. Test conditions

Pure nitrogen is used and the relatively low total enthalpy ($h_0 \lesssim 2$ MJ/kg) prevents dissociation of this test gas. The free-stream Mach number ranges between $9 \leq \mathrm{M}_\infty \leq 12$. Two tests conditions have been used for the different tests which scan a range of free-stream Reynolds number between 2.6×10^6 /m $\leq \mathrm{Re}_\infty \leq 16 \times 10^6$ /m. Typical Mach and Reynolds numbers are plotted in Fig. 4 for the two conditions used. The decaying trend with time is inherent to the working principle of the wind tunnel and the test time is limited to about 20 ms. The free-stream total temperature decreases during an experiment from 1800 K to 1000 K while the model temperature remains closely isothermal with $T_w \approx 293$ K. The wall to total temperature ratio consequently varies between

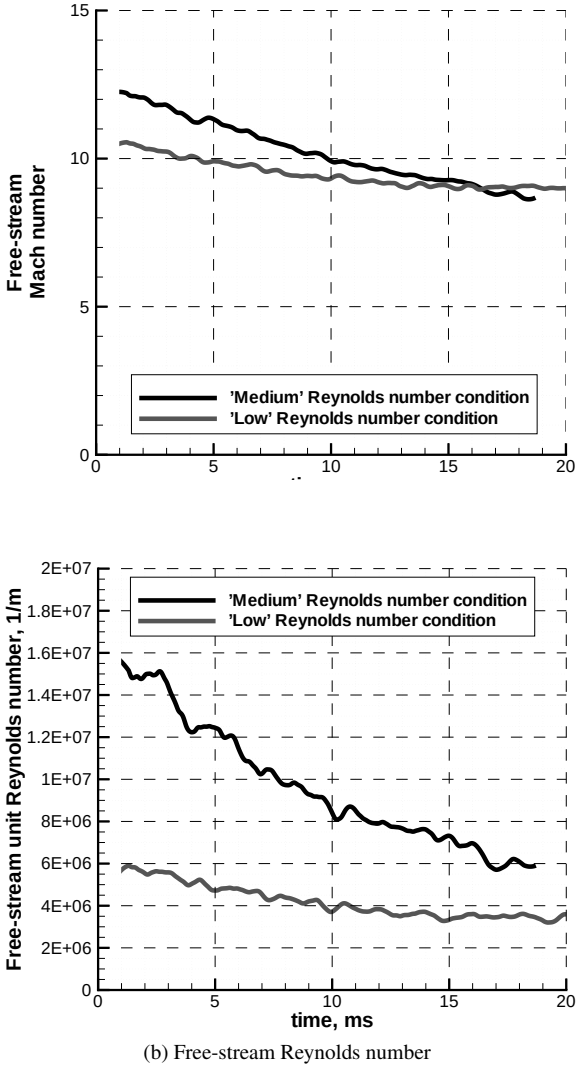

(b) Free-stream Reynolds number

Figure 4: Typical evolution of free-stream conditions during a test in the Longshot wind tunnel

The cone is fitted partially within the contoured nozzle, in its inviscid uniform core. Only the most rearward part of the cone (between 110 and 225 mm depending on the configuration used) is extending out

of the nozzle and allows for a limited flow visualization. This configuration allows for longer test times than if it was completely out of the nozzle. In this position, the model is still in the uniform part of the flow of the contoured nozzle as characterized in Ref. [24]. The model is slightly offset with respect to the nozzle axis to fit beside the static pressure probe and the hemispherical stagnation probe within the uniform part of the flow. It has been ensured that there was no influence between the various probes and their respective shock waves.

The angle of attack and sideslip of the model were both set to zero.

3. Experimental results

3.1. Wall heat fluxes

The distribution of wall heat fluxes along a model is commonly used to determine the transition location because of its good repeatability, reliability and accuracy [1; 28]. The length of the transition region is then determined as the distance between the minimum wall heat flux and the following maximum.

In the present case, wall heat fluxes along a generatrix of the cone are obtained from thermocouple measurements using the 1-dimensional model described in section 2.2.2. The results are plotted in Fig. 5 for three different nosetip radii: 0.2 mm, 1.75 mm and 4.75 mm for closely identical free-stream conditions.

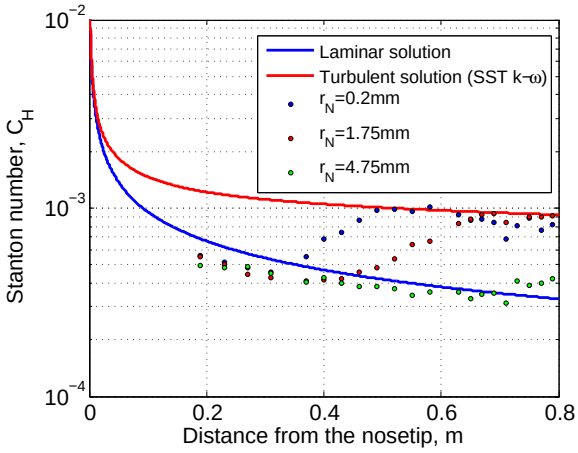

Figure 5: Transition location along the cone for different nosetip radii with $M_\infty \approx 10.7$ and $Re_\infty = 11 \times 10^6$ /m

The wall heat transfer coefficient initially decreases along the conical surface. Numerical predictions are in fair agreement, albeit slightly larger especially close to the nosetip. The minimum heat transfer location along the wall depends on the nosetip radii used. The boundary layer is for instance strongly stabilized by slight nose bluntness as already observed at lower hypersonic Mach numbers [9; 29; 30; 31].

The transition region for the sharpest nosetip tested extends from $s \approx 0.3$ m to $s \approx 0.55$ m. The onset of transition for the 1.75 mm nosetip is delayed to about $s \approx 0.4$ m, while the end of the transition region is for $s \approx 0.7$ m. The 4.75 mm blunt nose is stabilizing the boundary layer further and delays the onset of transition to $s \approx 0.7$ m, while a longer conical model would be required to reach a fully turbulent boundary layer.

A relatively long transition region is observed in all configurations investigated. The experimental wall heat transfer coefficient then approaches the numerical predictions for turbulent boundary layers, although it remains slightly lower than predicted values. Heat fluxes about 2.5 times larger than the laminar ones are encountered for the turbulent boundary layers.

3.2. Wall pressure

3.2.1. Wavelet analysis

Wavelet analysis allows to distinguish which frequency content exists in a signal at different time instants and is therefore particularly suited to the present purpose where large intermittencies are expected. This is a powerful and convenient tool for the study of turbulent flows as already applied in Ref. [32] and more recently to the study of hypersonic transition to turbulence [33].

The most important criterion when using wavelet analysis tool is the choice of the wavelet function to be used. Typically, this function should look like the flow features which are of interest. The wavelets belonging to the Morlet family (illustrated in Fig. 6b) are quite similar to the traces of the pressure disturbances plotted in Fig. 6a. A center frequency $\gamma_c = 1$ and a bandwidth $\gamma_b = 6$ is chosen for the present analysis [34]. This offers a good compromise between the frequency and the temporal resolution.

The use of the complex Morlet wavelet is justified by the possibilities to measure instantaneous frequencies and to extract the modulus of the wavelet coefficients from which the energy density of the fluctuations can be determined. The smallest scale for the wavelet analysis is chosen with respect to the sampling frequency of the signal and the maximum frequency of interest (limited by the sensors at 1 MHz). Larger scales are then chosen to cover four octaves, each octave being divided into 64 levels.

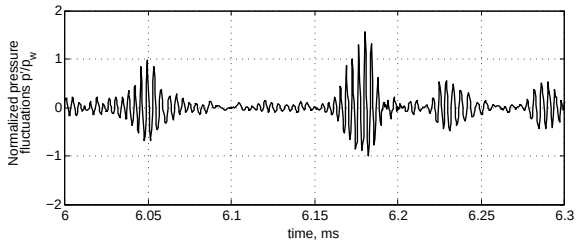

(a) Typical wall pressure signal

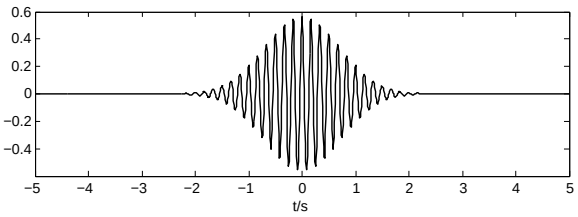

(b) Complex Morlet wavelet

Figure 6: Similarities between the pressure disturbances and a Morlet wavelet function.

The wavelet analysis is performed on PCB pressure measurements after nondimensionalizing them using a theoretical inviscid wall pressure (obtained by solving the Taylor-Maccoll equations for each time instant). Data have also been digitally high-pass filtered at 11 kHz so that only the high frequency content of the boundary layer pressure fluctuations is considered.

The square of the modulus of the complex wavelet coefficients obtained for some of the pressure sensors along the cone is given in Fig. 7 for a typical experiment using a nosetip radius of 1.75 mm. The color code is identical for each plot. The resulting power spectrum depicts the intermittency of the transition process with the succession of numerous energetic wave packets. Frequency content above 500 kHz was relatively poor in the present case and has not been plotted for clarity.

Most of the energetic fluctuations are contained within a narrow frequency band which depends on the location along the cone. The frequencies of the major disturbances in Fig. 7 are decreasing from 300 kHz at the most upstream measuring location down to about 150 kHz at the end of the cone. This shift to lower frequencies is expected to be a consequence of the boundary layer which gets thicker as it flows along the cone. Previous studies at lower Mach numbers have shown a similar behavior for second mode acoustic disturbances with the most amplified frequencies tuned to the local boundary layer thickness as $f \approx \frac{u_e}{2\delta}$ [8; 35].

The boundary layer along the model is also influenced by the decaying free-stream Reynolds number (Fig. 4b) which thickens the boundary layer over the time lapse considered. This consequently affects the frequencies of the major disturbances and explains the slight shift observed for each measuring location.

Some disturbances are amplified as the flow runs along the model and ultimately lead to a fully turbulent boundary layer by the end of the cone for experiments performed with a sufficiently large Reynolds number. Such a turbulent spectrum is plotted for comparison purposes in Fig. 8. It was obtained during a test with a higher free-stream unit Reynolds number and shows a broader spectrum with energy contained over a wide range of frequencies.

Harmonics of the major frequencies are picked up in the spectrum at the most downstream measurement locations. This corresponds to the locations where disturbances have a large amplitude and where nonlinear effects start to occur, right before the breakdown into a turbulent boundary layer. The very rapid growth of the harmonics quickly fills the power spectrum at large frequencies and completes the boundary layer destabilization process. This is better illustrated by plotting the Morlet spectrum [36] as in Fig. 9 which was obtained by summing the wavelet coefficients within the following time range: 9 ms $\leq t \leq$ 11 ms.

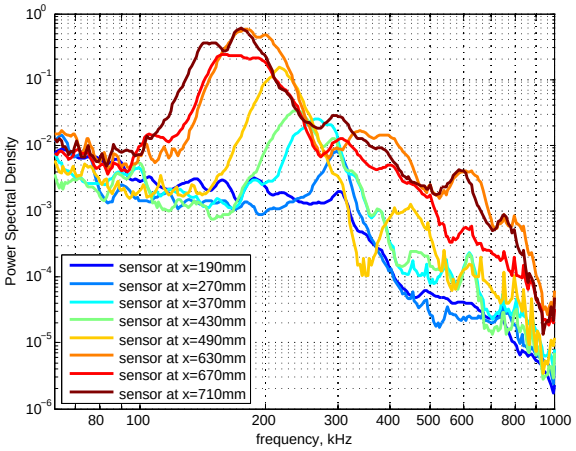

Figure 9: Morlet spectrum of the disturbances along the cone with $r_N = 1.75$ mm, $M_\infty = 10$ and $Re_\infty = 5.3 \times 10^6$ /m

3.2.2. *Convection velocities*

The nature of the disturbances can be inferred from the present measurements provided their convection velocity and the thickness of the boundary layer can

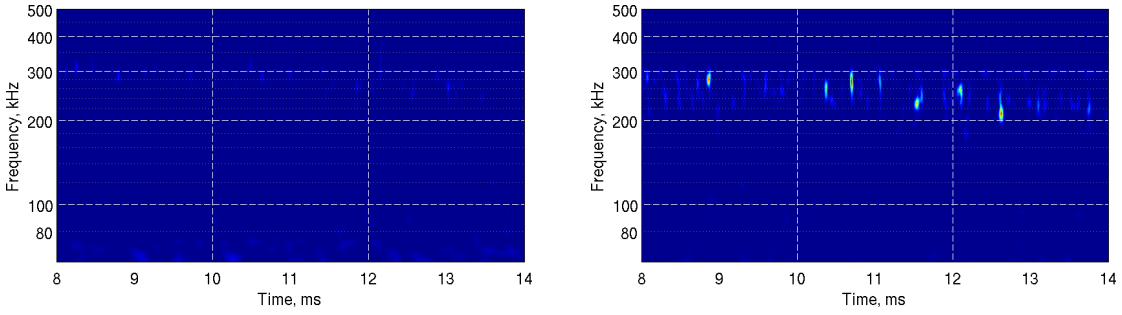

(a) sensor at $s = 270\,\text{mm}$

(b) sensor at $s = 370\,\text{mm}$

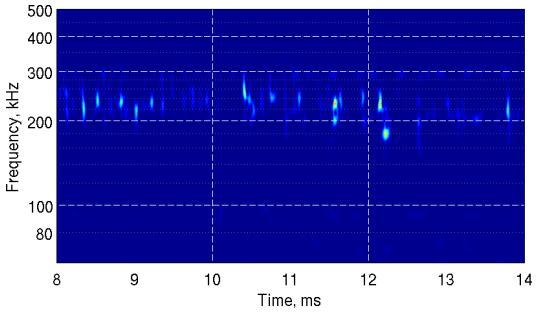

(c) sensor at $s = 430\,\text{mm}$

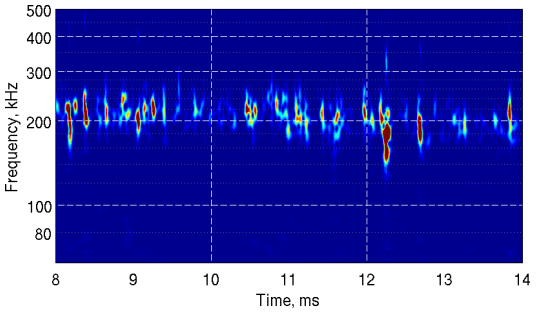

(d) sensor at $s = 490\,\text{mm}$

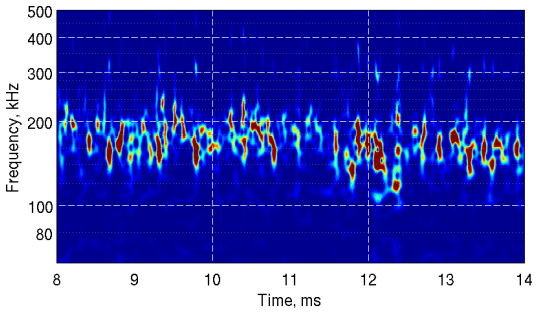

(e) sensor at $s = 670\,\text{mm}$

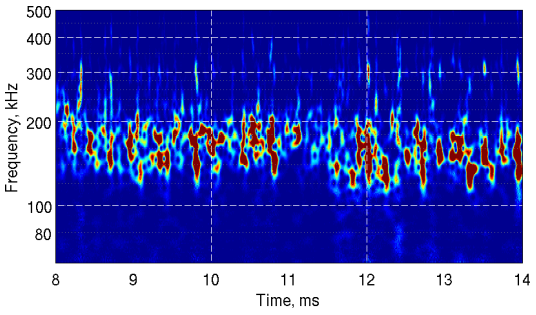

(f) sensor at $s = 710\,\text{mm}$

Figure 7: Power spectrum obtained from the wavelet analysis of the pressure fluctuations along the cone equipped with $r_N = 1.75\,\text{mm}$. Free-stream Mach number decays between $10.1 \gtrsim \text{M}_\infty \gtrsim 9.5$ from $t = 8\,\text{ms}$ to $t = 14\,\text{ms}$. Unit Reynolds number decays from $5.8 \times 10^6\,/\text{m} \gtrsim \text{Re}_\infty \gtrsim 4.8 \times 10^6\,/\text{m}$ over the same time window.

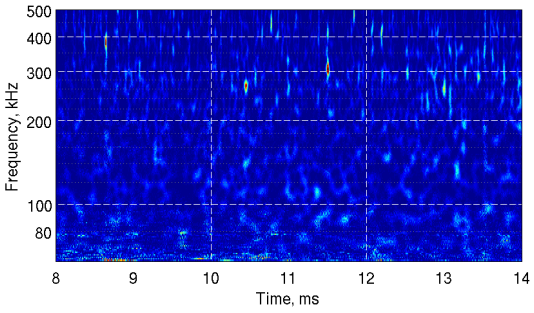

Figure 8: Power spectrum obtained from the wavelet analysis of a fully turbulent boundary layer $r_N = 1.75\,\text{mm}$ at $s = 490\,\text{mm}$ ($11 \gtrsim \text{M}_\infty \gtrsim 10.7$ and $11.7 \times 10^6\,/\text{m} \gtrsim \text{Re}_\infty \gtrsim 9.4 \times 10^6\,/\text{m}$ from $t = 8\,\text{ms}$ to $t = 14\,\text{ms}$).

be estimated. The phase speed can be estimated from the streamwise array of PCB pressure sensors using cross-correlation tools.

The best results have been obtained by discarding the frequency content of the sensors below 100 kHz. Signals were divided into several short windows of 0.2 ms with an overlap of 50% for the cross-correlation analysis. Thresholds have been applied to discard automatically cross-correlations coefficients lower than 0.2. Some coefficients have also been discarded when they were lower than 70% of the largest one within that time window. The corresponding time delay between two pressure traces is then determined for each of the selected cross-correlation coefficients. Since the distance between two sensors is accurately known, the convection velocities are determined straightforwardly.

Figure 10 depicts the convection velocities obtained for three different conical geometries. Results are compared to the free-stream velocity (determined from independent measurements following the method described in Ref. [23] and accurate to $2\sigma = \pm 5\%$) and the corresponding theoretical boundary layer edge velocity (derived from a Taylor-Maccoll flow solution). The color of each dot is representative of the cross-correlation coefficients, the darker ones corresponding to the largest values.

To a very good approximation, the disturbances within the boundary layer are convected with the boundary layer edge velocity during the transition process, i.e. $u_c/u_e \approx 1$. Convection velocities are sensibly the same for the three nosetip radii tested. No significantly different convection velocities could be observed for the different locations considered along the cone, suggesting that the instability waves are convected with the local flow velocity during the whole transition process. The larger scatter for the convection velocities of the disturbances in the blunt case are due to the stabilizing effect of the large nosetip radius (Fig. 5): the corresponding lower amplitude disturbances are more difficult to distinguish in the measurements and cross-correlations algorithms are less accurate. No significant influence of the Reynolds number is observed. These convection velocities are in good agreement with the measurements performed on similar geometries at lower Mach number and reported in Ref. [37].

3.3. *Flow visualization*

The destabilization process of a hypersonic boundary layer has been observed as early as in the seventies using Schlieren or Shadowgraph techniques as shown

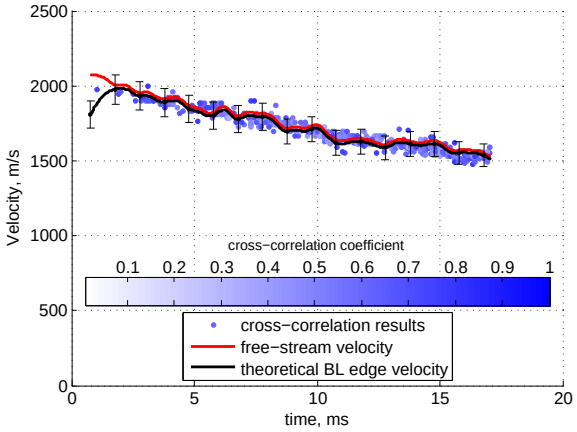

(a) Nosetip radius $r_N = 0.75$ mm ($11 \gtrsim M_\infty \gtrsim 9.7$ and 6.0×10^6 /m $\gtrsim Re_\infty \gtrsim 3.2 \times 10^6$ /m).

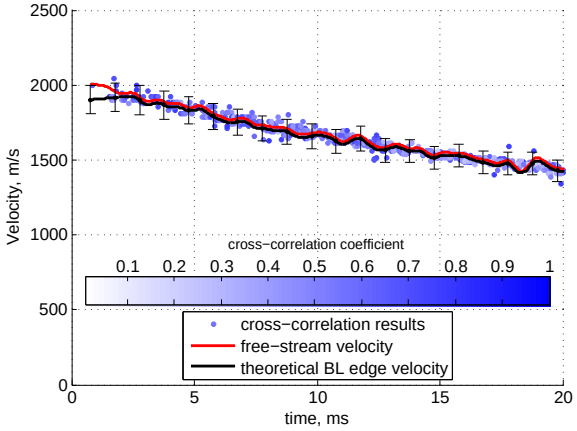

(b) Nosetip radius $r_N = 1.75$ mm ($11 \gtrsim M_\infty \gtrsim 9.5$ and 7.8×10^6 /m $\gtrsim Re_\infty \gtrsim 4.2 \times 10^6$ /m).

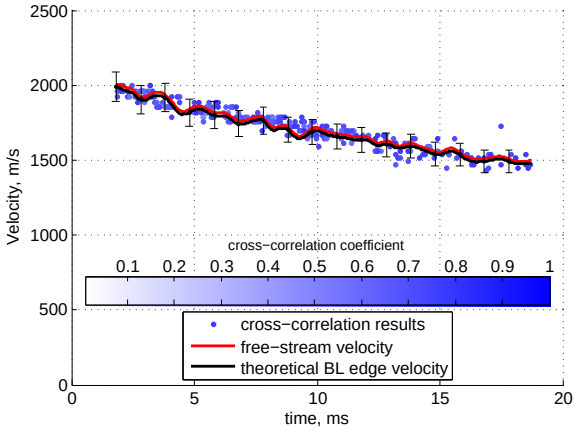

(c) Nosetip radius $r_N = 10$ mm ($12 \gtrsim M_\infty \gtrsim 10.3$ and 16×10^6 /m $\gtrsim Re_\infty \gtrsim 9.1 \times 10^6$ /m).

Figure 10: Effects of nosetip bluntness on the convection velocity of the dominant disturbances.

in Ref. [38]. The main difficulty is to illuminate the flow for a brief amount of time in order to freeze in space the flow disturbances. Only few other attempts have been successful in visualizing the hypersonic boundary layer disturbances. Among the most recent ones, are the results reported in Refs. [21; 39; 40] which used a continuous light source associated to the short exposure time of a high-speed camera. The flow structures still appear slightly blurred though, due to both the exposure time used (being still of several hundreds of nanoseconds) and the large flow velocities involved.

A novel Schlieren technique recently developed at VKI allows to improve such flow visualization results by using a specific light source having an exposure time as short as few nanoseconds [41]. It requires a high-power short duration laser which is used as an indirect light source for the Schlieren setup. The speckles and fringes due to the laser coherence have been successfully removed using an intermediate fluorescent material. This fluorescence provides a uniform illumination of the flow and is short enough to freeze in space all the hypersonic flow structures. The principle has been successfully applied using a conventional double cavity laser with a repetition rate of 15 Hz. Nevertheless, the short test time in the Longshot wind-tunnel prevents from obtaining several pairs of images per test. In order to overcome this limitation, an ILA High Speed PIV system has been used allowing to use a repetition rate of 2.5 kHz per cavity, and with a flash duration of 200 ns which is still short enough to obtain good quality images. The pictures were acquired with a Phantom SA-1 high-speed camera. The rest of the Schlieren setup is classical. The knife edge was aligned to the surface of the cone in order to be sensitive to density gradients normal to the surface.

Typical flow visualization results are given in Fig. 11 for different free-stream Reynolds numbers using a cone with a 1.75 mm radius nosetip.

A laminar boundary layer is illustrated in Fig. 11a as identified by the white line present at the edge of the boundary layer. Few oscillating structures are visible on the right-hand side on the image and correspond to the premises of a growing wave packet. Increasing the free-stream unit Reynolds number leads to the apparition of waves further upstream the cone, as in Fig. 11b.

The waves have a rope-shape structure and are running along the surface over long distances before they destabilize the boundary layer. Their wavelength is approximately twice the boundary layer thickness ($\lambda \approx 2\delta$) which is similar to that reported in Refs. [8; 35]. Since their convection velocities are closely approximated by the local flow velocity, one retrieves the following relationship established at lower Mach numbers and relating the frequency of the disturbances to the boundary layer thickness: $f \approx {}^{u_e}/_{2\delta}$. These are characteristics supporting the hypothesis of the second mode nature of the waves.

Increasing further the free-stream unit Reynolds number leads to the apparition of a turbulent spot at the most downstream location (Fig. 11c). The location of the first turbulent spot moves upstream when the Reynolds number is increased even more (Fig. 11d). At $\mathrm{Re}_\infty = 6.08 \times 10^6$ /m, a globally turbulent boundary layer is observed (Fig. 11e).

A much larger number of images would be required though to determine the transition location for each free-stream condition since the destabilization process is associated with a strong intermittency factor, with numerous wave packets and turbulent spots passing by a given location (Fig. 7e). Fig. 11e depicts for instance a boundary layer with lower fluctuations in the center of the image. This is probably due to a relatively young portion of turbulent boundary layer which was earlier surrounded by two turbulent spots. This hypothesis is supported by the presence of larger noise (inclined structures) within the shock layer and right above these older turbulent spots. Similar observations are valid for Figs. 11c and 11d where extensions of turbulent boundary layers were visible.

The convection velocities of the major disturbances can also be determined since pairs of images were obtained in each case. Measuring their wavelengths allows to infer their corresponding frequencies. Preliminary comparisons with the synchronized wall pressure measurements reveals a good agreement. Detailed comparisons will be the purpose of future publications.

4. Conclusion

Boundary layer transition experiments have been performed in the Longshot hypersonic wind tunnel over an 800 mm long 7 ° half-angle cone. The free-stream Mach number varies between $9.5 \leq \mathrm{M}_\infty \leq 12$ and the free-stream unit Reynolds number varies between 2.6×10^6 /m $\leq \mathrm{Re}_\infty \leq 16 \times 10^6$ /m.

Instrumentation includes thermocouples and pressure sensors flush-mounted to the surface. An overview of the results collected has been presented.

The determination of wall heat fluxes along the cone allows to determine the transition location and its

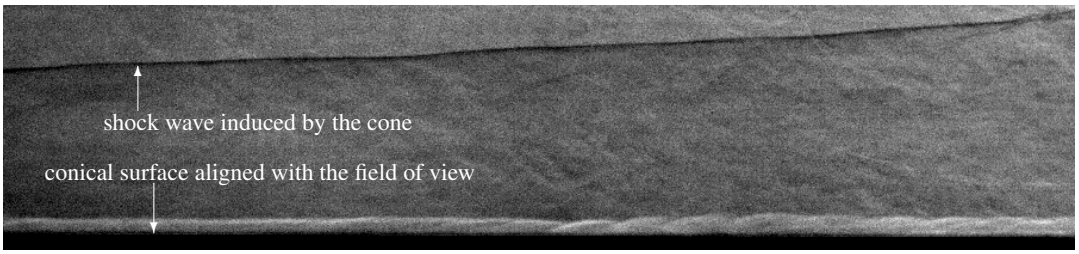

(a) $M_\infty = 9.6$ and $Re_\infty = 2.64 \times 10^6$ /m

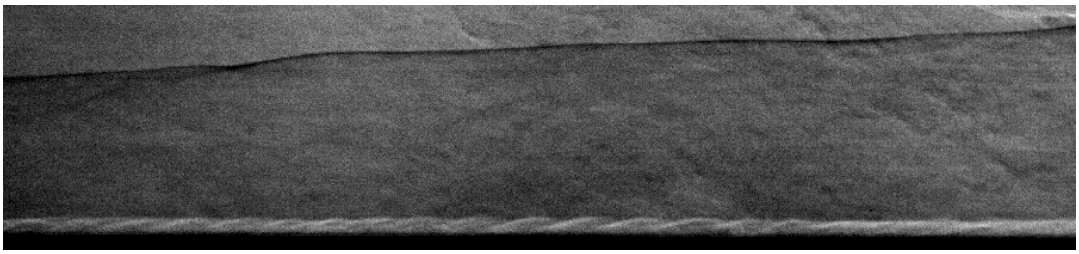

(b) $M_\infty = 10.1$ and $Re_\infty = 3.76 \times 10^6$ /m

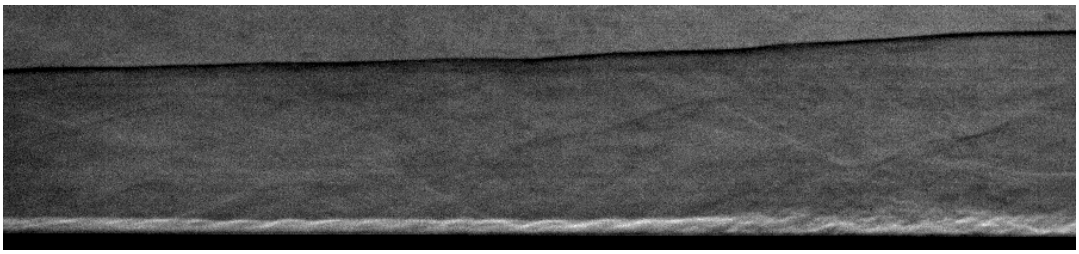

(c) $M_\infty = 10.5$ and $Re_\infty = 5.04 \times 10^6$ /m

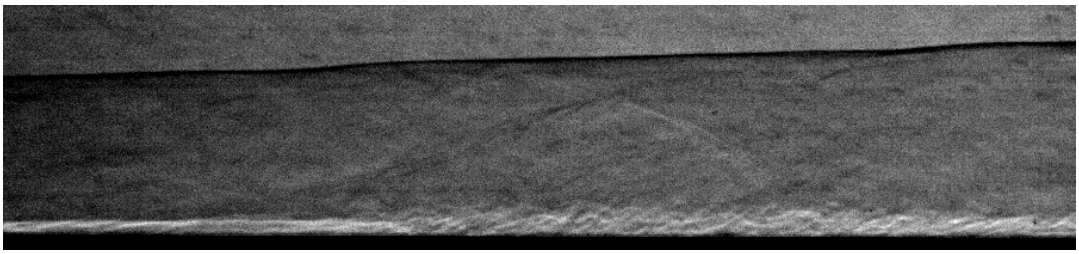

(d) $M_\infty = 10.8$ and $Re_\infty = 5.76 \times 10^6$ /m

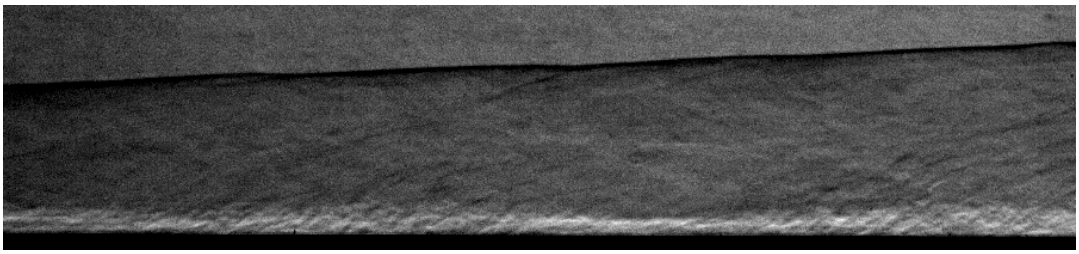

(e) $M_\infty = 11$ and $Re_\infty = 6.08 \times 10^6$ /m

Figure 11: LIF based Schlieren flow visualization on the 1.75 mm radius nosetip 7 ° half angle cone for different free-stream conditions. Flow is from left to right. Fields of view extend from 590 mm to 765 mm where distances are given from a theoretically sharp nosetip and along the surface.

extension. A nose bluntness of 4.75 mm has a strong stabilizing effect on the boundary layer with a laminar region extending twice longer than for a 0.2 mm sharp nosetip. Comparison with numerical predictions reveals a fair agreement although numerical predictions seem to overestimate the experimental values by 10 to 20%, especially close to the nosetip. The length of the transition region is approximately half of the laminar extension.

Wavelet analysis of the boundary layer pressure disturbances reveals large energy content between 150 and 300 kHz depending on the location along the cone. Numerous wave packets and turbulent spots are observed prior to a fully turbulent boundary layer.

The convection velocity of the waves is obtained from the cross-correlation of streamwise pressure measurements and is closely approximated by the boundary layer edge velocity during the whole transition process. No significant influence of the nosetip bluntness has been observed on these convection velocities.

Optical flow visualization using a novel Schlieren technique allowed to observe the structure of the disturbances. Their rope shape, wavelengths and estimated frequencies scaling as $f \approx {}^{u_e}/_{2\delta}$ all support the hypothesis that second mode instabilities are responsible for the transition in the present cases with large free-stream Mach numbers.

Results obtained from linear stability theory are now required to evaluate this conjecture. Such results and the knowledge of the transition location will allow to determine the N factor of the wind-tunnel representative of the quality of its flow. Further analysis of the data gathered and the comparison between flow images and the synchronized wall measurements are required to extend the boundary layer transition knowledge to higher Mach numbers.

Acknowledgments

The author gratefully acknowledge FRIA (Fonds pour la formation à la Recherche dans l'Industrie et dans l'Agriculture) for the financial support of this project. Best thanks are due to Steve Vanlanduit and Alexandru Nila (Vrije Universiteit Brussel) for the loan of their ILA High Speed PIV system. Thank you Gennaro Serino for reviewing the draft of this paper.

References

[1] E. R. vanDriest, The problem of aerodynamic heating, Aeronautical Engineering Review 15 (10) (1956) 26–41.

[2] S. R. Pate, Effects of wind-tunnel disturbances on boundary-layer transition with emphasis on radiated noise: a review, in: 11th AIAA Aerodynamic testing conference, no. AIAA paper 1980-0431, 1980.

[3] R. J. Sanator, J. P. DeCarlo, D. T. Torrillo, Hypersonic boundary layer transition data for a cold-wall slender cone, AIAA Journal 3 (4) (1965) 758–760.

[4] P. E. Everhart, H. H. Hamilton, Experimental investigation of boundary layer transition on a cooled 7.5deg. total angle cone at Mach 10, Technical Note TN D-4188, NASA (October 1967).

[5] E. J. Softley, B. C. Graber, R. E. Zempel, Experimental observation of transition of the hypersonic boundary layer, AIAA Journal 7 (2) (1969) 257–263.

[6] J. D. Whitfield, F. A. Iannuzzi, Experiments on roughness effects on cone boundary layer transition up to Mach 16, AIAA Journal 7 (3) (1969) 465–470.

[7] A. Demetriades, Hypersonic viscous flow over a slender cone, part III : laminar instability and transition, in: 7th AIAA Fluid and Plasma Dynamics Conference, no. AIAA paper 1974-535, 1974.

[8] K. F. Stetson, E. R. Thompson, J. C. Donaldson, L. G. Siler, Laminar boundary layer stability experiments on a cone at Mach 8, Part 1, sharp cone, in: 16th AIAA Fluid and plasma dynamics conference, no. AIAA paper 1983-1761, 1983.

[9] K. F. Stetson, E. R. Thompson, J. C. Donaldson, L. G. Siler, Laminar boundary layer stability experiments on a cone at Mach 8, Part 2: blunt cone, in: 22nd AIAA Aerospace Sciences Meeting, no. AIAA paper 1984-0006, 1984.

[10] K. Fujii, Experiment of the two dimensional roughness effect on hypersonic boundary layer transition, Journal of Spacecraft and Rockets 43 (4) (2006) 731–738.

[11] M. Estorf, R. Radespiel, S. P. Schneider, H. B. Johnson, S. Hein, Surface pressure measurements of second mode instability in quiet hypersonic flow, in: 46th AIAA Aerospace sciences meeting and exhibit, 2008.

[12] K. M. Casper, S. J. Beresh, J. F. Henfling, R. W. Spillers, B. Pruett, S. P. Schneider, Hypersonic wind tunnel measurements of boundary layer pressure fluctuations, in: 39th AIAA Fluid Dynamics Conference, no. AIAA paper 2009-4054, 2009.

[13] A. Wagner, K. Hannemann, V. Wartemann, H. Tanno, K. Ito, Free piston driven shock tunnel hypersonic boundary layer transition experiments on a cone configuration, in: Hypersonic laminar-turbulent transition, no. RTO-MP-AVT-200, 2012, pp. 12–1 – 12–12.

[14] D. Masutti, Ground testing investigation of hypersonic transition phenomenon for a re-entry vehicle, Ph.D. thesis, Technische Universiteit Delft and von Karman Institute for Fluid Dynamics (2013).

[15] T. Roediger, H. Knauss, E. Kraemer, M. Estorf, S. P. Schneider, B. V. Smorodsky, Hypersonic instability waves measured using fast-response heat flux gauges, in: 46th AIAA Aerospace sciences meeting and exhibit, no. AIAA paper 2008-638, 2008.

[16] H. Knauss, T. Roediger, J. Srulijes, Novel sensor for fast heat flux measurements, Journal of Spacecraft and Rockets 46 (2) (2009) 255–265.

[17] L. M. Mack, The stability of the compressible boundary layer according to a direct numerical solution, AGARDograph 97 Part I, NATO (1965).

[18] L. M. Mack, Linear stability theory and the problem of supersonic boundary layer transition, AIAA Journal 13 (3) (1975) 278–289.

[19] A. Maslov, A. Shiplyuk, A. Sidorenko, P. Polivanov, A. Fe-

dorov, V. Kozlov, N. Malmuth, Hypersonic laminar flow control using a porous coating of random microstructure, in: 44th AIAA Aerospace Sciences Meeting and Exhibit, no. AIAA paper 2006-1112, 2006.

[20] D. C. Berridge, K. M. Casper, S. J. Rufer, C. R. Alba, D. R. Lewis, S. J. Beresh, S. P. Schneider, Measurements and computations of second-mode instability waves in three hypersonic wind tunnels, in: 40th AIAA Fluid Dynamic Conference and Exhibit, no. AIAA paper 2010-5002, 2010.

[21] K. M. Casper, S. J. Beresh, J. F. Henfling, R. W. Spillers, High-speed Schlieren imaging of disturbances in a transitional hypersonic boundary layer, in: 51st AIAA Aerospace Sciences Meeting, no. AIAA paper 2013-0376, 2013.

[22] R. Narasimha, The laminar-turbulent transition zone in the boundary layer, Progress in Aerospace Sciences 22 (1985) 29–80.

[23] G. Grossir, S. Paris, P. Rambaud, B. Van Hove, Design of static pressure probes for improved free-stream characterization in hypersonic wind-tunnels, in: 52nd AIAA Aerospace Sciences Meeting, no. AIAA paper 2014-1410, 2014.

[24] G. Grossir, S. Paris, K. Bensassi, P. Rambaud, Experimental characterization of hypersonic nozzle boundary layers and free-stream noise levels, in: 51st AIAA Aerospace Sciences Meeting, no. AIAA paper 2013-1130, 2013.

[25] J. A. Fay, F. R. Riddell, Theory of stagnation point heat transfer in dissociated air, Journal of the Aeronauticals Sciences 25 (2) (1958) 73–85.

[26] H. Olivier, Thin film gauges and coaxial thermocouples for measuring transient temperatures, Tech. rep., RWTH Aachen, http://www.swl.rwth-aachen.de/en/industry-solutions/thermocouples/ (2000).

[27] D. L. Schultz, T. V. Jones, Heat-transfer measurements in short-duration hypersonic facilities, in: AGARDograph No. 165, no. AGARD-AG-165, NATO, 1973.

[28] S. R. Pate, Dominance of radiated aerodynamic noise on boundary layer transition in supersonic-hypersonic wind tunnels, Technical report AEDC-TR-77-107, Arnold Engineering Development Center (March 1978).

[29] J. L. Potter, J. D. Whitfield, Effects of slight nose bluntness and roughness on boundary layer transition in supersonic flows, Journal of Fluid Mechanics 12 (4) (1962) 501–535.

[30] K. F. Stetson, Nosetip bluntness effects on cone frustum boundary layer transition in hypersonic flow, in: 16th AIAA Fluid and Plasma Dynamics Conference, no. AIAA paper 1983-1763, 1983.

[31] M. R. Malik, R. E. Spall, C. L. Chang, Effect of nose bluntness on boundary layer stability and transition, in: 28th Aerospace Sciences Meeting, no. AIAA paper 1990-112, 1990.

[32] M. Farge, Wavelet transforms and their applications to turbulence, Annual Review of Fluid Mechanics 24 (1992) 395–457.

[33] D. Masutti, F. Pinna, E. Günaydınoğlu, T. Sopek, O. Chazot., Natural and induced transition on a 7deg. half-cone at Mach 6, in: Hypersonic laminar-turbulent transition, no. AVT-200, NATO, 2012.

[34] A. Teolis, Computational signal processing with wavelets, Birkhäuser, 1998.

[35] A. Demetriades, Laminar boundary layer stability measurements at Mach 7 including wall temperature effects, Technical report AFOSR-TR-77-1311, AFOSR (November 1977).

[36] C. Tropea, A. L. Yarin, J. F. Foss, Handbook of experimental fluid mechanics, Springer, 2007.

[37] R. L. Kimmel, A. Demetriades, J. C. Donaldson, Space-time correlation measurements in a hypersonic transitional boundary layer, AIAA Journal 34 (12) (1996) 2484–2489.

[38] A. Demetriades, Hydrodynamic stability and transition to turbulence in a hypersonic boundary layer over a sharp cone, Technical report AFOSR TR-75-1435, Air Force Office of Scientific Research (July 1975).

[39] S. Laurence, A. Wagner, K. Hannemann, V. Wartemann, H. Lüdeke, H. Tanno, K. Itoh, Time-resolved visualization of instability waves in a hypersonic boundary layer, AIAA Journal 50 (1) (2012) 243–246.

[40] K. M. Casper, S. J. Beresh, J. F. Hrenfling, R. W. Spillers, Toward transition statistics measured on a 7-degree hypersonic cone for turbulent spot modeling, in: 52nd Aerospace Sciences Meeting, no. AIAA paper 2014-0427, 2014.

[41] T. Regert, G. Grossir, S. Paris, L. Blay Esteban, Schlieren visualization for high-speed flows based on laser-induced fluorescence, Experiments in Fluids 55 (2) (2014) 1667.

In-flight Experiment Design and Ground Testing of a Re-Entry CubeSat

Işıl Şakraker

Aeronautics and Aerospace Department, von Karman Institute for Fluid Dynamics, Belgium, isil.sakraker@vki.ac.be

Supervisor: Olivier Chazot

Professor, Aeronautics and Aerospace Department, von Karman Institute for Fluid Dynamics, Belgium, olivier.chazot@vki.ac.be

Promotor: Gaëtan Kerschen

Professor , Department of Aerospace and Mechanical Engineering, University of Liege, g.kerschen@ulg.ac.be

Abstract

Real flight atmospheric entry tests are required to validate numerical/experimental tools in order to reduce the high conservative safety margins applied to the spacecraft thermal protection systems. This study covers the development of a flight-to-ground extrapolation methodology for non conventional vehicle geometries. The test case is QARMAN, which is a 3U CubeSat with thermal shield performing an atmospheric entry.

Keywords: Atmospheric Entry, Plasma Flows, In-Flight Experiments, Experimental Aerothermodynamics, CubeSats

1. Introduction

Spacecraft, returning back to Earth, experience a very harsh environment during the encounter with the particles of the atmosphere. One of the major issues of atmospheric entry is the extreme aerothermodynamic heating and the exothermic chemical reactions due to the gas-surface interaction at hypersonic velocities. There is a constant effort by the space agencies to increase the understanding of the re-entry flight dynamics to optimize the spacecraft and especially its thermal protection system design. During the design process, the need of real flight tests is indispensable for ground test and numerical tool validations. However due to the high costs, such missions are rarely launched and thus there is an increasing interest in small affordable entry probes. This study discusses an aerothermodynamic instrumentation payload on a triple unit CubeSat platform that will be launched to 380 km altitude with the rest of the QB50 network [1]. QARMAN, QubeSat for Aerothermodynamic Research and Measurements on AblatioN, is a triple unit (3U) CubeSat respecting the CubeSat standards; a rectangular prism with dimensions $34 \times 10 \times 10$ cm weighing 3 kg. It has an ablative thermal protection material at the nose and will perform an atmospheric entry representative of real missions with 7.5 km/s at 120 km with a peak heat flux of 2.6 MW/m^2. The objectives of the in-flight experiments are to retrieve real flight data on ablator efficiency (temperature, pressure, recession) and temperature/pressure/skin friction measurements for transition on the side panels. Overall, this challenging mission targets to demonstrate the use of nano and pico satellite technology to atmospheric entry research by providing successful real flight data for highly affordable costs when compared to other missions of the space agencies that cost hundreds of million Euros.

It is important to investigate how such non conventional geometry can be tested in the subsonic plasma wind tunnel VKI Plasmatron. The current ground to flight extrapolation methodology is seen to be insufficient since a flight to ground extrapolation method is needed. This paper discusses the proposed way of duplicating the hypersonic flight behind the shock of a non-axisymmetric and blunt body in the subsonic ground facility in terms of aerothermochemistry.

2. Ground Testing Methodology

2.1. Background and Methodology

The stagnation point heating of a vehicle flying at hypersonic velocities can be given by the Eq. 1 of Fay and Riddel [2] for thermo-chemical equilibrium:

$$\dot{q}_w = 0.763 Pr^{1/2} (\rho_e \mu_e)^{1/2} \left(\frac{dU_e}{ds} \right) \Bigg|_{edge}^{1/2} \left(\frac{\rho_w \mu_w}{\rho_e \mu_e} \right)^{0.1} (h_e - h_w) \quad (1)$$

The three independent parameters are the density ρ, the velocity gradient dU/ds and the enthalpy h at the boundary layer edge. The density is a function of the pressure and the enthalpy therefore the three independent parameters are pressure, enthalpy and velocity gradient at the boundary layer edge. The *Local Heat Transfer Simulation (LHTS)* approach states that for a full simulation of the stagnation region of a reactive hypersonic flow, three properties at the boundary layer edge must be identical for flight and for ground [3].

$$Enthalpy : h_e^{flight} = h_e^{ground} \quad (2)$$

$$Pressure : p_e^{flight} = p_e^{ground} \quad (3)$$

$$Velocity\ gradient : \beta_e^{flight} = \beta_e^{ground} \quad (4)$$

Among the three parameters, the boundary layer edge pressure can be determined accurately. The enthalpy and the velocity gradient are more challenging. The following sections will cover the two parameters.

The ground testing methodology consists of a combination of experimental and numerical campaigns. Initially an experimental campaign is necessary to build the test conditions corresponding to the entry vehicle trajectory: pressure and enthalpy. On the other hand, the velocity gradient depends on the test probe geometry which comes from both actual vehicle geometry and flight conditions. The velocity gradient matching procedure is not trivial especially for non-axisymmetric geometries like QARMAN. At VKI Plasmatron, the everyday use is a ground-to-flight extrapolation. This means the TPS sample or payload testing often starts with a standard probe geometry and then is extrapolated to flight conditions/geometry which does not always match the wanted vehicle geometry. The third parameter is often disregarded and the topic is addressed for the IXV re-entry vehicle by Panerai [4]. This study introduces a new approach of a flight-to-ground extrapolation which allows to simulate correctly a given hypersonic vehicle by determining correctly the test probe geometry in the subsonic ground facility.

2.2. Accurate Ground Tests: Enthalpy Determination

The ground testing methodology requires accurate knowledge of the flow produced in the test chamber of Plasmatron. Due to the errors in the heat flux, dynamic pressure measurements and the lack of accurate knowledge of copper recombination efficiency behavior when exposed to plasma, the enthalpy can have high uncertainties around 20%. The aim is to reduce these levels to around 5% and two independent methods are proposed.

The first method is to measure the same free stream with different sized probes, namely Damköhler probes. The second method is by using optical emission spectroscopy.

2.2.1. Damköhler Probes

Three water cooled copper calorimeters having different probe radii are used in the Damköhler probe campaigns. The idea behind lies on the Damköhler number definition.

$$Da = \frac{\tau_f}{\tau_c} \quad (5)$$

Where τ_f is the characteristic time of the flow and τ_c is the characteristic time of the chemistry. For given conditions, the probe radius drives the velocity gradient, then the Damköhler number in the boundary layer. One can conclude that low velocity gradient values promote chemical equilibrium while high velocity gradient values tend to 'freeze' the boundary layer. At the same free stream conditions all the probes will measure a different heat flux due to a change in the boundary layer chemistry. If the copper catalycity (γ) were known accurately enough, all the three measurements would lead to the same free stream enthalpy. Due to the lack of exact knowledge of this parameter, VKI's rebuilding code is used to compute the enthalpy for a range of catalycity values using the heat flux measurement and the radius of the calorimeter probe. Using the $h - \gamma$ curves from three different sized probes exposed to the same plasma, an accurate enthalpy interval can be extracted. There are several studies conducted at VKI with these probes [5; 6; 7]. However none of their campaigns included the desired test conditions of QARMAN trajectory.

The results of those studies are promising considering they led to catalycity intervals of $\Delta\gamma = 4.10^{-3}$ and uncertainties down to 10% in enthalpy. Even though the previous studies did not give the desired uncertainty level of 5%, there is an improvement of about 10% and the combination with other methods will improve the numbers.

2.2.2. *REDES*

REDES (Real-time Enthalpy Determination with Emission Spectroscopy) has two modes. The first mode uses a method adopted from Fletcher [8] for generic air plasma [9]. It considers the peaks and the integrated areas of N_2^+ first negative $\Delta\nu = 0$ and CN Violet $\Delta\nu = 0$ sequences. The theoretical spectrum for a given total pressure can be computed. Later the peak or the integral ratios are compared with preloaded 'theoretical ratio vs. temperature' curves and the temperature is retrieved. Using Mutation library of VKI, the temperature data is automatically converted to enthalpy assuming local thermal equilibrium. Fig. 1 shows the peak and the integral options of the method. The uncertainty of the temperature is around 5%.

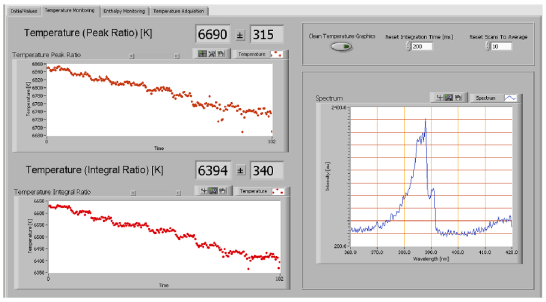

Figure 1: REDES Real-time Temperature monitoring using N_2^+ first negative and CN Violet.

Application of REDES to deduce recombination efficiency of different heat flux sensors. This method is used in the work of Leite [10] under the supervision of the author to determine the copper catalycity for three different heat flux sensors: water cooled calorimeter, copper slug and Gordon gage. The previously mentioned $h - \gamma$ curves, or S-curves, are built for QARMAN trajectory conditions. An example is given in Fig. 2. This study has significant importance when determining the enthalpy in the same way of the Damköhler probes since all three probes are exposed to the same plasma conditions and they all should measure the same free stream enthalpy given the catalycities are known.

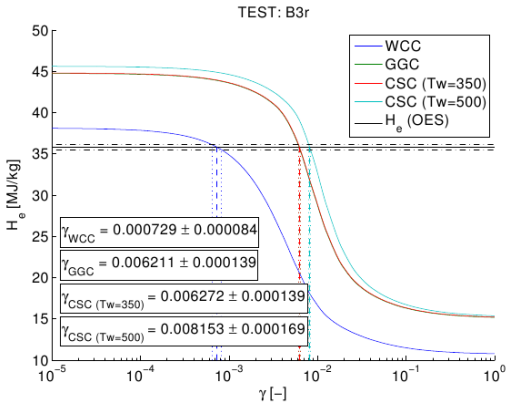

Figure 2: S-Curve and Reference Catalycity Results [10].

Recent studies at VKI showed that this method overpredicts the enthalpy due to the plasma instabilities. The acquisition frequency with the used spectrometer (nominally 1 Hz) is lower than the plasma oscillation frequency (about 60 Hz). This 'long' integration time leads to higher enthalpy measurement. The overprediction rate depends highly on the operating conditions and no full study has been done to quantify them yet, instead a new setup is proposed. The second mode of REDES uses a Boltzmann plot with O and N atomic lines. This mode is now being converted to so-called 'the mirror method' with a research master student. The setup is based on the work of Bachmann *et al.*[11]. Instead of a spectrometer, a high speed camera is introduced. The plasma image is split into two parts which allows, through correct filtering, measuring two intended O and N line intensities for Boltzmann method to deduce the temperature, thus enthalpy.

2.3. *Accurate Ground Tests: Velocity Gradient Determination*

An extensive literature survey has been conducted to find an accurate expression to replace the velocity gradient term in the Fay-Riddel equation, thus in the LHTS method, to find the correct sample probe for Plasmatron. It has been seen that two different approaches were taken since the 50s. One considers the pressure distribution at and around the stagnation point. The experimental work of Boison and Curtis covers a series of pressure measurements at supersonic Mach numbers [12]. The other approach takes the stagnation line profile instead, it determines the value at the boundary layer edge, such as Olivier [13]. For further reading refer to [14; 15; 16; 17]. The common part among all the studies is that they all consider

an axisymmetric shape and the most blunt body is a spherical cone.

The unconventional geometry of QARMAN does not allow a direct usage of the equations found in the literature. A new approach has been developed in order to find the equivalent test probe geometry iteratively.

2.3.1. *Iterative Procedure and its Application to QARMAN Spacecraft*

To start with, it is important to state that the stagnation line profile approach has been adopted. The velocity gradient to be used in LHTS is defined as the derivative of the radial velocity component in the radial direction at the boundary layer edge and along the stagnation line.

The iterative method contains 4 major steps and is summarized in Fig 3. Each step is briefly explained and applied to QARMAN vehicle at 66 km of its trajectory.

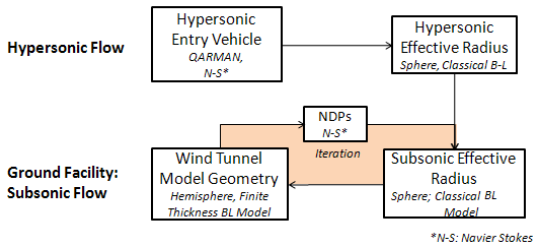

Figure 3: Iterative approach steps.

Step 1. The first step is to have the CFD computations of the vehicle according to the trajectory calculations. It is important that the stagnation line grid is resolved sufficiently. This step is solving Navier-Stokes equations as generally applied by commercial CFD codes. As one will see from the stagnation line profiles, the edge of the boundary layer cannot be detected directly. The velocity gradient equations in literature all comprise a spherical radius and the velocity gradient. At this point there is one equation and two unknowns. Therefore it is convenient to select an appropriate boundary layer edge and retract the needed spherical (equivalent radius). To do so, there are two different options: one is to select the point where the temperature profile stops to be linear after the shock; the other is to run an inviscid computation with the same conditions and take the velocity gradient profile at the wall of the vehicle. The latter shows that the viscous and inviscid computations defer from each other at the same location where the temperature profile stops to be linear. This shows that even if high non equilibrium conditions exist, the thermal, the chemical and the dynamic boundary layer thicknesses are comparable.

Among the many options, the Lunev formula, given in Eq. 6, is the adopted expression to go to the next step. Lunev suggests an expression, very similar to Modified Newtonian Theory (MNT) however based on Thin Shock Layer Theory.

$$\frac{1}{\beta} = \frac{1}{R_{eff,Hypersonic}} \times \sqrt{\frac{8}{3}\frac{(P_s - P_\infty)}{\rho_\infty}} \tag{6}$$

where β is the velocity gradient, P_s is the stagnation pressure, P_∞ and ρ_∞ is the free stream pressure and density respectively.

Step 2. The second step is to show that the sphere found in the first step is equivalent to the QARMAN vehicle. The equivalent, or effective radius denoted by $R_{eff,H}$ is found to be 12.8 cm taken from the inviscid solution of QARMAN at the wall using Lunev formulation.

The flow in front of this sphere is solved later by both commercial code CFD++ and the Stagnation Line code of VKI. The result is shown in Fig. 4 for temperature and in Fig. 5 for density. It is important to note that the sphere is solved with the classical boundary layer theory.

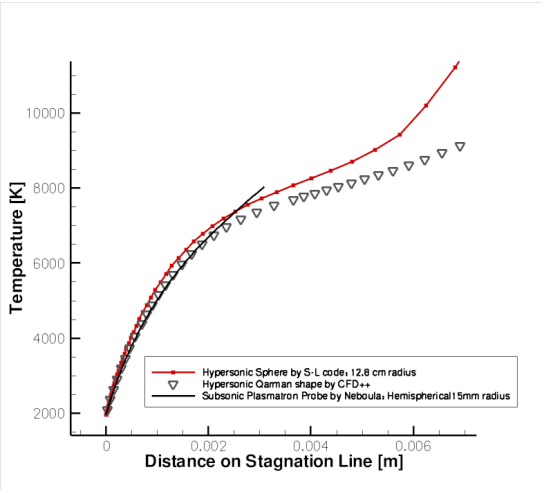

Figure 4: Temperature profile comparison of step 1, 2 and 4 at 66 km.

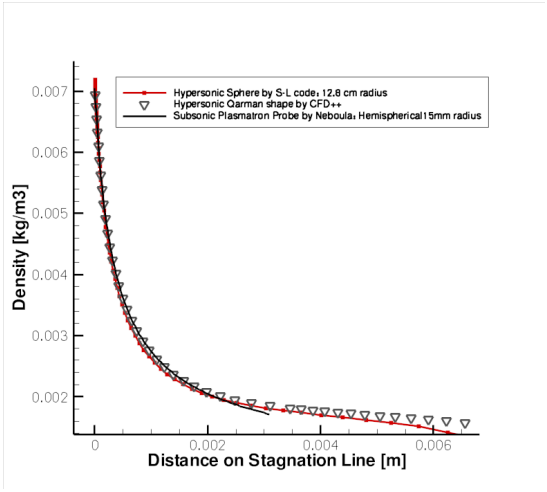

Figure 5: Density profile comparison of step 1, 2 and 4 at 66 km.

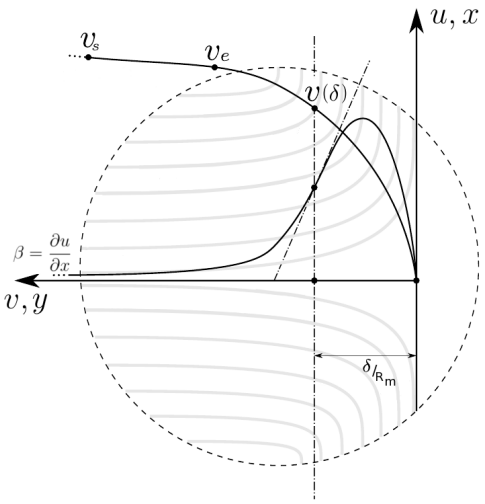

Figure 6: Velocity profile and velocity gradient in front of a wall exposed to subsonic plasma.

Step 3. This step is where an equivalent subsonic radius of a sphere is found. It mainly consists of equating the heat fluxes in the hypersonic and subsonic regimes. Given the same pressure and the enthalpy are provided at the boundary layer edge, the only difference in the two regimes is the velocity gradient expression given in terms of pressure. It should be noted that due to the pressure distribution differences, the subsonic equivalent sphere $R_{eff,Subsonic}$ is not the same as $R_{eff,Hypersonic}$. The relation between the two is given in Eq. 7. There is no assumption on the boundary layer model at this stage, therefore the subsonic sphere is still equivalent in classical boundary layer model.

$$R_{eff,Subsonic} = R_{eff,Hypersonic} \times \frac{\sqrt{P_e \Delta P_s}^{ground}}{P_s^{flight}} \quad (7)$$

Step 4. This stage is the iterative part of the whole process. The spherical subsonic body is converted to the hemispherical sample probe geometry for testing in VKI Plasmatron. The flow in Plasmatron is solved with the Finite Thickness boundary layer model using the in-house ICP code. Therefore the $R_{eff,Subsonic}$, or $R_{eff,S}$, cannot be used as the probe geometry. In subsonic regime, the velocity gradient and the resultant velocity are depicted in Fig. 6.

Using ICP code, the flow at the stagnation line can be represented by five Non-Dimensional Parameters (NDPs). They are important when rebuilding the free stream conditions from measured heat fluxes in everyday use of Plasmatron. For this, the NDPs at the boundary layer edge should be taken. The edge of the boundary layer is taken as the inflection point of the velocity gradient profile as the second order derivatives in the equation are canceled out and the boundary layer can be solved with simple first order equations. This was initially proposed by Kolesnikov [3]. The NDP expressions are given as:

$$NDP1 = \delta = \frac{\Delta}{R_m} \quad (8)$$

$$NDP2 = u_{1e} = \frac{\partial u}{\partial x} \cdot \frac{R_m}{v_s} \quad (9)$$

$$NDP3 = u_{1y} = \frac{{R_m}^2}{v_s} \cdot \frac{\partial}{\partial y}\left(\frac{\partial u}{\partial x}\right) \quad (10)$$

$$NDP4 = \bar{v} = \frac{v(\delta)}{v_s} \quad (11)$$

$$NDP5 = \frac{v(\delta)}{v_e} \quad (12)$$

Starting from the momentum equation, the $R_{eff,S}$ can be converted to R_m which is the radius of a hemispherical probe geometry as follows:

$$R_{eff,S} = \frac{R_m}{NDP2 \cdot \left(1 + \frac{NDP5 \cdot NDP3}{NDP2^2}\right)} = \frac{R_m}{f(NDP)} \quad (13)$$

The iteration begins by using the NDPs of an initially guessed R_m. This procedure is repeated until the R_m found from the procedure and the R_m used to deduce the NDPs are matched. This step is also conducted for the QARMAN trajectory at 66 km. The radius of the probe to be used in Plasmatron is found to

be 15 mm. The stagnation line profile is computed using the boundary layer code of VKI for the 66 km edge conditions. *It should be noted that the edge conditions are built in a separate Plasmatron campaign using REDES. The pressure and enthalpy are known from the trajectory calculations; the pressure is matched and the ICP power is adjusted until the same enthalpy is measured in the free stream. This is repeated for 8 selected points along the QARMAN trajectory. This campaign has been reported in the VKI PhD Symposium 2013.* The results are also given in Figs. 4 and 5. The subsonic flow in front of the probe geometry is in very good agreement with the QARMAN hypersonic CFD.

3. QARMAN In-Flight Experiment Design

3.1. QARMAN Flight Scenario

QARMAN is a triple unit CubeSat with two distinctive characteristics: an ablative TPS in the front unit and an aerodynamic drag augmentation device. The two mission objectives are: using aerodynamic drag to control the stability and de-orbiting for atmospheric entry; and performing an Earth atmospheric entry.

The current mission operation plan of QARMAN is sketched in Fig. 7. The AeroSDS will assure that QARMAN reaches 120 km of altitude with the desired entry conditions by reducing the speed down to 7.5 km/s. The peak heating is expected to be between 2.5-2.6 MW/m^2 at around 61km. For protecting the vehicle, the ablative TPS of the front unit will be a cork based material whereas the side panel heat shield will be silicon based ceramic. At 50km of altitude, QARMAN will start to disintegrate.

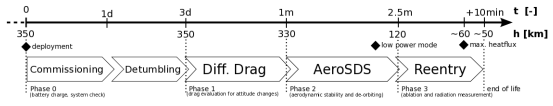

Figure 7: QARMAN flight scenario. Courtesy: Thorsten Scholz

3.2. Payloads for Aerothermodynamic Research

The overview of all the aerothermodynamic payloads of QARMAN is summarized in Table 1. A CubeSat platform, different than other spacecrafts, has high interdependency between its subsystems and payloads. A dedicated methodology has to be built for a mission like QARMAN where the satellite platform meets aerothermodynamic research. There is a number of references in the literature concerning the space mission designs (i.e [18]). The developed methodology was presented in VKI PhD Symposium in 2013. In this paper the payloads XPL01 to 05 are covered. The initial methodology is briefly summarized and more details are provided under measurement chain design and payload head design sections. [1] All the payloads presented here are also parts of a Flush Air Data Sensing system (FADS) system which will be used to rebuild the entry trajectory by temperature and pressure measurements. The trajectory reconstruction technique will be the focus of further future research.

Table 1: Overview of the Aerothermodynamic Payloads.

Payload	Objective	Parameter
XPL01	TPS Efficiency	Temperature
XPL02	TPS Pressure	Pressure
XPL03	Vehicle Stability	Pressure
XPL04	Laminar to Turbulence Transition	Pressure Temperature
XPL05	Side Panel Heating	Temperature
XPL06	Radiation	Species

3.2.1. XPL01

A first analysis on the payload mission objectives and requirements is conducted. The subject trades have shown that 'temperature' is the sufficient parameter of interest to satisfy the payload objectives concerning TPS recession, heating and material response. A preliminary investigation is then performed including the first estimation of the temperature during the flight (preliminary CFD); the critical locations/instants are determined and the performance thresholds expected from the measurement mean are defined. Later on, available measurement techniques are investigated and thermocouple type K is chosen as the best fit to the performance thresholds given in Tables 2 and 3.

Data Acquisition Chain Design. The measurement chain with correct filtering and signal conditioning that can fit the constraints of the spacecraft bus is designed and tested on a breadboard (Fig. 8). This chain is further tested in the VKI Plasmatron facility, inserted in a cork P50 sample exposed to plasma flow and the acquisitions are simultaneously made by identical sensors at the Plasmatron acquisition system for

[1] Note that the scope of this paper does not include the XPL06.

Table 2: Performance Thresholds of one sensor unit.

Type	Unit	Desired	Acceptable
Range	K	$273 - 2200$	$273 - 1523$
Accuracy	$\pm K$	$(0.0025 \times T) + 273.15$	$(0.0075 \times T) + 273.15$
Frequency between 150-120km	Hz	1/60	1/240
Frequency below 120km	Hz	1	0.5
Response Time	s	0.1	0.5
Mass (Sensor + cable + housing)	g	9.9	16.8
Volume	cm^3	0.118	0.353
Required ADC Resolution	bit	12	11
Power	$mW\,h$	0.83	2.08
TRL	[-]	9	4

comparison (Fig. 9). The results showed very good agreement and they can be seen in Fig. 10. The different cases correspond to filtering and grounding where the filtered thermocouple showed very good agreement with the reference thermocouple.

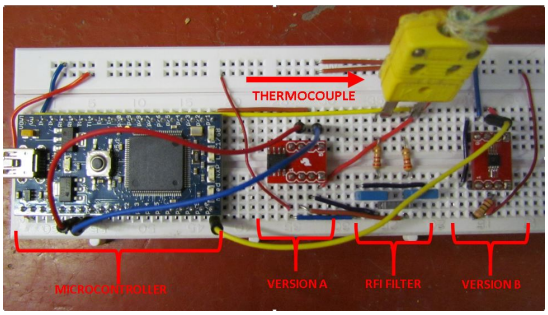

Figure 8: Thermocouple type K breadboard.

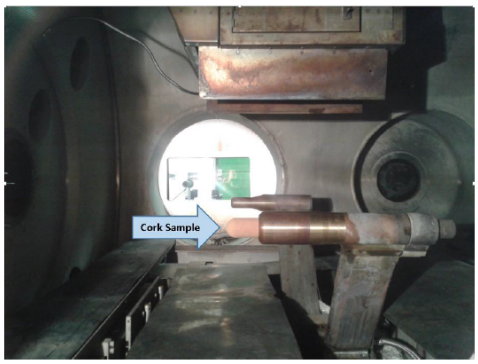

Figure 9: Plasmatron test with conditions $P = 100mbar$ and $\dot{q} = 708; 1250; 1500; 1640 kW/m^2$ with a sample of 15mm radius.

The engineering model of this design has been manufactured and extensively tested at VKI. It is currently integrated in two satellite platforms and it is ready to be launched in May 2014. The current TRL of 6 is expected to be 9 after the launched. The two QB50p satellites are going to put in an orbit of 624 km, 10:30 LTAN and 98 degrees inclination.

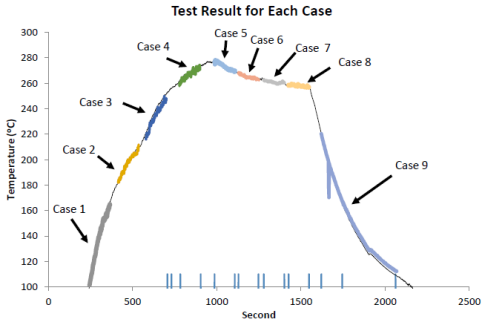

Figure 10: VKI Plasmatron Test with comparison to Plasmatron acquisition chain (Shown by black line).

Payload Head Design. The second part of the preliminary configuration consists of the sensor head. A thermal plug concept is foreseen. Six aligned thermocouples are going to put axially as depicted in Fig. 11. The depths for thermocouple positions are proposed as 2.5, 5, 10, 20, 30 and 40 mm with an additional one in the back at 50 mm before the insulator. These depths are chosen to catch the typical low density ablator temperature distribution as shown in Fig. 12. The thermal plug is to be inserted in a correctly adjusted hole without disturbing either the measurement junctions or the smoothness of the TPS.

A thermal plug with 2 thermocouples has been machined and instrumented to check the feasibility of this concept. This is shown in Fig. 13 (note that the glue as used in this sample will not be used in the real

Table 3: Details of performance thresholds.

Type	Desired	Acceptable
Range	Surface temperature at peak heat flux (by CFD)	Range of TC Type K
Accuracy	TC Type R accuracy	TC Type K accuracy
Frequency between 150-120km	Initial heating of TPS prior to re-entry	Safety factor 4.0 considering available power in the Low Power Mode
Frequency below 120 km	Analogous to ground tests	Safety factor 2.0 considering available power
Response Time	Analogous to ground tests	Safety factor 5.0. Should be less than acceptable acquisition frequency
Mass	Sensor head $1g$ + Cable $2.25g$ ($15cm$ long at $0.015kg/m$) + Installation $5g$ + Safety factor 1.2	Sensor head $1g$ + Cable $3g$ ($15cm$ long at $0.015kg/m$) + Installation $10g$ + Safety factor 1.2
Volume	Diameter 1mm, Length 15cm	Diameter 1.5mm, Length 20cm
Required ADC Resolution	To achieve $1°C$ output resolution	To achieve $0.5°C$ output resolution
Power	Calculated for desired frequency, desired response time and 10 minutes acquisition time at 0.05 W	Calculated for accepted frequency, accepted response time and 10 minutes acquisition time at 0.05 W
TRL	Flight heritage	Tested in laboratory environment

plugs). No major difficulties were encountered.

At this point it is important to determine the positions of the thermal plugs on the front TPS. This positioning also concerns the XPL02. Different scenarios are considered as shown in Fig. 14. T#s show the thermal plugs whereas the P#s show the pressure ports. The figure also depicts the selection criteria. The scenario 4 is chosen as the optimum to start with. Selection criteria consist of redundancy, weight, mission risk, dependency. integration, simplicity, DAQ simplicity and scientific contribution. The axial positioning of the sensors are done using the CFD computations. The centers of the thermal plugs are proposed to be positioned at 22 and 46 mm away from the stagnation (center) point diagonally where the XPL06 payload will have the optical path.

3.2.2. XPL02

A first analysis on the payload mission objectives and requirements is conducted. The main objective is to monitor the pressure in the front TPS and the secondary is to provide information behind the shock to the Flush AirData Sensing (FADS) system. The subject trades have shown that pressure is the interesting and sufficient parameter to satisfy the payload objectives concerning TPS pressure. A preliminary investigation is then performed including the first estimation of the pressure during the flight (preliminary CFD); the critical locations/instants are determined and the performance thresholds expected from the measurement mean are defined. Later on, available measurement techniques are investigated and two pressure sensors are found to fit the performance thresholds given in Table 4.

Data Acquisition Chain Design. The absolute pressure sensor breadboard tests are currently being conducted in Minitorch facilities and the results will be reported by end May 2014.

Payload Head Design. The positioning of the pressure ports are shown in Fig. 14 together with the thermal plugs of XPL01. As the CFD computations at dif-

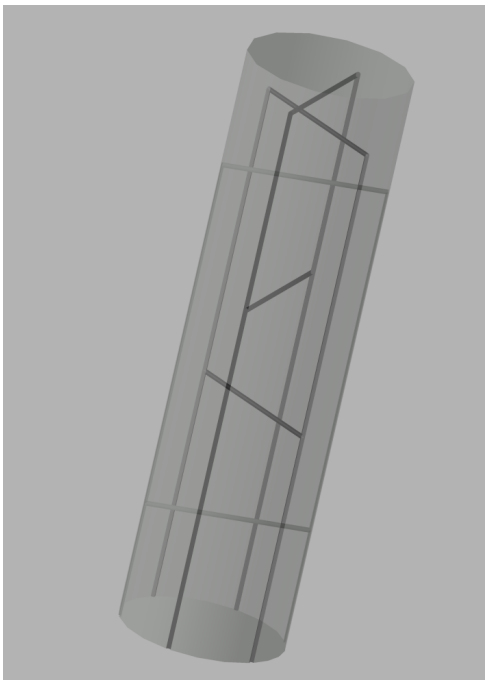

Figure 11: Thermal Plug - Side View.

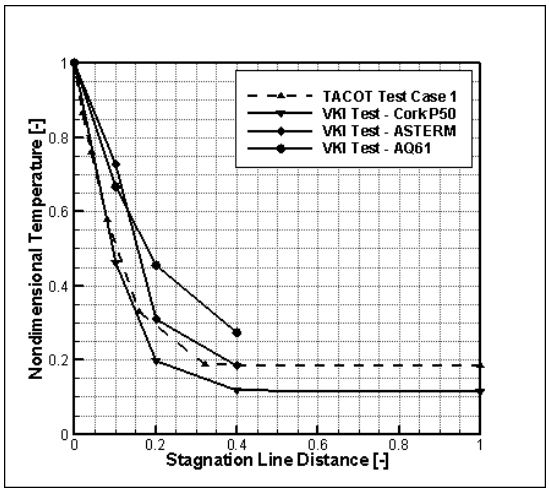

Figure 12: Temperature distribution at random time along the stagnation line for two different materials: Cork P50 tested at VKI [19] and the theoretical material TACOT [20]

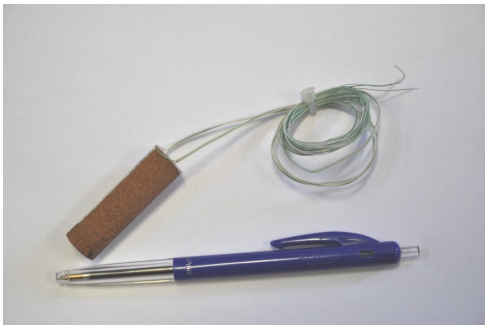

Figure 13: Thermal Plug with 2 type K thermocouples.

ferent altitudes shows in Fig. 15, the meaningful place to put the pressure holes are at 20 and 57 mm diagonally away from the stagnation point. It is intended to perform a CFD validation and these two points will be used to reconstruct the profiles along the trajectory. The scenario 4 has three pressure ports which allows to have a redundant system.

The literature survey showed no additional tubing inside the TPS is needed. Instead a pressure spool that will be fixed on the bonding structure of the TPS is sufficient to make sure the pressure pipe and the pressure path are aligned. An additional tube would also affect the recession since it will be consumed at a different rate than the ablator. This would result in disturbances in the stagnation region which can be fatal for QARMAN. Three different spool designs have been made and the design is optimized to be the spool depicted in Fig. 16.

3.2.3. XPL03

The objective of this payload is to determine the attitude and stability of QARMAN at the end of phase 2 and during re-entry (phase 3). It is planned to behave as a part of FADS system and will eventually be compared to the attitude determination subsystem of QARMAN. (In order to complete the FADS system, this payload will be combined with XPL04 and XPL05) The subject trades showed that the possible subjects are differential pressure and absolute pressure. It is decided to continue with both subjects and as the vehicle design is improved, to select one or combine the two. The performance thresholds are given in Table 5.

Data Acquisition Chain Design. The differential pressure sensor NPC-1220-015D-3-S is chosen and its circuit has been designed and built on a breadboard. An RF filter is found necessary. The Fig. 17 shows the breadboard. The data acquisition chain has been tested in VKI Minitorch test chamber at subatmospheric pressures. More details can be found in [21] and [22].

Payload Head Design. The positioning of the sensors relies on the CFD computations. A full 3D with AeroSDS is required in this case different than XPL01

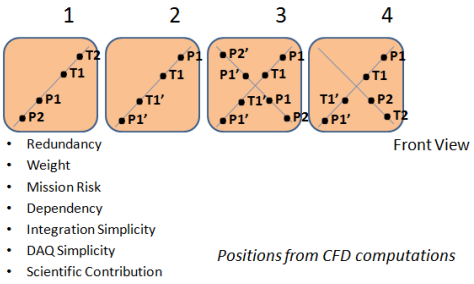

Figure 14: TPS XPL01 and XPL02 positioning scenarios.

Table 4: Desired performance thresholds of XPL02 single sensor unit.

Parameter to measure	Absolute pressure
Number of sensors	3 x pressure sensor
Total mass [g]	30
Energy consumption / piece [mW.h]	4.17
Data size per measurement [bit]	10
Total data size [kB]	1.5
Acquisition frequency [Hz]	2
Number of measurements	600
Total duration [min]	10
Response time [ms]	0.1
Power per piece [W]	0.250

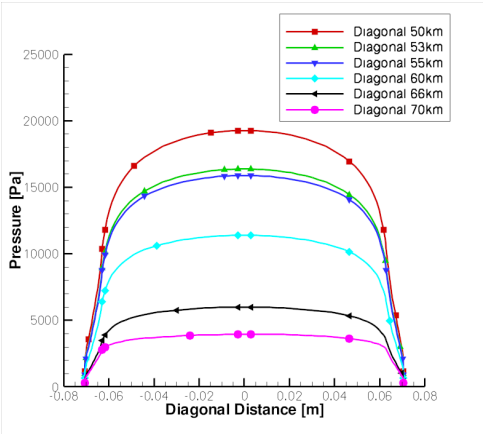

Figure 15: Diagonal pressure distributions. CFD computation of QARMAN front unit at different altitudes.

and XPL02 positioning. It also relies on the side panel TPS material (not an ablator) and the subsystem design for the tubing. The Fig. 18 shows the distributions and the intervals are determined as 10 cm and

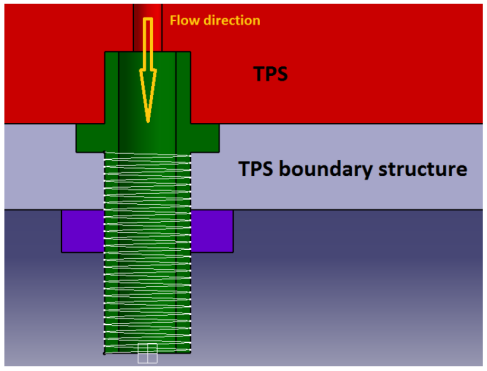

Figure 16: Optimized pressure spool design.

Table 5: Desired performance thresholds of XPL03 single sensor unit.

Parameter to measure	Absolute & differential pressure
Number of sensors	2 x pressure sensor
Total mass [kg]	0.060
Energy consumption / piece [mW.h]	840
Data size per measurement [bit]	10
Total data size [kB]	302.4
Acquisition frequency [Hz]	0.1
Number of measurements	120960
Total duration [h]	336
Response time [ms]	0.1
Power per piece [W]	0.250

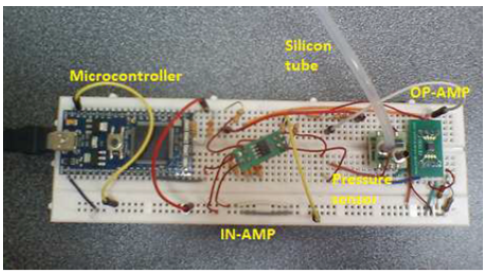

Figure 17: Breadboard for differential pressure.

22.5 cm (± 1cm) away from the front face.

The current designs split into two considering a machinable SiC TPS and a SiC based CMC material. In case of a SiC TPS, the spool depicted in Fig. 16 can already be manufactured together with the side panel which removes the necessity of fixing a second part.

In case of a CMC, a new spool design has to be made based on the previous design of XPL02 considering the junction between the two structures (TPS and side panel).

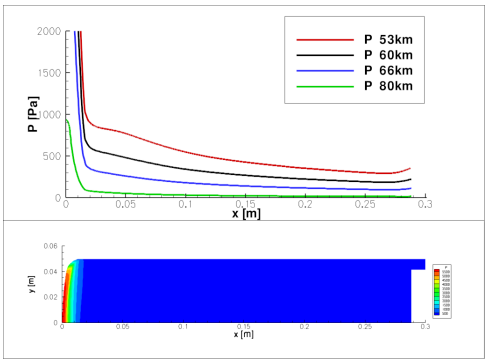

Figure 18: Side panel pressure distribution for different altitudes.

3.2.4. XPL04

The primary objective of this payload is to determine laminar to turbulent boundary layer transition with a precision (resolution) of the sensors placed. Initially, the 'skin friction' was considered as a result of the subject trades. A severe literature survey has been conducted on the theory and the application of the Preston tubes which is a means to measure the skin friction. Preston tube practically works as a Pitot probe however distributed as a thin total pressure probe close to the wall and a static pressure measurement hole. These two pressures allow, through a calibration, measuring the skin friction. However; it was concluded that such a disturbance element, even if in orders of 1mm, on the side panel will cause a significant wake and therefore extra heating. A series of experiments were conducted at VKI S4 wind tunnel with Mach 3.5 [23]. Eventually a roughness element of two angles was proposed to measure the pressure differences to obtain the skin friction. This solution is found to be risky due to the wake heating. The subject trade was continued and the application of the Turbomachinery Department of VKI is found to be the most feasible solution. They are combining temperature and pressure measurements to locate the transition on cascades. The pressure and temperature, thus the density, come by a sudden change when the boundary layer becomes turbulent. Although this is a qualitative method, it satisfies the payload objective. XPL04 will have two pressure sensors; combined with XPL03 and XPL05, it will provide the necessary and sufficient data to achieve the objective. In total a number of 4 pressure sensors are currently considered. The transition payload can work only on one side panel where the XPL03 is going to work on two facing walls. A possible combination of differential and absolute sensors may lead to a better resolution for the transition location determination. The concept is currently under design phase.

3.2.5. XPL05

The XPL05 consists of a payload to determine the temperature evolution on the side panel. The objectives are to validate CFD but also to combine the data with XPL03 in order to satisfy the objectives of XPL04 of laminar to turbulence transition detection. The traded subject is simply the 'temperature'. By concept, the temperature sensors should be put as close as possible to the pressure ports of XPL03 and XPL04 in order to determine the local density using the ideal gas law. The performance thresholds are kept the same as XPL01 as given in Table 2. The CFD shows the expected temperature range is lower than in the case of front TPS however the fitting measurement technique is again a thermocouple type K for such high temperatures and the technique is kept the same. The power, data and mass budgets allow 10 temperature sensing element for the side panels. However it should be noted that there will not be 10 pressure sensing elements on the side panel, therefore a part of thermocouples go with the pressure ports and some individually. The concept requirement is that all temperature sensing elements should be aligned to capture the temperature evolution preferably in the centerline. At the current stage, it is under discussion together with XPL03 and XPL04 whether to use two side panels or one. The optimistic scenario is to place the sensors on two facing panels, which also fits the objective of XPL03.

The data acquisition chain is identical to XPL01 and note that it will be flown and hopefully space qualified by May 2014.

4. Conclusion

Hypersonic flow testing is very challenging and complex due to the high temperature effects. The numerical and experimental methods have to be validated by real flight tests, which come with very high costs. A flight-to-ground extrapolation methodology is proposed with regard to the existing ground-to-flight extrapolation methodology. The main contribution is that it includes unconventional spacecraft geometries that are not studied up to now.

In order to make a correct flight-to-ground extrapolation one has to determine accurately the flow conditions in the ground facility since the full simulation rule is to duplicate the pressure, enthalpy and the velocity gradient at the boundary layer edge. At VKI Plasmatron, current enthalpy determination tools have significant uncertainties. To determine the enthalpy, Damköhler probes and the spectroscopy tool REDES are used.
Additionally, a velocity gradient determination procedure is proposed for the non-axisymmetric blunt shapes. Taking the example of QARMAN vehicle the proposed methodology is applied. It has been seen that the stagnation line profile of the resultant test probe geometry has a very good agreement with the non-axisymmetric hypersonic QARMAN vehicle. The discrepancy between the hypersonic QARMAN vehicle and the hypersonic sphere can be explained by the high thermal and chemical non equilibrium conditions behind the shock considering the small size of the vehicle. This aspect is still under investigation. However it can be concluded that the resultant test probe geometry provides a conservative way of testing the payloads of a non conventional vehicle.

Finally, the aerothermodynamic in flight experiments of QARMAN are presented. The payload design methodology suggests a two parts approach: payload head design and the measurement chain design. The completed breadboard test results are shown to be consistent with other independent measurements. Payload head designs are currently ongoing however the first design of the thermal plug (XPL01) is presented.

Acknowledgments

The authors are thankful to Dr. Cem O. Asma for his sincere interest and kind guidance. The authors are grateful to Mr. Pascal Collin for his unique dedication to the operation of the VKI Plasmatron facility.

References

[1] Qb50 project, www.qb50.eu, last accessed: 10.02.2014.
[2] J. A. Fay, F. R. Riddell, Theory of stagnation point heat transfer in dissociated air, in: VKI, An Introduction to Hypersonic Aerodynamics 13 p(SEE N 90-13334 05-02), 1958.
[3] A. Kolesnikov, Extrapolation from high enthalpy tests to flight based on the concept of local heat transfer simulation, RTO AVT Course on "Measurement Techniques for High Enthalpy and Plasma Flows", Rhode-Saint-Genese, Belgium (October 1999).
[4] F. Panerai, Aerothermochemistry characterization of thermal protection systems, Ph.D. thesis, Universite degli Studi di Perugia and von Karman Institute for Fluid Dynamics (2012).
[5] H. W. Krassilchikoff, Procedures for the determination of the cold copper catalycity, Master's thesis, von Karman Institute for Fluid Dynamics, vKI-PR2006-18 (2006).
[6] G. de Croombrugghe, Investigation of gas surface interactions in plasma wind tunnels for catalycity characterization, Master's thesis, von Karman Institute For Fluid Dynamics, vKI PR 2012-01 (2012).
[7] M. Marotta, Investigation on the driving phenomena characterization gsis in plasmatron facility, Master's thesis, von Karman Institute for Fluid Dynamics, vKI PR 2011-17 (2011).
[8] D. G. Fletcher, Nonintrusive diagnostic strategies for arcjet stream characterization, RTO AVT Course on Measurement Techniques for High Enthalpy and Plasma Flows, Rhode-Saint-Genese, Belgium (October 1999).
[9] P. S. Lopez, Non-intrusive real time enthalpy determination in plasma flows, Tech. Rep. SR 2012-41, von Karman Institute for Fluid Dynamics (2012).
[10] J. P. P. Leite, Assessment of ground testing conditions for in-flight experiment development, Master's thesis, PR2013-08, von Karman Institute for Fluid Dynamics, Rhode-Saint-Genese (2013).
[11] B. Bachmann, R. Kozakov, G. Gott, K. Ekkert, J.-P. Bachmann, J. Marques, H. Schopp, D. Uhrlandt, J. Schein, High-speed three-dimensional plasma temperature determination of axially symmetric free-burning arcs, JOURNAL OF PHYSICS D: APPLIED PHYSICS 46.
[12] J. Boison, A. Curtiss, An experimental investigation of blunt body stagnation point velocity gradient, ARS Journal (1959) 130–135.
[13] H. Olivier, Influence of the velocity gradient on the stagnation point heating in hypersonic flow, Shock Waves 5 (1995) 205–216.
[14] L. Lees, Recent developments in hypersonics, ARS Semi-Annual Meeting, San Francisco, California, 1957.
[15] E. V. Zoby, E. M. Sullivan, Effects of corner radius on stagnation-point velocity gradients on blunt axisymmetric bodies, Tech. Rep. NASA-TM-X-1067, NASA (1965).
[16] J. C. Ellison, Experimental stagnation point velocity gradients and heat transfer coefficients for a family of blunt bodies at mach 8 and angles of attack, Tech. Rep. TN D-5121, NASA Langley (1969).
[17] E. V. Zoby, Empirical stagnation point heat transfer relation in several gas mixtures at high enthalpy levels, Tech. Rep. TN D-4799, NASA Langley (1968).
[18] J. Wertz, W. Larson, Space Mission Analysis and Design, Microcosm Press, 1999.
[19] G. Bailet, Feasibility analysis and conceptual design of an atmospheric re-entry cubesat demonstrator, Master's thesis, PR2011-02, von Karman Institute for Fluid Dynamics, Rhode-Saint-Genese (2011).
[20] J. Lachaud, A. Martin, I. Cozmuta, B. Laub, Ablation workshop test case,, 4th Ablation Workshop, Albuquerque, New Mexico, 2011.
[21] I. E. Akyol, Design of data acquisition subsystem of qarman payloads and validation in plasma facilities-hardware, Tech. rep., SR 2013-16, von Karman Institute for Fluid Dynamics (2013).
[22] R. T. Nadal, Design and testing of the pressure payloads and data acquisition of qarman cubesat, Master's thesis, Universite de Liege, von Karman Institute for Fluid Dynamics (2013).
[23] N. Verstappen, Skin friction measurements with a preston and

inclined hole probe in the s-4, Tech. rep., SR 2008-04, von Karman Institute for Fluid Dynamics (2008).

Post-flight Reconstruction Using Conventional and Novel Instrumentation

Bart Van Hove

Aeronautics and Aerospace Department, von Karman Institute for Fluid Dynamics, Belgium, vanhove@vki.ac.be

Supervisor: Olivier Chazot

Professor and Head of the Department of Aeronautics and Aerospace, Aeronautics and Aerospace Department, von Karman Institute for Fluid Dynamics, Belgium, chazot@vki.ac.be

Supervisor: Özgür Karatekin

Royal Observatory of Belgium, Belgium, o.karatekin@observatory.be

University Promotor: Chris Lacor

Professor, VUB Dept. Mechanical Engineering, Belgium, chris.lacor@vub.ac.be

Abstract

Apart from their value for planetary exploration, vehicles landing on the surface of other planets present a rare opportunity to investigate vehicle performance and atmospheric conditions. We developed trajectory and atmosphere reconstruction tools that attempt to fully exploit in-flight measurements. Both conventional and novel measurement systems have been considered. In particular, Flush Air Data Systems (FADS) are currently making their entrance on planetary exploration vehicles to Mars. We present methodology to derive flow angles and atmospheric density from such measurements, apply it to a hypersonic wind tunnel probe and consider ESA EXPERT as a case study to quantify the uncertainty on FADS reconstructed quantities during an Earth entry. We conclude that an accurate estimate of the atmospheric density is feasible and suggest attainable objectives for the VKI Longshot wind tunnel to serve as a FADS calibration facility.

Keywords: 6-DOF, reconstruction, hypersonic, atmosphere, trajectory, FADS, Flush Air Data System, IMU, Inertial Measurement Unit, EDL, entry, EXPERT, Longshot, simulation.

1. Introduction

Successfully landing vehicles on other planets is a challenging and rare achievement. Therefore in-flight measurements must be fully exploited to gain knowledge on the vehicle's behavior and the planetary environment. For this purpose, we develop tools for the reconstruction of trajectory and atmospheric profiles during Entry, Descent and Landing (EDL) of planetary entry vehicles. Entry vehicles are instrumented for real time guidance (e.g. reaction control systems and parachute deployment) and for post-flight reconstruction of trajectory parameters, aerodynamic coefficients and atmospheric conditions. These reconstructed quantities are closely coupled, for example aerodynamic coefficients are a function of angle of attack, aerodynamic forces, velocity and atmospheric density. Another example is the atmospheric pressure, which is typically derived from atmospheric density and vehicle altitude.

Entry vehicles are conventionally equipped with accelerometers and gyroscopes. By integrating those inertial measurements, an accurate 6 degree of freedom (6-DOF) trajectory can be obtained. However, because the inertial sensors are confined to the vehicle interior, deriving exterior quantities such as the atmospheric density requires modeled or estimated information. The density is most often estimated from a measured deceleration and predicted drag coefficient. This makes the drag coefficient an estimated input instead of a reconstructed output, and conflates the uncertainty on the density with that on the drag coeffi-

cient. Other exterior quantities include angle of attack and side slip angle.

In recent years, some vehicles are instrumented with an additional set of sensors directly exposed to the flow around the vehicle (e.g. Space Shuttle, EXPERT, MSL, ExoMars). This grid of pressure sensors integrated in the heat shield is commonly called a Flush Air Data System (FADS) and allows the flow angles and atmospheric density to be estimated independently of predicted aerodynamic behavior. However, FADS systems rely on surface pressure distribution and shock layer flow models. These can be developed from analytical relations, wind tunnel testing and computational fluid dynamics (CFD).

The PhD research presented here aims to accurately reconstruct atmospheric profiles during EDL exploiting any in-flight measurements available. The current focus is on hypersonic/supersonic entry up to parachute deployment on Mars and Earth. Density is a quantity of particular interest because atmospheric pressure and temperature are derived from it, and because density is used to normalize reconstructed aerodynamic forces and moments for comparison with ground predictions. The arrival of a novel in-flight measurement system (FADS) warrants a fresh look at reconstruction strategies and uncertainty quantification, as well as methods to optimally combine results from various reconstruction strategies.

This thesis project is part of the preparatory work for ESA's set of ExoMars missions in 2016-2018. The recently approved 2016 ExoMars EDM (EDL Demonstrator Module) aims to be Europe's first successful landing on the surface of Mars. Royal Observatory of Belgium PhD advisor Özgür Karatekin is co-PI of the ExoMars EDM science team (AMELIA) responsible for extracting scientifically valuable information from in-flight EDM measurements, such as atmospheric profiles. ExoMars EDM will enter the Martian atmosphere during dust season, presenting the first opportunity to study dust impact on the atmospheric conditions in-situ. The EDM heat shield is instrumented with FADS sensors from which atmospheric density can be derived more accurately than from conventional in-flight measurements.

The work presented here covers the development and validation of entry reconstruction and simulation tools for high velocity planetary entry. Both conventional inertial measurements and novel heat shield instrumentation (FADS) have been considered. Our reconstruction tools utilizing conventional inertial measurements have been applied to in-flight data from Mars Phoenix Lander (25 May 2008), and validated against independent reconstructions. Currently lacking in-flight measurements, we have applied part of our FADS methodology to a wind tunnel model at Mach 14 in the VKI Longshot wind tunnel. These tests were performed with nitrogen gas under operating conditions similar to the ESA EXPERT trajectory. Finally, we applied the complete FADS methodology to an EXPERT case study and quantified the required accuracy of the FADS modeling and wind tunnel environment for application to the EXPERT FADS instrumentation.

2. Reconstruction from conventional measurements

2.1. Approach

Conventional in-flight measurements are inertial acceleration and angular velocity measurements by accelerometers and gyroscopes contained in one or several inertial measurement units (IMU). Together, the accelerometers and gyroscopes constrain a 6-DOF (translation and rotation) trajectory that can be reconstructed by integration. In a second step, using the trajectory and some assumptions, atmospheric conditions are derived.

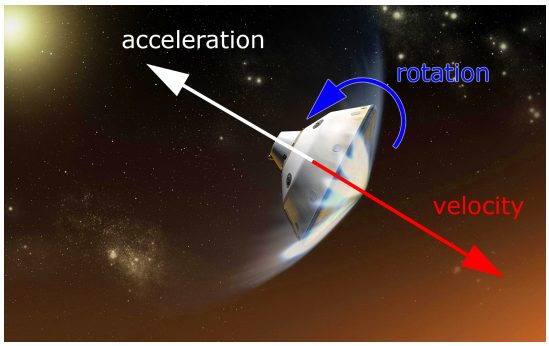

Figure 1: Hypersonic entry (adapted NASA artist concept)

The atmosphere reconstruction starts from an atmospheric density estimate ρ_∞ obtained from the axial acceleration a_{aero} measured in-flight and aerodynamic drag coefficient C_D predicted on ground:

$$\rho_\infty(h) = 2\frac{m \cdot |\vec{a}_{aero}|}{C_D \cdot S_{ref} \cdot |\vec{v}_{rel}|^2} \quad (1)$$

This method conflates the substantial uncertainty on the aerodynamic drag coefficient with that on the reconstructed density, but is the only option to derive

atmospheric conditions from IMU data. FADS instrumentation would provide a density estimate independently of aerodynamic modeling. The density estimate ρ_∞ is then integrated over altitude assuming hydrostatic equilibrium, to derive atmospheric pressure p_∞. The ideal gas law then combines density ρ_∞ and pressure p_∞ to derive atmospheric temperature T_∞.

$$p_\infty(h) = p_\infty(h_0) - \int_{h_0}^{h} g \cdot \rho_\infty \cdot dh \tag{2}$$

$$T_\infty(h) = \frac{\mu \cdot p_\infty}{R \cdot \rho_\infty} \tag{3}$$

Notice that to reconstruct atmospheric conditions, the trajectory needs to be accurately known. In the above equations, altitude h, aerodynamic acceleration $\vec{a}_{aero}$ and velocity relative to the atmosphere $\vec{v}_{rel}$ are required. Also vehicle mass and reference surface area.

2.2. *Validation with Mars Phoenix dataset*

The above reconstruction strategy has been employed for the majority of planetary exploration missions [1][2][3][4]. We applied our code to the Mars Phoenix Lander dataset and compared our reconstructed trajectory and atmosphere to reconstructions by independent authors. The Mars Phoenix dataset is representative of a conventionally instrumented entry vehicle and available on the Planetary Data System [5].

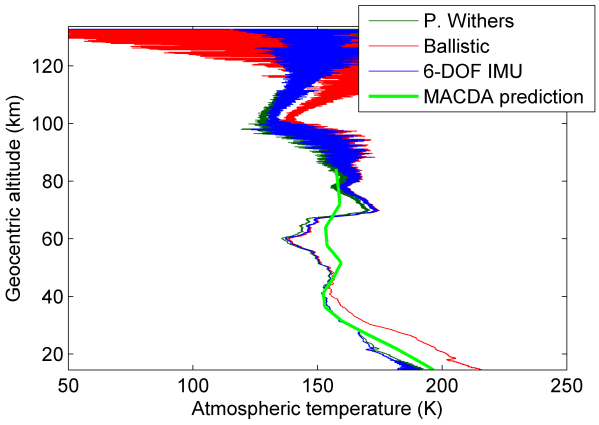

Figure 2: Phoenix reconstructed temperature profiles

We evaluate our 6-DOF reconstructed trajectory by comparing key quantities at parachute deployment in Table 1. Bias errors or discrepancies are integrated over the entire time interval from entry interface to parachute opening to yield maximal values at this final time instant. Our trajectory matches well with an independent NASA reconstruction [2]. Figure 2 shows two of our atmospheric temperature reconstructions: one assuming a 3-DOF head-on ballistic trajectory (red, accelerometer data only) and one utilizing the complete 6-DOF IMU dataset (blue, including attitude measurements by gyroscopes). The ballistic assumption has a significant impact on the reconstruction because Phoenix trimmed at a higher than expected angle of attack, which we will discuss below. Our temperature reconstruction matches great with an independent result [1] and does not deviate far from a climate model prediction assimilated with orbital observations (Mars Analysis Correction Data Assimilation or MACDA).

Table 1: Phoenix reconstructed trajectory at parachute deployment

	units	NASA	This study
Time	(s)	227.8	228.0
Altitude	(km)	13.3	13.9
Velocity	(m/s)	387.6	387.9
α_T (°)	4.73	4.65	

3. Planetary entry simulator

3.1. *Development*

Given the limited amount of in-flight measurements, especially for entries on planets other than Earth, a trajectory simulator was developed to produce our own datasets. Additionally, this will allow us to quantify the impact of atmospheric conditions (seasons, dust loading, wind velocities) and vehicle characteristics (instrumentation, geometry, aerodynamics). The simulator is a 6-DOF trajectory calculator for vehicles without reaction control mechanisms such as Phoenix and ExoMars EDM. Complete support for aerodynamics and a large number of flight mechanical and aerodynamic conventions has been implemented. Appropriate equations of motion are integrated with a 4th order Runge Kutta routine.

The simulator code was validated by comparing its outputs with those of POST II (Program to Optimize Simulated Trajectories). POST has a development history spanning many decades and has been used in the design of most NASA Mars missions. In subsequent comparisons, features of increasing fidelity and complexity were added. Figure 3 shows the Z acceleration sensed by the vehicle's accelerometers and the vertical pitch rate, both matching to machine precision with POST II results produced by the NASA

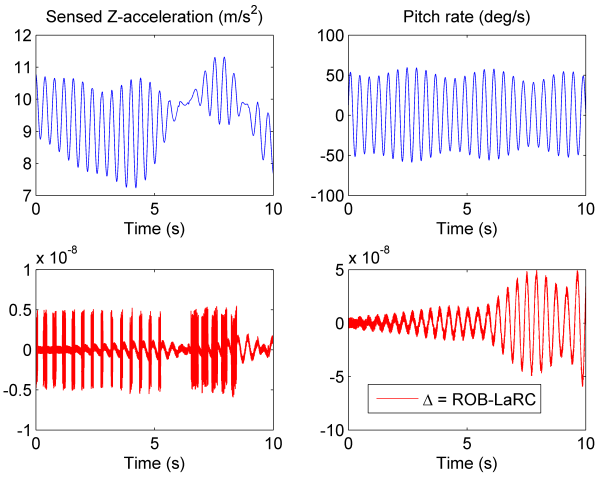

Figure 3: Simulator outputs versus LaRC POST II: nominal value (top) and absolute difference (bottom)

Langley Research Center (LaRC). This particular test case involved complex aerodynamics including static and dynamic forces and moments, off-center center of gravity and aerodynamic reference locations, an ellipsoid planet reference surface and numerous navigational coordinate conventions.

In Figure 2, assuming a ballistic trajectory was shown to have a significant impact on the reconstructed temperature profile. Phoenix was in fact designed as a ballistic capsule, but unexpectedly trimmed at a non-zero angle of attack. Using the simulator, probable causes for this can be identified. Specifically, an off-center center of gravity (CG) away from the vehicle symmetry axis or a bias error in the prediction of the aerodynamic moment coefficient C_m can both contribute to a trim angle change. In Figure 4, the total angle of attack reconstructed from the 6-DOF Phoenix IMU dataset (blue) is compared to various trajectory simulations.

The Phoenix aerodynamic database published by NASA [6] was used to describe vehicle behavior. The resulting trajectory simulation (black) reveals two known aerodynamic instabilities at 70 and 110 seconds, but a near zero trim angle during the rest of the high velocity entry. We produced two additional simulations (red, green) in which the CG was shifted by a realistic value of 2 mm, and in one case a 3-sigma adder error imposed on the aerodynamic moment prediction. The latter simulation corresponds best to the reconstructed angle of attack and suggests that these causes likely contributed to the observed trim angle.

This analysis emphasizes the importance of accurate knowledge of vehicle characteristics and aerodynamics for correct interpretation of in-flight measurements. We have also demonstrated our capacity to assess the impact of uncertainty/error on such information by performing trajectory simulations.

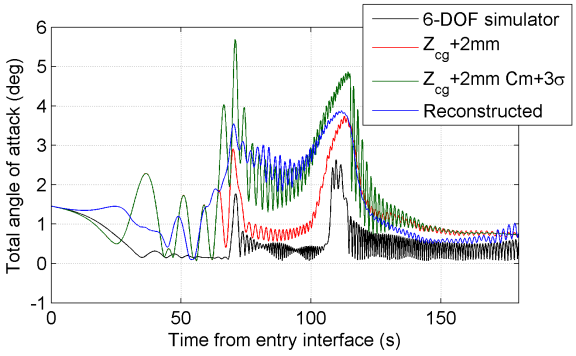

Figure 4: Phoenix total angle of attack: reconstruction and simulations

4. FADS methodology

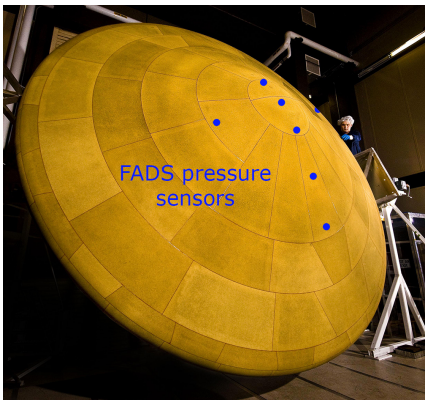

Figure 5: NASA MSL with FADS instrumented heat shield

Conventional inertial measurements (IMUs) allow for an accurate trajectory reconstruction, but are confined to the vehicle interior. Flush Air Data System (FADS) instrumentation measures the pressure distribution on the heat shield surface. It thus provides direct information on the flow field behind the bow shock (the shock layer). The recently successful NASA MSL mission (Mars Science Laboratory, 2012) is the only planetary exploration vehicle to date with an instrumented heat shield (Figure 5). The next will be ESA's ExoMars EDM demonstrator (2016).

From the measured surface pressure distribution, the direction of the oncoming flow (angle of attack

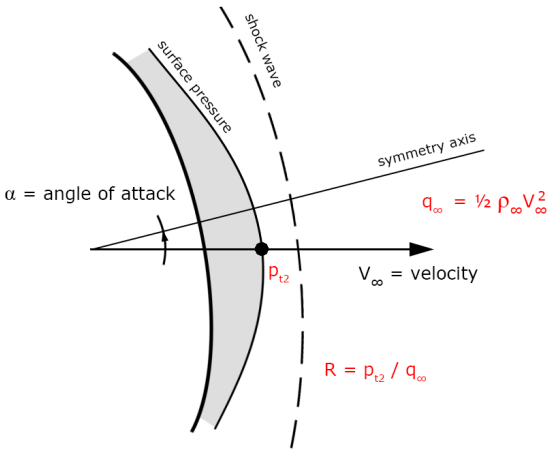

Figure 6: FADS density reconstruction method

α and side slip angle β), as well as the local maximum pressure or stagnation pressure p_{t2} can be derived. The stagnation pressure depends on the atmospheric density upstream of the shock wave, and is of interest for atmosphere reconstruction.

4.1. Approach

Our method for reconstructing atmospheric density from heat shield surface pressure measurements consists of three steps (Figure 6). The vehicle orientation relative to the oncoming flow is illustrated by the symmetry axis and velocity vector. The surface pressure distribution recorded by FADS sensors contains a local maximum equal to the stagnation pressure p_{t2}. The stagnation pressure is related to the dynamic pressure q_∞ upstream of the shock wave. The shock wave pressure ratio $R = p_{t2}/q_\infty$ allows us to derive this dynamic pressure. Finally, atmospheric density ρ_∞ is obtained by multiplying the dynamic pressure by $2/V_\infty^2$. The velocity magnitude is thus required independently, e.g. from inertial measurements.

The derivation of atmospheric density from FADS measurements requires a **surface pressure distribution** (to obtain α, β and p_{t2}) and a **shock wave pressure ratio** model (to obtain q_∞ and subsequently ρ_∞). The aerodynamic drag coefficient is not required as was the case for reconstruction from IMUs only. In fact, it could now be reconstructed for verification of pre-flight predictions. We used modified Newtonian flow theory to model the **surface pressure distribution** on hypersonic vehicles at high Mach numbers. It neglects viscous effects such as the boundary layer, but should be accurate above Mach 5. The surface pressures p_i at the FADS pressure port locations are then approximated by

$$p_i = (p_{t2} - p_\infty) \cdot cos(\theta_i)^2 + p_\infty \tag{4}$$

with θ_i the incidence angle between the flow and the heat shield surface and calculated from the pressure port location, angle of attack α and side slip angle β. The known pressure port locations are expressed by cone angles λ_i and clock angles ϕ_i.

$$\theta_i = f(\lambda_i, \phi_i, \alpha, \beta) \tag{5}$$

Atmospheric pressure p_∞ is small compared to p_{t2} and may be estimated or neglected. The solved for conditions are then stagnation pressure p_{t2} and flow angles α and β. For this the above equations must be inverted and pressure model fitted to the FADS measurements, which are usually greater in number than the three solved for variables. For this purpose an iterative non-linear least squares solver was developed, partly during a stay at NASA Langley.

A common analytical relation for the **shock wave pressure ratio** is the Rayleigh pitot tube formula:

$$R = \frac{p_{t2}}{q_\infty} = \frac{2}{\gamma M_\infty^2} \left(\frac{(\gamma+1)^2 M_\infty^2}{4\gamma M_\infty^2 - 2(\gamma-1)} \right)^{\frac{\gamma}{\gamma-1}} \left(\frac{1-\gamma+2\gamma M_\infty^2}{\gamma+1} \right) \tag{6}$$

with M_∞ the Mach number. This relation is derived for a constant heat capacity ratio $\gamma = c_p/c_v$ which is appropriate when gas temperatures are low. Such conditions are called *cold gas* or *perfect gas*. The Rayleigh pitot tube formula can be simplified in the limit of very high Mach numbers:

$$R \approx \left(\frac{(\gamma+1)^2}{4\gamma} \right)^{\frac{\gamma}{\gamma-1}} \left(\frac{4}{\gamma+1} \right) \tag{7}$$

In planetary entry scenarios, post-shock temperatures are very high and γ varies significantly through the shock wave. A more accurate model including high temperature effects was developed and consists of solving the shock wave conservation equations (mass, energy, momentum) while accurately calculating high temperature gas properties with the Mutation library developed by T. Magin [7].

Figure 7 shows our numerical predictions of the shock wave pressure ratio for air on a velocity-altitude

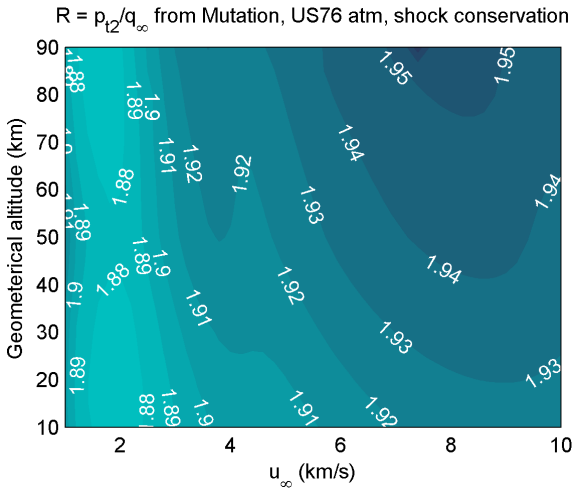

Figure 7: Shock wave pressure ratio model with high temperature effects

grid designed for fast interpolation during reconstruction. The atmospheric conditions on the velocity-atltitude grid were provided by the standard US76 atmosphere. We will show later that this results in negligible errors in application to realistic non-standard atmospheres. These numerical results differ significantly from the cold gas Rayleigh pitot tube solution of 1.84. A similar calculation will later be performed for CO_2 on Mars, expecting even larger deviations.

4.2. Application to wind tunnel model

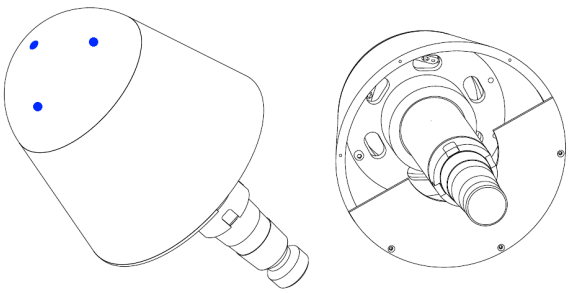

Figure 8: Hemispherical FADS probe

In the absence of in-flight measurements, we applied our FADS methodology in a wind tunnel test campaign. The VKI Longshot is a hypersonic Mach 14 wind tunnel with low to moderate gas temperatures. It is suitable to test our pressure distribution model with non-linear least squares solver to determine flow angles and stagnation pressure. The density derivation currently cannot be validated in this facility as an independent density measurement is not available. Testing was performed with a hemispherical probe equipped with five pressure sensors, three of which are indicated in blue on Figure 8. Currently only nitrogen gas (Earth) has been used. Utilizing Longshot's CO_2 (Mars) capabilities including an independent density measurement would allow us to validate the FADS density derivation. However, the derivation of flow angles and stagnation pressure does not depend significantly on the choice of gas and does not require wind tunnel density to be known.

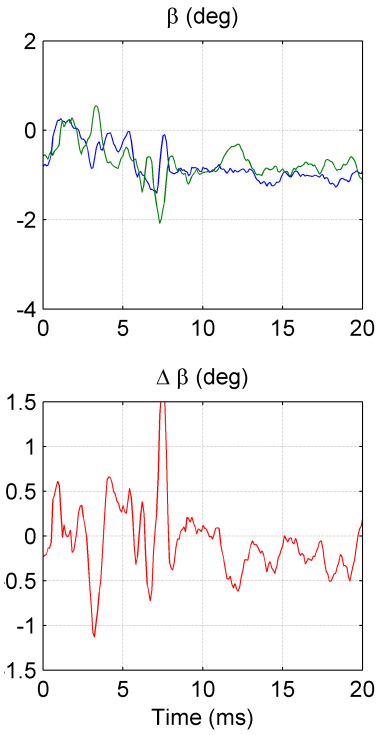

Figure 9: Repeatability test for side slip angle

The probe was positioned near the center of the uniform flow jet and recorded pressure signals. Using the least-squares inverted modified Newtonian flow equation, angle of attack α and side slip angle β were reconstructed from the FADS measurements. These can be compared with the known flow angles at which the model was set up. A range of α and β positions was tested. Figure 9 shows that wind tunnel repeatability with identically set up models is very satisfactory.

The wind tunnel stagnation pressure is routinely measured by a permanent reference probe. When the FADS probe is installed head-on into the flow, its central pressure tap should register the same stagnation pressure value. Instead, the FADS probe consistently measured a 3% lower stagnation pressure, Fig-

Table 2: Monte Carlo input uncertainties Longshot FADS calibration

input	3-σ	source
FADS pressures	2%	estimate of sensor accuracy
tunnel p_∞	100%	experimental mismatch
tunnel p_{t2}	3%	mismatch FADS / reference probes
FADS model α	0.006°	experimental setup
FADS model β	0.0833°	experimental setup
FADS sensors λ,ϕ	0.1°	estimated manufacturing precision

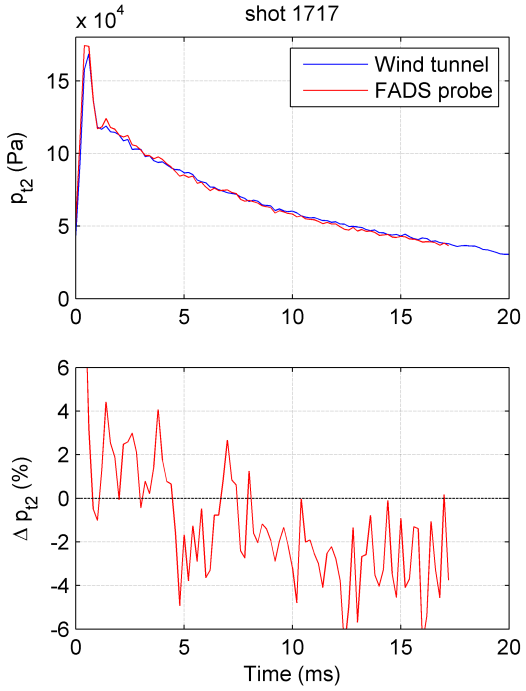

Figure 10: Stagnation pressure discrepancy

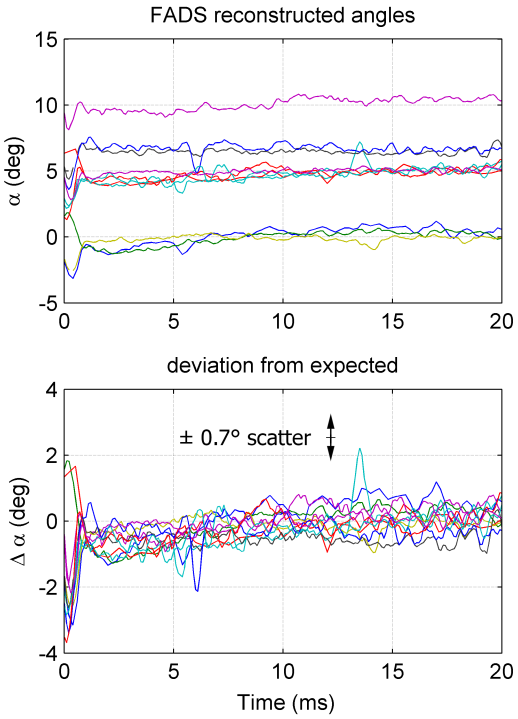

Figure 11: FADS reconstructed angle of attack

ure 10. The cause of this discrepancy is as yet unknown, the difference is outside the expected sensor accuracy range of ±2%. In the EXPERT case study below, we will show that a 3% accurate stagnation pressure match still permits a reasonably accurate reconstruction of density during entry.

The flow angle reconstruction contains more significant anomalies. The probe was carefully set up at various angles of attack (vertical plane) and side slip (horizontal plane). Figures 11 and 12 show the reconstructed flow angles (top) and their deviation from the expected angles at which the probe was installed (bottom). After 10 ms, the transient effects due to flow establishment and probe recoil have ceased. In the remainder of the 20 ms test time, the reconstructed angles of attack are scattered about the expected values by 0.7°, while the side slip angles have twice the scatter and a negative bias of about 1°. This is likely due to a single pressure sensor on the side of the FADS probe with unsatisfactory performance.

Equipping the probe with more sensors would reduce the impact of a single sensor and facilitate the identification of faulty sensors. To assess the benefit of increasing the number of sensors on the wind tunnel probe, a Monte Carlo analysis was run to quantify the uncertainty range within which the Longshot wind tunnel can constrain a FADS surface pressure distribution model. This correspond to the model uncertainty

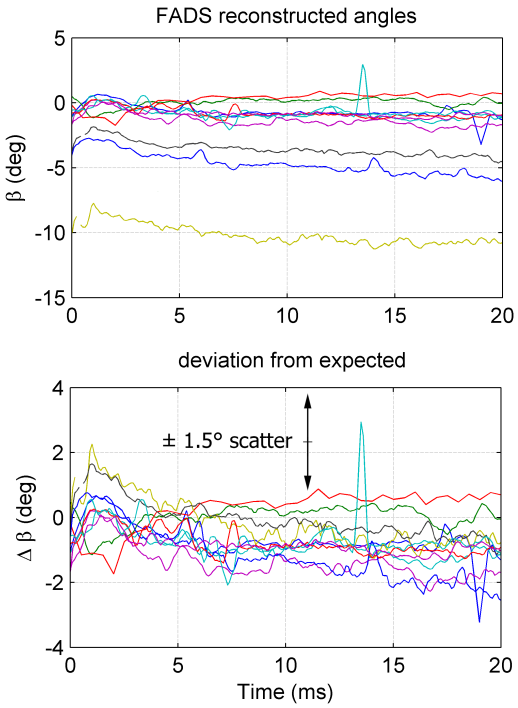

Figure 12: FADS reconstructed side slip angle

on α, β and p_{t2} when reconstructed by a surface pressure distribution model calibrated by or produced with the wind tunnel.

Table 2 lists the input uncertainties that went into the analysis. The angles λ and ϕ represent the pressure tap locations on the FADS probe and depend only on the manufacturing precision of the probe. The stagnation pressure accuracy was based on the mismatch mentioned above. The wind tunnel static pressure p_∞ has a negligible impact in the surface pressure distribution model as it is much smaller than the stagnation pressure. Its uncertainty on the other hand is very high, as an investigation is currently ongoing on a mismatch between expected and recently measured values. Uncertainty on the probe's surface pressure measurements is set to the sensor accuracy.

Figures 13 and 14 show the resulting uncertainty on the reconstructed flow angles from FADS instrumentation, given the input uncertainties in Table 2. Remember that these correspond to the accuracy with which the wind tunnel can constrain a surface pressure model. When applying the model to an actual entry reconstruction[1], these values will be conflated

[1] At appropriate free stream flow conditions, i.e. similar to those in the wind tunnel

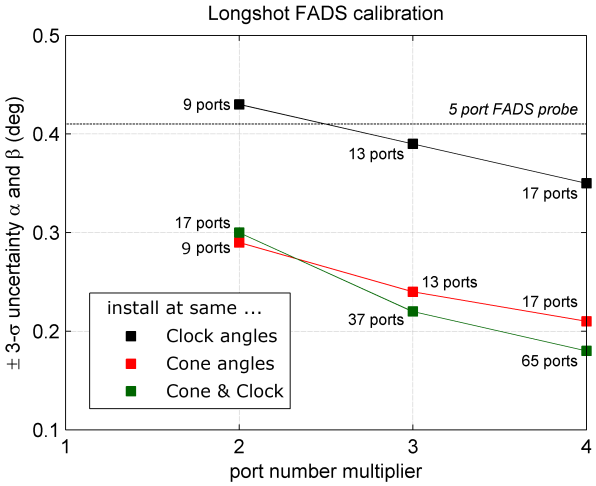

Figure 13: Flow angle uncertainty of Longshot calibrated FADS

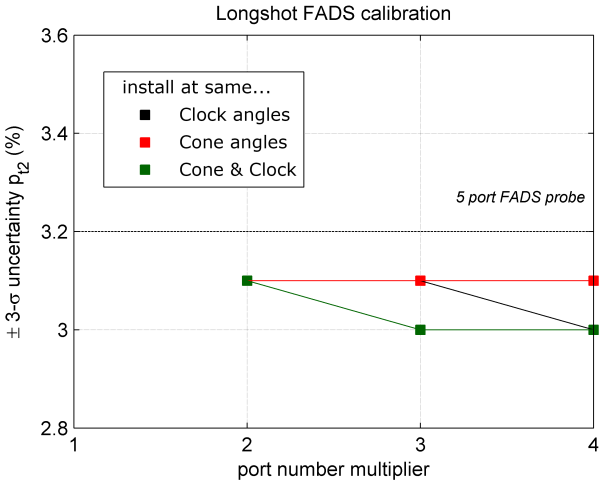

Figure 14: Stagnation pressure uncertainty of Longshot calibrated FADS

with other uncertainty sources, e.g. from vehicle sensor or trajectory parameter reconstruction.

The pressure port layout on the hemispherical FADS probe consisted of a central stagnation point sensor and four equally spaced off-stagnation sensors, at cone angles $\lambda = 45°$ away from the probe symmetry axis (4+1 = 5 sensors in total). Figure 13 shows the impact of multiplying the number of off-stagnation sensors along certain directions. For example doubling the number of off-stagnation sensors by installing additional sensors at the same clock angles, means placing an additional sensor between every off-stagnation sensor and the stagnation point (4+4+1 = 9 sensors). Conversely, installing at the same cone an-

gles would imply an additional sensor between every two off-stagnation sensors, resulting in 9 sensors positioned on a circumferential circle. Conserving both cone and clock angles refers to the superposition of both examples, resulting in a total of 8+8+1 = 17 sensors.

Installing more sensors could halve the reconstructed flow angle uncertainty (Figure 13). Installing them at the same cone angles is most beneficial. That is, additional sensors should all be installed at $\lambda = 45°$ to improve flow angle reconstruction. This makes sense, as the sensors farthest away from the stagnation point are most sensitive to flow angularity. The current FADS probe should be able to reconstruct the flow angles to within 0.4°, which is significantly below the scatter observed in the experimental results shown before. This supports a misbehaving sensor or may suggest flow irregularities[2] responsible for the scatter.

On the other hand, the accuracy with which a FADS surface pressure model produced in the wind tunnel would reconstruct stagnation pressure, does not benefit from additional sensors (Figure 14). It depends mainly on the accuracy with which the wind tunnel reference value is measured. This should be interpreted conversely as a good thing: the flow angle reconstruction does not suffer from a poorly known reference stagnation point measurement.

5. EXPERT case study

Our FADS methodology requires a surface pressure distribution model, and a shock wave pressure ratio model. In the previous section we applied the surface pressure model (modified Newtonian flow) to a FADS probe in the VKI Longshot wind tunnel, and concluded we could constrain the model by no less than 0.4° on the reconstructed flow angles and 3% on the reconstructed stagnation pressure. We also lacked the facilities to validate the shock wave pressure ratio model including high temperature effects described before. We will now apply our pressure ratio model to a simulated EXPERT entry, and assess the impact of the wind tunnel uncertainties on the reconstruction of that entry.

EXPERT is ESA's soon to be launched hypersonic flight testbed, and comes equipped with a similar FADS pressure tap layout as used in our wind tunnel testing (Figure 15). Also, its trajectory is planned

[2]The wind tunnel stagnation pressure is known to vary slightly throughout the uniform flow jet [8]

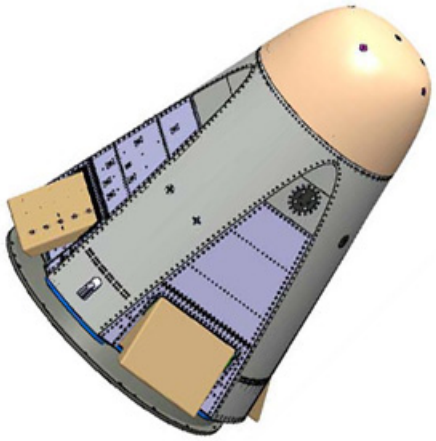

Figure 15: ESA hypersonic testbed EXPERT

to cross the Longshot flow conditions (Figure 16). We obtained a simulation of EXPERT's trajectory and simulated FADS pressure signals using our modified Newtonian flow model and pressure ratio model based on shock conservation equations and high temperature gas properties calculated by Mutation. Multiple pressure ratio models were then employed to reconstruct the a priori known atmospheric density back from the simulated signals. In the simulated case, the Mutation model naturally retrieves the density back exactly. This does not affect any conclusions but excludes independent validation.

To complement the previously described wind tunnel investigation, we performed a Monte Carlo analysis to predict realistic uncertainties on an EXPERT entry reconstruction utilizing a surface pressure model constrained by Longshot wind tunnel experiments. The uncertainty on the wind tunnel derived FADS model was conflated with realistic vehicle sensor and trajectory reconstruction uncertainties.

Figure 17 shows shock wave pressure ratios predicted along the EXPERT trajectory. The perfect gas Rayleigh pitot tube formula (PG) and its high Mach number approximation (PG high Mach) vary minimally with altitude and assume cold gas conditions. By contrast, the two remaining models include high temperature effects. They are our own model using Mutation, and a polynomial expression produced independently by other authors [9]. Notice the convergence with the (Mach dependent) perfect gas prediction at about Mach 4. At Mach 12 and above, high temperature effects account for a 4% to 6% departure from cold gas predictions. Our numerical solutions

Table 3: Monte Carlo input uncertainties EXPERT FADS

input	3-σ	source
FADS pressures	1.5%	EXPERT sensor accuracy
FADS sensors λ,ϕ	0.1°	estimated manufacturing precision
Pressure ratio model	1%	1/4th cold gas error
IMU V_∞	1%	typical reconstruction error
IMU p_∞	15%	typical reconstruction error
IMU altitude	600 m	typical reconstruction error

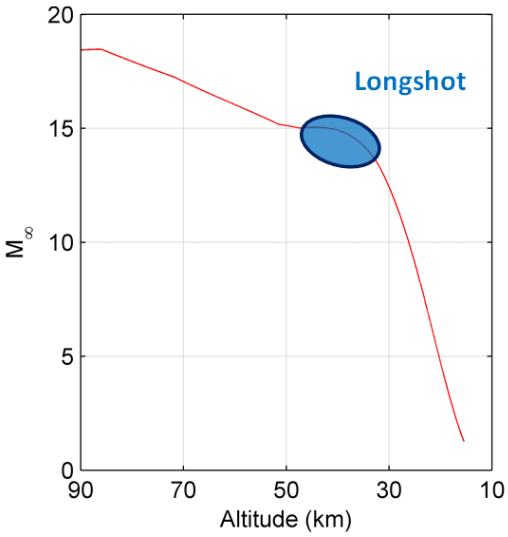

Figure 16: Mach number EXPERT trajectory

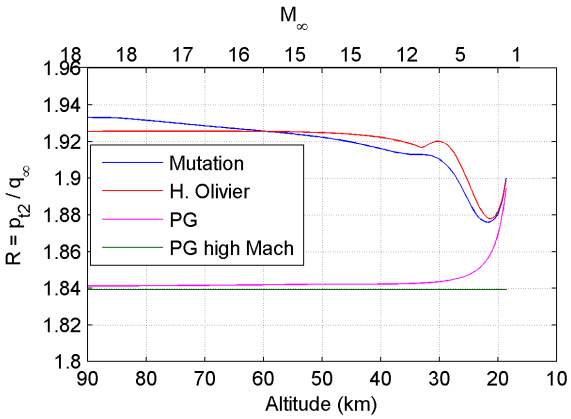

Figure 17: Various shock wave pressure ratio predictions along EXPERT trajectroy

don't deviate far from those of other authors.

Recall that our pressure ratio model was interpolated on an altitude-velocity grid based on the standard US76 atmosphere. We imposed a sinusiodal density disturbance on the density-altitude profiles used to simulate the FADS signals, to quantify the error inflicted by the standard atmosphere interpolation grid. Figure 18 shows this error to be negligible. The overall conclusion is that the high temperature effects are significant and fast interpolation on pre-calculated solutions is feasible.

Finally, we ran a Monte Carlo analysis to estimate realistic uncertainties on reconstructed quantities from EXPERT's FADS system. The analysis is performed at the point of the EXPERT trajectory that corresponds to the Longshot operating conditions. The final uncertainty depends on the accuracy of the surface pressure distribution and shock wave pressure ratio models, that of the reconstructed trajectory (e.g. altitude and velocity) and the accuracy of EXPERT's FADS instrumentation. Table 3 describes this part of these input uncertainties. The high temperature pressure ratio model has an estimated uncertainty of 1%, about a quarter of the error made by neglecting high temperature effects, which is known to be the main error made by perfect gas models.

Not listed in Table 3 are the uncertainties associated with the surface pressure distribution model. For these, two alternative sets are presented in Table 4. The first corresponds to our current efforts using the VKI Longshot to constrain the surface pressure model. The other is a hypothetical set of uncertainties we suggest as an attainable obective for future wind tunnel FADS calibration. In the objectives, the stagnation pressure uncertainty is brought down to the pressure sensor accuracy, and the reconstructed flow angle uncertainty to values achievable by increasing the number of pressure sensors (Figure 13).

The predicted performance for the FADS system on EXPERT using a pressure surface model calibrated by Longshot is shown in Figures 19 and 20. Four sets of solutions were obtained: for two sets of Longshot un-

Table 4: Remaining Monte Carlo input uncertainties EXPERT FADS

input	3-σ	source
α	0.5°	current FADS probe sensor layout
β	0.5°	current FADS probe sensor layout
p_{t2}	3%	mismatch FADS / reference probes
α	0.2°	objective FADS probe sensor layout
β	0.2°	objective FADS probe sensor layout
p_{t2}	2%	realistic objective

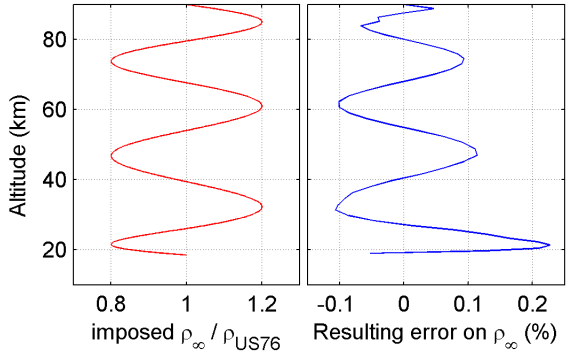

Figure 18: Impact of interpolation on standard atmosphere grid

certainties and two EXPERT pressure sensor layouts. The 1+4 layout is used on the real vehicle, whereas the 1+8 layout has four additional sensors equally spaced between the four existing off-stagnation point sensors[3]. In every of the four solution sets, the angular distance of the pressure taps from the stagnation point was varied around the $\lambda = 25°$ value actually used on EXPERT.

We find that the prime quantity of interest, the atmospheric density ρ_∞, can be reconstructed within 3 to 4%, depending on the accuracy of the surface pressure model. The red points at 4% correspond to our recent efforts in the VKI Longshot, the blue points at 3% to the suggested objective. Stagnation pressure reconstruction depends similarly on the quality of the surface pressure model. The 1% higher uncertainty on the density is due to the uncertainty on the shock wave pressure ratio model. Increasing the number of pressure sensors on the nose of EXPERT only benefits the flow angle reconstruction. At least as much can be gained however, by placing the sensors farther away from the stagnation point.

[3] All at identical cone angles: recall that this is most beneficial.

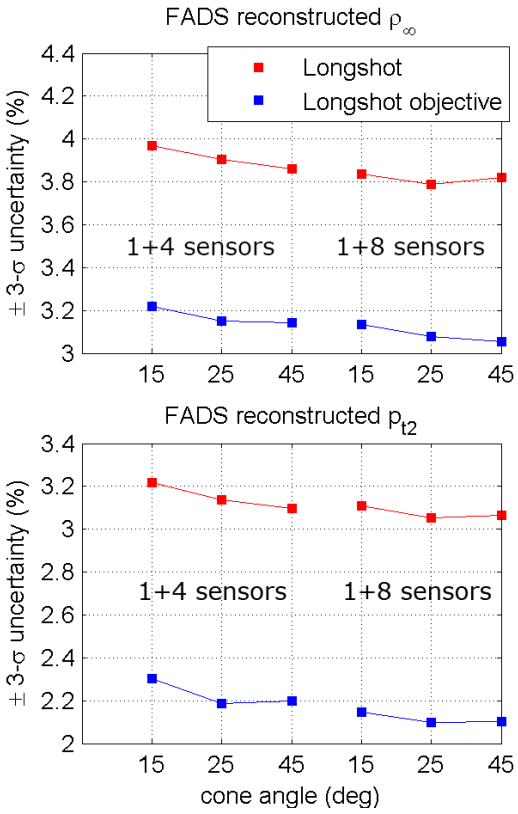

Figure 19: Monte Carlo EXPERT FADS performance

6. Conclusion

We reviewed our entry reconstruction and simulation tools utilizing both conventional inertial (IMU) and novel heat shield (FADS) instrumentation. The conventional reconstruction tools have been completely validated on Mars Phoenix Lander in-flight measurements. Similarly, all functionality in our six degree of freedom simulator matches exactly with NASA's well validated entry simulator.

We also presented FADS methodology to recon-

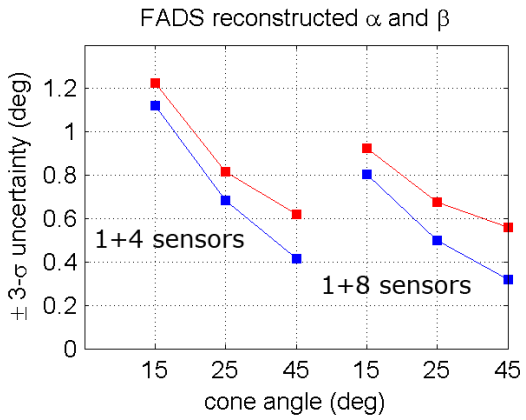

Figure 20: Monte Carlo EXPERT FADS performance

struct flow angles, stagnation pressure and atmospheric density from heat shield measurements. It consists of a surface pressure distribution model (modified Newtonian flow) and numerical calculations of shock wave pressure ratios, including high temperature effects. Lacking in-flight measurements, we applied these to a hypersonic wind tunnel probe and in a preliminary EXPERT case study. The Mach 14 Longshot wind tunnel we used is currently incapable of validating the pressure ratio model. We obtained promising performance from the surface pressure model, but were unable to experimentally constrain it to its potential accuracy. An uncertainty analysis pointed out that installing more sensors along the circumference of the FADS probe would significantly increase accuracy. It is also of interest to utilize Longshot's CO_2 capabilities and measure the wind tunnel density independently, e.g. by tunable diode laser absorption spectroscopy (TDLAS).

Both the surface pressure and pressure ratio models were applied to a simulated EXPERT trajectory. Our high temperature pressure ratio model differs substantially from cold gas approximations and matches well with work by independent authors. Its implementation on an altitude-velocity interpolation grid is both fast and accurate. A uncertainty analysis for where EXPERT's trajectory corresponds to the wind tunnel conditions was performed, for current and desired wind tunnel performance. In both cases the final uncertainty on reconstructed atmospheric density from FADS measurements is at most 4%, a significant improvement over the typical drag coefficient method employed for conventionally instrumented vehicles.

Acknowledgments

The PhD candidate is supported by the Royal Observatory of Belgium (Uccle) to develop reconstruction tools for ESA's 2016 Entry, Descent and Landing Demonstrator Module (EDM) of the ExoMars program. He gratefully acknowledges the NASA Langley Research Center for hosting him during a very productive stay. Juan Cruz in particular has been an outstanding colleague and mentor. The von Karman Institute continues to offer sound education, expertise and test facilities. Special thanks go to Guillaume Grossir and Sebastien Paris for executing the FADS wind tunnel testing, and Bruno Dias and Thierry Magin for adapting the Mutation code to solve shock conservation equations. Paul Withers from Boston University has been very helpful in the development of the IMU reconstruction tools. Thank you Damien Le Quang for reviewing the draft.

References

[1] P. Withers et al., Analysis of entry accelerometer data: A case study of Mars Pathfinder, Journal of Planetary and Space Science 51 (1) (2003) 541–561.

[2] R. C. Blanchard and P. N. Desai, Mars Phoenix Entry, Descent, and Landing Trajectory and Atmosphere Reconstruction, Journal of Spacecraft and Rockets 48 (5) (2011) 809–821.

[3] P. Withers and M. D. Smith, Atmospheric entry profiles from the Mars Exploration Rovers, Icarus 185 (1) (2006) 133–142.

[4] B. Kazeminejad, Methodology Development for the Reconstruction of the ESA Huygens Probe Entry and Descent Trajectory, Ph.D. thesis, Karl-Franzens University Graz, Institute for Physics, Austria (2005).

[5] L. F. Huber, Atmospheric Structure Experiment (ASE) Data Archive (PHX-M-ASE-2-EDL-V1.0), `http://atmos.nmsu.edu/PDS/data/phxase_0001/`, [Online; accessed February 2012] (2008).

[6] K. T. Edquist, P. N. Desai and M. Schoenenberger, Aerodynamics for Mars Phoenix Entry Capsule, Journal of Spacecraft and Rockets 48 (5) (2011) 713–726.

[7] T. Magin et al., Nonequilibrium radiative heat flux modeling for the Huygens entry probe, Journal of Geophysical Research 111 (E07S12).

[8] G. Grossir, S. Paris, K. Bensassi and P. Rambaud, Experimental characterization of hypersonic nozzle boundary layers and free-sream noise levels, in: 51st AIAA Aerospace Sciences Meeting, no. 1130 in AIAA 2013, 2013.

[9] P. zur Nieden and H. Olivier, Determination of Atmospheric Densities from Reentry Flight Data, Journal of Spacecraft and Rockets 44 (2) (2007) 332–337.

NUMERICAL MODELING FOR AEROTHERMODYNAMICS

On the Heat Flux Prediction Capabilities of Residual Distribution Methods Applied to Hypersonic Flows[☆]

Jesús Garicano Mena

Aeronautics and Aerospace Department, von Karman Institute for Fluid Dynamics, Belgium, jesus.garicano.mena@vki.ac.be

Supervisor: Herman Deconinck

Professor and Dean of the Faculty, Aeronautics and Aerospace Department, von Karman Institute for Fluid Dynamics, Belgium, deconinck@vki.ac.be

Co-Supervisor: Andrea Lani

Research Engineer, Aeronautics and Aerospace Department, von Karman Institute for Fluid Dynamics, Belgium, lani@vki.ac.be

University Promotor: Gérard Degrez

Professor, Université Libre de Bruxelles Service Aéro-Thermo-Mécanique, Belgium, Gerard.Degrez@ulb.ac.be

Abstract

In the present contribution we evaluate the heat flux prediction capabilities of second-order accurate Residual Distribution methods in the context of atmospheric entry problems around blunt bodies.
Our departing point is the computation of subsonic air flows -with air modeled either as chemically reacting and possibly out of thermal equilibrium gas mixture) around probe-like geometries, as those typically employed into high enthalpy wind tunnels. We confirm the agreement between the solutions obtained with the Residual Distribution method and the solutions computed with other Finite Volume based codes.
Straightforward application of the same technique for hypersonic cases involving strong shocks exhibit severe deficiencies. We investigate new variants of residual distribution schemes in an attempt to mitigate this problem.

Keywords: Residual Distribution, Flux Difference Splitting, Heat Flux, Hypersonic Flow, Non-equilibrium Flow.

1. Introduction

Numerical simulation of hypersonic flows is a challenging activity, since the complexity characterizing compressible flow aerodynamics have to be addressed together with additional high-temperature effects due to chemical (*CNEQ*) and/or thermal non equilibrium (*TCNEQ*) phenomena (see Ref. [1]).
Residual Distribution (*RD*[1]) Methods evince several advantageous features for the computation of compressible flows. Among them, we stress the following:

- A maximum principle (Local Extrema Diminishing) borrowed from Finite Volume (*FV*), which allows to capture discontinuities monotonically on general unstructured grids;
- Being based on finite element (*FE*) approximation theory, it is possible to obtain, on a compact stencil, second-order order accurate solutions on unstructured grids;
- Less grid sensitivity on simplicial meshes, thanks to a built-in multidimensional dissipation property.

The reasons above motivate our interest in the applicability of **RD** schemes to the simulation of atmospheric entry flow problems. Though successful examples of *RD* hypersonic heat flux computations are

[☆]Results reported in this work where presented at the AIAA SciTech meeting, in January, 2014.

[1] *RD* methods are also known under the name of Fluctuation Splitting (*FS*) schemes.

already available in the literature (*i.e.* the one concerning a sharp nosed double cone configuration, reported in Ref. [2] and [3]), the prediction of the convective heating induced by the extremely hot gas encountered in the shock layer downstream a strong bow shock is not yet fully mastered, not only with the method in question but also by standard *FV* schemes on arbitrary unstructured meshes. Indeed, it turns out that standard *RD* methods are affected by the same numerical shock instabilities (*e.g.* the carbuncle, see Ref. [4]) observed within *FV* flow computations. As examples, consult Ref. [5] or [6] (this last one for unstructured grids).
Hence, our first task is to determine whether it is possible to use *RD* methods to predict accurate wall heat flux distributions for flow fields without shock discontinuities. Subsequently, we will investigate how to employ these *RD* methods for more complex configurations, involving strong shocks.

2. Governing equations

The system of equations describing the flows of our interest accounts for the conservation of mass, momentum and energy. In compact, vector form it is:

$$\frac{\partial \vec{U}}{\partial t} + \nabla \cdot \bar{\bar{F}}^c = \nabla \cdot \bar{\bar{F}}^d + \vec{S}, \tag{1}$$

where $\vec{U}$ stands for the vector of conserved variables. For a two temperatures, N chemical species model, $\vec{U}$ includes the species densities ρ_s, the momentum ρu_j and the total ρE and electronic-vibrational energies ρe^v:

$$\vec{U} = \left[\rho_s, \quad \rho u_j, \quad \rho E, \quad \rho e^v\right]^t. \tag{2}$$

Tensors $\bar{\bar{F}}^c$ and $\bar{\bar{F}}^d$ describe the convective and diffusive fluxes of the conserved quantities, while vector $\vec{S}$ contains the chemical and internal energy modes source terms.

The components of the convective flux tensor are given by:

$$\vec{F}^c_j = \left[\rho_s u_j, \quad \rho u_i u_j + p\delta_{i,j}, \quad \rho H u_j, \quad \rho e^v u_j\right]^t, \tag{3}$$

whereas the diffusive flux tensor is:

$$\vec{F}^d_j = \left[-\rho_s u_{s,j}, \quad \tau_{i,j}, \quad \tau_{i,j} u_j - q_i, \quad -q_{v,i}\right]^t. \tag{4}$$

Quantity $\vec{u}_s$ stands for the sth-species diffusive velocity, which are obtained from the Stefan-Maxwell system (Ref. [7]).

Viscous stress tensor components $\tau_{i,j}$ are given, under the hypothesis of negligible bulk viscosity effects, by:

$$\tau_{i,j} = \mu\left[\left(\frac{\partial u_j}{\partial x_i} + \frac{\partial u_i}{\partial x_j}\right) - \frac{2}{3}\frac{\partial u_j}{\partial x_j}\right]. \tag{5}$$

Roto-translational heat flux components are defined as:

$$q_i = -\lambda\frac{\partial T}{\partial x_i} - \lambda_v\frac{\partial T_v}{\partial x_i} - \sum_s \rho_s h_s u_i. \tag{6}$$

while for the vibrational heat flux, one has:

$$q_{v,i} = -\lambda_v\frac{\partial T_v}{\partial x_i} - \sum_s \rho_s h^v_s u_i. \tag{7}$$

The source term $\vec{S}$ is given by:

$$\vec{S} = \left[\dot{\omega}_s, \quad \vec{0}_{3x1}, \quad 0, \quad \Omega_v\right]^t. \tag{8}$$

with the mass production term for a given species s:

$$\frac{\dot{\omega}_s}{M_s} = \sum_{reactions}\left(\nu''_{s,r} - \nu'_{s,r}\right)\left\{k_{r,f}\prod_{species}\left(\frac{\rho_k}{M_k}\right)^{\nu'_{k,r}} - k_{r,b}\prod_{species}\left(\frac{\rho_k}{M_k}\right)^{\nu''_{k,r}}\right\}. \tag{9}$$

Here $k_{r,f}$ and $k_{r,b}$ stand for the forward and backward reaction rates for the rth reaction; $\nu'_{k,r}$ and $\nu''_{k,r}$ are the stoichiometric coefficients and M_k is the molar weight for the k-th species.
Finally the term Ω_v accounts both for the energy exchange (relaxation) between translational and vibrational modes and the energy gained through dissociation or recombination:

$$\Omega_v = \sum_{species}\rho_s\frac{e^*_{v,s} - e_{v,s}}{\tau_s} + \sum_{species}\hat{D}_s\dot{\omega}_s. \tag{10}$$

Details on the definition of the parameters D_s, μ, λ, λ_v, $k_{r,f}$, $k_{b,f}$, τ_s ...can be found in reference [8] and further references therein.
The behavior of gases in *CNEQ* conditions can be modeled with Eqs. 1 simply by assuming that the vibrational and the roto-translational mode are at equilibrium, which translates into removing the conservation equation for the vibrational energy.
To finalize, notice that system of Eqs. 1 can be reduced to the one describing the behavior of an inert, ideal gas provided that:

- one single species is considered,

- the conservation of vibrational energy $\rho e^v$is neglected, and
- the source term $\vec{S}$ is identically zero .

In that case, Eq. 1 boils down to:

$$\frac{\partial \vec{U}}{\partial t} + \nabla \cdot \bar{\bar{F}}^c = \nabla \cdot \bar{\bar{F}}^d, \tag{11}$$

where now $\vec{U}$ contains just the gas density ρ, the momentum components ρu_j and the total energy ρE.

3. The residual distribution method

In this section we introduce briefly the **RD** discretization for the System of Equations 1. Extensive explanations on this topic are available in references [9], [10] and [4].
The solution is expressed by means of a finite element representation on P1 linear simplices.

$$\vec{U}^h(\vec{x},t) = \sum_{j=1}^{\#DOF} \vec{U}_j(t)\, N_j(\vec{x}) \tag{12}$$

where the nodal basis functions N_j fulfill the property:

$$N_j(\vec{x}_k) = \delta_{jk}, \tag{13}$$

The steady state residual for element Ω is defined as:

$$\vec{\Phi}^\Omega = \int_\Omega \left(\frac{\partial \vec{F}_j^c}{\partial x_j} - \frac{\partial \vec{F}_j^d}{\partial x_j} - \vec{S}^U \right) dv = \vec{\Phi}^{c,\Omega} - \vec{\Phi}^{d,\Omega} - \vec{\Phi}^{S,\Omega}, \tag{14}$$

and gathers contributions from the convective, dissipative and source terms.
The nodal system of equations is obtained by distributing fractions of the cell residuals $\vec{\Phi}^\Omega$ to the nodes forming part of the cell:

$$\vec{\Phi}_l^c = \sum_{\Omega_i \in \Xi_l} \vec{\Phi}_l^{c,\Omega_i}, \tag{15}$$

The convective contribution to the nodal equation of the cell residual is expressed generically as:

$$\vec{\Phi}_l^c = \sum_{\Omega_i \in \Xi_l} B_l^{\Omega_i}(K^\pm) \cdot \vec{\Phi}^{c,\Omega_i} \tag{16}$$

in terms of the so called distribution matrices $B_l^{\Omega_i}$, which depend in turn on the nodal upwind parameters:

$$K_j = \frac{1}{n_D}\left(A_{j,x}\, n_{j,x} + A_{j,y}\, n_{j,y} + A_{j,z}\, n_{j,z} \right), \tag{17}$$

where A_{j,x_d} is the Jacobian of the advective flux along direction x_d, n_{j,x_d} are the components of the vectors normal to the element faces and n_D is the problem dimensionality.
Different forms of the $B_l^{\Omega_i}$ matrices define different schemes. A scheme preserving linear solutions(*i.e.* providing second-order of accuracy at steady state, Ref. [10]) is the low diffusion A (*LDA*) defined as:

$$B_l^{\Omega_i,LDA} = (K_l)^+ \cdot \left(\sum_j \left(K_j\right)^+ \right)^{-1}, \tag{18}$$

This can be employed for the simulation of smooth flow fields.

For the simulation of shocked flow configurations a number of schemes is available, defined by different blendings of the *LDA* scheme with the quasi-monotone N scheme:

$$\vec{\Phi}_l^{c,\Omega_i,B} = \Theta^{\Omega_i} \vec{\Phi}_l^{c,\Omega_i,N} + (I - \Theta)\, \vec{\Phi}_l^{c,\Omega_i,LDA}, \tag{19}$$

with the N scheme contribution given by:

$$\vec{\Phi}_l^{c,\Omega_i,N} = K_l^+ \cdot \left(\vec{U}_l - \vec{U}_{inlet}^{\Omega_i} \right). \tag{20}$$

The *inlet* state $\vec{U}_{inlet}^{\Omega_i}$ reads:

$$\vec{U}_{inlet}^{\Omega_i} = \sum_{l=1} \left(K_l^-\right)^{-1} \cdot \sum_{l=1} K_l^- \cdot \vec{U}_l. \tag{21}$$

Different choices of Θ^{Ω_i} result in different variants of the blended scheme. The two most common are:

- The original B scheme of Ref. [4], where Θ^{Ω_i} is a diagonal matrix whose entries are defined by the ratios of the components of the characteristic decomposition of the nodal residual over the cell residual:

$$\Theta^{\Omega_i} = diag(\theta_k), \text{ with } \theta_k = \frac{\vec{l}_k \cdot \vec{\Phi}_l^{c,\Omega_i}}{\vec{l}_k \cdot \sum_l \vec{\Phi}_l^{c,\Omega_i}} \tag{22}$$

  and where $\vec{l}_k$ is the kth left eigenvector.

- The Bx scheme of Ref. [11], where Θ is the identity matrix times a scalar shock sensor θ, based on a field variable (*i.e.* pressure, temperature or density):

$$\Theta^{\Omega_i} = \theta^{\Omega_i} I. \tag{23}$$

Distribution of diffusive contributions to the cell residual is performed, when a $P1$ element mesh is used, by Galerkin discretization:

$$\vec{\Phi}_j^d = \int_\Omega N_j \nabla \cdot \bar{\bar{F}}^v \, dv \tag{24}$$

Source terms can be distributed either with the Galerkin method or together with the advective residual.

From the distribution process introduced before results a system of differential equations controlling the time evolution of the solution at the grid nodes. For l-th node, it reads:

$$\Xi_l \frac{d\vec{U}_l}{dt} + \vec{\Phi}_l^c - \vec{\Phi}_l^d - \vec{\Phi}_l^S = \vec{0}, \tag{25}$$

where Ξ_l stands for the volume of the median dual cell around l-th node.

The discretization of Eq. 25 is accomplished by means of the *COOLFluiD* solver, described in Ref. [12]. Eq. 25 is marched in pseudo-time until a steady state solution is reached, by using an implicit backward Euler integrator. The resulting linear system of equations is then solved by one of the Krylov subspace methods provided by the `PETSc` solver library, Ref. [13].

All thermophysical properties and non-equilibrium terms are provided by the `MUTATION` library (see Ref. [14]). Concerning boundary conditions, isothermal wall (and supersonic inlet) boundary conditions are enforced strongly, whereas far-field, subsonic outlet and inviscid wall boundary conditions are weakly imposed, as detailed in Ref. [9].

4. Results

4.1. Non-equilibrium subsonic flow around a circular cross-section probe

The first configuration we want to discuss consists of a cylindrical body (diameter $\phi = 8\,mm$) placed transversely in an incoming subsonic air stream. This configuration corresponds to a probe employed inside a high enthalpy wind tunnel (details in Ref. [7]). The upstream conditions for this case (Table 1) are such that the molecular species are strongly dissociated, and hence chemical non-equilibrium has to be accounted for.

For this computation we have employed *LDA* (Eq. 18) in its *CRD* form[2], see Ref [3].

[2]The character c is appended to the name of a scheme to identify its *CRD* variants, like in *LDAc*.

Table 1: Non-Equilibrium Subsonic Flow around a Circular Cross-Section Probe. Testcase definition.

M_∞	$\rho_\infty\,[kg/m^3]$	$p_\infty\,[Pa]$	$T_\infty\,[K]$	$T_{Wall}\,[K]$
0.526	$4.8084e-04$	1500.	6000.	400.
Composition				
$y_{N,\infty}$	$y_{O,\infty}$	$y_{N2,\infty}$	$y_{NO,\infty}$	$y_{O2,\infty}$
0.5765	0.2326	$5.87e-04$	0.193	$3.72e-6$

Our objective with this simulation is twofold: first, to assess the compatibility between the *RD* method and the complex thermochemical models needed for the simulation of non-equilibrium flows; and second, study whether accurate prediction of heat flux by means of *RD* is possible.

Regarding the first sub-objective, the non-linear residual for the translational-rotational temperature decreased without problem below 10^{-6}. Figure 2 shows a view of the Mach and pressure fields. Notice the separation of the flow over the leeward side of the cylinder(Fig. 2(b)): the symmetry of the recirculation in the separated region is evident.

With respect to the second objective, as can be observed in Fig. 3, the heat flux predicted by the *LDAc* scheme agrees with the results of Ref. [7] over the region where the flow remains attached. We cannot elucidate at the moment which of (even *if any of*) the two simulations is the correct over the separated region: further grid refinement studies are necessary.

As a conclusion, no major difficulties should arise in the application of *RD* techniques for the prediction of convective heat flux in subsonic, *TCNEQ* flows.

4.2. Inert ideal gas, hypersonic flow around cylinder

The second configuration we have considered is the $Ma = 17.5$ hypersonic flow around the mid section of a $\phi = 2\,m$ diameter cylinder, a problem proposed in Ref. [15]. Table 2 summarizes the conditions defining the testcase.

Table 2: Inert Ideal Gas, Hypersonic Flow around cylinder. Testcase definition.

$U_\infty\,[m/s]$	$p_\infty\,[Pa]$	$T_\infty\,[K]$	$T_{Wall}\,[K]$
5000.	57.65	200.	500.

We have chosen this testcase to analyze whether *RD* methods are capable of predicting heat flux when strong discontinuities are present in the domain.

Since we have to deal with a non-smooth flow field, we must employ a scheme that can handle steep gradients, *i.e.* any of the variants of the blended schemes described in section 3. According to our experience, the classical B blended scheme of Ref. [4], as well as its *CRD* variant, have proven to be not robust enough for the simulation of this problem. Hence, we have resorted to the Bx scheme of Dobes. Actually, we have preferred to use its *CRD* reformulation, the BCx scheme (see Ref. [16]), since contour integration based variants of a given scheme can be generalized more easily to *TCNEQ* problems.

Nevertheless, the shock detector described in Ref. [11] turns out to be particularly dissatisfying, because it is problem dependent and requires tuning in order to obtain an accurate shock capture. This has lead us to look for alternatives; in particular the shock detector given in Ref. [6] has been chosen. The new shock detector function σ is defined as:

$$\sigma^{\Omega_i} = 1 - \frac{1 - \cos(\pi Z)}{2}), \tag{26}$$

where

$$Z = min(1, max(0, z)) \text{ and } z = \frac{\phi_{max} - \phi}{\phi_{max} - \phi_{min}},$$

with ϕ defined as

$$\phi = \frac{\max\limits_{l \in \Omega_i} v_l}{\min\limits_{l \in \Omega_i} v_l}, \text{ with } v = p,\ T \text{ or } \rho,$$

and one takes typically $\phi_{max} = 3$ and $\phi_{min} = 2$.
The usage of this shock detector (based on pressure) makes possible a parameter free, sharp capture of the shock profile with a much easier convergence to the steady state, as shown in Fig. 4(a) and Fig. 4(b).
Unfortunately, solutions obtained with the BCx scheme and the shock detector of Eq. 26 do not provide accurate heat flux predictions. Fig. 6 shows wall heat flux predicted by *RD* on an unstructured grid obtained by splitting the quadrilaterals of a structured mesh along the diagonal. There are two such uniform splittings possible: considering the quadrilaterals just above and below the symmetry line, in the kind we call < the diagonals run at $\approx +45/-45$ deg, while in the one we denote as > diagonals run at $\approx 225/135$ deg. Thanks to the properties of the detector σ^{Ω_i}, it is possible to locate accurately the numerical shock wave: this has allowed us to run simulations with increased resolution across the shock region: in Fig. 6 predicted heat flux for two situations (20 and 60 nodes **across** the shock wave) are shown. The reference *FV* solution of Ref. [15] appears in blue.

It is evident from the figure that the choice of the diagonalization has an impact on the shape of the heat flux distribution. We have observed that the trends shown here depend neither on whether additional dissipation is applied across the shock wave by means of a *carbuncle fix* (Ref. [17]), nor on the magnitude of that artificial dissipation relative to the value of the dissipation coming from the physical diffusive terms; actually, we have found that the usage of a carbuncle fix has not been necessary for any of the simulations we have performed.
Previous results have lead us to investigate several alternative strategies to modify the numerical dissipation locally across the shock wave. Some of them start from the relationship between *LDA* and *N* schemes reported in Ref. [10]:

$$\vec{\Phi}_l^{c,\Omega_i,Nc} = \vec{\Phi}_l^{c,\Omega_i,LDAc} + \vec{\delta}_l^{Diss,Nc}, \tag{27}$$

where $\vec{\delta}_l^{Diss,Nc}$ is the crosswind dissipation that added to the *LDAc* scheme gives back the *Nc* scheme. Eq. 27 substituted into the definition of B scheme (Eq. 19) yields:

$$\vec{\Phi}_l^{c,\Omega_i} = \vec{\Phi}_l^{c,\Omega_i,LDAc} + \Theta^{\Omega_i}\vec{\delta}_l^{Diss,Nc} \tag{28}$$

A first possibility to modify the dissipation across the captured shock wave is substituting the *Nc* scheme contribution to Eq. 28 by some other term of dissipative nature, situation expressed by:

$$\vec{\Phi}_l^{c,\Omega_i} = \vec{\Phi}_l^{c,\Omega_i,LDAc} + \Theta\vec{\delta}_l^{Diss,*}. \tag{29}$$

As an example of the approach described by Eq. 29, we have considered the dissipative term of the Lax-Friedrichs (*LxF*) scheme (Ref. [18]):

$$\vec{\delta}_l^{Diss,LxF} = \max_{k \in \Omega_i} \lambda_k \sum_m \left(\vec{U}_l - \vec{U}_m\right), \tag{30}$$

where λ_k are the eigenvalues of a cell averaged state. This scheme guarantees a higher level of dissipation across the shock wave.
Yet another alternative to have an increased local dissipation exploits the known equivalence, reported in Ref. [19], between *RD* schemes and 1st order *FV* flux functions on the median dual mesh. This time we depart from Eq. 28 and substitute the complete cell-to-nodal contribution from the *Nc* scheme by some other monotonicity preserving scheme:

$$\vec{\Phi}_l^{c,\Omega_i} = \Theta^{\Omega_i}\vec{\Phi}_l^{c,\Omega_i,FV} + \left(I - \Theta^{\Omega_i}\right)\vec{\Phi}_l^{c,\Omega_i,LDAc}, \tag{31}$$

In particular, we have substituted the *Nc* scheme in Eq. 31 by the *HLL* flux function (Ref. [20]):

$$\vec{\Phi}_l^{c,\Omega_i} = \Theta^{\Omega_i}\vec{\Phi}_l^{c,\Omega_i,HLL} + \left(I - \Theta^{\Omega_i}\right)\vec{\Phi}_l^{c,\Omega_i,LDAc}. \tag{32}$$

Back to Eq. 29, there are clear similarities between it and the classical strategy applied for the (stabilized) *FE* simulation of compressible flows: *SUPG FE* methods consist of a central discretization supplemented by a stabilization of *upwind* nature and a shock capturing term (Ref. [21]). The form of this approach when applied (for simplicity) to a scalar problem is:

$$\Phi_l^{c,\Omega_i,SUPG+SC} = \left(\frac{1}{n_d+1} + \frac{1}{2\Omega_i}\tau\vec{a}\cdot\vec{n}_l\right)\Phi^{c,\Omega_i} + \int_{\Omega_i}\delta_{SC}\nabla N_l\cdot\nabla U\,dv. \quad (33)$$

From this point of view, the *RD* distribution of the cell residual by the *LDAc* accomplished in Eq. 29 would parallel the central and the stabilization terms in Eq. 33, while the dissipation term would play the role of a shock capturing term. There is however an important conceptual difference to point out: matrix Θ does not have residual character while shock capturing term used in *SUPG FE* discretization does. Nevertheless we can restore the residual character by taking as shock capturing term:

$$\delta_{SC} = \frac{\sqrt{\left\|\frac{\partial}{\partial t}\vec{U} + \nabla\cdot\bar{\bar{F}}^c - \nabla\cdot\bar{\bar{F}}^d\right\|^2_{A_0^{-1}}}}{\sqrt{\left\|\nabla\xi\cdot\nabla\vec{U}\right\|^2_{A_0^{-1}} + \left\|\nabla\eta\cdot\nabla\vec{U}\right\|^2_{A_0^{-1}} + \left\|\nabla\zeta\cdot\nabla\vec{U}\right\|^2_{A_0^{-1}}}}, \quad (34)$$

described by Kirk in Ref. [22], and superposing it to the *LDAc* distribution:

$$\vec{\Phi}_l^{c,\Omega_i} = \vec{\Phi}_l^{c,\Omega_i,LDAc} + \int_{\Omega_i}\delta_{SC}\nabla N_l\cdot\nabla\vec{U}\,dv. \quad (35)$$

These three new schemes (Eqs. 30, 32 and 35) turn out to be more dependent on the grid than the original *BCx* scheme, something which is natural since we have traded the *multidimensional upwinding* property built into the *N* scheme (see Ref. [9]) for more dissipation. Out of the three, the more dissipative is, as we will ilustrate immediately, the superposition of the *LDAc* distribution and the *HLL FV* flux function: the *HLL* flux, though an upwind scheme, is not multidimensional upwind and hence is negatively affected by the inherently misaligned simplicial grids employed here. As for the the combination of the *LDAc* scheme with the *LxF* dissipation (Eq. 27), albeit the central nature of the dissipative term, it has proven to be moderately dissipative. The scheme combining *LDAc* scheme and the *SUPG* shock capturing term (Eq. 35) -which we have so far employed in combination with an explicit time-stepping strategy for inviscid simulations- has shown encouraging results on inviscid testcases; implementation of an implicit variant is underway.

For the rest of the contribution, we illustrate the properties of the *BCx* scheme supplemented with the new shock detector function 26, of the *BLDA* − *LxFCx* scheme, and of the *BLDA* − *HLLCx* scheme. To illustrate the properties of these schemes, we show the flow solutions obtained on a mesh (13000 nodes / 25000 elements) constructed to have the inlet boundary as closely aligned to the numerical shock surface as possible. In order to avoid grid induced asymmetries, the mesh has been built to be symmetric along the stagnation streamline obtained: the mesh particularly employed is of the type <.

Fig. 7-9- show the *T* and *Ma* number fields predicted by each of the aforementioned schemes; heat flux profiles are shown in Fig. 10. Observe how the more dissipative variants - *BLDA* − *LxFCx* and *BLDA* − *HLLCx* - capture the shock wave over a thicker region than *BCx*. Notice also the evident irregularities in the post-shock temperature isolines for all schemes. These irregularities are born as the flow is processed by the numerical shock wave, and they are believed, when advected into the boundary layer, to spoil the heat flux prediction, Ref. [6]. Oddly enough, these irregularities do not show up in the *Ma* number field, neither do they appear on the pressure or entropy fields.

Concerning the predicted heat flux, *BCx* and *BLDA* − *LxFCx* schemes predict a heat flux significantly higher than the reference solution, while *BLDA* − *HLLCx* underpredicts it. As a comment, the shock thickness for *BLDA* − *LxFCx* or *BLDA* − *HLLCx* is relatively small because the mesh is quite fine around the shock wave; with a coarser grid or one which is poorly aligned with the shock wave, a much larger shock thickness would be obtained: this suggests that these schemes could take advantage of automatic grid refinement algorithms.

The following question arises then naturally: Does the *density* of the mesh across the captured shock surface have an effect on the quality of the post-shock temperature field? We can take advantage of the excellent localization properties of the shock detector function in Eq. 26 (recall Fig. 4(b)) to answer this question: Considering the shock wave contained by those elements where the detector is active (*i.e.* larger than zero), it is straightforward to subdivide each *shocked* element by introducing a new node in its barycenter. Thus, an isotropic refinement across the shock region is effectively obtained.

To test the impact on the refinement we depart from a solution computed with *BCx* scheme on a mesh of 6993 nodes / 13400 elements, again symmetric and of type <, and we perform several successive shock-refinement steps. The results are plotted in Fig. 11. Scheme *BLDA* − *HLLCx* loses the symmetry of the heat flux after one refinement step, because as it is known, the dimensionally splitted *HLL* flux

function cannot handle properly the isotropic grid emerging in the shock region. In combination with schemes BCx and $BLDA - LxFCx$, shock refinement has barely an effect on the predicted heat flux. This result is consistent with the findings in Ref. [23], where complex mesh adaption techniques are combined with a particular residual distribution technique: while the overall quality of the surface quantities is improved with mesh adaption, near the stagnation region the heat flux is quite insensitive to the improvement in the mesh.

At this point, the lack of dissipation across the shock and the insufficient mesh refinement have been eliminated as responsible for the poor predicted heat flux at the wall. The next step we take is to avoid completely the numerical capture of the shock wave; we can do this by making use again of the shock detector in Eq. 26: we identify all the nodes belonging to the captured shock profile and derive the 4th order polynomial that approximates them in the Least Squares sense with the additional restriction of $\frac{dx}{dy}|_{y=0} = 0$ at the stagnation streamline.The location of the shock wave obtained with this *extract-approximate* strategy is compared with respect to the location of the shock wave predicted by a shock fitting *RD* code - described in Ref. [24]- is shown in Fig. 12: the agreement between them is excellent.

Since there is an analytical expression available for the shock wave location, it is straightforward to compute the normal vector to the shock wave and to apply the *Rankine-Hugoniot* relations exactly to obtain the flow quantities after the shock. These quantities are used as inlet condition for a simulation on yet another mesh of the type <, again with 6993 nodes / 13400 elements. Since in this case the flow field is smooth, we employ just the *LDAc* scheme: the T and Ma number fields are shown in Fig. 13: the T isolines are now completely smooth and no wiggles are visible. The corresponding heat flux is plotted in Fig. 14. Notice as well the dramatic difference between these solutions and those obtained when capturing the shock wave (Fig. 11(a)).

We see then that the difficulty with the heat flux is related to the capture of the shock wave. More precisely, we believe that the real problem is not that there is a captured shock in the domain, but rather in the lack of control over the solution across the numerical shock, *i.e.* over the increments in entropy and over the total enthalpy: if an inlet value with a total enthalpy different from the correct post shock value is plugged in the stagnation streamline, a heat flux with an important peak in the symmetry line, similar to that in Fig. 10(a) is retrieved. This point adds even more weight to previous findings in the literature (Ref. [5] in *FV* context, Ref. [22] for stabilized *FE*), insisting on the need for numerical schemes capable of preserving total enthalpy across shocks.

5. Conclusions

In the present contribution the flow field and heat flux prediction capabilities of *RD* methods applied to the computation of high temperature flow fields have been investigated.

The *RD* method presented has proven to be capable of producing accurate flow solutions and heat flux prediction for flows where no shock waves are present, even if the gas is modeled as in non-equilibrium conditions.

Concerning the computation of *shocked* flows, the blended BCx scheme has been provided with an accurate, parameter free shock detector function never used before in a *RD* context. This shock detector function has been employed to derive two additional blended schemes: $BLDA - LxFCx$ and $BLDA - HLLCx$.

The heat flux prediction properties in presence of strong shock waves of these three schemes have been analyzed in detail. None of them, in its current form at least, has been able to provide an acceptable heat flux at the stagnation point. Nevertheless, out of this study we have found strong evidence of the irrelevance of the level and nature of the numerical dissipation across the numerical shock wave, while conservation of total enthalpy has been identified as a needed property for our schemes.

A strategy to perform shock fitted computations, relying on the good properties of the shock detector function introduced before, has been laid out and preliminarly tested, confirming the previous assertions, and setting the derivation of total enthalpy conserving inviscid schemes as our priority.

Acknowledgments

This contribution owes a great deal to many insightful discussions with Prof. Degrez. Raffaele Pepe kindly provided the reference shock location used for comparison with the *extract-approximate* results.

J. Garicano Mena is supported by a FNRS FRIA fellowship.

References

[1] J. D. Anderson, Hypersonic and High Temperature Gas Dynamics, McGraw Hill, New York, 1989.

[2] Lani, A., Garicano Mena, J. and Deconick, H., A residual distribution method for symmetrized systems in thermochemical nonequilibrium, in: Proceedings of the 20th AIAA Computational Fluid Dynamics Conference, AIAA, Honolulu (Hawaii), 2011.

[3] Lani, A., Panesi, M. and Deconinck, H., Conservative residual distribution method for viscous double cone flows in thermochemical nonequilibrium, Communications in Computational Physics 13 (2013) 479–501.

[4] Sermeus, K., Multi-Dimensional Upwind Discretization and Application to Compressible Flows, Ph.D. thesis, Université Libre de Bruxelles (2013).

[5] Kitamura, K., Shima, E., Nakamura, Y. and Roe, P.L., Evaluation of Euler fluxes for hypersonic flow computations, AIAA Journal 48 (4) (2010) 763–776.

[6] Gnoffo, P. A., Updates to multi-dimensional flux reconstruction for hypersonic simulations on tetrahedral grids, in: Proceedings of the 48th AIAA Aerospace Science Meeting and Exhibit, AIAA, Orlando(FL), 2010.

[7] Barbante, P.F., Accurate and efficient modelling of high temperature nonequilibrium air flows, Ph.D. thesis, Universite Libre de Bruxelles (2001).
[8] Gnoffo, P., Gupta, R. and Shinn, J., Conservation equations and physical models for hypersonic air flows in thermal and chemical non-equilibrium, TP 2867, NASA (1989).
[9] van der Weide, E., Compressible flow simulation on unstructured grids using multi-dimensiona upwind schemes, Ph.D. thesis, Technische Universitet Delft (1998).
[10] Ricchiuto, M., Construction and analysis of compact residual distribution discretizations for conservation laws on unstructured meshes, Ph.D. thesis, Université Libre de Bruxelles (2005).
[11] Dobes, J., Numerical Algorithms for the Computation of Steady and Unsteady Compressible Flow over Moving Geometries : Application to Fluid-Structure Interaction, Ph.D. thesis, Université Libre de Bruxelles (2007).
[12] Lani, A., An object oriented and high-performance platform for aerothermodynamic simulations, Ph.D. thesis, Université Libre de Bruxelles (2008).
[13] S. Balay, J. Brown, , K. Buschelman, V. Eijkhout, W. D. Gropp, D. Kaushik, M. G. Knepley, L. C. McInnes, B. F. Smith, H. Zhang, PETSc users manual, Tech. Rep. ANL-95/11 - Revision 3.4, Argonne National Laboratory (2013).
[14] Panesi, M., Physical models for nonequilibrium plasma flow , Ph.D. thesis, Universit degli studi di Pisa (2009).
[15] Gnoffo, P. A., White, J. A., Computational aerothermodynamic simulation issues on unstructured grids, in: Proceedings of the 37th AIAA Aerospace Science Meeting and Exhibit, AIAA, Portland(OR), 2004.
[16] Villedieu, N., High order discretisation by residual distribution schemes, Ph.D. thesis, Université Libre de Bruxelles (2009).
[17] Garicano Mena, J., Lani, A., Sermeus, K. and Deconinck, H., An effective treatment of numerical shock wave instabilities with residual distribution schemes: Application to hypersonic nonequilibrium flows around blunt bodies, in: 7th European Symposium on Aerothermodynamics for Space Vehicles, Brugge, Belgium, 2011.
[18] Abgrall, R. and Mezine, M., Construction of 2nd-order accurate monotone and stable RDS for steady flow problems, Journal of Computational Physics 195 (2004) 474–507.
[19] Abgrall, R., Toward the Ultimate Conservative Scheme: Following the Quest.
[20] Harten, A., Lax, P.D. and van Leer, B. , On Upstream Differencing and Godunov-Type Schemes for Hyperbolic Conservation Laws , SIAM Review 25 (1) (1983) 35–61.
[21] Hughes, T.J.R. and Mallet, M., A new finite element formulation for computational fluid dynamics: IV. A discontinuity-capturing operator for multidimensional advective-diffusive systems, Computer Methods in Applied Mechanics and Engineering 25 (3) (58) 329–336.
[22] Kirk, B. S. and Carey, G. F., Development and validation of a SUPG finite element scheme for the compressible Navier-Stokes equations using a modified inviscid flux discretization.
[23] Wood, W. A., Multi-dimensional Upwind Fluctuation Splitting Scheme with Mesh Adaption for Hypersonic Viscous Flow, Ph.D. thesis, Virginia Polytechnic Institute (2001).
[24] Paciorri, R and Bonfiglioli, A., A Shock-fitting technique for 2D unstructured grids, Computers and Fluids 38 (2009) 715–726.

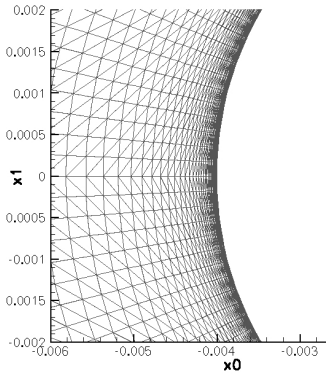

Figure 1: Subsonic *CNEQ* flow around cylinder. Closeup of mesh near stagnation point. Gas flows from left to right.

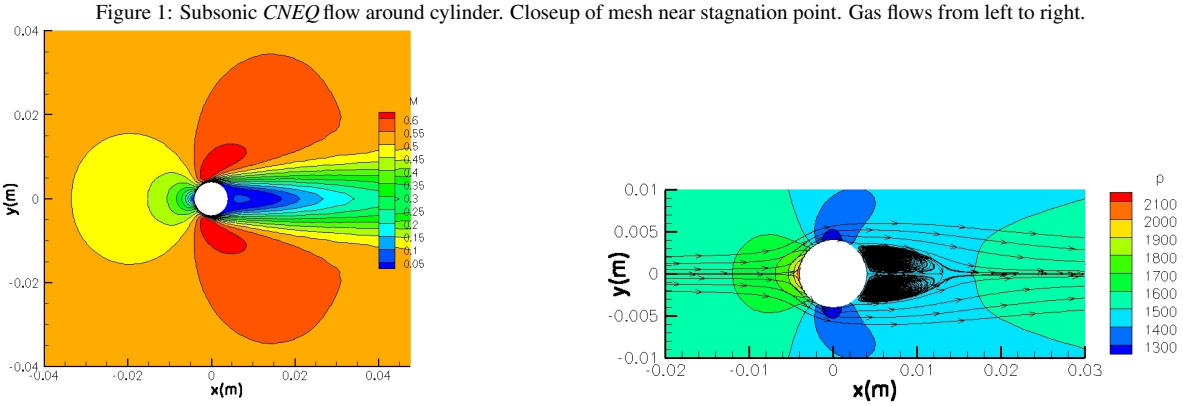

(a) Mach number field.

(b) Pressure field and streamlines.

Figure 2: Subsonic *CNEQ* flow around cylinder. *COOLFluiD RD* solution.

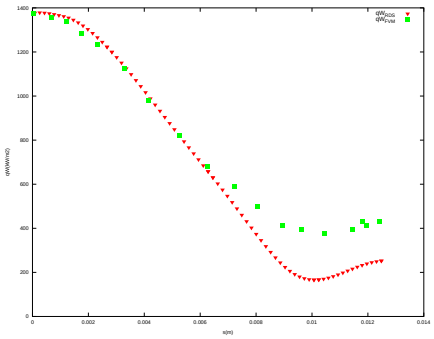

Figure 3: Subsonic *CNEQ* flow around cylinder. Heat flux (W/m^2). *RD* (red) *Vs* Barbante (green, Ref. [7]) results.

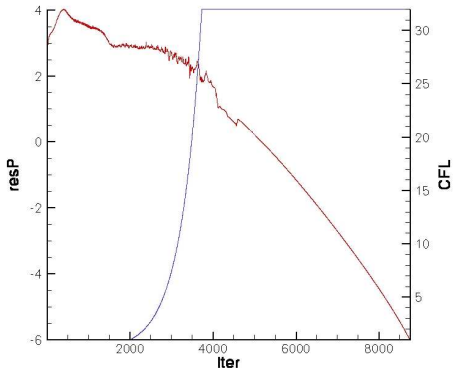

(a) Convergence history.

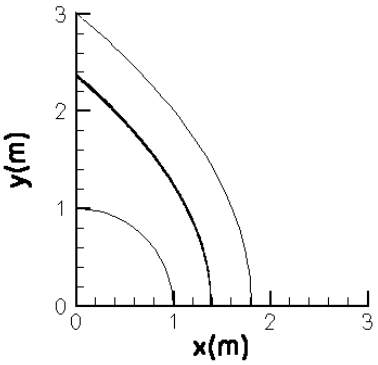

(b) Shock detector function active on blackened area.

Figure 4: Hypersonic flow around cylinder. BCx scheme with shock detector Eq. 26 .

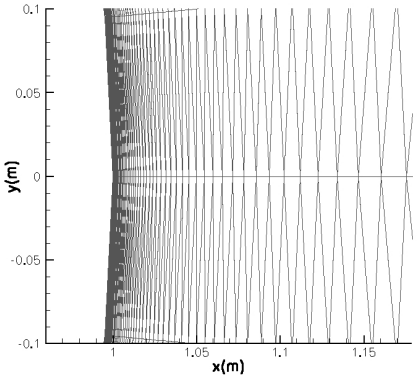

(a) Mesh of '<' kind .

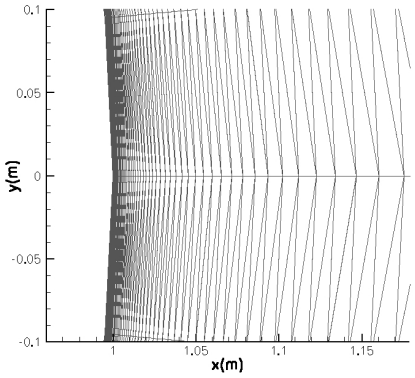

(b) Mesh of '>' kind.

Figure 5: Hypersonic flow around cylinder. Possible uniform diagonalizations.

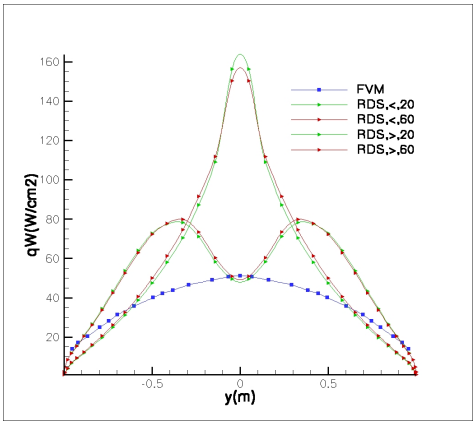

Figure 6: Hypersonic flow around cylinder. Heat flux (W/cm^2). *RD COOLFluiD* (red, green) *Vs* Gnoffo (blue, Ref. [15]) results.

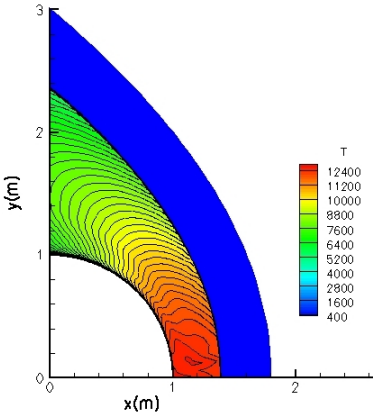

(a) Temperature (K).

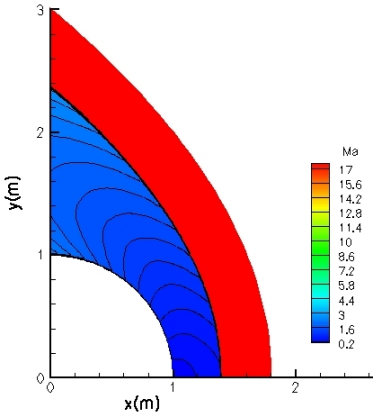

(b) Mach number.

Figure 7: Hypersonic flow around cylinder. BCx scheme.

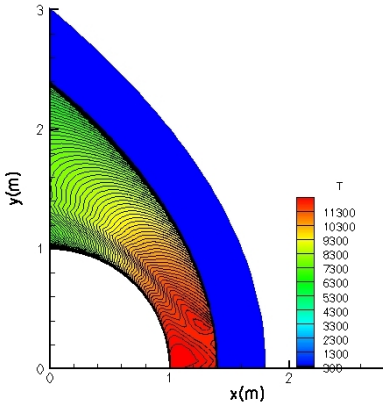

(a) Temperature (K).

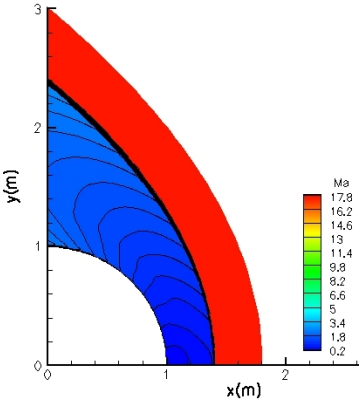

(b) Mach number.

Figure 8: Hypersonic flow around cylinder. $BLDA - LxFCx$ scheme.

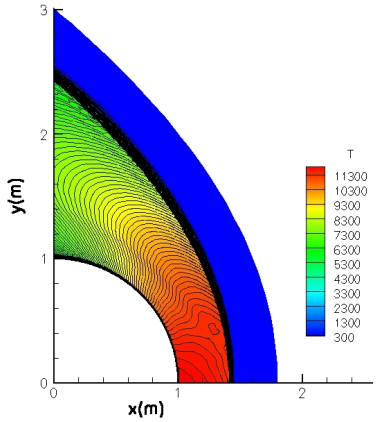

(a) Temperature (K).

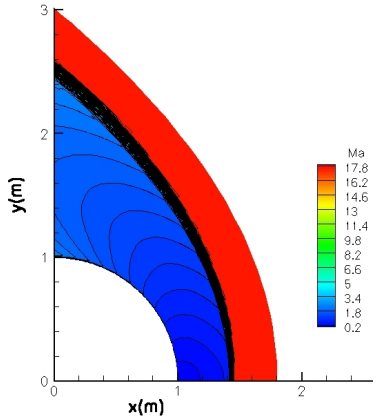

(b) Mach number.

Figure 9: Hypersonic flow around cylinder. $BLDA - HLLCx$ scheme.

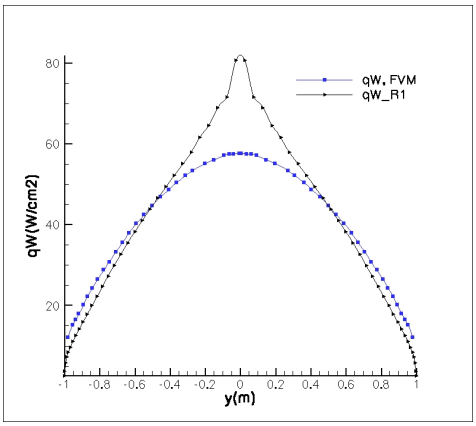

(a) BCx (black) Vs FV (blue, Ref. [15]) solution.

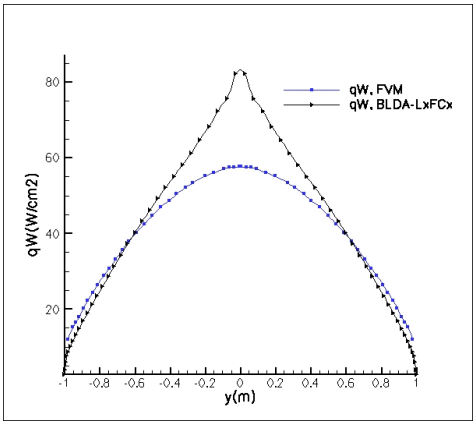

(b) $BLDA - LxFCx$ (black) Vs FV (blue, Ref. [15]) solution.

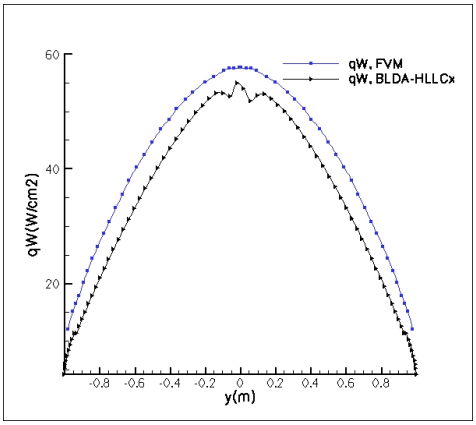

(c) $BLDA - HLLCx$ (black) Vs FV (blue, Ref. [15]) solution..

Figure 10: Hypersonic flow around cylinder. Heat flux (W/cm^2).

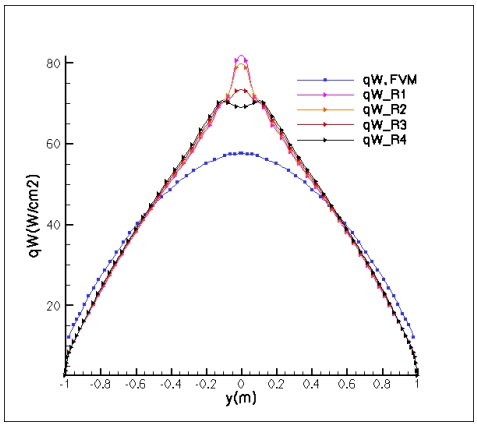

(a) *BCx Vs FV* (blue, Ref. [15]) solution.

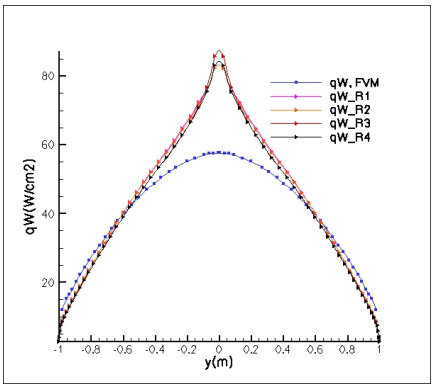

(b) *BLDA − LxFCx Vs FV* (blue, Ref. [15]) solution.

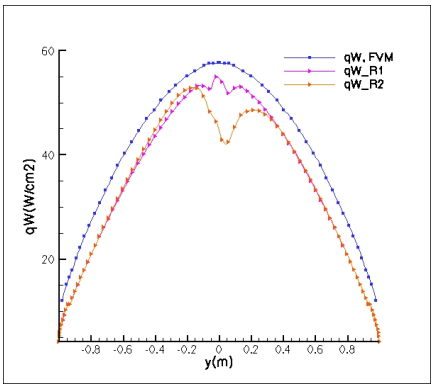

(c) *BLDA − HLLCx Vs FV* (blue, Ref. [15]) solution.

Figure 11: Refinement across the shock wave: 1st, 2nd, 3rd and 4th levels → pink, orange, red and black.

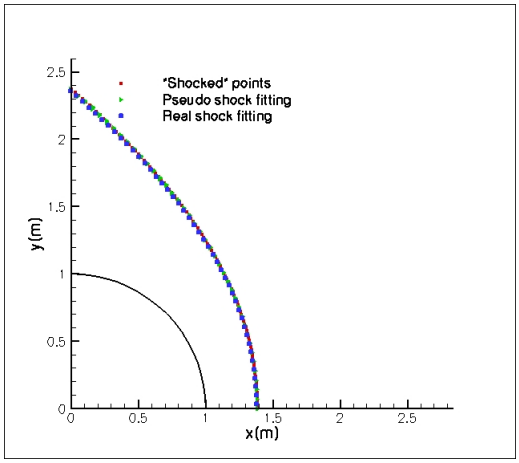

(a) Shock position (only 1st quadrant shown).

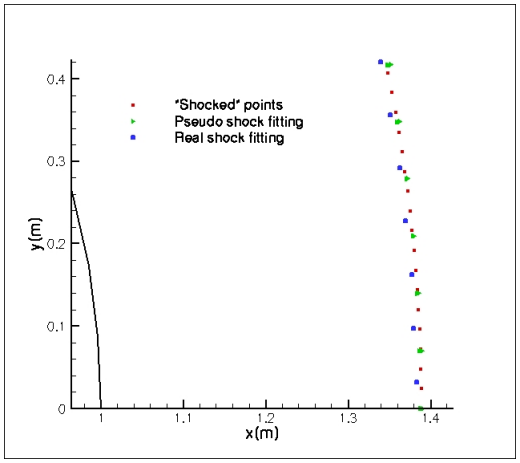

(b) Closeup around stagnation line.

Figure 12: Hypersonic flow around cylinder. Shock location from shock-fitting simulation [24] *Vs* Extracted/Approximated from simulation in Fig. 7.

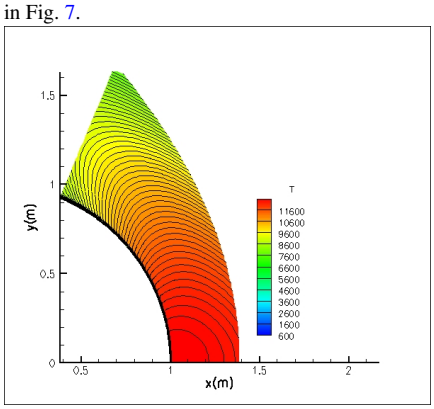

(a) Temperature (K).

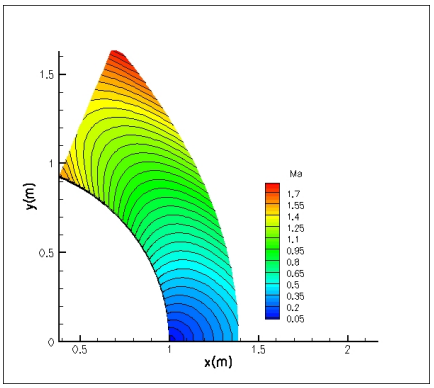

(b) Mach number.

Figure 13: Hypersonic flow around cylinder. *LDAc* scheme on post-shock region.

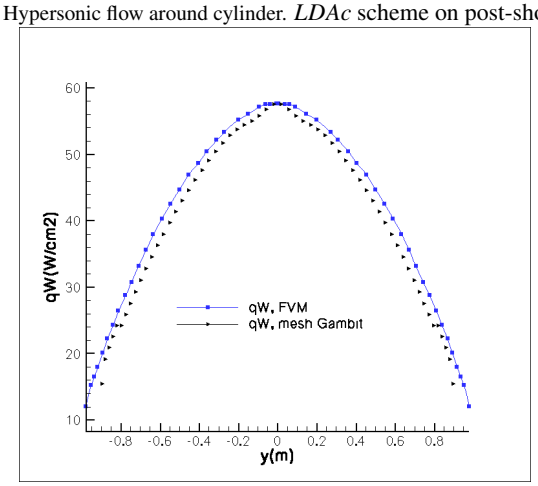

Figure 14: Hypersonic flow around cylinder: Heat flux (W/cm^2).

Physico-chemical Models for Rarefied Gas-Kinetic Simulations with Application to Atmospheric Entry Flows

Erik Torres

Aeronautics and Aerospace Department, von Karman Institute for Fluid Dynamics, Belgium, torres@vki.ac.be

Supervisor: Thierry Magin

Associate Professor, Aeronautics and Aerospace Department, von Karman Institute for Fluid Dynamics, Belgium, magin@vki.ac.be

University Supervisor: Stefanos Fasoulas

Professor, Institute of Space Systems, University of Stuttgart, Germany, fasoulas@irs.uni-stuttgart.de

Abstract

A state-to-state model for internal energy exchange and molecular dissociation of nitrogen is integrated into the framework of a direct simulation Monte Carlo (DSMC) flow solver. Necessary rate data for the full set of elementary processes are provided by a quantum chemical database developed at NASA Ames Research Center. The DSMC implementation requires detailed knowledge of all reaction cross sections as a function of relative translational energy. In the present work a methodology is proposed to extract these cross sections from available temperature-dependent rate coefficients. Due to the high computational cost of simulating the full range of inelastic collision processes of the N_2–N system ($\approx 23 \times 10^6$ reactions), a reduced model with fewer internal levels (e.g. uniform rovibrational bin method) will be used. To verify its implementation we perform several heat bath simulations of internal energy exchange and molecular dissociation of nitrogen. The results of our DSMC simulations are then compared with solutions to the equivalent system of master equations.

Keywords: Hypersonic flow, DSMC, nitrogen, dissociation, state-to-state

1. Introduction

Accurately predicting the flow field around a hypersonic flight vehicle and its interaction with the vehicle's surface is a challenging task. This is due to the tight coupling of compressible fluid dynamics with high-temperature gas effects. At flight speeds typical of orbital return, e.g. 10 km/s and above, a strong bow shock is formed ahead of the blunt-nosed capsule. Severe compression of the incoming gas across the shock causes the temperature to rise to several thousand Kelvin above the free-stream value. At such high temperatures molecular species become vibrationally excited and may partially dissociate. A fraction of the newly formed atomic species will later recombine in the boundary layer near the vehicle's surface and release heat in the process. These thermochemical processes have a strong influence on flow field features, such as shock standoff distance and thickness. Furthermore, additional physical phenomena such as radiation of gaseous species add to the thermal loads the vehicle has to endure during reentry.

The direct simulation Monte Carlo (DSMC) method was pioneered by Bird in the 1960's [1]. Over the course of the last decades it has become the method of choice within the aerospace community for numerical simulations in the transition range between continuum and free molecular flow regimes.

The most widespread model for internal energy exchange in use by the DSMC community was originally proposed by Borgnakke and Larsen [2]. The Larsen-Borgnakke model assumes that post-collision energies of the colliding molecules can be sampled from a joint equilibrium distribution of the translational and internal energy modes. The rate at which relaxation toward thermal equilibrium occurs is controlled by rotational/vibrational collision numbers $Z_r = \tau_r \cdot \nu$, $Z_v = \tau_v \cdot \nu$. These numbers are tuned to

values such that the characteristic relaxation times for rotation τ_r and vibration τ_v known from experiments (Parker [3], Millikan and White [4]) can be matched.

In the early formulation of the Larsen-Borgnakke model the internal energy was assumed as continuously distributed, therefore no distinction between individual quantum states of a given species was made. In later iterations the continuous distributions were replaced with discrete ones for vibration [5] and rotation [6]. However, the selection of post-collision levels still assumed an equilibrium distribution.

The problem of modeling chemical reactions within DSMC was initially addressed by Bird [7]. His approach is commonly known as the total collision energy (TCE) method. In later work the original TCE cross-sections were modified to include a term dependent on the molecule's vibrational energy, hence the name "vibrationally favored dissociation" (VFD) model [8]. Bird's Quantum-Kinetic [9] model is a way to directly couple the discrete Larsen-Borgnakke model for vibrational excitation with the dissociation rate. In this model it is assumed that dissociation occurs when a molecule is excited to a vibrational level with an energy above the dissociation threshold. The rate of dissociation is then indirectly linked to the vibrational excitation rate.

The models just mentioned have been widely used in the past for large-scale DSMC computations of high-speed, chemically reacting flows. The associated algorithms are fairly easy to implement and their added computational cost is relatively low. However it is a fact that they also have some shortcomings. Phenomenological models are not based on first-principles physics but rely instead on tuning parameters to mimic macroscopic experimental behavior (i.e. relaxation rates, etc.). Experimental data in the literature with the level of detail and range of validity we would require is scarce and it is not known how accurately these models will perform at the extreme conditions of high-speed reentry. In order to alleviate this problem, research has shifted recently to the high-fidelity state-to-state approach, relying on reaction cross-sections derived from quantum-mechanical calculations.

This paper is organized as follows: In section 2 we introduce the concept of state-to-state models and section 3 is devoted to a short description of the NASA *ab initio* quantum database for the N_2 + N system. Section 4 introduces the coarse grain model for rovibrational energy exchange and molecular dissociation of nitrogen (uniform bin model). More details on our implementation of the bin model in DSMC are given in section 5. Specifically, subsection 5.1 describes how the state-specific reaction cross-sections are obtained from rate coefficients. In subsection 5.2 we describe how to determine the state-specific total cross-section for inelastic collisions and how to calculate the probabilities of reaction, while subsection 5.3 is concerned with the necessary adaptations to the DSMC algorithm. The results of our simulations are presented in section 6. Finally, we give summarize and give an outlook on future work in section 7.

2. Approaches to state-specific models in DSMC

In the state-specific approach each molecule's internal state, defined by its internal quantum numbers, has to be stored during the simulation. Particles of a given chemical species (i.e. N_2) with different internal quantum states are each considered to belong to a separate "pseudo-species" (i.e. $N_2\,(v, J)$). For molecular nitrogen the total number of rotational and vibrational levels in the electronic ground state alone is 9390. Therefore, the number of separate species to be considered in a state-specific description is orders of magnitude larger than in the traditional approach, even if only a pure gas is considered.

Since each quantum state of a molecule is treated as a separate species, transitions between states become equivalent to chemical reactions. This includes transitions of a molecule between different pre- and post-collision quantum numbers (i.e. excitation/deexcitation), but also the state-specific chemical reactions such as dissociation/recombination and exchange reactions. Because dissociation can now occur with a given probability from any initial combination of quantum states, the number of separate dissociation reactions for a single type of molecule increases with the total number of internal levels considered.

One immediate consequence of such a detailed description is that a full set of state-specific cross-sections is required to determine the outcome of each collision. These cross-section data must typically be obtained by methods of quantum chemistry. This remains a formidable task and for many mixtures of interest, (i.e. Earth, Mars atmosphere) cross-section data are at present not available. The complexity of the calculations has prevented a construction of a full database of cross-sections for all possible combinations of collision partners. Quantum chemical data have been limited mostly to single-component systems, such as hydrogen or nitrogen, where only collisions of a molecule with an atom are taken into account. One of the most detailed sources of cross-

section data existing nowadays are based on the *ab-initio* quasi classical trajectory calculations (QCT) of Jaffe et al [10] for the N_2 – N-system.

An early implementation of a state-to-state model in DSMC was done by Anderson and co-workers [11]. They considered a gas with only a few internal states defined at arbitrary energy levels. The cross-sections in their model are computed explicitly from expressions which are designed such that detailed balance is satisfied. If, however these cross-sections are applied to the internal levels of a real gas, the transition rates will generally not match those known from experiment. Therefore their model cross section is not suited for application to treat real gases. In a later publication, Dunn and Anderson [12] extended this model to dissociation/recombination reactions. Bruno et al. implemented a vibrationally-specific model for nitrogen [13]. In this work 66 distinct vibrational levels for the nitrogen molecule were considered. For atom-diatom collisions (i.e. $N_2(v)$ + N), cross section data based on quasi-classical trajectory (QCT) calculations performed by the group at the University of Bari were available for both excitation/deexcitation and dissociation/recombination. This was one of the earliest instances where QCT databases were used successfully within DSMC. More recently, Sohn and Levin [14] have combined cross-sections based on the forced harmonic oscillator (FHO) model for VT transitions and on QCT for dissociation reactions in state-to-state simulations of shock waves in nitrogen. Kim and Boyd [15] have used the previously mentioned NASA database of Jaffe et al. [10] to study the $N_2 - N$ system with the full 9390 rovibrational levels of the nitrogen molecule.

3. NASA Ames N_2 + N QCT database

The NASA Ames N3 database [10] contains chemical rate data for the elementary reactions involving molecular and atomic nitrogen listed in Table 1. The nitrogen molecule may initially encounter itself in one of the 9390 rovibrational energy states belonging to the electronic ground state. Each rovibrational energy level is identified by a unique pair of rotational and vibrational quantum numbers (v, J). Using this numbering scheme one may re-order them into a total of 61 vibrational levels, each of them comprising its own distinct number of rotational levels.

If a global index i is used instead, the two notations

Table 1: Elementary processes considered in the NASA Ames database

Excitation / de-excitation:	$N_2(i) + N \rightleftharpoons N_2(j) + N$
Dissociation:	$N_2(i) + N \rightleftharpoons 3\,N$
Pre-dissociation:	$N_2(i) \rightleftharpoons 2\,N$

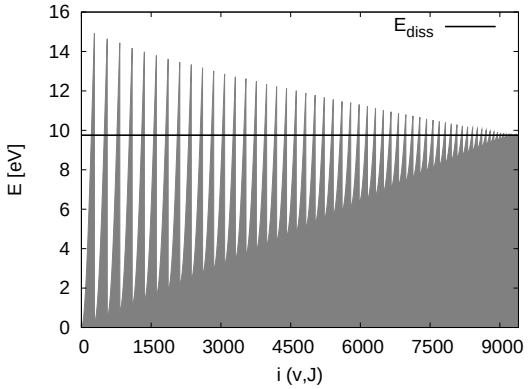

Figure 1: Internal energies of the 9390 rovibrational levels of N_2 sorted by increasing vibrational and rotational numbers $v, J(v)$. The horizontal line marks the minimum energy required to dissociate the nitrogen molecule from its rovibrational ground state $(v = 0, J = 0)$: $E_{\mathrm{diss}} = 9.75\mathrm{eV}$.

are related by

$$i = i(v, J), \quad \text{with} \quad v = 0, \ldots, v_{\max} \quad \text{and} \quad J = 0, \ldots, J_{\max}(v),$$

with the inverse relation given as

$$v = v(i), \quad J = J(i), \quad i = 1, \ldots, 9390.$$

In Figure 1 we plot the energy of each rovibrational level ordered with increasing $v, J(v)$ starting from the vibrational ground state $v = 0$ up to $v_{\max} = 60$. For all levels with the same vibrational number the energy increases monotonically from $J = 0$ to $J_{\max}(v)$ and the largest variation in energy is found within the lowest vibrational levels.

If the levels are re-sorted as a function of increasing energy (see Figure 2), contiguous levels will have non-sequential (v, J) quantum numbers. However this representation makes it much easier to distinguish the truly bound and quasi-bound states. Truly

bound states are those whose energy lies below E_{diss}, which is the minimum amount of energy required for dissociation from the rovibrational ground state ($v = 0, J = 0$), whereas quasi-bound levels lie above this threshold.

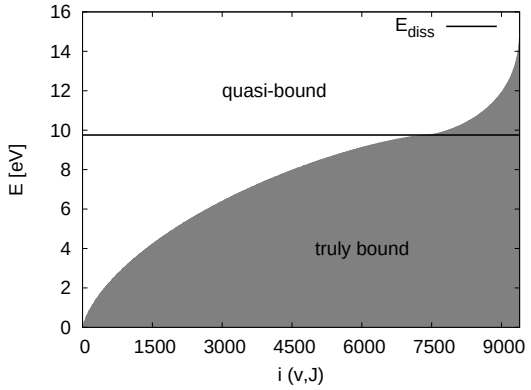

Figure 2: Rovibrational levels re-sorted according to increasing energy. Levels with energy lower than $E_{\text{diss}} = 9.75\text{eV}$ are called truly bound. Those with higher energies are called quasi-bound or pre-dissociated.

The NASA Ames database contains reaction rate data for the three types of elementary processes listed in Table 1:

1. Excitation/deexcitation reactions are collisional processes involving only changes of internal energy of the nitrogen molecule. During an excitation reaction part of the translational energy of the two colliding particles is converted into rovibrational energy of the molecule (thus $E_j > E_i$). Conversely during a deexcitation reaction a certain amount of internal energy is released by the molecule and the translational energy between the colliding particles increases. In the special case when $j = i$, the internal energy of the molecule remains unchanged and we speak of an elastic collision.
2. A dissociation reaction occurs when the nitrogen molecule is split into two atoms during the collision. Breaking up this chemical bond requires an amount of energy equal to $E_{\text{diss}} = 2\,E_N = 9.75\,\text{eV}$, where E_N is the energy of formation of a single nitrogen atom in the electronic ground state. If a collision partner provides enough additional translational energy, dissociation is possible both for molecules initially in a truly bound or a quasi-bound state.
3. The third process, called pre-dissociation, can occur spontaneously without the need of a collision partner for N_2(i). Only molecules in quasi-bound states have enough internal energy to dissociate via this mechanism. In previous work [16] it was shown that for the cases of interest pre-dissociation has a negligible effect on the overall dissociation rate and it is neglected in the present work.

If we were to consider all possible combinations of pre- and post-collision energy states for the 9390 levels of N_2, the total number of distinct excitation/deexcitation and dissociation reactions to take into account would be on the order of 90 million. However, in practice it turns out that many transitions have negligibly small probabilities of occurrence. Still others are so-called forbidden transitions, whose probability is exactly zero due to quantum-mechanical selection rules. This reduces the overall number of processes for which rate data is available to approximately 23 million.

A limitation of the current database is the lack of data for collisional processes involving two nitrogen molecules (i.e.: $N_2(i_1) + N_2(i_2) \longrightarrow ...$). Therefore it is not possible to study the reaction dynamics starting from a gas composed only of pure molecular nitrogen. For the simulations using the current rate data there always needs to be some atomic nitrogen present to start the reactions listed above and encounters between nitrogen molecules are modeled simply as elastic collisions.

4. Uniform rovibrational coarse grain model

The full N3 database has been used in previous studies involving conventional CFD flow solvers by Magin et al [17], while Kim and Boyd [15] have worked on integrating the database with the DSMC method. Simulations using the full set of levels are still computationally expensive due to the large number of processes involved and they have been mostly limited to master equation studies in heat baths and simple flow configurations, such as normal shock waves.

In order to make the information of the N3 database accessible to a wider range of flow problems, several attempts have been made to develop models of reduced complexity [18; 19; 20]. One approach are so-called coarse-grain models, where the goal is to approximate the full set of rovibrational levels of N_2

with a much smaller number of suitably averaged internal states. This smaller number of states automatically leads to a significant reduction in the size of the associated state-specific reaction mechanism. The details of the reduction vary for different coarse grain models, but the main idea is always to collect the information (degeneracy, internal energy, reaction rates) belonging to a certain subset of the original rovibrational levels into a single internal energy "bin". These bins will have specific properties which are averages over the constituting levels. In this work we use the coarse grain uniform rovibrational (URVC) bin model [21] and a short description of the binning procedure follows.

Having sorted the levels according to their energy as shown in Figure 2, we define an energy mesh of equally-spaced (hence uniform) intervals. In our current approach the number of intervals is arbitrary, except for the fact that we keep truly bound and quasi-bound levels in separate intervals. We define the degeneracy of bin k, $\overline{g}_k$ as the sum over all level degeneracies $\overline{g}_i$ contained within the bin:

$$\overline{g}_k = \sum_{i \in I_k} g_i, \tag{1}$$

where I_k is the set of all rovibrational levels i contained within bin k. The level populations within each bin are fixed by

$$\frac{n_i}{n_k} = \frac{g_i}{\overline{g}_k}, \qquad i \in I_k. \tag{2}$$

The bin energy $\overline{E}_k$ is defined as the weighted average over the level energies within the bin:

$$\overline{E}_k = \frac{1}{\overline{g}_k} \sum_{i \in I_k} g_i \, E_i. \tag{3}$$

Applying the weighted averaging to the excitation rate coefficients k^E_{ij}, we obtain:

$$\overline{k}^E_{kl}(T) = \frac{1}{\overline{g}_k} \sum_{i \in I_k} g_i \sum_{j \in I_l} g_j \, k^E_{ij}(T) \quad \ldots \quad k, l \in K_{BP}, \tag{4}$$

where $\overline{k}^E_{kl}$ becomes the bin-specific excitation rate coefficient. The indices k and l stand for the pre-collision and post-collision bins respectively. The overall set of bins containing all truly bound and quasi-bound levels is designated K_{BP}. Obtaining the the bin-specific dissociation rate coefficients $\overline{k}^D_k$ is done analogously:

$$\overline{k}^D_k(T) = \frac{1}{\overline{g}_k} \sum_{i \in I_k} g_i \, k^D_i(T) \quad \ldots \quad k \in K_{BP} \tag{5}$$

At this point the rate data provided in the NASA Ames database can be used with only minor modifications for master equation studies. The original rate coefficients for all processes, which were originally tabulated at nine distinct temperatures between 7500 and 50000K, are lumped into bins following the procedure just outlined. In a subsequent step these coefficients are fitted to temperature-dependent expressions of the form:

$$\overline{k}^E_{kl}(T) = A^E_{kl} \, T^{b^E_{kl}} \, \exp\left(-\frac{E^E_{\mathrm{a},kl}}{\mathrm{k_B} \, T}\right), \quad k < l \tag{6}$$

$$\overline{k}^D_k(T) = A^D_k \, T^{b^D_k} \, \exp\left(-\frac{E^D_{\mathrm{a},k}}{\mathrm{k_B} \, T}\right), \tag{7}$$

$$\overline{k}^E_{kk}(T) = \overline{k}^{el}_k(T) = A^{el}_k \, T^{b^{el}_k}. \tag{8}$$

This results in a pair of bin-specific Arrhenius fit parameters (A, b) for each type of excitation, dissociation and elastic rate coefficient. The fits for excitation (Eqn. (6)) include an exponential term with the energy threshold $E^E_{\mathrm{a},kl}$ for the given reaction. This threshold has been chosen as the minimum amount of energy required for the reaction to proceed. In the case of excitation from bin k to another bin l with higher energy it corresponds to: $E^E_{\mathrm{a},kl} = \overline{E}_l - \overline{E}_k$.

When fitting the forward excitation rate coefficients of equation (6) the data are directly extracted from the database. The corresponding deexcitation rate coefficients however are computed making use of the equilibrium constant given by statistical mechanics:

$$K^E_{\mathrm{eq},kl}(T) = \left[\frac{n_{\mathrm{N_2}(l)}}{n_{\mathrm{N_2(k)}}}\right]_{\mathrm{eq}} = \frac{\overline{g}_l}{\overline{g}_k} \exp\left(-\frac{\overline{E}_l - \overline{E}_k}{\mathrm{k_B} \, T}\right), \tag{9}$$

$$\overline{k}^E_{lk}(T) = \frac{\overline{k}^E_{kl}(T)}{K^E_{\mathrm{eq},kl}(T)} \tag{10}$$

We choose to ignore the deexcitation rate coefficients given in the database because there exist some uncertainties in both the forward and backward rate coefficients. These uncertainties arise as a result of the Monte-Carlo sampling used in generating the QCT

database. This means that it is generally not possible to obtain the correct value of the equilibrium constant as given by equation (9) when we take the ratio of k^E_{kl} / k^E_{lk} directly using both coefficients from the database.

The fit for the dissociation rate coefficient from bins composed of truly bound levels has the form of Eqn. (7). The energy threshold in this case is the difference between the formation energy of the pair of nitrogen atoms and that of the pre-collision bin of the molecule: $E^D_{\mathrm{a},k} = 2\,E_\mathrm{N} - \overline{E}_k$. For dissociation from bins containing only quasi-bound levels $\overline{E}_k > 2\,E_\mathrm{N}$ and $E^D_{\mathrm{a},k} = 0$. The equilibrium constant for the dissociation reaction is given by Eqn. (11). The rate coefficient for recombination is determined via detailed balance using Eqn. (12):

$$K^D_{\mathrm{eq},k}(T) = \left[\frac{n_\mathrm{N}^2}{n_{\mathrm{N_2(k)}}}\right]_\mathrm{eq} = \ldots$$
$$= \frac{\left[g_\mathrm{N}\,Q^t_\mathrm{N}(T)\right]^2}{\overline{g}_k\,Q^t_{\mathrm{N}_2}(T)} \exp\left(-\frac{2E_\mathrm{N} - \overline{E}_k}{\mathrm{k_B}\,T}\right) \qquad (11)$$

$$\overline{k}^R_k(T) = \frac{k^D_k(T)}{K^D_{\mathrm{eq},k}(T)}. \qquad (12)$$

Here $g_\mathrm{N} = 12$ is the degeneracy of the nitrogen atom in its electronic ground state including the contribution of nuclear spin. The translational partition functions of N and N_2 are given respectively by the expressions:

$$Q^t_\mathrm{N}(T) = \left(\frac{2\pi\,m_\mathrm{N}\,\mathrm{k_B}T}{\mathrm{h_P}^2}\right)^{3/2} \qquad (13)$$

$$Q^t_{\mathrm{N}_2}(T) = \left(\frac{2\pi\,m_{\mathrm{N}_2}\,\mathrm{k_B}T}{\mathrm{h_P}^2}\right)^{3/2} \qquad (14)$$

We have also extracted data to determine the elastic collision rate (Eqn. 8). Since no internal energy is exchanged in such a collision, the energy threshold is automatically zero and the exponential term disappears. For master equation studies and in the framework of continuum CFD the elastic rate data is never required, since an implicit assumption is that the velocity distribution function is always nearly Maxwellian. However, it is needed at the DSMC level for determining the total collision cross-section.

5. State-to-state cross-sections for the URVC model

After applying our uniform binning approach we are left with a reduced set of state-to-state reaction rate coefficients. In a hydrodynamic description these rate coefficients are employed to calculate the chemical source terms needed both in the individual species mass balance and overall energy equations. For application at the kinetic level though (e.g. DSMC), we require the equivalent bin-specific reaction cross-sections. The cross-sections are used to determine both the overall collision frequency between particles as well as the relative rate of occurrence of the different types of elastic and inelastic collisions.

5.1. Inversion of the URVC rate coefficients

The temperature-dependent rate coefficient for a given reaction $k_R(T)$ is related its corresponding cross-section $\sigma_R(E_t)$ via Equation (15). Strictly speaking, Equation (15) only holds when the velocity distributions of both colliding species are maxwellian. The cross-section is a function of the relative translational energy between the two colliding particles, i.e. $E_t = \frac{\mu_{AB}}{2}\,g^2$, where μ_{AB} is the collision pair's reduced mass and $g = |\mathbf{c}_A - \mathbf{c}_B|$ is the magnitude of the pair's relative velocity.

$$k_R(T) = \frac{1}{\sqrt{\pi\,\mu_{AB}}}\left(\frac{2}{\mathrm{k_B}T}\right)^{3/2} \times$$
$$\times \int_{E_{\mathrm{a},R}}^{\infty} \sigma_R(E_t)\,\exp\left(-\frac{E_t}{\mathrm{k_B}T}\right) E_t\,dE_t \qquad (15)$$

The integral's lower bound is the energy threshold $E_{\mathrm{a},R}$, which corresponds to the minimum net energy required for the reaction to proceed. It is zero for exothermic reactions but takes on positive values for endothermic reactions. Table 2 summarizes the reaction types considered in the URVC model with their respective energy threshold $E_{\mathrm{a},R}$. We broadly distinguish between internal energy exchange reactions, where the participating nitrogen molecule merely changes its internal state during the collision and dissociation reactions, where the molecule splits into two atoms.

Note that we have formally included collisions where the molecule's internal state remains unchanged (i.e. $k = l$) in the first group. Since the URVC model implies lumping a number of the original rovibrational levels into a single bin, this type of collision

Table 2: Reactions considered in the URVC model for the N_2 + N system

Reaction	$E_{a,R}$
Internal energy exchange N_2 (k) + N → N_2 (l) + N	
1) Excitation ($k < l$)	$\overline{E}_l - \overline{E}_k$
2) Deexcitation ($k > l$)	0
3) "Elastic" ($k = l$)	0
Dissociation N_2 (k) + N → N + N + N	
1) from truly bound state	$2E_N - \overline{E}_k$
2) from quasi-bound state	0

actually represents an aggregate of inelastic (level-to-level transitions within the same bin) as well as strictly elastic collisions (i.e. $(v, J) = (v', J')$). However, within the uniform bin model the individual levels are no longer distinguishable and we treat these collisions as elastic. For dissociation reactions another aspect becomes important. Since the average energy of a bin composed only of truly bound levels will always be lower than the minimum required to form the two nitrogen atoms (i.e. $\overline{E}_k < 2E_N, \quad k \in K_B$), this type of dissociation is always endothermic. However, the average energy of a bin composed of quasi-bound levels will always be larger than $2E_N$. Thus, we treat these reactions as exothermic with zero energy threshold. This is one reason why truly bound and quasi-bound levels should not be lumped together within the same bin.

Whenever the cross-section is known as a function of relative translational energy, either as an analytical expression or in tabulated form, obtaining the rate coefficient via Equation (15) is relatively simple. Numerical integration techniques are available to accurately determine the result. Unfortunately the inverse operation, i.e. determining the correct functional dependence of $\sigma_R(E_t)$ for a given $k_R(T)$ is not at all straightforward. In fact, without additional information on the shape of the cross-section the inverse problem is ill-posed. There may exist an infinity of cross-section shapes which would all in principle satisfy Equation (15). Most of these solutions would be far from the "true" shape of the cross-section and many of them would be problematic from a practical point of view: First, for the cross-section to be physically meaningful it should be non-negative over the whole energy range. The cross-section is directly related to the probability of occurrence of the reaction and can therefore never be negative. Furthermore, if we are dealing with an endothermic reaction, $\sigma_R(E_t)$ must be exactly zero below the threshold $E_{a,R}$. This is equivalent to saying that if the pre-collision translational energy E_t is less than $E_{a,R}$, there is not enough energy available to form the reaction products. Both these constraints narrow down our search to only certain types of cross-section shapes. It would be possible in principle to use a numerical inversion technique, such as Tikhonov regularization [22] or the approach proposed by Minelli et al. [23] to obtain a good enough approximation to the cross-section. However both methods rely on iterative solution finding procedures. Considerable computational time may be required to obtain even a single cross-section fulfilling the required constraints. Furthermore, it has been our experience that the cross-sections obtained via these methods are extremely sensitive to the initial guesses provided by the user and several attempts need to be made to find an acceptable solution. Therefore these procedures seem to be of practical use only when applied to a small number of reactions. Since we need to invert hundreds, if not thousands of rate coefficients depending on the overall number of internal energy bins considered, we will instead resort to an analytical inversion method. Our approach is inspired by the procedure outlined in chapter 6.3 of Bird [24]. The first assumption we need to make is that all our rate coefficients can be approximated by Arrhenius-type expressions of the form

$$k_R(T) = A_R\, T^{b_R} \exp\left(-\frac{E_{a,R}}{k_B T}\right), \tag{16}$$

where the two parameters A_R and b_R result from fitting the tabulated rate coefficients over the temperature range of interest. The appropriate value of the energy threshold $E_{a,R}$ needs to be taken into account at the time of generating the fits (see Table 2). The quality of the fit greatly depends on choosing the correct value of $E_{a,R}$. Next we assume an analytical expression with two adjustable parameters for the cross-section:

$$\sigma_R(E_t) = \begin{cases} \dfrac{C_R\,(E_t - E_{a,R})^{\eta_R}}{E_t} & \text{if} \quad E_t > E_{a,R}, \\ 0 & \text{otherwise.} \end{cases} \tag{17}$$

We wish to retrieve the functional dependence of Equation (16) for the rate coefficient upon substitution of (17) into Equation (15). This automatically determines the two parameters:

$$C_R = \frac{A_R}{2 \cdot \Gamma(3/2 + b_R)} \sqrt{\frac{\pi \mu_{12}}{2}}\, \mathrm{k_B}^{-b_R}, \qquad \eta_R = b_R + 1/2. \tag{18}$$

Excitation/deexcitation cross-sections need to verify detailed balance relations. According to this principle the cross-section for deexcitation from bin l to a lower-energy bin k is related to the corresponding excitation cross-section:

$$\sigma^E_{l,k}(E_t) = \frac{\overline{g}_k \cdot E'_t}{\overline{g}_l \cdot E_t} \cdot \sigma^E_{k,l}(E'_t), \tag{19}$$

with

$$E'_t = E_t + \overbrace{\left(\overline{E}_l - \overline{E}_k\right)}^{E^E_{\mathrm{a},kl}}. \tag{20}$$

The quantity E'_t is the relative translational energy of the collision pair after deexcitation. Note that the difference $\overline{E}_l - \overline{E}_k$ in Equation (20) is equal to the energy threshold needed for the transition $k \to l$.

As an example, in Figure 3 we plot a pair of cross-section for transitions between bins 5 and 6 out of a 10-bin system. The excitation cross-section $\sigma^E_{5,6}$ remains zero until the energy threshold has been reached. The corresponding deexcitation cross-section $\sigma^E_{6,5}$ has no such threshold.

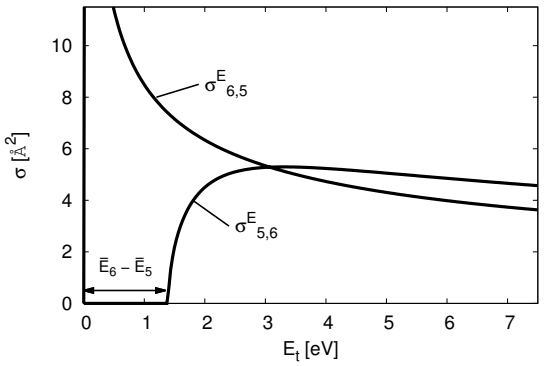

Figure 3: Excitation/deexcitation cross-sections between bins 5 and 6 from a 10-bin system

5.2. State-specific total cross-section for the pair $N_2(k) + N$

The overall number of collisions per unit time and unit volume between particles of two different species A,B is determined by:

$$N_{AB} = \frac{1}{2}\, n_A\, n_B \left(\overline{\sigma^T_{AB} \cdot g}\right). \tag{21}$$

The quantity in parenthesis represents a weighted average of the total cross-section for the colliding pair σ^T_{AB} multiplied by the pair's relative velocity g over the pair's joint velocity distribution:

$$\left(\overline{\sigma^T_{AB} \cdot g}\right) = \iint \sigma^T_{AB} \cdot |\mathbf{c}_A - \mathbf{c}_B|\; f_A\, f_B\, d\mathbf{c}_A\, d\mathbf{c}_B. \tag{22}$$

A common choice in DSMC is to use a total cross-section based on the variable hard sphere (VHS) model [25]:

$$\sigma^T_{AB,\mathrm{VHS}} = \frac{\pi\, d^2_{\mathrm{ref},AB}}{\Gamma(5/2 - \omega_{AB})} \left(\frac{\mathrm{k_B} T_{\mathrm{ref}}}{E_t}\right)^{\omega_{AB} - 1/2}. \tag{23}$$

The sub-index $(.)_{AB}$ in Equation (23) stands for one of the possible species pairings (e.g. in a mixture of molecular and atomic nitrogen: N_2–N_2, N_2–N or N–N). The reference diameters $d_{\mathrm{ref},AB}$ and exponents ω_{AB} are parameters tuned to approximate the viscosity and diffusion coefficients of the gas mixture over a given range around the reference temperature T_{ref}. Table 3 lists VHS parameters for an N_2–N mixture valid from 1000 K up to about 5000 K [26].

Table 3: Typical VHS parameters for particle pairings in a nitrogen mixture, The reference temperature for all cases is $T_{\mathrm{ref}} = 2880$ K

pair AB	$d_{\mathrm{ref},AB}$ [m]	ω_{AB}
N_2 - N_2	3.2×10^{-10}	0.68
N_2 - N	2.9×10^{-10}	0.69
N - N	2.6×10^{-10}	0.70

The VHS model is widely used in the conventional approach to DSMC, where we would generally assume that the VHS cross-section gives us the overall collision rate and internal energy exchange is treated using the Larsen-Borgnakke model. However when using a state-to-state approach the total cross-sections may depend not just on the identity of the species involved, but also on the pre-collision internal states of the particles. This was already noted by Kim [15]. For

our bin model this means that we will have as many total cross-sections for the collision N_2 (k) + N as there are bins. The total cross-section for a collision pair N_2(k) + N is now calculated as the sum over all inelastic cross-sections:

$$\sigma_k^T = \sum_{l=1}^{n_{\text{bins}}} \left\{\sigma_{k,l}^E\right\} + \sigma_k^D \tag{24}$$

Note that we have simplified the notation omitting the sub-index $N_2 - N$ for each of the cross-sections. Here, $\sigma_{k,l}^E$ represents the full set of excitation and deexcitation cross-sections from pre-collision bin k to all other post-collision bins l. In Figure 4 we show several of the state-specific total cross-sections for N_2-N computed from our URVC model and compare them to the VHS cross-section generated from the parameters from Table 3. It is evident that the VHS cross-section is much smaller than all the total cross-sections we extracted from the bin model.

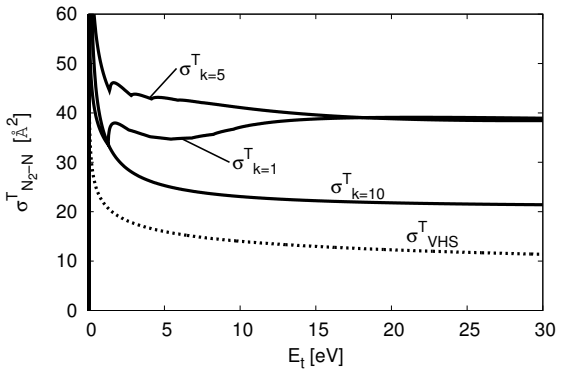

Figure 4: Total cross-sections for N_2(k) + N of the 10-bin system (solid lines) vs. typical VHS cross-section (dotted line)

If we plot the partial sum for each of the terms in Equation (24) we obtain the picture given in Figure 5a. There we can see the cumulative sum of all inelastic and elastic cross-sections for bin 5 out of a 10-bin system. The vertical distance between lines represents the magnitude of the given cross-section. Starting with deexcitation to the lowest bin at the bottom, i.e. $\sigma_{5,1}^E$, we first go through all possible bound stated after the collision: $l = 1, \ldots, 10$. The last interval, marked σ_5^D corresponds to the dissociation cross-section for bin 5. As can be seen, excitation cross-sections to higher-lying bins, i.e. $l > 5$ do not contribute to the total cross-section below the energy threshold $\overline{E}_l - \overline{E}_5$ and dissociation starts playing a role only at relative energies higher than $2E_N - \overline{E}_5$. The overall envelope of all the curves corresponds to the state-specific total cross-section σ_5^T.

The relative frequency, or probability of a given outcome after the collision is then given by the ratio of each individual cross-section to the total one:

$$\begin{aligned} P_{k,l}^E &= \frac{\sigma_{k,l}^E}{\sigma_k^T} \qquad l = 1, \ldots, n_{\text{bins}} \\ P_k^D &= \frac{\sigma_k^D}{\sigma_k^T} \end{aligned} \tag{25}$$

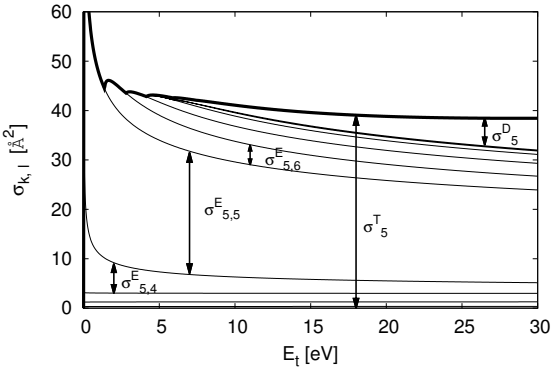

(a) Cumulative sum of excitation/deexcitation cross-sections for pre-collision bin $k = 5$. to post-collision bins $l = 1, \ldots, 10$ plus dissociation. The width between individual lines represents single-event cross-sections

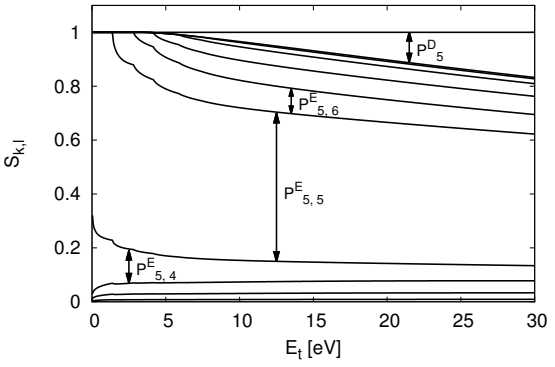

(b) Cumulative probabilities $S_{k,l}$ of transitions from pre-collision bin $k = 5$ to post-collision bins $l = 1, \ldots, 10$ plus dissociation. The width between individual lines represents single-event probabilities

Figure 5: Cumulative cross-sections and probabilities for bin 5 out of 10

Finally, we define the corresponding cumulative

probabilities for bin k as:

$$\begin{aligned} S_{k,1} &= P^E_{k,1} \\ S_{k,2} &= S_{k,1} + P^E_{k,2} \\ &\vdots \\ S_{k,10} &= S_{k,9} + P^E_{k,10} \\ S_{k,11} &= S_{k,10} + P^D_k \stackrel{!}{=} 1 \end{aligned} \tag{26}$$

Plotting these cumulative probabilities for the 10-bin system results in Figure 5b. Now all cross-sections have been normalized by σ_5^T and for a given translational energy E_t their overall sum always equals unity. Using this representation it is very easy to recognize the relative importance of a given transition. For example, it is evident that more than half of the collisions will be elastic over the whole energy range.

5.3. DSMC implementation

Use of the bin model requires several modifications to the standard DSMC collision algorithm. Assuming we use Bird's NTC method [27] to select the collision pairs, we first need to determine the collision probability for each one of them:

$$P_{\text{coll}} = \frac{\sigma^T_{AB} \cdot g}{(\sigma_T \cdot g)_{\max}}. \tag{27}$$

If the collision involves N_2–N_2 or N–N pairs, we determine σ^T_{AB} using Equation (23) and the VHS parameters of Table 3. For N–N pairs only elastic collisions are possible. Standard elastic collision routines using isotropic hard sphere scattering are computed. The same is done for N_2–N_2 collisions, but only because no detailed chemistry data for this pair is available at the moment. Therefore, no internal energy exchange or dissociation is allowed in this situation. In the case of N_2–N pairs though, we compute the bin-specific total cross-section using Equation (24). Next we follow the scheme in Figure 6 to decide the outcome of the collision. For this we require the cumulative probabilities $S_{k,l}$ as defined in Equation (26). We now compare each of these probabilities to the randomly generated number $0 \le R_f \le 1$ until one of the conditions is fulfilled.

If the outcome of the collision is a transition to another bin, we determine the post-collision translational energy:

$$E'_t = E_t + \overline{E}_k - \overline{E}_l. \tag{28}$$

After re-labeling the N_2(k) particle to its new bin, we now perform an elastic collision between the

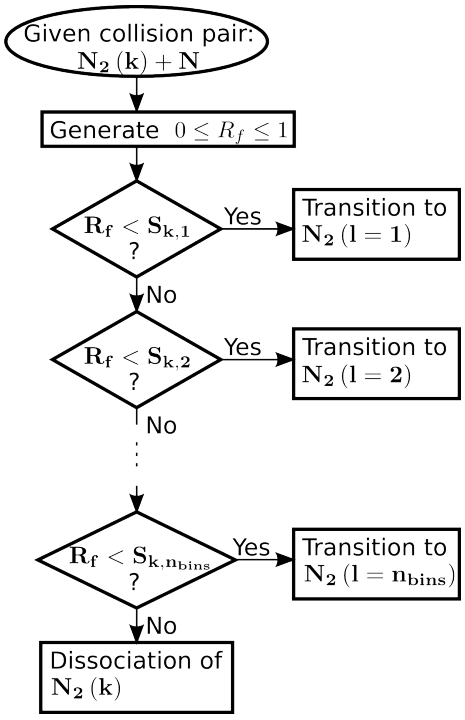

Figure 6: Procedure for selecting the post-collision state of a N_2 (k)-molecule

N_2(l) + N pair using hard sphere scattering and the remaining translational energy E'_t.

For dissociation, the collision is handled in two separate stages. In the first step the dissociation energy $2E_N$ is deducted from the overall energy available to the collision pair:

$$E^I_t = E_t + \overline{E}_k - 2E_N \tag{29}$$

The remaining energy is then partitioned at random into two fractions:

$$E^*_t = R_f \cdot E^I_t \tag{30}$$

$$E'_t = \left(1 - R_f\right) \cdot E^I_t, \qquad 0 \le R_f \le 1 \tag{31}$$

The first value E^*_t is stored in memory in a special array along with a pointer referring to the present N_2 molecule. This molecule is now marked for dissociation and its bin label is reset to zero. However, before the molecule is split into two atoms, E'_t will be used to compute an elastic collision between the $N_2(0)$ +N pair. After all regular collisions have been performed, we loop over the N_2 particles previously marked for dissociation. For each one of them two new nitrogen

atoms are generated. We use the N_2-molecule's velocity as the center-of-mass velocity of the N−N pair and the energy E_t^* as their relative translational energy to compute an elastic collision between the two newly created atoms. Finally, the molecule is removed from the global particle list and replaced with the two newly created atoms.

6. Results

In this section we demonstrate the results of integrating the URVC model into an existing DSMC solver. To verify the implementation we perform several transient relaxation studies in a constant-volume, adiabatic heat bath. The flow configuration is radically simplified by assuming that the gas is spatially homogeneous and does not interact with any external boundaries. In this case we can treat the gas as being confined to a single DSMC cell and may disregard the particle's motion between collisions. Using a fluid dynamic description this situation is governed by the system of master equations consisting of a species continuity equation for each bin of N_2, one for atomic nitrogen and a conservation equation for the total energy.

6.1. Adiabatic heat bath, internal energy exchange only

For the first set of calculations all parts of the URVC model related dissociation were disabled. The state-specific total cross-section employed in this case lacks the contribution of the dissociation cross-section and any collisions involving N_2 (k) + N may only result in transitions to other bound states. The equivalent simplification in the system of master equations is to impose dissociation and recombination rates equal to zero. Consequently the overall concentrations of molecular and atomic nitrogen in the heat bath remain frozen throughout the simulation. We initialize the heat bath with equal parts of molecular and atomic nitrogen, $n_{N_2} = n_N = 5.0 \times 10^{23}\,\mathrm{m}^{-3}$ using approximately 100000 particles in total. The initial particle velocities are sampled from a Maxwell distribution at $T_t = 10000\,\mathrm{K}$ whereas the initial bin populations of N_2 correspond to a Boltzmann distribution at $T_{\mathrm{int}} = 2000\,\mathrm{K}$.

Figure 7 shows the time evolution of translational and internal temperatures during the simulation. As internal energy excitation reactions take place the number of nitrogen molecules transitioning to higher-lying bins increases. Thermal equilibrium within the bath is achieved once all excitation and their corresponding deexcitation rates balance out. After this point the bin populations and temperatures characterizing the translational and internal mode also remain constant.

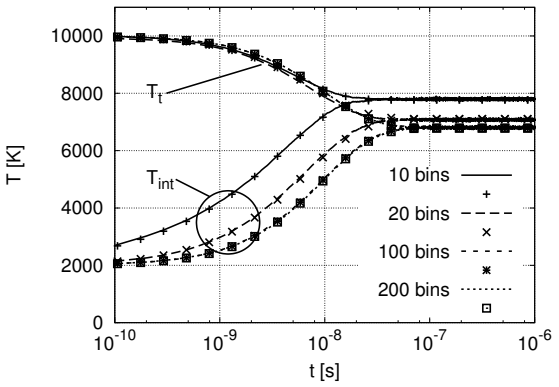

Figure 7: Profiles of translational and internal temperature. Lines represent the DSMC results and symbols the equivalent master equation results.

The internal temperature of N_2 is defined implicitly by Equation (32). This expression relates the bin populations $\overline{n}_k$ to the internal temperature. A mixture will be in thermal equilibrium when the bin populations of N_2 follow a Boltzmann distribution at the gas temperature. For non-equilibrium populations, Equation (32) may be solved iteratively to obtain T_{int}. In that case the difference between the translational gas temperature T_t and T_{int} is an indicator of the degree of thermal nonequilibrium.

$$\sum_{k\in K} \frac{\overline{n}_k}{n_{N_2}} \overline{E}_k = \frac{\sum_{k\in K} \overline{g}_k \overline{E}_k \exp\left(-\dfrac{\overline{E}_k}{k_B T_{\mathrm{int}}}\right)}{\sum_{k\in K} \overline{g}_k \exp\left(-\dfrac{\overline{E}_k}{k_B T_{\mathrm{int}}}\right)} \tag{32}$$

The temperature profiles in Figure 7 are repeated for four different values of n_{bins}. The influence of this parameter on the results is noticeable in two ways. First, the choice of n_{bins} affects the time at which thermal equilibrium is reached. For $n_{\mathrm{bins}} = 10$ it lies close to 2.5×10^{-8} seconds, whereas for $n_{\mathrm{bins}} = 100$ it increases slightly to around $9.0{\times}10^{-8}$ seconds. The final equilibrium temperature is also affected. When using 10 bins the gas reaches equilibrium at around 7700 K but with $n_{\mathrm{bins}} = 100$ the final equilibrium temperature lies closer to 6800 K. There is nearly perfect overlap

of the curves for $n_{\text{bins}} = 100$ and 200 and this asymptotic behavior leads us to conclude that, at least for this situation, the characteristics of the full rovibrational model can be captured well enough with 100 uniform bins. The variation of the equilibrium temperature can be explained by how the choice of n_{bins} influences the thermodynamic properties of the gas. Figure 8 shows the c_v of pure N_2 with n_{bins} as a parameter. As we reduce n_{bins} from 200 down to 10, the difference between the c_v-curves becomes especially noticeable below 10000 K. The contribution of the internal mode to c_v is largest for $n_{\text{bins}} \geq 100$ and becomes progressively smaller as n_{bins} is reduced. Thus, when using a small number of bins the gas can absorb less energy in its internal mode and consequently the final equilibrium temperature in Figure 7 rises to a higher level.

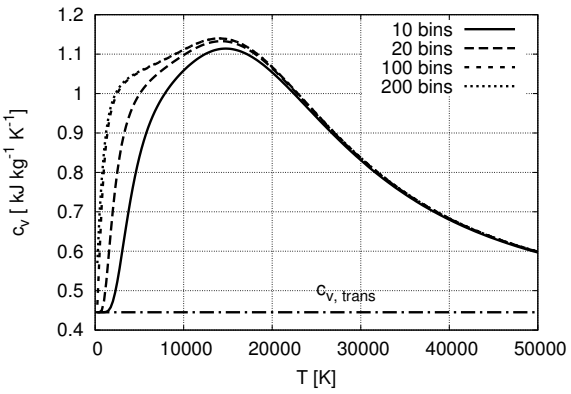

Figure 8: Comparison of constant-volume heat capacity of pure N_2 depending on n_{bins}. The horizontal line marks the contribution of the translational mode: $c_{v,\text{trans}} = \frac{3}{2}\frac{k_B}{m_{N_2}}$

6.2. *Adiabatic, constant volume heat bath including dissociation*

After having verified our implementation of internal energy exchange we are now ready to add the bin-specific dissociation reactions to the model. Although we again simulate a constant-volume homogeneous heat bath, this test case is intended to mimic the flow immediately behind a strong shock wave, typical of atmospheric entry. The gas starts out with a translational temperature of 62546.0 K and the density is equal to 1.64×10^{-4} kg/m^3. The initial bin populations of N_2 follow a Boltzmann distribution at $T_{\text{int}} = 300.0$ K. A small fraction of atomic nitrogen ($y_N = 0.014$) is also present in the initial mixture. This initial atomic nitrogen is necessary for any of the URVC reactions to occur at all, since we have no rate data for N_2–N_2-collisions and are treating them as elastic collisions. The DSMC simulation was initialized with approximately 100000 particles, which during the course of time gradually increase up to slightly under 200000 due to dissociation. The time step was set to 10^{-8} seconds, well below the mean collision time during the whole simulation.

In Figure 9a we plot translational and internal temperature profiles for this test case. It takes about 10^{-5} seconds for the gas to reach thermal equilibrium at slightly above 20000 K. During the early stages of the process internal energy exchange reactions seem to play the dominant role. The mass fractions of N and N_2 in Figure 9b are essentially constant up to about 2.5×10^{-6} seconds.

As in the previous test case these simulations were repeated for four different values of n_{bins}. We can see that both the temperature profiles, as well as the mixture compositions are affected by this parameter. We also see that the overall number of bins has a strong influence on the final equilibrium composition. For 10 bins, the final mass fraction of N is almost 80%, while for 100 bins it is closer to 70%. For $n_{\text{bins}} = 200$ the final concentrations remain essentially unchanged and it may be concluded that 100 bins is a large enough number to obtain accurate results.

In Figure 10 we plot the bin populations extracted from both the DSMC and master equation solutions. We show the populations at four different times during the early stages of the simulation. We have no comparison available for later times, because the DSMC was only run up to 10^{-2} seconds. It can be seen that at the earliest time (10^{-8} s) only the lowest-lying bin is significantly populated. Moreover, the initial populations deviate very strongly from thermal equilibrium, i.e. a straight line. It is only at about 10^{-4} seconds and at later times that the internal mode reaches thermal equilibrium at the internal temperature T_{int}.

6.3. *Neglecting recombination*

It is worthwhile to assess the influence of recombination on the overall solution. In Figure 11 we re-plot the results of the previous test case comparing the behavior of the heat bath with and without the effect of recombination reactions. Judging from the overlap of both sets of curves it is clear that at the early stages, up to about $t = 10^{-1}$ seconds, recombination does not play a role. Only after this point do the species mass fractions for the case including recombination (solid lines in Figure 11b start to level off and slowly approach the final equilibrium values. However, if we

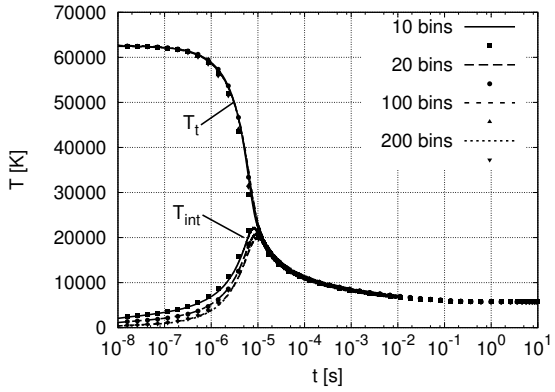

(a) Mixture translational temperature and internal temperature of N_2

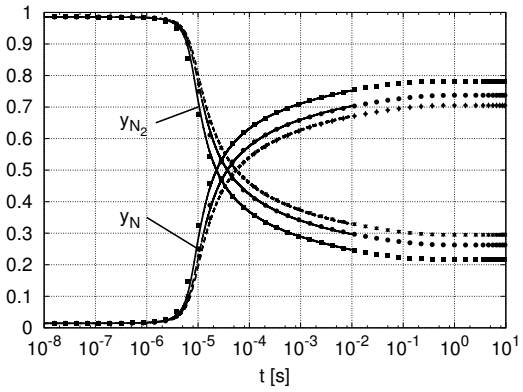

(b) Mass fractions profiles of N_2 and N.

Figure 9: Comparison of DSMC calculations (lines) with master equation results (symbols).

neglect recombination, the mass fractions of N_2 and N keep on decreasing/increasing beyond the equilibrium values. Simultaneously the temperature of the heat bath continues to decrease when dissociation is not balanced out by recombination. If we kept running the calculation for even longer, this process would continue until all of the original molecular nitrogen had dissociated. However, since the dissociation rate itself becomes smaller and smaller as the temperature decreases, this process would take an extremely long time.

In our DSMC implementation we have neglected recombination and this is mainly for practical reasons. Considering the time scales at which the differences in the two solutions start to appear, we can argue that recombination is of minor importance in practical applications. If we think of the previous test case in terms of the gas flow behind a standing shock wave,

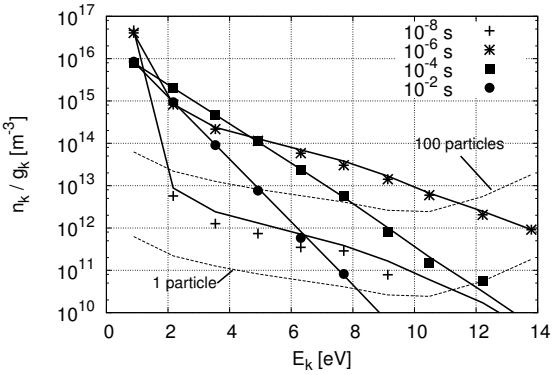

Figure 10: Bin populations for the 10-bin system extracted at four given times. Symbols represent DSMC, solid lines master equation results. The two dashed lines mark the threshold below which fewer than 100 or 1 DSMC particles are available to represent a population

we would interpret the time axis as being proportional to the distance a volume of gas has traveled after passing through the shock. Using this interpretation it can be said that recombination takes place very far behind the actual shock wave. Since we are mostly interested in applying the bin model in calculations of hypersonic flows over blunt body configurations at rarefied conditions, the length scales at which recombination would start to occur are much larger than our flow domain would be. The only place where recombination might be important is near the surface of the body itself. Usually the surface is much cooler and this encourages recombination to occur. However, we must also consider that the DSMC method would only be applied to the early stages of atmospheric entry at very high altitude. Under such conditions free-stream pressures are extremely low and the recombination rates are small.

7. Conclusion and future work

In this paper we have presented a methodology to incorporate detailed chemistry data provided by an *ab initio* quantum chemistry database for the N_2–N system into the direct simulation Monte Carlo method. We have used a coarse grain model (URVC bin model) to reduce the complexity of the original reaction mechanism. A key point of the current work is the extraction of cross-section data for DSMC simulations from existing rate coefficients. We implemented and tested our approach using constant-volume adiabatic

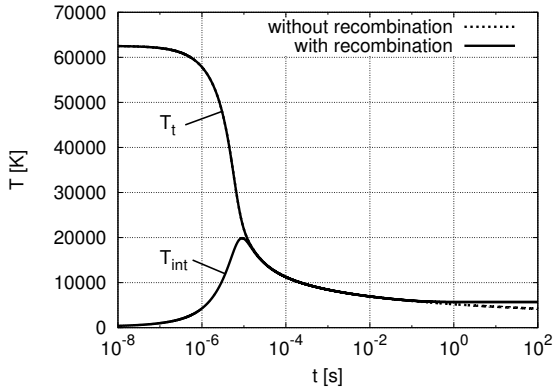

(a) Temperatures

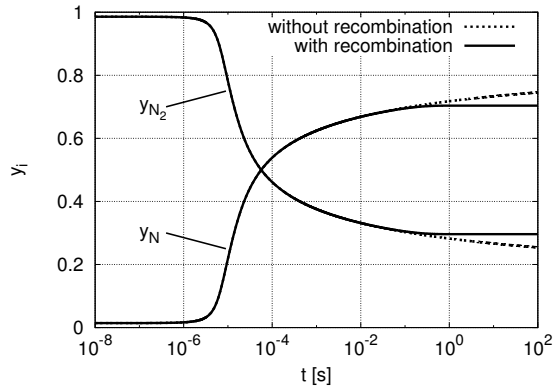

(b) Mass fractions

Figure 11: Master equation calculations for the 200 bin system, with (solid lines) and without recombination (dotted lines)

heat bath simulations. Comparing the dynamic behavior of the DSMC solutions to those obtained via the master equations we obtain very good agreement. We have also found that the behavior of the full N_2 database consisting of 9390 rovibrational levels can be approximated very well with 100 uniform bins. As a next step we will perform simulations of normal shock waves using the present coarse grain model and compare with more conventional chemistry models for DSMC. The current implementation does not yet take into account recombination reactions. Therefore it is impossible at present to retrieve the correct chemical equilibrium composition in our heat bath calculations. Since recombination may be of importance in boundary-layer flows, future work will be devoted to include it in the model.

References

[1] G. Bird, Approach to translational equilibrium in a rigid sphere gas, Physics of Fluids 6 (1963) 1518–1519.

[2] C. Borgnakke, P. Larsen, Statistical collision model for monte carlo simulation of polyatomic gas mixture, Journal of Computational Physics 18 (1975) 405–420.

[3] J. Parker, Rotational and vibrational relaxation in diatomic gases, Physics of Fluids 2(4) (1959) 449–462.

[4] R. Millikan, D. White, Systematics of vibrational relaxation, Journal of Chemical Physics 39(12) (1963) 3209–3214.

[5] F. Bergemann, I. Boyd, Rarefied Gas Dynamics: Experimental Techniques and Physical Systems (Progress in Aeronautics and Astronautics), American Institute of Aeronautics and Astronautics, 1994, Ch. 3. New Discrete Vibrational Energy Model for the Direct Simulation Monte Carlo Method, pp. 174–183.

[6] I. Boyd, Relaxation of discrete rotational energy distributions using a monte carlo method, Physics of Fluids A 5(9) (1993) 2278–2286.

[7] G. Bird, Simulation of multi-dimensional and chemically reacting flows, in: 11th International Symposium on Rarefied Gas Dynamics, 1978.

[8] B. Haas, I. Boyd, Models for vibrationally-favored dissociation applicable to a particle simulation, in: 29th Aerospace Sciences Meeting, 1991.

[9] G. Bird, The q-k model for gas-phase chemical reaction rates, Physics of Fluids 23 (2011) 106101.

[10] R. Jaffe, D. Schwenke, G. Chaban, W. Huo, Vibrational and rotational excitation and relaxation of nitrogen from accurate theoretical calculations, in: 46th AIAA Aerospace Sciences Meeting and Exhibit, Reno, Nevada, 2008.

[11] J. Anderson, J. Foch, M. Shaw, R. Stem, B. Wu, Statistical theory of electronic energy relaxation, in: Proceedings of the 15th International Symposium on Rarefied Gas Dynamics, 1986.

[12] S. Dunn, J. Anderson, Direct monte carlo simulation of chemical reaction systems: Dissociation and recombination, Journal of Chemical Physics 102(7) (1995) 2812–2815.

[13] D. Bruno, M. Capitelli, E. F., S. Longo, P. Minelli, Direct simulation of non-equilibrium kinetics under shock conditions in nitrogen, Chemical Physics Letters 360 (2002) 31–37.

[14] Z. Sohn, D. Levin, State specific vibrational relaxation and dissociation models for nitrogen in shock regions, in: 28th International Symposium on Rarefied Gas Dynamics, Zaragoza, 2012.

[15] J. Kim, I. Boyd, State resolved thermochemical modeling of nitrogen using dsmc, in: 43rd AIAA Thermophysics Conference, 2012.

[16] M. Panesi, R. Jaffe, D. Schwenke, T. Magin, Rovibrational internal energy transfer and dissociation of $n_2^1\left(\sigma_g^+\right) - n\left(^4s_u\right)$ system in hypersonic flows, The Journal of Chemical Physics 138 (4) (2013) 044312.

[17] T. Magin, M. Panesi, A. Bourdon, R. Jaffe, D. Schwenke, Rovibrational internal energy excitation and dissociation of molecular nitrogen in hypersonic flows, in: 10th AIAA/ASME Joint Thermophysics and Heat Transfer Conference, Chicago, Illinois, 2010.

[18] A. Munafo, M. Panesi, R. Jaffe, T. Magin, A. Lani, Vibrational state to state kinetics in expanding and compressing nitrogen flows, in: 10th AIAA/ASME Joint Thermophysics and Heat Transfer Conference, 2010.

[19] M. Panesi, T. Magin, A. Munafo, A. Bourdon, R. Jaffe, D. Schwenke, Rovibrational internal energy excitation and dissociation of nitrogen in hypersonic flows, in: Center for

Turbulence Research Proceedings of the Summer Program, 2010.

[20] A. Munafo, T. Magin, M. Panesi, A. Bourdon, R. Jaffe, D. Schwenke, Mechanism reduction for rovibrational energy excitation and dissociation of molecular nitrogen in hypersonic flows, in: 42nd AIAA Thermophysics Conference, Honolulu, Hawaii, 2011.

[21] T. Magin, M. Panesi, A. Bourdon, R. Jaffe, D. Schwenke, Coarse-grain model for internal energy excitation and dissociation of molecular nitrogen, Chemical Physics 398 (2012) 90–95.

[22] Y. Bondar, M. Ivanov, Dsmc dissociation model based on two-temperature chemical rate constant, in: 45th AIAA Aerospace Sciences Meeting and Exhibit, Reno, Nevada, 2007.

[23] P. Minelli, E. F., D. Bruno, M. Capitelli, S. Longo, Extracting cross sections from rate coefficients: Application to molecular gas dissociation, Journal of Thermophysics and Heat Transfer 25(3) (2011) 374–377.

[24] G. Bird, Molecular Gas Dynamics and the Direct Simulation of Gas Flows, Oxford University Press, 1994.

[25] G. Bird, Monte-carlo simulation in an engineering context, in: 12th International Symposium on rarefied gas dynamics, 1980.

[26] K. Stephani, D. Goldstein, P. L. Varghese, Consistent treatment of transport properties for five-species air direct simulation monte carlo/navier-stokes applications, Physics of Fluids 24 (2012) 077101.

[27] G. Bird, Perception of numerical methods in rarefied gasdynamics, in: 16th International Symposium on rarefied gas dynamics, 1988.

Assessment of Gas-Surface Interaction Modeling for Lifting Body Re-Entry Flight Design

Alan Viladegut

Aeronautics and Aerospace Department, von Karman Institute for Fluid Dynamics, Belgium, alan.viladegut@vki.ac.be

Supervisor: Olivier Chazot

Professor, Aeronautics and Aerospace Department, von Karman Institute for Fluid Dynamics, Belgium, chazot@vki.ac.be

University Supervisor: Roberto Flores

Professor, Aerospace Department, Universitat Politècnica de Catalunya, Spain, rflores@cimne.upc.edu

Abstract

A description of the reacting processes involved in hypersonic boundary layers is given. Two Damköhler numbers characterize the level of both volume and surface reactions. Two types of catalytic models are described: microscopic and macroscopic. The second is based on quantification of catalycity with typical variables used in Plasma facilities. An update of the γ-model currently used at the VKI-Plasmatron is proposed based on new experiments in both Air and N_2 mixtures.

Keywords: Catalycity, Plasmatron, Reaction Rate, Boundary Layer, Damköhler, Equilibrium, Frozen.

1. Introduction

Space vehicles re-entering an atmosphere at hypersonic velocities face extreme heat flux conditions. A bow shock wave appears in front of the vehicle after which molecules dissociate into atoms and the gas becomes a mixture of species. Diffusive effects are confined inside a thin boundary layer close to the body. The processes involved within this layer are responsible for the energy balance at the wall of the Thermal Protection System (TPS). If conduction inside the TPS is neglected, both convective and diffusive heatings should be compensated by radiative heat flux. An accurate characterization of the flow diffusive properties and an appropriate gas-surface interaction model is necessary for both payload integrity and overall mission efficiency.

One important term in the energy balance at the wall is the diffusive heat flux. It is induced by species concentration gradients within the so called chemical boundary layer. Its expression can be found in Eq 1, where ρ is the gas density, c_i the mass fraction of i-species, D the mass diffusion coefficient and h_i is the enthalpy.

$$\dot{Q}_d = \sum \rho D \frac{\partial c_i}{\partial \eta} h_i \tag{1}$$

Many efforts has been made since the late 50's to account for chemical reactions in hypersonic boundary layers. Lees [1] introduced in 1956 the relevance of the Lewis number ($Le = \rho D c_p / \lambda$) in both frozen and equilibrium boundary layers. Then, in 1958 Fay and Riddell [2] gave a mathematical expression that is still in use for flight extrapolation methodologies such as the Local Heat Transfer Simulation developed at IPM by Kolesnikov [3] and adapted at VKI [4]. Also in 1958 Goulard [5] extended the conservative assumption of full recombination at the wall used by Lees and Fay and Riddell to finite rate catalytic activity, being the first to introduce the concept of *Recombination Efficiency* (γ) for re-entry applications. It is the purpose of this work to introduce to the reader the effect of catalytic reactions in a chemical boundary layer, to review different aproaches for modelling catalycity and to propose a path for improving one of these models from experimental data base produced at the VKI-Plasmatron facility.

1.1. Characterization of Chemical Boundary Layers

Two main sources are responsible for mass diffusion within the boundary layer: volume and surface reactions. The non-dimensional parameters known as Damköhler numbers were proposed by Rosner [6] in 1963 to quantify the relevance of these chemical reactions in the boundary layer problem. They are the ratio between a characteristic time of the flow τ_f and a characteristic time of the reaction τ_c. Rosner gave a definition for both volume and surface reactions. He distinguished between a gas Damköhler $Da_g = (\delta^2/D)/\tau_c$ for the former and a wall Damköhler $Da_w = k_w\delta/D$ for the latter, being k_w and δ the reaction rate constant and the boundary layer thickness respectively. These definitions turn to be a comparison between diffusion and reaction characteristics of the problem and they can play an important role on the heat flux computation (Nusselt number can go much beyond unity) during the TPS design phase depending on their order of magnitude.

It is possible to differenciate three regimes depending on the balance between species diffusion and volume reactions:

- $Da_g \to 0$ Frozen Regime: The characteristic reaction time is much higher than the time used by species to diffuse across the boundary layer (computed with the velocity gradient $\beta = \partial u_e/\partial x$ as β^{-1}). Recombination effects can be neglected in this regime and no bulk reaction shall be considered.

- $0 << Da_g << \infty$ Non-Equilibrium Regime: Recombination is taking place and should be taken into account in the heat balance equation.

- $Da_g \to \infty$ Equilibrium Regime: Reaction processes are much faster than diffusion. Atoms are recombined into molecules so fast that LTE is reached and chemical composition of the mixture is imposed by the boundary layer temperature profile.

Equivalently, three catalytic regimes could be identified for surface reactions:

- $Da_w \to 0$ Non-Catalytic Regime: Diffusion is much faster than reaction and surface production rates ($\dot{\omega}$) are set to zero as boundary condition.

- $0 << Da_w << \infty$ Finite-Rate-Catalytic Regime: Recombination is taking place and should be considered in the heat balance equation.

- $Da_w \to \infty$ Diffusion Limited Regime: Diffusion due to surface reaction is so slow that the speed of the reaction has to stop to its upper limit. The system is considered Full-Catalytic. Atom mass concentration is usually imposed to zero under this situation. This is not fully correct since the species composition cannot go beyond equilibrium. Barbato [7] proposed the definition of a wall in Local Equilibrium. However, at typical TPS temperatures during re-entry the difference between Full-Catalytic and Local Equilibrium Wall is negligible.

Despite this analysis could be appropriate for CFD codes, it gives the idea that a Full-Catalytic wall is the worst case scenario for the heat flux. This is not completely true since the coupling between volume and surface reactions must not be forgotten. Indeed, the relevance of catalycity would be negligible in the heat flux computation if $Da_g \to \infty$. On the other hand, diffusive heat flux is very sensitive to catalycity under Frozen Regimes. This means that the precision required for the implemented catalytic model will be relevant only under certain flight conditions.

Many TPS designs have been based on the Full-Catalytic assumption. This is an extremely conservative hypothesis since the surface material is usually low in terms of catalycity. The result is an oversized TPS that increases both costs and weight. Modern designs use *Finite-Rate-Catalytic* models that normally depend on wall temperature T_w and in some cases pressure P. However, their uncertainty is still high and more work on the subject must be done.

2. Catalytic Modeling

The presence of a third body is generally required during a recombination process between two atoms into a molecule. It could be either another atom/molecule if the process is a volume reaction or the wall itself for surface reactions. The third body remains unchanged after the process. Catalycity is nothing else than a quantification of the wall microscopic properties that enhance recombination while acting as a third body. There are different but equivalent ways to express these properties. The Da_w proposed by Rosner [6] and previously described seems convenient for flight extrapolation. Direct modeling of the reaction rate constant (k_w) and the so-called γ-model are extensively used for CFD calculations. State-of-the-art numerical models is briefly described

in Section 2.1 and an extension of the γ-model currently used at VKI is proposed in Section 2.2.

2.1. A microscopic approach

The reaction rate ($\dot{\omega}$) for each wall process is a function of three variables: partial density of reactants ($\rho_i = \rho c_i$), reaction order (n) and reaction rate constant (k_w). The relation is given by Eq 2. The backward reaction rate constant is neglected in the production rate for surface reactions [8; 9]. Mass conservation at the wall requires diffusion of atoms towards the surface. Thus, Eq 3 is implemented as boundary condition. This expression becomes more complex in multispecies mixtures [10; 11; 12]. The units of k_w will vary depending on the reaction order. For instance, it has velocity units assuming first order reaction ($n = 1$). Either k_w or γ require modeling for wall boundary conditions implementation in CFD.

$$\dot{\omega} = k_w \left(\rho c_i\right)^n \tag{2}$$

$$\rho D \left.\frac{\partial c_i}{\partial \eta}\right|_w = k_w \rho c_i \tag{3}$$

It is important to mention that k_w and γ are directly related by the expression in Eq 4 given by Goulard [5] for binary mixtures. He defines γ as the ratio of the number of atoms recombining on a surface per unit area and time to the total number of atoms striking the surface per unit area and time.

$$\gamma = k_w \sqrt{\frac{2\pi m}{k_B T_w}} \tag{4}$$

Many microscopic catalytic models can be found in literature. Most of them are based in different steps to describe wall processes. The relevance of each process depends on T_w and P and stablishes different levels of catalycity. Each step is represented in Figure 1

- Diffusion of atoms towards the wall.
- Chemical Adsorption: Atoms attach to the surface through a chemical bond. They are known as adatoms.
- Eley-Rideal Mechanism: A gas-phase atom reacts with an adatom. It takes place at low T_w when there are large numbers of adatoms spread over the surface. It is related to low catalycity.
- Langmuir-Hinshelwood Mechanism: At higher T_w, adatoms diffuse throughout the surface until they react with another adatom. Catalycity increases with T_w.
- Thermal Desorption: Adatoms leave the surface in the form of an atom at even higher T_w.
- Diffusion of molecules away from the wall.

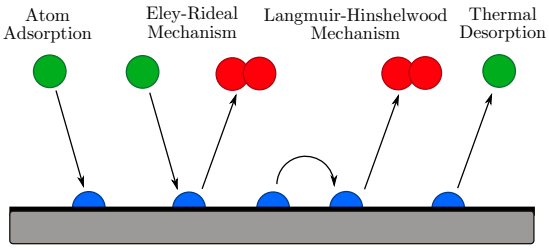

Figure 1: Processes in wall reaction.

It is worth to remark the work of Seward [13] who proposed a description for adsorption, E-R recombination and thermal desorption processes and balanced them at steady state. New parameters such as surface coverage θ and sticking coefficient S were introduced among others to model catalycity. They turned out to be extensively used in nowadays models. For instance, Nasuti [14] in 1996 and Barbato [15] in 2000 followed the same strategy but considering all four processes for each reaction. Moreover, they proposed to express $\dot{\omega}$ as an Arrhenius function where activation energies (E_a) had also to be defined. In addition, Armenise [16] extended the modeling by considering non-Boltzmann behavior on the vibrational distribution functions near the surface in 2006. It was not until 2010 that Di Benedetto and Bruno [17] proposed that a model simplification might be convenient for further experimental validation. However, the model they offer is still dependent on E_a databases and other coefficients difficult to extract from experiments in plasma facilities.

Furthermore, the effect of P can be seen in Thoemel's thesis [18]. He showed kinetic Monte Carlo computation results for a mixture of O and CO where the increase of P (and partial pressures) turned into a *Recombination Efficiency* reduction. It is worth to mention also his study of material roughness effect on catalycity determination [19]. Following the idea of Y. C. Kim [20], he considered atoms diffusion to account for the wet surface seen by the gas due to material roughness.

2.2. A macroscopic approach

The introduction of catalytic models as wall boundary condition in hypersonic CFD simulations requires their experimental validation under similar conditions.

However, the measurement of θ, S or E_a can be rather tedious in plasma facilities. While models described in Section 2.1 focus on reaction process description, it seems more convenient to look at boundary layer diffusion characteristics for model validation. This is a new macroscopic approach that wants to be studied using VKI-Plasmatron facility in order to update the current γ-model.

If only surface reactions took place in the boundary layer ($Da_g = 0$), species diffusion would be the direct consequence of these reactions. Extending the hypothesis to binary mixtures and first order reactions, k_w (and hence γ) could be directly identified by the evaluation of the diffusion velocity at the wall. Since the frozen boundary layer assumption is rather limiting, it is necessary to introduce the effect of volume reactions in the modeling. This is confirmed by Panerai [21] who measured different recombination efficiencies for different velocity gradients β under the same freestream conditions at the VKI-Plasmatron. Velocity gradient is modified with the size of the probe introduced into the plasma torch, which in turn defines the boundary layer thickness δ and qualitatively imposes the Da_g [22].

3. Testing for Catalytic Model Development

3.1. The VKI-Plasmatron Facility

Plasma facilities are used to reproduce the high temperature environment encountered during re-entry. Induced Coupled Plasma (ICP) wind tunnels are specially suitable for catalytic studies due to the gas purity they provide. The VKI-Plasmatron is a 1.2MW ICP facility able to use 2kV at 400kHZ to create the plasma and expand it into a 2.5m long and 1.4m diameter test chamber through a 160mm diameter torch. ICP computations, a non-equilibrium boundary layer solver (CERBOULA) and Optical Emission Spectroscopy (OES) assist the data post-processing and the freestream enthalpy (H_e) determination.

A copper calorimeter is normally used for heat flux measurements in the Plasmatron. Together with gas mass flow, static and dynamic pressures and plasma power, the non-equilibrium boundary layer solver is able to calculate H_e if an appropriate γ is introduced on the wall boundary condition. The Minimax method to estimate a reference copper *Recombination Efficiency* (γ_{ref}) is presented by Krassilchikoff [23] and a model dependent on P at $T_w = 350K$ is proposed by Panerai [21]. The H_e rebuilding procedure is normally done with a 50mm diameter probe (also called *Standard Probe*). However, results published by Panerai on CMC and Mullite samples suggest that different probe configurations, and hence different Da_g, could also modify the *Recombination Efficiency*. OES technique could also be used to obtain H_e. The emited light is collected with a 150 mm focal lenght converging lens (Thorlabs GmbH, Munich, Germany) and transmited to the Spectrometer (HR-4000 Ocean Optics, Dundedin, FL) through a 400 μm diameter optical fiber (Premium Fiber Ocean Optics, Dunedin, FL). An uncertainty of 15% is expected in both methodologies.

Static pressure conditions are measured with an absolute pressure transducer (Memberanovac DM 12, Leybold Vacuum, OC Oerlikon Corporation AG, Switzerland) with ±0.7 hPa accuracy. Dynamic pressure data is taken from the database of Marotta [24] developed with a variable reluctance pressure transducer (DP-15, Valydine Engineering Corp, Northridge, CA USA) of ±0.2% uncertainty. Due to torch instabilities, uncertainties increase to ±2% for both static and dynamic P.

3.2. Experimental Modeling

A new testing campaign is carried out at the VKI-Plasmatron in order to verify the effect of volume reactions on catalycity in both N_2 and Air mixtures. Heat fluxes have been measured using three identical copper calorimeters located at the center of the *VKI Damköhler Probes* [22]. They are three water cooled holders of different diameters that enhance or reduce volume recombination by changing the size of the boundary layer from one to another. They are shown in Figure 2. Thus, the *Equilibrium Probe* (115mm diameter and low β) presents a higher Da_g than the *Frozen Probe* (30mm diameter and high β) for the same freestream conditions. The *Standard Probe* (50mm diamter) is within the two and it is normally used as a reference to target the freestream conditions.

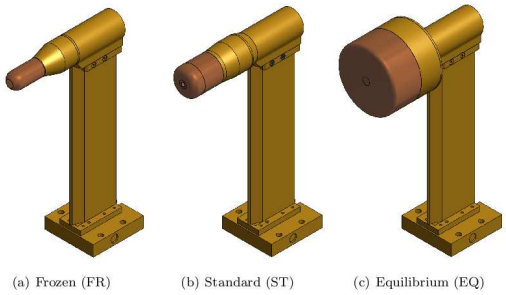

Figure 2: VKI Damköhler probes.

A simple scheme of the test configuration can be seen in Figure 3. First, Plasmatron is started up at 16 g/s and P is adjusted, target freestream conditions are stablished by injecting the *Stantard Probe* into the plasma torch. After reference heat flux measurement, the probe is ejected and replaced by the *Equilibrium Probe* without changing any freestream condition. The same is followed on the *Frozen Probe*. Acquisition frequency is 1 Hz. Nitrogen heat flux measurements at different pressures are summarized in Tables 1-3 for this testing campaign. They are plotted in Figure 4 for 15 mbar. Indeed, higher β makes boundary layer gradients steeper and it affects the heat flux. Same target conditions are applied on Air plasma (see Tables 4-6 in Appendix).

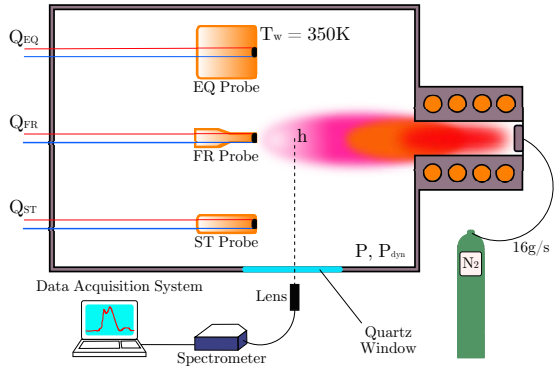

Figure 3: Test Scheme for Air and N_2.

Table 1: Heat flux measurements at 15 mbar on N_2.

Test	$\dot{Q}_w^{ref}$ kW m^{-2}	$\dot{Q}_w^{ST}$ kW m^{-2}	$\dot{Q}_w^{EQ}$ kW m^{-2}	$\dot{Q}_w^{FR}$ kW m^{-2}
1	300	301.8	149.7	448.2
2	500	512.7	154.4	724.3
3	700	717.1	268.5	979.1
4	900	913.3	339.3	1272.0
5	1100	1089.9	475.5	1572.5
6	1300	1306.8	556.9	1775.5
7	1500	1518.0	723.1	2076.5
8	1700	1727.3	821.8	2297.9
9	2000	2009.9	1133.8	2642.8

Testing the three probes under equal freestream conditions of enthalpy H_e and P assuming LTE, and having $T_w = 350K$ in all calorimeters, the effect of volume reactions is seen in Figure 5 for N_2 and in Figure 6 for Air at 15 mbar. Freestream enthalpy is determined with the two different methods described

Table 2: Heat flux measurements at 50 mbar on N_2.

Test	$\dot{Q}_w^{ref}$ kW m^{-2}	$\dot{Q}_w^{ST}$ kW m^{-2}	$\dot{Q}_w^{EQ}$ kW m^{-2}	$\dot{Q}_w^{FR}$ kW m^{-2}
10	300	306.0	109.8	511.9
11	500	504.9	212.1	944.9
12	700	705.3	304.6	1010.6
13	900	917.1	426.3	1315.7
14	1100	1112.9	545.4	1617.3
15	1300	1309.7	645.2	1814.1
16	1500	1522.9	763.8	2135.9
17	1700	1713.5	832.9	2528.3
18	2000	2003.9	1154.3	2892.2

Table 3: Heat flux measurements at 100 mbar on N_2.

Test	$\dot{Q}_w^{ref}$ kW m^{-2}	$\dot{Q}_w^{ST}$ kW m^{-2}	$\dot{Q}_w^{EQ}$ kW m^{-2}	$\dot{Q}_w^{FR}$ kW m^{-2}
19	300	316.1	110.8	529.8
20	500	526.6	160.7	733.9
21	700	720.2	380.0	980.7
22	900	910.5	616.1	1280.1
23	1100	1113.8	859.6	1538.5
24	1300	1314.5	906.0	1831.1
25	1500	1505.3	1108.3	2187.2
26	1700	1728.0	1202.7	2339.9
27	2000	1906.9	1307.1	2704.4

above, one for each gas mixture. H_e is estimated by means of the γ_{ref}-model in N_2 and through Optical Emission Spectroscopy (OES) in Air. The *Recombination Efficiency* is obtained using the non-equilibrium boundary layer solver in both mixtures. This software is able to iteratively compute H_e for every possible value of γ. This relation is know as S-curve (Figure 7) and is given for each heat flux and probe configuration. The common edge enthalpy on all the probes leads to its corresponding catalycity. The results show that a half order of magnitude difference in γ is possible between the probes under Air and it reaches one order of magnitude under N_2. In addition, it turns out that catalycity also increases with the freestream enthalpy.

An update of the current γ-model is required. The strategy to follow is the addition of new inherent-to-the-flow variables such as the the freestream enthalpy H_e and the Da_g to account boundary layer volume reactions. Despite the Da_g can neither be simply computed nor measured, an equivalent paramater that

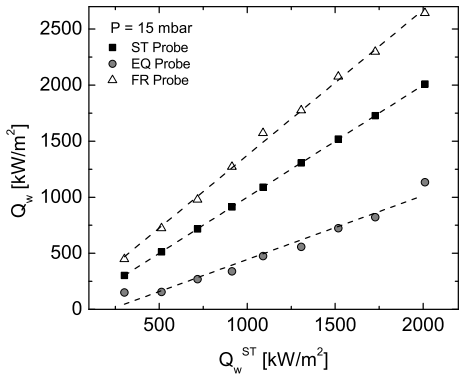

Figure 4: Heat Flux measurements results at 15 mbar.

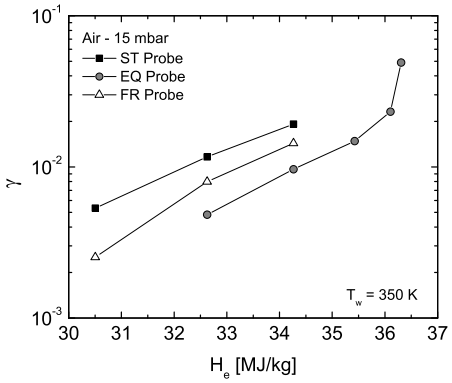

Figure 6: Enthalpy and Catalycity results on Air at 15mbar.

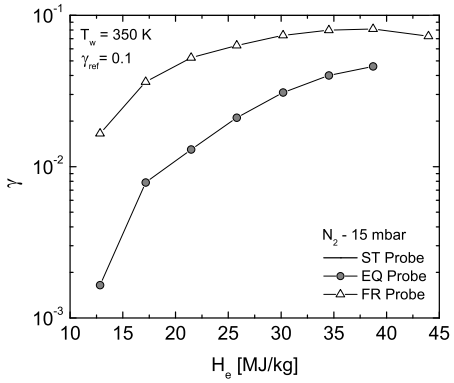

Figure 5: Enthalpy and Catalycity results on N_2 at 15mbar.

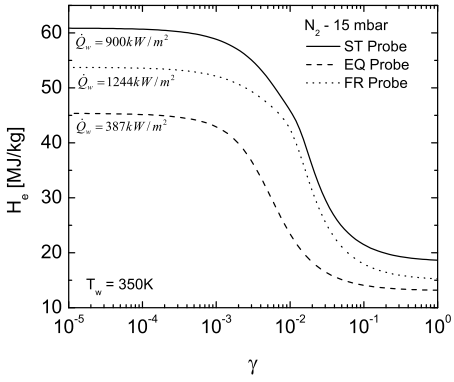

Figure 7: Enthalpy and Catalycity relation for *Damköhler Probes* on N_2 at 15mbar. This case corresponds to $H_e = 25MJ/kg$ condition seen in Figure 5. Heat fluxes are extrapolated from Figure 4.

could be used is β. Then, the new catalytic model here proposed should be of the form: $\gamma = f(T_w, P, H_e, \beta)$.

4. Conclusion

The effect of chemical reactions on the overall heat flux computation has been reviewed. Diffusion of species within the chemical boundary layer is a direct consequence of both volume and surface reactions. The boudary layer characterization in terms of both Da_g and Da_w has been presented. Different but equivalent ways to quantify surface reactions have been discussed. The Da_w being appropriate to characterize the boundary layer in terms of Non-Catalytic and Full-Catalytic regimes, the reaction rate constant k_w and the *Recombination Efficiency* γ seem more suitable for Finite-Rate-Catalytic modeling.

A brief literature research reveals that most authors assume different microscopic processes to describe one single surface reactions. These models introduce parameters whose validation in plasma facility turns to be rather laborious. A new macroscopic model is proposed for the VKI-Plasmatron facility. The purpose is to offer a γ-model based on typical fluid variables that could be measured or computed from testing campaigns.

The current model used at VKI is only intended to rebuild the freestream enthalpy of the plasma, serving as wall boundary condition in the non-equilibrium boundary layer solver. However, recent experiments on Air and N_2 mixtures reveal that this model only based on T_w and P could be too simplistic. The fact that *Recombination Efficiency* could change with both H_e and Da_g (or β) requires the introduction of these parameters as new independent variables. Therefore, the new model proposed is of the form: $\gamma =$

$f(T_w, P, H_e, \beta)$.

Despite a new set of variables is defined, a quantitative value of γ cannot be easily given for an appropriate model validation. There are still many questions to be adressed at the VKI-Plasmatron:

- H_e determination: Two methods has been used in the testing campaign and both present their own epistemic uncertainties. The γ_{ref} method assumes a catalytic model on copper that does not include the effect of either Da_g or H_e. This means that the enthalpy retrieved from the non-equilibrium boundary layer solver CERBOULA might not be fully correct. Regarding OES, plasma torch fluctuations are likely to introduce an overestimation depending on the amplitude of this fluctuation. In some cases, a 500 K oscillation could lead to an error of 30% on the measurement [25].

- Coupling Experiments-ICP Simulations: ICP simulations are required to account for the plasma power, dynamic pressure and probe configuration in the non-equilibrium boundary layer solver. These effects are resumed in the so-called NDP's (Non Dimensional Paramenters [21]). Their determination from Navier-Stokes solution to be introduced in CERBOULA is still an important source of uncertainty.

- Assumption of the same γ for all surface reactions. Atom recombination in Air mixtures is described only by the type $2X \rightarrow X_2$ if NO formation is neglected. CERBOULA assumes the same catalycity for both O and N recombination. This could be a too simplistic assumption and more studies on that direction must be done.

References

[1] L. Lees, Laminar Heat Transfer Over Blunt-Nosed Bodies at Hypersonic Flight Speeds, Jet Propulsion 26, Num. 4 (1956) 259–269.

[2] J. A. Fay, F. R. Riddell, Theory of Stagnation Point Heat Transfer in Dissociated Air, Journal of the Aeronautical Sciences 25, Num. 2 (1958) 73–85.

[3] A. F. Kolesnikov, The Concept of Local Simulation for Stagnation Point Heat Transfer in Hypersonic Flows: Application and Validation, AIAA Paper 2000-2515.

[4] P. F. Barbante, O. Chazot, Flight Extrapolation of Plasma Wind Tunnel Stagnation Region Flowfield, Journal of Thermophysics and Heat Transfer 20, Num. 3 (2006) 493–499.

[5] R. Goulard, On Catalytic Recombination Rates in Hypersonic Stagnation Heat Transfer, Jet Propulsion 28, Num. 11 (1958) 737–745.

[6] D. E. Rosner, Scale Effects and Correlations in Nonequilibrium Convective Heat Transfer, AIAA Journal 1, Num. 7 (July 1963) 1550–1555.

[7] J. M. M. Barbato, D. Giordano, C. Bruno, Comparison of Catalytic Wall Conditions for Hypersonic Flow, Journal of Spacecrafts and Rockets 33, Num. 5 (September-October 1996) 620–627.

[8] P. W. Atkins, Physical Chemistry, Oxford University Press, 1994.

[9] P. M. Chung, Chemically Reacting Non-Equilibrium Boundary Layers, Advances in Heat Transfer, 1965.

[10] J. D. Ramshaw, Self-Consistent Binary Diffusion in Multicomponent Gas Mixture, J. Non-Equilib. Thermodyn. 15 (1990) 295–300.

[11] P. F. Barbante, Accurate and Efficient Modelling of High Temperature Nonequilibrium Air Flows, Ph.D. thesis, von Karman Institute for Fluid Dynamics / Université Libre de Bruxelles (2001).

[12] C. D. Scott, Wall Catalytic Recombination and Boundary Conditions in Non-Equilibrium Hypersonic Flows, Second Joint Europe/US Short Course in Hypersonics.

[13] W. A. Seward and E. J. Jumper, Model for Oxygen Recombination on Silicon-Dioxide Surfaces, Journal of Thermophysics 5, Num. 3 (July-September 1991) 284–291.

[14] M. B. F. Nasuti, C. Bruno, Material-Dependent Catalytic Recombination Modeling for Hypersonic Flows, Journal of Thermophysics and Heat Transfer 10, Num. 1 (January-March 1996) 131–136.

[15] C. B. M. Barbato, S. Reggiani, J. Muylaert, Model for Heterogeneous Catalysis on Metal Surfaces with Applications to Hypersonic Flows, Journal of Thermophysics and Heat Transfer 14, Num. 3 (July-September 2000) 412–420.

[16] M. C. I. Armenise, M. Barbato, E. Kustova, State-to-State Catalytic Models, Kinetics, and Transport in Hypersonic Boundary Layers, Journal of Thermophysics and Heat Transfer 20, Num. 3 (2006) 465–476.

[17] S. D. Benedetto, C. Bruno, Novel Semi-Empirical Model for Finite Rate Catalysis with Application to PM1000 Material, Journal of Thermophysics and Heat Transfer 24, Num. 1 (January-March 2010) 50–59.

[18] J. Thoemel, Surface Catalysis in High Enthalpy Flows, Ph.D. thesis, von Karman Institute for Fluid Dynamics / Rheinisch-Westfälische Technische Hochschule Aachen (2012).

[19] O. C. J. Thoemel, P. Barbante, Aspects of Advanced Catalysis Modeling for Hypersonic Flows, Center for Turbulence Research Proceedings of the Summer Program 2008.

[20] Y. C. Kim, M. Boudart, Recombination of O, N, and H Atoms on Silica: Kinetics and Mechanisms, Langmuir - American Chemical Society 7 (1991) 2999–3005.

[21] F. Panerai, Aerothermochemistry Characterization of Thermal Protection Systems, Ph.D. thesis, von Karman Institute for Fluid Dynamics / Università Degli Studi Di Perugia (2012).

[22] S. Herpin, Chemical Aspects of Hypersonic Stagnation Point Heat Transfer, VKI Project Report VKI Project Report 2005-10.

[23] H. W. Krassilchikoff, Procedure for the Determination of the Cold Copper Catalycity, VKI Project Report VKI Project Report 2006-18.

[24] Marotta, Investigation on the Driving Phenomena Characterization GSI in Plasmatron Facility, VKI Project Report VKI Project Report 2011-17.

[25] J. P. S. Pinto, O. Chazot, Spectroscopy in Subsonic ICP Facility, To be published.

Appendix

Heat flux measurements on Air are resumed in the following Tables 4-6.

Table 4: Heat flux measurements at 15 mbar on Air.

Test	$\dot{Q}_w^{ref}$ kW m^{-2}	$\dot{Q}_w^{ST}$ kW m^{-2}	$\dot{Q}_w^{EQ}$ kW m^{-2}	$\dot{Q}_w^{FR}$ kW m^{-2}
1	300	302.2	132.3	321.7
2	500	505.9	184.0	492.3
3	700	704.5	337.1	734.2
4	900	898.9	484.0	971.2
5	1100	1109.9	619.5	1189.5
6	1300	1298.0	777.4	1379.6
7	1500	1499.2	920.9	1570.3
8	1700	1720.5	1121.4	1822.0
9	2000	2059.7	1381.9	2098.1

Table 5: Heat flux measurements at 50 mbar on Air.

Test	$\dot{Q}_w^{ref}$ kW m^{-2}	$\dot{Q}_w^{ST}$ kW m^{-2}	$\dot{Q}_w^{EQ}$ kW m^{-2}	$\dot{Q}_w^{FR}$ kW m^{-2}
10	1300	1338.5	821.1	1492.2
11	1500	1518.7	987.4	1726.4
12	1700	1740.0	1136.9	1900.6
13	2000	2018.9	1389.7	2315.1

Table 6: Heat flux measurements at 100 mbar on Air.

Test	$\dot{Q}_w^{ref}$ kW m^{-2}	$\dot{Q}_w^{ST}$ kW m^{-2}	$\dot{Q}_w^{EQ}$ kW m^{-2}	$\dot{Q}_w^{FR}$ kW m^{-2}
14	300	276.6	122.4	367.8
15	500	524.2	262.3	642.6
16	700	703.4	415.0	1184.0
17	900	926.5	577.2	124.2
18	1300	1309.4	743.5	1797.2
19	1500	1536.5	822.4	1849.9
20	1700	1713.1	977.2	2083.0
21	2000	2001.4	1187.7	2412.6

WHO’S WHO

Who's who



Alejandro
Alvarez Laguna



Francesco
Baldani



Filip
Ballien



Aurélie Bellemans



Christopher
Chahine



Julien
Clinckemaille



Nicolas
De Cock



Giulia
Dell'Era



Lamberto
Dell'elce



Fabrizio
Fontaneto



Clara
García Sánchez



Jesus
Garicano Mena



Sara
Gonzalez Ruiz



Gabriele
Grasso



Koen
Groot



Guillaume
Grossir



Daniel
Guariglia



Mohamed Hassanine
Aissa



Bernd
Helber



Imre
Horváth



Bart
Janssens



Ugur
Karban



Miguel Alonso
Mendez



Jorge
Pinho



Işil
Şakraker



Jérôme
Sans



Sebastian
Scholl



Pierre-Louis
Schrooyen



James B.
Scoggins



Gennaro
Serino



Alessia
Simonini



Chiara
Spaccapaniccia



Erik
Torres



Roberto
Tomasssini



Stefano
Vagnoli



Bart
Van Hove



Alan
Viladegut



Martin
Vymazal

PhD candidates who have not presented a paper at the symposium



Jayson
Babajee



Gilles
Bailet



Georgios
Bellas Chatzigeorgios



Khalil
Bensassi



Henny
Bottini



Stefano
D'Angelo



Leandro
Dantas De Santana



Cis
De Maesschalck



Jorge
Fernandes Lopes de Sousa



Victor
Fernández Villace



Michaël
Joly



Damien
Le Quang



Silvania
Lopes



Marcos
Lema Rodriguez



Alessandro
Munafo



Mehmet
Mersinligil



Lasse
Müller



Fatma
Ceyhun Şahin



Nikolaos
Stergiannis



Orkun
Temel



Peter
Tóth



Laura
Villafañe